CHIRAL ORGANIC CHROMOPHORIC SYSTEMS IN THE ENHANCEMENT OF CIRCULARLY POLARIZED LUMINESCENCE

EDITED BY: Tao Wu, You-Xuan Zheng, Giovanna Longhi and Ga-Lai Law

PUBLISHED IN: Frontiers in Chemistry

frontiers Research Topics

ISSN 1664-8714
ISBN 978-2-88966-708-6
DOI 10.3389/978-2-88966-708-6

About Frontiers

Frontiers is more than just an open-access publisher of scholarly articles: it is a pioneering approach to the world of academia, radically improving the way scholarly research is managed. The grand vision of Frontiers is a world where all people have an equal opportunity to seek, share and generate knowledge. Frontiers provides immediate and permanent online open access to all its publications, but this alone is not enough to realize our grand goals.

Frontiers Journal Series

The Frontiers Journal Series is a multi-tier and interdisciplinary set of open-access, online journals, promising a paradigm shift from the current review, selection and dissemination processes in academic publishing. All Frontiers journals are driven by researchers for researchers; therefore, they constitute a service to the scholarly community. At the same time, the Frontiers Journal Series operates on a revolutionary invention, the tiered publishing system, initially addressing specific communities of scholars, and gradually climbing up to broader public understanding, thus serving the interests of the lay society, too.

Dedication to Quality

Each Frontiers article is a landmark of the highest quality, thanks to genuinely collaborative interactions between authors and review editors, who include some of the world's best academicians. Research must be certified by peers before entering a stream of knowledge that may eventually reach the public - and shape society; therefore, Frontiers only applies the most rigorous and unbiased reviews.
Frontiers revolutionizes research publishing by freely delivering the most outstanding research, evaluated with no bias from both the academic and social point of view. By applying the most advanced information technologies, Frontiers is catapulting scholarly publishing into a new generation.

What are Frontiers Research Topics?

Frontiers Research Topics are very popular trademarks of the Frontiers Journals Series: they are collections of at least ten articles, all centered on a particular subject. With their unique mix of varied contributions from Original Research to Review Articles, Frontiers Research Topics unify the most influential researchers, the latest key findings and historical advances in a hot research area! Find out more on how to host your own Frontiers Research Topic or contribute to one as an author by contacting the Frontiers Editorial Office: frontiersin.org/about/contact

CHIRAL ORGANIC CHROMOPHORIC SYSTEMS IN THE ENHANCEMENT OF CIRCULARLY POLARIZED LUMINESCENCE

Topic Editors:
Tao Wu, Academy of Sciences of the Czech Republic (ASCR), Czechia
You-Xuan Zheng, Nanjing University, China
Giovanna Longhi, University of Brescia, Italy
Ga-Lai Law, Hong Kong Polytechnic University, Hong Kong

Citation: Wu, T., Zheng, Y.-X., Longhi, G., Law, G.-L., eds. (2021). Chiral Organic Chromophoric Systems in the Enhancement of Circularly Polarized Luminescence. Lausanne: Frontiers Media SA. doi: 10.3389/978-2-88966-708-6

Table of Contents

frontiers in Chemistry

ORIGINAL RESEARCH
published: 09 April 2020
doi: 10.3389/fchem.2020.00237

Chiral Diketopyrrolopyrrole-Helicene Polymer With Efficient Red Circularly Polarized Luminescence

Kais Dhbaibi[1,2], Chengshuo Shen[1,3], Marion Jean[4], Nicolas Vanthuyne[4], Thierry Roisnel[1], Marcin Górecki[5,6], Bassem Jamoussi[7], Ludovic Favereau[1] and Jeanne Crassous[1]**

[1] Univ Rennes, CNRS, Institut des Sciences Chimiques de Rennes, ISCR-UMR 6226, Rennes, France, [2] Faculty of Science of Gabès, University of Gabès, Gabes, Tunisia, [3] State Key Lab of Metal Matrix Composites, School of Chemistry and Chemical Engineering, Shanghai Jiao Tong University, Shanghai, China, [4] Aix Marseille University, CNRS, Centrale Marseille, iSm2, Marseille, France, [5] Dipartimento di Chimica e Chimica Industriale, University of Pisa, Pisa, Italy, [6] Institute of Organic Chemistry, Polish Academy of Sciences, Warsaw, Poland, [7] Department of Environmental Sciences, Faculty of Meteorology, Environment and Arid Land Agriculture, King Abdulaziz University, Jeddah, Saudi Arabia

Chiral diketopyrrolopyrrole (DPP)-helicene polymers were synthesized to develop efficient red circularly polarized (CP) light emitters. These original chiral dyes display intense electronic circular dichroism (ECD) and CP luminescence (CPL) in the far-red spectral region owing to the presence of excitonic coupling between achiral DPPs within the chiral environment of the polymeric structure. This work affords an interesting example illustrating the potential of π-conjugated helical polymers for chiral optoelectronic applications.

Keywords: helicene, diketopyrrolopyrrole, circularly polarized luminescence, red emitters, exciton coupling, chiral polymers

OPEN ACCESS

Edited by:
Giovanna Longhi,
University of Brescia, Italy

Reviewed by:
Tsuyoshi Kawai,
Nara Institute of Science and Technology (NAIST), Japan
Juan Manuel Cuerva,
University of Granada, Spain

***Correspondence:**
Ludovic Favereau
ludovic.favereau@univ-rennes1.fr
Jeanne Crassous
jeanne.crassous@univ-rennes1.fr

Specialty section:
This article was submitted to Physical Chemistry and Chemical Physics, a section of the journal Frontiers in Chemistry

Received: *26 January 2020*
Accepted: *12 March 2020*
Published: *09 April 2020*

Citation:
Dhbaibi K, Shen C, Jean M, Vanthuyne N, Roisnel T, Górecki M, Jamoussi B, Favereau L and Crassous J (2020) Chiral Diketopyrrolopyrrole-Helicene Polymer With Efficient Red Circularly Polarized Luminescence. Front. Chem. 8:237. doi: 10.3389/fchem.2020.00237

INTRODUCTION

Circularly polarized (CP) light has received renewed attention owing to its superior potential over unpolarized one in a diverse range of domains such as (chir)optoelectronics (stereoscopic displays, organic light-emitting diodes (OLEDs), optical information processing, etc.) as well as in bio-imaging and chiral sensing (Riehl and Richardson, 1986; Berova et al., 2000, 2012; Carr et al., 2012; Maeda and Bando, 2013; de Bettencourt-Dias, 2014; Kumar et al., 2015a; Zinna and Di Bari, 2015, 2018; Zinna et al., 2015, 2017; Brandt et al., 2016; Longhi et al., 2016; Li et al., 2017; Han et al., 2018; Tanaka et al., 2018). Until recently, luminescent chiral lanthanides complexes have been the most studied molecular CPL emitters since this family of compounds can display relatively high level of circularly polarized emission, characterized by a luminescence dissymmetry factor $g_{lum} = 2(I_L\text{-}I_R)/(I_L+I_R)$, of more than 1 (Carr et al., 2012; Zinna et al., 2015; Zinna and Di Bari, 2018). However, lanthanide complexes often possess low luminescent quantum yield (ϕ) and stability issues, which may difficultly render their integration in optoelectronic devices such as CP-OLEDs, chiral photovoltaics and transistors for example. To circumvent these aspects, the development of chiral emitting small organic molecules (SOM) has gained increasing interest, also benefiting from their tunable photophysical and chiroptical properties from the blue to the near-infrared spectral region (Li et al., 2017; Han et al., 2018). One particularly appealing synthetic strategy to design efficient CPL emitters has consisted in developing chirally perturbed π-extended achiral chromophores, mostly based on C_2-symmetric chiral moieties (chiral binaphthyl or 1,2-diamino-cyclohexane derivatives) linked to bodipy or perylene organic dyes (Tsumatori et al., 2010; Langhals et al., 2011; Kumar et al., 2013, 2014, 2015b; Sánchez-Carnerero et al., 2014; Sheng et al., 2016). In

addition, helicenes have recently shown to be very good scaffolds for the development of emissive materials with strong CPL activity (Gingras, 2013; Chen and Shen, 2016; Dhbaibi et al., 2018, 2020; Zhao et al., 2019; Shen et al., 2020). Following this approach, we recently reported helical π-conjugated helicene-diketopyrrolopyrrole (DPP) dyes [*P*-**H6(DPP)$_2$** and (*P*,*P*)-**DPP(H6DPP)$_2$**, **Figure 1**] (Dhbaibi et al., 2018) as red CPL emitters, (Shen et al., 2014; Saleh et al., 2015; Pascal et al., 2016; Sakai et al., 2016; Biet et al., 2017; Nishimura et al., 2017) arising from an intramolecular exciton coupling (Berova et al., 2012) between the achiral DPP units placed within the chiral environment of the helicene. Based on purely π-π* transitions, this design afforded promising g_{lum} factors of 6–9 × 10^{-4} at 610–650 nm associated with fluorescence quantum yields (ϕ) of 35–40%. To our knowledge, this study remains the only example of DPP based CPL emitters, despite the promising potential of diketopyrrolopyrrole and its derivatives in a broad range of applications such as OLEDs, photovoltaic devices, organic transistors, and fluorescent probes (Nielsen et al., 2013; Grzybowski and Gryko, 2015; Heyer et al., 2015; Kaur and Choi, 2015; Data et al., 2016).

With the aim of deeper exploring this innovative and promising synergy between chiral helicene and achiral diketopyrrolopyrrole dye, we report here the synthesis and chiroptical properties of novel π-conjugated helical polymeric CPL emitters, namely *rac*-, (*P*)- and (*M*)-**(H6DPP)$_n$**, **Figure 1**. These new examples display intense electronic circular dichroism (ECD) in the visible region and strong red CPL with g_{lum} = 1.4 × 10^{-3} at 660 nm, associated with a high ϕ of ∼35 %. This first example of chiral helicene-DPP based polymer exhibits higher CPL response than the molecular chiral helicene-DPP dyes previously reported, and brings interesting aspects for the design of efficient polymeric red and near infra-red CPL emitters.

RESULTS AND DISCUSSION

Synthesis of Polymer (H6DPP)$_n$

The helicene-DPP polymers were prepared using the Sonogashira coupling between a helicene decorated with two alkynyl functions and a DPP core substituted with two bromothiophene units. In a first attempt to synthesize polymer **(H6DPP)$_n$**, the

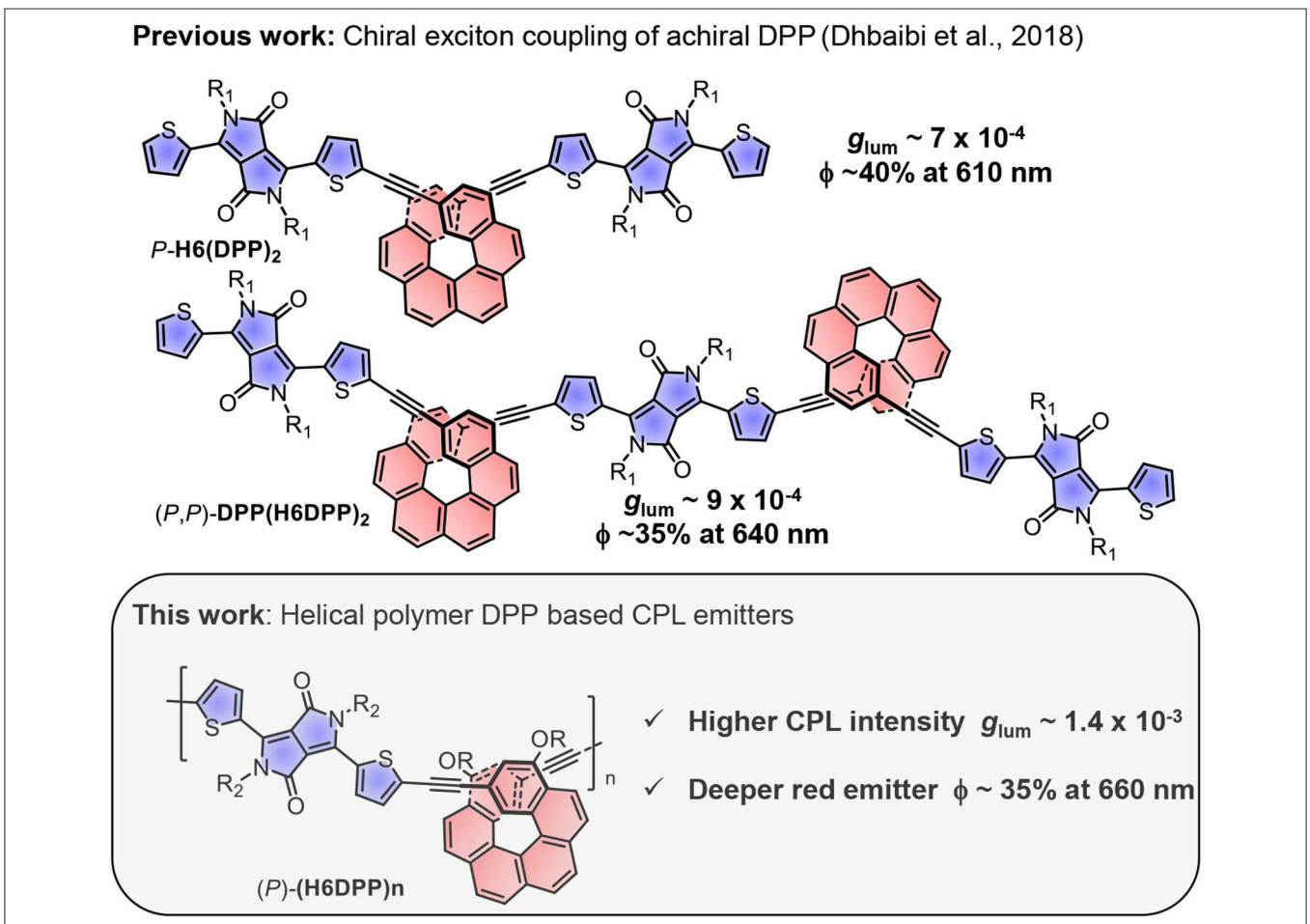

FIGURE 1 | Chemical structures of CPL emitters based on helicene-diketopyrrolopyrrole polymers and their corresponding polarized and unpolarized luminescence characteristics (*P* enantiomers are shown).

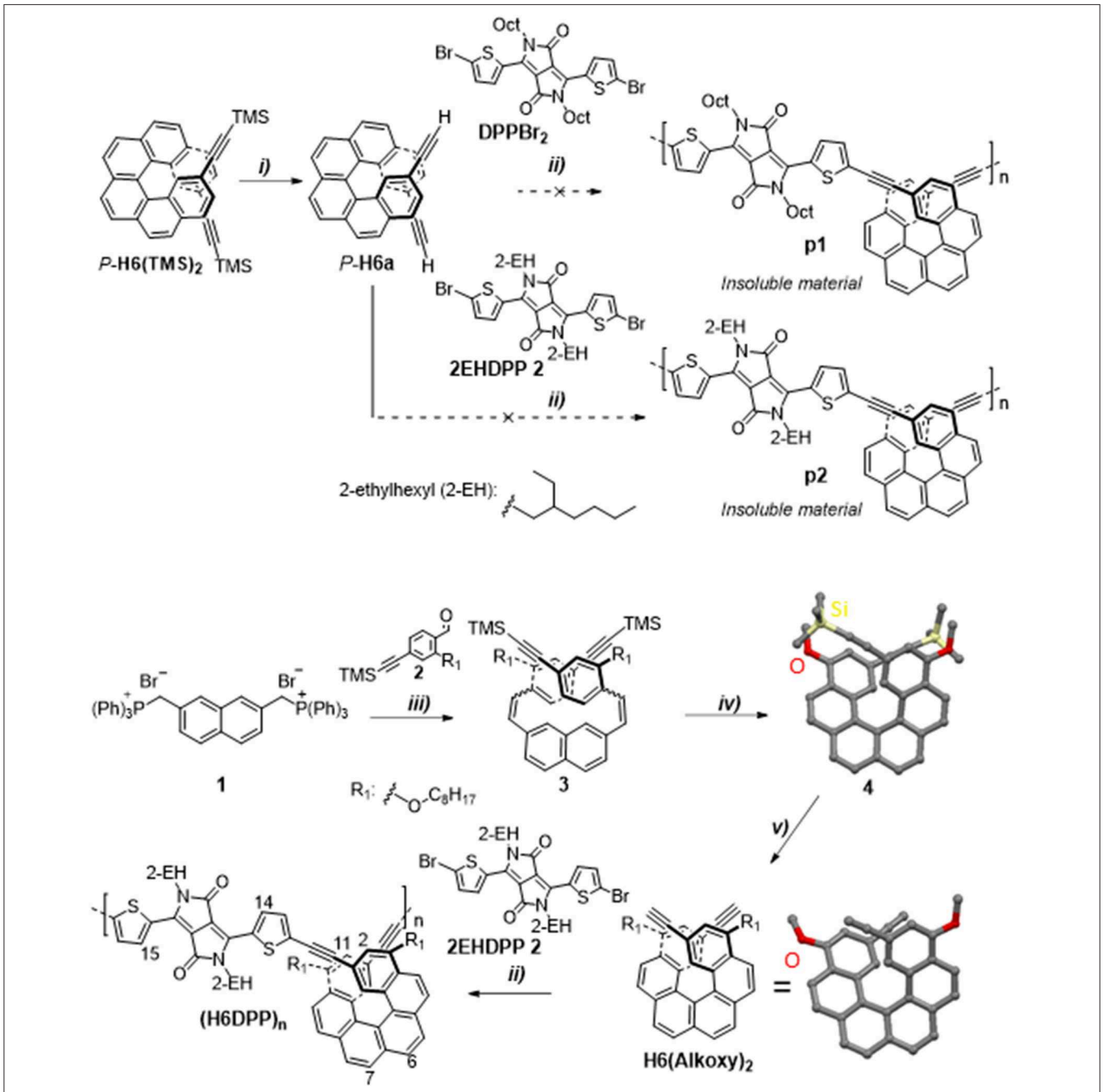

FIGURE 2 | Synthesis of enantiopure *P*-**(H6DPP)**$_n$. TMS: trimethylsilyl. Reaction conditions: (i) TBAF, $CHCl_3$; (ii) $Pd(PPh_3)_4$, CuI, Et_3N/toluene, 50°C; (iii) *n*-BuLi, THF,−78°C to rt, 60%; (iv) hν, I_2 (1 equiv.), propylene oxide (50 equiv.), toluene, 50%; (v) TBAF, $CHCl_3$, 52%, chiral HPLC. X-ray crystal structures of *rac*-**4** and *rac*-**H6(Alkoxy)$_2$** (octyl chains and hydrogen atoms have been omitted for clarity).

coupling was performed using enantiopure *P*- and *M*-2,15-bis-(ethynyl)[6]helicene (*P*- and *M*-**H6a**) (Anger et al., 2012) with 3,6-bis(5-bromothiophen-2-yl)-2,5-diketopyrrolopyrrole, **DPPBr$_2$**, respectively (**Figure 2**, where only *P* enantiomer is described) (Wu et al., 2015). While the reactions seemed to proceed efficiently, they resulted in the formation of insoluble dark blue material (**p1**, **Figure 2**). To circumvent this solubility issue, we introduced widely used branched 2-ethylhexyl (2-EH) chains on the DPP unit in place of the linear octyl ones (Huo et al., 2009; Palai et al., 2010). Although this fragment has a chiral center, we used its racemic form since a weak influence of these additional stereogenic centers is expected on the photophysical and chiroptical properties of the final polymer in diluted solution. Unfortunately, this new approach also afforded insoluble blue solid when a stoichiometric mixture of *P*-**H6a** and **2EHDPP 2** was subjected to the Sonogashira

coupling conditions (**p2**, **Figure 2**). To further increase the solubility of the obtained polymer material, the helicenic fragment was also functionalized with additional linear octyloxy chains through a new synthetic pathway involving 2-(octyloxy)-4-((trimethylsilyl)ethynyl)benzaldehyde, **2**, as starting material for the synthesis of the helicene fragment. Indeed, the latter was engaged in a double Wittig reaction with naphthyl-2,7-dimethylphosphonium bromide salt, **1**, to give 2,7-bis(2-(octyloxy)-4-((trimethylsilyl)ethynyl)styryl)naphthalene, **3**, in 60% yield. The resulting *cis*/*trans* stilbene mixture was subsequently submitted to a photocyclisation reaction with propylene oxide as an acid scavenger to afford *rac*-2,15-bis-((trimethylsilyl)ethynyl)-4,13-bis-(octyloxy)[6]helicene (**4**) in 50% yield, followed by deprotection reaction of the two remaining TMS groups to yield **H6(Alkoxy)$_2$** (**Scheme 1**). Fully characterized by NMR spectroscopy and mass spectrometry (see **Supplementary Information**), the structures of the two latters were further ascertained by X-ray crystallographic analysis (see **Scheme 1** and **Supplementary Information**). Both *rac*-**4** and *rac*- **H6(Alkoxy)$_2$** crystallized in a *P*-1 space group and displayed helicity (dihedral angle between the two terminal rings) of 41.1° and 54.4°, respectively, which is in the range of classical carbo[6]helicenes (Gingras, 2013; Chen and Shen, 2016; Dhbaibi et al., 2019). Moreover, the lateral octyloxy chains point toward the outside of the molecules, which may disfavor the formation of polymer aggregates in solution.

Rac-**H6(Alkoxy)$_2$** was then submitted to chiral HPLC separation to give *P*-(+) and *M*-(–) in 99 and 98.5% of *ee*, respectively (see **Supplementary Information** for detailed experimental conditions). These enantiomers, as well as the racemic compound, were finally engaged in the polymerization reaction with **2EHDPP 2** and gave expected soluble polymers which were firstly filtered over a silica plug, then further purified by size-exclusion chromatography (SEC, $CHCl_3$) before precipitated using $CHCl_3$/MeOH solvent mixture to yield *P*-, *M*-, and *rac*-**(H6DPP)$_n$** in ∼45% yield for each polymer (see **Supplementary Information**). These novel chiral dyes are soluble in common organic solvents such as THF, $CHCl_3$, and CH_2Cl_2, and were characterized by ^{1}H NMR and SEC using a polystyrene standard in THF. The obtained NMR spectrum displays characteristic signals for both helicene and DPP starting materials: for instance, shielded $H^{2,11}$ and deshielded $H^{6,7}$ helicenic protons at 6.75 and 8.50 ppm respectively, and deshielded DPP protons $H^{14,15}$ at 9.10 ppm (see **Supplementary Information**). The number average molecular mass (M_n) for *rac*-, *P*-, and *M*-**(H6DPP)$_n$** were estimated to be 6.9×10^3, 5.3×10^3, and 6.4×10^3, respectively, which correspond to a low degree of polymerization, *ca.* 5-6 (helicene-DPP) units (see **Supplementary Information**). The thermal stability of *rac*-**(H6DPP)$_n$** was also evaluated by thermogravimetric analysis (TGA) and resulted in an onset decomposition temperature at 300°C with a 10% weight loss.

UV-Vis, ECD, and Electrochemical Characterizations

The ground state photophysical and chiroptical properties of DPP-helicene polymers were investigated in CH_2Cl_2 solutions and compared with corresponding precursors and previously reported **DPP(H6DPP)$_2$**. UV-Vis spectrum of **(H6DPP)$_n$** polymer displays two main absorption signatures between 300 and 425 nm and between 530 and 675 nm that correspond to a combination of helicene and DPP transitions for the higher energy region and only from DPP transitions for the low energy part. The latter absorption region is red-shifted by 70 nm in comparison with DPP precursor, characterized by $\varepsilon = 7.0 \times 10^4$ M^{-1} cm^{-1} at 565 nm and 35×10^4 M^{-1} cm^{-1} at 635 nm for **2EHDPP 2** and **(H6DPP)$_n$**, respectively, resulting from the extension of the π-conjugation via the alkynyl bridges between the DPP dye and the helicene units. These observations are supported by comparison with **DPP(H6DPP)$_2$** UV-vis spectrum, where contributions of both "DPP-helicene" and "helicene-DPP-helicene" fragments are superimposed in the red region (see **Supplementary Information** for additional details). Going from oligomer **DPP(H6DPP)$_2$** to polymer **(H6DPP)$_n$** does not strongly red-shift the overall absorption signature (λ_{max} = 620 and 635 nm for **DPP(H6DPP)$_2$** and **(H6DPP)$_n$** lowest absorption bands, respectively), which suggests that electronic communication between each bis(ethynyl)DPP unit through the π-conjugated helicene is relatively limited along the polymer. The observed difference of 15 nm results probably from the presence of the electron donating octyloxy groups on the helicene fragment for **(H6DPP)$_n$**.

ECD of *P*- and *M*-**(H6DPP)$_n$** displays expected mirror-image spectra with intense responses ranging from 280 to 700 nm (**Figure 3**). *P*-**(H6DPP)$_n$** exhibits an intense negative ECD band ($\Delta\varepsilon = -576$ M^{-1} cm^{-1}) at 309 nm which is 19 nm red-shifted compared to helicene *P*-**H6(Alkoxy)$_2$**, a broad strong positive band between 347 and 500 nm with a maximum at 391 nm ($\Delta\varepsilon = +940$ M^{-1} cm^{-1}) and a shoulder at 414 nm ($\Delta\varepsilon = +740$ M^{-1} cm^{-1}), a negative contribution at 565 nm ($\Delta\varepsilon = -88$ M^{-1} cm^{-1}) followed by a positive one with a maximum at 640 nm ($\Delta\varepsilon = +481$ M^{-1} cm^{-1}). This lowest bisignate DPP-centered signal is clearly reminiscent of what we observed for *(P,P)*-**DPP(H6DPP)$_2$** (**Figure 4**), which was attributed to a chiral excitonic coupling between the DPP-centered π-orbitals in the helical arrangement (Bouvier et al., 2018; Dhbaibi et al., 2018, 2020). Elongating the number of helicene-DPP association within polymer *P*-**(H6DPP)$_n$** appears as an efficient strategy to obtain very intense ECD signature across the whole spectrum and especially in the red region thanks to the increase of the excitonic coupling intensity. Indeed, this higher sensitivity to red circularly polarized light for *P*-**(H6DPP)$_n$** is confirmed by the evaluation of the associated dissymmetry factor $g_{abs} = \Delta\varepsilon/\varepsilon = +1.8 \times 10^{-3}$ at 649 nm, i.e., a 40 % increase in comparison with (*P,P*)-**DPP(H6DPP)$_2$** ($g_{abs} = +1.3 \times 10^{-3}$ at 610 nm).

The electrochemical behavior of **(H6DPP)$_n$** was investigated by cyclic voltammetry (CV, **Figure S17** and **Table S1**), which displays pseudo-reversible oxidation process at ca. +0.81 V and a reversible reduction one at −1.24 V vs. SCE, respectively assigned to the oxidation and the reduction of the DPP unit(s). The calculated HOMO and LUMO energy level were −5.21 eV and a LUMO level of −3.16 eV, respectively, leading to an estimated electrochemical band gap of 2.05 eV.

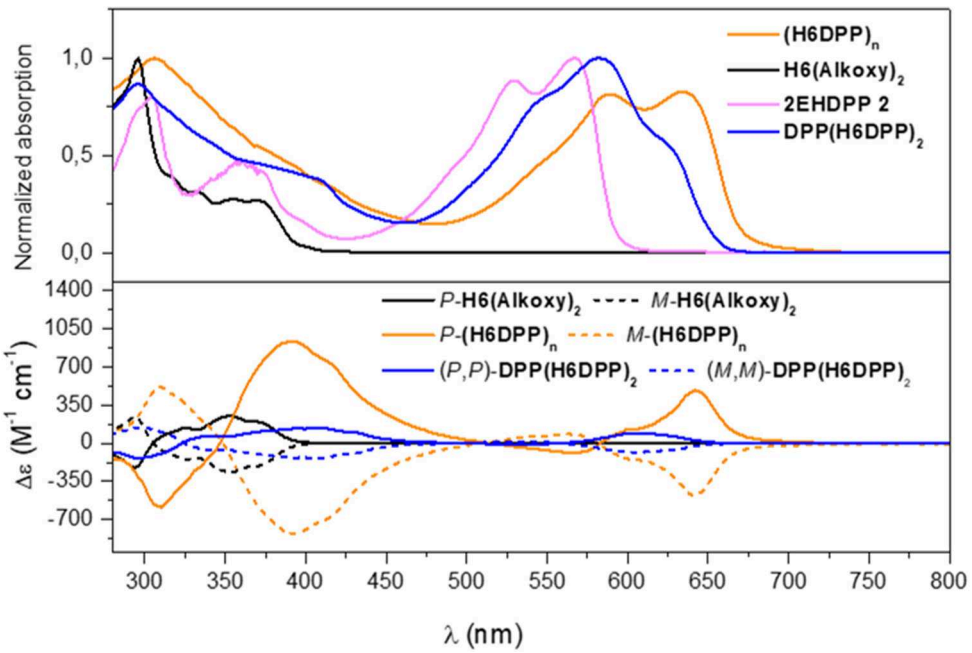

FIGURE 3 | UV-vis (top) and ECD (bottom) spectra of **H6(Alkoxy)$_2$** (black), **2EHDPP 2** (purple), **DPP(H6DPP)$_2$** (blue) and **(H6DPP)$_n$** (orange) in CH_2Cl_2 at 298 K (~10^{-5} M).

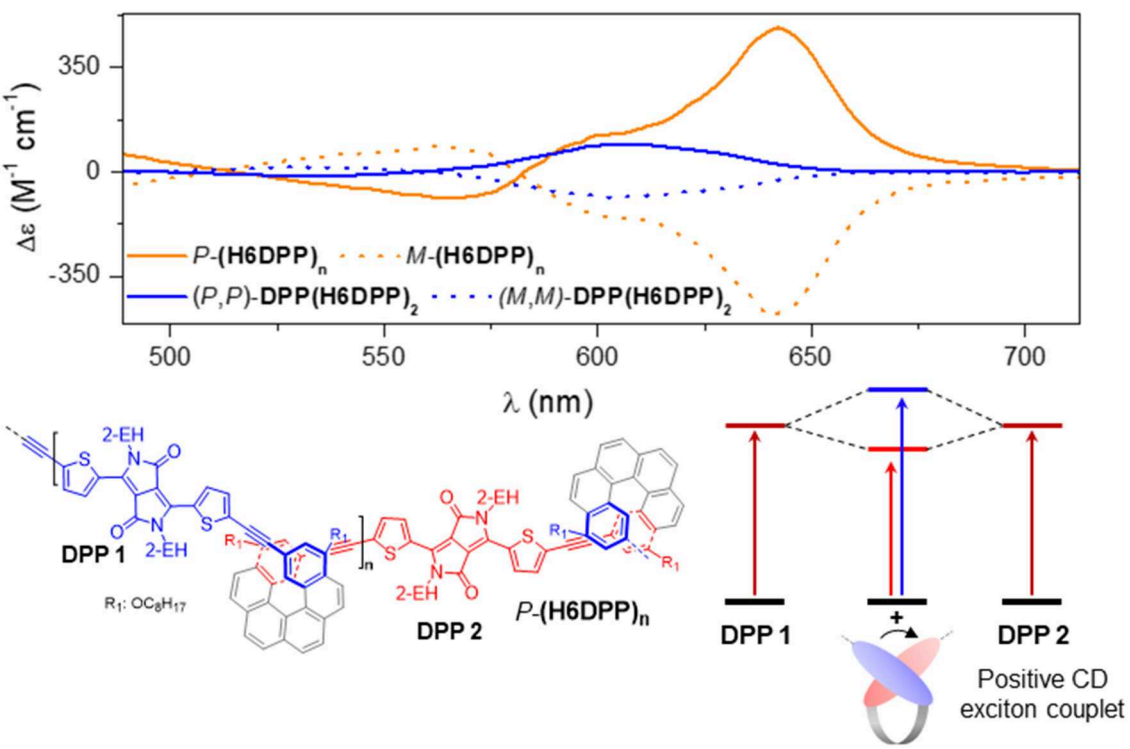

FIGURE 4 | Enlargement of 490–710 nm region of the ECD spectra of **DPP(H6DPP)$_2$** (blue) and **(H6DPP)$_n$** (orange) in CH_2Cl_2 at 298 K (~10^{-5} M), with schematic illustration of the chiral exciton coupling process in **(H6DPP)$_n$**.

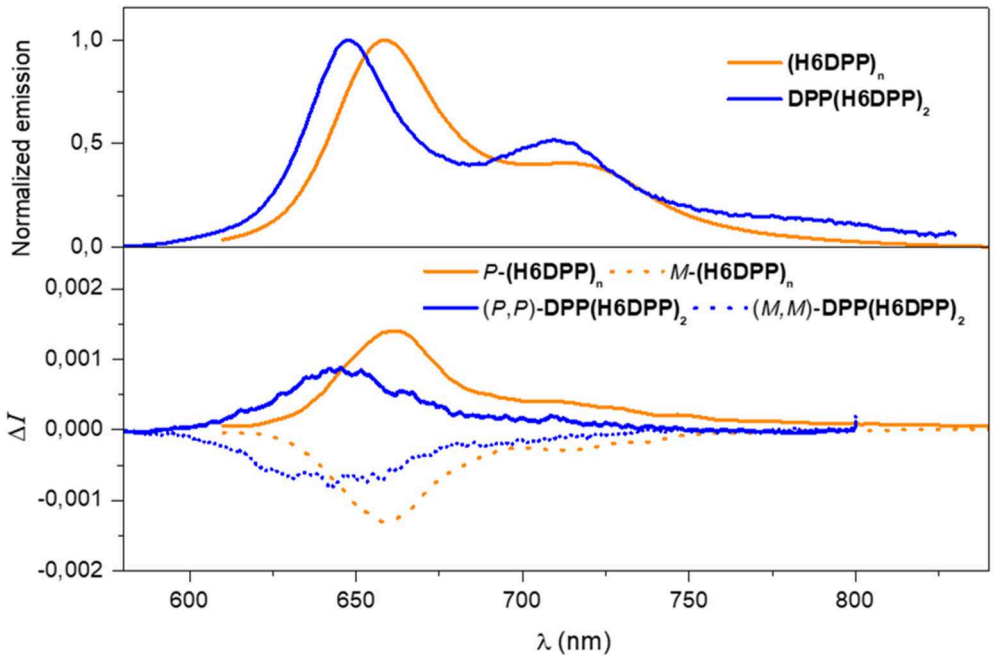

FIGURE 5 | Normalized fluorescence (top) and CPL (bottom) spectra of **DPP(H6DPP)$_2$** (blue) and **(H6DPP)$_n$** (orange) in CH_2Cl_2 at 298 K. CPL spectra for *P* and *M* enantiomers are shown, respectively, in solid and dotted lines.

Unpolarized (PL) and Circularly Polarized Luminescence (CPL)

To our delight, **(H6DPP)**$_n$ displays intense unpolarized vibronic emission arising from the DPP-ethynyl fragment with a maximum intensity at 660 nm and a quantum yield of 35%. Interestingly, these values suggest that embedding DPP-helicene fragment within a polymer material is also an efficient strategy to make deeper red emitter while keeping a high fluorescence efficiency since **DPP(H6DPP)$_2$** exhibits similar luminescence quantum yield (ϕ = 35%) but its emission is blue shifted (λ_{max} = 650 nm). In order to rule out the possibility of charge transfer character the emission of the polymer was carried out in solvents of different polarity including toluene, tetrahydrofuran, and dichloromethane in which the polymer was fully soluble (**Figure S13**). A similar spectral behavior was found in these solvents with a structured signals and no significant shift of the emission spectra, indicating that the nature of the emission is mainly based on π-π^* transitions localized on the DPP units. The fluorescence kinetics of the polymer was also performed at 650 nm (**Figure S14**) and fits a single-exponential decay function with a decay time constant of 2.08 ns.

Regarding circularly polarized luminescence (CPL), mirror-image spectra were also obtained for *P*- and *M*-**(H6DPP)**$_n$ with a maximum and a structural signature similar to unpolarized emission, highlighting the synergy of the DPP-helicene association also in the polymer chiral excited-state (**Figure 5**). Moreover, g_{lum} factor of $+1.3 \times 10^{-3}$ was determined for *P*-**(H6DPP)**$_n$, which suggests a relatively similar chiral geometry of the ground and emitting excited states (g_{lum}/g_{abs} = 0.72) and represents also a *ca.* 40% increase in comparison with *(P,P)*-**DPP(H6DPP)$_2$** ($g_{lum} = +\ 0.9 \times 10^{-3}$). The obtained g_{lum} values for polymers **(H6DPP)**$_n$ are in the same range of reported SOM CPL emitters (10^{-4}-10^{-2}), and are among the most efficient ones for the far red and near infrared region (i.e., for $\lambda_{max} > 650$ nm, $3 \times 10^{-4} < g_{lum} < 4.3 \times 10^{-3}$) (Tanaka et al., 2018).

CONCLUSIONS

In summary, we have successfully prepared novel helical conjugated polymers based on the association between enantiopure carbo[6]helicene derivative and diketopyrrolopyrrole dye via the Sonogashira cross-coupling. These polymers show strong ECD signal in the visible region ($\Delta\varepsilon \times 482$ M^{-1} cm^{-1} at 642 nm, for *P*-**(H6DPP)**$_n$) and strong CPL emission response signals ($g_{lum} = +1.3 \times 10^{-3}$ at 662 nm) along with high fluorescence quantum efficiency (φ_f = 35 %). Extending the efficiency of exciton coupling process in chiral polymers allow efficient preparation of CPL emitters deeper in the red and near-infrared region. Our results provide an alternative approach to the metalation and the push-pull functionalization methodologies to extend and to improve the chiroptical responses of the helicene molecules by taking advantages of the strong synergy between the chiral environment controlled by the helicene center and the interesting photophysical properties offered by the corresponding dye. The polymers based on the helicene unit that we presented in this work can be used as a new class of candidates for efficient CPL materials in optoelectronics and bioimaging applications.

DATA AVAILABILITY STATEMENT

All datasets generated for this study are included in the article/**Supplementary Material**.

AUTHOR CONTRIBUTIONS

KD and CS synthesized and characterized the molecules. MJ and NV performed the HPLC resolution. TR performed the X-ray analysis. MG performed CPL measurements. BJ, LF, and JC supervised the work, analyzed the results and wrote the manuscript.

ACKNOWLEDGMENTS

We acknowledge the Ministère de l'Education Nationale, de la Recherche et de la Technologie, the Centre National de la Recherche Scientifique (CNRS). KD is grateful for financial support from the University of Gabès, the University of Rennes 1, and Campus France. The PRISM core facility (Biogenouest©, UMS Biosit, Université de Rennes 1 - Campus de Villejean - 35043 RENNES Cedex, FRANCE) is acknowledged for the NMR characterizations and ECD measurements. MG thanks the Bekker Program of the Polish National Agency for Academic Exchange (NAWA). Prof. Lorenzo Di Bari is warmly thanked for his advices and for fruitful discussions.

SUPPLEMENTARY MATERIAL

The Supplementary Material for this article can be found online at: https://www.frontiersin.org/articles/10.3389/fchem.2020.00237/full#supplementary-material

REFERENCES

Anger, E., Srebro, M., Vanthuyne, N., Toupet, L., Rigaut, S., Roussel, C., et al. (2012). Ruthenium-vinylhelicenes: remote metal-based enhancement and redox switching of the chiroptical properties of a helicene core. *J. Am. Chem. Soc*. 134, 15628–15631. doi: 10.1021/ja304424t

Berova, N., Nakanishi, K., and Woody, R. W. (2000). *Circular Dichroism: Principles and Applications*. New York, NY: John Wiley & Sons

Berova, N., Polavarapu, P. L., Nakanishi, K., and Woody, R. W. (2012). *Comprehensive Chiroptical Spectroscopy: Applications in Stereochemical Analysis of Synthetic Compounds, Natural Products, and Biomolecules*. Hoboken, NJ: John Wiley & Sons.

Biet, T., Cauchy, T., Sun, Q., Ding, J., Hauser, A., Oulevey, P., et al. (2017). Triplet state CPL active helicene-dithiolene platinum bipyridine complexes. *Chem. Commun.* 53, 9210–9213. doi: 10.1039/c7cc05198k

Bouvier, R., Durand, R., Favereau, L., Srebro-Hooper, M., Dorcet, V., Roisnel, T., et al. (2018). Helicenes grafted with 1,1,4,4-Tetracyanobutadiene Moieties: π-Helical push-pull systems with strong electronic circular dichroism and two-photon absorption. *Chem. Eur. J.* 24, 14484–14494. doi: 10.1002/chem.201802763

Brandt, J. R., Wang, X., Yang, Y., Campbell, A. J., and Fuchter, M. J. (2016). Circularly polarized phosphorescent electroluminescence with a high dissymmetry factor from PHOLEDs based on a platinahelicene. *J. Am. Chem. Soc*. 138, 9743–9746. doi: 10.1021/jacs.6b02463

Carr, R., Evans, N. H., and Parker, D. (2012). Lanthanide complexes as chiral probes exploiting circularly polarized luminescence. *Chem. Soc. Rev*. 41, 7673–7686. doi: 10.1039/c2cs35242g

Chen, C.-F., and Shen, Y. (2016). *Helicene Chemistry: From Synthesis to Applications*. Springer.

Data, P., Kurowska, A., Pluczyk, S., Zassowski, P., Pander, P., Jedrysiak, R., et al. (2016). Exciplex enhancement as a tool to increase OLED device efficiency. *J. Phys. Chem.* 120, 2070–2078. doi: 10.1021/acs.jpcc.5b11263

de Bettencourt-Dias, A. (2014). *Luminescence of Lanthanide Ions in Coordination Compounds and Nanomaterials*. Hoboken, NJ: John Wiley & Sons.

Dhbaibi, K., Favereau, L., and Crassous, J. (2019). Enantioenriched Helicenes and Helicenoids Containing Main-Group Elements (B, Si, N, P). *Chem. Rev*. 119, 8846–8953. doi: 10.1021/acs.chemrev.9b00033

Dhbaibi, K., Favereau, L., Srebro-Hooper, M., Jean, M., Vanthuyne, N., Zinna, F., et al. (2018). Exciton coupling in diketopyrrolopyrrole-helicene derivatives leads to red and near-infrared circularly polarized luminescence. *Chem. Sci*. 9, 735–742. doi: 10.1039/c7sc04312k

Dhbaibi, K., Favereau, L., Srebro-Hooper, M., Quinton, C., Vanthuyne, N., Arrico, L., et al. (2020). Modulation of circularly polarized luminescence through excited-state symmetry breaking and interbranched exciton coupling in helical push-pull organic systems. *Chem. Sci.* 11, 567–576. doi: 10.1039/C9SC05231C

Gingras, M. (2013). One hundred years of helicene chemistry. Part 3: applications and properties of carbohelicenes. *Chem. Soc. Rev*. 42, 1051–1095. doi: 10.1039/c2cs35134j

Grzybowski, M., and Gryko, D. T. (2015). Diketopyrrolopyrroles: synthesis, reactivity, and optical properties. *Adv. Opt. Mater*. 3, 280–320. doi: 10.1002/adom.201400559

Han, J., Guo, S., Lu, H., Liu, S., Zhao, Q., and Huang, W. (2018). Recent progress on circularly polarized luminescent materials for organic optoelectronic devices. *Adv. Opt. Mater*. 6:1800538. doi: 10.1002/adom.201800538

Heyer, E., Lory, P., Leprince, J., Moreau, M., Romieu, A., Guardigli, M., et al. (2015). Highly fluorescent and water-soluble diketopyrrolopyrrole dyes for bioconjugation. *Angew. Chem. Int. Ed*. 54, 2995–2999. doi: 10.1002/anie.201411274

Huo, L., Hou, J., Chen, H.-Y., Zhang, S., Jiang, Y., Chen, T. L., et al. (2009). Bandgap and molecular level control of the low-bandgap polymers based on 3,6-dithiophen-2-yl-2,5-dihydropyrrolo[3,4-c]pyrrole-1,4-dione toward Highly Efficient Polymer Solar Cells. *Macromolecules* 42, 6564–6571. doi: 10.1021/ma9012972

Kaur, M., and Choi, D. H. (2015). Diketopyrrolopyrrole: brilliant red pigment dye-based fluorescent probes and their applications. *Chem. Soc. Rev*. 44, 58–77, doi: 10.1039/c4cs00248b

Kumar, J., Nakashima, T., and Kawai, T. (2014). Inversion of supramolecular chirality in bichromophoric perylene bisimides: influence of temperature and ultrasound. *Langmuir*. 30, 6030–6037. doi: 10.1021/la500497g

Kumar, J., Nakashima, T., and Kawai, T. (2015a). Circularly polarized luminescence in chiral molecules and supramolecular assemblies. *J. Phys. Chem. Lett*. 6, 3445–3452. doi: 10.1021/acs.jpclett.5b01452

Kumar, J., Nakashima, T., Tsumatori, H., Mori, M., Naito, M., and Kawai, T. (2013). Circularly polarized luminescence in supramolecular assemblies of chiral bichromophoric perylene bisimides. *Chem. Eur. J*. 19, 14090–14097. doi: 10.1002/chem.201302146

Kumar, J., Tsumatori, H., Yuasa, J., Kawai, T., and Nakashima, T. (2015b). Self-discriminating termination of chiral supramolecular polymerization: tuning the length of nanofibers. *Angew. Chem. Int. Ed*. 54, 5943–5947. doi: 10.1002/anie.201500292

Langhals, H., Hofer, A., Bernhard, S., Siegel, J. S., and Mayer, P. (2011). Axially chiral bichromophoric fluorescent dyes. *J. Org. Chem*. 76, 990–992. doi: 10.1021/jo102254a

Li, M., Lin, W.-B., Fang, L., and Chen, C.-F. (2017). Recent Progress on Circularly Polarized Luminescence of Chiral Organic Small Molecules. Acta Chim. Sin. 75, 1150–63. doi: 10.6023/A17090440

Longhi, G., Castiglioni, E., Koshoubu, J., Mazzeo, G., and Abbate, S. (2016). Circularly polarized luminescence: a review of experimental and theoretical aspects. *Chirality* 28, 696–707. doi: 10.1002/chir.22647

Maeda, H., and Bando, Y. (2013). Recent progress in research on stimuli-responsive circularly polarized luminescence based on π-conjugated molecules. *Pure Appl. Chem*. 85, 1967–1978. doi: 10.1351/pac-con-12-11-09

Nielsen, C. B., Turbiez, M., and McCulloch, I. (2013). Recent advances in the development of semiconducting DPP-containing polymers for transistor applications. *Adv. Mater*. 25, 1859–1880. doi: 10.1002/adma.201201795

Nishimura, H., Tanaka, K., Morisaki, Y., Chujo, Y., Wakamiya, A., and Murata, Y. (2017). Oxygen-bridged diphenylnaphthylamine as a scaffold for full-color circularly polarized luminescent materials. *J. Org. Chem*. 82, 5242–5249. doi: 10.1021/acs.joc.7b00511

Palai, A. K., Mishra, S. P., Kumar, A., Srivastava, R., Kamalasanan, M. N., and Patri, M. (2010). Synthesis and characterization of red-emitting poly(aryleneethynylene)s Based on 2,5-Bis(2-ethylhexyl)-3,6-di(thiophen-2-yl)pyrrolo[3,4-c]pyrrole-1,4(2H,5H)-dione (DPP). *Macromol. Chem. Phys*. 211, 1043–1053. doi: 10.1002/macp.200900706

Pascal, S., Besnard, C., Zinna, F., Di Bari, L., Le Guennic, B., Jacquemin, D., et al. (2016). Zwitterionic [4]helicene: a water-soluble and reversible pH-triggered ECD/CPL chiroptical switch in the UV and red spectral regions. *Org. Biomol. Chem*. 14, 4590–4594. doi: 10.1039/c6ob00752j

Riehl, J. P., and Richardson, F. S. (1986). Circularly polarized luminescence spectroscopy. *Chem. Rev*. 86, 1–16. doi: 10.1021/cr00071a001

Sakai, H., Kubota, T., Yuasa, J., Araki, Y., Sakanoue, T., Takenobu, T., et al. (2016). Protonation-induced red-coloured circularly polarized luminescence of [5]carbohelicene fused by benzimidazole. *Org. Biomol. Chem*. 14, 6738–6743. doi: 10.1039/C6OB00937A

Saleh, N., Srebro, M., Reynaldo, T., Vanthuyne, N., Toupet, L., Chang, V. Y., et al. (2015). enantio-Enriched CPL-active helicene-bipyridine-rhenium complexes. *Chem. Commun*. 51, 3754–3757. doi: 10.1039/c5cc00453e

Sánchez-Carnerero, E. M., Moreno, F., Maroto, B. L., Agarrabeitia, A. R., Ortiz, M. J., Vo, B. G., et al. (2014). Circularly polarized luminescence by visible-light absorption in a chiral O-BODIPY dye: unprecedented design of CPL organic molecules from achiral chromophores. *J. Am. Chem. Soc*. 136, 3346–3349. doi: 10.1021/ja412294s

Shen, C., Anger, E., Srebro, M., Vanthuyne, N., Deol, K. K., Jefferson, T. D., et al. (2014). Straightforward access to mono- and bis-cycloplatinated helicenes displaying circularly polarized phosphorescence by using crystallization resolution methods. *Chem. Sci*. 5, 1915–1927. doi: 10.1039/c3sc53442a

Shen,C., Gan, F., Zhang, G., Ding, Y., Wang, J., Wang, R., et al. (2020). Tunable circularly polarized luminescence of helicene-derived aggregation-induced emission adducts. *Mater. Chem. Front*. 4, 837–844. doi: 10.1039/C9QM00652D

Sheng, Y., Ma, J., Liu, S., Wang, Y., Zhu, C., and Cheng, Y. (2016). Strong and reversible circularly polarized luminescence emission of a chiral 1,8-naphthalimide fluorophore induced by excimer emission and orderly aggregation. *Chem. Eur. J*. 22, 9519–9522. doi: 10.1002/chem.201600891

Tanaka, H., Inoue, Y., and Mori, T. (2018). Circularly polarized luminescence and circular dichroisms in small organic molecules: correlation between excitation and emission dissymmetry factors. *ChemPhotoChem*. 2, 386–402. doi: 10.1002/cptc.201800015

Tsumatori, H., Nakashima, T., and Kawai, T. (2010). Observation of chiral aggregate growth of perylene derivative in opaque solution by circularly polarized luminescence. *Org. Lett*. 12, 2362–2365. doi: 10.1021/ol100701w

Wu, X. F., Fu, W. F., Xu, Z., Shi, M., Liu, F., Chen, H. Z., et al. (2015). Spiro linkage as an alternative strategy for promising nonfullerene acceptors in organic solar cells. *Adv. Funct. Mater*. 25, 5954–5966. doi: 10.1002/adfm.201502413

Zhao, W.-L., Li, M., Lu, H.-Y., and Chen, C.-F. (2019). Advances in helicene derivatives with circularly polarized luminescence. *Chem. Commun*. 55, 13793–13803. doi: 10.1039/c9cc06861a

Zinna, F., and Di Bari, L. (2015). Lanthanide circularly polarized luminescence: bases and applications. *Chirality* 27, 1–13. doi: 10.1002/chir.22382

Zinna, F., and Di Bari, L. (2018). *Lanthanide-Based Multifunctional Materials*. eds P. Martín-Ramos and M. Ramos Silva (Amsterdam: Elsevier).

Zinna, F., Giovanella, U., and Di Bari, L. (2015). Highly circularly polarized electroluminescence from a chiral europium complex. *Adv. Mater*. 27, 1791–1795. doi: 10.1002/adma.201404891

Zinna, F., Pasini, M., Galeotti, F., Botta, C., Di Bari, L., and Giovanella, U. (2017). Design of lanthanide-based OLEDs with remarkable circularly polarized electroluminescence. *Adv. Funct. Mater*. 27:1603719. doi: 10.1002/adfm.201603719

Conflict of Interest: The authors declare that the research was conducted in the absence of any commercial or financial relationships that could be construed as a potential conflict of interest.

frontiers in Chemistry

ORIGINAL RESEARCH
published: 21 April 2020
doi: 10.3389/fchem.2020.00306

Simple Perylene Diimide Cyclohexane Derivative With Combined CPL and TPA Properties

Pablo Reine[1], Ana M. Ortuño[1], Inês F. A. Mariz[2], Maria Ribagorda[3], Juan M. Cuerva[1], Araceli G. Campaña[1], Emerlinda Maçôas[2] and Delia Miguel[4]**

[1] Departamento de Química Orgánica, Facultad de Ciencias, Unidad de Excelencia de Química Aplicada a Biomedicina y Medioambiente (UEQ), Universidad de Granada, Granada, Spain, [2] Centro de Química Estrutural, Instituto Superior Técnico, Universidade de Lisboa, Lisbon, Portugal, [3] Departamento de Química Orgánica, Facultad de Ciencias, C.U. Cantoblanco, Universidad Autónoma de Madrid, Madrid, Spain, [4] Departamento de Fisicoquímica, Facultad de Farmacia, UEQ, Universidad de Granada, Granada, Spain

OPEN ACCESS

Edited by:
Giovanna Longhi,
University of Brescia, Italy

Reviewed by:
Santiago De La Moya,
Complutense University of Madrid, Spain
Narcis Avarvari,
UMR6200 Institut des Sciences et Technologies Moléculaires d'Angers (MOLTECH ANJOU), France

***Correspondence:**
Emerlinda Maçôas
ermelinda.macoas@tecnico.ulisbo.pt
Delia Miguel
dmalvarez@ugr.es

Specialty section:
This article was submitted to Physical Chemistry and Chemical Physics, a section of the journal Frontiers in Chemistry

Received: 06 March 2020
Accepted: 27 March 2020
Published: 21 April 2020

Citation:
Reine P, Ortuño AM, Mariz IFA, Ribagorda M, Cuerva JM, Campaña AG, Maçôas E and Miguel D (2020) Simple Perylene Diimide Cyclohexane Derivative With Combined CPL and TPA Properties. Front. Chem. 8:306. doi: 10.3389/fchem.2020.00306

In this work we describe the linear and non-linear (chiro)optical properties of an enantiopure bis-perylenediimide (PDI) cyclohexane derivative. This compound exhibits upconversion based on a two-photon absorption (TPA) process with a cross-section value of 70 GM together with emission of circularly polarized luminescence (CPL), showing a g_{lum} in the range of 10^{-3}. This simple structure represents one of the scarce examples of purely organic compounds combining both TPA and CPL responses, together with large values of molar absorptivity and fluorescence quantum yield with emission in the 500–600 nm. Self-assembly induced by introduction of a poor solvent allows for a spectacular shift of the emission into the near-infrared (NIR, 650–750 nm) by formation of well-defined rotationally displaced dimers. Therefore, we are here presenting a versatile platform whose optical properties can be simply tuned by self-assembly or by functionalization of the electron-deficient aromatic core of PDIs.

Keywords: perylene diimide (PDI), electronic circular dichroism (ECD), circularly polarized luminiscence (CPL), two-photon absorption, non-linear emission

INTRODUCTION

Organic materials presenting circularly polarized luminescence (CPL) (Riehl and Richardson, 1977; Kumar et al., 2015; Sanchez-Carnerero et al., 2015; Longhi et al., 2016; Tanaka et al., 2018) have recently emerged as promising candidates for advanced optical applications (Zinna et al., 2015; Han et al., 2018; Shi et al., 2018; Zheng et al., 2018; Burrezo et al., 2019; David et al., 2019; Jiménez et al., 2019; Pop et al., 2019; Yang and Zhong, 2019). Thus for example, CPL emitters have been proposed as chiroptical sensors (Staszak et al., 2019), for smart sensing methodologies (Imai et al., 2018; Reine et al., 2018a,b; Zinna et al., 2019), to encode information in light (Andréassons and Pischel, 2018), in patterning processes using security inks (Andres et al., 2014), or constituents of CPL organic light-emitting diodes OLEDs (Brandt et al., 2016; Di Nuzzo et al., 2017). This property is characterized by the preferential emission of left (I_L) or right handed (I_R) circularly polarized light with respect to the entire emission $(I_L+I_R)/2$, being usually described by the dimensionless Kuhn factor of the emission, $g_{lum} = 2(I_L-I_R)/(I_L+I_R)$. For simple organic molecules (SOMs), these values usually range from 0.01 to 0.0001, being scarce values higher than 0.01 (Sato et al., 2017; Ito et al., 2018; Takaishi et al., 2018, 2019, 2020; Han et al., 2019; Reine et al., 2019; Schaack et al., 2019; Zheng et al., 2019).

Although the development of this technique is approaching its maturity, the coupling of CPL with other types of optical response can open new avenues in the design, fabrication and application of optical materials. In particular, the coupling of CPL with non-linear excitation opens the possibility of obtaining higher energy emission from low energy photons. Two-photon absorption (TPA) is a non-linear optical property that depends on the third-order optical susceptibility (χ^3) and it scales with the square of the light intensity used in the excitation process (He et al., 2008). In a two-photon process, low energy photons can cooperatively excite the chromophore, yielding an excited state indistinguishable of that obtained by a one photon excitation. The use of low energy photons (usually NIR light) and the non-linear dependence of the excitation offers the possibility of light actuation at larger penetration depths (e.g., deeper penetration in biological tissue) and intrinsic localization in space. Thus, the TPA process is routinely applied in photolithography to obtain 3D nanopatterning with high aspect ratio. It also finds widespread application in optical imaging of 3D-biological samples in biomedical research, with particular relevance in the study of neuronal activity in awake, behaving animals over long periods of time (Lecoq et al., 2019). Many different types of organic chromophores have been explored in an attempt to improve the TPA properties, from SOM, to polymers, nanoparticles and composites tailored for diverse applications (Zou et al., 2011; Marcelo et al., 2015; Mariz et al., 2015; Santos et al., 2018). The non-linear excitation of a chiral chromophore opens the additional possibility of observing upconverted CPL. Therefore, some efforts have been carried out to combine TPA and CPL (TPCPL) in the same molecule. To our knowledge, very few examples have been described including chiral nanographenic SOMs developed by our group (Cruz et al., 2018a,b, 2019) and chiral Cd(II) 1D structures (Deng et al., 2019). It is remarkable that, up to the moment, there is just one photonic system enabling TPA-induced CPL based on chiral perovskites (Chen et al., 2019).

The combination of TPA and CPL is a promising field of research that will unfold through carefully planned systematic studies. Many opportunities exist for the development of new and simple architectures combining reasonable g_{lum} values and TPA cross sections (σ_2) together with good quantum yields (Φ_F). Among such possibilities simple organic molecules (SOMs) are appreciated owing to their high solubility and processability (Kumar et al., 2015; Sanchez-Carnerero et al., 2015; Longhi et al., 2016; Tanaka et al., 2018).

For the sake of simplicity, we propose as a new approach a chiral arrangement of achiral PDIs to take advantages of the intrinsic photophysical properties of such chromophores. Following a similar strategy, pyrenes have been extensively used in the context of CPL (Hashimoto et al., 2016; Takaishi et al., 2018; Ohishi and Inouye, 2019). Nevertheless, the possibility of forming excimer inter- or intramolecularly drops the quantum yield of the emission. Moreover, simple pyrenes cannot be excited using the most common excitation sources providing high peak power femtosecond pulses in the NIR (700–1,000 nm) that are necessary for the observation of TPA. On the other hand, PDIs are remarkable emitters, with near unit emission yield in all common solvents including aliphatic, aromatic, chlorinated, and dipolar solvents. Their emission wavelength can be tuned via functionalization of either the electron-deficient aromatic core or the imide units. The imide substituents can be used to control their self-assembly into a plethora of supramolecular architectures (Wurthner et al., 2016). It is noteworthy that PDIs (Kawai et al., 2007; Ikeda et al., 2012) and also the smaller analogs napthtalene diimides (Salerno et al., 2017; Keshri et al., 2020) have been successfully used in the context of CPL-SOMs with high quantum yields in solution and/or aggregated forms (Tsumatori et al., 2010).

Different types of chiral scaffolds have been used to place the achiral chromophores in a chiral environment. Remarkable examples are binaphtyl-type skeletons (Hara et al., 2019; Takaishi et al., 2019), dibenzo[b,d]furane (Ito et al., 2017), cyclophanes (Morisaki et al., 2014; Liang et al., 2019; Wang et al., 2020), or [n]-helicenes (Dhbaibi et al., 2020). In this work, we considered as chiral scaffold enantiopure and commercially available (*1R,2R*)-(-)-1,2-diaminecyclohexane for its simplicity and its easy functionalization. This chiral unit has been recently used in the design of CPL emitters based on naphthalimides (Wang et al., 2019) and efficient CPL-OLEDs based on thermally activated delayed fluorescent enantiomers of aromatic-imides (Li et al., 2018).

Herein we present the interesting linear and non-linear (chiro)optical properties of compound (*R,R*)-**1** (**Figure 1**) built upon the combination of the chiral diamine and a PDI derivative. This compound can be easily prepared following known procedures (Che et al., 2007; Park et al., 2017). We show that, despite its simple structure, it can compete in terms of quantum yields, g_{lum} and even TPA cross sections with previously described TPCPL emitters requiring a more demanding synthetic approach.

RESULTS AND DISCUSSION

Compound (*R,R*)-**1** was prepared by direct condensation between anhydride **2** and commercially available (*1R,2R*)-(–)-1,2-diaminecyclohexane with good yields (**Figure 2**). Precursor **2** can be synthetized using a known protocol (Che et al., 2007) from perylene diimide and the corresponding solubilizing chains. At this point we checked some solubilizing chains, finding that at least 13 carbon atoms are required to ensure a reasonable solubility in all the solvents studied.

With compound (*R,R*)-**1** fully characterized by means of ^{1}H-NMR, ^{13}C-NMR and HRMS (**Figures S1**, **S2**), we then analyzed the corresponding linear optical properties in different solvents covering a wide range of polarity, in order to evaluate a possible solvatochromic effect. As it can be seen in **Figure 3A** (for other solvents see **Figure S4**), with the exception of water, a similar shape of the absorbance spectra was observed in all solvents. Three main vibronic bands are observed centered at ≈ around 455, 485, and 525 nm characteristic of the PDI units, thus confirming that the inclusion of short aliphatic chains does not alter the spectroscopical properties of PDI (Langhals, 2005; Kawai et al., 2007). The absorbance maximum appeared around

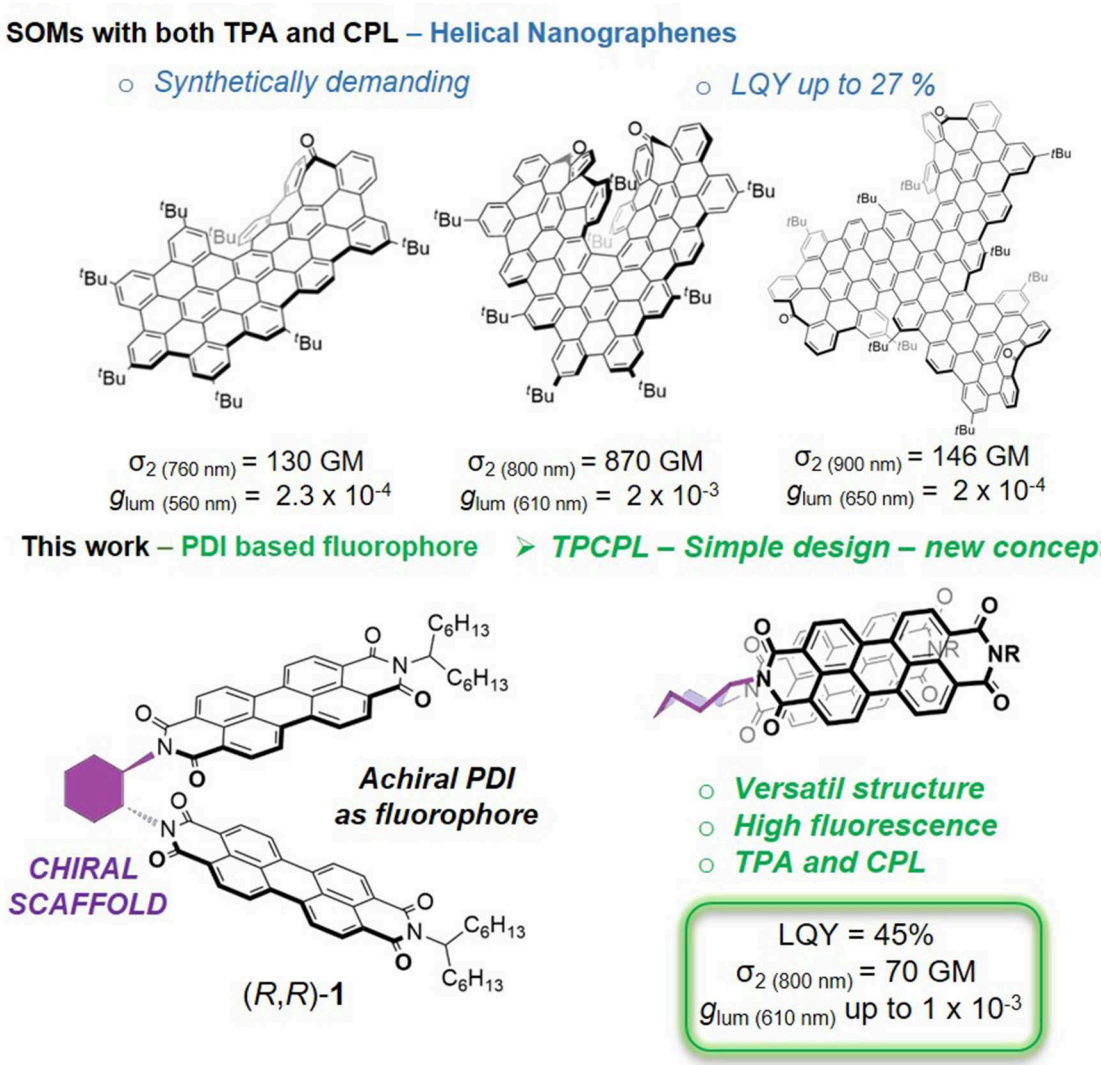

FIGURE 1 | SOMs exhibiting both TPA and CPL responses. **(Top)** Reported examples. **(Bottom)** This work.

525 nm with no obvious polarity dependent solvatochromic effect from benzene (Bz) to dimethylsulfoxide (DMSO). The molar absorptivity remained almost constant at 1×10^5 $M^{-1}cm^{-1}$ as the polarity of the solvent increases from benzene to dimethylformamide (DMF) (**Figure S3**). In more polar solvents (DMSO and acetonitrile) the molar absorptivity drops considerably and the relative intensity of the vibronic bands is significantly altered suggesting the existence of aggregation. Except from water, all organic solvents presented two main emission peaks with well-defined maxima at ≈ 530 and 580 nm. Similarly to the absorption spectra, the fluorescence spectra show no obvious polarity dependent solvatochromic effect (emission maxima between 530 nm for acetonitrile and acetone and 540 nm for benzene, toluene and DMSO). Although in most of the solvents the emission is again typical of monomeric PDI, we observed an additional broad and unstructured band in the NIR in more polar solvents as DMSO, but also in tetrahydrofuran (THF) and acetone in **Figure S4**. This band is attributed to the formation of aggregates or excimer-like interactions (**Figure 3B**). When (*R,R*)-**1** is directly suspended in water most of the compound precipitates and a broad unstructured emission band centered at 690 nm is observed due to dispersed aggregates in solution. No clear absorption is directly observed but the corresponding excitation spectrum shows again a broad and unstructured feature centered at 500 nm (**Figure S5**). For the sake of completeness, the influence of the excitation wavelength in the emission spectra is also shown for dioxane (Diox) and DMSO in **Figure S5**. For dioxane the excitation spectrum has a clear vibronic structure, it overlaps perfectly with the absorption spectrum and it is independent on the emission wavelength showing that all the compound is in its monomeric form. For DMSO, the excitation spectrum has also a clear vibronic structure but it depends on the emission wavelength and it does not have a perfect overlap with the absorption spectrum. The

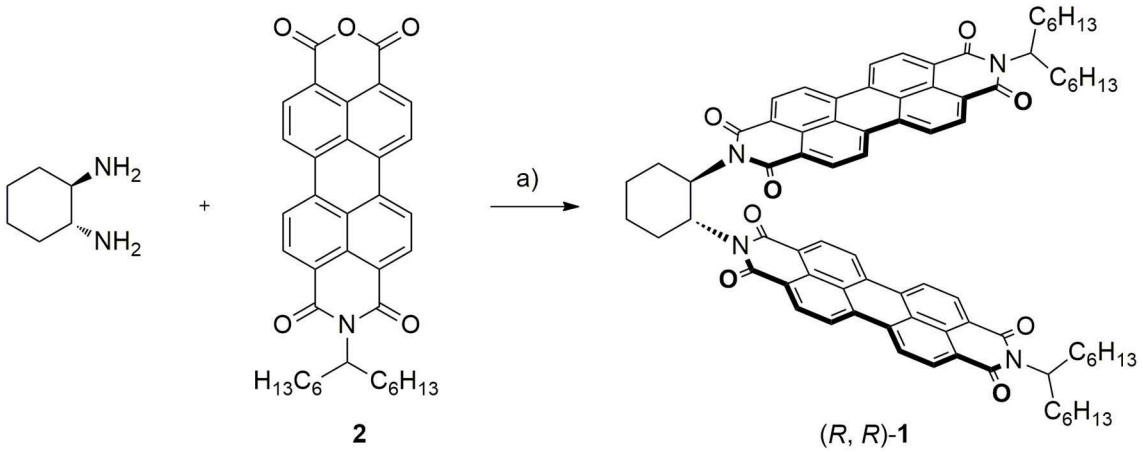

FIGURE 2 | Synthetic route yielding (*R,R*)-**1**. Reagents and conditions: a) (*1R*, *2R*)-(–)-1,2-Cyclohexanediamine (1 Eq.), **2** (2.2 Eq), Imidazole as solid solvent (350 Eq.), 140°C, 1 h (27%).

excitation maximum appears at 528 nm when collected at typical wavelengths of monomeric emission (574 nm) and it appears blue-shifted to 492 nm for emission collected in the aggregate band at 690 nm. Dioxane and water feature extreme cases where all the compound is either monomeric or aggregated in higher-order aggregates. DMSO is an intermediate situation where we have contributions from both monomeric and different types of aggregates.

Fluorescence quantum yields measured for all solvents show a general trend with higher values in less polar solvents (40-60% in Bz, Tol, Diox, $CHCl_3$, DCM) and considerably lower values in more polar solvents (5–20% in acetone, DMF, ACN and DMSO) as shown in **Figure S3**.

In an attempt to control the self-assembly of (*R,R*)-**1**, diluted solutions of compound (*R,R*)-**1** (*ca* 10^{-6} M) were prepared in different dioxane: water mixtures ranging from 0 to 99.5% water (pure water was avoided due to the partial insolubility of compound (*R,R*)-**1**). Since the compound is monomeric in dioxane and the solvent is completely miscible in water, the systematic addition of the poor solvent, while keeping the concentration in the micromolar range, can lead to the formation of lower order aggregates. As can be seen in **Figures 4A,B** there is a clear difference in both absorption and emission spectra not only in the wavelength maxima but mainly in the ratio and the intensity of the bands. The increased amount of water promotes a decrease of the intensity of both absorption and emission bands. The integrated absorption drops by almost 70% (**Figure 4A**) while the integrated emission drops by more than one order of magnitude (**Figure 4B**). **Figures 4C,D** illustrate the significantly different behavior of the initial pure dioxane solution featuring the monomer and the 99.5% water solution featuring the aggregate. Interestingly, at high water percentages (>94%) we observe the formation of a well-defined aggregate with a clear vibronic structure in the absorption (**Figure 4D**) and a broad unstructured emission centered at 690 nm. The excitation spectrum does not depend on the emission wavelength and the emission is also excitation-wavelength independent. These observations confirm that there is only one lower order aggregate in solution, which we assign to a rotationally displaced dimer based on the similarities between its absorption spectrum and that of a model PDI derivative with anti-cooperative supramolecular self-assembly into dimers (Gershberg et al., 2016). Additionally, we observed an increase in the absorption and emission intensity of the dimer with the concentration of (*R,R*)-**1** in solutions with more than 94% of water (**Figure S6**), which excludes both the possibility of intramolecular aggregation in the ground state and the formation of excimers.

Chiroptical properties (ECD and CPL) were also recorded in 0 vol% and 99.5 vol% water content dioxane solutions. In neat dioxane, ECD spectra exhibits three main bands at 490, 520, and 540 nm attributed to the PDI skeleton and a value of $g_{abs} = 1 \times 10^{-3}$(**Figure 5A**). We could also record CPL of (*R,R*)-**1** in dioxane, thus obtaining a g_{lum} value of 4×10^{-4} at 550 nm, which is in the range of simple organic molecules. Moreover, ECD and CPL of the opposite enantiomer were also recorded in both pure dioxane and 99.5% water mixture to check the absence of lineal interferences. In dioxane we obtained a mirror CPL spectra to the previous one (**Figure S7**), thus confirming the value of g_{lum} obtained is attributed to compound (*R,R*)-**1** emission, discarding any possible artifacts (Riehl and Richardson, 1977). However, the experiment in 99.5%water solution afforded a CPL spectra with the same sign to that obtained for the (*R,R*)-**1** enantiomer. With this experiment we can asseverate that the ΔI emission obtained in almost neat water solution was due to an artifact promoted by linear polarization contributions and not actually due to circularly polarized emission (See **Figure S8**). Moreover, ECD and CPL spectra of compound (*R,R*)-**1** in different solvents were measured (**Figure S9**) and, in both cases, we obtained maximum values of dissymmetry factors when DMSO was used, with a $g_{abs} = 2 \times 10^{-3}$ and a $g_{lum} = 1 \times 10^{-3}$.

Geometry of compound **1** was also optimized by DFT calculations and the corresponding UV-vis and ECD spectra were also simulated with the aid of TD-DFT (See

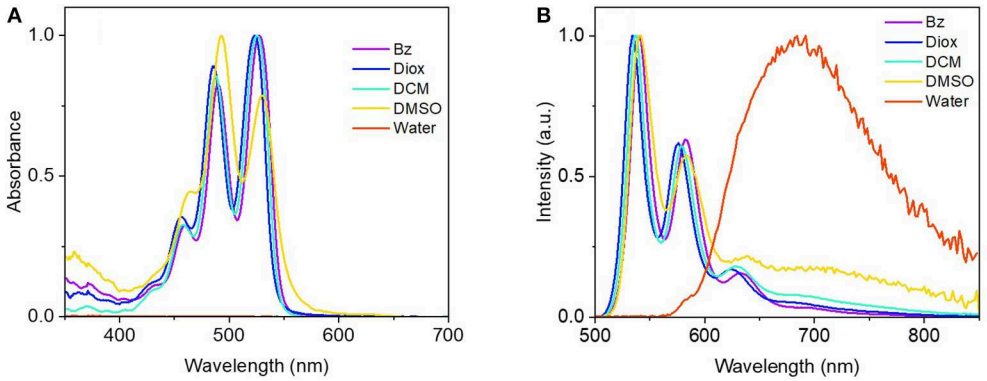

FIGURE 3 | Normalized UV-vis absorbance **(A)** and fluorescence spectra [**(B)**, $\lambda_{exc} = 485$ nm] of (*R,R*)-**1** in an illustrative set of solvents of increasing polarity (Bz, benzene; Diox, dioxane; DCM, dichloromethane; DMSO, dymethylsulfoxide) at a concentration of ca. 10^{-6}M. Additional solvents are shown in **Figure S4**. Note that the absorption of a (*R,R*)-**1** suspension in water is not clearly observed due to precipitation and formation of dispersed aggregates.

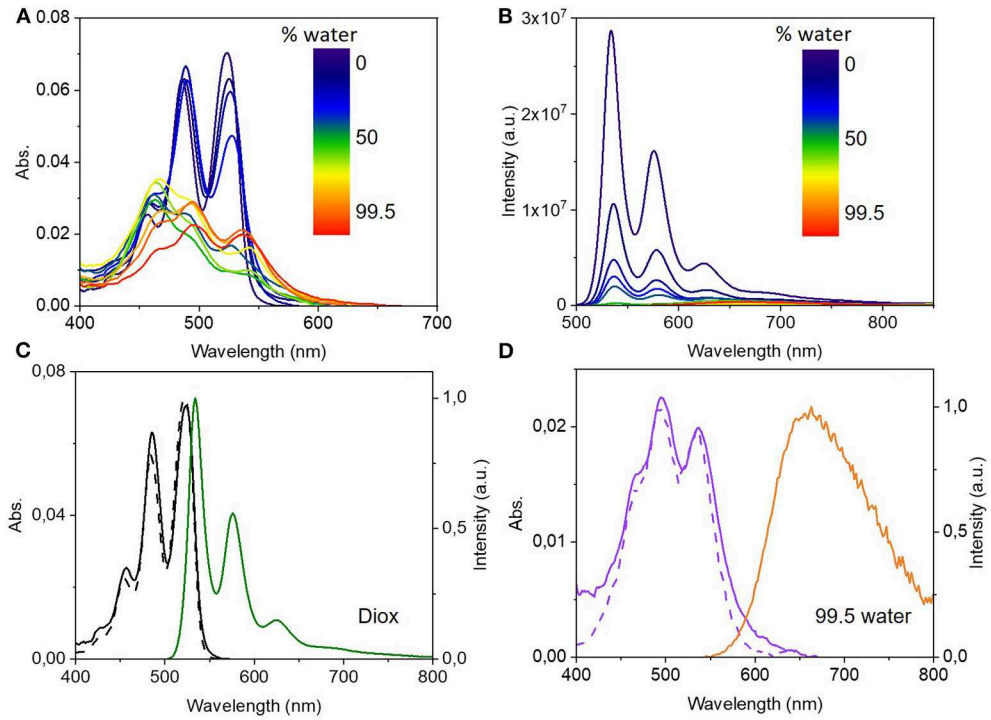

FIGURE 4 | Top: UV-Vis absorbance **(A)** and fluorescence spectra ($\lambda_{exc} = 535$ nm) **(B)** of (*R,R*)-**1** in dioxane:water mixtures with increasing water percentage from 0 to 99.5%. Bottom: UV-Vis absorption (black and violet lines), excitation (dashed lines) and fluorescence emission spectra (green and orange lines, $\lambda_{exc} = 535$ nm) of (*R,R*)-**1** in 0 vol% **(C)** and 99.5 vol% **(D)** water content in dioxane.

Figures S10–S13 and **Tables S1**, **S2**). The calculated ECD signals matched well with experimental ones, as can be seen in **Figure S12**.

In addition to ECD and CPL, two-photon absorption (TPA) and emission (TPE) of a 10^{-6}M solution of compound (*R,R*)-**1** in dioxane were analyzed (**Figure 6**). The emission spectrum under two-photon excitation at 730 nm (red dots in **Figure 6B**) is similar to the one obtained under one-photon excitation at 456 nm (solid black line). The maximum value of TPA cross-section (σ_2) was 70 GM at 730 nm, which corresponds to a one-photon energy of 365 nm. The observed blue shifted two-photon absorption with respect to the one-photon absorption maxima is typical of the PDI monomer. This particular spectral shape is attributed to the centrosymmetric structure of the PDI core that causes the TPA under the intense $S_0 - S_1$ transition to be quasi-forbidden by symmetry. The TPA cross-section is about one order of magnitude higher than that reported for unsubstituted PDIs (Pagoaga et al., 2016). Core substituted PDIs

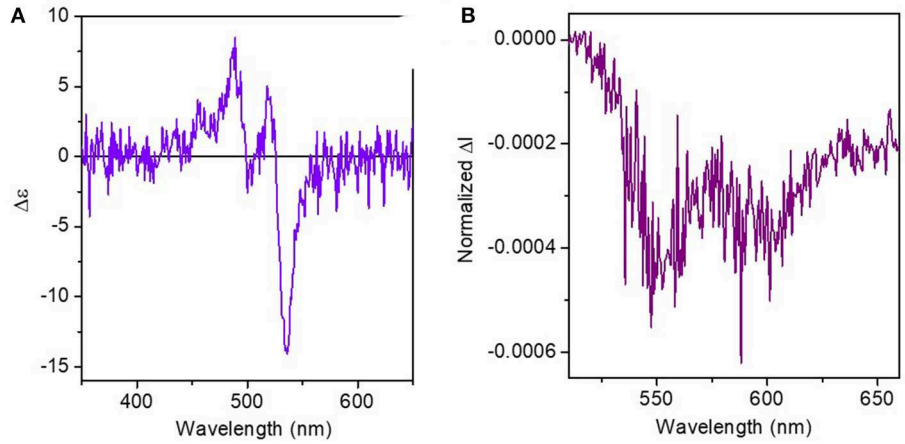

FIGURE 5 | (A) ECD and **(B)** CPL spectra of compound (*R,R*)-**1** in dioxane at *ca.* 10^{-5} M.

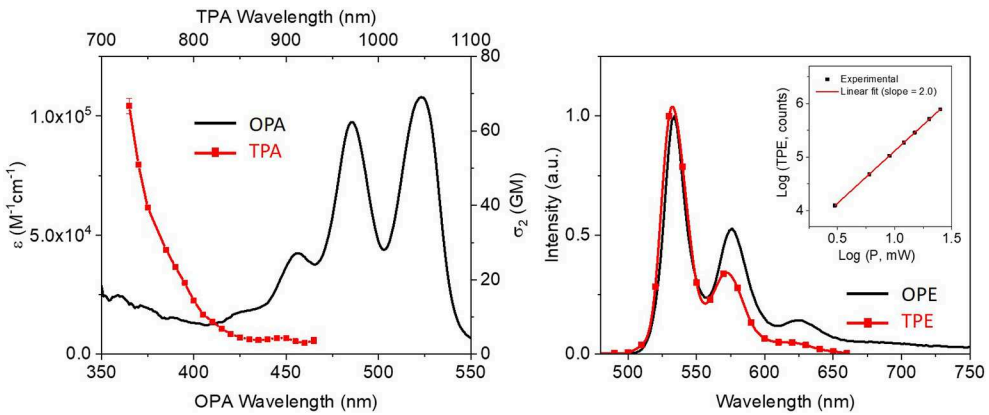

FIGURE 6 | Comparison between one and two-photon absorption and emission of (*R,R*)-**1** in dioxane at *ca.* 10^{-6} M: the left plot shows the one-photon absorption (OPA, black) and two-photon absorption (TPA, red) spectra and the right plot shows the one-photon emission (OPE, black) and two-photon emission (TPE, red). The inset on the right plot represents the Log-Log plot of the photon counts due to non-linear emission as a function of the excitation power. A slope of 2 confirms the biphotonic nature of the process.

with strong electron donor or electron acceptor groups can have similar TPA values. Remarkably, although the cross-section value is 10 times lower than the one described for our previously reported superhelicene (**Figure 1**, top middle) (Cruz et al., 2018a) it is only half of the ones described for both nanoribbon (Cruz et al., 2018b) and the triskelion-shape nanographenes (Cruz et al., 2019) (see **Figure 1**, top left and top right, respectively) but with a simpler and more versatile structure. Due to the order of magnitude lower emission yield and the low concentration of the aggregate in water a reliable estimate of the TPA cross-section of the aggregate was not possible.

MATERIALS AND METHODS

Synthesis of Compound (*R,R*)-1

Compound **1** was prepared according to the protocol previously described by the group of Park et al. (2017). Thus, commercially available (*1R, 2R*)-(−)-1,2-cyclohexanediamine (28.4mg, 0.25 mmol), anhydride **2** (Che et al., 2007) (315 mg, 0.55 mmol) and imidazole (6g) as a solid solvent were heated at 140°C under nitrogen atmosphere for 1 h. Then, 1M HCl was poured into the flask and the formed precipitate was filtrated. The product was purified by flash chromatography in ethyl acetate to afford derivative (*R,R*)-**1** in a 17% yield. Spectroscopic data are detailed in the SI.

Absorbance and Emission Measurements

A JASCO V-540 spectrophotometer was used to record the linear absorption spectra. The fluorescence spectra were recorded using a Horiba Jobin Yvon Fluorlog 3-22 Spectrofluorimeter with a xenon lamp of 450 W. All the spectra were collected at μM concentration in spectroscopic grade solvents. The fluorescence quantum yields were measured at 492 nm using Rhodamine 6G in methanol as a standard ($\Phi_F = 0.94$).

TPA Measurements

The TPA spectra were measured by the two-photon induced fluorescence (TPF) method using a Ti:sapphire laser (Tsunami BB, Spectra-Physics, 710–990 nm, 1.7 W, 100 fs, 82 MHz). A modified setup that follows the one described by Xu and Webb was used to estimate the TPA cross-section in the 710–920 nm region (Xu and Webb, 1996). Two different standards (Rhodamine 6G in methanol and Fluorescein pH11) where used to account for the collection efficiency and excitation pulse characteristics (de Reguardati et al., 2016). The two-photon absorption cross-section was calculated from the following equation:

$$\sigma_2 = \left(\frac{F_2}{\phi C n}\right)_s \left(\frac{\phi C n \sigma_2}{F_2}\right)_{ref}$$

where F_2 stands for two-photon induced fluorescence intensity, Φ is the one-photon excited fluorescence quantum yield, n refers to the refractive index in solution, C is the concentration and s and ref are relative to the sample and the TPA standard used as reference, respectively. The emission intensity dependence on the excitation power was checked to be quadratic as expected for a biphotonic process. The two-photon emission was measured within a narrow wavelength bandwidth centered at 580 nm selected by the H20Vis Jobin Yvon monochromator placed at the entrance of a PMC-100-4 photomultiplyer tube (Becker and Hickl GmbH). The integrated intensity over the entire emission band was extrapolated using the emission spectra corrected by the detector sensitivity.

CD and CPL Measurements

ECD and CPL experiments were carried out in an Olis DSM172 spectrophotometer equipped with a Xe lamp of 150W. The spectra were recorded at 2.5×10^{-5} M concentrations in HPLC grade solvents and at room temperature. For ECD measurements, a fixed slit-width of 1 mm and 0.1 s of integration time were selected and the ECD spectra shown in **Figure 5** and **Figures S7–S9** are average spectra calculated from 30 scans. In CPL measurements, a fixed wavelength by a dual excitation of 402 and 420 nm provided by two LED sources was used. CPL spectra in **Figure 5** and **Figures S7, S8** were collected by averaging 200 scans and with 1s of integration time.

Theoretical Calculations

Geometry calculation of (*R,R*)-**1** was carried out by DFT methods using the Gaussian 09 software (Frisch et al., 2009). The optimizations were carried out at the CAM-B3LYP/6-31G(d,p) theory level for C, H, N, and O atoms in dichloromethane. The solvent was implemented by using the polarizable continuum model with the integral equation formalism (IEFPCM) available in Gaussian 09. Frequency analysis were performed to confirm that the geometries optimized corresponded to energy minima.

DATA AVAILABILITY STATEMENT

All datasets generated for this study are included in the article/**Supplementary Material**.

AUTHOR CONTRIBUTIONS

PR and AO carried out the synthesis and ECD and CPL measurements. EM was responsible for the linear and non-linear optical characterization, in addition to writing and editing tasks. IM performed the optical characterization and corresponding data analysis. AC performed DFT calculations. MR AC, JC, EM, and DM were responsible of the management, methodology, resources and writing—review and editing.

ACKNOWLEDGMENTS

We thank the Ministerio de Ciencia, Innovación y Universidades (PG2018-101181-B-I00), the Ministerio de Economía y Competitividad (CTQ2017-85454-C2-1-P) and the European Research Council (ERC-2015-STG-677023) for financial support. AC and PR also thank MINECO for RyC-2013-12943 and FPU contracts. EM thanks the Fundação para a Ciência e a Tecnologia, POCI and FEDER (PTDC/NAN-MAT/29317/2017, PTDC/QUI-QFI/29319/2017, and UIDB/00100/2020. We thank the UGR CSIRC for access to computational facilities.

SUPPLEMENTARY MATERIAL

The Supplementary Material for this article can be found online at: https://www.frontiersin.org/articles/10.3389/fchem.2020.00306/full#supplementary-material

REFERENCES

Andréassons, J., and Pischel, U. (2018). Molecules for security measures: from keypad locks to advanced communication protocols *Chem. Soc. Rev.* 47, 2266–2279. doi: 10.1039/C7CS00287D

Andres, J., Hersch, R. D., Moser, J. E., and Chauvin, A., S. (2014). A new anti-counterfeiting feature relying on invisible luminescent full color images printed with lanthanide-based inks *Adv. Funct. Mater.* 24:5029. doi: 10.1002/adfm.201400298

Brandt, J. R., Wang, X., Yang, Y., Campbell, A. J., and Fuchter, M. J. (2016). Circularly polarized phosphorescent electroluminescence with a high dissymmetry factor from PHOLEDs based on a platinahelicene. *J. Am. Chem. Soc.* 138, 9743–9746. doi: 10.1021/jacs.6b02463

Burrezo, P. M.;, Jiménez, V. G., Blasi, D., Ratera, I., Campaña, A. G., and Veciana, J. (2019). Organic free radicals as circularly polarized luminescence emitters. *Angew. Chem. Int. Ed.* 58, 16282–16288. doi: 10.1002/anie.201909398

Che, Y., Datar, A., Balakrishnan, K., and Zang, L. (2007). Ultralong nanobelts self-assembled from an asymmetric perylene tetracarboxylic diimide. *J. Am. Chem. Soc.* 129, 7234–7235. doi: 10.1021/ja071903w

Chen, W., Zhang, S., Zhou, M., Zhao, T., Qin, X., Liu, M., et al. (2019). Two-photon absorption-based upconverted circularly polarized luminescence

generated in chiral perovskite nanocrystals. *J. Phys. Chem. Lett.* 10, 3290–3295. doi: 10.1021/acs.jpclett.9b01224

Cruz, C. M., Castro-Fernández, S., Maçôas, E., Cuerva, J. M., and Campaña, A. G. (2018a). Undecabenzo[7]superhelicene: a helical nanographene ribbon as a circularly polarized luminescence emitter. *Angew. Chem. Int. Ed.* 57, 14782–14786. doi: 10.1002/anie.201808178

Cruz, C. M., Márquez, I. R., Castro-Fernández, S., Cuerva, J. M., Maçôas, E., and Campaña, A. G. (2019). A triskelion-shaped saddle–helix hybrid nanographen. *Angew. Chem. Int. Ed.* 58, 8068–8072. doi: 10.1002/anie.201902529

Cruz, C. M., Márquez, I. R., Mariz, I. F. A., Blanco, V., Sánchez-Sánchez, C., Sobrado, J. M., et al. (2018b). Enantiopure distorted ribbon-shaped nanographene combining two-photon absorption-based upconversion and circularly polarized luminescence. *Chem. Sci.* 9, 3917–3924. doi: 10.1039/C8SC00427G

David, A. H. G., Casares, R., Cuerva, J. M., Campaña, A. G., and Blanco, V. (2019). A [2] rotaxane-based circularly polarized luminescence switch. *J. Am. Chem. Soc.* 141, 18064–18074. doi: 10.1021/jacs.9b07143

de Reguardati, S., Pahapill, J., Mikhailov, A., Stepanenko, Y., and Rebane, A. (2016). High-accuracy reference standards for two-photon absorption in the 680-1050 nm wavelength range. *Opt. Exp.* 24, 9053–9066. doi: 10.1364/OE.24.009053

Deng, W. T., Qu, H., Huang, Z.-Y., Shi, L., Tang, Z.-Y., Cao, X.-Y., et al. (2019). Facile synthesis of homochiral compounds integrating circularly polarized luminescence and two-photon excited fluorescence. *Chem. Commun.* 55, 2210–2213. doi: 10.1039/C8CC08947G

Dhbaibi, K., Favereau, L., Srebro-Hooper, M., Quinton, C., Vanthuyne, N., Arrico, L., et al. (2020). Modulation of circularly polarized luminescence through excited-state symmetry breaking and interbranched exciton coupling in helical push–pull organic systems. *Chem. Sci.* 11, 567–576. doi: 10.1039/C9SC05231C

Di Nuzzo, D., Kulkarni, C., Zhao, B., Smolinsky, E., Tassinari, F., Meskers, S. C. J., et al. (2017). Circular polarization of electroluminescence achieved via self-assembly of a light-emitting chiral conjugated polymer into multidomain cholesteric films. *ACS Nano* 11, 12713–12722. doi: 10.1021/acsnano.7b07390

Frisch, M. J., Trucks, G. W., Schlegel, H. B., Scuseria, G. E., Robb, M. A., Cheeseman, J. R., et al. (2009). Gaussian 09 Revision D.01. Wallingford, CT: Gaussian Inc.

Gershberg, J., Fennel, F., Rehm, T. H., Lochbrunner, S., and Wurthner, F. (2016). Anti-cooperative supramolecular polymerization: a new K_2-K model applied to the self-assembly of perylene bisimide dye proceeding via well-defined hydrogen-bonded dimers. *Chem. Sci.* 7, 1729–1737. doi: 10.1039/C5SC03759J

Han, J., Guo, S., Lu, H., Liu, S., Zhao, Q., and Huang, W. (2018). Recent progress on circularly polarized luminescent materials for organic optoelectronic devices. *Adv. Opt. Mater.* 6:1800538. doi: 10.1002/adom.201800538

Han, J., Yang, D., Jin, X., Jiang, Y., Liu, M., and Duan, P. (2019). Enhanced circularly polarized luminescence in emissive charge-transfer complexes. *Angew. Chem. Int. Ed.* 58, 7013–7019. doi: 10.1002/anie.201902090

Hara, N., Okuda, K., Shizuma, M., Tajima, N., and Imai, Y. (2019). Control of circularly polarised luminescence using a suitable wired structure connecting a binaphthyl with two pyrenes. *Chem. Select* 4, 10209–10213. doi: 10.1002/slct.201902176

Hashimoto, Y., Nakashima, T., Shimizu, D., and Kawai, T. (2016). Photoswitching of an intramolecular chiral stack in a helical tetrathiazole. *Chem. Commun.* 52, 5171–5174. doi: 10.1039/C6CC01277A

He, G. S., Tan, L. S., Zheng, Q., and Prasad, P. N. (2008). Multiphoton absorbing materials: molecular designs, characterizations, and applications. *Chem. Rev.* 4, 1245–1330. doi: 10.1021/cr050054x

Ikeda, T., Masuda, T., Hirao, T., Yuasa, J., Tsumatori, H., Kawai, T., et al. (2012). Circular dichroism and circularly polarized luminescence triggered by self-assembly of tris(phenylisoxazolyl)benzenes possessing a perylenebisimide moiety. *Chem. Commun.* 48, 6025–6027. doi: 10.1039/C2CC31512B

Imai, Y., Nakano, Y.;, Kawai, T., and Yuasa, J. (2018). A smart sensing method for object identification using circularly polarized luminescence from coordination-driven self-assembly. *Angew. Chem. Int. Ed.* 57, 8973–8978. doi: 10.1002/anie.201803833

Ito, H., Sakai, H., Okayasu, Y., Yuasa, J., Mori, T., and Hasobe, T. (2018). Significant enhancement of absorption and luminescence dissymmetry factors in the far-red region: a Zinc(II) homoleptic helicate formed by a pair of achiral dipyrromethene ligands. *Chem. Eur. J.* 24, 16889–16894. doi: 10.1002/chem.201804171

Ito, S., Ikeda, K., Nakanicshi, S., Imai, Y., and Asami, M. (2017). Concentration-dependent circularly polarized luminescence (CPL) of chiral N,N′-dipyrenyldiamines: sign-inverted CPL switching between monomer and excimer regions under retention of the monomer emission for photoluminescence. *Chem. Commun.* 53, 6323–6326. doi: 10.1039/C7CC01351E

Jiménez, J.-R., Doistau, B., Cruz, C. M., Besnard, C., Cuerva, J. M., Campaña, A. G., et al. (2019). Chiral molecular ruby [Cr(dqp)2]3+ with long-lived circularly polarized luminescence. *J. Am. Chem. Soc.* 141, 13244–13252. doi: 10.1021/jacs.9b06524

Kawai, T., Kawamura, K., Tsumatori, H., Ishikawa, M., Naito, M., Fujiki, M., et al. (2007). Circularly polarized luminescence of a fluorescent chiral binaphtylene-perylenebiscarboxydiimide dimer. *ChemPhysChem* 8, 1465–1468. doi: 10.1002/cphc.200600747

Keshri, S. K., Takai, A., Ishizuka, T., Kojima, T., and Takeuchi, M. (2020). Conformational dynamics of monomer- versus dimer-like features in a naphthalenediimide-based conjugated cyclophane. *Angew. Int. Ed. Chem.* 59:5407. doi: 10.1002/anie.201914414

Kumar, J., Nakashima, T., and Kawai, T. (2015). Circularly polarized luminescence in chiral molecules and supramolecular assemblies. *J. Phys. Chem. Lett.,* 2015, 6, 3445–3452. doi: 10.1021/acs.jpclett.5b01452

Langhals, H. (2005). Control of the interactions in multichromophores: novel concepts. Perylene Bis-imides as Components for Larger Functional Units. *Helv. Chim. Acta* 88, 1309–1343. doi: 10.1002/hlca.200590107

Lecoq, J., Orlova, N., and Grewe, B. F. (2019). Wide. Fast. Deep: recent advances in multiphoton microscopy of *in vivo* neuronal activity. *J. Neurosci.* 39, 9042–9052. doi: 10.1523/JNEUROSCI.1527-18.2019

Li, M., Li, S.-H., Zhang, D., Cai, M., Duan, L., Fung, M.-K., et al. (2018). Stable enantiomers displaying thermally activated delayed fluorescence: efficient OLEDs with circularly polarized electroluminescence. *Angew. Chem. Int. Ed.* 57, 2889–2893. doi: 10.1002/anie.201800198

Liang, X., Liu, T. T., Yan, Z.-P., Zhou, Y., Su, J., Luo, X.-F., et al. (2019). Organic room-temperature phosphorescence with strong circularly polarized luminescence based on paracyclophanes. *Angew. Chem. Int. Ed.* 58, 17220–17225. doi: 10.1002/anie.201909076

Longhi, G., Castiglioni, E., Koshoubu, J., Mazzeo, G., and Abbate, S. (2016). Circularly polarized luminescence: a review of experimental and theoretical aspects. *Chirality* 28, 696–707. doi: 10.1002/chir.22647

Marcelo, G., Pinto, S., Cañeque, T., Mariz, I. F. A., Cuadro, A. M., Vaquero, J. J., et al. (2015). Nonlinear emission of quinolizinium-based dyes with application in fluorescence lifetime imaging. *J. Phys. Chem. A* 119, 2351–2362. doi: 10.1021/jp507095b

Mariz, I. F. A., Siopa, F., Rodrigues, C. A. B., Afonso, C. A. M., Chen, X., Martinho, J. M. G., et al. (2015). A 1,3,5-triazine based polymer as a nonlinear near-infrared antenna for two-photon activated volumetric optical memory devices. *J. Mater. Chem. C,* 3, 10775–10782. doi: 10.1039/C5TC02085A

Morisaki, Y., Gon, M., Sasamori, T., Tokitoh, N., and Chujo, Y. (2014). Planar chiral tetrasubstituted [2.2]paracyclophane: optical resolution and functionalization. *J. Am. Chem. Soc.* 136, 3350–3353. doi: 10.1021/ja412197j

Ohishi, Y., and Inouye, M. (2019). Circularly polarized luminescence from pyrene excimers. *Tetrahedron Lett.* 60:151232. doi: 10.1016/j.tetlet.2019.151232

Pagoaga, B., Mongin, O., Caselli, M., Vanossi, D., Momicchioli, F., Blanchard-Desce, M., et al. (2016). Optical and photophysical properties of anisole- and cyanobenzene-substituted perylene diimides. *Phys. Chem. Chem. Phys.* 18, 4924–4941. doi: 10.1039/C5CP07758C

Park, G. E., Choi, S., Lee, D. H., Godumala, M., Uddin, M. A., Woo, H. Y., et al. (2017). Perylene diimide isomers containing a simple sp3-core for non-fullerene-based polymer solar cells. *J. Mat. Chem. A* 5, 663–771. doi: 10.1039/C6TA09394A

Pop, F., Zigon, N., and Avarvari, N. (2019). Main-group-based electro- and photoactive chiral materials. *Chem. Rev.* 119, 8435–8478. doi: 10.1021/acs.chemrev.8b00770

Reine, P., Campaña, A. G., Álvarez de Cienfuegos, L., Blanco, V., Mota, A. J., Longhi, G., et al. (2019). Chiral double stapled o-OPEs with intense circularly polarized luminescence. *Chem. Commun.* 55, 10685–10688. doi: 10.1039/C9CC04885E

Reine, P., Justicia, J., Morcillo, S. P., Abbate, S., Vaz, B., Ribagorda, M., et al. (2018a). Pyrene-Containing *ortho*-Oligo(phenylene)ethynylene foldamer as a ratiometric probe based on circularly polarized luminescence. *J. Org. Chem.* 83, 4455–4463. doi: 10.1021/acs.joc.8b00162

Reine, P., Ortuño, A. M., Resa, S., Álvarez de Cienfuegos, L., Blanco, V., Ruedas-Rama, M. J., et al. (2018b). OFF/ON switching of circularly polarized luminescence by oxophilic interaction of homochiral sulfoxide-containing *o*-OPEs with metal cations. *Chem. Commun.* 54, 13985–13988. doi: 10.1039/C8CC08395A

Riehl, J. P., and Richardson, F. S. (1977). Circularly polarized luminescence spectroscopy. *Chem. Rev.*, 77, 773–792.

Salerno, F., Berrocat, J. A., Haedler, A. T., Zinna, F., Meijer, E. W., and di Bari, L. (2017). Highly circularly polarized broad-band emission from chiral naphthalene diimide-based supramolecular aggregates. *J. Mat. Chem. C* 5, 3609–3615. doi: 10.1039/C7TC00281E

Sanchez-Carnerero, E. M., Agarrabeitia, A. R., Moreno, F., Maroto, B. L., Muller, G., Ortiz, M. J., et al. (2015). Circularly polarized luminescence from simple organic molecules. *Chem. Eur. J.* 21, 13488–13500. doi: 10.1002/chem.201501178

Santos, C. I. M., Mariz, I. F. A., Pinto, S. N., Goncalves, G., Bdikin, I., and Marques, P. (2018). Selective two-photon absorption in carbon dots: a piece of the photoluminescence emission puzzle. *Nanoscale* 10, 12505–12514.doi: 10.1039/C8NR03365J

Sato, S., Yoshii, A., Takahashi, S., Furumi, S., Takeuchi M., and Isobe, H. (2017). Chiral intertwined spirals and magnetic transition dipole moments dictated by cylinder helicity. *Proc. Nat. Acad. Sci. U.S.A.* 114, 13097–13101. doi: 10.1073/pnas.1717524114

Schaack, C., Arico, L., Sidler, E., Góreki, M., Di Bari, L., and Diederich, F. (2019). Helicene monomers and dimers: chiral chromophores featuring strong circularly polarized luminescence. *Chem. Eur. J.* 25, 8003–8007. doi: 10.1002/chem.201901248

Shi, Y., Duan, P., Huo, S., Li, Y., and Liu, M. (2018). Endowing perovskite nanocrystals with circularly polarized luminescence. *Adv. Mater.* 30:1705011. doi: 10.1002/adma.201705011

Staszak, K., Wieszczycka, K., Marturano, V., and Tylkowski, B. (2019). Lanthanides complexes – Chiral sensing of biomolecules. *Coord. Chem. Rev.* 397, 76–90. doi: 10.1016/j.ccr.2019.06.017

Takaishi, K., Iwachido, K., and Ema, T. (2020). Solvent-induced sign inversion of circularly polarized luminescence: control of excimer chirality by hydrogen bonding. *J. Am. Chem. Soc.* 142, 1774–1779. doi: 10.1021/jacs.9b13184

Takaishi, K., Iwachido, K., Takehana, R., Uchiyama, M., and Ema, T. (2019). Evolving fluorophores into circularly polarized luminophores with a chiral naphthalene tetramer: proposal of excimer chirality rule for circularly polarized luminescence. *J. Am. Chem. Soc.* 141, 6185–6190. doi: 10.1021/jacs.9b02582

Takaishi, K., Takehana, R., and Ema, T. (2018). Intense excimer CPL of pyrenes linked to a quaternaphthyl. *Chem. Commun.* 54, 1449–1452. doi: 10.1039/C7CC09187G

Tanaka, H., Inoue, Y., and Mori, T. (2018). Circularly polarized luminescence and circular dichroisms in small organic molecules: correlation between excitation and emission dissymmetry factors. *ChemPhotoChem.* 2, 386–402. doi: 10.1002/cptc.201800015

Tsumatori, H., Nakashima, T., and Kawai, T. (2010). Observation of chiral aggregate growth of perylene derivative in opaque solution by circularly polarized luminescence. *Org. Lett.* 12, 2362–2365. doi: 10.1021/ol100701w

Wang, J., Zhuang, G., Chen, M., Lu, D., Li, Z., Huang, Q., et al. (2020). Selective synthesis of conjugated chiral macrocycles: sidewall segments of (–)/(+)-(12,4) carbon nanotubes with strong circularly polarized luminescence. *Angew. Chem. Int. Ed.* 59, 1619–1626. doi: 10.1002/anie.201909401

Wang, Y.-F., Lu, H.-Y., Chen, C., Li, M., and Chen, C.-F. (2019). 1,8-Naphthalimide-based circularly polarized TADF enantiomers as the emitters for efficient orange-red OLEDs. *Org. Electron.* 70, 71–77. doi: 10.1016/j.orgel.2019.03.020

Wurthner, F., Saha-Moller, C. R., Fimmel, B., Ogi, S., Leowanawat, P., and Schmidt, D. (2016). Perylene bisimide dye assemblies as archetype functional supramolecular materials. *Chem. Rev.* 116, 962–1052. doi: 10.1021/acs.chemrev.5b00188

Xu, C., and Webb, W. W. (1996). Measurement of two-photon excitation cross sections of molecular fluorophores with data from 690 to 1050 nm. *J. Opt. Soc. Am. B* 13, 481–491. doi: 10.1364/JOSAB.13.000481

Yang, G., and Zhong, H. (2019). Multi-dimensional quantum nanostructures with polarization properties for display applications. *Isr. J. Chem.* 59, 639–648. doi: 10.1002/ijch.201900001

Zheng, D., Zheng, L., Yu, C., Zhan, Y., Wang, Y., and Jiang, H. (2019). Significant enhancement of circularly polarized luminescence dissymmetry factors in quinoline oligoamide foldamers with absolute helicity. *Org. Lett.* 21, 2555–2559. doi: 10.1021/acs.orglett.9b00450

Zheng, H., Li, W., Li, W., Wang, X., Tang, Z., Zhang, S., et al. (2018). Uncovering the circular polarization potential of chiral photonic cellulose films for photonic applications. *Adv. Mater.* 30:1705948. doi: 10.1002/adma.201705948

Zinna, F., Giovanella, U., and Di Bari, L. (2015). Highly circularly polarized electroluminescence from a chiral europium complex. *Adv. Mater.* 27:1719. doi: 10.1002/adma.201404891

Zinna, F., Voci, S., Arrico, L., Brun, E., Homberg, A., Bouffier, L., et al. (2019). Circularly-polarized electrochemiluminescence from a chiral bispyrene organic macrocycle. *Angew. Chem. Int. Ed.* 58, 6952–6956. doi: 10.1002/anie.201901303

Zou, L., Liu, Y., Ma, N., Macoas, E., Martinho, J. M. G., Pettersson, M., et al. (2011). Synthesis and photophysical properties of hyperbranched polyfluorenes containing 2,4,6-tris(thiophen-2-yl)-1,3,5-triazine as the core. *Phys. Chem. Chem. Phys.* 13, 8838–8846. doi: 10.1039/C0CP03014G

Conflict of Interest: The authors declare that the research was conducted in the absence of any commercial or financial relationships that could be construed as a potential conflict of interest.

The handling Editor declared a past co-authorship with several of the authors PR, MR, JC, AC, and DM.

frontiers in Chemistry

ORIGINAL RESEARCH
published: 24 April 2020
doi: 10.3389/fchem.2020.00303

Enhanced Circularly Polarized Luminescence Activity in Chiral Platinum(II) Complexes With Bis- or Triphenylphosphine Ligands

Qian-Ying Yang, Hua-Hong Zhang, Xue-Ling Han, Shi-Dao Weng, Yuan Chen, Jia-Li Wu, Li-Zhi Han, Xiao-Peng Zhang and Zai-Feng Shi*

Key Laboratory of Water Pollution Treatment & Resource Reuse of Hainan Province, College of Chemistry and Chemical Engineering, Hainan Normal University, Haikou, China

Distinct circularly polarized luminescence (CPL) activity was observed in chiral (C^N^N)Pt(II) [(C^N^N) = 4,5-pinene-6′-phenyl-2,2′-bipyridine] complexes with bis- or triphenylphosphine ligands. Compared to the pseudo-square-planar geometry of chiral (C^N^N)Pt(II) complexes with chloride, phenylacetylene (PPV) and 2,6-dimethylphenyl isocyanide (Dmpi) ligands, the coordination configuration around the Pt(II) nucleus of chiral (C^N^N)Pt(II) complexes with bulk phosphine ligands is far more distorted. The geometry is straightforwardly confirmed by X-ray crystallography. The phosphines' participation enhanced the CPL signal of Pt(II) complexes profoundly, with the dissymmetry factor (g_{lum}) up to 10^{-3}. The distorted structures and enhanced chiroptical signals were further confirmed by time-dependent density functional theory (TD-DFT) calculations.

Keywords: circularly polarized luminescence, platinum(II) complexes, phenylphosphine ligands, chiral enhancement, crystal structures

OPEN ACCESS

Edited by:
Tao Wu,
Institute of Organic Chemistry and Biochemistry (ASCR), Czechia

Reviewed by:
Francesco Zinna,
University of Pisa, Italy
Cheng-Hui Li,
Nanjing University, China

****Correspondence:***
Xiao-Peng Zhang
zxp_inorganic@126.com

Specialty section:
This article was submitted to Physical Chemistry and Chemical Physics, a section of the journal Frontiers in Chemistry

Received: *21 February 2020*
Accepted: *26 March 2020*
Published: *24 April 2020*

Citation:
Yang Q-Y, Zhang H-H, Han X-L, Weng S-D, Chen Y, Wu J-L, Han L-Z, Zhang X-P and Shi Z-F (2020) Enhanced Circularly Polarized Luminescence Activity in Chiral Platinum(II) Complexes With Bis- or Triphenylphosphine Ligands. Front. Chem. 8:303. doi: 10.3389/fchem.2020.00303

INTRODUCTION

Circularly polarized luminescence (CPL) materials have attracted considerable attention because of their enormous potential in 3D displays (Zinna et al., 2015; Song F. et al., 2018; Zhang et al., 2020), quantum information (Wagenknecht et al., 2010), chiroptical sensors (Carr et al., 2012; Guo et al., 2019; Wu et al., 2019), photodetectors (Yang et al., 2013; Chen C. et al., 2019) and anti-counterfeiting security (Yang et al., 2020; Yu et al., 2020). Especially these phosphorescent transition metal complexes, which have remarkable metal-center chirality, tunable emission properties, and unusually high phosphorescence efficiency, are receiving increasing interests in recent years (Han et al., 2018). Such CPL-active materials as Pt (Shen et al., 2014), Ir (Han et al., 2017; Hellou et al., 2017; Yan et al., 2019a), Au (Yang et al., 2020; Zhu et al., 2020), Cu (Jin et al., 2019; Deng et al., 2020; Yao et al., 2020), Zn (Aoki et al., 2017; Chen Y. et al., 2019) Cd (Deng et al., 2019), and Cr (Jiménez et al., 2019) complexes can exhibit various emission colors from blue to red. The dissymmetry factor g_{lum} ($g_{lum} = 2\Delta I/I = 2(I_L - I_R)/(I_L + I_R)$, where I_L and I_R indicate, respectively, the intensity of the left and right circularly polarized light), can reach up to 10^{-2} order. Furthermore, the rotatory strength of the transition probably leading to CPL activity can be distinctly enhanced by the spin–orbit coupling (SOC) effect of transition metals (Gendron et al., 2019). Therefore, those chiral luminescent complexes containing heavy metal atoms are likely to show a polarized emission.

Phosphorescent CPL-active Pt(II) complexes are known for their high emission quantum yield and large g_{lum} values, and they hold promise for use in novel optoelectronic devices. To obtain more efficient CPL materials, helicene skeleton (Shen et al., 2014; Biet et al., 2017), 1,1′-binaphthyls (Song J. et al., 2018; Song et al., 2019; Jiang et al., 2020), and other moieties were incorporated into phosphorescent Pt(II) systems, and a distinct enhancement in the phosphorescence and g_{lum} value can be reached. Chiral-at-metal phosphorescent Pt(II) complexes have been prepared by utilizing *trans*-spanning bipyridyl (Schulte et al., 2017) and substituted (2-thienyl)pyridine ligands (Usuki et al., 2019), displaying strong spectral responses both in circular dichroism (CD) and CPL. In addition, due to their square-planar geometry, molecules of Pt(II) complexes can form helical assemblies *via* Pt···Pt, $\pi-\pi$ stacking, and hydrophobic–hydrophobic interactions, with a high dissymmetry factor (g_{lum}) of 10^{-2} order (Ikeda et al., 2015, 2018; Zhang et al., 2015a; Tanaka et al., 2016; Park et al., 2019). More intriguingly, circularly polarized organic light-emitting phosphorescent diodes (CP-PHOLEDs) have been fabricated by using chiral Pt(II) complexes as the emitting layer, showing a display level brightness and a high g_{lum} factor (Brandt et al., 2016; Fu et al., 2019; Yan et al., 2019b).

In a previous work, two couples of chiral dinuclear Pt(II) complexes, [(−)-(C^N^N)Pt]$_2$dppmCl$_2$ (−)-**1** and [(+)-(C^N^N)Pt]$_2$dppmCl$_2$ (+)-**1**, (−)-(C^N^N)Pt]$_2$dppeCl$_2$ (−)-**2,** and [(+)-(C^N^N)Pt]$_2$dppeCl$_2$ (+)-**2**, linked by bis(diphenylphosphino)methane (dppm) and bis(diphenylphosphino)ethane (dppe), were prepared (**Scheme 1**). Distinct CPL signals triggered by an intramolecular Pt···Pt interaction (Zhang et al., 2018) were observed. In this work, new chiral Pt(II) complexes with longer bridging ligands, [bis(diphenylphosphino)propane (dppp), bis(diphenylphosphino)butane (dppb), bis(diphenylphosphino)pentane (dpppe), and bis(diphenylphosphino)hexane (dpph)], were prepared and characterized by single-crystal X-ray crystallography. Comparisons of the chiroptical spectra to the precursors and impactors on CPL enhancement were presented.

RESULTS AND DISCUSSION

Synthesis

The precursors mononuclear complexes (−)-(C^N^N)PtCl and (+)-(C^N^N)PtCl were prepared according to previous procedures (Zhang et al., 2014, 2015b). The target dinuclear and mononuclear Pt(II) complexes have been facilely synthesized though the coordination reaction between different phosphine ligands and precursors in the proper proportion at room temperature (**Scheme 1**). The new obtained complexes were fully characterized by NMR and MS spectra. The preparation of their enantiomers was done using the same procedure.

Synthesis of [(−)-(C^N^N)Pt]$_2$dpppCl$_2$, (− p3

Under an argon atmosphere, a solution (30/10 ml CH_2Cl_2/CH_3OH) of (−)-(C^N^N)PtCl (278 mg, 0.50 mmol) and dppp (103 mg, 0.25 mmol) was stirred at room temperature for 12 h. Then, the solvent was removed under reduced pressure. The residue was washed with *n*-hexane and was further purified by recrystallization in chloroform. Lastly, green-yellow powders were obtained (65%). MS (electrospray ionization, ESI) (*m*/*z*): $[M]^{2+}$ Calcd. for $C_{73}H_{68}N_4P_2Pt_2$, 725.7; found, 726.4. Anal. Calcd. for $C_{73}H_{68}N_4P_2Pt_2Cl_2$ [(−)-**3**]: C, 57.52; H, 4.50; N, 3.68%. Found: C, 57.54; H, 4.48; N, 3.67%. ^{1}H NMR (400 MHz, $CDCl_3$, 298 K): δ 8.48 (s, 4H), 8.38 (s, 2H), 7.66–7.80 (m, 10H), 7.35 (m, 10H), 7.28 (t, J = 7.2 Hz, 2H), 7.11 (d, J = 7.2 Hz, 2H), 6.57 (t, J = 7.2 Hz, 2H), 6.38 (d, J = 7.2 Hz, 2H), 6.30 (t, J = 7.2 Hz, 2H), 6.04 (s, 2H), 3.13 (d, J = 14.0 Hz, 4H), 2.87 (m, 6H), 2.57 (m, 2H), 2.27 (m, 2H), 1.89 (m, 2H), 1.30 (s, 6H), 0.95 (d, J = 10.0 Hz, 2H), 0.43 (s, 6H). ^{13}C NMR (100 MHz, $CDCl_3$, 298 K): δ 162.8, 156.5, 153.8, 150.6, 147.7, 147.1, 146.6, 143.9, 137.5, 135.4, 133.5, 133.4, 133.3, 131.5, 131.0, 130.7, 130.4, 130.1, 129.5, 129.4, 129.2, 129.1, 125.4, 124.5, 120.8, 119.8, 45.3, 39.4, 39.0, 33.5, 31.2, 29.8, 27.5, 25.8, 21.4.

Synthesis of [(−)-(C^N^N)Pt]$_2$dppbCl$_2$, (− b4

The synthesis method was the same as the one used in preparing (−)-**3**, but replacing dppp with dppb. The product yield was 65%. MS (ESI) (*m*/*z*): $[M]^{2+}$ Calcd. for $C_{74}H_{70}N_4P_2Pt_2$, 732.7; found, 733.4. Anal. Calcd. for $C_{74}H_{70}N_4P_2Pt_2Cl_2$ [(−)-**4**]: C, 57.77; H, 4.59; N, 3.64%. Found: C, 57.76; H, 4.59; N, 3.62%. ^{1}H NMR (400 MHz, $CDCl_3$, 298 K): δ 8.41 (d, 2H, J = 8.0 Hz, 2H), 8.32 (s, 2H), 8.29 (t, J = 8.0 Hz, 2H), 7.65–7.75 (m, 10H), 7.32–7.41 (m, 10H), 7.28–7.31 (m, 4H), 6.75 (t, J = 7.2 Hz, 2H), 6.41 (t, J = 8.0 Hz, 2H), 6.38 (t, J = 8.0 Hz, 2H), 6.10 (s, 2H), 3.11 (d, J = 16.0 Hz, 4H), 2.82 (m, 2H), 2.59 (m, 6H), 2.29 (m, 2H), 1.92 (t, J = 5.2 Hz, 4H), 1.31 (s, 6H), 1.03 (d, J = 9.6 Hz, 2H), 0.44 (s, 6H). ^{13}C NMR (100 MHz, $CDCl_3$, 298 K): δ 163.2, 156.5, 154.2, 150.7, 147.3, 146.7, 146.5, 143.5, 137.4, 135.7, 133.7, 133.6, 133.1, 133.0, 131.6, 131.4, 130.9, 130.3, 129.6, 129.5, 129.2, 129.1, 125.6, 125.5, 124.6, 120.7, 119.9, 45.4, 39.5, 39.1, 33.5, 31.2, 29.9, 27.9, 25.9, 24.6, 21.5.

Synthesis of [(−)-(C^N^N)Pt]$_2$dpppeCl$_2$, (− p5

The synthesis method was the same as the one used in preparing (−)-**3**, but replacing dppp with dpppe. The product yield was 60%. MS (ESI) (*m*/*z*): $[M]^{2+}$ Calcd. for $C_{75}H_{72}N_4P_2Pt_2$, 739.7; found, 740.5. Anal. Calcd. for $C_{75}H_{72}N_4P_2Pt_2Cl_2$ [(−)-**5**]: C, 58.03; H, 4.67; N, 3.61%. Found: C, 58.06; H, 4.65; N, 3.59%. ^{1}H NMR (400 MHz, $CDCl_3$, 298 K): δ 8.64 (s, 2H), 8.62 (d, J = 8.0 Hz, 2H), 8.28 (t, J = 8.0 Hz, 2H), 7.81 (d, J = 8.0 Hz, 2H), 7.62–7.73 (m, 8H), 7.54 (m, 2H), 7.40–7.49 (m, 12H), 6.98 (t, J = 7.2 Hz, 2H), 6.73 (t, J = 7.2 Hz, 2H), 6.59 (d, J = 7.2 Hz, 2H), 6.13 (s, 2H), 3.14 (d, J = 14.0 Hz, 4H), 2.67 (m, 4H), 2.53 (m, 2H), 2.25–2.30 (m, 4H), 1.95 (m, 4H), 1.88 (t, J = 4.4 Hz, 2H), 1.29 (s, 6H), 0.96 (d, J = 10.0 Hz, 2H), 0.46 (s, 6H). ^{13}C NMR (100 MHz, $CDCl_3$, 298 K): δ 163.3, 156.7, 154.5, 151.3, 148.3, 147.5, 146.6, 143.4, 137.1, 135.2, 133.8, 133.7, 133.6, 132.1, 131.9, 131.1, 130.4, 129.8, 129.6, 129.5, 129.4, 125.9, 125.6, 125.1, 121.1, 119.5, 45.5, 39.4, 39.1, 33.5, 31.1, 29.8, 27.2, 26.4, 25.9, 21.6.

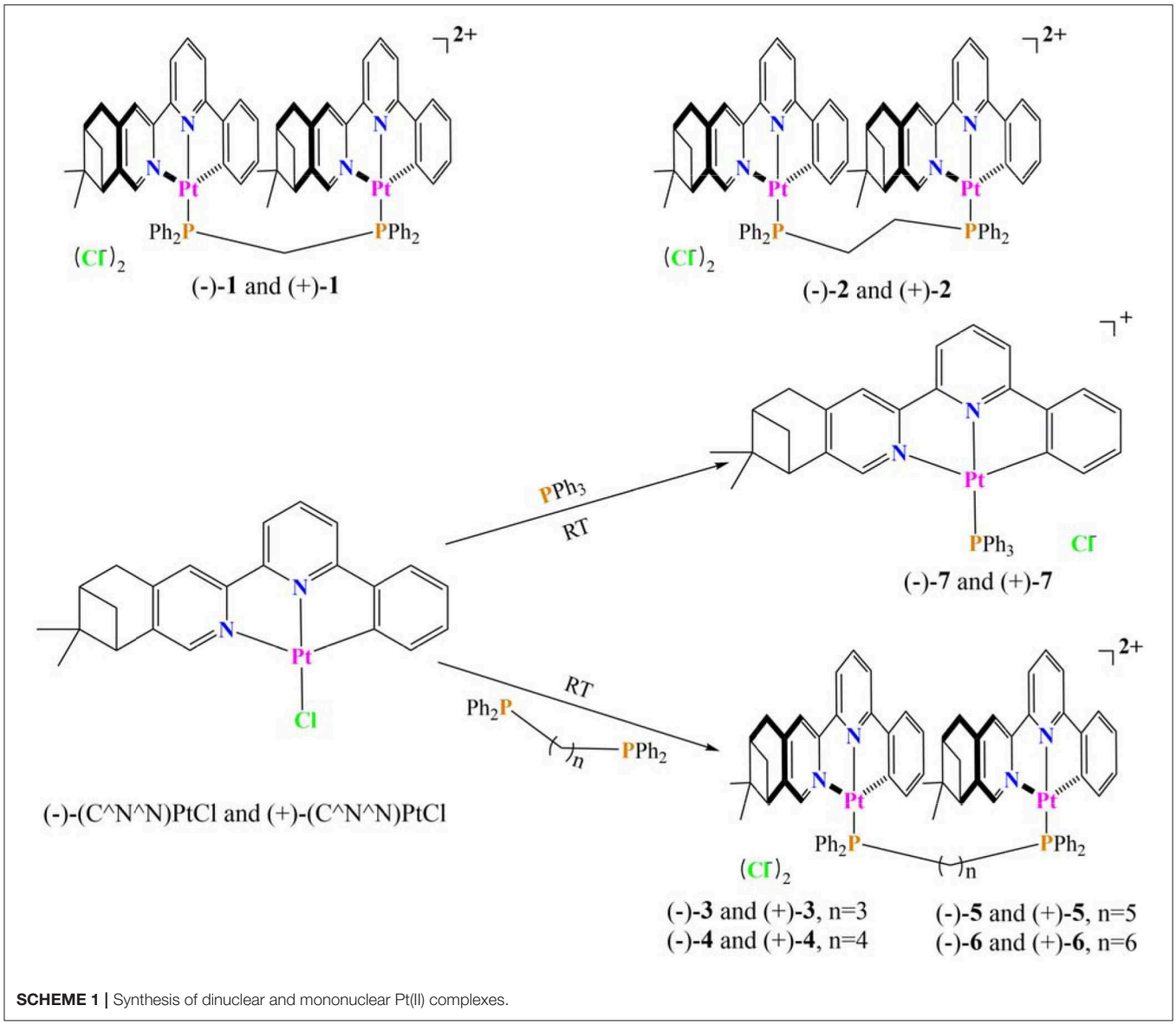

SCHEME 1 | Synthesis of dinuclear and mononuclear Pt(II) complexes.

Synthesis of [(–)-(C^N^N)Pt]$_2$dpphCl$_2$, (– h6

The synthesis method was the same as the one used in preparing (–)-**3**, but replacing dppp with dpph. The product yield was 60%. MS (ESI) (*m*/*z*): $[M]^{2+}$ Calcd. for $C_{76}H_{74}N_4P_2Pt_2$, 746.7; found, 747.5. Anal. Calcd. for $C_{76}H_{74}N_4P_2Pt_2Cl_2$ [(–)-**6**]: C, 58.27; H, 4.76; N, 3.58%. Found: C, 57.28; H, 4.74; N, 3.57%. ^{1}H NMR (400 MHz, $CDCl_3$, 298 K): δ 8.66 (s, 2H), 8.63 (d, J = 8.0 Hz, 2H), 8.27 (t, J = 8.0 Hz, 2H), 7.76 (t, J = 8.0 Hz, 6H), 7.69 (t, J = 8.0 Hz, 4H), 7.53 (m, 4H), 7.45 (m, 10H), 7.03 (t, J = 7.2 Hz, 2H), 6.81 (t, J = 7.2 Hz, 2H), 6.62 (d, J = 7.2 Hz, 2H), 6.19 (s, 2H), 3.16 (d, J = 14.0 Hz, 4H), 2.72 (m, 2H), 2.58 (m, 8H), 2.26 (m, 2H), 1.90 (t, J = 4.4 Hz, 6H), 1.30 (s, 6H), 0.99 (d, J = 9.6 Hz, 2H), 0.49 (s, 6H). ^{13}C NMR (100 MHz, $CDCl_3$, 298 K): δ 163.3, 156.7, 154.5, 151.3, 148.2, 147.5, 146.6, 143.3, 137.1, 135.3, 133.7, 133.6, 133.5, 132.0, 131.9, 131.2, 130.4, 129.8, 129.6, 129.5, 129.4, 129.3, 125.8, 125.5, 125.0, 121.0, 119.3, 45.4, 39.4, 39.0, 33.4, 31.0, 30.5, 27.1, 26.9, 25.9, 21.5.

Synthesis of (–of C^N^N)PtPPh$_3$Cl, (– P7

The synthesis method was the same as the one used in preparing (–)-**3**, but replacing dppp with triphenylphosphine (PPh_3), and the molar ratio of (–)-(C^N^N)PtCl to PPh_3 is 1:1. The product yield was 70%. MS (ESI) (*m*/*z*): $[M]^+$ Calcd. for $C_{41}H_{36}N_2PPt$, 782.2; found, 782.9. Anal. Calcd. for $C_{41}H_{36}N_2PPtCl$ [(–)-**7**]: C, 60.18; H, 4.43; N, 3.42%. Found: C, 60.20; H, 4.41; N, 3.41%. ^{1}H NMR (400 MHz, $CDCl_3$, 298 K): δ 8.86 (s, 1H), 8.81 (d, J = 8.0 Hz, 1H), 8.32 (t, J = 8.0 Hz, 1H), 7.87 (dd, J_1 = 12.0 Hz, J_2 = 7.2 Hz, 6H), 7.78 (d, J = 8.0 Hz, 1H), 7.58 (td, J_1 = 7.2 Hz, J_2 = 2.0 Hz, 3H), 7.49 (td, J_1 = 7.2 Hz, J_2 = 2.0 Hz, 7H), 7.02 (t, J = 7.2 Hz, 1H), 6.62 (t, J = 7.2 Hz, 1H), 6.43 (d, J = 8.0 Hz, 1H), 6.06 (s, 1H), 3.20 (d, J = 18.8 Hz, 2H), 2.53–2.59 (m, 1H), 2.28

(m, 1H), 1.91 (t, $J = 5.2$ Hz, 1H), 1.33 (s, 3H), 1.01 (d, $J = 9.6$ Hz, 1H), 0.49 (s, 3H). ^{13}C NMR (100 MHz, $CDCl_3$, 298 K): δ 163.5, 156.9, 156.8, 154.6, 151.5, 148.1, 147.4, 146.0, 143.5, 138.9, 135.7, 135.6, 134.8, 134.7, 132.2, 132.1, 130.8, 129.5, 129.3, 129.2, 128.9, 128.7, 128.6, 125.8, 125.5, 125.1, 121.3, 119.2, 119.1, 45.8, 39.4, 39.1, 33.4, 31.1, 26.0, 21.6.

Crystal Structures

Suitable crystals (–)-**4** and (–)-**7** for X-ray analysis were obtained by the interface diffusion of *n*-hexane into the mixed dichloromethane/acetone (V/V = 1:2) solution of respective compounds at 273 K. Although single crystals of (–)-**3** could not be obtained, green-yellow blocks of (–)-**3**-OTf were isolated *via* the same interface diffusion, where Cl^- was substituted by OTf^- through counterion metathesis. The crystal structure of (–)-**3**-OTf falls in the *P*1 space group of the triclinic system (**Table 1**), and only one enantiomer molecule is included in the asymmetrical unit (**Figure 1**). Whereas, both complexes (–)-**4** and (–)-**7** crystallize in the monoclinic space group $P2_1$ with two separated molecules in the asymmetrical unit (**Figure 1** and **Table 1**). The Flack values of (–)-**3**-OTf, (–)-**4**, and (–)-**7** are −0.018(8), −0.022(7), and −0.017(6), respectively, confirming the absolute configuration of the molecules.

In the crystal structures of (–)-**3**-OTf, (–)-**4**, and (–)-**7**, Pt–N (1.98–2.17 Å), distance is slightly larger than the Pt–C (1.97–2.04 Å) bond, similar to the previously reported bond lengths of analogous Pt(II) complexes (**Table S1**) (Lu et al., 2002, 2004; Shao and Sun, 2007; Zhang et al., 2018). The Pt–P (2.23–2.26 Å) bond is also consistent with that in phosphino Pt(II) complexes. In the structure of complex (–)-**3**-OTf, the angles N2–Pt1–C1 (158.8(2)°) and N4–Pt2–C2 (158.7(3)°) deviate substantially from linearity due to the chelate ring strain (**Table S2**). Interestingly, the N1–Pt1–P1 [176.10(16)°] and N3–Pt2–P2 [173.60(15)°] angles are also slightly distorted from linearity. Even then, the angle N3–Pt2–P2 is found at 168.75(17)° in the crystal structure of (–)-**4** (**Table S2**), which is much smaller than the reported values in pinene-containing (C^N^N)PtCl, (C^N^N)PtPPV, and (C^N^N)PtDmpi complexes (Zhang et al., 2014, 2015a,b, 2016). In addition, the torsion angles between the benzene plane and lateral pyridine plane of C^N^N ligands have been examined, as shown in **Table S3**, and the angles range from 1.3 to 14.5°. It can be inferred that the Pt(II) cation situates in a more distorted square-planar coordination environment in the phosphino-coordinating system.

As shown in **Figure 1**, two $[(-)\text{-}(C^N^N)Pt]^+$ segments bridged by the dppp ligand in (–)-**3**-OTf are arranged parallel to each other with a torsion angle θ (0.74°) along the Pt–Pt axis (θ defined by the angle between the Pt1–Pt2–N1 and Pt1–Pt2–N3 planes). However, $[(-)\text{-}(C^N^N)Pt]^+$ moieties in (–)-**4** are staggered packed along the Pt–Pt axis, with θ values of 11.74° and 16.34°. Because flexibility and steric hindrance increase with the elongation of the bridging ligand, the intramolecular Pt· · ·Pt distances observed in (–)-**3**-OTf, (–)-**4**, and (–)-**7** are outside the range (3.09–3.50 Å) predicted for an effective Pt· · ·Pt interaction (Zhang et al., 2018). However, weak intramolecular π–π interactions (the distance between two aromatic rings: 3.5–4.1 Å) are expected in both (–)-**3**-OTf and (–)-**4** resulting from the face-to-face conformation of two $[(-)\text{-}(C^N^N)Pt]^+$ planes. In addition, the distances for the closest intermolecular Pt· · ·Pt contact are over 4.0 Å in (–)-**3**-OTf, (–)-**4**, and (–)-**7**; therefore, any effective intermolecular Pt· · ·Pt interaction is absent (**Figure S1**).

TABLE 1 | Crystallographic data of (–)-**3**-OTf, (–)-**4**, and (–)-**7**.

	(–)-**3**-OTf	(–)-**4**	(–)-**7**
Formula	$C_{78}H_{78}F_6N_4O_9P_2Pt_2S_2$	$C_{162}H_{178}Cl_{12}N_8O_3P_4Pt_4$	$C_{43}H_{40}Cl_5N_2PPt$
Mr (g mol^{-1})	1,845.68	3,614.76	988.08
Crystal system	Triclinic	Monoclinic	Monoclinic
Space group	*P*1	$P2_1$	$P2_1$
a (Å)	12.0402(10)	15.4780(4)	12.9794(3)
b (Å)	13.7250(11)	21.6484(4)	13.2011(4)
c (Å)	13.8815(13)	22.3757(4)	23.8617(6)
α (°)	68.595(8)	90.00	90.00
β (°)	64.906(9)	94.539(2)	95.244(2)
γ (°)	74.035(7)	90.00	90.00
V (Å^3)	1,914.4(3)	7,474.0(3)	4,071.41(19)
Z	1	2	4
T (K)	153(2)	153(2)	153(2)
Radiation, λ (Å)	0.71073	0.71073	0.71073
D_{calcd} (g/cm^{-3})	1.601	1.606	1.612
μ (mm^{-1})	3.819	4.046	3.847
F(000)	918	3,612	1,960
Crystal size (mm^3)	0.26 × 0.23 × 0.20	0.29 × 0.26 × 0.20	0.28 × 0.26 × 0.21
θ range (°)	2.07–26.00	2.30–29.53	2.21–27.10
Reflections measured	15,561	37,976	24,890
Unique reflections	10,849	22,792	15,192
R_{int}	0.0404	0.0422	0.0384
Reflections with $F^2 > 2\sigma(F^2)$	9,558	20,357	14,217
Number of parameters	922	1,741	905
Goodness-of-fit on F^2	1.044	1.042	1.067
R_1 [$F^2 > 2\sigma(F^2)$]	0.0490	0.0581	0.0424
wR_2 (all data)	0.1165	0.1543	0.1089
$\Delta\rho_{max}$, $\Delta\rho_{min}$ (e Å^{-3})	2.184, −1.230	3.493, −2.426	1.523, −1.580
Flack parameter	−0.018(8)	−0.022(7)	−0.017(6)

Absorption and Emission Properties

As shown in **Figure 2** and **Figures S2–S4**, all of the chiral dinuclear Pt(II) complexes show characteristic absorption bands ($\varepsilon > 10^4$ L mol^{-1} cm^{-1}) in the UV region similar to those of bis-(diphenylphosphino)alkane bridged dinuclear Pt(II) complexes. The mononuclear Pt(II) complex (–)-**7** also exhibits a similar intense absorption below 400 nm. According to previous studies, the intense bands (<400 nm) are attributed to intraligand π–π^* transitions. In addition, weak absorptions in the region of 400–450 nm are designated as a mixture of metal-to-ligand charge transfer (^{1}MLCT) and ligand-to-ligand charge transfer (^{1}LLCT) transitions (Lu et al., 2002, 2004; Shao and Sun, 2007; Zhang et al., 2018). From the crystal structures of (–)-**3**-OTf, (–)-**4**, and (–)-**7**, it can be found that effective intramolecular/intermolecular Pt···Pt interactions are absent and that two $[(C^N^N)Pt]^+$

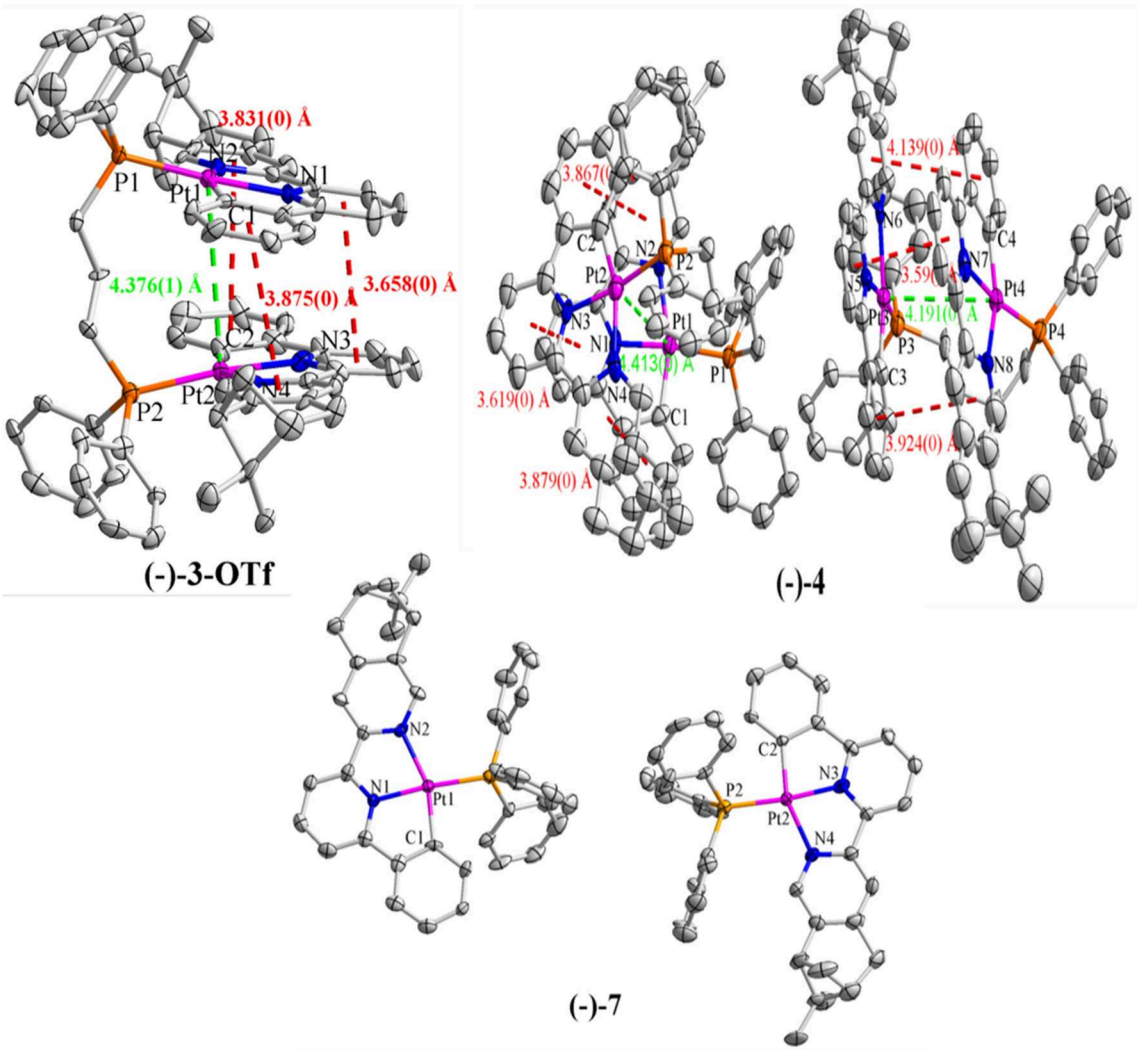

FIGURE 1 | X-ray crystal structures of (–)-**3**-OTf, (–)-**4**, and (–)-**7**, with the *green dashed lines* indicating the Pt···Pt distances and the *red dashed lines* indicating the π–π distances. H atoms, solvent molecules, as well as anions are omitted for clarity.

units manifest like two separated moieties (Sun et al., 2006). Correspondingly, the absorptions of all the complexes only extend to ∼470 nm, which agrees well with the spectrum of (–)-**2**, demonstrating the nonexistence of metal-metal-to-ligand charge transfer transition (^{1}MMLCT) (Zhang et al., 2018).

All of the chiral dinuclear and mononuclear Pt(II) complexes are highly emissive in solution. For all the dinuclear Pt(II) complexes, a broad and structureless emission band at 546 nm is seen, which resembles that of the mononuclear relative (–)-**7** (**Figure S5**). Similar to the absorption spectra, the emission energy of all the complexes also reflects the absence of effective intramolecular/intermolecular Pt···Pt interactions. The emission of all the complexes can be ascribed to a triplet metal-to-ligand charge transfer (^{3}MLCT) excited state (Lu et al., 2002, 2004; Shao and Sun, 2007; Zhang et al., 2018). At 77 K, the emissions are significantly blue-shifted and evolve to be more structured (**Figure S5**), a characteristic nature for ^{3}MLCT excited states. An intense emission peak and a shoulder are observed at 515 and 550 nm, respectively, and the spacing of about 1,100 cm^{-1} correlates to the characteristic skeletal stretching of the free C^N^N ligand.

Chiroptical Properties

The chiroptical spectra (CD and CPL) of all the chiral Pt(II) complexes are plotted in **Figure 2** (complexes **3** and **7**) and **Figures S2**–**S4** (complexes **4**–**6**). Although the bridging ligands are different, complexes (–)-**3**, (–)-**4**, (–)-**5**, and (–)-**6** show similar CD signals with an intense negative Cotton effect at approx. 310 nm and a weak negative effect at approx. 380–400 nm in CH_2Cl_2 solution. Because the two $[(C^N^N)Pt]^+$ units behave like two discrete parts, a similar CD profile is expected in the mononuclear Pt(II) complex (–)-**7**. The variance values of the absorption dissymmetry factor g_{abs} (defined as $g_{abs} = \Delta\varepsilon/\varepsilon$) are quite small for chiral dinuclear complexes (–)-**3** (-5.1×10^{-4}

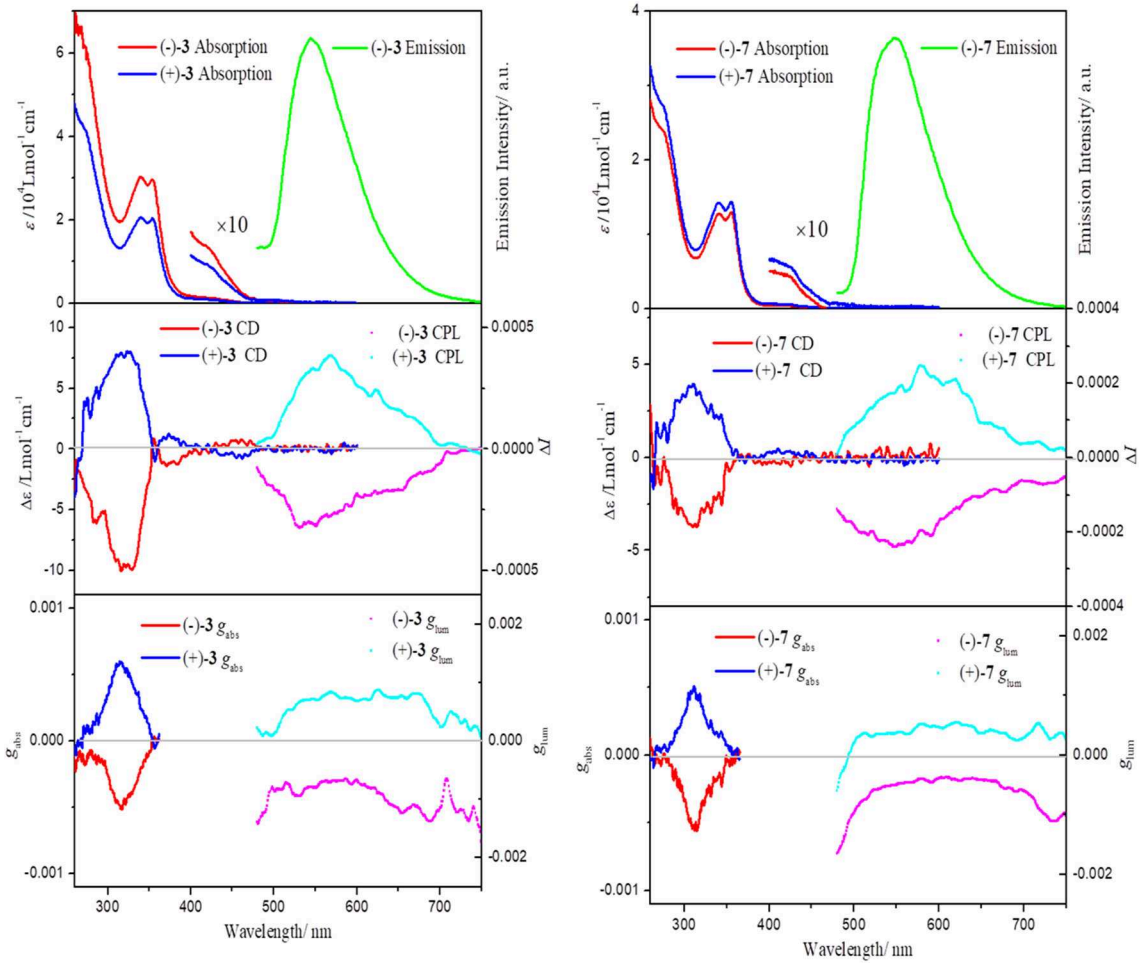

FIGURE 2 | Absorption and emission spectra of (–)-**3** and (–)-**7** in CH_2Cl_2 (5×10^{-5} mol L^{-1}) at $T = 298$ K, $\lambda_{ex} = 420$ nm (*top*). CD spectra in CH_2Cl_2 (5×10^{-5} mol L^{-1}) at $T = 298$ K (*middle*) and CPL spectra in CH_2Cl_2 (10^{-3} mol L^{-1}) at $T = 298$ K (*middle*). g_{abs} and g_{lum} factors are shown at the *bottom*.

at 316 nm), (–)-**4** (-6.9×10^{-4} at 310 nm), (–)-**5** (-7.8×10^{-4} at 310 nm), and (–)-**6** (-7.6×10^{-4} at 311 nm). The g_{abs} for mononuclear Pt(II) complex (–)-**7** also does not differ much, with a value of -5.5×10^{-4} at 311 nm. Thus, these bridging ligands (bridging carbon atoms number > 2) have little impact on the CD signals, and it can be inferred that the chiroptical properties of ground electronic states mainly come from an independent $[(-)\text{-}(C^{\wedge}N^{\wedge}N)Pt]^{+}$ unit.

In the precursor monomer Pt(II) complexes, the chiral block pinene substituent prohibits either a helical or axial geometry; its contribution to chirality-at-metal is also limited. Correspondingly, the CPL activity of the monomer state of chiral Pt(II) complexes grafted with pinene groups was very weak, with low g_{lum} values ($\sim 10^{-4}$ order), and the mirror-imaged CPL spectra could not be obtained (Zhang et al., 2015a; Lu et al., 2017). The bulky bis- or triphenylphosphine ligands selected in this study both adopt a distorted square-planar coordination of Pt(II), as evidenced in their X-ray-determined crystal structures. As expected, the CPL signals of chiral dinuclear Pt(II) complexes exhibit almost mirror image spectra with respect to their enantiomers (complex **3** in **Figure 2** and complexes **4**–**6** in **Figures S2**–**S4**). The g_{lum} values around the maximum emission wavelength are $-1.5 \times 10^{-3}/+1.2 \times 10^{-3}$ for (–)-**3**/(+)-**3** (**Figure 2**), $-1.2 \times 10^{-3}/+1.6 \times 10^{-3}$ for (–)-**4**/(+)-**4**, $-1.4 \times 10^{-3}/+1.0 \times 10^{-3}$ for (–)-**5**/(+)-**5**, and $-1.3 \times 10^{-3}/+1.0 \times 10^{-3}$ for (–)-**6**/(+)-**6** (**Figures S2**–**S4**). These are comparable to the values reported for helicene- and binaphthyl-derived Pt(II) complexes or helical assemblies of square-planar Pt(II) complexes, with CPL values from 10^{-3} to 10^{-2} order (Shen et al., 2014; Schulte et al., 2017; Ikeda et al., 2018; Song et al., 2019). Similarly, CPL signals can be unambiguously detected for mononuclear complexes (–)-**7** and (+)-**7** with opposite g_{lum} values [(–)-**7**: -1.0×10^{-3}; (+)-**7**: $+1.0 \times 10^{-3}$ at 546 nm) (**Figure 2**). A comparison of the CPL measurements for chiral mononuclear complexes (–)-$(C^{\wedge}N^{\wedge}N)$PtCl and (–)-$(C^{\wedge}N^{\wedge}N)$PtPPV has been performed. No appreciable CPL activity was detectable (**Figure 3**). A similar phenomenon has been observed for chiral (–)-$(C^{\wedge}N^{\wedge}N)$PtDmpi complexes before (Zhang et al., 2015a).

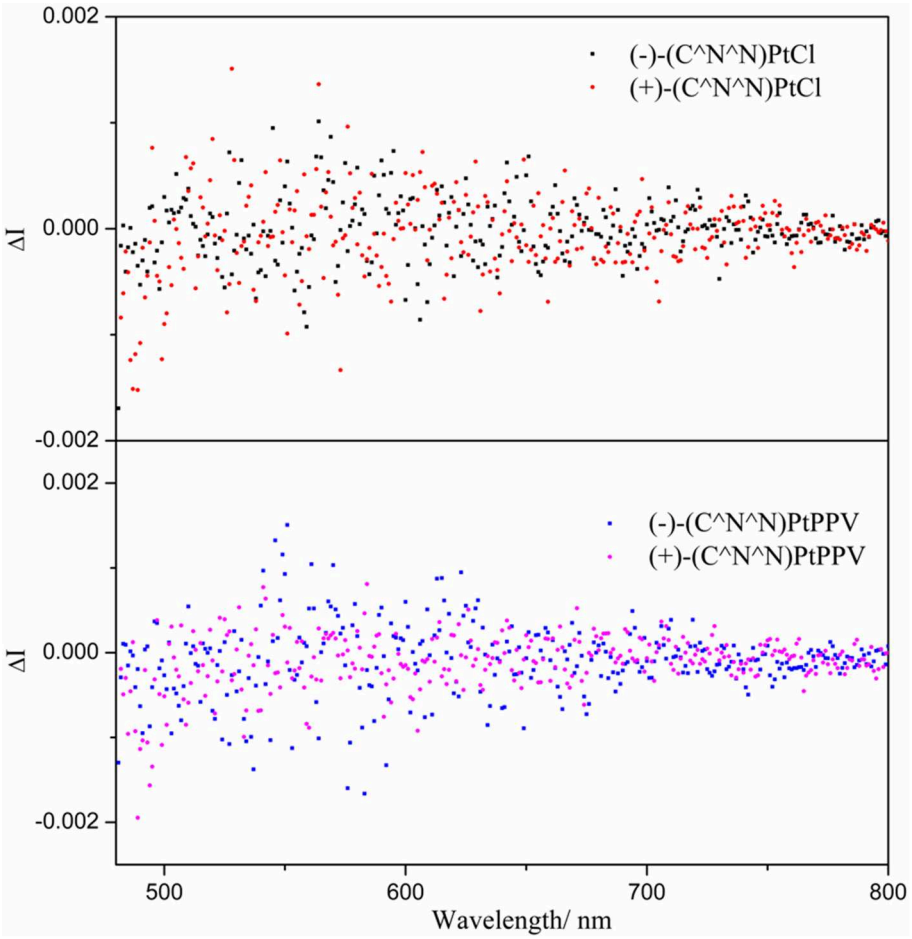

FIGURE 3 | CPL spectra of (–)-(C^N^N)PtCl and (+)-(C^N^N)PtCl, (–)-(C^N^N)PtPPV and (+)-(C^N^N)PtPPV in CH_2Cl_2 (10^{-3} mol L^{-1}) at $T = 298$ K.

TABLE 2 | Bond angles around the Pt(II) nucleus of the opitimized configurations obtained from calculation.

Bond angles	(–)-1	(–)-2	(–)-3	(–)-4	(–)-5	(–)-6	(–)-7	(–)-(C^N^N)PtCl	(–)-(C^N^N)PtPPV	(–)-(C^N^N)PtDmpi
C1–Pt1–N2	157.69	158.08	157.76	157.70	157.42.	157.76				
C2–Pt2–N4	157.10	158.03	157.85	157.64	157.76	157.37				
N1–Pt1–P1	175.38	171.59	176.82	173.69	171.80	175.81				
N3–Pt2–P2	176.41	171.67	175.85	174.69	176.14	170.97				
C1–Pt1–N2							157.60	160.52	158.95	159.37
N1–Pt1–P1 (Cl1, C2)							175.42	177.30	178.82	178.52

Complexes (–)-**3**, (–)-**4**, (–)-**5**, (–)-**6**, and (–)-**7** show negative CPL activity; similar spectra have been observed for (–)-**2**. Therefore, the chiroptical properties of excited states mainly originate from monomeric ^{3}MLCT (Zhang et al., 2018). Unlike the change of CPL activity induced by the Pt· · ·Pt interaction, $\pi-\pi$ stacking effects have little influence on the CPL signals in this system. The CPL activity mostly derives from discrete molecules as a monomeric form. The incorporation of bulky ligands with steric hindrance favors a more distorted coordination geometry for central Pt atoms and enlarges the asymmetry at the metal center, leading to an enhancement in the CPL activity.

TD-DFT Calculation

Time-dependent density functional theory (TD-DFT) calculations were carried out, shedding light on the differences in the structural parameters and frontier molecular orbitals of optimized configurations. The optimized configurations of all the chiral dinuclear and mononuclear Pt(II) complexes are shown in **Figure S6**. Also, the calculated results of the

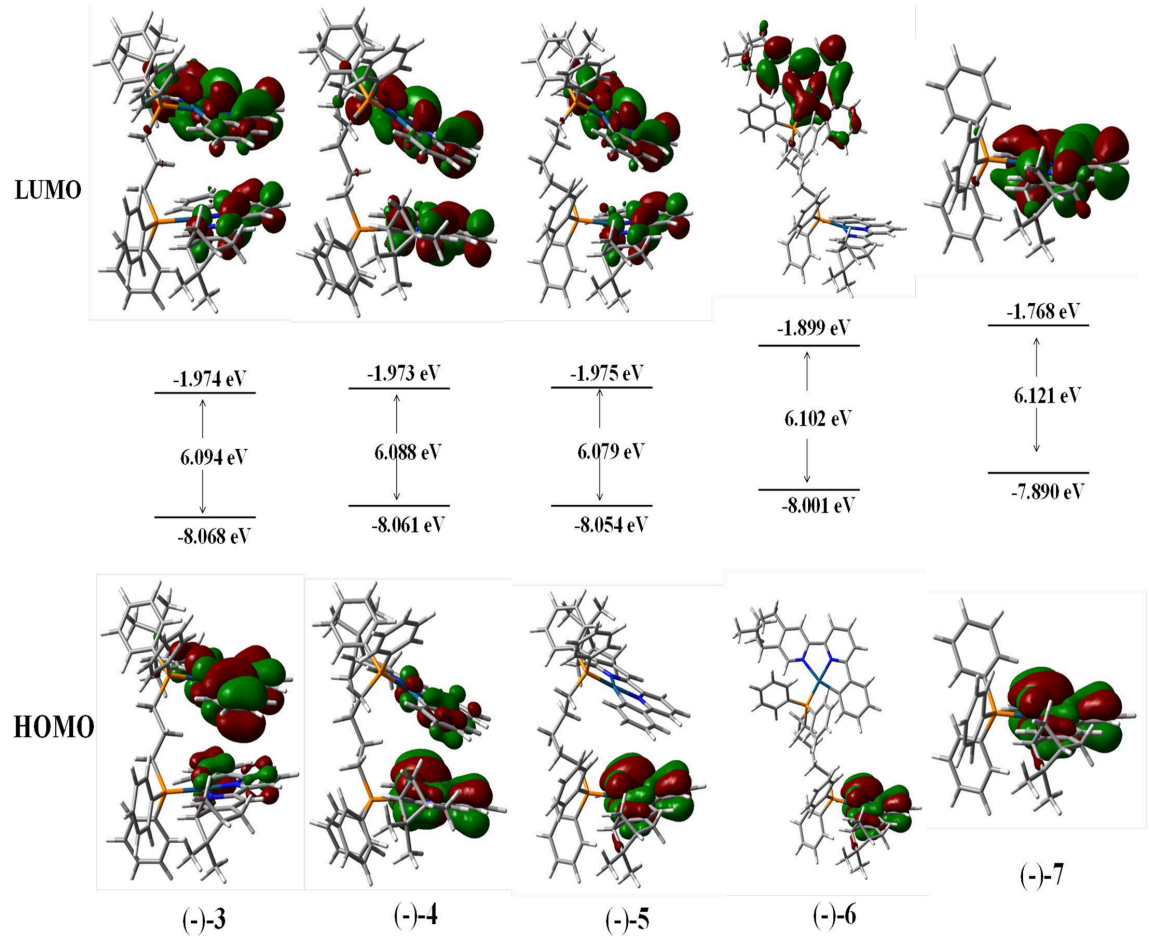

FIGURE 4 | Contour plots of the highest occupied (HOMO) and lowest unoccupied (LUMO) molecular orbitals of (–)-**3**, (–)-**4**, (–)-**5**, (–)-**6**, and (–)-**7**.

reference mononuclear compounds (–)-(C^N^N)PtCl, (–)-(C^N^N)PtPPV, and (–)-(C^N^N)PtDmpi have been provided. The bond angles around the metal nucleus of chiral Pt(II) complexes coordinated with bis- or triphenylphosphine ligands are further away from linearity than those of the reference mononuclear compounds (**Table 2**), which is consistent with the results of the crystal structures. In optimized configurations with phosphine ligands, the angles of C1–Pt1–N2 and C2–Pt2–N4 are in the range of 157.10–158.08°, and the angles of N1–Pt1–P1 and N3–Pt2–P2 range from 170.97° to 176.82°. It is further confirmed that the Pt(II) nucleus in bulk bis- or triphenylphosphine systems adopts a more distorted coordination geometry.

The calculations of the frontier molecular orbitals of (–)-**3**, (–)-**4**, (–)-**5**, (–)-**6**, and (–)-**7** have been explored. The highest occupied molecular orbital (HOMO) and the lowest unoccupied molecular orbital (LUMO) of all the complexes are mainly contributed by the aromatic rings of (–)-(C^N^N) ligands and Pt atoms (**Figure 4**). Due to the longer bridging ligands, neither obvious bonding orbitals between the two Pt centers nor bonding orbitals between the two aromatic C^N^N planes can be visualized in (–)-**3**, (–)-**4**, (–)-**5**, and (–)-**6** (**Figure 4**), while strong and weak bonding orbitals between the two Pt centers are visible in complexes (–)-**1** and (–)-**2**, respectively (Zhang et al., 2018). The HOMO–LUMO band gaps of (–)-**3**, (–)-**4**, (–)-**5**, (–)-**6**, and (–)-**7** are calculated to be 6.094, 6.088, 6.079, 6.102, and 6.121 eV, respectively (**Figure 4**), revealing that the bridging ligands (bridging carbon atoms > 2) cause little difference in band gaps. In addition, the CD spectra have been simulated, and the computed spectra in dichloromethane are in good agreement with the experimental profiles (**Figures S7–S11**).

CONCLUSION

In summary, we introduced bulky bis- or triphenylphosphine ligands into the phosphorescent pinene-containing (C^N^N)Pt(II) complexes and their structures were determined by single-crystal X-ray analysis. The geometries around the Pt(II) nucleus upon coordinating with bis- or triphenylphosphine were more distorted than those in chloride, phenylacetylene, and 2,6-dimethylphenyl isocyanide systems, which was further

verified by DFT calculations. Enhanced CPL activity was observed, with g_{lum} up to 10^{-3} order. This study may pave a new way for the preparation of CPL-active phosphorescent metal complexes by introducing bulky ligands.

DATA AVAILABILITY STATEMENT

The datasets generated for this study can be found in the Cambridge Crystallographic Data Centre (https://www.ccdc.cam.ac.uk/structures/) under the identifiers 1984372-1984374.

AUTHOR CONTRIBUTIONS

The preparation and characterization of all the complexes were done mainly by Q-YY, X-LH, and J-LW. The spectra measurement was done mainly by Q-YY, H-HZ, and YC. The TD-DFT calculation was done mainly by S-DW, L-ZH, and Z-FS. The manuscript was written by Q-YY with the guidance of X-PZ.

FUNDING

This work was supported by the National Natural Science Foundation of China (no. 21961009) and the Natural Science Foundation of Hainan Province (no. ZDYF2019140 and 219MS041).

SUPPLEMENTARY MATERIAL

The Supplementary Material for this article can be found online at: https://www.frontiersin.org/articles/10.3389/fchem.2020.00303/full#supplementary-material

REFERENCES

Aoki, R., Toyoda, R., Kögel, J. F., Sakamoto, R., Kumar, J., Kitagawa, Y. et al. (2017). Bis(dipyrrinato)zinc(II) complex chiroptical wires: exfoliation into single strands and intensification of circularly polarized luminescence. *J. Am. Chem. Soc.* 139, 16024–16027. doi: 10.1021/jacs.7b07077

Biet, T., Cauchy, T., Sun, Q., Ding, J., Hauser, A., Oulevey, P., et al. (2017). Triplet state CPL active helicene–dithiolene platinum bipyridine complexes. *Chem. Commun*. 53, 9210–9213. doi: 10.1039/C7CC05198K

Brandt, J. R., Wang, X., Yang, Y., Campbell, A. J., and Fuchter, M. J. (2016). Circularly polarized phosphorescent electroluminescence with a high dissymmetry factor from PHOLEDs based on a platinahelicene. *J. Am. Chem. Soc*. 138, 9743–9746. doi: 10.1021/jacs.6b02463

Carr, R., Evans, N. H., and Parker, D. (2012). Lanthanide complexes as chiral probes exploiting circularly polarized luminescence. *Chem. Soc. Rev*. 41, 7673–7686. doi: 10.1039/C2CS35242

Chen, C., Gao, L., Gao, W., Ge, C., Du, X., Li, Z., et al. (2019). Circularly polarized light detection using chiral hybrid perovskite. *Nat. Commun*. 10:1927. doi: 10.1038/s41467-019-09942-z

Chen, Y., Li, X., Li, N., Quan, Y., Cheng, Y., and Tang, Y. (2019). Strong circularly polarized electroluminescence based on chiral salen-Zn(ii) complex monomer chromophores. *Mater. Chem. Front*. 3, 867–873. doi: 10.1039/C9QM00039A

Deng, M., Mukthar, N. F., Schley, N. D., and Ung, G. (2020). Yellow circularly polarized luminescence from C1-symmetrical copper(I) complexes. *Angew. Chem. Int. Ed*. 132, 1244–1247. doi: 10.1002/ange.201913672

Deng, W.-T., Qu, H., Huang, Z.-Y., Shi, L., Tang, Z.-Y., Cao, X.-Y., et al. (2019). Facile synthesis of homochiral compounds integrating circularly polarized luminescence and two-photon excited fluorescence. *Chem. Commun*. 55, 2210–2213. doi: 10.1039/C8CC08947G

Fu, G., He, Y., Li, W., Wang, B., Lü, X., He, H., et al. (2019). Efficient polymer light-emitting diodes (PLEDs) based on chiral [Pt(C^{wedge}N)(N^{wedge}O)] complexes with near-infrared (NIR) luminescence and circularly polarized (CP) light. *J. Mater. Chem. C* 7, 13743–13747. doi: 10.1039/c9tc04792a

Gendron, F., Moore, B. II., Cador, O., Pointillart, F., Autschbach, J., Le Guennic, B., et al. (2019). Ab Initio study of circular dichroism and circularly polarized luminescence of spin-allowed and spin-forbidden transitions: from organic ketones to lanthanide complexes. *J. Chem. Theory Comput*. 15, 4140–4155. doi: 10.1021/acs.jctc.9b00286

Guo, Y., Han, Y., and Chen, C.-F. (2019). Construction of chiral nanoassemblies based on host-guest complexes and their responsive CD and CPL properties: chirality transfer from 2,6-helic[6]arenes to a stilbazolium derivative. *Front. Chem*. 7:543. doi: 10.3389/fchem.2019.00543

Han, J., Guo, S., Lu, H., Liu, S., Zhao, Q., and Huang, W. (2018). Recent progress on circularly polarized luminescent materials for organic optoelectronic devices. *Adv. Optical Mater*. 6:1800538. doi: 10.1002/adom.201800538

Han, J., Guo, S., Wang, J., Wei, L., Zhuang, Y., Liu, S., et al. (2017). Circularly polarized phosphorescent electroluminescence from chiral cationic Iridium (III) isocyanide complexes. *Adv. Optical Mater*. 5:1700359. doi: 10.1002/adom.201700359

Hellou, N., Srebro-Hooper, M., Favereau, L., Zinna, F., Caytan, E., and Toupet, L. (2017). Enantiopure cycloiridiated complexes bearing a pentahelicenic N-heterocyclic carbene and displaying long-lived circularly polarized phosphorescence. *Angew. Chem. Int. Ed*. 56, 8236–8239. doi: 10.1002/ange.201704263

Ikeda, T., Hirano, K., and Haino, T. (2018). A circularly polarized luminescent organogel based on a Pt(II) complex possessing phenylisoxazoles. *Mater. Chem. Front*. 2, 468–474. doi: 10.1039/C7QM00564D

Ikeda, T., Takayama, M., Kumar, J., Kawai, T., and Haino, T. (2015). Novel helical assembly of a Pt(II) phenylbipyridine complex directed by metal–metal interaction and aggregation-induced circularly polarized emission. *Dalton Trans*. 44, 13156–13162. doi: 10.1039/c5dt01284h

Jiang, Z., Wang, J., Gao, T., Ma, J., Chen, R., and Liu, Z. (2020). Rational design of axially chiral platinabinaphthalenes with aggregation-induced emission for red circularly polarized phosphorescent organic light-emitting diodes. *ACS Appl. Mater.* 12, 9520–9527. doi: 10.1021/acsami.9b20568

Jiménez, J.-R., Doistau, B., Cruz, C. M., Besnard, C., Cuerva, J. M., Campaña, A. G., et al. (2019). Chiral molecular ruby [Cr(dqp)2]3+ with long-lived circularly polarized luminescence. *J. Am. Chem. Soc.* 141, 13244–13252. doi: 10.1021/jacs.9b06524

Jin, Y., Li, S., Han, Z., Yan, B.-J., Li, H.-Y., Dong, X.-Y., et al. (2019). Cations controlling the chiral assembly of luminescent atomically precise copper (I) clusters. *Angew. Chem. Int. Ed*. 58, 12143–12148. doi: 10.1002/anie.201906614

Lu, G.-Z., Su, N., Li, Y., and Zheng,Y.-X. (2017). Efficient electroluminescence of platinum complexes containing pinene sterically hindered spacer. *J. Organomet. Chem*. 842, 39–46. doi: 10.1016/j.jorganchem.2017.05.011

Lu, W., Chan, M. C., Zhu, N., Che, C. M., Li, C., and Hui, Z. (2004). Structural and spectroscopic studies on Pt. . .Pt and π-π interactions in luminescent multinuclear cyclometalated platinum (II) homologues tethered by oligophosphine auxiliaries. *J. Am. Chem. Soc*. 126, 7639–7651. doi: 10.1021/ja039727o

Lu, W., Zhu, N., and Che, C. M. (2002). Tethered trinuclear cyclometalated platinum (II) complexes: from crystal engineering to tunable emission energy. *Chem. Commun*. 8, 900–901. doi: 10.1039/B200723A

Park, G., Kim, H., Yang, H., Park, K. R., Song, I., Oh, J. H., et al. (2019). Amplified circularly polarized phosphorescence from co-assemblies of platinum(II) complexes. *Chem. Sci*. 10, 1294–1301. doi: 10.1039/c8sc04509g

Schulte, T. R., Holstein, J. J., Krause, L., Michel, R., Stalke, D., Sakuda, E., et al. (2017). Chiral-at-metal phosphorescent square-planar Pt (II)-complexes from an achiral organometallic ligand. *J. Am. Chem. Soc*. 139, 6863–6866. doi: 10.1021/jacs.7b03963

Shao, P., and Sun, W. (2007). Trinuclear platinum(II) 4, 6-Diphenyl-2, 2'-bipyridyl complex with bis(diphenylphosphinomethyl) phenylphosphine auxiliary ligand: synthesis, structural characterization, and photophysics. *Inorg. Chem*. 46, 8603–8612. doi: 10.1021/ic700757x

Shen, C., Anger, E., Srebro, M., Vanthuyne, N., Deol, K. K., Jefferson, T. D. Jr., et al. (2014). Straightforward access to mono- and bis-cycloplatinated helicenes displaying circularly polarized phosphorescence by using crystallization resolution methods. *Chem. Sci*. 5, 1915–1927. doi: 10.1039/C3SC53442A

Song, F., Xu, Z., Zhang, Q., Zhao, Z., Zhang, H., Zhao, W., et al. (2018). Highly efficient circularly polarized electroluminescence from aggregation-induced emission luminogens with amplified chirality and delayed fluorescence. *Adv. Funct. Mater*. 28:1800051. doi: 10.1002/adfm.201800051

Song, J., Wang, M., Xu, X., Qu, L., Zhou, X., and Xiang, H. (2019). 1D-helical platinum (II) complexes bearing metal-induced chirality, aggregation-induced red phosphorescence, and circularly polarized luminescence. *Dalton Trans*. 48, 4420–4428. doi: 10.1039/C8DT03615B

Song, J., Wang, M., Zhou, X., and Xiang, H. (2018). Unusual circularly polarized and aggregation-induced near-infrared phosphorescence of helical platinum(II) complexes with tetradentate salen ligands. *Chem. Eur. J*. 24, 7128–7132. doi: 10.1002/chem.201801414

Sun, W., Zhu, H., and Barron, P. M. (2006). Binuclear cyclometalated platinum(II) 4,6-Diphenyl-2,2'-bipyridine complexes: interesting photoluminescent and optical limiting materials. *Chem. Mater*. 18, 2602–2610. doi: 10.1021/cm060161n

Tanaka, S., Sato, K., Ichida, K., Abe, T., Tsubomura, T., Suzuki, T., et al. (2016). Circularly polarized luminescence of chiral Pt(pppb)Cl (pppbH= 1-pyridyl-3-(4,5-pinenopyridyl) benzene) aggregate in the excited state. *Chem. Asian J*. 11, 265–273. doi: 10.1002/asia.201500985

Usuki, T., Uchida, H., Omoto, K., Yamanoi, Y., Yamada, A., Iwamura, M., et al. (2019). Enhancement of the photofunction of phosphorescent Pt(II) cyclometalated complexes driven by substituents: solid-state luminescence and circularly polarized luminescence. *J. Org. Chem*. 84, 10749–10756. doi: 10.1021/acs.joc.9b01285

Wagenknecht, C., Li, C.-M., Reingruber, A., Bao, X.-H., Goebel, A., Chen, Y.-A., et al. (2010). Experimental demonstration of a heralded entanglement source. *Nat. Photonics* 4, 549–552. doi: 10.1038/nphoton.2010.123

Wu, T., Bouř, P., and Andrushchenko, V. (2019). Europium(III) as a circularly polarized luminescence probe of DNA structure. *Sci. Rep*. 9:1068. doi: 10.1038/s41598-018-37680-7

Yan, Z.-P., Liao, K., Han, H.-B., Su, J., Zheng, Y.-X., and Zuo, J.-L. (2019a). Chiral iridium (iii) complexes with four-membered Ir–S–P–S chelating rings for high-performance circularly polarized OLEDs. *Chem. Commun*. 55, 8215–8218. doi: 10.1039/c9cc03915e

Yan, Z. P., Luo, X. F., Liu, W. Q., Wu, Z. G., Liang, X., Liao, K., et al. (2019b). Configurationally stable platinahelicene enantiomers for efficient circularly polarized phosphorescent organic light-emitting diodes. *Chem. Eur. J*. 25, 5672–5676. doi: 10.1002/chem.201900955

Yang, J.-G., Li, K., Wang, J., Sun, S., Chi, W., Wang, C., et al. (2020). Controlling metallophilic interactions in chiral Au(I) double salts towards excitation wavelength-tunable circularly polarized luminescence. *Angew. Chem. Int. Ed*. 59, 6915–6922. doi: 10.1002/anie.202000792

Yang, Y., da Costa, R. C., Fuchter, M. J., and Campbell, A. J. (2013). Circularly polarized light detection by a chiral organic semiconductor transistor. *Nat. Photon*. 7, 634–638. doi: 10.1038/nphoton.2013.176

Yao, L., Niu, G., Li, J., Gao, L., Luo, X., Xia, B., et al. (2020). Circularly polarized luminescence from chiral tetranuclear copper(I) iodide clusters. *J Phys Chem Lett*. 11, 1255–1260. doi: 10.1021/acs.jpclett.9b03478

Yu, H., Zhao, B., Guo, J., Pan, K., and Deng, J. (2020). Stimuli-responsive circularly polarized luminescent films with tunable emission. *J. Mater. Chem. C* 8, 1459–1465. doi: 10.1039/C9TC06105C

Zhang, D.-W., Li, M., and Chen, C.-F. (2020). Recent advances in circularly polarized electroluminescence based on organic light-emitting diodes. *Chem. Soc. Rev*. 49, 1331–1343. doi: 10.1039/C9CS00680J

Zhang, X., Zhu, L., Wang, X., Shi, Z., and Lin, Q. (2016). Mechano-induced multi-functional optical switches based on chiral cyclometalated platinum(II) complexes. *Inorg. Chim. Acta* 442, 56–63. doi: 10.1016/j.ica.2015.11.028

Zhang, X.-P., Chang, V. Y., Liu, J., Yang, X.-L., Huang, W., Li, Y., et al. (2015a). Potential switchable circularly polarized luminescence from chiral cyclometalated platinum(II) complexes. *Inorg. Chem*. 54, 143–152. doi: 10.1021/ic5019136

Zhang, X.-P., Mei, J.-F., Lai, J.-C., Li, C.-H., and You, X.-Z. (2015b). Mechano-induced luminescent and chiroptical switching in chiral cyclometalated platinum(II) complexes. *J. Mater. Chem. C* 3, 2350–2357. doi: 10.1039/C4TC02800G

Zhang, X.-P., Wang, L.-L., Qi, X.-W., Zhang, D.-S., Yang, Q.-Y., Shi, Z.-F., et al. (2018). Pt Pt interaction triggered tuning of circularlypolarized luminescence activity in chiral dinuclear platinum(II) complexes. *Dalton Trans*. 47, 10179–10186. doi: 10.1039/c8dt02277a

Zhang, X.-P., Wu, T., Liu, J., Zhang, J.-X., Li, C.-H., and You, X.-Z. (2014). Vapor-induced chiroptical switching in chiral cyclometalated platinum(II) complexes with pinene functionalized C^N^N ligands. *J. Mater. Chem. C* 2, 184–194. doi: 10.1039/C3TC31997K

Zhu, M., Chen, S., Du, W., Qin, C., Liu, D., Tang, L., et al. (2020). A new approach to assemble the thiolated [Au1Ag22 (S-Adm)12]3+ superatom complex into a framework material: directly linked by SbF6- anions. *Angew. Chem. Int. Ed*. doi: 10.1002/anie.202000073. [Epub ahead of print].

Zinna, F., Giovanella, U., and Bari L. D. (2015). Highly circularly polarized electroluminescence from a chiral europium complex. *Adv. Mater*. 27, 1791–1795. doi: 10.1002/adma.201404891

Conflict of Interest: The authors declare that the research was conducted in the absence of any commercial or financial relationships that could be construed as a potential conflict of interest.

The handling editor declared a past co-authorship with one of the authors X-PZ.

frontiers in Chemistry

MINI REVIEW
published: 09 June 2020
doi: 10.3389/fchem.2020.00448

Irreverent Nature of Dissymmetry Factor and Quantum Yield in Circularly Polarized Luminescence of Small Organic Molecules

Yuya Nagata[1] *and Tadashi Mori*[2]*

[1] *Institute for Chemical Reaction Design and Discovery (WPI-ICReDD), Hokkaido University, Sapporo, Japan,* [2] *Department of Applied Chemistry, Graduate School of Engineering, Osaka University, Osaka, Japan*

Recently, a rational modification of small organic molecules has attracted considerable attention for designing advanced materials with enhanced circularly polarized luminescence (CPL) activity. A particular emphasis has been placed on fully allowed π-π* transition of rigid aromatic systems, due to their relatively superior emission properties or quantum yields of luminescence (Φ_{lum}). However, their dissymmetry factors (g_{lum}), differential left and right CPL intensities, are typically disappointingly low at least in one to two orders of magnitude. Truly useful organic CPL materials, rated by a circular polarization luminosity index (Λ_{CPL}) per single molecule, possess both $|g_{lum}|$ and Φ_{lum} values high. However, how to improve these two factors simultaneously with a proper molecular design is an open question. Here, we addressed this issue by theoretical and statistical inspection on a possible relation of the g_{lum} and Φ_{lum} values. According to the analysis, we propose simple, unpretentious, yet pertinent guidelines for designing superior organic CPL materials for the future with large Λ_{CPL} values.

Keywords: dissymmetry factor, luminescence quantum yield, circularly polarized luminescence, structure-chiroptical property relationship, allowed π-π* transition

OPEN ACCESS

Edited by:
Giovanna Longhi,
University of Brescia, Italy

Reviewed by:
Cheng Yang,
Sichuan University, China
Ken-ichi Sugiura,
Tokyo Metropolitan University, Japan

***Correspondence:**
Tadashi Mori
tmori@chem.eng.osaka-u.ac.jp

Specialty section:
This article was submitted to Physical Chemistry and Chemical Physics, a section of the journal Frontiers in Chemistry

Received: *15 February 2020*
Accepted: *28 April 2020*
Published: *09 June 2020*

Citation:
Nagata Y and Mori T (2020) Irreverent Nature of Dissymmetry Factor and Quantum Yield in Circularly Polarized Luminescence of Small Organic Molecules. Front. Chem. 8:448. doi: 10.3389/fchem.2020.00448

INTRODUCTION

An increasingly considerable attention has been paid recently to circularly polarized luminescence (CPL) behavior (Riehl and Muller, 2011; Longhi et al., 2016). Not only their potential applications in chemical sensors (Bradberry et al., 2014), biological probes (Muller, 2009), and three-dimensional displays (Schadt, 1997), but also the exclusive chiroptical and photophysical property of CPL reflects the structural information of chiral molecules or molecules in chiral environment in their excited states (Richardson and Riehl, 1977; Riehl and Richardson, 1986). Every so often, the CPL signal is relatively weak but can be unique and selective; accordingly, the CPL materials are believed to be applicable to various smarter photonic materials and discerning biological censors (Han et al., 2018; Ma et al., 2019). At an early stage, the materials had been developed for derivatives of lanthanoids, due to their intrinsic characteristics that electronic forbidden f–f transitions commonly afford better dissymmetry factor (or a degree of chirality, g_{lum}, vide infra) (Carr et al., 2012; Zinna and Di Bari, 2015). Recent advance in supramolecular chirality is another trend in the CPL chemistry, where improved responses have been frequently reported through

molecular aggregation, agglomeration, flocculation, as well as their combinations (Kumar et al., 2015; Sang et al., 2020). However, systematic investigations to pursue a so-called structure–property relationship to attain a reliable strategy and a design principle for the superior CPL materials, even for more simple isolated molecular systems, have been quite limited. As such, current studies on the CPL materials are mostly based on a cut-and-try basis. Further discussions and many examples are available in recent review articles (Sanchez-Carnerero et al., 2015; Tanaka et al., 2018b).

Naturally, an observed difference between emission intensities of left- and right-handed circularly polarized light (I_L-I_R) at a given frequency ν in the CPL measurement on chiral substance depends on an intensity of an incident excitation light. Therefore, a degree of chirality in the CPL response is generally discussed with the polarization efficiency, or the dissymmetry factor of luminescence (g_{lum}). Thus, the g_{lum} value is a difference emission intensity divided by an averaged intensity at a given frequency ν, which is defined as follows:

$$g_{lum}(\nu) = 2\,\frac{I_L(\nu) - I_R(\nu)}{I_L(\nu) + I_R(\nu)} \tag{1}$$

By definition, minimum and maximum g_{lum} factors are -2 and $+2$. Most of the studies that explore better CPL molecules thus pursue molecules with larger absolute g_{lum} value (i.e., $|g_{lum}|$), as this parameter is frequently the most limiting factor, particularly in small organic molecules where g_{lum} factors are typically as low as in an order of 10^{-5} to 10^{-3} range.

In the 1960s and 1970s, the CPL chemistry on small organic molecules had been limited to constraint cyclic ketones, where relatively larger g_{lum} values were obtained due to the electronically forbidden n–π^* transition. In most of these molecules, chiral distortion of carbonyl moiety is usually released in their excited states, the degree of which is highly dependent on the nature of the molecule. Accordingly, g_{lum} prediction of chiral ketones is specifically challenging. Recent emphasis has been rather placed on electronically allowed π-π^* transition of rigid aromatic systems, for reasons such as below. Firstly, these systems often afford much improved fluorescence probability. Second, a facile structural modification is conceivable that can fine-tune absorption and emission wavelengths and bandwidths, and possibly the degree of dissymmetry as well. Also, the degree of excited-state relaxation in such systems has been found surprisingly systematic, although slightly dependent on the structural motifs or types of chirality. Such statistical analyses afforded empirical linear correlations between the dissymmetry factors of luminescence and absorption, allowing us an empirical yet a rational design (Tanaka et al., 2018b).

In order to fully understand the overall CPL efficiency, other photophysical parameters beside the dissymmetry factor (g_{lum}) should be also taken into consideration (**Figure 1**). As more materials-oriented intrinsic index of CPL efficiency, we propose a circular polarization luminosity (Λ_{CPL}) per single chiral molecule in the excited state, which is defined as follows:

$$\Lambda_{CPL} = f \times \Phi_{lum} \times \frac{|g_{lum}|}{2} \tag{2}$$

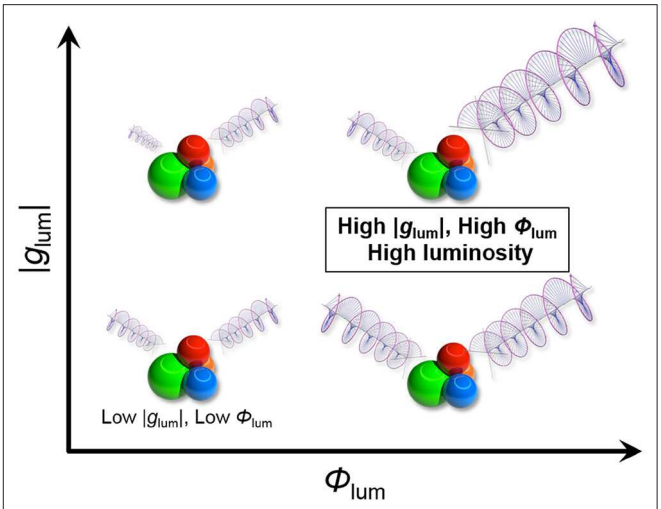

FIGURE 1 | Conceptual diagram for two-dimensional improvement of CPL materials.

where f and Φ_{lum} are efficiencies of light absorption (oscillator strength) and emission intensity (quantum yield), respectively. By definition, minimum and maximum Λ_{CPL} values are 0 and 1. Hypothetically, molecules with larger Λ_{CPL} values at desired excitation and emission wavelengths are considered as satisfactory chiroptical materials. In the following discussion, we made an effort to understand a possible relationship among the photophysical parameters in the CPL behavior, particularly that between g_{lum} and Φ_{lum}.

THEORETICAL CONSIDERATION

In real spectra, the CPL and fluorescence bands are characterized by distinct parameters, which are called rotational (R) and dipole (D) strengths, respectively. In isotropic solution, the following equations generally fold (in cgs unit) for the CPL (I_L-I_R) and total ($I_L + I_R$) emission intensities from chiral substance as a function of ν:

$$I_L(\nu) - I_R(\nu) = \frac{16\,\nu^3\,\rho(\nu)}{3\,c^3\,\hbar^4}\,R \tag{3}$$

$$I_L(\nu) + I_R(\nu) = \frac{8\,\nu^3\,\rho(\nu)}{3\,c^3\,\hbar^4}\,D \tag{4}$$

where h is the reduced Planck's constant, c is the speed of light, and $\rho(\nu)$ is a Gaussian band shape.

Theoretically, the value D is defined as the square of an electric transition dipole moment ($\boldsymbol{\mu}$) for an electronic transition between an emissive state j and a ground state i:

$$D = \langle \Psi_j | \boldsymbol{\mu} | \Psi_i \rangle^2 \tag{5}$$

According to Rosenfeld (Rosenfeld, 1929), the value R can be expressed as a product of wavefunction overlap integrals between

the electric ($\boldsymbol{\mu}$) and magnetic ($\boldsymbol{m}$) transition dipole moments, as follows:

$$R = \mathrm{Im}\left[\langle\Psi_j|\boldsymbol{\mu}|\Psi_i\rangle \cdot \langle\Psi_i|\boldsymbol{m}|\Psi_j\rangle\right] \tag{6}$$

where Im refers to an imaginary component of the scalar product between real vector $\boldsymbol{\mu}$ and imaginary vector $\boldsymbol{m}$. In most situations, this is also expressed as:

$$R = |\boldsymbol{\mu}|\,|\boldsymbol{m}|\cos\theta \tag{7}$$

where θ is the angle between the two dipole moments. This obviously demonstrates a non-orthogonal nature of $\boldsymbol{\mu}$ and $\boldsymbol{m}$ of chiral materials. By substituting Equations (3) and (4) for Equation (1), the dissymmetry factor can be simplified with R and D as follows:

$$g_{lum} = 4 \times \frac{R}{D} \tag{8}$$

Equation (8) clearly suggests the linear correlation between the g_{lum} value against the inverse of D. That is, g_{lum} should be reciprocally proportional to the square of transition probability, if the value R is independent to D. This is empirically in accord with the fact that classical examples of CPL responsive materials were based on the molecules with forbidden transitions, in which better g_{lum} factors were frequently reported. In a different expression, Equation (8) is also stated as:

$$g_{lum} = 4 \times \frac{|\boldsymbol{m}|\cos\theta}{|\boldsymbol{\mu}|} \tag{9}$$

Thus, g_{lum} is proportional to reciprocal amplitude of $\boldsymbol{\mu}$, under conditions that $\boldsymbol{\mu}$ is independent to $\boldsymbol{m}$. For further details on the relevant theoretical consideration and numerical expressions, see refs (Richardson and Riehl, 1977) and (Riehl and Richardson, 1986).

The quantum yield of emission Φ_{lum} is determined by the rate of radiative and non-radiative decays, as follows:

$$\Phi_{\mathrm{lum}} = \frac{k_r}{k_r + k_{nr}} = \frac{1}{1 - \left(-\frac{k_{nr}}{k_r}\right)} \tag{10}$$

In order to assess a possible correlation between g_{lum} and Φ_{lum} values, we may consider the following relations (Carr et al., 2012; Kumar et al., 2015; Tanaka et al., 2018b; Sang et al., 2020) that are valid only at the condition of $k_{\mathrm{nr}}/k_{\mathrm{f}} \ll 1$, for which the molecules have relatively good emission properties. This allows to expand the Equation (10) to:

$$\Phi_{\mathrm{lum}} \approx 1 - \frac{k_{nr}}{k_r}, \text{ in the limit of } \frac{k_{nr}}{k_r} \ll 1 \tag{11}$$

The rate of emission is dependent on f and the square of the frequency of the electronic transition ν. Here, we ignore the difference between absorption and emission processes as structural relaxation in the excited state can be negligible in rigid aromatic systems. Also, the experimental emission and absorption intensities are proportional to the square of corresponding electric transition dipole moments. Thus, Φ_{lum} is related to the electronic transition dipole moment $\boldsymbol{\mu}$ as follows:

$$1 - \Phi_{lum} \propto |\boldsymbol{\mu}|^{-2} \tag{12}$$

Subsequently, Equations (9) and (12) can be rearranged to:

$$g_{lum} \propto |\boldsymbol{m}|\cos\theta \times \sqrt{1 - \Phi_{\mathrm{lum}}} \tag{13}$$

Therefore, under the condition that Φ_{lum} and $\boldsymbol{m}$ can be regarded independent, g_{lum} values are dependent to the square of (1 – Φ_{lum}). That is:

$$g_{lum} \propto \sqrt{1 - \Phi_{\mathrm{lum}}}, \text{ in the limit of } \frac{k_{nr}}{k_r} \ll 1 \tag{14}$$

Finally, Equation (2) can be also reorganized into:

$$\begin{aligned} \Lambda_{\mathrm{CPL}} \propto |\boldsymbol{\mu}|^2 \times \Phi_{\mathrm{lum}} \times \frac{|\boldsymbol{m}|\cos\theta}{|\boldsymbol{\mu}|} &= |\boldsymbol{\mu}|\,|\boldsymbol{m}|\cos\theta \times \Phi_{\mathrm{lum}} \\ &= R \times \Phi_{\mathrm{lum}} \end{aligned} \tag{15}$$

Thus, as the first approximation, the circular polarization luminosity (Λ_{CPL}), a key parameter for the excellent CPL materials, is eventually related to the rotational strength (R) and the emission quantum yield (Φ_{lum}). Note that this equation holds without the condition of $k_{\mathrm{nr}}/k_{\mathrm{f}} \ll 1$.

STATISTICAL ANALYSES

We have recently collected all the reported CPL data that were associated with circular dichroisms (CDs) for small organic molecules up to the year 2017 (Tanaka et al., 2018b). We found the direct correlation between dissymmetry factors of luminescence and absorption, affording an empirical linear correlation of $|g_{\mathrm{lum}}| = 0.81 \times |g_{\mathrm{abs}}|$ ($r^2 = 0.60$) as a global fit for all the CPL and CD data of the electronically allowed π-π* transition of rigid aromatic systems. For comparison and clarity, the same data were plotted in log–log format depicted in **Figure 2A**. Although some scattered data were apparent, statistical analysis led to the same conclusion that there is a linear correlation between two dissymmetry factors with a slop of ≈1. As discussed above, the g_{lum} value will be correlated to the square of (1 – Φ_{lum}), unless there is extensive bias. Such an analysis was performed as shown in **Figure 2B**, utilizing all the chiral molecules used in the same review (Tanaka et al., 2018b). As clearly seen, data were more dispersed and direct correlation was not obtained between g_{lum} and Φ_{lum}, at least among these samples, both in global plot and among sub-class of chirality, which was categorized in different colors.

DISCUSSION

Before providing our supposition on the above observations, we better comment on a limitation of our evaluations. Possible issues on reliability of our data analyses may include the following: (1)

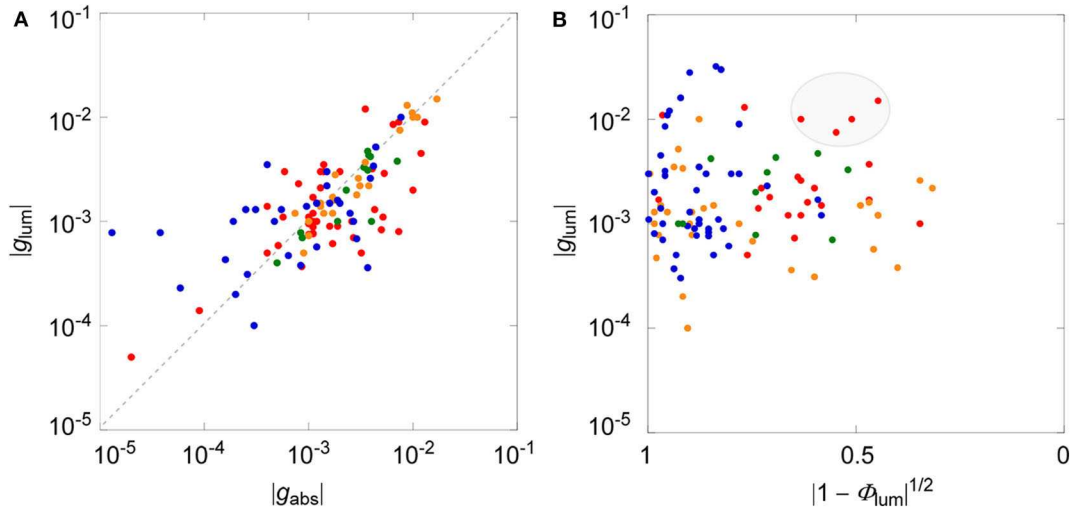

FIGURE 2 | (A) Log–log plot between luminescence (g_{lum}) and absorption (g_{abs}) dissymmetry factors. **(B)** Log plot between g_{lum} and square of 1—luminescence quantum yield (Φ_{lum}). Blue, helicenes and derivatives; red, planar chiral cyclophanes; orange, binaphthyls with axial chirality; green chiral BODIPY derivatives. Data are taken from Tanaka et al. (2018b).

Limiting examples: Our analyses were rather limited in terms of numbers of available data ($N \approx 100$) in indefectible statistical point of view. (2) Exclusion of negative data: In particular, data with low Φ_{lum} values ($<10^{-3}$) are almost completely neglected as such systems have been rarely published. Such trend is also true for those with low g_{lum} values ($<10^{-5}$). (3) Measurement conditions: Measurements to be compared are better to be identical. Also, both the CPL and luminescence experiments should be executed under the comparable conditions. From time to time, Φ_{lum} and g_{lum} were evaluated at specific peak wavelengths that were not always matching each other (e.g., g_{lum} was reported at a relatively feeble shoulder position of emission). In such cases, both parameters are maximized at individual wavelengths, but the correlation may be lost, or at least deteriorated. In other instances, very wide slit widths are employed in the CPL experiment. The g_{lum} values tend to be observed smaller as widths of slit (window of light propagation) in the CPL spectroscopy are increased. This is often inevitable, however, for samples of weak signal (i.e., low luminescence and/or dissymmetry factor). (4) Sample quality: As well as the purity and optical purity of the chiral samples, additional experimental issues such as aggregation, band overlap, and vibronic contribution should be carefully considered and possibly be eliminated or corrected. Such propositions, however, have been overlooked in most of the reports.

Although we admit that more studies are certainly needed to have a definite relevancy between g_{lum} and Φ_{lum} values, we may deduce the following (tentative) suppositions.

(1) The plots between g_{lum} and Φ_{lum} values, even among the sub-class of different types of chiral molecules, provided substantially dispersed ones (**Figure 2B**). They did not provide a linear (or any meaningful) relationship, as has been expected by theory or by intuition from the classical examples. This immediately indicates that there is some bias between these values. We believe that this is due, at least in part, to the fact that the data of low Φ_{lum} values were missing simply because such numbers were reluctant to be included in a publication. In fact, the plots based on the reported values were widely dispersed with the exception of a region with low Φ_{lum} values (right-hand side).

(2) At a first glance, the fact that there was no immediate correlation between g_{lum} and Φ_{lum} values was somewhat disappointing. However, it was also realized that the g_{lum} values were still expanded in a whole range between 10^{-5} and 10^{-1} within the selected Φ_{lum} domain. This observation clearly infers that the g_{lum} values may be improved irrespective to the emission property, in spite of possible correlation in Equation (14). As such, we suggest the rather straightforward strategy for designing superior CPL materials having better circular polarization luminosity (Λ_{CPL}), that is, to inspect a systematic structural modification on certain molecules already demonstrating high Φ_{lum} value in a trial-and-error manner.

(3) In this regard, we can point to some data located at the top-middle position in **Figure 2B** (highlighted in a gray ellipse), those simultaneously possessing relatively larger g_{lum} and Φ_{lum} values. These include some planar chiral rigid cyclophane derivatives that may be quite promising as the starting points for more improved CPL materials with larger g_{lum} value concomitantly keeping high Φ_{lum} value. In another respect, it is worth noting that there have been substantially growing numbers of investigations recently that report the improved CPL responses based on molecular symmetry with helicene derivatives (Tanaka et al., 2018a,c; Isla et al., 2019; Schaack et al., 2019; Zhao et al., 2019).

CONCLUDING REMARKS

Although the number of reported examples of CPL active small organic molecules has been rapidly increasing, mostly being explored in a cut-and-try basis, a structure–property relationship that can guide the design principle has not been established. Thus, to design desired CPL response in molecular systems is still challenging. In most of the CPL studies in organic molecules, the dissymmetry factor of luminescence (g_{lum}) is the limiting factor because the reported values are considerably smaller, usually in several orders of magnitude than the limiting value. Alternatively, other photophysical parameters, in particular the luminescence quantum yields (Φ_{lum}), are also an important factor to develop the truly useful CPL materials.

In this contribution, we tried to determine the possible correlation between g_{lum} and Φ_{lum} values, both in theoretical formula and experimental observations. It was a little surprise that the observed g_{lum} values of π-π^* transition of rigid aromatic molecules are independent to their Φ_{lum} values, despite the expected correlation derived from Equation (14). Rather, a direct relationship between the circular polarization luminosity (Λ_{CPL}) and rotational strength (R) found in Equation (15) seems more substantial. Our analyses also advocate that the g_{lum} values can be improved irrespective to Φ_{lum}. Therefore, the most straightforward means to develop the improved CPL materials could be a methodical structural modification of aromatic systems that already enjoy the high Φ_{lum} values, which will directly maximize the circular polarization luminosity (Λ_{CPL}), the real measure for the superior CPL materials. We hope our analyses and suppositions may be of benefit for future design of materials of better CPL responses.

AUTHOR CONTRIBUTIONS

TM wrote the first draft of the manuscript. Both authors contributed to manuscript revision, and read and approved the submitted version.

FUNDING

Financial support for TM by Grant-in-Aids for Scientific Research, Challenging Exploratory Research, and Promotion of Joint International Research (Fostering Joint International Research) (Grant Numbers JP16H06041, JP16KK0111, JP17H05261, JP18K19077, and JP18H01964) from JSPS, by the Asahi Glass Foundation and the Murata Science Foundation, Tonen General Sekiyu Research/Development Encouragement & Scholarship Foundation, and by the Cooperative Research Program of Network Joint Research Center for Materials and Devices are greatly acknowledged.

ACKNOWLEDGMENTS

TM thanks Emeritus Prof. Yoshihisa Inoue for a fruitful discussion.

REFERENCES

Bradberry, S. J., Savyasachi, A. J., Martinez-Calvo, M., and Gunnlaugsson, T. (2014). Development of responsive visibly and NIR luminescent and supramolecular coordination self-assemblies using lanthanide ion directed synthesis. *Coord. Chem. Rev.* 273, 226–241. doi: 10.1016/j.ccr.2014.03.023

Carr, R., Evans, N. H., and Parker, D. (2012). Lanthanide complexes as chiral probes exploiting circularly polarized luminescence. *Chem. Soc. Rev.* 41, 7673–7686. doi: 10.1039/c2cs35242g

Han, J., Guo, S., Lu, H., Liu, S., Zhao, Q., and Huang, W. (2018). Recent progress on circularly polarized luminescent materials for organic optoelectronic devices. *Adv. Optic. Mater.* 6:1800538. doi: 10.1002/adom.201800538

Isla, H., Saleh, N., Ou-Yang, J.-K., Dhbaibi, K., Jean, M., Dziurka, M., et al. (2019). Bis-4-aza(6)helicene: a bis-helicenic 2,2'-bipyridine with chemically triggered chiroptical switching activity. *J. Org. Chem.* 84, 5383–5393. doi: 10.1021/acs.joc.9b00389

Kumar, J., Nakashima, T., and Kawai, T. (2015). Circularly polarized luminescence in chiral molecules and supramolecular assemblies. *J. Phys. Chem. Lett.* 6, 3445–3452. doi: 10.1021/acs.jpclett.5b01452

Longhi, G., Castiglioni, E., Koshoubu, J., Mazzeo, G., and Abbate, S. (2016). Circularly polarized luminescence: a review of experimental and theoretical aspects. *Chirality* 28, 696–707. doi: 10.1002/chir.22647

Ma, J.-L., Peng, Q., and Zhao, C.-H. (2019). Circularly polarized luminescence switching in small organic molecules. *Chem. Eur. J.* 25, 15441–15454. doi: 10.1002/chem.201903252

Muller, G. (2009). Luminescent chiral lanthanide(III) complexes as potential molecular probes. *Dalton Trans.* 9692–9707. doi: 10.1039/b909430j

Richardson, F. S., and Riehl, J. P. (1977). Circularly Polarized Luminescence Spectroscopy. *Chem. Rev.* 77, 773–792. doi: 10.1021/cr60310a001

Riehl, J. P., and Muller, G. (2011). Circularly polarized luminescence spectroscopy and emission-detected circular dichroism. *Compreh. Chiropt. Spectr.* 65–90. doi: 10.1002/9781118120187.ch3

Riehl, J. P., and Richardson, F. S. (1986). Circularly polarized luminescence spectroscopy. *Chem. Rev.* 86, 1–16. doi: 10.1021/cr00071a001

Rosenfeld, L. (1929). Quantenmechanische theorie der natürlichen optischen aktivität von flüssigkeiten und gasen. *Z. Phys.* 52, 161–174. doi: 10.1007/BF01342393

Sanchez-Carnerero, E. M., Agarrabeitia, A. R., Moreno, F., Maroto, B. L., Muller, G., Ortiz, M. J., et al. (2015). Circularly Polarized Luminescence from Simple Organic Molecules. *Chem. Eur. J.* 21, 13488–13500. doi: 10.1002/chem.201501178

Sang, Y., Han, J., Zhao, T., Duan, P., and Liu, M. (2020). Circularly polarized luminescence in nanoassemblies: generation, amplification, and application. *Adv. Mater.* 32. doi: 10.1002/adma.201900110

Schaack, C., Arrico, L., Sidler, E., Gorecki, M., Di Bari, L., and Diederich, F. (2019). Helicene monomers and dimers: chiral chromophores featuring strong circularly polarized luminescence. *Chem. Eur. J.* 25, 8003–8007. doi: 10.1002/chem.201901248

Schadt, M. (1997). Liquid crystal materials and liquid crystal displays. *Annu. Rev. Mater. Sci.* 27, 305–379. doi: 10.1146/annurev.matsci.27.1.305

Tanaka, H., Ikenosako, M., Kato, Y., Fujiki, M., Inoue, Y., and Mori, T. (2018a). Symmetry-based rational design for boosting chiroptical responses. *Comms. Chem.* 1, 38. doi: 10.1038/s42004-018-0035-x

Tanaka, H., Inoue, Y., and Mori, T. (2018b). Circularly polarized luminescence and circular dichroisms in small organic molecules: correlation between

excitation and emission dissymmetry factors. *ChemPhotoChem* 2, 386–402. doi: 10.1002/cptc.201800015

Tanaka, H., Kato, Y., Fujiki, M., Inoue, Y., and Mori, T. (2018c). Combined experimental and theoretical study on circular dichroism and circularly polarized luminescence of configurationally robust D_3-symmetric triple pentahelicene. *J. Phys. Chem. A* 122, 7378–7384. doi: 10.1021/acs.jpca.8b05247

Zhao, W.-L., Li, M., Lu, H.-Y., and Chen, C.-F. (2019). Advances in helicene derivatives with circularly polarized luminescence. *Chem. Commun.* 55, 13793–13803. doi: 10.1039/C9CC06861A

Zinna, F., and Di Bari, L. (2015). Lanthanide circularly polarized luminescence: bases and applications. *Chirality* 27, 1–13. doi: 10.1002/chir.22382

Conflict of Interest: The authors declare that the research was conducted in the absence of any commercial or financial relationships that could be construed as a potential conflict of interest.

The reviewer CY declared a past co-authorship with one of the author TM to the handling editor.

frontiers in Chemistry

REVIEW
published: 12 June 2020
doi: 10.3389/fchem.2020.00458

The Progress and Perspective of Organic Molecules With Switchable Circularly Polarized Luminescence

*Yang Gao, Can Ren, Xiaodong Lin and Tingchao He**

College of Physics and Optoelectronic Engineering, Shenzhen University, Shenzhen, China

Circularly polarized luminescence (CPL) has been under intense research for future applications in high-resolution 3D displays, smart sensors, and information technologies. Different types of CPL materials have been developed, but neither the handedness nor the asymmetrical luminescence degree can be inferred from the material composition or the components. CPL materials with switchable handedness or emission wavelength play an important role, reducing the need for repetitive bottom-up synthesis. Here, we have presented switchable CPL behaviors toward multiple reported stimuli, including light irradiation, host–guest interaction, metal ions, pH, solvent, temperature, etc. This summary and discussion of the effective stimuli is aimed to promote rational future material exploration and boost related multidisciplinary applications.

Keywords: circularly polarized luminescence, asymmetrical emission factor, organic material, multiple stimuli, reversible switch

OPEN ACCESS

Edited by:
Tao Wu,
Institute of Organic Chemistry and Biochemistry (ASCR), Czechia

Reviewed by:
Chuan-Feng Chen,
Institute of Chemistry (CAS), China
Chuanliang Feng,
Shanghai Jiao Tong University, China

****Correspondence:***
Tingchao He
tche@szu.edu.cn

Specialty section:
This article was submitted to Physical Chemistry and Chemical Physics, a section of the journal Frontiers in Chemistry

Received: *09 March 2020*
Accepted: *01 May 2020*
Published: *12 June 2020*

Citation:
Gao Y, Ren C, Lin X and He T (2020) The Progress and Perspective of Organic Molecules With Switchable Circularly Polarized Luminescence. Front. Chem. 8:458. doi: 10.3389/fchem.2020.00458

INTRODUCTION

Circularly polarized luminescence (CPL) has been the subject of intense research due to its possible applications in new photonic/photoelectronic devices (Han J. et al., 2018; Zhang et al., 2020), smart sensors, high-resolution 3D displays, information technologies, etc. A variety of CPL materials have been developed to date, including rare-earth metal-based coordination complexes and organic and inorganic molecules/assemblies. Organic luminescent materials have enjoyed a major role in their development due to the wide range of possible structural components, moderate to high emission efficiency, and multiple intra-/inter-molecular interaction modes.

Although there are a number of known strategies to design CPL active materials and a large library of material structures are available (Pop et al., 2019; Sang et al., 2019; Zhao W. L. et al., 2019; Ouyang and Liu, 2020), it is as yet unrealistic to predict related CPL activities for any given structure. Neither the handedness nor the degree of asymmetry can be confidently or accurately predicted from the material composition or the components (e.g., enantiomer excess value). Thus, CPL materials with switchable emission characteristics have been the subject of intense research with the aim of obtaining strong CPL with selective handedness/emission wavelength. Recently, a number of novel approaches have been reported including facile applicable triggers, multiple emissive states, and high-quality emitters. For example, a helical structure incorporating pyrene units showed strong CPL in solution ($g_{lum} \sim 10^{-2}$) with handedness, which was invertible by changing the solvent from toluene to DMSO (Takaishi et al., 2020). Also, a switch from circularly polarized fluorescence to ultra-long phosphorescence was achieved for a chiral carbazole phosphor (Li et al., 2020).

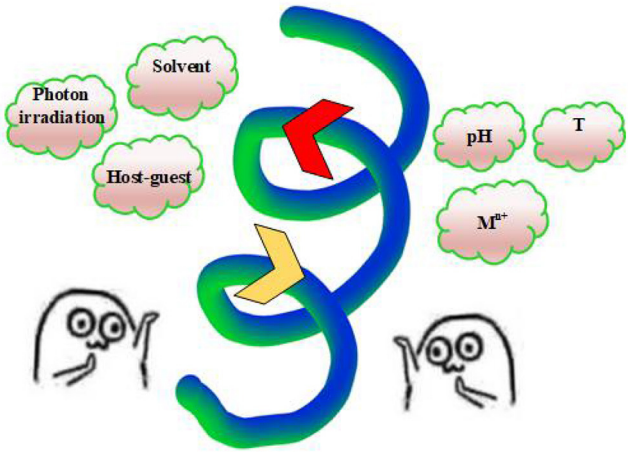

GRAPHICAL ABSTRACT | CPL materials with switchable handedness or emission wavelength toward multiple stimuli, including light irradiation, host-guest interaction, metal ions, pH, solvent, temperature, etc.

Though there have been some recent partial reviews (Ma J. L. et al., 2019; Sang et al., 2019), CPL emitters whose emission is switchable under various stimuli have not been comprehensively reviewed. To fill this gap, a review of switchable CPL behavior is presented herein, including the use of irradiation with light, host–guest interaction, metal ions, pH, temperature, and solvents as stimuli. The discussion will be focused on reversible behavior. Also, a brief explanation of how CPL measurements are performed is included. Hopefully, this review will help promote the design and exploration of future materials and boost development of related multidisciplinary applications.

MEASUREMENT

To describe CPL materials properly, a number of parameters related to both emission and polarization are involved. Concerning emission behaviors, features usually mentioned include the type of emission (fluorescence, phosphorescence), the emission wavelength (λ_{em}), quantum efficiency (Φ), and the emission lifetime (τ). To characterize spectroscopic features of chiral materials, circular dichroism (CD) and CPL spectra are often used to study the chirality in the ground and excited states, respectively. In the CD measurement, alternative left- and right-handed light beams pass through the chiral medium, which show different light propagation speeds. Different molar CD ($\Delta\varepsilon$) can be recorded, and the asymmetric factor of CD can be calculated according to

$$g_{abs} = \frac{\Delta\varepsilon}{\varepsilon} = 2 \times \frac{\varepsilon_L - \varepsilon_R}{\varepsilon_L + \varepsilon_R} \quad (1)$$

where ε_L and ε_R represents the extinction coefficients for left- and right-handed circularly polarized light, respectively.

The CPL measurement utilizes fluorescence spectrometry with additional compartments for the polarization detection. Usually the excitation beam is polarized with a polarizer before entering the sample, and a modulated circular polarizer is applied after the emission beam to obtain the separate intensity of the left-handed and right-handed CPL. The level of circular polarization in emission is termed as the dissymmetry or emission g-factor, which is formulated as followed:

$$g_{lum} = \frac{\Delta I}{I} = 2\times\frac{I_L - I_R}{I_L + I_R} \quad (2)$$

The theoretical range of g_{lum} is from -2 to $+2$. For organic molecules in solution, the g_{lum} value appears usually in the range of $10^{-5}\sim10^{-3}$. While in aggregated state or in condensed state, the value increases to $10^{-3}\sim10^{-1}$.

A switch of the CPL behaviors will be discussed in the context of the aforementioned parameters toward various stimuli.

IRRADIATION WITH LIGHT

Irradiation with light can influence the CPL behaviors through photo cyclization/de-cyclization, photo induced isomerization, and selected population of specific excited state. Moreover, photoreactions are usually induced by UV radiation and reversed by lower-energy visible light or heat treatment. An on-off switch based on photo cyclization was observed for a photochromic tetrathiazole attached pyrene dye (Hashimoto et al., 2016). When the individual pyrene units were attached via a chiral phenylamine spacer to a tetrathiazole core, the π-π stacking of two phenylthiazoles resulted in a helical conformation of the core, and two pyrene units were arranged in close proximity. Thus, an intramolecular pyrene excimer was formed (**Figure 1**), and a CPL signal at 500 nm with a large $|g_{lum}|$ (0.01) was observed. When the helical conformation of the photochromic core was destroyed by UV-light driven cyclization, the pyrene units were separated from each other, and the CPL was quenched. A reversible off-on CPL switch was observed for enantiomeric glutamate gelators modified with a spiropyran moiety (**Figure 2**) upon alternated UV and visible irradiation

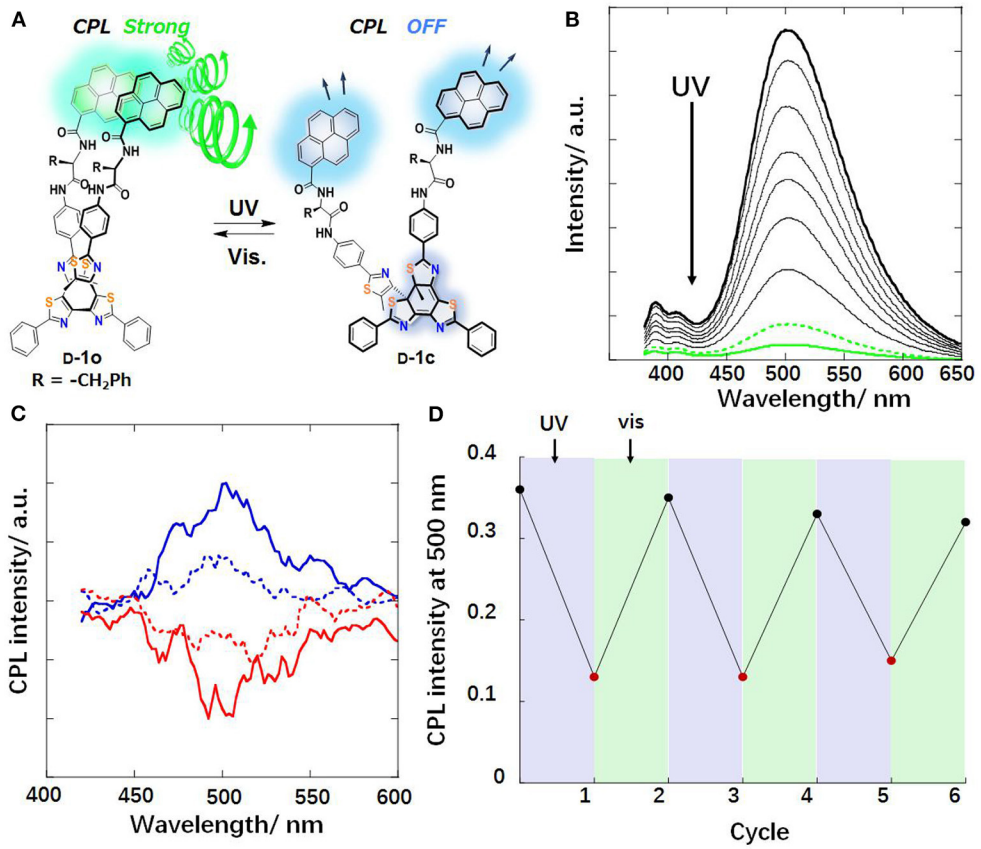

FIGURE 1 | (A) Chemical and CPL change of pyrene stack with tetrathiazole D-1 toward light irradiation. **(B)** Fluorescence spectral change of L-1o upon UV irradiation ($4.6\times10^{-6}M, CHCl_3$). Solid thick black line: 1o-form, solid green line: 1c-form, dashed green line: at photo stationary state (PSS), other traces were recorded at an irradiation interval of 5 s. **(C)** CPL spectra of 1o (1.7×10^{-4}M, $CHCl_3$). D-form: upper solid blue line; L-form: lower solid red line; dashed lines: at PSS. **(D)** Reversible CPL intensity changes of D-1o (500 nm, $CHCl_3$) (Reproduced with permission; Hashimoto et al., 2016). Copyright 2016, Royal Society of Chemistry.

(Miao et al., 2017). Chirality transfer from the chiral glutamate part to the luminophore was facilitated in the gel state. Upon UV irradiation (365 nm), the spiropyran unit changed from a colorless closed ring form to a blue zwitterionic merocyanine state accompanied by a red CPL signal (662 nm). After exposure to visible light, the CPL phenomenon was suppressed. This reversible process worked for over 30 cycles when applied in a re-writable printing application.

Light irradiation induced *Z-E* isomerization of a cyanostilbene-based chromophore resulted in different assembled structures and different related CPL behaviors. Upon exposure to UV-light, cyanostilbene-conjugated glutamide (**Figure 3**) assembled into different morphologies with inversed CPL sign (Jin X. et al., 2018). The rigid planar (Z)-PCNP formed nanobelts with a lamellar structure, exhibiting left-handed CPL (g_{lum} $\sim4.5\times10^{-3}$). Upon irradiation at 365 nm, co-existing rigid Z- and flexible E- isomers assembled to form nanotoroids, which showed right-handed CPL (g_{lum} $\sim6.6\times10^{-3}$). Similarly, a host–guest supra-gelator, which was formed by encapsulating a chiral Z-cyanostilbene gelator (CG) inside the cavity of γ-cyclodextrin (CD) (**Figure 4**), showed reversible off-on CPL, which could be switched using UV-irradiation and heating (Ji et al., 2019). The super-gelator assembled into a bilayer structure and showed CPL signal at 450 nm with slightly enhanced g_{lum} value ($\sim7.9\times10^{-3}$). The handedness of the super-gel followed the chirality of the CG unit. When the super-gelator was subjected to UV irradiation, isomerization of Z-CG to E-CG took place, the gel collapsed to a suspension of nanospheres, and the CPL signal gradually disappeared. After heating the suspension to form a solution and natural cooling down, the supra-gel was reproduced with the same CPL activity. Moreover, the reversible process was pretty robust, as confinement of the CG unit inside the cavity of γ-CD make it resistant to fatigue.

Besides the above photo chemical mechanism, the CPL switch was also observed for the photophysical mechanism. Light irradiation at selected wavelength can populate specific excited states, select the emissive state energy, then manipulate the emission probability and the emission lifetime. When a chiral ester chain was linked to the N-position of a carbazole phosphor (Li et al., 2020), an H-type aggregate in the condensed state showed CPL at 369 and 379 nm (g_{lum} ~0.0031) upon photoexcitation at 365 nm. Moreover, chiral phosphorescence

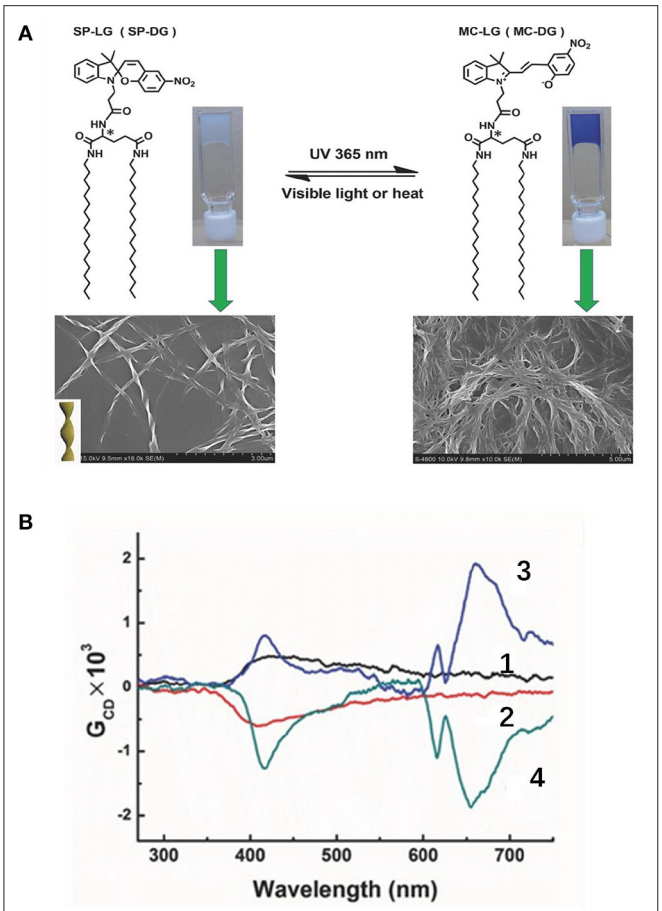

FIGURE 2 | (A) Reversible molecular structure change of spiropyran-modified glutamate gelator between a colorless closed ring state and a blue zwitterionic emissive state toward alternating UV and visible light irradiation, with the related SEM images of SP-LG xerogels (lower part). **(B)** CPL spectra before UV irradiation (SP-LG (1), SP-DG (2) gels) and after UV irradiation for 8 min (MC-LG (3), MC-DG (4) gels). Reproduced with permission (Miao et al., 2017). Copyright 2017, John Wiley and Sons.

at 550 and 596 nm (g_{lum} ~0.0027) was observed at room temperature (CP-RTP) after removal of the photo excitation (**Figure 5**). With extended irradiation time (365 nm, <40 s), ultralong lifetime CP-RTP (CP-OURTP) was observed by naked eye at room temperature or at low temperature. With elevated temperature at 50°C, the signal of CP-OURTP diminished within 5 min. After lowering the temperature and repeating photo-activation, the CP-OURTP signal recovered without photo bleaching. Thus, a reversible irradiation turn-on and thermal turn-off CP-OURTP system was developed.

HOST–GUEST INTERACTION

Engineered rotaxanes with different sizes were demonstrated as containers to encapsulate various guests. Association–disassociation of the host–guest interaction can serve as a switch for further excimer formation, chirality transfer, chirality inversion, and modulate the on-off state of CPL behaviors. When two polycyclic aromatic chromophores (PAH) (NDI, Pyrene, perylene, and fluorene) were linked to the same face of modified crown-ethers, the close geometrical contact between the PAH units resulted in the formation of intramolecular excimers (Homberg et al., 2018). G_{lum} values as high as $\sim 10^{-2}$ were observed. After selective binding the crown-ether with metal ions such as Na^+ and Ca^{2+}, the central cryptand acquired a new geometry in which the chromophores were situated far away from each other. The excimers were thus disrupted and the related CPL suppressed.

When the host was changed to chiral (P-/M-) 2,6-helic[6]arene cycle, the complexation with guest 4-[(4′-N, N-diphenylamino)styryl]-N-methylpyridinium iodide in water showed mirror-imaged CD and CPL signals (Guo et al., 2019). The chirality transfer from the host to the guest resulted in chiral emission of the guest, which was absent for the guest alone. Moreover, the chirality transfer was tunable by temperature and pH. In detail, higher temperature (up to 70°C) caused faster rotation and motion of both the host and the guest, then deteriorated the chirality transfer. Similarly, either lower or higher pH other than the neutral condition caused lower CPL signals due to either destructed assembly or weakened host–guest interaction. By selecting different inclusion units for a [2]rotaxane, David et. al reported a molecular machine based on-off CPL switch (David et al., 2019). A crown-ether macrocycle with an emitting 2,2′-bipyrene unit was threaded with a secondary ammonium unit, which was linked with chiral D- or L- phenylalanine moieties (**Figure 6**). When H-bonding was formed between the luminophore and the chiral center under acidic conditions, CPL signals appeared and the handedness was determined by the phenylalanine unit. By contrast under basic conditions, the location of the macrocycle shifted along the thread to the triazolium group, which disabled the aforementioned chirality transfer. Such an on-off switch worked *in-situ* and only had impact on the CPL signal without quenching the photoluminescence.

In a similar concept, alternative addition of potassium ions (K^+) and cryptand were applied to invert the chirality of a G-quadruplex DNA (G4 DNA) (Chen et al., 2019). Parallel arrangement G4 DNA can be changed to anti-parallel arrangement by addition of K^+, and the inclusion of luminescent ThT (3,6-dimethyl-2-(4-dimethylaminophenyl)-benzo-thiazolium) cations produced different handedness (490 nm, g_{lum} ~0.5×10^{-3} to 1.5×10^{-3}, 10°C). Moreover, the ordered assembly of G4 DNA and ThT was promoted at low temperature (10°C), which could switch CPL on. Higher temperature (10–70°C) dissolved the assembly and turned the CPL off. Thus, switching of both handedness and intensity was realized for the assembled complex of G4 DNA and ThT.

METAL IONS

Metal-ligand interaction has been demonstrated as a facile method to tune CPL performance, by modifying the active chromophores through changes in their conformation, chemical

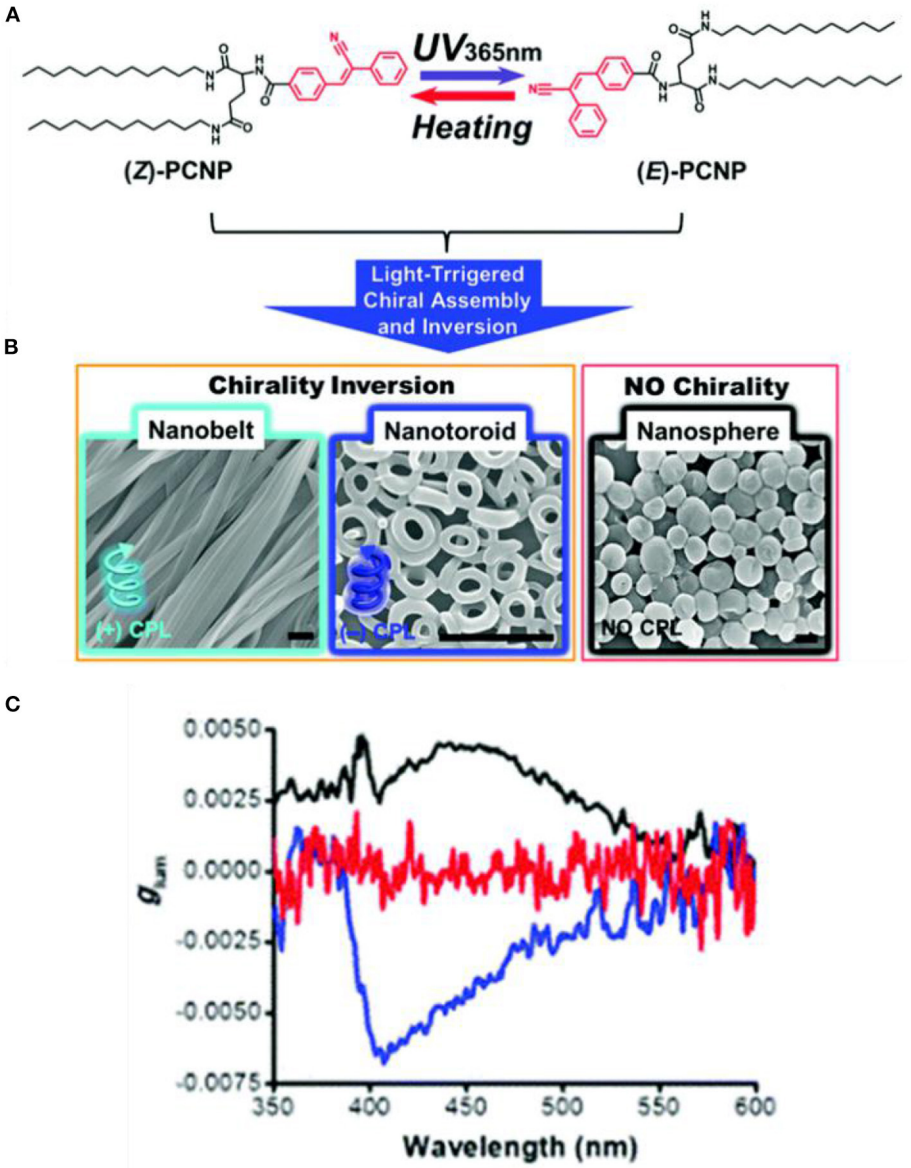

FIGURE 3 | (A) Z-E isomerization of PCNP under UV irradiation. **(B)** SEM images of the different assembled nanostructures with different irradiation duration (365 nm). From left to the right: Nanobelts (0 min); nanotoroids (15–120 min); and nanospheres (150 min). Scale bar: 1 mm. **(C)** Glum curves of nanobelts (black), nanotoroids (blue), and nanospheres (red). Reproduced with permission (Jin X. et al., 2018). Copyright 2018, Royal Society of Chemistry.

composition, electronic structure, assembly behavior, etc. This is often reversible by extracting the metal ion with strong chelating ligands. Multiple metal ions have been applied, including Zn^{2+}, Ag^{+}, Ni^{2+}, and Al^{3+}.

Turn-on of CPL upon coordination of Zn^{2+} with terpyridine, salen, and dipyrromethene units is accompanied by geometrical changes. A terpyridine suspended bis- aza[6]helicenic unit changed from trans, trans-N,N orientation to cis, and cis-N,N orientation upon coordination with Zn^{2+} ions (**Figure 7A**), which resulted in the flip-over of one helicene moiety and charge-transfer from the helicene to the terpyridine part (Isla et al., 2016). Correspondingly, the positive CD signal at 341 nm decreased slightly and the emission shifted from 420 to 480 nm with greatly enhanced intensity (Φ_{FL} from 0.08 to 0.19), while g_{lum} values decreased slightly to $+1.2 \times 10^{-3}$ and -1.4×10^{-3} for (P, P) and (M, M)-isomers, respectively. Moreover, the Zn^{2+}-terpyridine coordination was reversible by adding a competitive ligand N, N, N′, and N′-tetrakis(2-pyridylmethyl)ethane-1,2-diamine so that the CPL behavior could be recovered. BINOL based polymer enantiomers with Salen units showed turn-on CPL (465 nm, g_{lum} ~8×10^{-3}) upon coordination with Zn^{2+} (0.3–4.0 equiv) (Meng et al., 2018), with the handedness being determined by the chiral BINOL unit. The CPL signal was induced by effective chirality transfer from the binaphthyl moiety

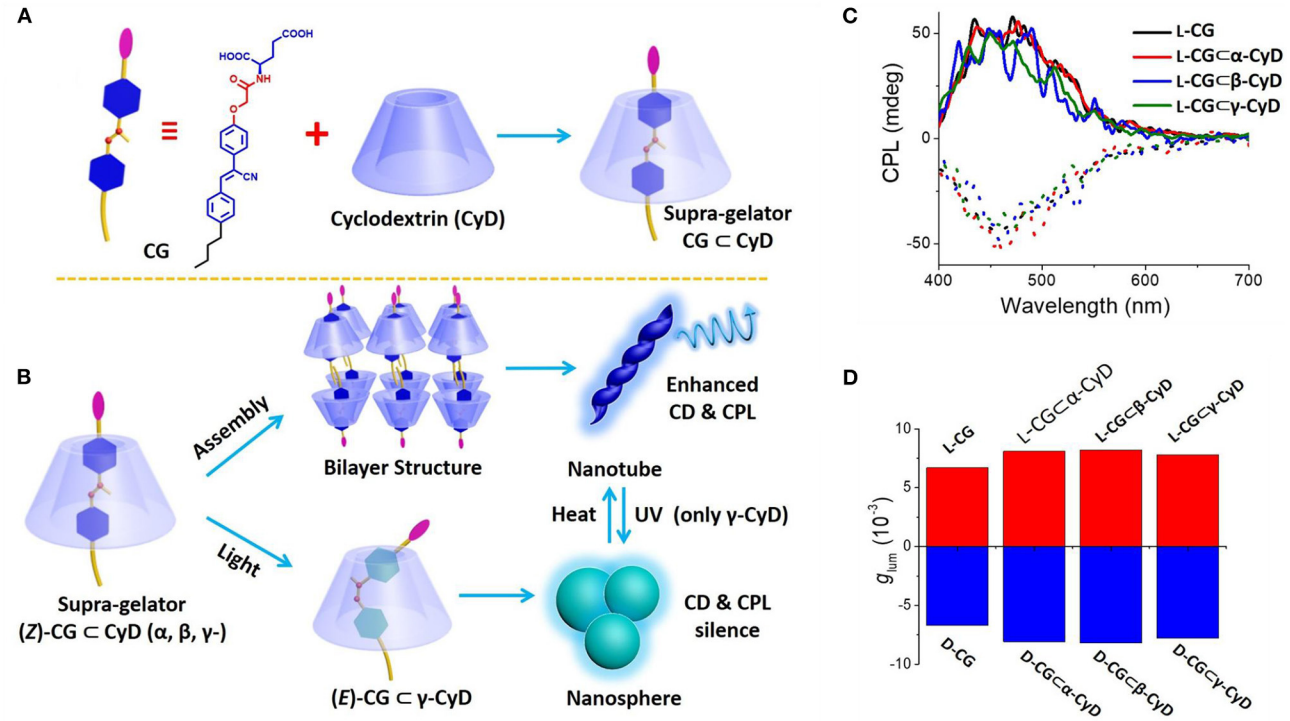

FIGURE 4 | (A) Molecular structure of hydrogelator CG and schematic formation of supra-gelator CG-CyDs. **(B)** Suggested gelation route of supra-gelator CG-CyDs (upper), UV irradiation induced Z–E isomerization in CG-CyD and the morphology change between nanotube and nanosphere (bottom). **(C)** CPL curves of CG and CG-CyDs hydrogels. **(D)** Glum values plot of CG and CG-CyDs hydrogels. The dashed lines refer to the counterparts of the D-configuration CG based gels. [CG] = 6.5 mM, [CG-CyD] = 6.5 mM. Reproduced with permission (Ji et al., 2019). Copyright 2019, Royal Society of Chemistry.

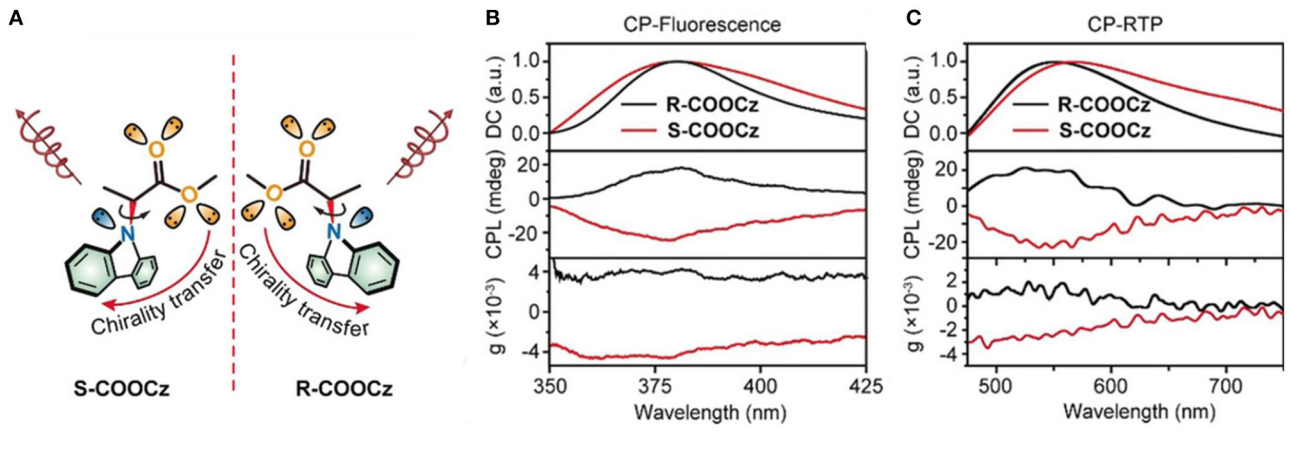

FIGURE 5 | (A) Molecular design of chiral CP-OURTP molecules (S- and R- COOCz). **(B)** CP-Fluorescence curves excited at 295 nm. **(C)** CP-RTP curves excited at 365 nm. Reproduced with permission (Li et al., 2020). Copyright 2020, John Wiley and Sons.

to the Zn^{2+}-Salen unit. Addition of EDTA as a competitive Zn^{2+} binder can switch-off the CPL signal. Another example of Zn^{2+} coordinated complex with turn-on CPL in the far-red region (wavelength: 700–850 nm, Φ_{FL}: 0.23) was reported in 2018 (Ito et al., 2018). In this system, a pair of achiral benzo[a]phenanthrene-fused dipyrromethene ligands formed a helical structure upon coordination with Zinc(II) (**Figure 7B**), which showed strong exciton-coupled chiroptical responses in both ground state (g_{abs}~0.20) and the excited state (g_{lum} ~0.022). Notably, the asymmetrical luminescence factor was the largest yet reported among rare-earth- and precious-metal-free small molecules.

Besides the on-off switch, a switch of the CPL emission colors were also reported for Zn(II) complexes in case of imidazole

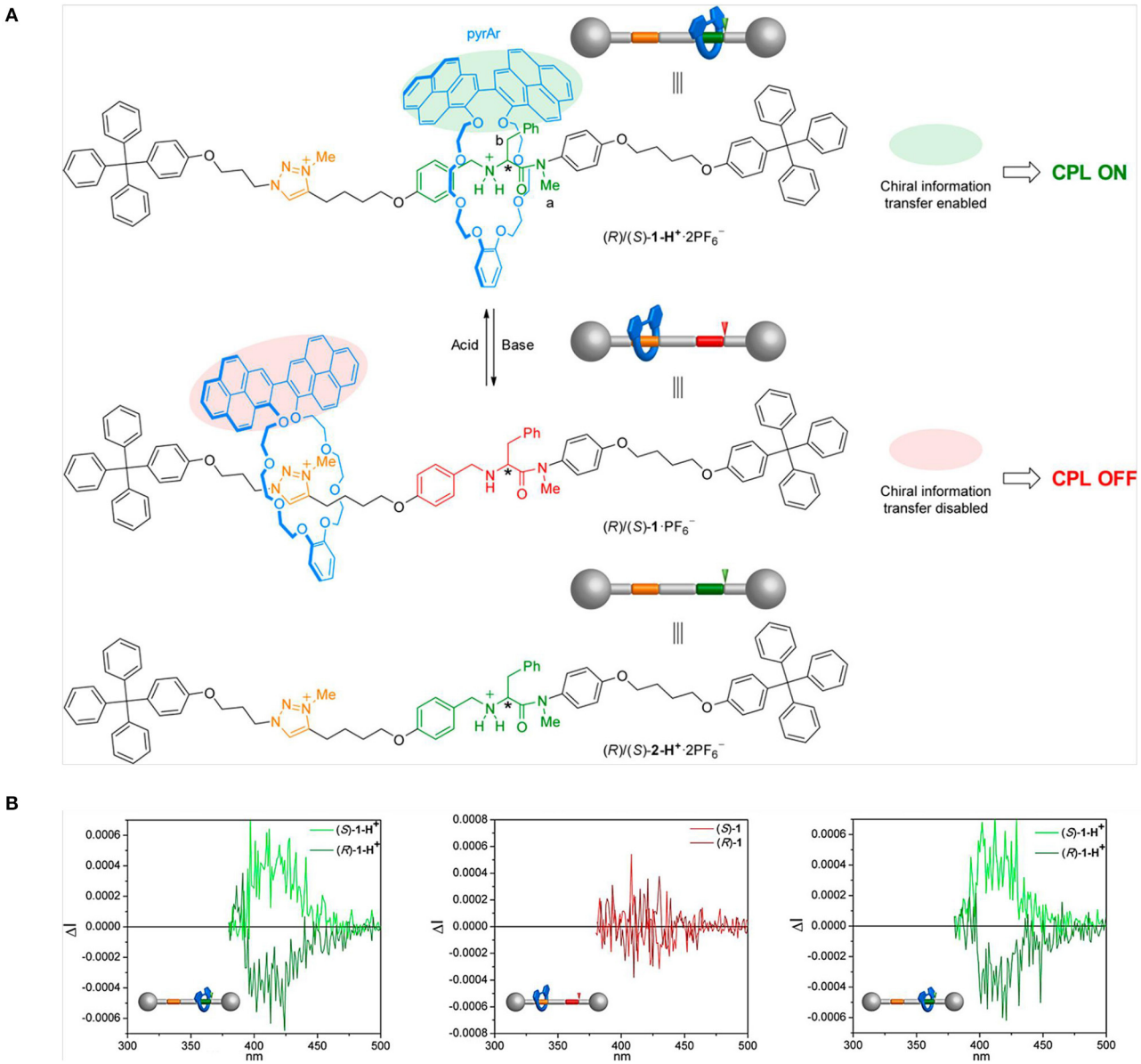

FIGURE 6 | (A) On–off CPL switching of rotaxanes (R)/(S)-1-H^+·$2PF_6$ by acid/base- controlled chirality transfer from the thread to the pyrene containing macrocycle. **(B)** CPL spectra of 1-H^+·2PF6$^-$ (left), 1·PF6$^-$ (middle), and 1-H^+ (right), obtained by protonation of 1·PF6$^-$ with CF_3CO_2H in $CHCl_3$, condition: normalized ΔI scale, λ_{exc} = 355 nm, ca. 1 × 10^{-5} M. Reproduced with permission (David et al., 2019). Copyright 2019, American Chemical Society.

or histidine ligand, which originated from changes in their compositions or their assembly behavior. CPL activities of pyrene bridged dual chiral imidazole units (L^S) were found to be dependent on the ratio of ligand to Zn^{2+} (Imai and Yuasa, 2019). When the molar ratio of $[Zn^{2+}]/[L^S]_0$ was <0.33, a complexation with the formula of (Zn_1L_3)n appeared with blue pyrene monomer emission (445 nm, 467 nm), and no CPL signal was detected. When the molar ratio of $[Zn^{2+}]/[L^S]_0$ increased to 0.33–0.67, a (Zn_2L_3)n complex formed that showed yellow emission (535 nm) (**Figure 7C**). The CPL signal was switched on, showing good asymmetrical behavior ($|g_{lum}|$ ~0.01) and emission quantum yield (Φ_{FL}~0.10). By contrast, the ligand with L- chirality did not show a similar CPL switch. Pyrene-conjugated L-histidine assembled into nanofibers and formed gels in a mixture of EtOH/H_2O (v/v 1:4), which exhibited right-handed CPL (500 nm). After complexation with Zn^{2+}, the newly formed histidine-based penta-coordinated Zn(II) complex assembled into nanospheres, and the gel collapsed to form a suspension (Niu et al., 2019). Accordingly, the π stacking of the pyrenes unit shifted from a T-shaped to a nearly paralleled arrangement, the related CPL signal shifted from the excimer emission to the monomer emission, and the CPL handedness was inverted from

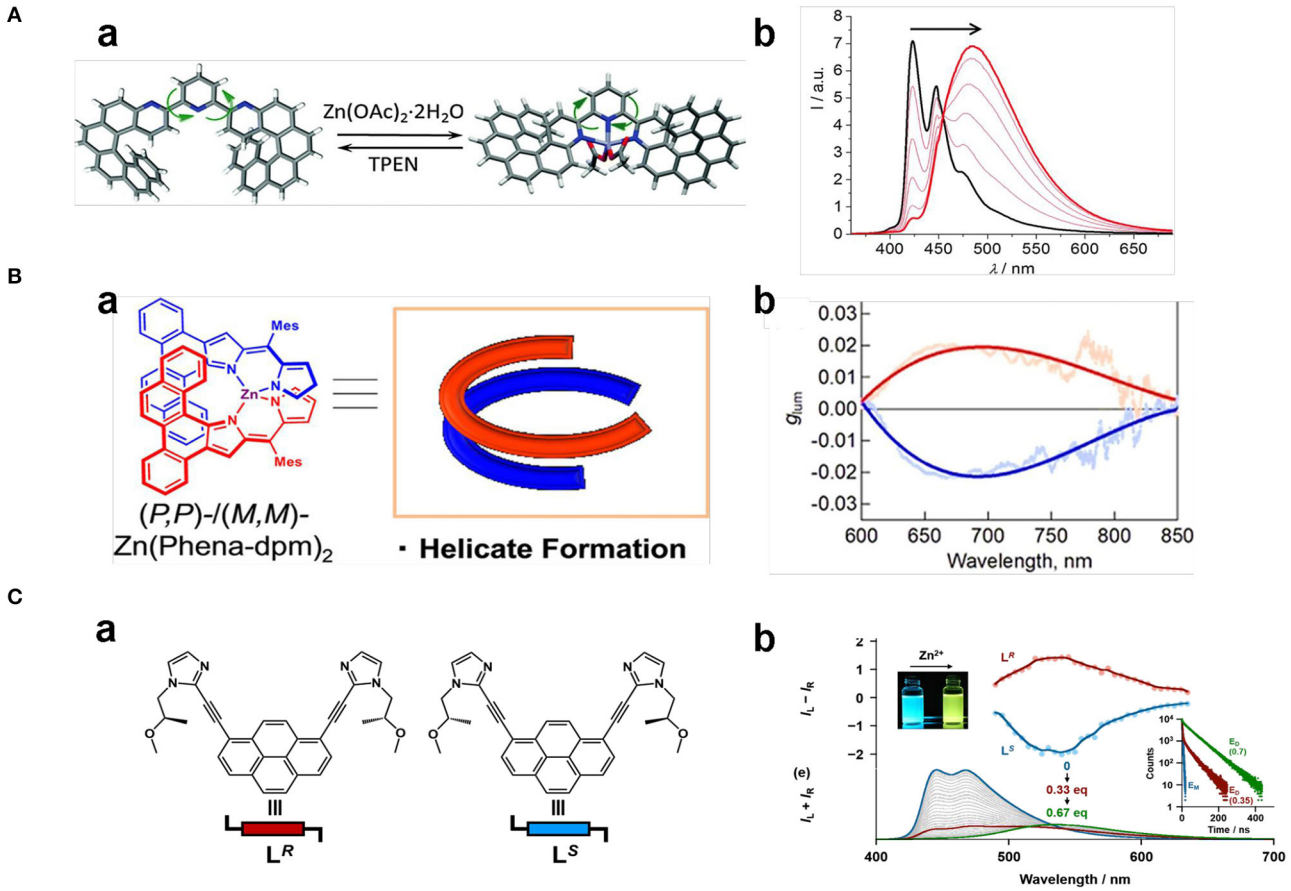

FIGURE 7 | (A) (a) Reversible Zn(II) complexation–decomplexation process of (P,P)-1 upon addition of $Zn(OAc)_2$ and TPEN. (b) Complexion-related fluorescence change of (P,P)-1 (λ_{ex} = 350 nm, 2.2 × 10^{-5} M in CH_2Cl_2. **(B)** (a) Zinc(II) helicate ($Zn(Phena\text{-}dpm)_2$) formed by coordinating with two achiral phenanthrene-fused dipyrromethene ligands. (b) Smoothed g_{lum} curves of M,M (red line) and P, P enantiomer (blue line) measured in toluene (λ_{ex} =580 nm), respectively. **(C)** (a) Chemical structures of chiral ligands L^R and L^S. (b) Emission color change (upper left) and emission spectral change (lower left, λ_{ex} = 380 nm) of L^S toward Zn^{2+}, CPL of L^R and L^S (middle) (2.0 × 10^{-5} M) in the presence of Zn^{2+} (1.4 × 10^{-5} M), emission decay profiles of L^S (2.0 × 10^{-5} M) (right) without Zn^{2+} (blue), with low ratio of Zn^{2+} (7.0 × 10^{-6} M (red), λ_{em} = 446 nm), and with high ratio of Zn^{2+} (1.4 × 10^{-5} M (green), λ_{em} = 535 nm). **(A)** Reproduced with permission (Isla et al., 2016). Copyright 2016, Royal Society of Chemistry). **(B)** Reproduced with permission (Ito et al., 2018). Copyright 2018, John Wiley and Sons. **(C)** Reproduced with permission (Imai and Yuasa, 2019). Copyright 2019, Royal Society of Chemistry.

right handedness to left handedness (**Figure 8A**). Such emission switch of wavelength and handedness was reversible by removing the Zn(II) ions with the strong chelator EDTA.

Ni^{2+} and Al^{3+} worked similarly through complexation to modify both the assembly behavior and CPL properties of organic molecules. A chiral phenylalanine-derived hydrogelator and a pyridine modified achiral coumarin co-assembled to form chiral gels, showing CPL at around 450 nm ($g_{lum} \sim 10^{-2}$) with handedness being dependent on the position of the pyridine nitrogen atom (Wang et al., 2019). The introduction of Ni^{2+} removed the influence of the N-position and resulted in all the isomers producing the same P-helix and left-handed emission (**Figure 8B**). The different handedness was inferred to result from different dominant hydrogen-bonding interactions, including carboxylic acid-pyridine hydrogen bonds and amide hydrogen bonds. Thus, CPL with opposite handedness was obtained by tuning the nitrogen position and the metal additive. Aluminum ion (Al^{3+}, $AlCl_3$, ethanol) (Jin Q. et al., 2018) was found to turn-on the CPL of glutamide-derived amphiphilic Schiff base containing a 1-hydroxyl-2-naphthaldehyde group. Inhibition of photon-induced electron transfer (PET) or excited-state induced proton transfer (ESIPT) enhanced the blue emission and specific chirality transfer from the ligand to the chromophore resulted in observable CPL emission (465 nm, $|g_{lum}| \sim 6.21 \times 10^{-4}$).

Along with the coordination mechanism, metal ion also affected the assembly through carbophilic and oxophilic interactions. For instance, CPL activity of ortho-oligo-(phenylene)ethylene (OPE) foldmers can be tuned by adding either carbophilic Ag^+ or oxophilic Ca^{2+}, Sc^{3+}, and Zn^{2+} ions. A series of ortho-oligo-(phenylene)ethylene (OPE) foldmers were confined into chiral helical structure by introducing enantiopure 2,3-dihydroxybutane diethers, exhibiting strong CPL responses (g_{lum} values up to 1.1× 10^{-2}) and a low but acceptable fluorescence efficiency (Φ_{FL} ~0.069 in CH_2Cl_2).

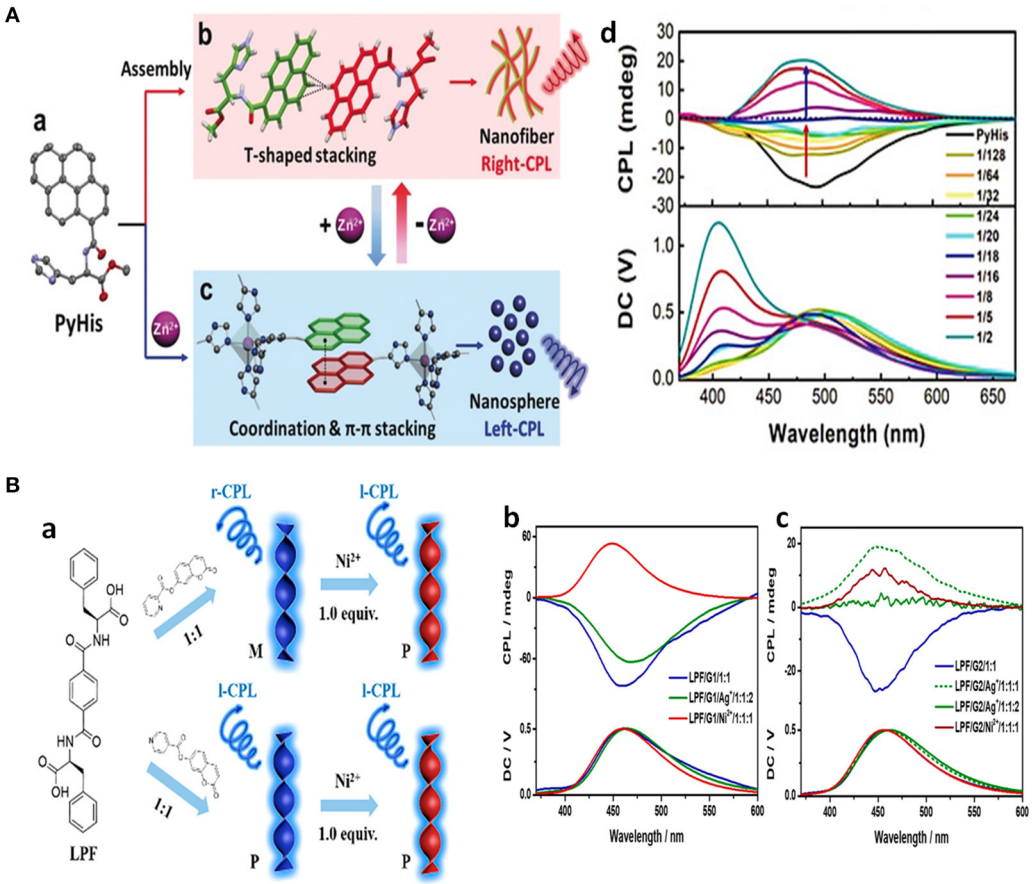

FIGURE 8 | (A) Schematic illustration about assembly changes and CPL changes of the chiral gelator PyHis toward Zn^{2+}. (a) Single-crystal structure. (b) T-shaped stacking of pyrenes in PyHis nanofibers, showing right-handed CPL. (c) π-π stacking of pyrenes with distorted triangular bipyramid $[Zn(PyHis)_5]^{2+}$ complex, which formed nanospheres with increasing amount of Zn^{2+} and showed left-handed CPL. (d) CPL spectra change of l-PyHis gel upon increased amount Zn^{2+} (λ_{ex} =330 nm). **(B)** Schematic illustration of CPL behaviors dependent on pyridyl-N location of coumarin derivatives, and further Ni^{2+} (a). PL and fluorescence spectra of pyrenes of LPF/G1 (b), LPF/G2 (c) hydrogels with different amount of Ag^{+} or Ni^{2+} ions, excited at 320 nm. (a) Reproduced with permission (Niu et al., 2019). Copyright 2019, John Wiley and Sons. (b) Reproduced with permission (Wang et al., 2019). Copyright 2019, American Chemical Society.

When Ag^{+} was introduced, its strong affinity toward alkyne units resulted in its confinement within the OPE cavity. As a result, the conformation changed from a helical structure to a planar-like structure, which resulted in a decrease of g_{lum} values by up to one order of magnitude (Morcillo et al., 2016). Recovery of the asymmetrical optical properties can be achieved by adding a stoichiometric amount of competitive CH_3CN to extract the confined Ag^{+} ions. When such an OPE helical skeleton was functionalized at both the C1 and C2 stereogenic positions with a pyrene unit, dual wavelength CPL emission in the blue (centered at 400 nm) and green (centered at 500 nm), originated from the OPE helicate and pyrene excimer located, respectively (**Figure 9**). Similar CPL silencing from the OPE unit upon carbophilic association with Ag^{+} ion was observed (Reine et al., 2018), while the CPL signal from the pyrene units was retained. With careful screening of the bridge between the chiral 2,3-dihydroxybutane diethers moiety and the pyrene units, the CPL signal [ΔI (400 nm)/ΔI (500 nm)] of one foldmer [(P,1S,2S)-2, CH_2 bridge] acted as a ratiometric probe toward Ag(I) concentration.

When the OPE unit was modified with sulfoxides at the end positions, oxophilic metal cations (Ca^{2+}, Sc^{3+}, and Zn^{2+}) interacted with oxygen atoms, promoted the folding of OPE to form helical conformation, and turned on the chiroptical properties (Reiné et al., 2018). Meanwhile, the helical conformation avoided aggregation induced emission quenching of the fluorophore itself. Consequently, the metal complexes exhibited both glum values and high Φ_{Fl}. A representative example was the Sc^{3+} complex, of which the g_{lum} and Φ_{Fl} were -7.1×10^{-3} and 0.38, respectively.

pH

Manipulating pH value has been demonstrated to be a broadly applicable tool to tune both the wavelength and the intensity

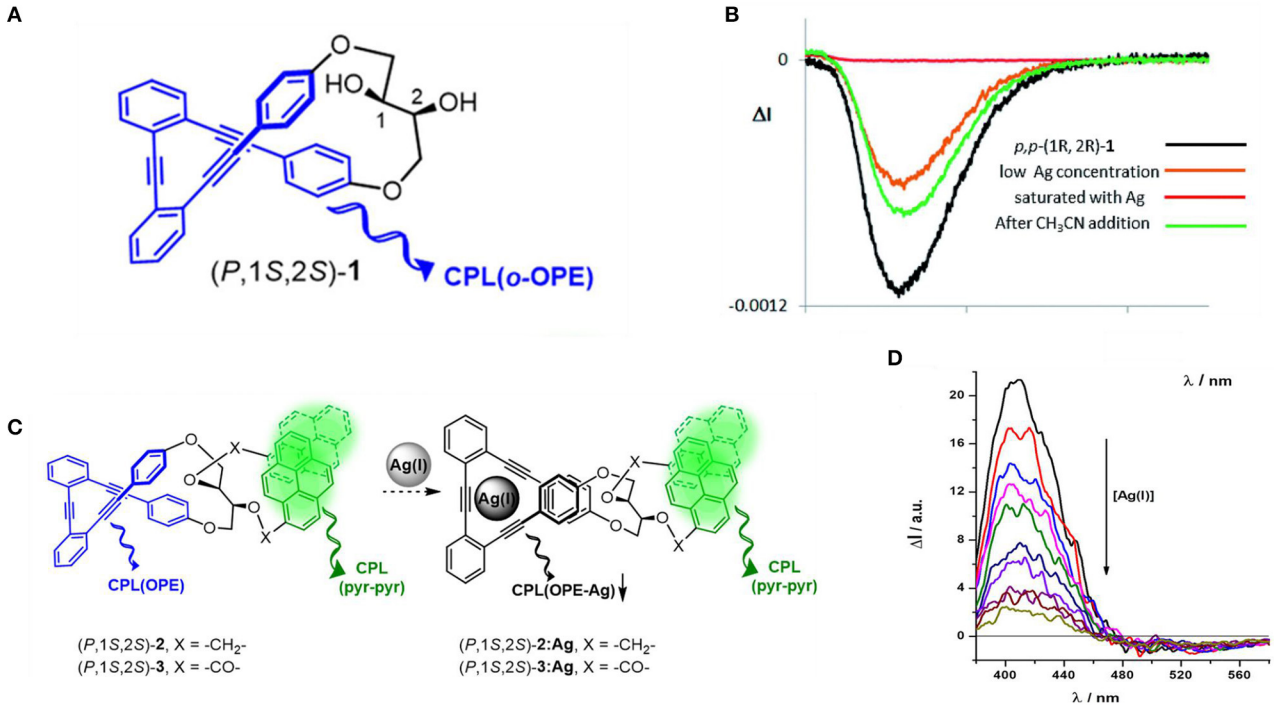

FIGURE 9 | (A) Chemical structure of helical oligo(phenylethylene) (*P*,1s,2s)-**1**. **(B)** CPL titration curves with increasing amount of $AgBF_4$ until saturation, and with following addition of CH_3CN. **(C)** Schematic mechanism of a (*P*,1s,2s)-1 based ratiometric CPL probe based. **(D)** CPL titration curves of (*P*,1s,2s)-**2** with increasing amount of $AgBF_4$. **(A,B)** Reproduced with permission (Morcillo et al., 2016). Copyright 2016, Royal Society of Chemistry. **(C,D)** Reproduced with permission (Reine et al., 2018). Copyright 2018, American Chemical Society.

of CPL. The wavelength shift was achieved by protonation of N-heterocycle-containing chromophores or deprotonation of acidic protons. The intensity tune was exemplified by tuning the competing non-emissive pathways. Moreover, both changes could be facilely reversed by reverting to the original pH by adding appropriate amounts of acid or base. The CPL color of benzimidazole-fused [5]carbohelicene ([5]HeliBI) (**Figure 10A**) can be switched from yellow (570 nm) to red (650 nm) by protonation with trifluoroacetic acid to form (H^+- [5]HeliBI) (Sakai et al., 2016). Both yellow and red CPL show high g_{lum} values in the CH_2Cl_2 solution, which were estimated to be $\sim 9.45 \times 10^{-3}$ and $\sim 5.92 \times 10^{-3}$, respectively. Moreover, the process was reversible by deprotonation with pyridine. Similar reversible CPL emission tuned by acid/base addition (HBF_4, Na_2CO_3/NEt_3) was observed for both P- and M- 3-(2-pyridyl)-4-aza[6]helicene (Saleh et al., 2015). Bathchromic emission from 426 to 590 nm was observed after dual protonation, while the quantum yield, lifetime, and g_{lum} value ($\sim 10^{-3}$) remained almost the same (**Figure 10B**). For diaza [4] helicene functioned with a carboxylic acid group, lowering the pH from 7.3 to 0.4 resulted in protonation of the zwitterion form to the protonated from (Pascal et al., 2016), and the fluorescence emission was shifted from 709 nm (acetonitrile, QY$\sim$0.01%) for to 654 nm (QY $\sim$0.29%) (**Figure 10C**). Differently, no CPL signal was detected for the former, while CPL signal (600 nm) was turned on for the later with a g_{lum} value of $\sim 5 \times 10^{-4}$. Thus, an off-on CPL switch was achieved by increasing/lowering the acidity of the system. Turn-on of CPL by lowering pH was also observed for a co-assembled gel of achiral perylene bisimide dye and N,N'-bis(octadecyl)-L/D-Boc glutamic diamide gelator (**Figure 10D**), which was a result of chiral transfer from the chiral part to PBI and inhibited photon induced charge transfer in the PBI unit (Han D. et al., 2018). The CPL sign was the same as the chirality of the chiral gelator, and the bright yellow emission was centered at 558 nm. The g_{lum} was calculated to be a moderate $\sim 9 \times 10^{-3}$. When the co-gel was exposed to a basic atmosphere, such as ammonia, the CPL signal could be reversibly switched off. Thus, an on-off CPL switch was obtained by applying the co-gel to alternating acidic and basic conditions.

Besides the above-mentioned cases using Lewis acid/base and Brönsted acid/base activation, a photo-acid functionalized dye also showed pH dependent emission behavior. In the co-assembled gel of non-emissive photoacid 8-hydroxy-1,3,6-pyrenetrisulfonate (HPTS) and chiral amino-terminated dialkyl glutamide (LG) (**Figure 11**), the emission wavelength and the g_{lum} value was modulated by the composition of solvent or acid/base additive (Fan et al., 2019). A mixed molar ratio of 1:10 of HPTS:LG assembled in DMF:H_2O resulted in nanotube structure, with the components arranged in a lamellar motif. CD signals in the same range of absorption (250–450 nm) retained the chirality from the gelator, which proved that chirality transfer occurred from the gelator to the photoacid. Upon excitation in

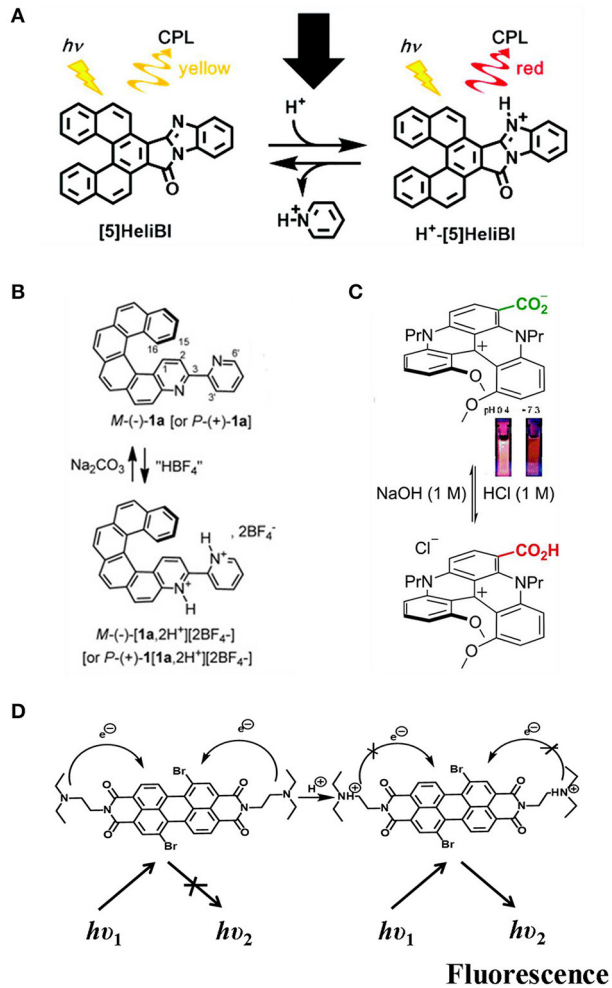

FIGURE 10 | (A,B) pH induced switchable CPL based on pyridine N- atom. **(C)** deprotonation of aromatic carboxylic acid. **(D)** protonation of tertiary amine. **(A)** Reproduced with permission (Sakai et al., 2016). Copyright 2016, Royal Society of Chemistry. **(B)** Reproduced with permission (Saleh et al., 2015). Copyright 2015, John Wiley and Sons. **(C)** Reproduced with permission (Pascal et al., 2016). Copyright 2016, Royal Society of Chemistry. **(D)** Reproduced with permission (Han D. et al., 2018). Copyright 2018, Royal Society of Chemistry.

a proton-accepting environment (mixed solvent of DMF:H_2O ratio < 7:3, or basic condition), excited-state induced proton transfer from the photoacid to the environment shifted the CPL signal from 420 nm (pristine HPTS) to 520 nm (deprotonated HPTS). Meanwhile, the g_{lum} of the green emission was increased to 10^{-3}.

CONTROLLED ASSEMBLY SWITCHABLE BY SOLVENT, TEMPERATURE, AND OTHER MISCELLANEOUS FACTORS

CPL materials usually showed higher g_{lum} values from aggregates or assembled states than from the monomers, and manipulation of the assembly behavior resulted in tunable CPL performances. Broadly applicable manipulating factors included solvent, temperature, and mechanical forces.

Solvents with varied polarity, hydrogen-bonding capabilities and solubility have been used to tune the electronic structure through intramolecular charge transfer (ICT), the assembly behaviors, and the formation of excimers, respectively. Modulating the intramolecular charge transfer process of axial chiral triarylboranes resulted in switchable CPL behaviors. For 2,2′-bis(diphenylamino)-6,6′-bis(dimesityl-boryl)-1,1′-binapthyl with a D-π-A structure (Sun Z. et al., 2019), increasing solvent polarity from cyclohexane (455 nm) to MeCN (521 nm) showed an obvious red-shifted emission from 440 to 512 nm (**Figure 12**). Correspondingly, reversal of CPL sign was observed for the (+)-isomer in cyclohexane (negative signal) and in MeCN (positive signal). Similar sign inversion was also detected by using an excess amount of fluoride ions (F^-), which complexed with the boron atoms to greatly enhance the emission intensity and asymmetry ($|g_{lum}| \sim 10^{-2}$). Handedness reversion by changing solvents was also observed due to reversal of the orientation of the helix. For a random polymer containing achiral fluorescent 5,7-bis(4-methyloxyphenyl)quinoxaline and chiral units modified with (S)-3-octyloxymethyl groups (Nishikawa et al., 2017), solvent change from n-octane to cyclooctane resulted in conformation change of the polymer from pure M- to P-helical, and the correspondent CPL shifted from right handedness to left handedness (**Figure 13A**). Moreover, the change of conformation was determined only by the chiral moiety, and the emission color can be tuned by modifying the luminescent part with different substituents. Thus, the polymer can be tuned orthogonally to prepare CPL materials with convertible handedness and variable emission colors. Furthermore, solvent tunable handedness was achieved for pyrene incorporated axially chiral 2-hydroxy 3, 3′-dimethylbinathyls with carefully designed substituents (**Figure 13B**). Highly polarized negative excimer emission in non-polar toluene (538 nm, g_{lum} ∼-0.012) was reversed to right-handedness in polar DMSO (520 nm, g_{lum} ∼0.012) (Takaishi et al., 2020). The sign switch was attributed to the reduced intermolecular H-bonding in the polar solvents and corresponding lower population of the left-handed excimer. This hypothesis was confirmed further by lowering the temperature. This resulted in the stronger negative emission being observed in toluene and lower positive emission being observed in acetone.

Along with switchable CPL behaviors in pure solvent, a ratio change between good solvent and poor solvent (mixture of THF and H_2O) has also been reported to produce tunable CPL. For a 1,8-naphthalimide fluorophore linked with chiral 1,2-diaminocyclohexane (DACH) (Sheng et al., 2016), excimer-type CPL with large g_{lum} ($\sim 10^{-2}$) was observed in THF or mixture of H_2O and THF with <90% water. Upon increasing the water content above 90%, the assembly changed from an irregular form to an ordered aggregate, and the CPL sign was reversed. Similar THF/water ratio dependent assembly and CPL performance were observed for R- or S-SPAn (Ma K. et al., 2019). With increasing water ratio, the orderly aggregates changed from 0D nanoshperes (THF/H_2O ∼50:50), 2D flake (THF/H_2O ∼85%) to 3D nanoflakes (THF/H_2O ∼90%).

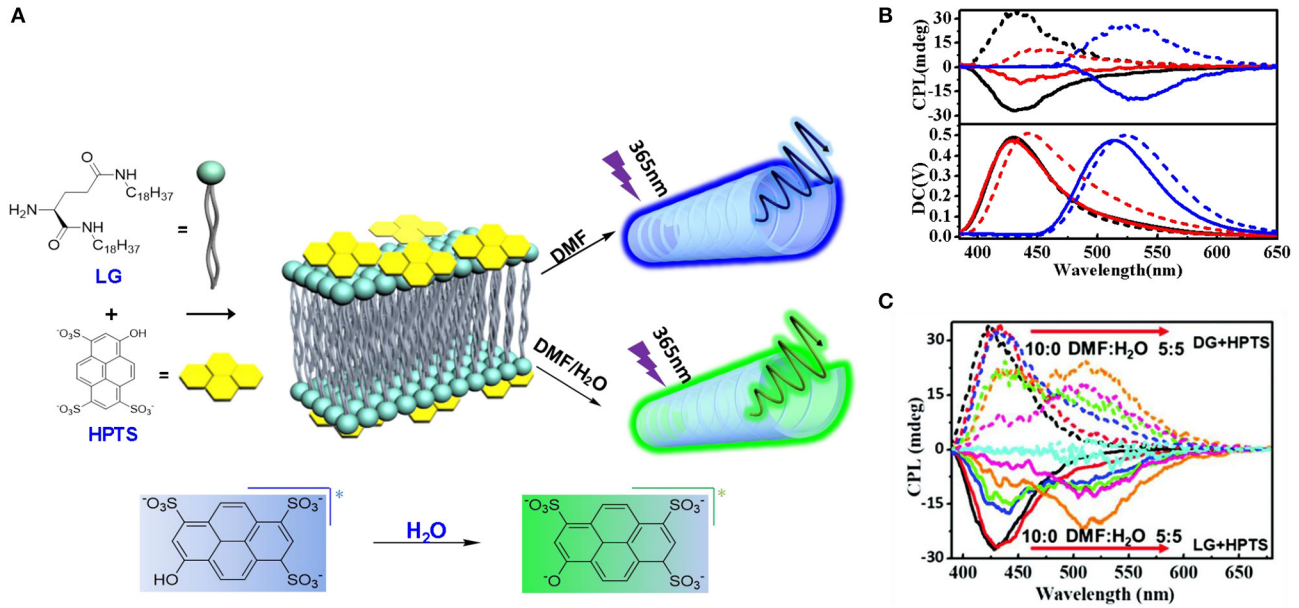

FIGURE 11 | (A) Chemical structure of LG and HPTS, and the schematic demonstration about CPL dependence on solvent by deprotonation (RO–). **(B)** CPL spectra of LG/HPTS (DMF/H_2O = 9 : 1) gels (black line) and LG/HPTS gels with acid (red line) and base (blue line). Solid lines refer to LG/HPTS and dotted lines represent the DG/HPTS system. **(C)** CPL spectra of LG/HPTS (dash) and DG/HPTS (line) supramolecular gels in mixed solvents of N,N-Dimethylformamide (DMF) and water (H_2O). The measurements were carried out in the solutions with a concentration of ~1.23×10^{-4} M at room temperature, under the excitation of 370 nm. Reproduced with permission (Fan et al., 2019). Copyright 2019, Royal Society of Chemistry.

Meanwhile, the emission wavelength shifted from 420 nm (Φ_{FL}: 0.6), 432 nm (Φ_{FL}: 0.04) to 460 nm (Φ_{FL}: 0.13). The related g_{lum} value increased from the value of 10^{-4}, 7.2×10^{-3}, to 2.9×10^{-2}, inferring favor of high g_{lum} with larger ordered structures.

The CPL behaviors were influenced by temperature through cooling to form ordered chiral assemblies or through heating to dissolve the assembly, which was utilized to tune either the CPL handedness or the emission wavelength. Upon lowering the temperatures, two-stage cooperative assembly of dithienogermole (DTG) molecules driven by dipole-dipole interaction of chiral phenylisoxazoles pendants was observed in methyl-cyclohexane (MCH), including a first nucleation stage and a later elongation stage. Correspondingly, CPL signals with different emission wavelengths and inverted handedness were observed (Hirano et al., 2019). When the temperature was initially dropped from 40 to 20°C, a weak positive CPL appeared at 566 nm (**Figure 14**). Further cooling to 10°C resulted in increased CPL at 566 nm, and a new negative signal at 472 nm was observed. After further cooling to −10°C, the positive signal disappeared, and only a negative signal at 514 nm was detected. Thus, the temperature dropping from 20 to −10°C fully inverted a positive signal at 566 nm (g_{lum} ~8×10^{-4}) to a negative signal at 514 nm (g_{lum} ~-3×10^{-4}). Similar sign change was also observed in the CD signals for both the S- and R- enantiomers, which suggested the assembly behavior dominated the chirality in both the ground and excited states. Thus, chirality inversion was achieved by controlled assembly at different temperatures. Similarly, L-glutamide-functionalized phenyl anthracene (g-PA) showed solvent- and cooling-rate-dependent CPL signals (Jintoku et al., 2015). In pure THF, no CPL signal was observed. In a mixture of n-hexane/THF (50:1), the organic gel showed clear excimer-type CPL signal at 526 nm, and the g_{lum} value is ~3.2×10^{-3}. Thus, the gel state enhanced chirality transfer from the L-glutamide unit to the excimer of anthracene. As the temperature elevated from 10 to 60°C, excimer emission was changed to monomer emission (426 nm) with decreasing g_{lum}. Moreover, the slower the reversed cooling process, the higher ratio of the excimer CPL at 10°C.

Moreover, CPL performance switched with mechanical triggers, and oxidation anions and co-assembled achiral isomers were reported. Mechanical mixing of difluoro-boron β-diketonate complexes with chiral amide ligands (DFB-Hex-amide) triggered CPL sign inversion (Louis et al., 2019). For the crystalline state obtained from thermal annealing, strong emission appeared in the blue-green range (475 nm, Φ_{FL} ~0.10–0.13), and the g_{lum} value reached the level of ~10^{-2} (**Figure 15**). After applying a shearing stress, the CPL signs for the two signals at 450 and 550 nm (Φ_{FL}~0.35) were inverted, and the g_{lum} value (500–550 nm) dropped to 3×10^{-3}. By referring to structural analogs and the fluorescence lifetime measurements, the signal at 450 nm was ascribed to the remaining microcrystals in the smeared sample, while the signal at 500–550 nm was assigned to the excimers. A CPL sign dependent on the amount of hypochlorite ion (ClO^-) present was observed for a chiral gel composed of an achiral phenothiazine derivative and a gelating chiral glutamic lipid (PTD-Z) through step-wise oxidation of the sulfur atom in the phenothiazine ring (Gong et al., 2019).

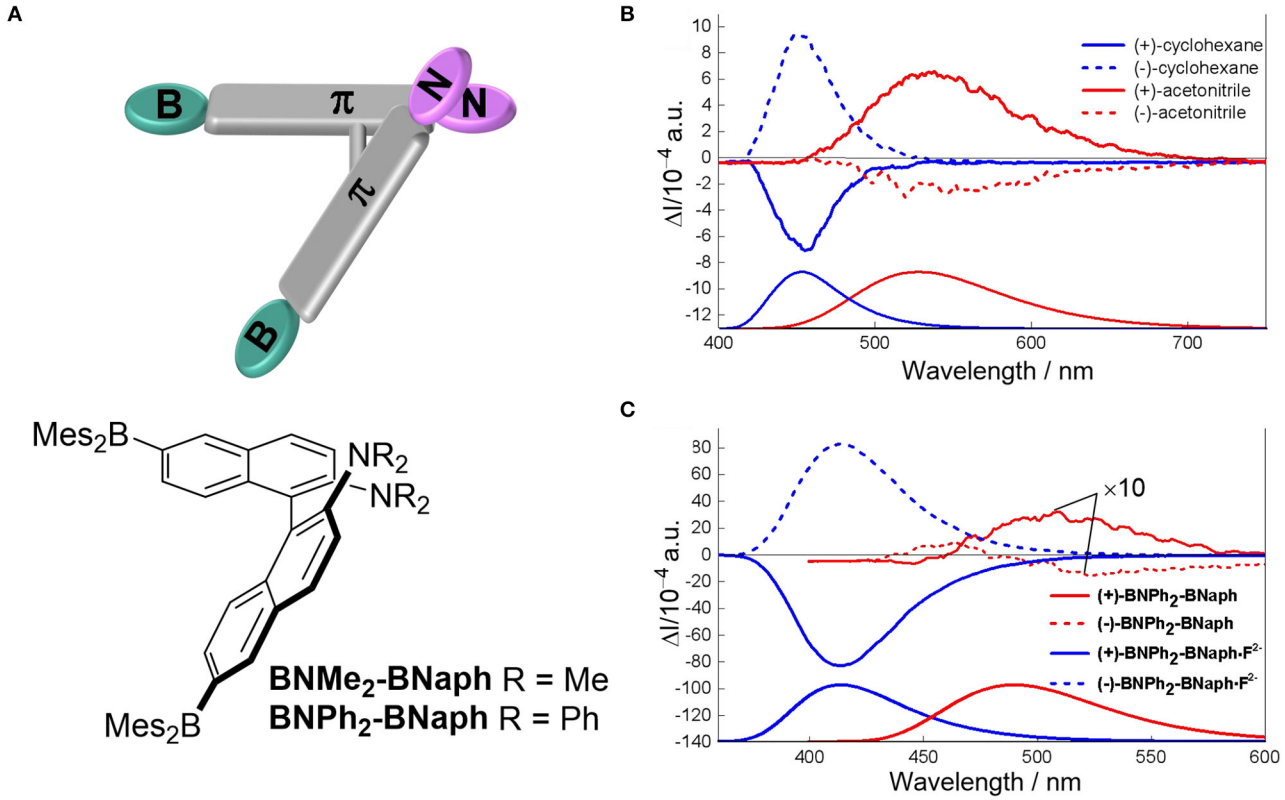

FIGURE 12 | (A) Illustration and chemical structure of chiral $BNPh_2$-BNaph. **(B)** CPL (top) and fluorescence (bottom) spectra of $BNPh_2$-BNaph in cyclohexane (blue) and MeCN (red), condition: 1.23×10^{-4} M, $\lambda_{ex} = 340$ nm. **(C)** CPL (top) and fluorescence (bottom) changes of $BNPh_2$-BNaph upon addition of F^- (tetrabutylammonium fluoride, 20 equiv). The measurements were carried out in THF solution (~1.23×10^{-4} M), under the excitation of 320 nm. Reproduced with permission (Sun Z. et al., 2019). Copyright 2019, John Wiley and Sons.

Initial titration experiments were carried out on a solution of PTD-Z (10 μM, mixed $CH_3CN/CHCl_3$). Addition of ClO^- from 0–80 μM was accompanied with emerging absorption at 375 nm and blue-shifted emission from 625 to 498 nm. Further addition of ClO^- to 10 equivalents of PTZ-D resulted in the formation of a sulfone. Structurally, the original left-handed helicoid structure of the PTZ-D gel changed to a right-handed structure. As a result, the original negative CD signal at 438 nm gradually shifted to a positive signal at 460 nm. Correspondingly, the negative CPL signal initially decreased, and then reversed to positive. The change was ascribed to the different dihedral angles related to the phenothiazine unit before and after oxidation. In Feng's work, co-assembled supramolecular gels composed of C2-symmetric hydrogelators (LPF and DPF) and achiral naphthylamine isomers showed inversed supramolecular chirality and CD/CPL signals when the amine groups of the isomers shifted from the α- position to the β- position (Yang et al., 2019). Along with the sign inversion, the CPL signals exhibited high |glum| values in the range of 5.62×10^{-3}-8.74×10^{-3}. Furthermore, the inversion was studied from the intermolecular hydrogen bonds and π-π stacking between the chiral and non-chiral components, which served as a rare example of achiral isomers used to form switchable CPL-active materials.

CONCLUSIONS AND PERSPECTIVES

Various CPL organic materials have been developed through tailoring either the molecular structures or their assembly behavior. Those with switchable CPL properties have been reviewed here, which possess considerable potential for applications in information processing and as intelligent sensors. The switchable behaviors have been classified based on different stimuli, including photo-irradiation, host–guest interaction, metal ions, pH, solvent, temperature, etc. Photoactive CPL switches have been developed mainly from photochemical active units, such as covalently linked photochromic diaryethene/spiropyran and chiral units or by chiral assembly of photo-isomerizable cyanostilenes. Recently, a novel strategy based on photophysical excitation of selected excited states has been applied to achieve convertible CPL and CP-OURTP. For host–guest interaction-based switches, cryptand molecules with tunable size and adjustable binding affinity have been used to control both the formation of chiral inclusion pairs and to modulate the chirality transfer process in-between the components. Recent progress has come from a robust on-off CPL shuttle based on a single molecular machine. Metal ions serve as a versatile methodology with which to

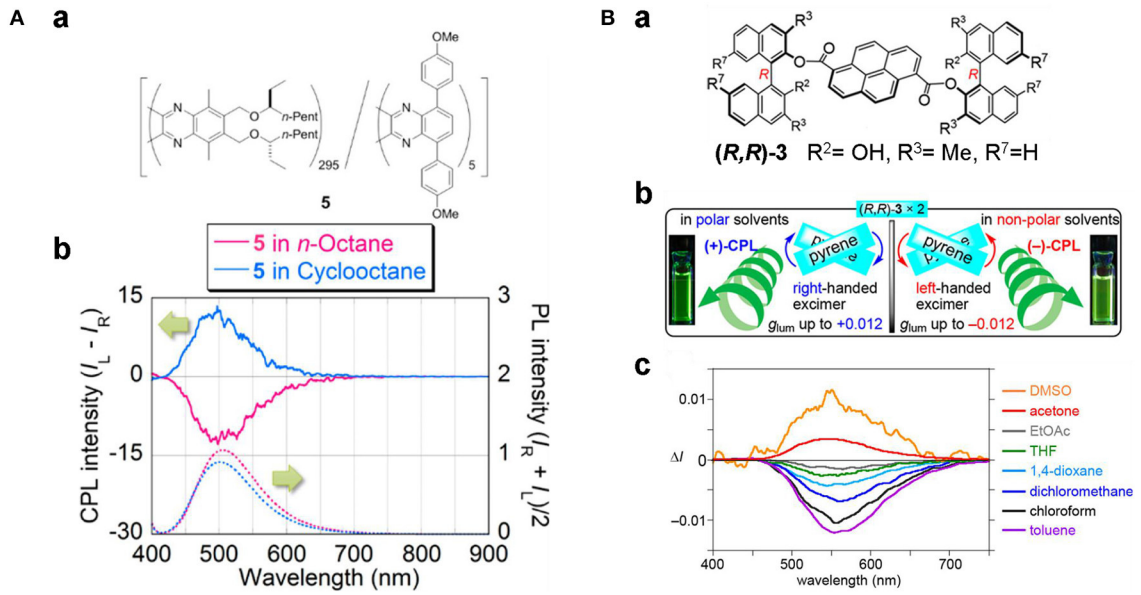

FIGURE 13 | (A) (a) Chemical sketch of polymer 5, and (b) CPL (upper) and PL (lower) spectra of **5** in n-octane (red) and cyclo-octane (blue) (2.70×10^{-2} g/L). **(B)** (a, b) Chemical structures and CPL illustration of (*R,R*)-**3**; (c) CPL spectra of **(*R,R*)-3** in different solvents. The solutions ($\sim 4.0 \times 10^{-3}$ M) were excited at 355 nm. **(A)** Reproduced with permission (Nishikawa et al., 2017). Copyright 2017, American Chemical Society. **(B)** Reproduced with permission (Takaishi et al., 2020). Copyright 2020, American Chemical Society.

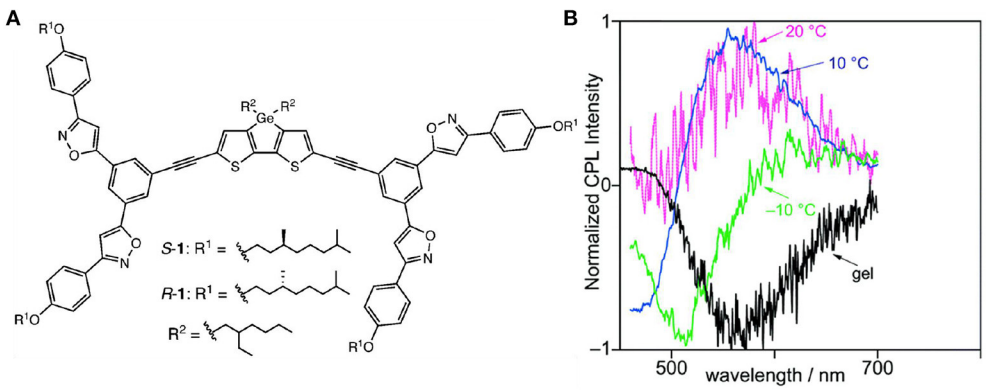

FIGURE 14 | (A) Skeleton of DTG possessing phenylisoxazoles and substituents. **(B)** CPL plots of S-1 from the methylcyclohexane solution ($\sim 4.9 \times 10^{-4}$ M) to gel, under the excitation of 420 nm. Reproduced with permission (Hirano et al., 2019). Copyright 2019, Royal Society of Chemistry.

switch the CPL behaviors by forming highly directional and rigid complexes, which can dictate related electronic band structures, molecular conformations and helical orientations. Thus, multiple metal ions have been applied to reach CPL switches in emission color, intensity, and handedness. A majority of acid-base active CPL switches tune the emission wavelength by protonation/deprotonation process, and a recent on-off switch works by governing the protonation induced electron transfer. Solvent and temperature based CPL switches make impacts by the facile operation. The switch processes work usually by controlling the assembly process, through tuning the solvent-solute interaction forces by tuning the polarity of the solvents, or by controlled cooling. Besides those widely applied stimuli, other methods not mentioned here make use of anions (Maeda et al., 2011; Zhao Z. H. et al., 2019), energy transfer (Feng et al., 2018; Sun M. J. et al., 2019), and stoichiometry (Li et al., 2019).

To sum up, various types of stimuli for CPL switches work by either tuning molecular/electronic structures to change the related dynamic assembly behaviors or

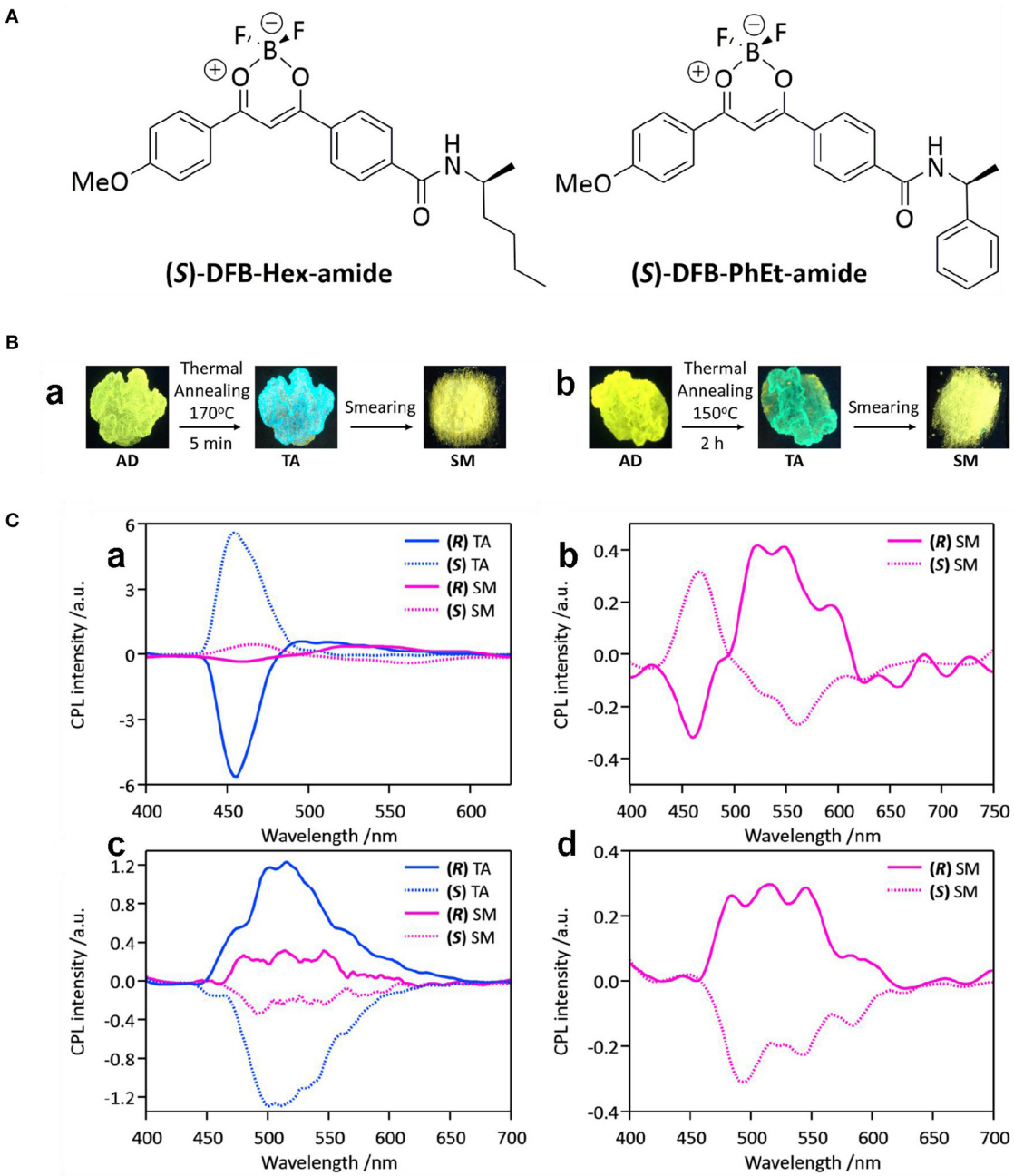

FIGURE 15 | (A) Chemical structures of (S)-DFB-Hex-amide and (S)-DFB-PhEt-amide. **(B)** Photographs of the samples obtained from deposition (AD), annealing (TA) and smearing (SM) for (S)-DFB-Hex-amide (a) and (S)-DFB-PhEt-amide (b). Under the excitation of 365 nm. **(C)** CPL spectra of (R/S)-DFB-Hex-amide (a and b) and (R/S)-DFB-PhEt-amide(c and d). Solid-state samples were deposited on paper. Blue color indicates the thermally annealed (TA) samples, while the pink color represents the mechanically smeared samples. (R) and (S) isomers are plotted using solid and dashed lines, respectively. Reproduced with permission (Louis et al., 2019). Copyright 2019, Royal Society of Chemistry.

tuning external interactions in-between chiral and achiral components/moieties. Meanwhile, the many switch modes can be classified into two general fashions, simple on or off CPL switches or switching between/among multiple emissive CPL states. Up till now, the former have been in the majority. Meanwhile, a large part of the CPL switches rely on the synchronous luminescence switch. Thus, CPL switches capable of switching among multiple emissive states and CPL switches independent on the luminescence switch are still less explored and under demand. Hopefully, the methodologies discussed in the review will help to promote further research.

AUTHOR CONTRIBUTIONS

YG and TH initiated the project. YG, CR, XL, and TH searched the data and wrote, revised, and completed the manuscript. All authors contributed to the article and approved the submitted version.

FUNDING

This work was supported by the Natural Science Foundation of Guangdong Province (2019A1515012094 and 2018A030310635), Shenzhen Basic Research Project of Science and Technology (JCYJ20170818142921044), and Natural Science Foundation of SZU (2018026).

ACKNOWLEDGMENTS

The authors wish to thank Prof. Andrew Grimsdale from Nanyang Technology University, Singapore, for the great comments on the manuscript.

REFERENCES

Chen, J., Chen, Y., Zhao, L., Feng, L., Xing, F., Zhao, C., et al. (2019). G-quadruplex DNA regulates invertible circularly polarized luminescence. *J. Mater. Chem. C* 7, 13947–13952. doi: 10.1039/c9tc04508b

David, A. H. G., Casares, R., Cuerva, J. M., Campana, A. G., and Blanco, V. (2019). A [2]rotaxane-based circularly polarized luminescence switch. *J. Am. Chem. Soc.* 141, 18064–18074. doi: 10.1021/jacs.9b07143

Fan, H., Jiang, H., Zhu, X., Guo, Z., Zhang, L., and Liu, M. (2019). Switchable circularly polarized luminescence from a photoacid co-assembled organic nanotube. *Nanoscale* 11, 10504–10510. doi: 10.1039/c9nr01959f

Feng, H.-T., Gu, X., Lam, J. W. Y., Zheng, Y.-S., and Tang, B. Z. (2018). Design of multi-functional AIEgens: tunable emission, circularly polarized luminescence and self-assembly by dark through-bond energy transfer. *J. Mater. Chem. C* 6, 8934–8940. doi: 10.1039/c8tc02504e

Gong, J., Yu, M., Wang, C., Tan, J., Wang, S., Zhao, S., et al. (2019). Reaction-based chiroptical sensing of ClO(-) using circularly polarized luminescence via self-assembly organogel. *Chem. Commun.* 55, 10768–10771. doi: 10.1039/c9cc05245c

Guo, Y., Han, Y., and Chen, C. F. (2019). Construction of chiral nanoassemblies based on host–guest complexes and their responsive CD and CPL properties: chirality transfer from 2,6-helic[6]arenes to a stilbazolium derivative. *Front. Chem.* 7:543. doi: 10.3389/fchem.2019.00543

Han, D., Han, J., Huo, S., Qu, Z., Jiao, T., Liu, M., et al. (2018). Proton triggered circularly polarized luminescence in orthogonal- and co-assemblies of chiral gelators with achiral perylene bisimide. *Chem. Commun.* 54, 5630–5633. doi: 10.1039/c8cc02777c

Han, J., Guo, S., Lu, H., Liu, S., Zhao, Q., and Huang, W. (2018). Recent progress on circularly polarized luminescent materials for organic optoelectronic devices. *Adv. Opt. Mater.* 2010:1800538. doi: 10.1002/adom.201800538

Hashimoto, Y., Nakashima, T., Shimizu, D., and Kawai, T. (2016). Photoswitching of an intramolecular chiral stack in a helical tetrathiazole. *Chem. Commun.* 52, 5171–5174. doi: 10.1039/c6cc01277a

Hirano, K., Ikeda, T., Fujii, N., Hirao, T., Nakamura, M., Adachi, Y., et al. (2019). Helical assembly of a dithienogermole exhibiting switchable circularly polarized luminescence. *Chem. Commun.* 55, 10607–10610. doi: 10.1039/c9cc05253d

Homberg, A., Brun, E., Zinna, F., Pascal, S., Gorecki, M., Monnier, L., et al. (2018). Combined reversible switching of ECD and quenching of CPL with chiral fluorescent macrocycles. *Chem. Sci.* 9, 7043–7052. doi: 10.1039/c8sc02935k

Imai, Y., and Yuasa, J. (2019). Off-off-on chiroptical property switching of a pyrene luminophore by stepwise helicate formation. *Chem. Commun.* 55, 4095–4098. doi: 10.1039/c9cc01138b

Isla, H., Srebro-Hooper, M., Jean, M., Vanthuyne, N., Roisnel, T., Lunkley, J. L., et al. (2016). Conformational changes and chiroptical switching of enantiopure bis-helicenic terpyridine upon Zn(2+) binding. *Chem. Commun.* 52, 5932–5935. doi: 10.1039/c6cc01748g

Ito, H., Sakai, H., Okayasu, Y., Yuasa, J., Mori, T., and Hasobe, T. (2018). Significant Enhancement of absorption and luminescence dissymmetry factors in the far-red region: a Zinc(ii) homoleptic helicate formed by a pair of achiral dipyrromethene ligands. *Chemistry* 24, 16889–16894. doi: 10.1002/chem.201804171

Ji, L., He, Q., Niu, D., Tan, J., Ouyang, G., and Liu, M. (2019). Host–guest interaction enabled chiroptical photo-switching and enhanced circularly polarized luminescence. *Chem. Commun.* 55, 11747–11750. doi: 10.1039/c9cc06305f

Jin, Q., Chen, S., Jiang, H., Wang, Y., Zhang, L., and Liu, M. (2018). Self-assembly of amphiphilic schiff base and selectively turn on circularly polarized luminescence by Al(3). *Langmuir* 34, 14402–14409. doi: 10.1021/acs.langmuir.8b03019

Jin, X., Yang, D., Jiang, Y., Duan, P., and Liu, M. (2018). Light-triggered self-assembly of a cyanostilbene-conjugated glutamide from nanobelts to nanotoroids and inversion of circularly polarized luminescence. *Chem. Commun.* 54, 4513–4516. doi: 10.1039/C8CC00893K

Jintoku, H., Kao, M.-T., Guerzo, A. D., Yoshigashima, Y., Masunaga, T., Takafujiac, M., et al. (2015). Tunable Stokes shift and circularly polarized luminescence by supramolecular gel. *J. Mater. Chem. C* 3, 5970–5975. doi: 10.1039/C5TC00878F

Li, H., Li, H., Wang, W., Tao, Y., Wang, S., Yang, Q., et al. (2020). Stimuli-responsive circularly polarized organic ultralong room temperature phosphorescence. *Angew. Chem. Int. Ed.* 59, 4756–4762. doi: 10.1002/anie.201915164

Li, P., Lu, B., Han, D., Duan, P., Liu, M., and Yin, M. (2019). Stoichiometry-controlled inversion of circularly polarized luminescence in co-assembly of chiral gelators with an achiral tetraphenylethylene derivative. *Chem. Commun.* 55, 2194–2197. doi: 10.1039/c8cc08924h

Louis, M., Sethy, R., Kumar, J., Katao, S., Guillot, R., Nakashima, T., et al. (2019). Mechano-responsive circularly polarized luminescence of organic solid-state chiral emitters. *Chem. Sci.* 10, 843–847. doi: 10.1039/c8sc04026e

Ma, J. L., Peng, Q., and Zhao, C. H. (2019). Circularly polarized luminescence switching in small organic molecules. *Chemistry* 25, 15441–15454. doi: 10.1002/chem.201903252

Ma, K., Chen, W., Jiao, T., Jin, X., Sang, Y., Yang, D., et al. (2019). Boosting the circularly polarized luminescence of small organic molecules via multi-dimensional morphology control. *Chem. Sci.* 10, 6821–6827. doi: 10.1039/c9sc01577a

Maeda, H., Bando, Y., Shimomura, K., Yamada, I., Naito, M., Nobusawa, K., et al. (2011). Chemical-stimuli-controllable circularly polarized luminescence from anion-responsive pi-conjugated molecules. *J. Am. Chem. Soc.* 133, 9266–9269. doi: 10.1021/ja203206g

Meng, F., Li, F., Yang, L., Wang, Y., Quan, Y., and Cheng, Y. (2018). The amplified circularly polarized luminescence emission response of chiral 1,10 -binaphthol-based polymers via Zn(II)-coordination fluorescence enhancement. *J. Polym. Sci. Pol. Chem.* 29, 1282–1288. doi: 10.1002/pola.29009

Miao, W., Wang, S., and Liu, M. (2017). Reversible quadruple switching with optical, chiroptical, helicity, and macropattern in self-assembled spiropyran gels. *Adv. Funct. Mater.* 27:1368. doi: 10.1002/adfm.201701368

Morcillo, S. P., Miguel, D., Alvarez de Cienfuegos, L., Justicia, J., Abbate, S., Castiglioni, E., et al. (2016). Stapled helical o-OPE foldamers as new circularly polarized luminescence emitters based on carbophilic interactions with Ag(i)-sensitivity. *Chem. Sci.* 7, 5663–5670. doi: 10.1039/c6sc01808d

Nishikawa, T., Nagata, Y., and Suginome, M. (2017). Poly(quinoxaline-2,3-diyl) as a multifunctional chiral scaffold for circularly polarized luminescent materials:

color tuning, energy transfer, and switching of the CPL handedness. *ACS Macro. Lett.* 6, 431–435. doi: 10.1021/acsmacrolett.7b00131

Niu, D., Jiang, Y., Ji, L., Ouyang, G., and Liu, M. (2019). Self-assembly through coordination and pi-stacking: controlled switching of circularly polarized luminescence. *Angew. Chem. Int. Ed. Engl.* 58, 5946–5950. doi: 10.1002/anie.201900607

Ouyang, G., and Liu, M. (2020). Self-assembly of chiral supra-amphiphiles. *Mater. Chem. Front* (4), 155-167. doi: 10.1039/C9QM00571D

Pascal, S., Besnard, C., Zinna, F., Di Bari, L., Le Guennic, B., Jacquemin, D., et al. (2016). Zwitterionic [4]helicene: a water-soluble and reversible pH-triggered ECD/CPL chiroptical switch in the UV and red spectral regions. *Org. Biomol. Chem.* 14, 4590–4594. doi: 10.1039/c6ob00752j

Pop, F., Zigon, N., and Avarvari, N. (2019). Main-Group-Based Electro- and Photoactive Chiral Materials. *Chem. Rev.* 119, 8435–8478. doi: 10.1021/acs.chemrev.8b00770

Reine, P., Justicia, J., Morcillo, S. P., Abbate, S., Vaz, B., Ribagorda, M., et al. (2018). Pyrene-Containing ortho-Oligo(phenylene)ethynylene foldamer as a ratiometric probe based on circularly polarized luminescence. *J. Org. Chem.* 83, 4455–4463. doi: 10.1021/acs.joc.8b00162

Reiné, P., Ortuño, A. M., Resa, S., Álvarez de Cienfuegos, L., Blanco, V., Ruedas-Rama, M. J., et al. (2018). OFF/ON switching of circularly polarized luminescence by oxophilic interaction of homochiral sulfoxide-containing o-OPEs with metal cations. *Chem. Commun.* 54, 13985–13988. doi: 10.1039/c8cc08395a

Sakai, H., Kubota, T., Yuasa, J., Araki, Y., Sakanoue, T., Takenobu, T., et al. (2016). Protonation-induced red-coloured circularly polarized luminescence of [5]carbohelicene fused by benzimidazole. *Org. Biomol. Chem.* 14, 6738–6743. doi: 10.1039/c6ob00937a

Saleh, N., Moore, B. 2nd, Srebro, M., Vanthuyne, N., Toupet, L., Williams, J. A., et al. (2015). Acid/base-triggered switching of circularly polarized luminescence and electronic circular dichroism in organic and organometallic helicenes. *Chemistry* 21, 1673–1681. doi: 10.1002/chem.201405176

Sang, Y., Han, J., Zhao, T., Duan, P., and Liu, M. (2019). Circularly polarized luminescence in nanoassemblies: generation, amplification, and application. *Adv. Mater.* e1900110. doi: 10.1002/adma.201900110

Sheng, Y., Ma, J., Liu, S., Wang, Y., Zhu, C., and Cheng, Y. (2016). Strong and reversible circularly polarized luminescence emission of a chiral 1,8-naphthalimide fluorophore induced by excimer emission and orderly aggregation. *Chemistry* 22, 9519–9522. doi: 10.1002/chem.201600891

Sun, M. J., Liu, Y., Zeng, W., Zhao, Y. S., Zhong, Y. W., and Yao, J. (2019). Photoluminescent anisotropy amplification in polymorphic organic nanocrystals by light-harvesting energy transfer. *J. Am. Chem. Soc.* 141, 6157–6161. doi: 10.1021/jacs.9b02055

Sun, Z. B., Liu, J. K., Yuan, D. F., Zhao, Z. H., Zhu, X. Z., Liu, D. H., et al. (2019). 2,2'-Diamino-6,6'-diboryl-1,1'-binaphthyl: a versatile building block for temperature-dependent dual fluorescence and switchable circularly polarized luminescence. *Angew. Chem. Int. Ed.* 58, 4840–4846. doi: 10.1002/anie.201813320

Takaishi, K., Iwachido, K., and Ema, T. (2020). Solvent-induced sign inversion of circularly polarized luminescence: control of excimer chirality by hydrogen bonding. *J. Am. Chem. Soc.* 142, 1774–1779. doi: 10.1021/jacs.9b13184

Wang, F., Ji, W., Yang, P., and Feng, C. L. (2019). Inversion of circularly polarized luminescence of nanofibrous hydrogels through co-assembly with achiral coumarin derivatives. *ACS Nano* 13, 7281–7290. doi: 10.1021/acsnano.9b03255

Yang, L., Wang, F., Auphedeous, D. Y., and Feng, C. (2019). Achiral isomers controlled circularly polarized luminescence in supramolecular hydrogels. *Nanoscale* 11, 14210–14215. doi: 10.1039/c9nr05033g

Zhang, D. W., Li, M., and Chen, C. F. (2020). Recent advances in circularly polarized electroluminescence based on organic light-emitting diodes. *Chem. Soc. Rev.* 49, 1331–1343. doi: 10.1039/c9cs00680j

Zhao, W. L., Li, M., Lu, H. Y., and Chen, C. F. (2019). Advances in helicene derivatives with circularly polarized luminescence. *Chem. Commun.* 55, 13793–13803. doi: 10.1039/c9cc06861a

Zhao, Z. H., Liang, X., He, M. X., Zhang, M. Y., and Zhao, C. H. (2019). Triarylborane-based [5]Helicenes with full-color circularly polarized luminescence. *Org. Lett.* 21, 9569–9573. doi: 10.1021/acs.orglett.9b03734

Conflict of Interest: The authors declare that the research was conducted in the absence of any commercial or financial relationships that could be construed as a potential conflict of interest.

frontiers in Chemistry

ORIGINAL RESEARCH
published: 17 June 2020
doi: 10.3389/fchem.2020.00501

Rational Design of the Platinahelicene Enantiomers for Deep-Red Circularly Polarized Organic Light-Emitting Diodes

Zhi-Ping Yan, Xu-Feng Luo, Kang Liao, You-Xuan Zheng and Jing-Lin Zuo**

State Key Laboratory of Coordination Chemistry, Jiangsu Key Laboratory of Advanced Organic Materials, School of Chemistry and Chemical Engineering, Nanjing University, Nanjing, China

[n]Helicene derivatives are most popular chiral structures to construct luminescent materials with circularly polarized (CP) light, which have revealed appealing application in chiral optoelectronics. Particularly, because of the unique phosphorescent emission, platinahelicene has great application prospects in CP organic light-emitting diode (CP-OLED). Herein, by decorating the pyridinyl-helicene ligand with trifluoromethyl (-CF_3) unit in a specific position, a pair of platinahelicene enantiomers was prepared and separated with extremely twisted structure showing not only superior thermal and configurational stability but also good CP luminescence (CPL) property with dissymmetry factors ($|g_{PL}|$) of 6×10^{-3}. Moreover, the evaporated CP-OLEDs based on platinahelicene enantiomers exhibited the deep-red emission with the peak at 653 nm as well as obvious CP electroluminescence (CPEL) signals with the $|g_{EL}|$ in 10^{-3} order. Therefore, the design strategy provides an efficient way to improve the CPL properties of platinahelicene to cope with the future application in CP-OLEDs.

Keywords: platinahelicene, circularly polarized light, thermal and configurational stability, CP-OLED, deep-red emission

OPEN ACCESS

Edited by:
Ralph Ernstorfer, Fritz-Haber-Institute, Germany

Reviewed by:
Yue Wang, Jilin University, China
Wai-Yeung Wong, Hong Kong Polytechnic University, Hong Kong

****Correspondence:***
You-Xuan Zheng
yxzheng@nju.edu.cn
Jing-Lin Zuo
zuojl@nju.edu.cn

Specialty section:
This article was submitted to Physical Chemistry and Chemical Physics, a section of the journal Frontiers in Chemistry

Received: *13 February 2020*
Accepted: *15 May 2020*
Published: *17 June 2020*

Citation:
Yan Z-P, Luo X-F, Liao K, Zheng Y-X and Zuo J-L (2020) Rational Design of the Platinahelicene Enantiomers for Deep-Red Circularly Polarized Organic Light-Emitting Diodes. Front. Chem. 8:501. doi: 10.3389/fchem.2020.00501

INTRODUCTION

In recent years, the exploration of chiral materials enabling circularly polarized (CP) light has attracted widespread attention in the field of chiral optoelectronics (Zhang et al., 2014). Compared with the traditional way of obtaining CP light (Grell et al., 2001) with polarizer, CP organic light-emitting diodes (CP-OLEDs) (Li et al., 2015, 2018) could emit CP light directly, which avoid brightness loss and complicated device structures. In term of current research (Han et al., 2018), it is still an important way to design chiral materials with excellent CPL properties for achieving high-performance CP-OLEDs. And the degree of circularly polarized photoluminescence (CPPL) or circularly polarized electroluminescence (CPEL) is characterized by the dissymmetry factor (g_{PL} or g_{EL}) defined as $g = 2\times \Delta I / I = 2 \times (I_L - I_R)/ (I_L + I_R)$. For example, Meijer and co-workers (Peeters et al., 1997) firstly obtained CP electroluminescence (CPEL) by using a chiral-substituted poly(p-phenylenevinylene) derivative as emitter. Since then, there has been some progress in chiral luminescent materials and efficient CP-OLEDs. Notably, although several reported chiral lanthanide complexes (Zinna et al., 2015, 2017) show excellent CPL properties with the $|g_{PL}|$ values over 1, the poor device performances make them difficult to be applied for practical OLEDs. On the contrary, chiral transition metal complexes [Ir(III), Pt(II)] and thermally activated delayed

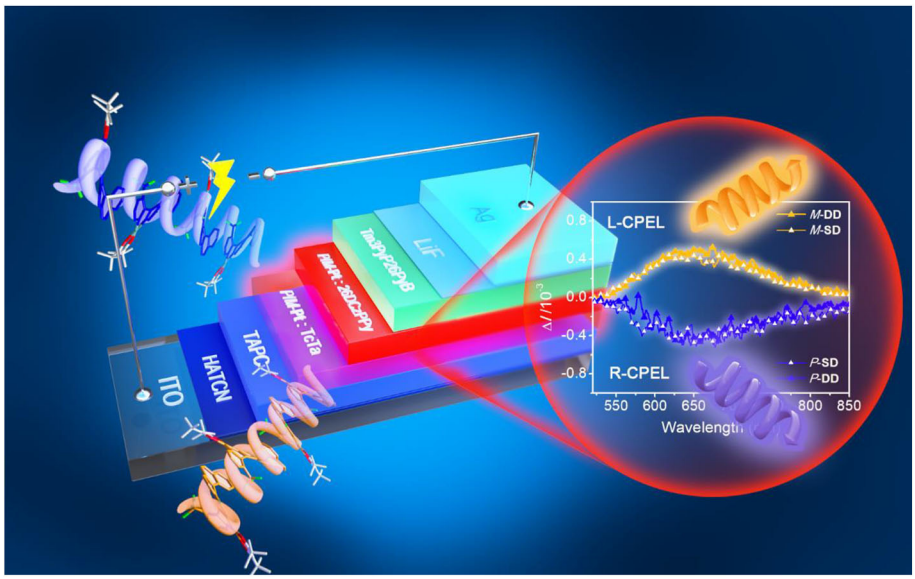

GRAPHICAL ABSTRACT | A pair of chiral deep-red platinahelicene enantiomers show good CPL property with $|g_{PL}|$ of 6.0×10^{-3}. And the fabricated CP-OLEDs exhibit EQE_{max} of 4.6% with the $|g_{EL}|$ at the degree of 10^{-3}.

fluorescence materials (Feuillastre et al., 2016; Han et al., 2017; Wu et al., 2019) exhibit increasingly satisfactory results in term of the electroluminescence properties. Nevertheless, most of these materials used in efficient OLEDs exhibit poor CPL properties with the $|g_{PL}|$ value in the range of 10^{-5} to 10^{-3} (Han et al., 2018; Yan et al., 2019b) and mostly $<5 \times 10^{-3}$. Hence, it is important to provide a design strategy to improve their CPL properties.

Generally, introducing chiral units to luminescent materials is an efficient way to construct CPL materials (Sakai et al., 2015; Sánchez-Carnerero et al., 2015). Compared with chiral carbon centers, the special conjugated screw-shaped structure of [n]helicene derivatives makes it possess intrinsic chirality, which is one of the most effective chiral units (Dhbaibi et al., 2019; Zhao et al., 2019). Particularly, platinahelicene (Norel et al., 2010; Hellou et al., 2017) has not only the chirality of helicene but also the properties of phosphorescent emission, making it a potential choice for efficient CP-OLEDs. For example, Crassous and co-workers ((Norel et al., 2010), (Shen et al., 2014)) developed a series of chiral platinahelicene exhibiting both phosphorescent and CP emission. Their elegant molecular design was based on the introduction of pyridinyl-helicene ligand into cyclometalated complexes. Later, a solution processed CP-OLED based on platinahelicene (Brandt et al., 2016) was reported by Fuchter group, achieving a very high $|g_{EL}|$ value of 0.38 with a maximum luminance (L_{max}) of 222 cd m^{-2} and a maximum current efficiency (η_{max}) of 0.25 cd A^{-1}, indicating the application of platinahelicene in CP-OLEDs. However, owing to the poor volatility, this kind of platinahelicene is difficult to be fabricated by vacuum deposition to gain better device performances. Subsequently, we modified the platinahelicene with the sterically hindered -CF_3 and -^{t}Bu group to enable the material to be sublimated for the preparation of evaporated devices (Yan et al., 2019a), showing the $|g_{EL}|$ of $(1.1–1.6) \times 10^{-3}$ with a L_{max} of 11,590 cd m^{-2} and a η_{max} of 22.52 cd A^{-1}, respectively. Meanwhile, the device performances are the highest values among the reported devices based on chiral phosphorescent Pt(II) complexes. Although the device performances were improved a lot, the $|g_{PL}|$ of 3.7×10^{-3} still need to be promoted.

Herein, we created helicene core through a special structure design combining the -CF_3 group and helicene structure, and further improving the CPL property of platinahelicene. Compared with the platinahelicene reported by Crassous and Fuchter (Norel et al., 2010; Brandt et al., 2016), (*RAC*)-**Pt** possesses superior thermal stability and could be easily sublimated owing to the introduction of additional large hindered groups (-CF_3, ^{t}Bu). Meanwhile, the special substitution position of the group not only makes the helicene structure more configurationally stable, but also endows this complex better CPL performance because of the more twisted structures. Therefore, based on our design strategy we successfully prepared a new kind of platinahelicene which was further prepared evaporated CP-OLED with good performance. In this way, *P*-**Pt** and *M*-**Pt** separated by (*RAC*)-**Pt** show higher g_{PL} of $-5.9 \times 10^{-3}/6.0 \times 10^{-3}$. And both deep-red electroluminescence ($\lambda_{max} = 653$ nm) and CP light activity were achieved by fabricating the evaporated OLEDs.

MATERIALS AND METHODS

General Method

NMR measurements were conducted on a Bruker AM 400 spectrometer. The mass spectra were recorded by an electrospray ionization (ESI) mass spectrometer (LCQ fleet, Thermo Fisher

Scientific) and Matrix Assisted Laser Desorption Ionization Time of Flight Mass Spectrometry (autoflex TOF/TOF, Bruker Daltonics), high-resolution mass spectra were recorded on a MICROTOF-Q III instrument. Ultraviolet-visible (UV-vis) absorption spectra were measured on a UV-3100 spectrophotometer and PL spectra were obtained from a Hitachi F-4600 photoluminescence spectrophotometer. The absolute photoluminescence quantum yields (Φ) and the decay lifetimes of the complex were measured by HORIBA FL-3 fluorescence spectrometer. Thermogravimetric analysis (TGA) was performed on a Pyris 1 DSC under nitrogen at a heating rate of 10°C min^{-1}. (*RAC*)-**Pt** was separated by CHIRALPAK IE (IE00CD-RH008) column which was employed as stationary phase and the hexane/dichloromethane (80/20) was employed as eluent. Cyclic-voltammetry measurement system carried out at room temperature in deaerated CH_3CN, employing a polished Pt plate as the working electrode, terta-n-butylammonium perchlorate (0.1 M) as the supporting electrolyte and Fc^+/Fc used as the reference, with the scan rate of 0.1 V/s. The HOMO and LUMO levels were obtained by the following equation: $E_{HOMO} = -(4.8+E_{oxonset})$ (eV), $E_{LUMO} = -(E_{HOMO}+E_g)$ (eV), and E_g was estimated from the UV-vis absorption spectra, $E_g = hc/\lambda_{abs}$. The circular dichroism (CD) and CPL spectra were measured in the same condition with UV-Vis absorption spectra and PL spectra. The CD spectra were measured on a Jasco J-810 circular dichroism spectrometer with "low" sensitivity. The circularly polarized photoluminescence (CPPL) and circularly polarized electroluminescence (CPEL) spectra were measured on a Jasco CPL-300 spectrophotometer based on "Continuous" scanning mode at 200 nm/min scan speed. The test mode adopts "Slit" mode with the E_x and E_m Slit width 3,000 μm and the digital integration time (D.I.T.) is 2.0 s with multiple accumulations (10 times or more).

Theoretical Calculation

All the DFT and TD-DFT calculations were carried out using Gaussian 16 software package. The initial structures were created according to the GaussView 6 based on crystal structures. The ground state geometry optimization with frequent calculations for all the complexes were performed using B3LYP exchange-correlation functional. On the basis of the optimized structures, vertical transition energy calculations were carried out with B3LYP functional, too. For all the calculations, a combination of basis sets that Lanl2dz for platinum and 6-31G (d,p) for the others were employed and the solvent effect were considered by C-PCM model in CH_2Cl_2.

Device Fabrication

All the final products were purified by sublimation before applied to device fabrication. Moreover, the OLEDs with the emission area of 0.1 cm^2 were fabricated on the pre-patterned ITO-coated glass substrate with a sheet resistance of 15 Ω sq^{-1}. The ITO glass substrates were cleaned with ITO lotion and deionized water and then dried in an oven at 120 °C. The devices were fabricated by vacuum deposition of the materials at $<10^{-4}$ Pa with the deposition rate of 1–2 Å s^{-1}. The platinahelicene and host were co-evaporated from two separate sources. The LiF and Al were deposited with the rate of 0.1 and 3 Å s^{-1}, respectively.

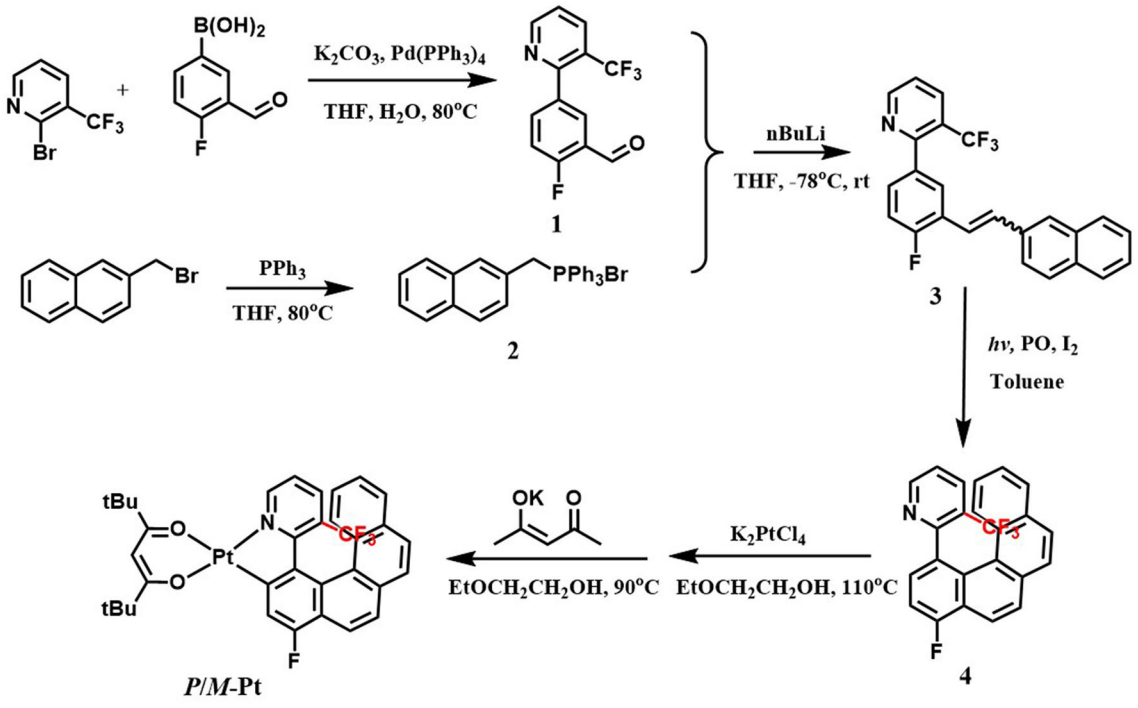

SCHEME 1 | Synthetic routes and molecular structure of (*RAC*)-**Pt**.

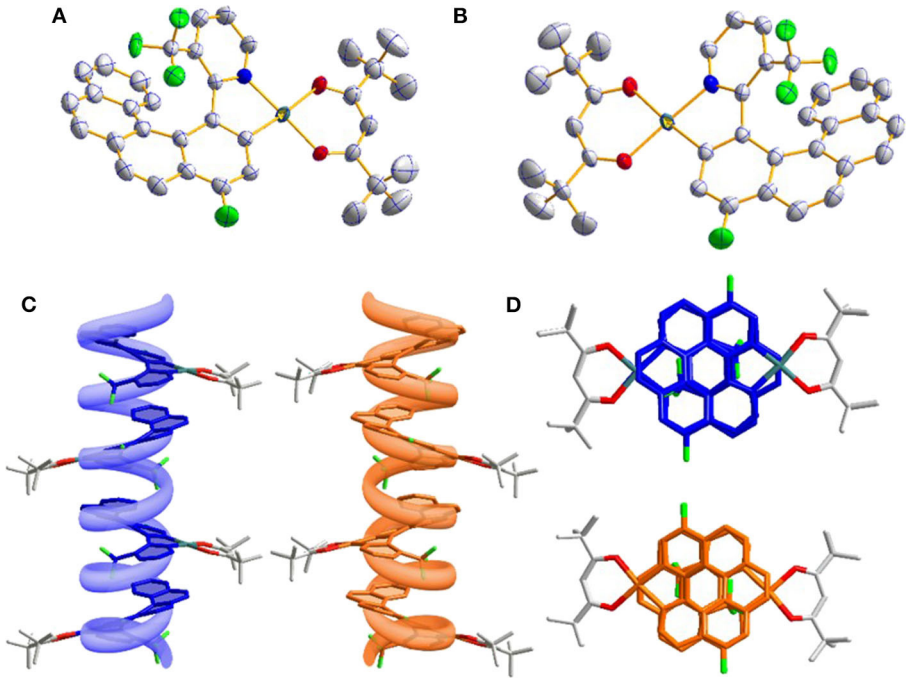

FIGURE 1 | (A) Oak Ridge thermal ellipsoidal plot (ORTEP) diagrams of *P*-**Pt** (CCDC no. 1844425) and **(B)** *M*-**Pt** (CCDC no. 1844426); **(C)** molecular packing in crystal along b axis observed from side view and **(D)** top view.

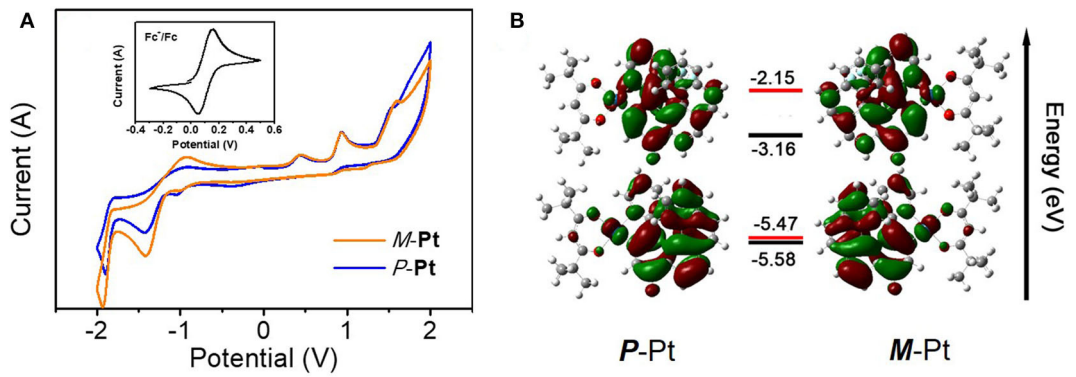

FIGURE 2 | (A) The cyclic voltammogram curves and **(B)** HOMO/LUMO energy levels (experiment: black; calculation: red) and electronic cloud distributions of *P*-**Pt** and *M*-**Pt**.

RESULT AND DISCUSSION

Preparation and Characterization of Platinahelicene

All experiments were performed under nitrogen atmosphere and the relevant procedures referred to the reported literature (Norel et al., 2010). The starting reactants and solvents were used as commercial grade without further purification. The synthetic routes of (*RAC*)-**Pt** are depicted in **Scheme 1**. The helicene ligand **4** and (C^N)Pt(μ-Cl) chloride-bridged dimmer were prepared by the reported methods. Then the platinahelicene was readily obtained by mixing the μ-chloro-bridged dimer with 2,2,6,6-tetramethylheptane-3,5-dione sodium salt. The target platinahelicene was purified by column chromatography and sublimation. Due to the rapid racemization at room temperature, the helicene ligand is difficult to be separated into stable enantiomers. On the contrary, with the introduction of coordination bond, *P*-**Pt** and *M*-**Pt** are configurationally stable, which could be separated by (*RAC*)-**Pt** by using chiral HPLC with enantiomeric purity higher than 99%.

1-Fluoro-4-(6-Trifluoromethyl-2-Pyridyl)-Benzo[*g*]Phenanthrene (4)

The mixture of *cis* and *trans* **3** (1.0 g, 2.55 mmol), I_2 (30 mg, 0.12 mmol) and 10 ml propylene oxide were dissolved in toluene (1,000 mL). The solution was irradiated for 4 h by 250 W mercury

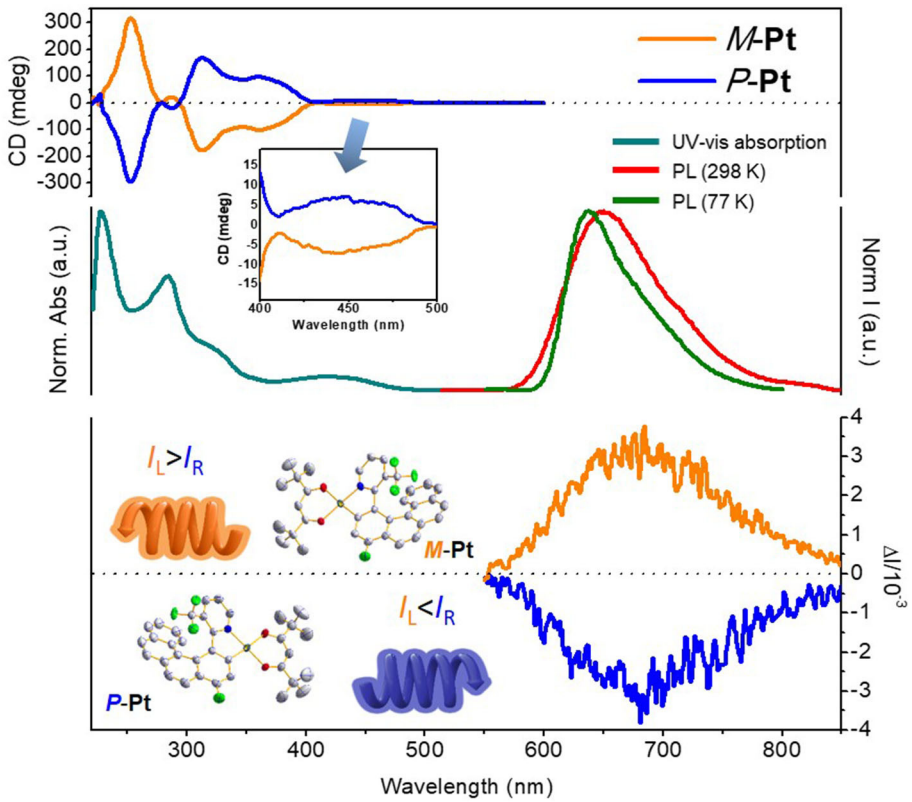

FIGURE 3 | Photophysical properties of platinahelicene in CH_2Cl_2 (5×10^{-5} mol L^{-1}): (top) CD spectra of *P*-**Pt** and *M*-**Pt**; (middle) Normalized absorption and PL spectra of (*RAC*)-**Pt**; (bottom) CPL spectra of *P*-**Pt** and *M*-**Pt**.

vapor lamps. The solvent was evaporated under reduced pressure and then the residue was purified by column chromatography [silica gel, ethyl acetate: petroleum ether 1:10 (v/v)] to afford **4** as a beige solid (598 mg, 60%). ESI-MS, calculated: m/z 392.11 for $[M+H]^+$ $(C_{24}H_{14}F_4N)^+$ found: m/z 392.25. ^{1}H NMR (400 MHz, $CDCl_3$): δ 9.05 (d, $J = 3.7$ Hz, 1H), 8.27 (d, $J = 8.6$ Hz, 1H), 8.03 (dd, $J = 19.2$, 8.1 Hz, 1H), 7.92 (dt, $J = 8.4$, 4.3 Hz, 2H), 7.89-7.77 (m, 3H), 7.72 (d, $J = 8.0$ Hz, 1H), 7.44 (dt, $J = 31.7$, 8.8 Hz, 1H), 7.30 (d, $J = 7.8$ Hz, 1H), 7.22 (t, $J = 7.4$ Hz, 1H), 6.99 (t, $J = 7.3$ Hz, 1H).

(6-Trifluoromethyl-2-[4′-(1′-fluoro-benzo[g]phenanthrenyl)]pyridinato-*N*, *C*)platinum-*tert*-butylacetylacetonate (*RAC*)-Pt

1) Preparation of the platinum μ-chloro-bridged dimer: To a solution of **4** (400 mg, 1.02 mmol) in ethoxyethanol (30 mL) was added K_2PtCl_4 (423 mg, 1.02 mmol). The suspension was gently warmed with stirring until all the platinum salt dissolved. The solution was then refluxed for 16 h to yield a dark green suspension. After cooled to room temperature, water (100 mL) was added. The precipitation was filtered and dried in air and then dark yellow solid (549 mg, 88%) was obtained.

2) Preparation of (*RAC*)-Pt: To a solution of μ-chloro-bridged dimer (549 mg, 0.44 mmol) in ethoxyethanol (25 mL) was added the 2,2,6,6-tetramethylheptane-3,5-dione sodium salt (217 mg, 0.97 mmol). The reaction mixture was refluxed overnight and then concentrated under reduced pressure. Purification by column chromatography (silica gel, ethyl acetate: petroleum ether 1:4 (v/v)), yielded (*RAC*)-**Pt** as orange-red solid (337 mg, 50%). MALDI-TOF-MS, calculated: 768.194 for M ($C_{35}H_{31}F_4NO_2Pt$), found: 768.382; HR-MS, calculated: 769.2011 for $[M+H]^+$ $(C_{35}H_{32}F_4NO_2Pt)^+$, found: 769.2013. ^{1}H NMR (400 MHz, $CDCl_3$): δ 9.25 (d, $J = 4.6$ Hz, 1H), 8.21 (d, $J = 8.5$ Hz, 1H), 8.11 (d, $J = 8.5$ Hz, 1H), 7.84 (q, $J = 8.6$ Hz, 2H), 7.79 (dd, $J = 8.0$, 5.1 Hz, 2H), 7.58 (d, $J = 9.3$ Hz, 1H), 7.34 (d, $J = 6.9$ Hz, 1H), 7.24 (t, $J = 7.3$ Hz, 1H), 7.05-6.99 (m, 1H), 6.92 (t, $J = 7.7$ Hz, 1H), 5.91 (s, 1H), 1.34 (d, $J = 6.2$ Hz, 18H).

The single crystals of two enantiomers were obtained by vacuum sublimation and the single crystal diffraction analysis further confirmed the preconceived structure. As shown in **Figures 1A**, **5B**, two symmetric enantiomers adopted twisted planar structures could be easily divided into *P* and *M* configurations. Interestingly, because the -CF_3 group is inserted into the helicene-like skeleton, the twist angle of pyridine and the coordinate five-membered rings is 17.3°, bigger than the relevant report (Norel et al., 2010; Yan et al., 2019a), and the consecutive twist angles between the fused rings (10.6, 12.1, 12.3,

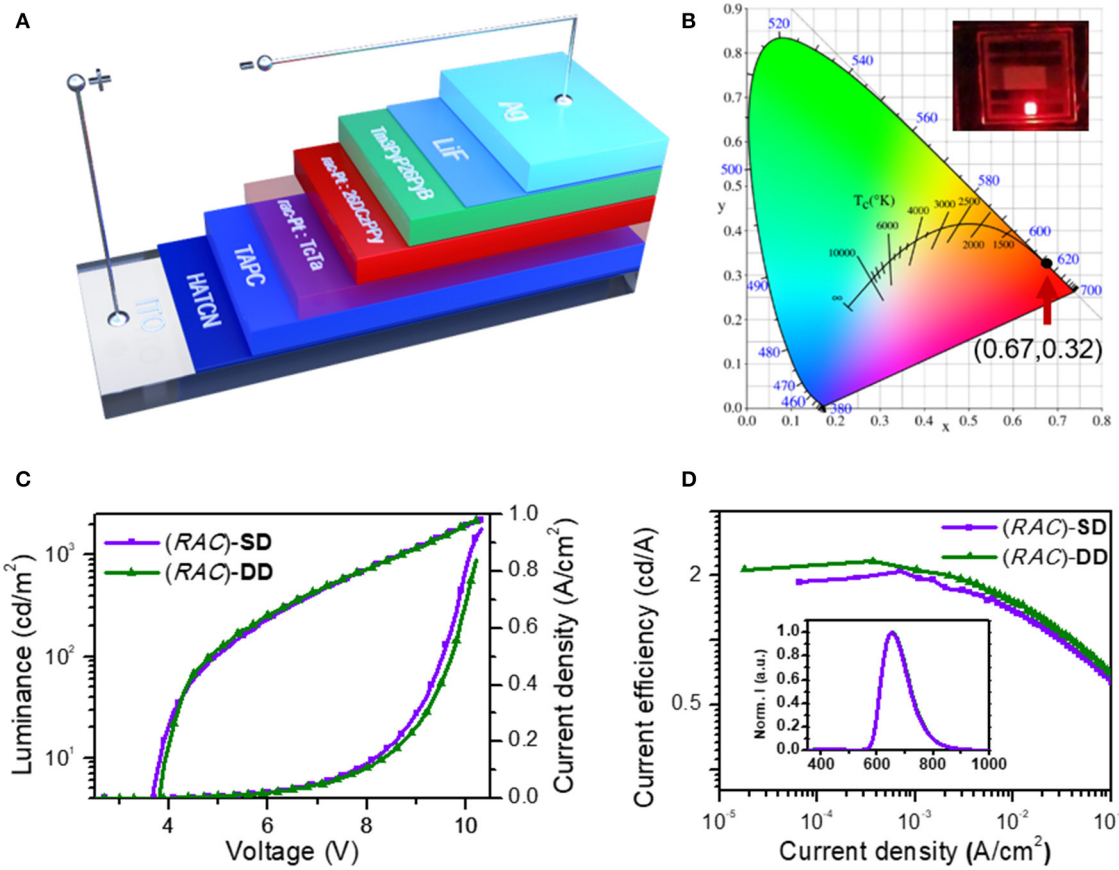

FIGURE 4 | Characteristics of (*RAC*)-**SD** (without TcTa layer) and (*RAC*)-**DD** (with TcTa layer): **(A)** device configuration of OLEDs; **(B)** CIE (x,y) coordinates of both devices; **(C)** current density-luminance-voltage (*J*-*L*-V) curves; **(D)** current efficiency-current density curves (inset: the normalized EL spectrum at 8 V).

and 9.9°) lead to a helical curvature (*hc*, the angle between the terminal helicene rings) value of 38.7° in *P*-**Pt** and *M*-**Pt**, which is smaller than the conventional organic or heteroatomic [6]helicene system (Graule et al., 2009). Although the helicene-based ligand shows a large distortion, the central Pt(II) still adopts a planar coordination form with the dihedral angle 5° between plane O_1-Pt-O_2 and N_1-Pt-C_1. Moreover, the smaller *hc* value leads to relative strong π-π interactions, as a result, *P*-**Pt** and *M*-**Pt** pile up in a parallel face-to-face style. As shown in **Figures 1C,D**, combining with the help of the special chiral *P* or *M* helicene unit, these strong interactions can self-assemble *P*-**Pt** and *M*-**Pt** to form *P* and *M* spiral structures, which may be a reason of the good CPL properties of the platinahelicene.

Thermal and Configurational Stability

Thermal and configurational stability was investigated by TGA and CD spectra, respectively, which are vital parameters for chiral materials to fabricate CP-OLEDs. As shown in **Figure S12**, the decomposition temperature (T_d, 5% loss of weight) of (*RAC*)-**Pt** is 321°C, which benefits the application during the operation of CP-OLEDs. Moreover, due to the introduction of large sterically hindered groups, these enantiomers are endowed with a better configurational stability, which could preserve the original configuration (**Figure S11**) even at 240°C under vacuum of 1×10^{-4} Pa overnight.

TABLE 1 | EL performances of the devices based on (*RAC*)-**Pt**, *P*-**Pt**, and *M*-**Pt**.

Device	V_{on} [a] [V]	L_{max} [b] [cd/m2]	$\eta_{c,max}$ [c] [cd/A]	$\eta_{c,L1000}$ [d] [cd/A]	EQE_{max} [e] [%]	$\eta_{p,max}$ [f] [lm/W]	g_{EL} [g] [10^{-3}]
(*RAC*)-**SD**	3.6	2,222	2.29	0.47	4.16	1.90	–
(*RAC*)-**DD**	3.6	2,201	2.33	0.52	4.44	1.88	–
P-**SD**	3.4	1,927	2.26	0.47	4.42	2.03	−1.1
M-**SD**	3.4	2,156	2.14	0.36	4.17	1.91	1.1
P-**DD**	3.6	1,754	2.23	0.47	4.06	1.87	−0.9
M-**DD**	3.6	1,840	2.32	0.48	4.60	1.97	1.3

[a] *Turn-on voltage recorded at a luminance of 1 cd/m²;* [b] *Maximum luminance;* [c] *Maximum current efficiency;* [d] *Current efficiency at 1,000 cd/m²;* [e] *Maximum external quantum efficiency;* [f] *Maximum power efficiency;* [g] g_{EL} *around maximum emission peak.*

Electrochemical Property and Theoretical Calculation

Cyclic voltammetry (CV) measurements and density functional theory (DFT) calculations were further conducted to investigate

the electronic and structural features of *P*-**Pt** and *M*-**Pt**. As depicted in **Figure 2A**, both complexes have irreversible oxidation and reduction waves and the electrochemical data are summarized in **Table S3**. The oxidation onsets of these two enantiomers reference Fc^+/Fc are the same with the value of 0.78 V. Moreover, both *P*-**Pt** and *M*-**Pt** display the first reduction potential at about −1.43 V. These results demonstrated the chiral configuration has ignored influence on the electrochemical properties of the enantiomers. Therefore, the calculated highest occupied molecular orbital (HOMO) and the lowest unoccupied molecular orbital (LUMO) levels for *P*-**Pt** and *M*-**Pt** are −5.58/−3.24 eV, respectively, which are helpful for the carriers' injection and transport in OLEDs.

To gain a better insight of the electron cloud distributions and structure features, the molecular simulations were further executed by density functional theory (DFT) preformed with Gaussian 09 software, and the accurate energy and location of HOMO/LUMO were calculated by QMForge program. As shown in **Figure 2B**, the HOMO/LUMO are mainly distributed in the helicene ligand (77.09/91.51%) together with *d* orbitals of Pt atom (18.11/6.64%), respectively. Obviously, the distributions of HOMO/LUMO on ancillary ligand are very small, indicating the little influence on the energy level of this Pt(II) complex.

Photophysical Property

To clarify the photophysical properties of (*RAC*)-**Pt**, room temperature UV-vis absorption spectrum in CH_2Cl_2 is depicted in **Figure 3** (middle). The short-wavelength absorption bands at 227 and 284 nm are mainly associated with π-π* transition, while the weak absorption bands peaking at 350–500 would be attributed to the mixed singlet and triplet metal-to-ligand charge transfer (^{1}MLCT and ^{3}MLCT) transitions because of the strong spin-orbital coupling effect of the Pt atom. The room temperature PL spectrum of (*RAC*)-**Pt** was further studied with the emission peak at 650 nm and the Commission Internationale de L'Eclairage (CIE) coordinates of (0.68, 0.32) demonstrating the deep-red emission. When measured at 77 K, the emission peak has a blue shift of 14 nm with the emission peak at 636 nm.

Furthermore, emission lifetime (τ) and absolute photoluminescence quantum yield (PLQY) were recorded for (*RAC*)-**Pt** in CH_2Cl_2 under nitrogen atmosphere. The phosphorescence lifetime of (*RAC*)-**Pt** (τ = 4.6 μs) is in range of the similar reported Pt(II) complexes (Shen et al., 2014). Moreover, as shown in **Figure S9**, the linear fit curve on logarithmic scale indicates the phosphorescent emission is basically the only pathway. But due to the deep-red emission with tail to the near-infrared region, the PLQY of (*RAC*)-**Pt** is only about 4%.

Chiroptical Property

CD spectra were reported for both enantiomers *P*-**Pt** and *M*-**Pt** in CH_2Cl_2. As depicted in **Figure 3** (top), *P*-**Pt** shows a strong negative cotton effect at 249 nm and positive cotton effects at 313, 363 and 446 nm, as well as corresponding to the UV-Vis absorption spectrum. The *M*-**Pt** reveals exactly the opposite CD spectrum further indicating that the two components are a pair of enantiomers. Furthermore, in the range of 350–500 nm, relatively weak cotton effect is observed, indicating the circular dichroism of the MLCT process.

CPL spectra of *P*-**Pt** and *M*-**Pt** were also preformed [**Figure 3** (bottom)] to prove the chiroptical properties of the luminescent molecular upon excitations. The *P*-**Pt** shows negative CPL signals in 550–850 nm region while the *M*-**Pt** shows symmetrical signals in the same position with the $|g_{PL}|$ of about 6.0×10^{-3} which is superior compared with the reported chiral Pt(II) complexes (Shen et al., 2014; Fu et al., 2019). In order to explore the application of materials in OLEDs, the CPL properties of *P*-**Pt** and *M*-**Pt** in doped films were also investigated. When the enantiomers were doped into the host material 26DCzPPy (2,6-bis(3-(9H-carbazol-9-yl)phenyl)pyridine) at a concentration of 5 wt% by vacuum evaporation, the $|g_{PL}|$ factors are smaller than that in the solution state with the values about 4.0×10^{-3}. Apparently, as for the CPL performance of *P*/*M*-**Pt**, the host material 26DCzPPy has a certain weakening effect. However, in order to obtain better device performance, 26DCzPPy was selected to further fabricate OLED owing to its unique bipolar characteristic.

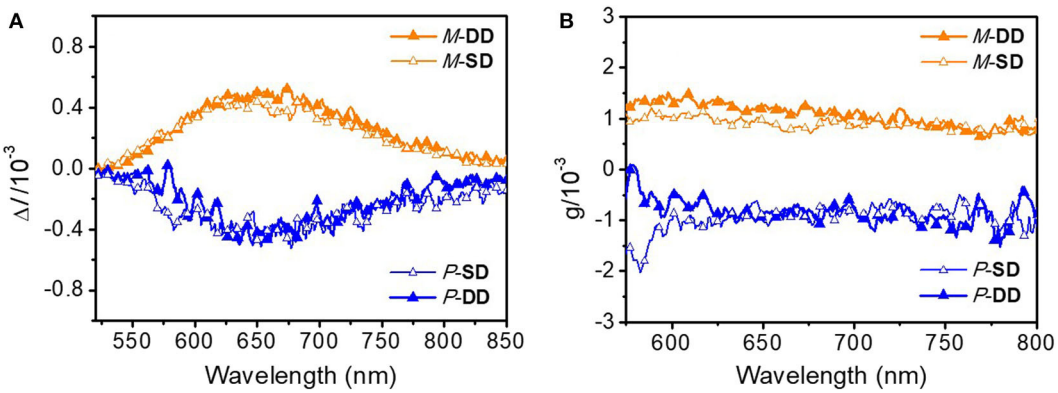

FIGURE 5 | (A) CPEL spectra of *P*-**SD**, *M*-**SD**, *P*-**DD**, and *M*-**DD** based on Δ*I* and **(B)** g_{EL} vs. wavelength curves of *P*-**SD**, *M*-**SD**, *P*-**DD,** and *M*-**DD**.

CP-OLED Characterization

Inspired by the unique phosphorescent emission, good thermal and configurational stability and chiroptical property, the application of these platinahelicene in the circularly polarized electroluminescent devices were also investigated. Considering the similar properties of enantiomers and racemate, initially (*RAC*)-**Pt,** was chosen to optimize the device structures. After reasonable structural optimization, the device adopting the single emissive layer of ITO/ HATCN (hexaazatriphenylene-hexacarbonitrile, 6 nm)/HATCN (0.2 wt%): TAPC (di-(4-(*N*, *N*-ditolyl-amino)phenyl)cyclohexane, 50 nm)/(*RAC*)-**Pt** (5 wt%): 26DCzPPy (10 nm)/Tm3PyP26PyB (1,3,5-*tris*(6-(3-(pyridin-3-yl)phenyl)pyridin-2-yl)benzene, 60 nm)/LiF (1 nm)/Al (100 nm) named (*RAC*)-**SD** showed the best performances (**Figure 4A**, **Figure S13**). Respectively, HATCN and LiF are served as the hole-injection and the electron-injection layers; TAPC and Tm3PyP26PyB are used as hole-transporting and electron-transporting layers; Bipolar 26DCzPPy is used as host material which could transport both hole and electrons. Meanwhile, trace HATCN co-doped with TAPC could reduce hole-injection potential energy to achieve low turn-on voltage. The EL spectra, luminance-voltage-current density (*L-V-J*) and current efficiency-current density characteristics of (*RAC*)-**SD** are depicted in **Figure 4**, and the key device data are summarized in **Table 1**. The device (*RAC*)-**SD** displays deep-red EL emission with the peak at 653 nm and the CIEs of (0.67, 0.32) are attained. Moreover, the turn-on voltage of (*RAC*)-**SD** is 3.6 V with the L_{max}, $\eta_{c,max}$, maximum external quantum efficiency (EQE_{max}) and maximum power efficiency ($\eta_{p,max}$) of 2,222 cd/m^2, 2.29 cd/A, 4.16% and 1.90 lm/W, respectively. Furthermore, in order to obtain better device performances, the double emissive layers device of ITO/ HATCN/ HATCN (0.2 wt%): TAPC (50 nm)/(*RAC*)-**Pt** (5 wt%): TcTa (4,4′,4″-tris(carbazol-9-yl)triphenylamine, 10 nm)/ (*RAC*)-**Pt** (5 wt%): 26DCzPPy (10 nm)/Tm3PyP26PyB (60 nm)/LiF (1 nm)/Al (100 nm) named (*RAC*)-**DD** was also fabricated. Generally, the introduction of TcTa to fabricate double emissive layers device could broaden electron-hole recombination area which would enhance the use of electron-hole pairs. As a result, there is a certain improvement of the device performances with the L_{max} of 2,201 cd/m^2, $\eta_{c,max}$ of 2.33 cd/A, EQE_{max} of 4.44% and $\eta_{p,max}$ of 1.88 lm/W, respectively.

Notably, as shown in **Figure 5**, the two different enantiomer-based OLEDs show obvious CPEL properties with opposite g_{EL} of -1×10^{-3} and 1×10^{-3} at 653 nm for *P*-**Pt** and *M*-**Pt**, respectively, which demonstrate the successful preparation of CP-OLEDs and the device performances of *P*-**SD**, *M*-**SD**, *P*-**DD,** and *M*-**DD** are listed in **Table 1** and **Figure S13**. Notably, although the device performance of *P*-**SD** shows better performance at low current density, *P*-**DD** with wider recombination area performs better at higher current density. However, it is obvious that the measured $|g_{EL}|$ factors are smaller than the chiral material in solution and film. The reason may be the reflected circularly polarized electroluminescence from metal electrode causing the spiral direction of CP light reverse which impair the intensity of CPEL (Zinna et al., 2017; Yan et al., 2019a). Anyway, successfully obtained CPEL signals indicate a feasible way to fabricate evaporated CP-OLEDs. Meanwhile, appropriate host material and device structure may also be required for better CPEL and EL performances.

CONCLUSION

In summary, a pair of chiral platinahelicene enantiomers with excellent thermal and configurational stability was designed and synthesized. Meanwhile, owing to the special structure design strategy, *P*-**Pt** and *M*-**Pt** show good CPL properties possessing $|g_{PL}|$ of 6.0×10^{-3} in solution and 4.0×10^{-3} in doped film, respectively. And the fabricated devices *P*-**SD**, *M*-**SD**, *P*-**DD,** and *M*-**DD** exhibited deep-red emission with the emission peak around 653 nm and the EQE_{max} of 4.6% as well as the $|g_{EL}|$ on the order of 10^{-3}.

DATA AVAILABILITY STATEMENT

All datasets generated for this study are included in the article/**Supplementary Material**.

AUTHOR CONTRIBUTIONS

Z-PY designed and synthesized the platiahelicene complexes, carried out relevant measurement, and wrote the manuscript. X-FL helped in material synthesis and purification. KL helped in the theoretical calculation. Y-XZ and J-LZ designed the whole research.

ACKNOWLEDGMENTS

We gratefully acknowledge the financial support from the National Natural Science Foundation of China (51773088, 21975119).

SUPPLEMENTARY MATERIAL

The Supplementary Material for this article can be found online at: https://www.frontiersin.org/articles/10.3389/fchem.2020.00501/full#supplementary-material

REFERENCES

Brandt, J., Wang, X., Yang, Y., Campbell, A., and Fuchter, M. (2016). Circularly polarized phosphorescent electroluminescence with a high dissymmetry factor from PHOLEDs based on a platinahelicene. *J. Am. Chem. Soc.* 138, 9743–9746. doi: 10.1021/jacs.6b02463

Dhbaibi, K., Favereau, L., and Crassous, J. (2019). Enantioenriched helicenes and helicenoids containing main-group elements (B, Si,

N, P). *Chem. Rev.* 119, 8846–8953. doi: 10.1021/acs.chemrev.9b00033

Feuillastre, S., Pauton, M., Gao, L., Desmarchelier, A., Riives, A. J., Prim, D., et al. (2016). Design and synthesis of new circularly polarized thermally activated delayed fluorescence emitters. *J. Am. Chem. Soc.* 138, 3990–3993. doi: 10.1021/jacs.6b00850

Fu, G., He, Y., Li, W., Wang, B., Lü, X., He, H., et al. (2019). Efficient polymer light-emitting diodes (PLEDs) based on chiral [Pt(C^N)(N^O)] complexes with near-infrared (NIR) luminescence and circularly polarized (CP) light. *J. Mater. Chem. C* 7, 13743–13747. doi: 10.1039/C9TC04792A

Graule, S., Rudolph, M., Vanthuyne, N., Autschbach, J., Roussel, C., Crassous, J., et al. (2009). Metal-bis(helicene) assemblies incorporating π-conjugated phosphole-azahelicene ligands: impacting chiroptical properties by metal variation. *J. Am. Chem. Soc.* 131, 3183–3185. doi: 10.1021/ja809396f

Grell, M., Oda, M., Whitehead, K. S., Asimakis, A., Neher, D., and Bradley, D. D. C. (2001). A compact device for the efficient, electrically driven generation of highly circularly polarized light. *Adv. Mater.* 13, 577–580. doi: 10.1002/1521-4095(200104)13:8<577::AID-ADMA577>3.0.CO;2-K

Han, J., Guo, S., Lu, H., Liu, S. J., Zhao, Q., and Huang, W. (2018). Recent progress on circularly polarized luminescent materials for organic optoelectronic devices. *Adv. Opt. Mater.* 6:1800538. doi: 10.1002/adom.201800538

Han, J., Guo, S., Wang, J., Wei, L., Zhuang, Y., Liu, S., et al. (2017). Circularly polarized phosphorescent electroluminescence from chiral cationic iridium(III) isocyanide complexes. *Adv. Optical Mater.* 5:1700359. doi: 10.1002/adom.201700359

Hellou, N., Srebro-Hooper, M., Favereau, L., Zinna, F., Caytan, E., Toupet, L., et al. (2017). Enantiopure cycloiridiated complexes bearing a pentahelicenic N-Heterocyclic carbene and displaying long-lived circularly polarized phosphorescence. *Angew. Chem. Int. Ed.* 56, 8236–8239. doi: 10.1002/anie.201704263

Li, M., Li, S. H., Zhang, D., Cai, M., Duan, L., and Fung, M. K. (2018). Stable enantiomers displaying thermally activated delayed fluorescence: efficient OLEDs with circularly polarized electroluminescence. *Angew. Chem. Int. Ed.* 57, 2889–2893. doi: 10.1002/anie.201800198

Li, T. Y., Jing, Y. M., Liu, X., Zhao, Y., Shi, L., Tang, Z., et al. (2015). Circularly polarised phosphorescent photoluminescence and electroluminescence of iridium complexes. *Sci. Rep.* 5:14912. doi: 10.1038/srep14912

Norel, L., Rudolph, M., Vanthuyne, N., Gareth. Williams, J. A., Lescop, C., Roussel, C., et al. (2010). Metallahelicenes: easily accessible helicene derivatives with large and tunable chiroptical properties. *Angew. Chem. Int. Ed.* 49, 99–102. doi: 10.1002/anie.200905099

Peeters, E., Christiaans, M., Janssen, R., Schoo, H., Dekkers, H., and Meijer, E. W. (1997). Circularly polarized electroluminescence from a polymer light-emitting diode. *J. Am. Chem. Soc.* 119, 9909–10. doi: 10.1021/ja971912c

Sakai, H., Shinto, S., Kumar, J., Araki, Y., Sakanoue, T., Takenobu, T., et al. (2015). Highly fluorescent [7]carbohelicene fused by asymmetric 1,2-dialkyl-substituted quinoxaline for circularly polarized luminescence and electroluminescence. *J. Phys. Chem. C* 119, 13937–13947. doi: 10.1021/acs.jpcc.5b03386

Sánchez-Carnerero, E., Agarrabeitia, A., Moreno, F., Maroto, B., Muller, G., Ortiz, M., et al. (2015). Circularly polarized luminescence from simple organic molecules. *Chem. Eur. J.* 21, 13488–13500. doi: 10.1002/chem.201501178

Shen, C., Anger, E., Srebro, M., Vanthuyne, N., Deol, K. K., Jefferson, T. D., et al. (2014). Straightforward access to mono- and bis-cycloplatinated helicenes displaying circularly polarized phosphorescence by using crystallization resolution methods. *Chem. Sci.* 5, 1915–1927. doi: 10.1039/c3sc53442a

Wu, Z. G., Han, H. B., Yan, Z. P., Luo, X. F., Wang, Y., Zheng, Y. X., et al. (2019). Chiral octahydro-binaphthol compound-based thermally activated delayed fluorescence materials for circularly polarized electroluminescence with superior EQE of 32.6% and extremely low efficiency roll-off. *Adv. Mater.* 31:1900524. doi: 10.1002/adma.201900524

Yan, Z. P., Liao, K., Han, H. B., Su, J., Zheng, Y. X., and Zuo, J. L. (2019b). Chiral iridium(III) complexes with four-membered Ir-S-P-S chelating rings for high-performance circularly polarized OLEDs. *Chem. Commun.* 55, 8215–8218. doi: 10.1039/C9CC03915E

Yan, Z. P., Luo, X. F., Liu, W. Q., Wu, Z. G., Liang, X., Liao, K., et al. (2019a). Configurationally stable platinahelicene enantiomers for efficient circularly polarized phosphorescent organic light-emitting diodes. *Chem. Eur. J.* 25, 5672–5676. doi: 10.1002/chem.201900955

Zhang, Y. J., Oka, T., Suzuki, R., and Ye, J. T. (2014). Electrically switchable chiral light-emitting transistor. *Science* 344, 725–728. doi: 10.1126/science.1251329

Zhao, W. L., Li, M., Lu, H. Y., and Chen, C. F. (2019). Advances in helicene derivatives with circularly polarized luminescence. *Chem. Commun.* 55, 13793–13803. doi: 10.1039/C9CC06861A

Zinna, F., Giovanella, U., and Bari, D. (2015). Highly circularly polarized electroluminescence from a chiral europium complex. *Adv. Mater.* 27, 1791–1795. doi: 10.1002/adma.201404891

Zinna, F., Pasini, M., Galeotti, F., Botta, C., Bari, L. D., and Giovanella, U. (2017). Design of lanthanide-based OLEDs with remarkable circularly polarized electroluminescence. *Adv. Funct. Mater.* 27:1603719. doi: 10.1002/adfm.201603719

Conflict of Interest: The authors declare that the research was conducted in the absence of any commercial or financial relationships that could be construed as a potential conflict of interest.

frontiers in Chemistry

PERSPECTIVE
published: 23 June 2020
doi: 10.3389/fchem.2020.00527

Temperature-Dependent Circularly Polarized Luminescence Measurement Using KBr Pellet Method

Yoshiro Kondo[1]*, *Satoko Suzuki*[1], *Masayuki Watanabe*[1], *Akio Kaneta*[1], *Paolo Albertini*[2] *and Koushi Nagamori*[1]

[1] JASCO Corporation, Hachioji, Japan, [2] JASCO Europe srl, Cremella, Italy

Circularly polarized luminescence (CPL) spectroscopy measures the difference in luminescence intensity between left- and right-circularly polarized light, and is often used to analyze the structure of chiral molecules in their excited state. Recently, it has found an increasing range of applications in the analysis of molecules that emit circularly polarized light and can be employed in 3D displays. Thus, the number of articles focusing on CPL spectroscopy has increased dramatically. However, since the luminescence dissymmetry factor (g_{lum}) for organic compounds is generally $<|0.01|$, CPL spectrometers must offer high sensitivity and produce spectra that are artifact-free for chiral molecules. Until now, the principal targets of CPL measurements have been solution samples. However, for practical device applications, it is also necessary to be able to measure the CPL spectra of solid-state samples. In addition, since electronic devices often operate at high temperatures, it is important to evaluate the thermal dependence of the CPL characteristics. Moreover, in the measurement of solid-state samples, the degree of anisotropy of the samples must be evaluated, because a large degree of anisotropy can cause artifacts. Therefore, we describe methods to evaluate the degree of anisotropy of solid-state samples and their high-temperature applications.

Keywords: CPL, europium complex, solid-state CPL measurement, temperature-dependent CPL measurements, KBr pellet

OPEN ACCESS

Edited by:
Giovanna Longhi,
University of Brescia, Italy

Reviewed by:
Takunori Harada,
Oita University, Japan
Zhipeng Liu,
Nanjing Forestry University, China

***Correspondence:**
Yoshiro Kondo
yoshiro.kondo@jasco.co.jp

Specialty section:
This article was submitted to Physical Chemistry and Chemical Physics, a section of the journal Frontiers in Chemistry

Received: *03 March 2020*
Accepted: *22 May 2020*
Published: *23 June 2020*

Citation:
Kondo Y, Suzuki S, Watanabe M, Kaneta A, Albertini P and Nagamori K (2020) Temperature-Dependent Circularly Polarized Luminescence Measurement Using KBr Pellet Method. Front. Chem. 8:527. doi: 10.3389/fchem.2020.00527

INTRODUCTION

Recently, circularly polarized luminescence (CPL) spectroscopy has attracted attention in the study of optically active substances. Circular dichroism (CD) spectroscopy is used for structural analysis of the ground state of such substances, while CPL spectroscopy is a complementarily method that can obtain information about the excited state.

The CPL signal is defined as the difference in luminescence intensity between left- and right-circularly polarized light, and the luminescence dissymmetry factor (g_{lum}) is defined as:

$$g_{lum} = \frac{2\,(I_L - I_R)}{(I_L + I_R)},$$

where I_L and I_R are the luminescence intensities of left- and right-hand circularly polarized light, respectively. g_{lum} takes a value from -2 to $+2$, and is $+2$ for only left circularly polarized light,

and −2 for only right circularly polarized light. The value measured by a CPL spectrometer is often output in the form of ΔI or θ (ellipticity in millidegrees). In a JASCO CPL-300 CPL spectrometer using lock-in detection, calibration is performed so that the following relationship is maintained between θ and g_{lum}:

$$g_{lum} = \frac{6.9813 \times 10^{-5} \times \theta}{I}$$

where I is the total luminescence intensity measured by the CPL spectrometer at the same time as the CPL spectrum.

In recent years, organic compounds exhibiting very large g_{lum} values have been synthesized. Sato et al. (2017) reported $g_{\mathrm{lum}} = \pm 0.152$ for cylindrical organic molecules, and Shen et al. (2015) reported $g_{\mathrm{lum}} = -2.3 \times 10^{-2}$ for supramolecular gels. However, for most organic compounds, g_{lum} is $<|0.01|$. Also, in the field of biomolecules, CPL of green fluorescent protein has been reported, but the g_{lum} value of 1.8×10^{-3} is small (Goto et al., 2010). In addition, in lanthanoid complexes, the CPL signal associated with f → f transitions has a large g_{lum}, but the CPL band is very sharp (Brittain and Richardson, 1976; Zinna and Bari, 2015; Zinna et al., 2015; Hasegawa et al., 2020).

Until now, the principal targets of CPL measurements have been solution samples. However, in recent years, CPL measurements of solid-state samples have attracted attention. Nakabayashi et al. (2014) reported a peak shift in the fluorescence spectrum and inversion of the sign in the CPL spectrum when binaphthyl-crown ether-pyrene was dispersed in a chloroform solution or a PMMA film. Kimoto et al. (2013) reported that the sign of the CPL spectrum of binaphthyl fluorophores was reversed in a KBr pellet and a PMMA film. This also suggests that it is possible to control the CPL properties by changing the environment of the chiral compound without using an enantiomer. Taniguchi et al. (2019) reported the observation of aggregation-induced enhanced (AIEnh) CPL of chiral perylene diimide fluorophores in a KBr pellet, a PMMA film and a *myo*-IPU-film. Louis et al. (2019) reported mechano-responsive CPL by thermal annealing and smearing of a solid-state sample.

Compounds that emit circularly polarized light have potential applications to optical devices such as displays (Brandt et al., 2016). However, in order to achieve this, it is necessary to be able to perform solid-state CPL measurements. In addition, since electronic devices often operate at high temperatures, it is important to evaluate the temperature dependence of the CPL characteristics. Although there have been some reports on solid-state CPL measurements of samples in KBr pellets (Nishiguchi et al., 2011; Taniguchi et al., 2015) and PMMA films (Kimoto et al., 2012, 2013; Nakabayashi et al., 2014), the number of studies is still quite small. Okazaki et al. (2016) and Kumar et al. (2014) studied the temperature dependence of CPL characteristics, but again these reports are limited. Moreover, in the measurement of solid-state samples, the degree of anisotropy of the samples must be evaluated, because a large degree of anisotropy can lead to artifacts. Anisotropic samples such as single crystals and oriented liquid crystals have a large degree of anisotropy and cannot be measured by conventional CPL spectrometers. However, solid samples such as those dispersed in KBr pellets, which do not exhibit anisotropy, can be measured by conventional CPL spectrometers. Here, we describe methods to evaluate the degree of anisotropy of solid-state samples, and high-temperature measurement techniques for such samples.

ARTIFACTS IN CPL MEASUREMENTS

Conventional CPL spectrometers employ a photoelastic modulator (PEM) and a lock-in amplifier. Normally, in lock-in detection, the CPL signal is detected at 50 kHz and the linearly polarized luminescence (LPL) signal is detected at 100 kHz. The 100 kHz signal is filtered by signal processing in the CPL spectrometer, but if it is too large, it cannot be completely removed, causing artifacts in the CPL spectrum. These artifacts cannot be ignored when measuring samples exhibiting large anisotropy such as single crystals or oriented liquid crystals. For the case of an ideal PEM and lock-in amplifier, only the 50 kHz signal will be detected. However, since this is impossible in reality, the degree of anisotropy must be evaluated. The following two cases can be considered for solid-state samples: (1) Highly oriented samples such as single crystals and liquid crystals, (2) samples in which molecules motion is restricted, but the molecules are randomly oriented, such as samples dispersed in KBr pellets, Nujol, and isotropic films.

In the case of (1), it is necessary to measure CPL spectra with a dedicated CPL spectrometer, for example using the method based on the Stokes-Mueller matrix analysis reported by Harada et al. (2012). In the case of (2), molecular motion is restricted, so that a LPL component due to fluorescence anisotropy may be detected. However, even using a conventional CPL spectrometer, artifacts due to fluorescence anisotropy can be eliminated using unpolarized incident light and 180° detection, or horizontally polarized incident light with 90° detection (Blok and Dekkers, 1990; Castiglioni et al., 2014).

The following methods can be used to determine whether a sample exhibits a large degree of anisotropy:

Before measuring CPL spectra, measure the LD spectrum of the sample and confirm that there is no signal associated with anisotropy.

Rotate the sample around the excitation light propagation axis and measure CPL spectra at different angles.

These methods are also effective for measuring CD spectra of solid samples (Castiglioni et al., 2009). If possible, it is desirable to measure enantiomers and confirm that the CD and CPL spectra exhibit mirror images.

PRINCIPLES OF CPL SPECTROSCOPY

In a CPL spectrometer, the beam from a light source is monochromated, and the sample is excited by unpolarized or linearly polarized light. The fluorescence in the left- and right-circularly polarized light emitted from the sample is then modulated into linearly polarized light at a frequency of 50 kHz using a PEM installed behind the sample. A polarizer behind the PEM passes either left- or right-circularly polarized fluorescent light in synchronization with the PEM modulation.

This fluorescence is monochromated and then detected. The CPL signal is obtained by lock-in detection of the difference between the fluorescence intensities for the left- and right-circularly polarized light, again synchronized with the PEM modulation. The total fluorescence spectrum of the sample can be obtained simultaneously with the CPL spectrum.

A CPL spectrometer can use a laser, LED, or xenon lamp as a light source. A laser can emit a high-intensity light beam, and a LED has the advantages of being inexpensive and having a long life. On the other hand, a xenon lamp emits a large amount of energy in the ultraviolet to near-infrared region, and the optimal excitation wavelength for a given sample can be selected using a monochromator. Also, the use of an ozone-free xenon lamp eliminates the need for nitrogen purging. Since commercially available CPL spectrometers have become widespread, ozone-free xenon lamps are widely used.

The monochromator is generally either a diffraction grating or a prism. Although the former allows easy wavelength control, polarization effects due to Woods' anomalies and higher-order light may affect the CPL spectra. By using a prism, these problems can be eliminated.

Fluorescence in circularly polarized light from the sample is detected at 90 or 180° with respect to the excitation-side monochromator. The 90° arrangement has the advantage of being little affected by scattered excitation light, but in the case of solid or highly viscous samples, it is susceptible to artifacts unless the sample is irradiated with horizontally polarized incident light (Blok and Dekkers, 1990; Castiglioni et al., 2014). On the other hand, in the case of the 180° arrangement, the influence of artifacts can be greatly reduced, just by performing measurements with unpolarized excitation light. In this configuration, the influence of scattered excitation light and stray light can be reduced by employing a double-prism monochromator.

Various accessories are available for CPL spectrometers. To measure thin films or KBr pellets, a special holder adapted to the sample shape can be used. In addition, Peltier thermostatted cell holders can be used to control the sample temperature, and some can be used in both CPL and CD spectrometers. In a 180° CPL spectrometer, magnetic circularly polarized luminescence (MCPL) measurements can be performed by placing a magnet in the sample chamber to produce a magnetic field that is parallel to the light beam. MCPL spectroscopy provides information about the electronic structure of the excited states of molecules. Usually, a photomultiplier tube with high sensitivity in the ultraviolet to visible region is used as a detector in a CPL spectrometer. To measure NIR CPL spectra, an InGaAs detector can instead be used. To our knowledge, there have been no reports on CPL measurements in the NIR region, but this will hopefully change.

CALIBRATION OF CPL SPECTROMETER

Wavelength calibration is indispensable in a CPL spectrometer. For an ultraviolet/visible spectrophotometer or a spectrofluorometer, calibration of the wavelength is generally performed using an emission line from a deuterium or mercury lamp. For example, the JASCO CPL-300 CPL spectrometer uses low-pressure mercury lamps for both the excitation and emission monochromators, and the wavelength can be calibrated.

Calibration of the CPL scale is essential for CPL spectrometers that use lock-in detection. One method of achieving this is to irradiate a sample solution with a known CD value at a certain wavelength using unpolarized light, and to measure the difference in intensity between the left- and right-circularly polarized transmitted light. Samples with known CD values include (1S)-(+)-10-camphorsulfonic acid (Schippers

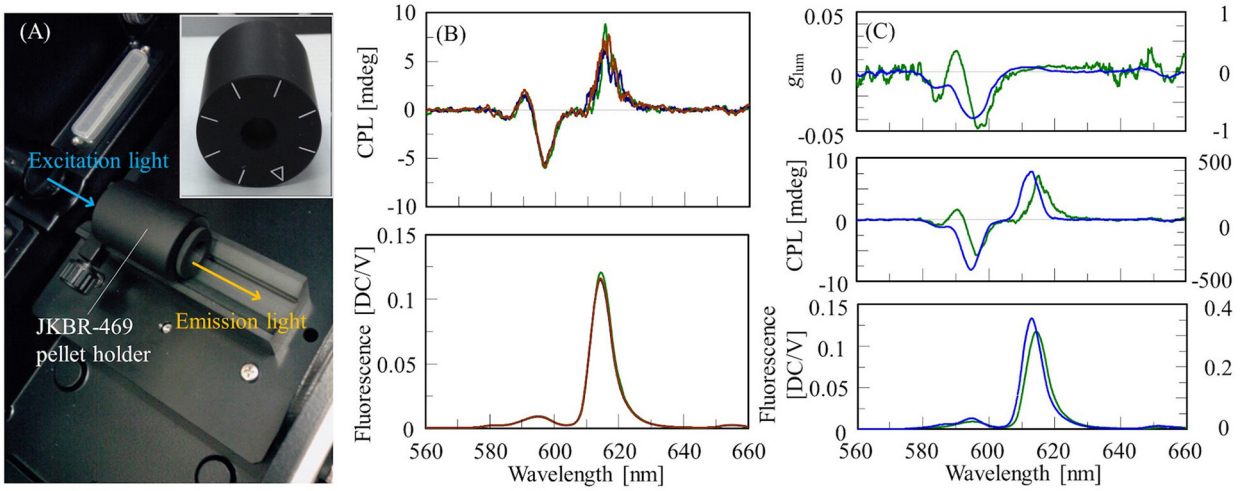

FIGURE 1 | (A) Sample compartment of CPL-300 with installed JKBR-469 pellet holder, and front view of JKBR-469. **(B)** CPL and fluorescence spectra of Eu(facam)$_3$/KBr pellet at rotation angles of 0° (green), 45° (blue), and 90° (red). **(C)** g_{lum}, CPL and fluorescence spectra of Eu(facam)$_3$/KBr pellet (green, left vertical axis) and in DMSO solution (blue, right vertical I axis).

and Dekkers, 1981) and (1S)-(+)-10-camphorsulfonic acid ammonium salt (Takakuwa et al., 1985). Since the latter is not hygroscopic, it is useful for calibrating CPL spectrometers.

CPL MEASUREMENTS USING KBR PELLET METHOD

To measure CPL spectra of solid-state samples using a conventional CPL spectrometer, available methods are the Nujol mull method, dispersing a sample in a film such as PMMA, and the KBr pellet method. In this section, we describe an example of measuring the CPL spectrum of a Eu(facam)$_3$/KBr pellet. The pellet was prepared at a sample concentration of 5% (w/w) using the same procedure as that used for IR measurements, and had a diameter of 10 mm. The CPL spectrum was obtained using a JASCO CPL-300 CPL spectrometer. The KBr pellet was placed in a JKBR-469 pellet holder, and the fluorescence in the 180° direction was detected (**Figure 1A**). The excitation wavelength was 373 nm, and the emission bandwidth was 7 nm. The excitation light was unpolarized, thus suppressing CPL artifacts. Generally, to eliminate the possibility of artifacts being present, it is necessary to measure enantiomers and confirm that the CPL spectra are mirror images of each other. However, it is not always practical to obtain an enantiomer of a sample. In such a case, the presence of artifacts can be detected by rotating a solid-state sample like a polarizer with respect to the excitation light and measuring at different angles. If the CPL spectrum changes, artifacts are likely to be present. The JKBR-469 pellet holder has a mark every 45°, and by checking if the CPL spectrum changes by rotating the sample, the presence of artifacts can be determined. In this study, the CPL spectrum of

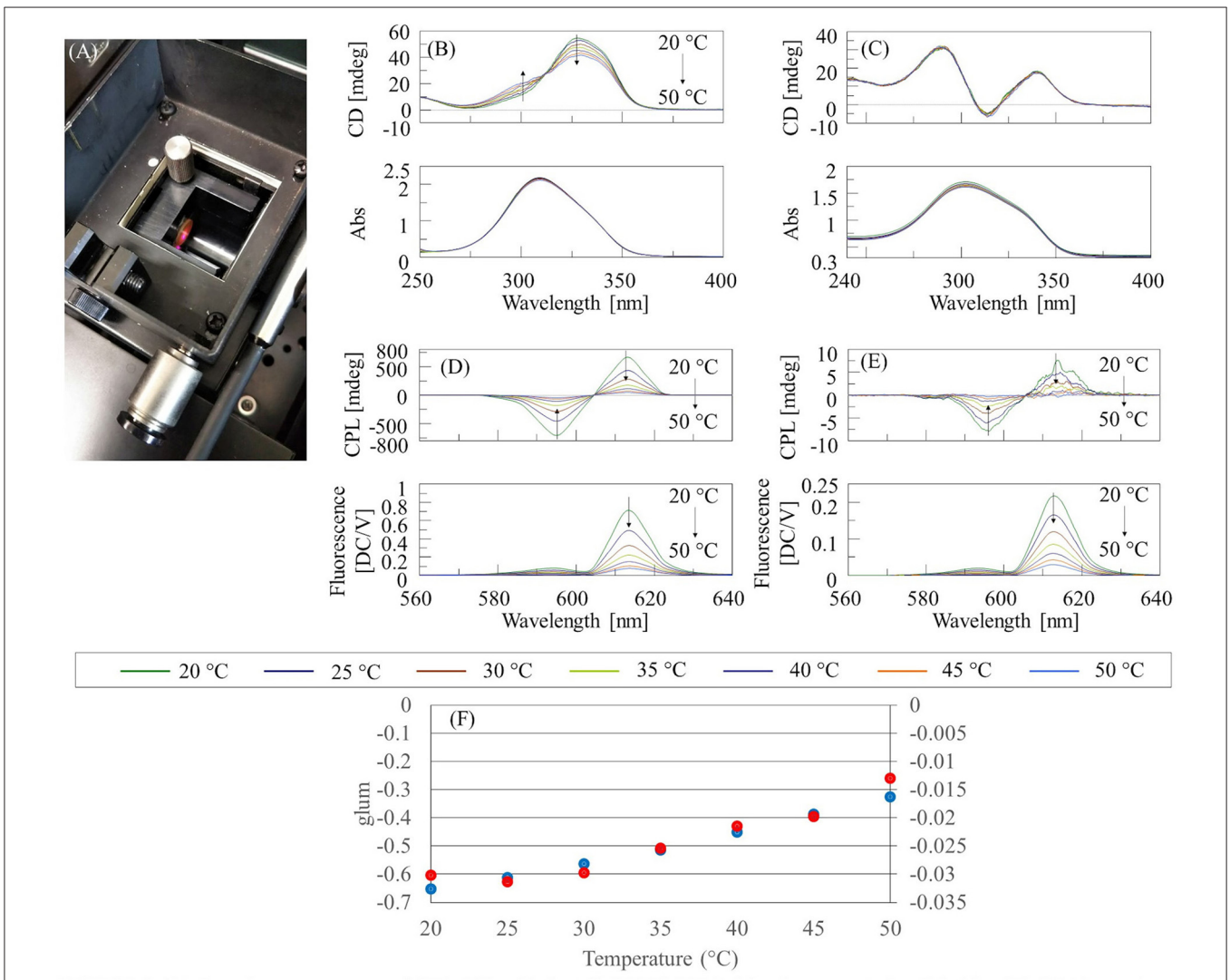

FIGURE 2 | (A) Sample compartment of CPL-300 with installed PTC-510 Peltier thermostatted cell holder **(B)** CD/absorption spectra of Eu(facam)$_3$/DMSO, **(C)** CD/absorption spectra of Eu(facam)$_3$/KBr pellet, **(D)** CPL/fluorescence spectra of Eu(facam)$_3$/DMSO, **(E)** CPL/fluorescence spectra of Eu(facam)$_3$/KBr pellet, and **(F)** g_{lum} for DMSO solution (blue) and KBr pellet (red) at 596 nm.

the Eu(facam)$_3$/KBr pellet was measured at 0°, 45°, and 90°, and no change was detected (**Figure 1B**).

CPL and fluorescence spectra of the Eu(facam)$_3$/KBr pellet and the DMSO solution are shown in **Figure 1C**. The concentration of the Eu(facam)$_3$/DMSO solution was 5 mg/mL, and the CPL spectra of Eu(facam)$_3$/DMSO and Eu(facam)$_3$/KBr were measured under the same conditions except for the number of accumulations. It is known that g_{lum} for Eu(facam)$_3$ changes dramatically depending on the solvent used (Brittain and Richardson, 1976). In the present study, the spectrum of Eu(facam)$_3$/KBr was different to that of Eu(facam)$_3$/DMSO. For the KBr pellet, g_{lum} was −0.048 at 597 nm, which is about 16 times smaller than the value of −0.777 at 596 nm for the DMSO solution.

TEMPERATURE-DEPENDENT CPL MEASUREMENTS USING KBR PELLET METHOD

The temperature dependence of the CPL and CD spectra of Eu(facam)$_3$/KBr and Eu(facam)$_3$/DMSO was investigated using a CPL-300 CPL spectrometer and a J-1500 CD spectrometer, respectively, together with a PTC-510 Peltier thermostatted cell holder (JASCO Corporation). The concentration of the Eu(facam)$_3$/DMSO solution was 5 mg/mL, and the optical path length was 0.1 mm for CD measurements, and 10 mm for CPL measurements. The diameter of the KBr pellet was 10 mm. The concentration of Eu(facam)$_3$ in the KBr pellet was 0.074% (w/w) for CD measurements, and 5% (w/w) for CPL measurements. The Eu(facam)$_3$/KBr pellets were mounted on the handmade holder of the PTC-510 (**Figure 2A**).

The temperature-dependent CD and absorption spectra of Eu(facam)$_3$/DMSO and Eu(facam)$_3$/KBr are shown in **Figures 2B,C**, respectively. It can be seen that the CD spectrum of Eu(facam)$_3$/DMSO changes with increasing temperature. On the other hand, for Eu(facam)$_3$/KBr, there is almost no change in the CD spectrum with increasing temperature. This indicates that the structure of Eu(facam)$_3$ in the ground state is more stable in the KBr pellet. No change is observed in the absorption spectrum of either Eu(facam)$_3$/DMSO or Eu(facam)$_3$/KBr. The temperature dependence of the CPL and fluorescence spectra of Eu(facam)$_3$/DMSO and Eu(facam)$_3$/KBr are shown in **Figures 2D**,**E**, respectively. For both samples, the CPL and fluorescence intensity decreases with increasing temperature. For Eu(facam)$_3$/DMSO, $|g_{lum}|$ decreases monotonically with increasing temperature, whereas for Eu(facam)$_3$/KBr, it remains almost constant up to 30°C and then decreases (**Figure 2F**). The different shapes of the CPL spectra in **Figures 1C, 2E** are due to the different emission bandwidths. When the Peltier thermostatted cell holder was used, the fluorescence intensity became weak, and so it was necessary to widen the bandwidth on the emission side. However, there was no problem in evaluating the relative change of g_{lum} with changing temperature.

FUTURE PROSPECTS

Recently, there have been reports on the design and synthesis of chiral molecules based on theoretical strategies (Tanaka et al., 2018), and such studies are expected to become more common in the future. Accordingly, the importance of CPL spectroscopy is expected to increase. The targets of CPL spectroscopy are expanding from conventional solution samples to solid-state samples and temperature-dependent samples. We hope that this report will help further the development of research using CPL spectroscopy.

DATA AVAILABILITY STATEMENT

All datasets generated for this study are included in the article/supplementary material.

AUTHOR CONTRIBUTIONS

YK conceived and wrote the article. MW and AK developed the CPL spectrometer. SS, PA, and KN edited the article. All authors contributed to the article and approved the submitted version.

REFERENCES

Blok, P. M. L., and Dekkers, H. P. J. M. (1990). Measurement of the circular polarization of the luminescence of photoselected samples under artifact-free conditions. *Appl. Spectrosc.* 44, 305–309.

Brandt, J. R., Wang, X., Yang, Y., Campbell, A. J., and Fuchter, M., J. (2016). Circularly polarized phosphorescent electroluminescence with a high dissymmetry factor from PHOLEDs based on a platinahelicene. *J. Am. Chem. Soc.* 138, 9743–9746. doi: 10.1021/jacs.6b02463

Brittain, H. G., and Richardson, F. S. (1976). Circular polarized emission studies on the chiral nuclear magnetic resonance lanthanide shift reagent Tris(3-trifluoroacetyl-*d*-camphorato)europium(III). *J. Am. Chem. Soc.* 98, 5858–5863.

Castiglioni, E., Abbate, S., Lebon, F., and Longhi, G. (2014). Chiroptical spectroscopic techniques based on fluorescence. *Method Appl. Fluoresc.* 2:024006. doi: 10.1088/2050-6120/2/2/024006

Castiglioni, E., Biscarini,. P., and Abbate, S. (2009). Experimental aspects of solid state circular dichroism. *Chirality* 21, 28–36. doi: 10.1002/chir.20770

Goto, H., Sawada, I., and Nomura, N. (2010). Circular dichroism and circular polarized luminescence from a green fluorescent protein – Initial research for chiroptical emission of biological materials. *Int. J. Polym. Mater.* 59, 786–792. doi: 10.1080/00914037.2010.483218

Harada, T., Kuroda, R., and Moriyama, H. (2012). Solid-state circularly polarized luminescence measurements: theoretical analysis. *Chem. Phys. Lett.* 530, 126–131. doi: 10.1016/j.cplett.2012.01.059

Hasegawa, M., Iwasawa, D., Kawaguchi, T., Koike, H., Saso, A., Ogata, S., et al. (2020). Chiroptical spectroscopic studies on lanthanide complexes with valinamide derivatives in solution. *ChemPlusChem.* 85, 294–300. doi: 10.1002/cplu.201900692

Kimoto, T., Amako, T., Tajima, N., Kuroda, R., Fujiki, M., and Imai, Y. (2013). Control of solid-state circularly polarized luminescence of binaphthyl organic fluorophores through environmental changes. *Asian J. Org. Chem.* 2, 404–410. doi: 10.1002/ajos.20130034

Kimoto, T., Tajima, N., Fujiki, M., and Imai, Y. (2012). Control of circularly polarized luminescence by using open-and closed-type binaphthyl

derivatives with the same axial chirality. *Chem. Asian. J.* 7, 2836–2841. doi: 10.1002/asia.201200725

Kumar, J., Nakashima, T., Tsumatori, H., and Kawai, T. (2014). Circularly polarized luminescence in chiral aggregates: Dependence of morphology on luminescence dissymmetry. *J. Phys. Chem. Lett.* 5, 316–321. doi: 10.1021/jz402615n

Louis, M., Sethy, R., Kumar, J., Katao, S., Guillot, R., Nakashima, T., et al. (2019). Mechano-responsive circularly polarized luminescence of organic solid-state chiral emitters. *Chem. Sci.*, 10, 843–847. doi: 10.1039/c8sc04026e

Nakabayashi, K., Amako, T., Tajima, N., Fujiki, M., and Imai, Y. (2014). Nonclassical dual control of circularly polarized luminescence modes of binaphthyl-pyrene organic fluorophores in fluidic and glassy media. *Chem. Commun*. 50, 13228–13230. doi: 10.1039/c4cc02946a

Nishiguchi, N., Kinuta, T., Nakano, Y., Harada, T., Tajima, N., Sato, T., et al. (2011). Control of the solid-state chiral optical properties of a supramolecular organic fluorophore containing 4-(2-arylethynyl)-benzoic acid. *Chem. Asian. J.* 6, 1092–1098. doi: 10.1002/asia.201000780

Okazaki, Y., Goto, T., Sakaguchi, R., Kuwahara, Y., Takafuji, M., Oda, R., et al. (2016). Facile and versatile approach for generating circularly polarized luminescence by non-chiral, low-molecular dye-on-nanotemplate composite system. *Chem. Lett.* 45, 448–450. doi: 10.1246/cl.060041

Sato, S., Yoshii, A., Takahashi, S., Furumi, S., Takeuchi, M., and Isobe, H. (2017). Chiral intertwined spirals and magnetic transition dipole moments dictated by cylinder helicity. *Proc. Natl. Acad. Sci. U.S.A.* 114, 13097–13101. doi: 10.1073/pnas.1717524114

Schippers, P. H., and Dekkers, H. P. M. J. (1981). Direct determination of absolute circular dichroism data and calibration of commercial instruments, *Anal. Chem.* 53, 778–782.

Shen, Z., Wang, T., Shi, L., Tang, Z., and Liu, M. (2015). Strong circularly polarized luminescence from the supramolecular gels of an achiral gelator: tunable intensity and handedness. *Chem. Sci*. 6, 4264–4272. doi: 10.1039/c5sc01056j

Takakuwa, T., Konno, T., and Meguro, H. (1985). A new standard substance for calibration of circular dichroism: ammonium d-10-camphorsulfonate. *Anal. Sci.* 1, 215–218.

Tanaka, H., Ikenosako, M., Kato, Y., Fujiki, M., Inoue, Y., and Mori, T. (2018). Symmetry-based rational design for boosting chiroptical responses. *Commun. Chem*. 1, 1–8. doi: 10.1038/s42004-018-0035-x

Taniguchi, A., Kaji, D., Hara, N., Murata, R., Akiyama, S., Harada, T., et al. (2019). Solid-state AIEnh-circularly polarized luminescence of chiral perylene diimide fluorophores. *RSC Adv*. 9, 1976–1981. doi: 10.1039/c8ra09785b

Taniguchi, N., Nakabayashi, K., Harada, T., Tajima, N., Shizuma, M., Fujiki, M., et al. (2015). Circularly polarized luminescence of chiral binaphthyl with achiral terthiophene fluorophores. *Chem. Lett*. 44, 598–600. doi: 10.1246/cl.150011

Zinna, F., and Bari, L. D. (2015). Lanthanide circularly polarized luminescence: bases and applications. *Chirality* 27, 1–13. doi: 10.1002/chir.22382

Zinna, F., Resta, C., Abbate, S., Castiglioni, E., Longhi, G., and Mineo, P., et al. (2015). Circularly polarized luminescence under near-UV excitation and structural elucidation of a Eu complex. *Chem. Commun*. 51, 11903–11906. doi: 10.1039/c5cc04283f

Conflict of Interest: YK, SS, MW, AK, and KN were employed by the company JASCO Corporation. PA was employed by the company JASCO Europe srl.

frontiers in Chemistry

ORIGINAL RESEARCH
published: 07 July 2020
doi: 10.3389/fchem.2020.00584

CPL Spectra of Camphor Derivatives in Solution by an Integrated QM/MD Approach

*Sara Del Galdo, Marco Fusè and Vincenzo Barone**

SMART Laboratory, Scuola Normale Superiore, Pisa, Italy

We extend a recently proposed computational strategy for the simulation of absorption spectra of semi-rigid molecular systems in condensed phases to the emission spectra of flexible chromophores. As a case study, we have chosen the CPL spectrum of camphor in methanol solution, which shows a well-defined bisignate shape. The first step of our approach is the quantum mechanical computation of reference spectra including vibrational averaging effects and taking bulk solvent effects into account by means of the polarizable continuum model. In the present case, the large amplitude inversion mode is explicitly treated by a numerical approach, whereas the other small-amplitude vibrational modes are taken into account within the harmonic approximation. Next, the snapshots of classical molecular dynamics computations are clusterized and one representative configuration from each cluster is used to compute a reference spectrum. In the present case, different clusters correspond to the two stable conformers of camphor in the S1 excited electronic state and, for each of them, to different numbers of strong solute-solvent hydrogen bonds. Finally, local fluctuation effects within each cluster are taken into account by means of the perturbed matrix model. The overall procedure leads to good agreement with experiment for absorption and emission spectra together with their chiral counterparts, thus allowing to analyze the role of different effects (stereo-electronic, vibrational, environmental) in tuning the overall experimental spectra.

Keywords: QM/MM, variational/perturbative, vibronic contributions, flexible systems, CPL

OPEN ACCESS

Edited by:
Ga-Lai Law,
Hong Kong Polytechnic University,
Hong Kong

Reviewed by:
Son Tung Ngo,
Ton Duc Thang University, Vietnam
Luca Evangelisti,
University of Bologna, Italy

****Correspondence:***
Vincenzo Barone
vincenzo.barone@sns.it

Specialty section:
This article was submitted to Physical Chemistry and Chemical Physics, a section of the journal Frontiers in Chemistry

Received: *21 April 2020*
Accepted: *05 June 2020*
Published: *07 July 2020*

Citation:
Del Galdo S, Fusè M and Barone V (2020) CPL Spectra of Camphor Derivatives in Solution by an Integrated QM/MD Approach. Front. Chem. 8:584. doi: 10.3389/fchem.2020.00584

1. INTRODUCTION

Circularly polarized luminescence (CPL) and electronic circular dichroism (ECD) are complementary techniques giving access to the properties of the excited and ground electronic states, respectively for chiral chromophores or chromophores embedded in chiral environments (Longhi et al., 2016; Tanaka et al., 2018). However, the magnetic dipole transition moment is generally much smaller than the electric one, thus hindering the investigation of systems showing strong luminescence (Riehl and Muller, 2012). Therefore, for both chiroptical spectroscopies, electric dipole forbidden and magnetic dipole allowed transitions represent a particularly appealing situation.

Camphor and its derivatives, and in particular their formally forbidden $n \rightarrow \pi^*$ carbonyl transitions, have been extensively studied by chiroptical methods, from both experimental and computational points of views (Dekkers and Closs, 1976; Schippers et al., 1983; Pritchard and Autschbach, 2010; Longhi et al., 2013; McAlexander and Crawford, 2015; Duong and Fujiki, 2017). Nevertheless, simulation of the camphor CPL is far from being straightforward because of

(i) the inherent dependence of the vibrational information from solvation interactions and (ii) the bisignate nature of the spectra. This latter phenomenon was recently qualitatively investigated by Longhi et al. (2013) and Duong and Fujiki (2017). According to Kasha's rule (Kasha, 1950), luminescence is expected to occur from the lowest excited electronic state. Therefore, within the Franck-Condon approximation, the first ECD and CPL transitions should have the same sign. In fact, the bisignate shape is a consequence of the pyramidalization of the carbonyl moiety, which gives rise to two low-energy conformers connected through a large amplitude motion (LAM) in the first excited state. This interconversion path needs to be properly accounted in order to reproduce and evaluate the different vibronic contributions in the spectra (Cerezo et al., 2016; Baiardi et al., 2017).

In this contribution, we apply a QM/MD approach to perform accurate simulations of camphor one-photon absorption (OPA) and emission (OPE) spectra and of their chiral counterparts ECD and CPL. We employ our recently developed ONIOM/EE-PMM (Del Galdo et al., 2019, 2020) procedure to model solvent effects on the electronic properties of the chromophore. The method belongs to the general category of multiscale procedures and merges variational and perturbative approaches in the calculation of spectroscopic features. Starting from extensive classical simulations of a target electronic state of a chromophore, effective clustering procedures are applied in order to identify a relevant set of sub-trajectories within the complete sampling. Within each cluster, one reference snapshot is utilized for an ONIOM calculation performed within the Electronic Embedding framework [ONIOM/EE, i.e., the variational approach (Dapprich et al., 1999; Vreven et al., 2006; Chung et al., 2015)]. Then, the local fluctuations within each sub-trajectory are treated via the Perturbed Matrix Method [PMM, i.e., the perturbative approach (Aschi et al., 2001; Del Galdo et al., 2018; Zanetti-Polzi et al., 2018)]. The procedure permits to strongly reduce the computational costs when compared to more conventional QM/MM approaches, without lowering the accuracy of the final results.

On top of this, the vibrational contributions to the final spectra are also modeled. We exploit for the purpose a general computational tool that allows the simulation of different kinds of one-photon spectroscopies and supports inclusion of mode-mixings, as well as Franck-Condon (FC) and Herzberg-Teller (HT) effects. Finally, internal coordinates are used in order to minimize the coupling between normal modes and LAMs, which are properly accounted for and treated separately.

2. METHODS

2.1. Combining QM and MM Methods, Step 1: Sampling Solute Internal Motions and Solvent Effects

Molecular Dynamics simulations of the ground and first excited electronic states of camphor in methanol were employed to generate the ensembles needed to evaluate the solvatochromic shifts on absorption and emission spectra. In view of the structural rigidity characterizing the camphor ground state, the corresponding MD simulation was run by constraining the solute at its equilibrium geometry. In this way, we did not take into account internal motions through classical approaches, thus adding their contribution *a posteriori* by means of full QM calculations of vibrational modulation effects by means of models based on the Franck-Condon principle (see sections 2.3). Conversely, as already reported (Longhi et al., 2013; Duong and Fujiki, 2017), in its first electronic state camphor undergoes an internal deformation associated to the carbonyl out of plane bending. After the characterization of the LAM (*vide infra*), we accounted for its effects by extracting the most representative conformers characterizing the excited state potential energy surface as a function of the carbonyl out of plane bending (namely the two minima of the curve reported in **Figure 1**). Then, both conformers were utilized for the classical MD sampling performed by constraining the solute geometry while the solvent molecules followed their unconstrained motion. The other internal degrees of freedom of the solute were taken into account in a separate step by full QM computations of vibronic effects within the harmonic approximation. For each MD ensemble the corresponding emission spectra were computed, thus obtaining the final spectra by proper weighting of the results. In **Table 1**, the relative stabilities of the two conformers are reported, which were used to compute the respective Boltzmann population at 300 K. Remembering that the solute was kept rigid during the MD runs for both ground and excited electronic states, the only properties differentiating the two simulation ensembles were the geometry of the solute and the atomic charges, the latter possibly including virtual sites (VSs) to represent oxygen lone pairs. The positions of VSs were determined by first locating the O-VS distance and the C-O-VS angle for the centroids of localized molecular orbitals at the sp2 oxygen atom of formaldehyde and propanone by using the Boys localization procedure, as reported in Macchiagodena et al. (2016) and Del Galdo et al. (2020). By averaging the (nearly identical) results, we obtained a value of

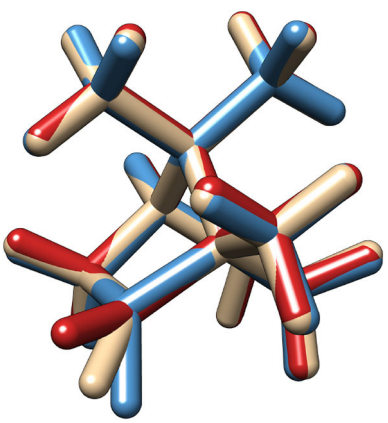

FIGURE 1 | Superimposed structures of the two most stable conformers (Conf.1 in blue and Conf.2 in red) and of the transition state between them in the first excite state.

TABLE 1 | Relative Electronic Energy (ΔE), Free Energy at 300 K (ΔG), Free Energy at 300 K in Solution (ΔG PCM) Values (kJ mol^{-1}) for the first excited state. Electronic energies computed at Cis(d) B2 levels of theory, vibrational and PCM correction computed at TD-DFT B3 level of theory[a].

	ΔE	ΔG	ΔG PCM	Pop.[a]
Conf. 1	0.00	0.00	0.00	96.97
Conf. 2	8.24	8.48	8.73	2.93
TS	15.37	16.19	17.00	0.10

[a]*Percent population factors (Pop., computed from the Boltzmann distribution) based on ΔG PCM.*

0.3067 Å for the distance and 111.3 degree for the angle. For the ground electronic state we imposed that the VSs, the O, the C and the other two atoms bound to C (i.e., the two C atoms) lie on the same plane (O-C(O)-C plane). Instead, for the excited state the VSs were constrained in the plane orthogonal to the plane defined by the normal to the C-C-C plane and oxygen atom. Separation of the charge between the oxygen nucleus and the VSs (having vanishing masses) was achieved by imposing that both VSs have the same charge and reproducing the classical dipole moment of the molecule in the target electronic state. The role of VSs was evaluated by performing two MD simulations (with and without their inclusion) for the ground electronic state. Specific solute-solvent interactions were analyzed by computing the probability of hydrogen bonding (HB) between the carbonyl oxygen and the hydroxyl group of methanol with the help of the so-called F function (Pagliai et al., 2003; Del Galdo et al., 2019, 2020), based on exponential decays for deviations from both radial and angular optimal values obtained from pure methanol simulations (we obtained 1.8 Å and 6 degrees for the optimum distance and angle, respectively and 0.2 Å and 5 degrees for the corresponding half width at half maximum, HWHM).

2.2. Combining QM and MM Methods, Step 2: The ONIOM/EE-PMM Method

Solvatochromic shifts on the different spectra of camphor were evaluated by the ONIOM/EE-PMM procedure we recently proposed (Del Galdo et al., 2019, 2020). The procedure merges variational and perturbative approaches to get a cheap yet accurate characterization of the perturbing effects exerted by an embedding environment on the quantum mechanical properties of a chromophore. The first step is the identification of a set of basins/clusters within a production MD run. For each sub-sampling, a reference frame is chosen as the most representative one of the corresponding cluster and its spectrum is evaluated by a variational procedure (ONIOM/EE) in which the QM model system (here the Camphor molecule) is embedded in a set of point charges representing the environment (here the methanol molecules) (Vreven et al., 2006). For all the other frames of each cluster, the fluctuations of environmental effects with respect to the reference configuration are computed *a posteriori* by a perturbative approach (PMM). In details, for each frame of each sub-trajectory, the system Hamiltonian is written as the diagonal matrix of the eigenvalues of the reference configuration plus a perturbation matrix representing the difference of the electrostatic potential between the considered frame and the reference value. Diagonalization of this matrix provides a set of eigenvalues (electronic states) representing the instantaneous effects of the embedding environment as provided by the MD trajectories. The operator representing the variation between the perturbing effects exerted by the environment in each frame and the reference, is modeled by exploiting the latest development of the PMM procedure, that is by expanding the perturbing electrostatic potential within the atomic region around each atomic center (atom-based expansion) (Zanetti-Polzi et al., 2018). Interested readers can find details of the procedure in Aschi et al. (2001), Zanetti-Polzi et al. (2018), Del Galdo et al. (2019), and Del Galdo et al. (2020) while specific computational details are reported in the following subsections.

2.3. Combining ONIOM/EE-PMM and Vibronic Calculation

The fist step is the simulation of the vibrational modulation (vibronic) effects in electronic spectra using models based on the Franck-Condon principle and a continuum description (PCM) of bulk solvent effects, as described in detail in Barone et al. (2009), Bloino et al. (2010), and Bloino et al. (2016). In particular, we employed the so-called time-independent (TI) approach, in which the band-shape is obtained as the sum of the individual transitions between the vibrational states of the initial and final electronic states. In order to best decouple the effect of the LAM, we employed the Vertical Gradient (VG) model (Baiardi et al., 2016), which requires the vibrational frequencies of the initial state, but only the forces of the final state at the equilibrium geometry of the initial one (Barone et al., 2009; Bloino et al., 2010, 2016).

Once computed the vibronic spectra for the reference structure of each conformer, they need to be combined with the outcome of the ONIOM/EE-PMM procedure to obtain the final spectra.

At the FC level, a simple shift by the transition energy and scaling by the transition moments for each snapshot leads, after proper averaging, to the final spectrum. Furthermore, on the grounds of previous experience (Del Galdo et al., 2020), effects related to environment fluctuations were considered negligible for magnetic transition dipole moments.

Inclusion of HT terms, accounting for the dependence of the transition dipole moments on the nuclei position, would require the computation of the derivatives of the perturbed transition dipole moments for each MD snapshot. Since this model would become too computationally demanding, we assumed, as in previous works (Del Galdo et al., 2020), that the difference between FC and FCHT spectra is explicitly evaluated only for the reference configuration, whereas the effect of solvent fluctuations is taken as half the value explicitly computed for the FC part as described above. In the following sections, the FCHT acronym will be used to indicate the inclusion of both FC and HT terms in the calculations.

2.4. Computational Details

All geometry optimizations and frequency calculations were carried out with a development version of the Gaussian suite of quantum chemical programs (Frisch et al., 2019), whereas all the MD simulations were performed with the GROMACS software (Berendsen et al., 1995). All the MD production runs of ground and first excited electronic states were performed by constraining the chromophore in the corresponding equilibrium geometry as obtained in the framework of the Density Functional Theory (DFT) (Lee et al., 1988) and its Time Dependent extension (TD-DFT) with the hybrid B3LYP functional (Becke, 1988; Lee et al., 1988) with additional empirical dispersion contributions (D3BJ) (Grimme et al., 2011) and the jul-cc-pVDZ (Dunning, 1989; Papajak et al., 2011) basis set (B3). For each simulation, the solute atomic charges were computed in vacuum at the proper equilibrium geometries by means of the CM5 model (Marenich et al., 2012) at the same level of theory. As mentioned above, two simulations of the ground state were performed including or not virtual sites on the oxygen atom to model directional effects related to sp2 lone pairs. Only the model including virtual sites was used for the simulations of the excited electronic state. All atom Lennard-Jones parameters were taken from the OPLS force field (Jorgensen et al., 1996) MD simulations under periodic boundary conditions were performed in the isothermal-isochoric ensemble (NVT) in order to avoid the additional parameters related to isobaric thermostats required by NPT simulations. The integration step was 2 fs and the temperature was kept constant (300 K) by the velocity-rescaling (Bussi et al., 2007) temperature coupling. Hard geometrical parameters were constrained using the LINCS algorithm (Hess et al., 1997). The particle mesh Ewald method (Darden et al., 1997) was used to compute long range interactions with grid search and cut-off radii of 1.1 nm. A cubic simulation box was utilized and the density was calibrated to obtain in the NVT MD simulations a pressure equal, within the noise, to that provided by a corresponding simulation of the pure solvent. The latter was carried out in the NVT ensemble at $T = 300$ K and imposing a box density equal to the experimental density of pure methanol at standard conditions (24.58 mol/l, Goodwin, 1987). All the production runs were 10 ns long. We analyzed the solvent effects within each simulation, by computing the probability of the carbonyl oxygen to be engaged in hydrogen bonds with methanol molecules as outlined above (that is, by means of the F function). For each production run, we partitioned the sampling into 4 clusters characterized by two, one (with either VS) or none solute-solvent hydrogen bond, respectively. The partitioning was performed using a threshold of 0.7 for the presence of an effective hydrogen bond. Next, for each cluster, the reference configuration used for the ONIOM/EE calculations is taken as a "collective frame" representative of the average configuration of the molecular environment for the corresponding cluster. To this aim, we extracted 30 snapshots sequentially from the trajectory, from each snapshot we cut a sphere of 30 Å centered around the solute and we assembled them into a collective configuration and we assigned to each environmental atom 1/30 of the actual atomic charge. The first 11 electronic states and the complete matrix of the corresponding dipole moments were computed for the 4 reference configurations exploiting the ONIOM/EE model with the QM part described at the TD-DFT/CAM-B3LYP (Yanai et al., 2004) level in conjunction with the jul-cc-pVDZ (Dunning, 1989; Papajak et al., 2011) basis set. For each electronic state, the corresponding atomic charges were also computed at the same computational level using the CM5 recipe. The above results were then utilized to apply the PMM approach for evaluating fluctuation effects within each cluster. Free energies were determined by adding to electronic energies zero-point energy, thermal, and PCM solvation contributions evaluated in the framework of the rigid rotor/harmonic oscillator approximation (Bloino et al., 2012; Cappelli et al., 2012; Mennucci, 2012). Transition energies have been corrected by the differences between TDDFT/CAMB3LYP/jul-cc-pVDZ and Cis(d) B2PLYPD3/jun-cc-pVTZ (Grimme and Neese, 2007; Jacquemin et al., 2009; Ottochian et al., 2020) (B2) results for isolated camphor. The LAM associated with the double-well potential has been characterized in the framework of the ICPH-model (Baiardi et al., 2017), using 251 DVR basis functions and a step size of 4°. Vibronic spectra were simulated starting from the structure and force constants computed taking into account solvent effects by PCM (Cappelli et al., 2012; Mennucci, 2012). OPE and CPL spectra were computed within the so-called time-independent (TI) approach, employing VG|FC and and VG|FCHT models. The default GAUSSIAN parameters of the class-based integral prescreening scheme were employed ($C_1^{max} = 50$, $C_2^{max} = 30$, $N_I^{max} = 10^9$). Normal modes connected with the LAM or methyl rotations were removed. Gaussian distribution functions with HWHM of 900, 550, and 450 cm^{-1} were used as broadening functions for pure electronic ONIOM/EE-PMM, vibronic PCM, and combined ONIOM/EE-PMM vibronic approaches, respectively. Spatial Distribution Functions plotted as isosurfaces and virtual sites were visualized employing the CAFFEINE software (Salvadori et al., 2016; Lazzari et al., 2020).

3. RESULTS

3.1. Characterization of the LAM

As already mentioned in the introduction, the lowest band in the camphor absorption spectrum is associated with the formally forbidden $n \rightarrow \pi^*$ carbonyl transition. However, experiments reveal the presence of a bisignate band in the CPL spectrum that can be connected with a breakdown of the Frank-Condon regime or with the involvement of more than one electronic state in the emission process. Since the second transition lies at a significantly higher energy than the first one, this behavior can be attributed, as previously suggested, to the flexibility of the system. Indeed, in its first electronic state camphor undergoes an internal deformation associated to the carbonyl out of plane bending: a LAM connects two minima through a flat transition state (see **Figure 1**). These kinds of LAMs are generally ill described by harmonic models (Baiardi et al., 2015, 2016), but use of internal coordinates strongly reduces the coupling of the LAM from the other modes, leading, to a good approximation, to an effective one-dimensional problem (Cerezo et al., 2016; Baiardi et al., 2017). The PES associated with the one-dimensional LAM

was explicitly computed through a scan along the CO out-of-plane (OOP) coordinate and it was used to solve numerically the vibrational Schrödiger equation with the help of a quasi-variational approach employing the discrete variable method (Light et al., 1985; Bačić and Light, 1989; Colbert and Miller, 1992; Light and Carrington, 2000; Baiardi et al., 2017). In the upper panels of **Figure 2** the PES of the first excited state along the LAM is reported together with the associated vibrational levels obtained with the DVR method, whereas in the bottom panels the ground state PES computed along the same path is reported. Moreover, the vibrational wave functions of those states relevant at 300 K (population above 0.5%) are drawn for both S1 and S0. The different colors highlight the dependence on the LAM of the electric and magnetic transition dipole moment and the angle between them. As expected, in the ground state only one conformer, corresponding to a flat CO structure, is observed along the LAM. On the other hand, the results of the excited state reveal the presence of two conformers corresponding to the out-of-plane bending of the CO, which are separated by a relatively high (18 kJ/mol) transition state (Conf. 1 and Conf. 2). It should also be noted that in S1 the accessible vibrational states at 300 K are well-localized and separated into the two wells. As observed before (Longhi et al., 2013; Duong and Fujiki, 2017), the sign of CPL shows a strong dependence on the LAM. However, as it can be seen in the panels of **Figure 2**, the most relevant variations are connected with the relative orientation between the two transition dipoles and with the magnitude of the electric transition dipole moment, whereas the corresponding magnetic moment is only negligibly affected by the LAM. Vibronic contributions of the other modes were then described by the Vertical Gradient (VG) model, neglecting the contribution of the LAM already accounted for explicitly. This approach is based on the assumption that the other modes rearrange faster than the LAM (Stendardo et al., 2012; Cerezo et al., 2016; Baiardi et al., 2017).

Finally, the strong dependence of the electric transition dipole moments on the nuclear position was accounted for by including Herzberg-Teller (HT) contributions.

3.2. Molecular Dynamics Results

The effectiveness of the interaction between camphor and the embedding solvent was at first assessed by computing the Spatial Distribution Function (SDF) of the methanol molecules around the solute for the ground state simulation. In **Figure 3**, we compare the results of the SDF calculation performed on simulations involving or not VSs. More precisely, we computed

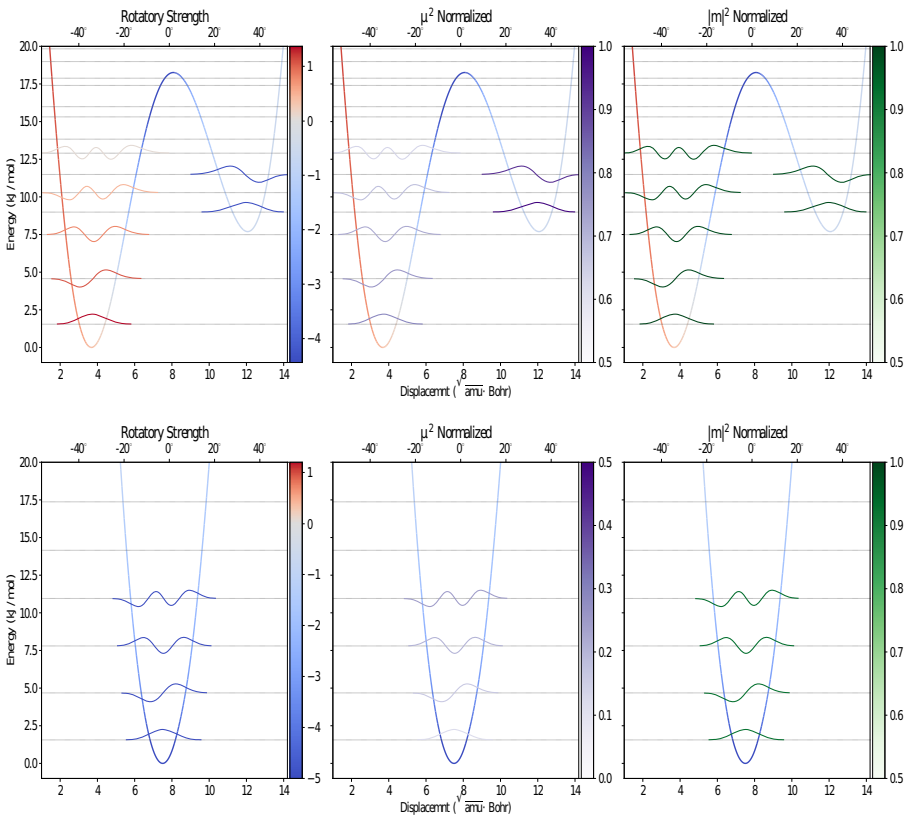

FIGURE 2 | Graphical representation of the PES along the CO out-of-plane bending for the S_1 **(upper)** and S_0 **(lower)** electronic states, computed at the B3LYP/Jul-cc-pVDZ (D3BJ) level of theory using the ICPH framework. The vibrational levels and wave functions with contribution above 0.5% at 300K, computed using the variational DVR-based approach, are also reported.

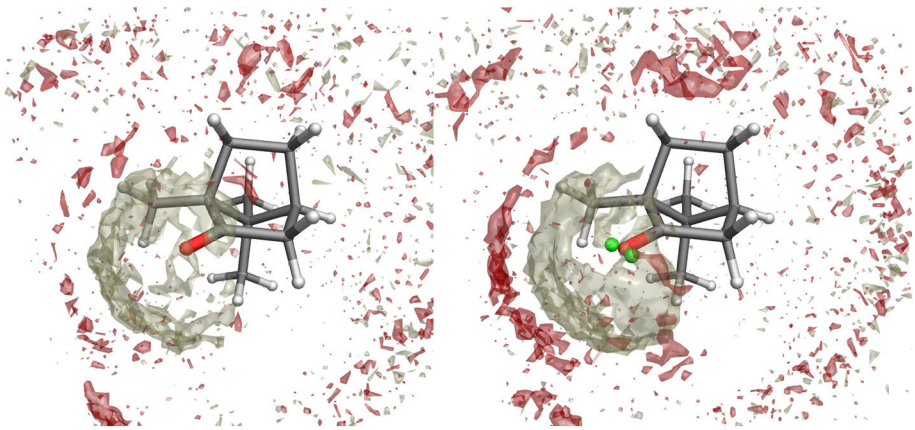

FIGURE 3 | Spatial Distribution Function of methanol molecules around camphor from the ground state simulation when the standard atomic charges **(left)** or the VSs representation **(right)** are employed. Density distributions of (hydroxyl) hydrogen and oxygen atoms in methanol are represented as white and red volumes, respectively.

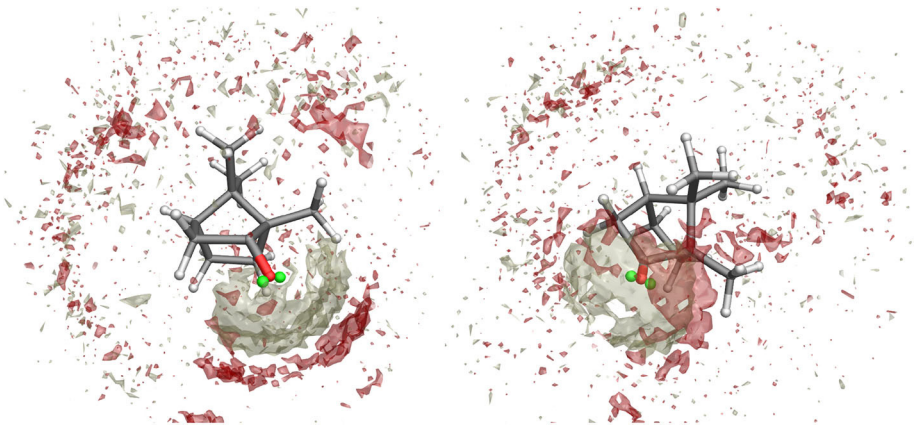

FIGURE 4 | Spatial Distribution Function of methanol molecules around camphor from the first excited state simulation of Conf. 1 **(left)** and 2 **(right)**. Density distributions of (hydroxyl) hydrogen and oxygen atoms in methanol are represented as white and red volumes, respectively.

the density distributions of (hydroxyl) hydrogen and oxygen atoms in methanol thus addressing the SDF of the partners of probable HB with camphor oxygen. It is apparent that inclusion of VSs increased the (average) number of methanol molecules around oxygen atom. Moreover, these results show that the arrangement of the solvent is slightly asymmetrical, with a more pronounced effect when the VSs are employed. As a consequence (i) we utilized this simulation as the statistical ensemble to evaluate the solvent effects on the absorption spectra and (ii) also for the production MD runs of the (first) excited electronic state we modeled the camphor including VSs. In **Figure 4**, the SDFs corresponding to the MD runs of the two conformers simulated to account for the first excited state of camphor are reported. The results suggest that the camphor oxygen (both in the ground and excited states) is engaged in HBs with the solvent molecules. In the following, for the sake of brevity, only the results obtained from the excited state simulations are reported while those corresponding to the ground state simulation can be found in the Supplementary Material (see **Figures S1**, **S2**). Nevertheless, it is worth noting that very similar results were found from the classical sampling. We computed the distribution of (i) the distance between each VS and the closest methanol hydroxyl hydrogen and (ii) the angle these two form with the oxygen in methanol. The results obtained from both the excited state simulations are reported in **Figure 5**. Nearly identical profiles are obtained for the two conformers and, within a given conformer, for each VS: while a clear peak appears in the radial distributions, a less pronounced one characterizes the angular distributions thus suggesting that some geometrical hindrance might weaken HB interactions. Next, we analyzed the HB probability for each excited state simulation by computing the F function described in the section 2. The results reported in **Figure 6** show that for both conformers, most of the classical sampling is characterized by the absence of any significant HB. However, we also obtained a non-negligible probability of having one HB for each VS. According to our computations, each methanol molecule was considered to interact with either one VS or the other, thus implying that a probability of around 1 for both the interaction

sites corresponds to a total number of 2 HBs for the molecule. On the basis of these results, we decided to partition both the excited state trajectories into a set of clusters, each characterized by a different number of HBs occurring between the camphor and the solvent. As shown in **Table 2**, the largest cluster accounts for the absence of any significant HB (noHB), then we identified two clusters characterized by one HB depending on the VS involved in the interaction (HB-VS1 and HB-VS2) and the fourth cluster includes the remaining snapshots where at least 2 HBs occur (twoHB). As mentioned above, very similar results were found when the ground state simulation was analyzed, thus allowing us to apply the same partitioning procedure to cluster the ground state trajectory (see **Table S1** for the results).

The partitioning is the first step toward application of the ONIOM/EE-PMM method, with the four clusters providing the different statistical ensembles from which the representative frames to be employed for the ONIOM/EE calculations were extracted. Then, the PMM procedure was applied to account for fluctuations (within each cluster) of the external electric potential tuning the electronic properties of the chromophore.

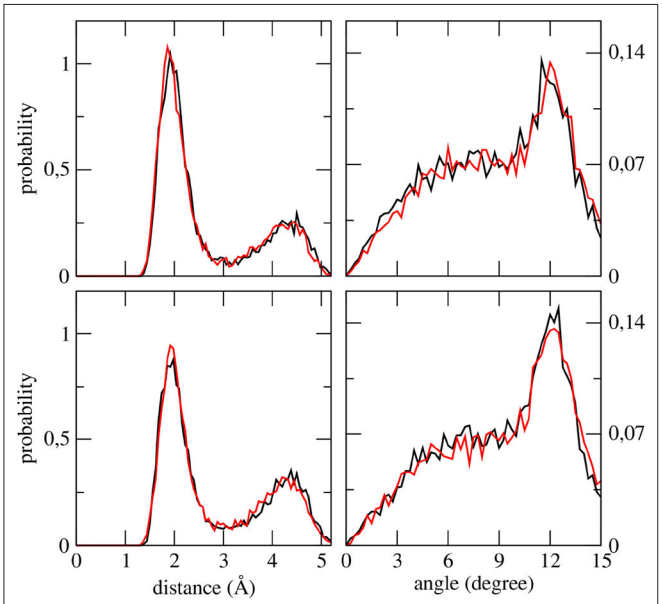

FIGURE 5 | Distribution functions of each VS—(methanol hydroxyl) H distance **(left)** and of each VS—(methanol hydroxyl) H—(methanol hydroxyl) O angles **(right)** as obtained from the first excited state simulation of camphor in methanol. Upper panels refer to the Conf. 1, lower panels refer to Conf. 2. For all the panels, data computed for the first and second VSs are shown as black and red lines, respectively.

3.3. Spectroscopic Results

In order to increase the accuracy of the results, all the transition energies were shifted with reference to the values computed in the gas-phase at the Cis(d) B2PLYPD3/jun-cc-pVTZ level, which is significantly more reliable than TD-DFT with hybrid

TABLE 2 | Population per cent of the clusters within the excited state simulation of Conf. 1 and 2.

	Conf. 1	Conf. 2
noHB	58.04	65.01
HB-VS1	18.79	17.35
HB-VS2	21.58	16.9
twoHB	1.59	0.74

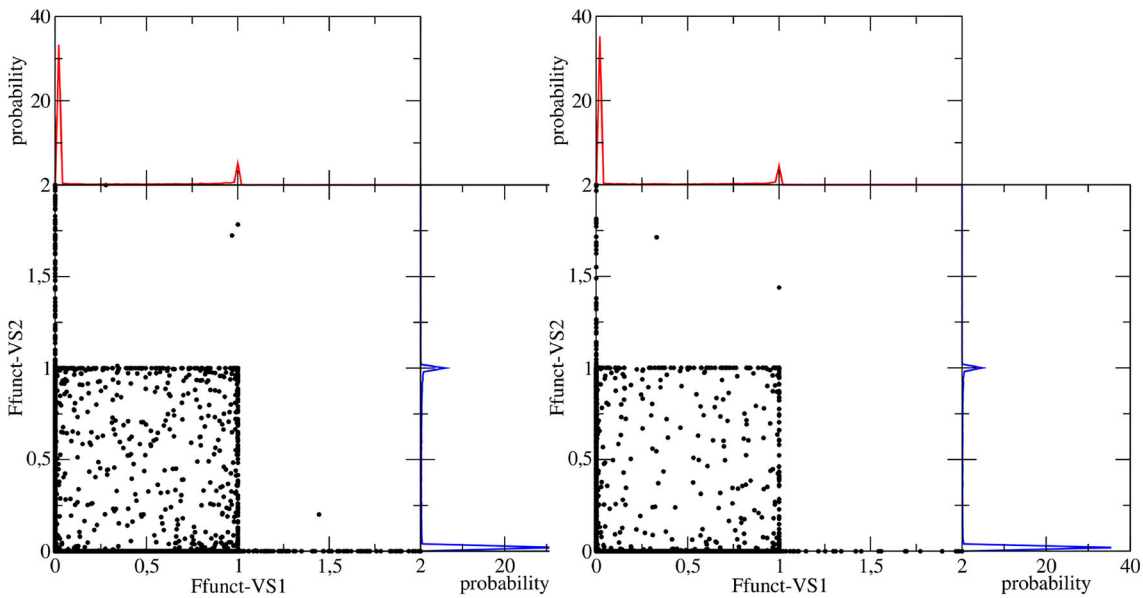

FIGURE 6 | Space defined by the values of the F function computed for the each VS in the camphor molecule. Left and right panels correspond to Conf. 1 and Conf. 2, respectively. In each panel the corresponding probability distributions of each F function are also shown.

functionals (Grimme and Neese, 2007; Jacquemin et al., 2009; Laurent and Jacquemin, 2013; Ottochian et al., 2020).

The first step was the simulation of the absorption spectra. The experimental results show an isolated well-defined band for both OPA and ECD spectra without any apparent vibronic sub-structure. According to Longhi et al. (2013), these results suggest a non-negligible interaction with the solvent molecules. In **Figure 7**, the electronic absorption spectra obtained at the ONIOM/EE-PMM level are reported. Indeed, the four clusters lead to quite different spectra both in terms of energy and intensity, thus contributing to the overall asymmetric shape of both OPA and ECD spectra (see **Figure S3** for unweighted cluster spectra). Vibrational modulation effects bring an additional contribution to the final spectra and the corresponding results

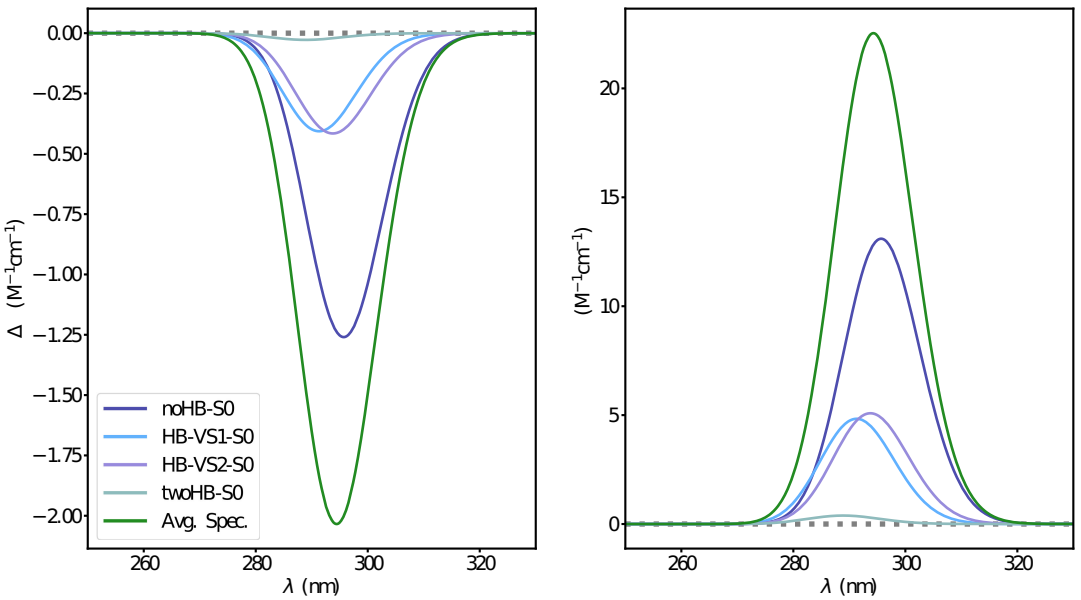

FIGURE 7 | Electronic ECD **(left)** and OPA **(right)** spectra of camphor in methanol obtained through the ONIOM/EE-PMM method. The different contributions from each cluster are shown.

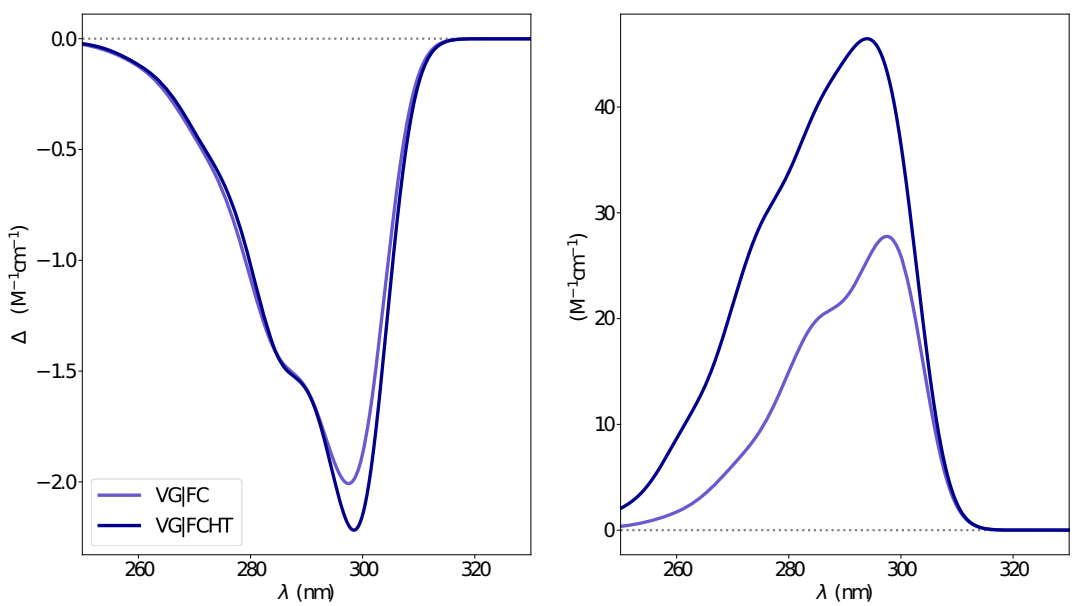

FIGURE 8 | Vibronic ECD **(left)** and OPA **(right)** spectra of camphor in methanol as obtained through VG|FC and VG|FCHT computational procedures in conjunction with PCM model to treat the environment effect.

including bulk solvent effect by mean of the PCM are reported in **Figure 8**. It is noteworthy that HT terms smooth the prominence of the first band and, especially for the OPA spectrum, cause a non-negligible intensity gain. Finally, as reported in **Figure 9**, a proper account of specific solvent effects by means of the overall ONIOM/EE-PMM procedure modulates the HT contributions and, in turn, improves the overall agreement with the experimental spectrum, as already observed in the case of the related camphorquinone molecule (Del Galdo et al., 2020).

After having tuned the procedure on absorption spectra we analyzed the corresponding emission spectra. As discussed in section 3.1, the excited electronic state must be described in terms of two disjoint conformers, whose relative stability is a key parameter in the reproduction of the overall spectra. Relying

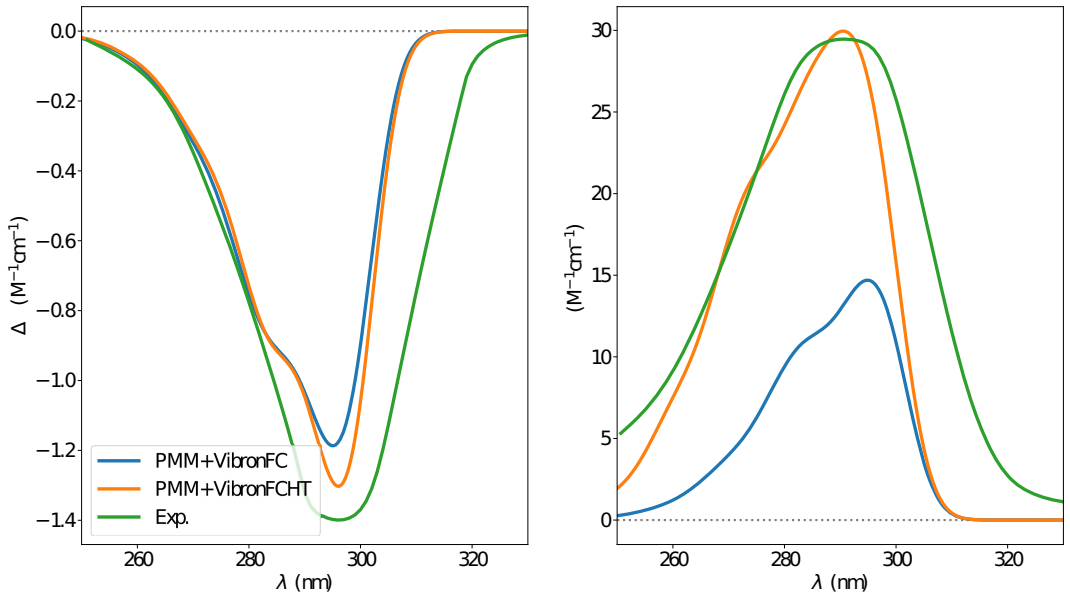

FIGURE 9 | ECD **(left)** and OPA **(right)** spectra of camphor in methanol as obtained by combining the ONIOM/EE-PMM procedure outcome with VG|FC (blue line) and VG|FCHT (orange line) models to simulate the vibronic coupling, the corresponding experimental spectrum is also reported (green line). Experimental spectra taken from Longhi et al. (2016).

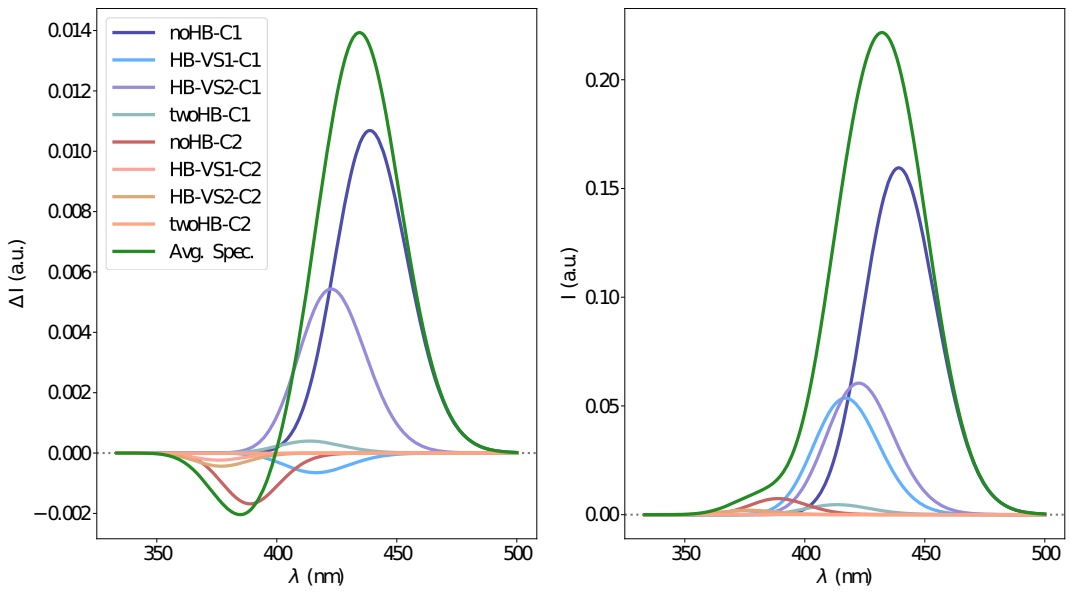

FIGURE 10 | Electronic CPL **(left)** and OPE **(right)** spectra of camphor in methanol obtained through the ONIOM/EE-PMM method. The different contributions from each cluster for each excited state simulations are shown.

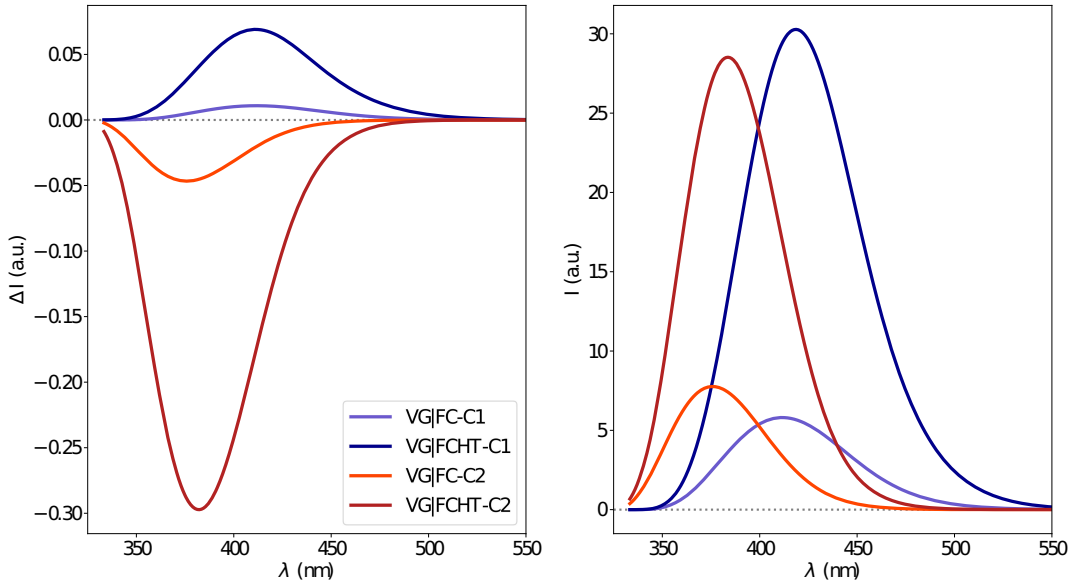

FIGURE 11 | Vibronic CPL **(left)** and OPE **(right)** spectra of camphor in methanol as obtained through VG|FC and VG|FCHT computational procedures in conjunction with PCM model to treat the environment effect.

on previous investigations (Barone et al., 2015; Fusè et al., 2019; Paoloni et al., 2020), we employed in this case the B2PLYP-D3 level of theory also accounting for bulk solvent effects by means of the PCM approximation. The results are reported in **Table 1**, and ΔG PCM values were used to compute Boltzmann population at 300 K in order to get the final simulated spectra.

The electronic emission spectra obtained through application of the ONIOM/EE-PMM method are reported in **Figure 10**. The differential contributions of both camphor conformers and, for each of them, of the different clusters, are clearly shown. In particular, the presence of different numbers of solute-solvent H-bonds led to quite asymmetrical spectra since these interactions shift the spectrum toward higher energies. On the other hand, the equilibrium between the two main solute conformers is responsible for the inversion of the sign of the transition. In fact, already at the ONIOM/EE-PMM level the bisignate nature of the CPL is well-reproduced. This clearly highlights the relevance of both proper sampling of the solvent distribution and proper weighting of conformer populations. Similarly to the absorption case, the HT term substantially affects the transition intensity. In **Figure 11**, the OPE and CPL vibronic spectra are reported. It is quite apparent that the CPL intensity of the less populated conformer is higher than that of the prevailing one and it partially compensates the lower population at 300 K. The result of combining vibronic and ONIOM/EE-PMM contributions in the emission spectra is shown in **Figure 12**. The results are in good agreement with the experimental ones, and it is worth recalling at this point that the full computational procedure does not involve any empirical correction. Moreover, it should be noted that the original CPL spectra from the work of Longhi et al. (2013) are quite noisy (the authors claimed that for both absorption and emission solute-solvent interactions are responsible for the quenching of the vibronic features) and the structure of the experimental CPL signal in **Figure 12** is probably due to digitization artifacts. Comparison of the simulated spectra with their experimental counterparts shows that the OPE band-shape is well reproduced by our approach, whereas the agreement is only fair for the CPL spectrum. One of the possible limitations of our computational protocol is the approximate VG vibronic model, which could be too rough to catch and accurately describe the contribution of the vibration on the spectra. Although more refined models could possibly lead to more accurate results, our integrated approach is capable to improve the final results of both ONIOM/EE-PMM and vibronic models taken individually, providing a simulated CPL spectrum significantly closer to the experimental one without any huge increase of the computational cost.

4. CONCLUSIONS

The main aim of the present contribution was the development of a cheap yet accurate multi-scale strategy for the study of solvatochromic shifts of medium-size flexible chromophores in condensed phases. Explicit treatment of a large amplitude motion and clustering of different MD simulations for each stationary point along the LAM allow the extension of our previous approach from semi-rigid to flexible molecules. At the same time, fitting of atomic charges for excited electronic states permits their MD simulation and the following computation of emission spectra. As a test case, we have chosen a flexible system characterized by remarkable chiroptical properties (namely, the camphor dye in methanol solution), which requires, inter alia, the challenging reproduction of significantly different ECD and CPL spectra. The computational strategy starts from the collection of transition energies and

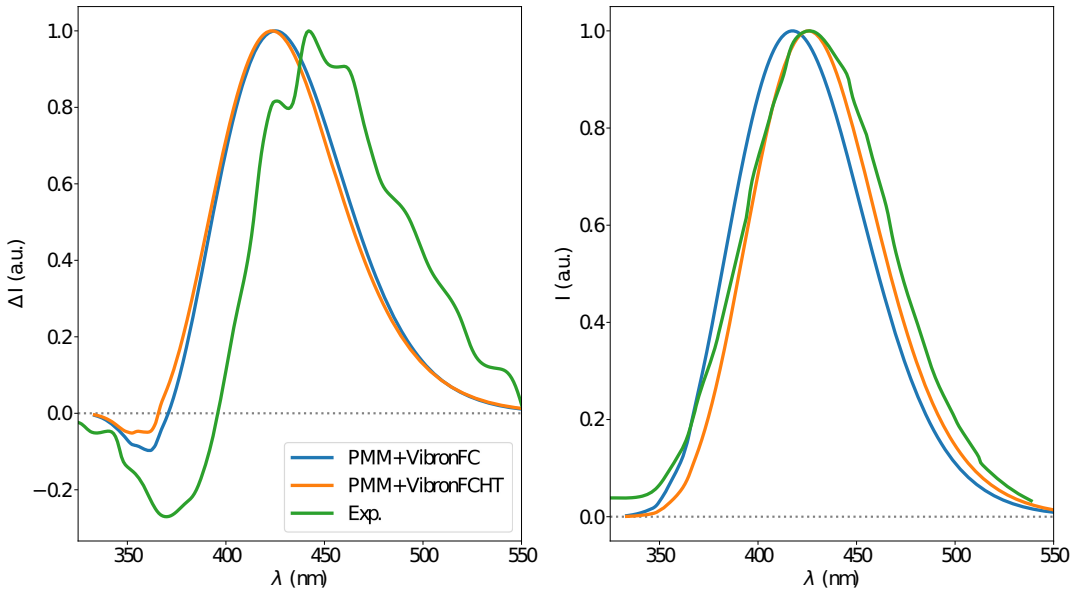

FIGURE 12 | CPL **(left)** and OPE **(right)** spectra of camphor in methanol as obtained by combining the ONIOM/EE-PMM procedure outcome with VG|FC (blue line) and VG|FCHT (orange line) models to simulate the vibronic coupling, the corresponding experimental spectrum is also reported (green line). Experimental spectra taken from Longhi et al. (2016).

dipole moments tuned by environmental effects provided by MD simulations. Next, vibrational modulation effects on the different electronic transitions are taken into account by a fully quantum mechanical approach including Franck-Condon and Herzberg-Teller contributions together with bulk solvent effects described by a polarizable continuum model. At variance with previous applications, a large amplitude motion has been explicitly considered by means of a discrete-variational approach. Specific chromophore-environment interactions and their fluctuations are described by a recently proposed hybrid procedure, which combines a variational approach (ONIOM/EE), with the PMM perturbative approach. In this way, it becomes possible to obtain accurate results without the need to perform explicit computations for a statistically significant number of solute-solvent configurations. For each stationary point of this flexible system (i.e., the two energy minima of the S1 electronic state and the transition state ruling their inter-conversion corresponding to the single minimum of the ground electronic state) we partitioned the overall simulations into four subsets (clusters) related to the presence or not of strong solute-solvent hydrogen bonds. Although the flexibility of the system increases the number of explicit QM computations with respect to semi-rigid chromophores, the proposed ONIOM/EE-PMM approach strongly reduces the computational effort with respect to a standard QM/MM computation. The good agreement between all the computational results and their experimental counterparts, gives confidence about the robustness and reliability of the overall procedure and permits the analysis of the role of different contributions (stereo-electronic, dynamic, environmental) in tuning the overall spectra.

DATA AVAILABILITY STATEMENT

The original contributions presented in the study are included in the article/**Supplementary Material**, further inquiries can be directed to the corresponding authors.

AUTHOR CONTRIBUTIONS

All authors listed have made a substantial, direct and intellectual contribution to the work, and approved it for publication.

FUNDING

This work has been supported by the Italian MIUR (PRIN 2017, project Physico-chemical Heuristic Approaches: Nanoscale Theory Of Molecular Spectroscopy, PHANTOMS), prot. 2017A4XRCA.

ACKNOWLEDGMENTS

The SMART@SNS Laboratory (http://smart.sns.it) is acknowledged for providing high- performance computer facilities. Prof. Julien Bloino and Dr. Andrea Salvadori are acknowledged for helpful discussions.

SUPPLEMENTARY MATERIAL

The Supplementary Material for this article can be found online at: https://www.frontiersin.org/articles/10.3389/fchem.2020.00584/full#supplementary-material

REFERENCES

Aschi, M., Spezia, R., Nola, A. D., and Amadei, A. (2001). A first-principles method to model perturbed electronic wavefunctions: the effect of an external homogeneous electric field. *Chem. Phys. Lett.* 344, 374–380. doi: 10.1016/S0009-2614(01)00638-8

Bačić, Z., and Light, J. C. (1989). Theoretical methods for rovibrational states of floppy molecules. *Annu. Rev. Phys. Chem.* 40, 469–498. doi: 10.1146/annurev.pc.40.100189.002345

Baiardi, A., Bloino, J., and Barone, V. (2015). Accurate simulation of resonance-Raman spectra of flexible molecules: An internal coordinates approach. *J. Chem. Theory Comput.* 11, 3267–3280. doi: 10.1021/acs.jctc.5b00241

Baiardi, A., Bloino, J., and Barone, V. (2016). General formulation of vibronic spectroscopy in internal coordinates. *J. Chem. Phys.* 144:084114. doi: 10.1063/1.4942165

Baiardi, A., Bloino, J., and Barone, V. (2017). Simulation of vibronic spectra of flexible systems: Hybrid DVR-harmonic approaches. *J. Chem. Theory Comput.* 13, 2804–2822. doi: 10.1021/acs.jctc.7b00236

Barone, V., Biczysko, M., Bloino, J., Cimino, P., Penocchio, E., and Puzzarini, C. (2015). CC/DFT route toward accurate structures and spectroscopic features for observed and elusive conformers of flexible molecules: pyruvic acid as a case study. *J. Chem. Theory Comput.* 11, 4342–4363. doi: 10.1021/acs.jctc.5b00580

Barone, V., Bloino, J., Biczysko, M., and Santoro, F. (2009). Fully integrated approach to compute vibrationally resolved optical spectra: from small molecules to macrosystems. *J. Chem. Theory Comput.* 5, 540–554. doi: 10.1021/ct8004744

Becke, A. D. (1988). Density-functional exchange-energy approximation with correct asymptotic behavior. *Phys. Rev. A* 38, 3098–3100. doi: 10.1103/PhysRevA.38.3098

Berendsen, H., van der Spoel, D., and van Druned, R. (1995). GROMACS: a message-passing parallel molecular dynamics implementation. *Comput. Phys. Commun.* 91, 43–56. doi: 10.1016/0010-4655(95)00042-E

Bloino, J., Baiardi, A., and Biczysko, M. (2016). Aiming at an accurate prediction of vibrational and electronic spectra for medium-to-large molecules: an overview. *Int. J. Quant. Chem.* 116, 1543–1574. doi: 10.1002/qua.25188

Bloino, J., Biczysko, M., and Barone, V. (2012). General perturbative approach for spectroscopy, thermodynamics, and kinetics: methodological background and benchmark studies. *J. Chem. Theory Comput.* 8, 1015–1036. doi: 10.1021/ct200814m

Bloino, J., Biczysko, M., Santoro, F., and Barone, V. (2010). General approach to compute vibrationally resolved one-photon electronic spectra. *J. Chem. Theory Comput.* 6, 1256–1274. doi: 10.1021/ct9006772

Bussi, G., Donadio, D., and Parrinello, M. (2007). Canonical sampling through velocity rescaling. *J. Chem. Phys.* 126:014101. doi: 10.1063/1.2408420

Cappelli, C., Bloino, J., Lipparini, F., and Barone, V. (2012). Toward *ab initio* anharmonic vibrational circular dichroism spectra in the condensed phase. *J. Phys. Chem. Lett.* 3, 1766–1773. doi: 10.1021/jz3006139

Cerezo, J., Mazzeo, G., Longhi, G., Abbate, S., and Santoro, F. (2016). Quantum-classical calculation of vibronic spectra along a reaction path: the case of the ECD of easily interconvertible conformers with opposite chiral responses. *J. Phys. Chem. Lett.* 7, 4891–4897. doi: 10.1021/acs.jpclett.6b02484

Chung, L. W., Sameera, W. M. C., Ramozzi, R., Page, A. J., Hatanaka, M., Petrova, G. P., et al. (2015). The ONIOM method and its applications. *Chem. Rev.* 115, 5678–5796. doi: 10.1021/cr5004419

Colbert, D. T., and Miller, W. H. (1992). A novel discrete variable representation for quantum mechanical reactive scattering via the S-matrix Kohn method. *J. Chem. Phys.* 96, 1982–1991. doi: 10.1063/1.462100

Dapprich, S., Komaromi, I., Byun, K., Morokuma, K., and Frisch, M. J. (1999). A new ONIOM implementation in Gaussian98. Part I. the calculation of energies, gradients, vibrational frequencies and electric field derivatives. *J. Mol. Struct. Theochem.* 461–462:1–21. doi: 10.1016/S0166-1280(98)00475-8

Darden, T., Tork, D., and Pedersen, L. (1997). Particle mesh Ewald: an n-log(n) method for Ewald sums in large systems. *J. Comput. Chem.* 18, 1463–1472.

Dekkers, H. P. J. M., and Closs, L. E. (1976). The optical activity of low-symmetry ketones in absorption and emission. *J. Am. Chem. Soc.* 98, 2210–2219. doi: 10.1021/ja00424a034

Del Galdo, S., Chandramouli, B., Mancini, G., and Barone, V. (2019). Assessment of multi-scale approaches for computing UV-VIS spectra in condensed phases: toward an effective yet reliable integration of variational and perturbative QM/MM approaches. *J. Chem. Theory Comput.* 15, 3170–3184. doi: 10.1021/acs.jctc.9b00120

Del Galdo, S., Fusè, M., and Barone, V. (2020). The ONIOM/PMM model for effective yet accurate simulation of optical and chiroptical spectra in solution: camphorquinone in methanol as a case study. *J. Chem. Theory Comput.* 16, 3294–3306. doi: 10.1021/acs.jctc.0c00124

Del Galdo, S., Mancini, G., Daidone, I., Zanetti Polzi, L., Amadei, A., and Barone, V. (2018). Tyrosine absorption spectroscopy: backbone protonation effects on the side chain electronic properties. *J. Comput. Chem.* 39, 1747–1756. doi: 10.1002/jcc.25351

Dunning, T. H. (1989). Gaussian basis sets for use in correlated molecular calculations. I. the atoms boron through neon and hydrogen. *J. Chem. Phys.* 90, 1007–1023. doi: 10.1063/1.456153

Duong, S. T., and Fujiki, M. (2017). The origin of bisignate circularly polarized luminescence (CPL) spectra from chiral polymer aggregates and molecular camphor: anti-Kasha's rule revealed by CPL excitation (CPLE) spectra. *Polym. Chem.* 8, 4673–4679. doi: 10.1039/C7PY00958E

Frisch, M. J., Trucks, G. W., Schlegel, H. B., Scuseria, G. E., Robb, M. A., Cheeseman, J. R., et al. (2019). *Gaussian Development Version, Revision J.02*. Wallingford, CT: Gaussian, Inc.

Fusè, M., Mazzeo, G., Longhi, G., Abbate, S., Masi, M., Evidente, A., et al. (2019). Unbiased determination of absolute configurations by vis-à-vis comparison of experimental and simulated spectra: the challenging case of diplopyrone. *J. Phys. Chem. B* 123, 9230–9237. doi: 10.1021/acs.jpcb.9b08375

Goodwin, R. D. (1987). Methanol thermodynamic properties from 176 to 673 k at pressures to 700 bar. *J. Phys. Chem. Ref. Data* 16, 799–892. doi: 10.1063/1.555786

Grimme, S., Ehrlich, S., and Goerigk, L. (2011). Effect of the damping function in dispersion corrected density functional theory. *J. Comput. Chem.* 32, 1456–1465. doi: 10.1002/jcc.21759

Grimme, S., and Neese, F. (2007). Double-hybrid density functional theory for excited electronic states of molecules. *J. Chem. Phys.* 127:154116. doi: 10.1063/1.2772854

Hess, B., Bekker, H., Berendsen, H. J. C., and Fraaije., J. G. E. M. (1997). LINCS: a linear constraint solver for molecular simulations. *J. Comput. Chem.* 18, 1463–1472. doi: 10.1002/(SICI)1096-987X(199709)18:12<1463::AID-JCC4>3.0.CO;2-H

Jacquemin, D., Wathelet, V., Perpete, E. A., and Adamo, C. (2009). Extensive TD-DFT benchmark: singlet-excited states of organic molecules. *J. Chem. Theory Comput.* 5, 2420–2435. doi: 10.1021/ct900298e

Jorgensen, W. L., Maxwell, D. S., and Tirado-Rives, J. (1996). Development and testing of the OPLS all-atom force field on conformational energetics and properties of organic liquids. *J. Am. Chem. Soc.* 118, 11225–11236. doi: 10.1021/ja9621760

Kasha, M. (1950). Characterization of electronic transitions in complex molecules. *Discuss. Faraday Soc.* 9, 14–19. doi: 10.1039/df9500900014

Laurent, A. D., and Jacquemin, D. (2013). TD-DFT benchmarks: a review. *Int. J. Quant. Chem.* 113, 2019–2039. doi: 10.1002/qua.24438

Lazzari, F., Salvadori, A., Mancini, G., and Barone, V. (2020). Molecular perception for visualization and computation: the proxima library. *J. Chem. Inf. Model.* 60, 2668–2672. doi: 10.1021/acs.jcim.0c00076

Lee, C., Yang, W., and Parr, R. G. (1988). Development of the colle-salvetti correlation-energy formula into a functional of the electron density. *Phys. Rev. B* 37, 785–789. doi: 10.1103/PhysRevB.37.785

Light, J. C., and Carrington, T. Jr. (2000). "Chapter 4: Discrete-variable representations and their utilization," in *Advances in Chemical Physics, Vol. 114* (New York, NY: John Wiley & Sons, Ltd), 263–310. doi: 10.1002/9780470141731.ch4

Light, J. C., Hamilton, I. P., and Lill, J. V. (1985). Generalized discrete variable approximation in quantum mechanics. *J. Chem. Phys.* 82, 1400–1409. doi: 10.1063/1.448462

Longhi, G., Castiglioni, E., Abbate, S., Lebon, F., and Lightner, D. A. (2013). Experimental and calculated CPL spectra and related spectroscopic data of camphor and other simple chiral bicyclic ketones. *Chirality* 25, 589–599. doi: 10.1002/chir.22176

Longhi, G., Castiglioni, E., Koshoubu, J., Mazzeo, G., and Abbate, S. (2016). Circularly polarized luminescence: a review of experimental and theoretical aspects. *Chirality* 28, 696–707. doi: 10.1002/chir.22647

Macchiagodena, M., Mancini, G., Pagliai, M., and Barone, V. (2016). Accurate prediction of bulk properties in hydrogen bonded liquids: amides as case studies. *Phys. Chem. Chem. Phys.* 18, 25342–25354. doi: 10.1039/C6CP04666E

Marenich, A. V., Jerome, S. V., Cramer, C. J., and Truhlar, D. G. (2012). Charge model 5: an extension of hirshfeld population analysis for the accurate description of molecular interactions in gaseous and condensed phases. *J. Chem. Theory Comput*. 8, 527–541. doi: 10.1021/ct200866d

McAlexander, H. R., and Crawford, T. D. (2015). Simulation of circularly polarized luminescence spectra using coupled cluster theory. *J. Chem. Phys.* 142:154101. doi: 10.1063/1.4917521

Mennucci, B. (2012). Polarizable continuum model. *WIREs Comput. Mol. Sci*. 2, 386–404. doi: 10.1002/wcms.1086

Ottochian, A., Morgillo, C., Ciofini, I., Frisch, M. J., Scalmani, G., and Adamo, C. (2020). Double hybrids and time-dependent density functional theory: an implementation and benchmark on charge transfer excited states. *J. Comput. Chem*. 41, 1242–1251. doi: 10.1002/jcc.26170

Pagliai, M., Raugei, S., Cardini, G., and Schettino, V. (2003). Hydrogen bond dynamics in liquid methanol. *J. Chem. Phys*. 119:6655. doi: 10.1063/1.1605093

Paoloni, L., Mazzeo, G., Longhi, G., Abbate, S., Fusè, M., Bloino, J., et al. (2020). Toward fully unsupervised anharmonic computations complementing experiment for robust and reliable assignment and interpretation of IR and VCD spectra from mid-IR to NIR: the case of 2,3-butanediol and trans-1,2-cyclohexanediol. *J. Phys. Chem. A* 124, 1011–1024. doi: 10.1021/acs.jpca.9b11025

Papajak, E., Zheng, J., Xu, X., Leverentz, H. R., and Truhlar, D. G. (2011). Perspectives on basis sets beautiful: Seasonal plantings of diffuse basis functions. *J. Chem. Theory Comput*. 7, 3027–3034. doi: 10.1021/ct200106a

Pritchard, B., and Autschbach, J. (2010). Calculation of the vibrationally resolved, circularly polarized luminescence of D–camphorquinone and (S,S)–trans–β–hydrindanone. *ChemPhysChem* 11, 2409–2415. doi: 10.1002/cphc.201000054

Riehl, J. P., and Muller, G. (2012). "Chapter 3: Circularly polarized luminescence spectroscopy and emission-detected circular dichroism," in *Comprehensive Chiroptical Spectroscopy: Instrumentation, Methodologies, and Theoretical Simulations, Vol. 1* (New York, NY: John Wiley & Sons, Ltd.), 65–90. doi: 10.1002/9781118120187.ch3

Salvadori, A., Del Frate, G., Pagliai, M., Mancini, G., and Barone, V. (2016). Immersive virtual reality in computational chemistry: applications to the analysis of QM and MM data. *Int. J. Quantum Chem*. 116, 1731–1746. doi: 10.1002/qua.25207

Schippers, P. H., Van der Ploeg, J. P. M., and Dekkers, H. P. J. M. (1983). Circular polarization in the fluorescence of $\beta\gamma$ -enones: distortion in the $1n\pi^\star$ state. *J. Am. Chem. Soc*. 105, 84–89. doi: 10.1021/ja00339a015

Stendardo, E., Avila Ferrer, F., Santoro, F., and Improta, R. (2012). Vibrationally resolved absorption and emission spectra of dithiophene in the gas phase and in solution by first-principle quantum mechanical calculations. *J. Chem. Theory Comput*. 8, 4483–4493. doi: 10.1021/ct300664d

Tanaka, H., Inoue, Y., and Mori, T. (2018). Circularly polarized luminescence and circular dichroisms in small organic molecules: correlation between excitation and emission dissymmetry factors. *ChemPhotoChem* 2, 386–402. doi: 10.1002/cptc.201800015

Vreven, T., Byun, K. S., Komáromi, I., Dapprich, S., Montgomery, J. A. Jr., Morokuma, K., et al. (2006). Combining quantum mechanics methods with molecular mechanics methods in ONIOM. *J. Chem. Theory Comput*. 2, 815–826. doi: 10.1021/ct050289g

Yanai, T., Tew, D. P., and Handy, N. C. (2004). A new hybrid exchange-correlation functional using the coulomb-attenuating method (CAM-B3LYP). *Chem. Phys. Lett*. 393, 51–57. doi: 10.1016/j.cplett.2004.06.011

Zanetti-Polzi, L., Del Galdo, S., Daidone, I., D'Abramo, M., Barone, V., Aschi, M., et al. (2018). Extending the perturbed matrix method beyond the dipolar approximation: comparison of different levels of theory. *Phys. Chem. Chem. Phys*. 20, 24369–24378. doi: 10.1039/C8CP04190C

Conflict of Interest: The authors declare that the research was conducted in the absence of any commercial or financial relationships that could be construed as a potential conflict of interest.

The reviewer LE declared a past co-authorship with one of the authors VB to the handling editor.

frontiers in Chemistry

REVIEW
published: 28 July 2020
doi: 10.3389/fchem.2020.00555

Beyond Chiral Organic (p-Block) Chromophores for Circularly Polarized Luminescence: The Success of d-Block and f-Block Chiral Complexes

Benjamin Doistau†, Juan-Ramón Jiménez*† and Claude Piguet*

Department of Inorganic and Analytical Chemistry, University of Geneva, Geneva, Switzerland

OPEN ACCESS

Edited by:
Giovanna Longhi,
University of Brescia, Italy

Reviewed by:
Dong Chen,
Zhejiang University, China
Lorenzo Di Bari,
University of Pisa, Italy

***Correspondence:**
Benjamin Doistau
Benjamin.Doistau@unige.ch
Juan-Ramón Jiménez
Juan.JimenezGallego@unige.ch

†These authors have contributed equally to this work

Specialty section:
This article was submitted to Physical Chemistry and Chemical Physics, a section of the journal Frontiers in Chemistry

Received: *04 March 2020*
Accepted: *29 May 2020*
Published: *28 July 2020*

Citation:
Doistau B, Jiménez J-R and Piguet C (2020) Beyond Chiral Organic (p-Block) Chromophores for Circularly Polarized Luminescence: The Success of d-Block and f-Block Chiral Complexes. Front. Chem. 8:555. doi: 10.3389/fchem.2020.00555

Chiral molecules are essential for the development of advanced technological applications in spintronic and photonic. The best systems should produce large circularly polarized luminescence (CPL) as estimated by their dissymmetry factor (g_{lum}), which can reach the maximum values of $-2 \leq g_{lum} \leq 2$ when either pure right- or left-handed polarized light is emitted after standard excitation. For matching this requirement, theoretical considerations indicate that optical transitions with large magnetic and weak electric transition dipole moments represent the holy grail of CPL. Because of their detrimental strong and allowed electric dipole transitions, popular chiral emissive organic molecules display generally moderate dissymmetry factors ($10^{-5} \leq g_{lum} \leq 10^{-3}$). However, recent efforts in this field show that g_{lum} can be significantly enhanced when the chiral organic activators are part of chiral supramolecular assemblies or of liquid crystalline materials. At the other extreme, chiral Eu^{III}- and Sm^{III}-based complexes, which possess intra-shell parity-forbidden electric but allowed magnetic dipole transitions, have yielded the largest dissymmetry factor reported so far with $g_{lum} \sim 1.38$. Consequently, 4f-based metal complexes with strong CPL are currently the best candidates for potential technological applications. They however suffer from the need for highly pure samples and from considerable production costs. In this context, chiral earth-abundant and cheap d-block metal complexes benefit from a renewed interest according that their CPL signal can be optimized despite the larger covalency displayed by d-block cations compared with 4f-block analogs. This essay thus aims at providing a minimum overview of the theoretical aspects rationalizing circularly polarized luminescence and their exploitation for the design of chiral emissive metal complexes with strong CPL. Beyond the corroboration that f–f transitions are ideal candidates for generating large dissymmetry factors, a special attention is focused on the recent attempts to use chiral Cr^{III}-based complexes that reach values of g_{lum} up to 0.2. This could pave the way for replacing high-cost rare earths with cheap transition metals for CPL applications.

Keywords: circularly polarized luminescence (CPL), coordination complexes, lanthanides, chromium(III), dissymmetry factor

INTRODUCTION

Chirality has raised human interest probably because of its ubiquity in nature (Barron, 2008), which originates from stereoselective reactions affording proteins, DNA, or more generally natural compounds (Mori, 2011). Chemists have then invested major efforts and energy to reproduce the nature efficiency with the artificial preparation of a plethora of chiral molecules and structures, such as curved aromatics (Rickhaus et al., 2017; Dhbaibi et al., 2019), coordination compounds (Knof and von Zelewsky, 1999; Seeber et al., 2006; Crassous, 2009, 2012), polyoxometalates (Hasenknopf et al., 2008), topologically complex architectures (Chambron et al., 1993; Jamieson et al., 2018), self-assembled systems (Mateos-Timoneda et al., 2004; Hembury et al., 2008; Liu et al., 2015), dynamics motors, and shuttles, to name a few (Leigh and Pérez, 2006; Feringa, 2007; Kudernac et al., 2011; van Leeuwen et al., 2017). In optics, the appeal for chiral systems is justified by their ability to rotate the plane of polarized light, a phenomenon that was discovered by the French scientist Jean-Baptiste Biot in collaboration with Jean-François Persoz in 1812. Subsequently, the physicist Aimé Cotton discovered the optical rotatory dispersion in 1895 and highlighted that chiral molecules displayed different absorption coefficients for right- and left-handed circularly polarized light, the amplitudes of which depend on the light wavelengths (Cotton effect). The latter feature gave birth to circular dichroism (CD) spectroscopy (Beychok, 1968; Schellman, 1975; Woody, 1995). The CD technique was extensively used to study the conformation and the configuration of enantiopure organic compounds (Berova et al., 2007; Pescitelli et al., 2011) and permitted to analyze the chirality and helicity of sophisticated supramolecular self-assembled architectures in solution (Pescitelli et al., 2014). Similarly to CD, which is based on the selective absorption of circularly polarized photons, some emissive chiral compounds may display a difference in intensity between right- and left-handed circularly polarized emitted light upon excitation with non-polarized light (Richardson, 1979; Riehl and Richardson, 1986; Riehl and Muller, 2004; Zinna and Di Bari, 2015; Longhi et al., 2016). The first circularly polarized luminescence (CPL) emission was observed in 1948 by Samoilov for a sodium uranyl acetate crystal. In 1960, Oosterhof reported the first CPL measurement in solution for an organic compound, namely, trans-b-hydrindanone, and for a coordination complex $[Cr(en)_3]^{3+}$ where en stands for ethylenediamine (Emeis and Oosterhoff, 1967). Several decades later, the development of CPL was promoted by the need for chiroptical features in versatile technological fields (Wu et al., 2015; Brandt et al., 2017), such as optoelectronics (Han et al., 2018), nanomaterials (Sang et al., 2019), chiral molecular conductors (Réthoré et al., 2005), magnetochiral devices (Rikken and Raupach, 1997; Train et al., 2011), chiral molecular switches (Feringa et al., 2000; Browne and Feringa, 2011; Isla and Crassous, 2016; Isla et al., 2016), macrostructure solvers (Roose et al., 2016), unidirectional motion controllers (Huck et al., 1996), semiconductor transistors (Yang et al., 2013), and CP-OLEDs (Gilot et al., 2010; Zinna et al., 2017).

PHYSICAL BASIS OF CPL AND STRATEGIES TO ACHIEVE STRONG CPL EMISSION

The development of CPL techniques required a quantificative parameter for comparing the amount of circularly polarized light emitted by a specific chromophore, the latter factor being independent of the non-polarized photophysical features. The dissymmetry factor g_{lum} ($-2 < g_{lum} < 2$) was thus set as the ratio between the difference of left and right circularly polarized emission and the global emitted intensity (Equation 1). Although this value is defined for each wavelength of the CPL spectrum, it is usually reported for the maximum intensity of the emission band.

$$g_{lum} = \frac{\Delta I}{\frac{1}{2}I} = \frac{I_L - I_R}{\frac{1}{2}(I_L + I_R)} \quad (1)$$

The time-dependent intensity difference of emitted light ΔI depends on the orientation of molecules regarding the selected polarization of the emitted light. Moreover, the excitation process is affected as well by molecule orientation since the transition probability depends on the relative orientation of the molecule transition dipole moment with respect to the incident electric field (Riehl and Muller, 2004). Consequently, working with crystals, solid samples, or more generally anisotropic media requires the explicit consideration of anisotropy in theoretical models. For matters of simplicity, the following review is restricted (i) to studies performed in isotropic media (solution) and (ii) to molecules showing excited-state lifetime one order of magnitude longer than their rotational correlation time, in order to allow relaxation to randomize the orientations of the molecules after selection of some preferential orientations upon excitation (Riehl and Muller, 2004). At room temperature, this latter criterion is fulfilled for excited-state lifetimes longer than 10 ns for molecules around 1 kD (Tóth et al., 1996).

The amplitude of the CPL signal for a $i \rightarrow j$ transition is governed by its rotatory strength (R_{ij}), which represents the probability of emitting (or absorbing for CD) a circularly polarized photon. In an isotropic medium, R_{ij} can be expressed by Equation (2), where ψ_i and ψ_j are the wave functions of the initial and final states, respectively. $\widehat{\mu}$ and $\widehat{m}$ are the electric and magnetic perturbation Hamiltonians, while $\overrightarrow{\boldsymbol{\mu}_{ij}}$ and $\overrightarrow{\mathbf{m}_{ij}}$ are respectively the electric transition dipole moment (ED) and magnetic transition dipole moment (MD) and θ is the angle between those two latter vectors.

$$R_{ij} = -i \langle \psi_i | \widehat{\mu} | \psi_j \rangle \langle \psi_i | \widehat{m} | \psi_j \rangle = -i \, \overrightarrow{\boldsymbol{\mu}_{ij}} \cdot \overrightarrow{\mathbf{m}_{ij}} = \left| \overrightarrow{\boldsymbol{\mu}_{ij}} \right| \left| \overrightarrow{\mathbf{m}_{ij}} \right| \cos\theta \quad (2)$$

Any contribution arising from the coupling between the electric dipole (ED) and electric quadrupole (EQ) moments is neglected in the rotatory strength equation since the consideration of an isotropic medium implies the orientation average (Gendron et al., 2019). The comparison of CPL intensities of different compounds showing different quantum yields requires some normalization of the rotatory strength by the global emission contribution which is ruled by the dipole strength (D_{ij}) depicted in Equation (3), where

$\overrightarrow{\mathbf{Q_{ij}}}$ is the electric transition quadrupole moment (Gendron et al., 2019).

$$D_{ij} = \left|\overrightarrow{\boldsymbol{\mu}_{ij}}\right|^2 + \left|\overrightarrow{\mathbf{m}_{ij}}\right|^2 + \left|\overrightarrow{\mathbf{Q}_{ij}}\right|^2 \quad (3)$$

The electric transition quadrupole moment being several orders of magnitude weaker than its dipole counterpart, it is often negligible and will be omitted in the following. The dissymmetry factor can now be related to the theoretical features with Equation (4).

$$g_{lum} = \frac{4R_{ij}}{D_{ij}} = 4\frac{\left|\overrightarrow{\boldsymbol{\mu}_{ij}}\right|\left|\overrightarrow{\mathbf{m}_{ij}}\right|\cos\theta}{\left|\overrightarrow{\boldsymbol{\mu}_{ij}}\right|^2 + \left|\overrightarrow{\mathbf{m}_{ij}}\right|^2} \quad (4)$$

For organic chromophores involving parity-allowed ED- and MD-forbidden transitions, the contribution of the magnetic transition dipole moment is often neglected in the denominator ($\left|\overrightarrow{\boldsymbol{\mu}_{ij}}\right| >> \left|\overrightarrow{\mathbf{m}_{ij}}\right|$), and the dissymmetry factor reduces to $g_{lum} = 4\left(\left|\overrightarrow{\mathbf{m}_{ij}}\right|/\left|\overrightarrow{\boldsymbol{\mu}_{ij}}\right|\right)\cos\theta$. However, this latter equation is too restrictive and cannot be applied for magnetic dipole-allowed and electric dipole-forbidden transitions, such as those found in f–f transitions, for which the amplitude of magnetic transition dipole moment can overpass its electric counterpart (Metcalf and Richardson, 1994). The introduction of a ratio $r = \left|\overrightarrow{\boldsymbol{\mu}_{ij}}\right|/\left|\overrightarrow{\mathbf{m}_{ij}}\right|$ into Equation (4) permits its rewriting as Equation (5), which highlights that a maximum value of g_{lum} is reached when the electric and magnetic transition dipole moments are (i) colinear ($\theta = 0$ or 180°) and (ii) of the same amplitude ($\left|\overrightarrow{\boldsymbol{\mu}_{ij}}\right| = \left|\overrightarrow{\mathbf{m}_{ij}}\right|$; $r = 1$) (Wada et al., 2018). The latter criterion contrasts with the usual misleading statement saying that $\left|\overrightarrow{\mathbf{m}_{ij}}\right|$ should be maximized while $\left|\overrightarrow{\boldsymbol{\mu}_{ij}}\right|$ is minimized, a situation encountered for organic chromophores upon neglecting $\left|\overrightarrow{\mathbf{m}_{ij}}\right|$ at the denominator of Equation (4). Nevertheless, the weak magnitude of magnetic dipole compared to electric dipole transition moments ($\left|\overrightarrow{\boldsymbol{\mu}_{ij}}\right| = 10^6\left|\overrightarrow{\mathbf{m}_{ij}}\right|$) indicates the ED-forbidden/MD-allowed transitions are promising for equalizing both transition dipole moments.

$$g_{lum} = 4\frac{r}{r^2+1}\cos\theta \quad (5)$$

From a theoretical point of view, the organic chromophores thus appear to be not particularly promising for CPL. However, their low cost, their easy synthetic accessibility, and the chemical inertness of carbon chemistry bring substantial advantages which (i) allow chiral resolution, (ii) afford enantiomerically pure compounds, and (iii) provide easy processability for material applications. As a consequence, CPL was systematically recorded and explored for myriads of organic chromophores exploiting central, axial, planar, or helical chirality (Sánchez-Carnerero et al., 2015; Chen and Yan, 2018; Tanaka et al., 2018a) with record values for 1,8-naphthalimide ($|g_{lum}(450\,nm)| = 0.014$) (Sheng et al., 2016), oligothiophenes ($|g_{lum}(520\,nm)| = 0.0093$) (Benincori et al., 2018; Dhbaibi et al., 2019) cyclo-2,8-chrysenylene ($|g_{lum}(443\,nm)| = 0.152$) (Sato et al., 2017), and 1,1′-bitriphenylenes ($|g_{lum}(449\,nm)| = 0.032$) (Sawada et al., 2012). Planar and helical chiralities, as found in helicenes, were highlighted to promote important dissymmetry factors because of the larger magnetic transition dipole moments induced by aromatic distortion. Hence, important efforts were made to rationalize this observation with the calculation of $\left|\overrightarrow{\boldsymbol{\mu}_{ij}}\right|$ and $\left|\overrightarrow{\mathbf{m}_{ij}}\right|$ and the determination of the θ angle (Sato et al., 2017; Ito et al., 2018; Tanaka et al., 2018b,c). The outstanding $|g_{lum}|$ value of 0.152 reported for the single-wall carbon nanotubes (Dhbaibi et al., 2019) cyclo-2,8-chrysenylene by Isobe and Sato was attributed to the unusually important magnetic transition dipole moment originating from a cyclic aromatic structure which allows and facilitates a magnetic field-induced current loop (Sato et al., 2017). In addition, due to the circular shape of the molecule, the first individual singlet-state electric transition dipole moments of the four chromophoric moieties might result in some compensation effects, as stated by Anderson for achiral nanorings (Sprafke et al., 2011). Hence, the combination of peculiar MD strength and ED weakness provides a large g_{lum} value. Apart from this exceptional chiral single-wall carbon nanotube, the dissymmetry factors lie in the $10^{-5} - 10^{-2}$ range for most of organic compounds (Sánchez-Carnerero et al., 2015; Chen and Yan, 2018; Tanaka et al., 2018a).

Despite the chemical advantages of organic molecules for application in material sciences (easy synthetic access, low cost, easy incorporation into devices, and processability) (Yang et al., 2013; Brandt et al., 2017; Han et al., 2018; Sang et al., 2019), the need for important dissymmetry factors prompted chemists to look into d-block chemistry. In particular, the second- and third-row metal complexes have attracted important attention due to (i) the synthetic accessibility, (ii) the chemical inertness due to large ligand-field strengths, (iii) the processability, and (iv) some easy characterization by NMR techniques for common diamagnetic Ir^{III}, Pt^{II}, Ru^{II}, or Os^{II} complexes. In addition, the important covalency in those complexes produces highly emissive charge transfer states which are not quenched by d–d states located at much higher energies. However, the associated dissymmetry factors still cover the expected range for ED-allowed/MD-forbidden transitions (10^{-5}-10^{-2}) (Han et al., 2018).

It is worth noting here that significant enhancement of g_{lum} could be observed occasionally in nano-assemblies or in aggregated systems as a result of the formation of chiral microstructural materials or films (Geng et al., 2003; Kumar et al., 2015; Roose et al., 2016; Sang et al., 2019), in particular for few electroluminescent systems, such as OLEDs (Brandt et al., 2016; Song F. et al., 2018). In addition, the incorporation of emissive moieties into anisotropic media, such as chiral liquid crystals displaying helical macrostructures, proved to be an efficient strategy for the generation of strong CPL emission (Watanabe and Akagi, 2014; Goto, 2018; Gao et al., 2019; Kim et al., 2019; Li et al., 2019; Yang X. et al., 2019). Focusing on isotropic solutions, some recent up-converted CPL studies evidenced enhanced g_{lum} compared to their downshifted counterparts. This observation suggests that triplet–triplet annihilation could be an innovative and unexpected approach to increase the CPL emission of organic compounds showing weak g_{lum} (Han et al., 2017a; Yang D. et al., 2019; Yang X. et al., 2019).

Further optimization of the dissymmetry factors requires the operation of MD-allowed/ED-forbidden transitions in complexes showing little covalence to avoid the relaxation of the parity rules due to the mixing of metal and ligand wave functions. In this context, the lanthanide f–f transitions and the first-row d–d transitions, for which covalence is still reasonably weak, appear as promising candidates to generate important g_{lum}. The high potential of these coordination compounds led to extensive theoretical studies in order to tackle potential spectral/structure relationships (Richardson, 1979; Riehl and Richardson, 1986; Riehl and Muller, 2004). The most comprehensive model used for rationalizing the influence of stereogenic centers on the optical activity (CD or CPL) is referred to as the independent systems/perturbation model (ISP) (Mason, 1971; Richardson, 1971; Mason and Seal, 1975, 1976; Strickland and Richardson, 1976). According to this approach, the rotatory strength emerges from two distinct mechanisms: the static coupling (SC) and the dynamic coupling (DC). The rotary strength due to SC arises from the intrinsic chirality of the emissive center which is, in the case of the coordination complexes, restricted to the metal and the ligand donor atoms. Intrinsic chirality of the first coordination sphere is ensured, for instance, for a D_3 symmetric transition metal or for a lanthanide complex displaying a distorted square anti-prismatic geometry with an optimal computed twist angle of 22.5° (Carr et al., 2012; Zinna and Di Bari, 2015). If the chromophore (i.e., the coordination sphere) is achiral, while a stereogenic center is located on a remote site (i.e., a chiral ligand), the optical activity is driven by the DC mechanism. In this case, the optical activity of the metal center derives from a multipole (metal)–dipole (ligand) interaction between the emissive metal's transition density and the stereogenic center's induced dipole moment. This coupling provides a non-orthogonal contribution of the electric transition dipole moment with respect to its magnetic counterpart, the scalar product of which affords non-zero terms for the rotatory strength. When the DC mechanism is solely active, the CPL intensity mainly depends on the electrostatic quadripole–dipole interaction, which is optimized for (i) highly polarizable stereogenic centers, (ii) short metal–stereogenic center distance (the quadripole–dipole interaction distance decreases as $1/r^8$), and (iii) energy matching between the optical transitions of the aromatic stereogenic center and those centered on the metal (Richardson, 1979; Zinna and Di Bari, 2015). Although the intrinsic chirality of the metal coordination sphere (SC) might appear to neophyte as the best tool for maximizing g_{lum}, the DC mechanism appears to be very efficient and may provide considerable rotatory strength. To date, the record $g_{lum} = 1.38$ belongs to the $Cs[Eu(hfbc)_4]$ (hfbc = heptafluorobutyrylcamphorate) complex, in which an essentially achiral square anti-prismatic coordination sphere (twist angle of −41.4°) results in a weak SC contribution, whereas the location of a camphor unit on the bound ligand is responsible for the impressive dissymmetry factor via the DC mechanism (Lunkley et al., 2008, 2011; Zinna and Di Bari, 2015).

Nonetheless, harnessing the potential of lanthanide f–f or of first-row d–d transitions requires overcoming the kinetic lability of the associated complexes, which hampers enantiomeric separations and/or provides efficient racemization pathways. In a first attempt to exploit labile lanthanide complexes, a chiral ligand is simply used to induce solely a DC mechanism. Actually, this approach is at the origin of the record dissymmetry factor reported to date (Aspinall, 2002; Lunkley et al., 2008, 2011). An alternative strategy to generate enantiomerically pure systems takes advantage of chiral ligands for inducing stereoselectivity within the coordination process (Cantuel et al., 2004; Gregolinski et al., 2008; Kotova et al., 2013). In this latter case, both SC and DC mechanisms should be active. Finally, the selection of some (rare) inert coordination complexes followed by chiral resolution and separation may afford enantiomerically pure complexes. Inert lanthanides complexes can be obtained for polydentate ligands (i.e., cryptates, DOTA) (Gregolinski et al., 2008; Walton et al., 2011; Carr et al., 2012; Dai et al., 2019) or *via* the design of supramolecular assemblies, in which the lanthanide is sequestered within inert stoppers (Zare et al., 2017a). Although the first-row transition metals are known to produce labile complexes, the preparation of inert complexes is possible with Cr^{III} (d^3) or Co^{III} (low-spin d^6) metals which possess large ligand-field stabilization energies, and with small and highly charged Fe^{III} centers (Hilmes et al., 1977; Cantuel et al., 2004; Dee et al., 2019; Jiménez et al., 2019). When emissive states can be implemented, those latter cheap transition metal complexes should be good candidates to provide large dissymmetry factors after chiral resolution.

THE SUCCESS OF LANTHANIDE COMPLEXES USING CHIRAL ORGANIC LIGANDS AND (SUPRA)MOLECULAR CONTROL

Theoretical Aspects of f–f Transitions

The absorption and emission properties of Ln^{3+}-based complexes arise from the parity-forbidden and spin-forbidden metal-centered f–f transitions, the proscribed character of which can be relaxed by spin–orbit coupling and by crystal-field effects (see below). Consequently, these transitions have generally low but no negligible molar absorption coefficients ($<10\ M^{-1}\cdot cm^{-1}$) and limited radiative rate constants ($k_{rad} < 10^3\ s^{-1}$). This results in long-lived excited states that give extended emissions reaching up to 10 ms for Ln^{3+} doped in low-phonon materials but reduced by one to four orders in magnitudes in Ln^{3+}-based molecular complexes possessing high-energy oscillators. According to quantum mechanics, in the absence of spin–orbit coupling, any electronic wave functions can be separated into two independent contributions arising from the spin wave function and the orbital wave function. Since the interaction between an electromagnetic wave responsible for the electronic transition only involves the orbital wave function, the orthogonal and normalized character of the non-perturbated spin wave functions implies that an electronic transition between two states is only possible when the spin does not change ($\Delta S = 0$), a first condition known as the spin rule. The interaction between the electromagnetic wave and the orbital part of the electronic wave functions further implies that an electric-dipole-allowed

electronic transition between two states requires a parity change between the two incriminated orbital wave functions ($\Delta L = \pm 1, \pm 3\ldots$), a condition often referred to as Laporte's rule. However, magnetic dipole transitions are allowed in the absence of change in parity ($\Delta L = 0, \pm 2\ldots$). Accordingly, f–f transitions obeying the spin rule are electric dipole forbidden but magnetic dipole allowed. The considerable spin–orbit coupling constants which characterize the 4f-block series indeed mix orbital and spin wave functions so that the spin-selection rule ($\Delta S = 0$) is relaxed for 4f−4f transitions. Concerning the parity rules controlling the electronic transitions, two different situations have to be considered. For centrosymmetric systems, the electronic f–f transitions are electric-dipole (ED) forbidden by the Laporte selection rule, but some intensity can be gained through the operation of symmetry-allowed but weak magnetic-dipole (MD, oscillator strength 10^{-6}, **Table 1**) transitions and electric quadrupole (EQ, oscillator strength 10^{-10}, **Table 1**) transitions. In molecular complexes, minor vibronic coupling mechanisms cannot be completely ruled out. For non-centrosymmetric systems produced by weak static crystal-field effects, the Laporte rule is partially relaxed and the mixing of electronic configurations with opposite parity gives rise to the so-called Judd–Ofelt forced ED transitions, possessing oscillator strength in the order of 10^{-4} (note that allowed ED transitions have oscillator strengths in the 0.01–1 range) (Malta and Carlos, 2003; Tanner, 2013). Altogether, the original selection rules based on spin S and orbital L quantum numbers should be replaced with some looser versions of them, which rely on the total momentum J quantum number (**Table 1**, column 5). In this context, the f–f transitions with $\Delta J = 0, \pm 1$ (except $0 \leftrightarrow 0$) are MD allowed and can benefit from the large magnetic moments displayed by these ions. Consequently, the weak ED transition mechanisms do not always dominate the transition dipole moment, as it does in organic molecules and in the major part of d-block complexes. This can lead to large rotatory strengths comparable with the dipole strength, and in the context of CPL that can afford large dissymmetry factors, g_{lum} (Equation 4). For instance, the $^5D_0 \rightarrow {}^7F_1$ transition of Eu^{3+} is an example of an MD-allowed and ED-forbidden transition that leads to large g_{lum}, typically, $g_{lum} > 0.1$ (Harada et al., 2009; Dai et al., 2016; Neil et al., 2016; Uchida et al., 2016; Zercher and Hopkins, 2016; Kono et al., 2017; Leonzio et al., 2017). Exceptionally, the complex $Cs[Eu[(+)\text{-}(hfbc)_4]$ displays $g_{lum} = +1.38$ at 595 nm ($^5D_0 \rightarrow {}^7F_1$), which represents the highest dissymmetric factor reported to date (Lunkley et al., 2008). The emissive $^5D_0 \rightarrow {}^7F_2$ and $^5D_0 \rightarrow {}^7F_3$ transitions of the aforementioned complex that do not satisfy the MD selection rule indeed yield lower but still remarkable dissymmetry factors of >0.2. Surprisingly, the Sm^{3+}-based complexes possessing two MD-allowed $^4G_{5/2} \rightarrow {}^6H_{5/2}$ and $^4G_{5/2} \rightarrow {}^6H_{7/2}$ transitions have been considerably less exploited for CPL although the analog $Cs[Sm[(+)\text{-}(hfbc)_4]$ has been shown to produce large dissymmetry factors of +1.15 and −1.15 at 553 and 598 nm, respectively (Lunkley et al., 2011). Other chiral Sm^{3+} complexes have been also reported (Petoud et al., 2007; Kreidt et al., 2018; Cotter et al., 2019). Aside from Eu^{3+} and Sm^{3+}, other lanthanides ions, such as Nd^{3+}, Tb^{3+}, Dy^{3+}, and Yb^{3+} have been used in chiral complexes as optically active luminescence-polarized emitters, and they will be described in the following section (Maupin et al., 1998, 2000; Dickins et al., 1999; Morita et al., 2000; Petoud et al., 2007; Casanovas et al., 2017; Leonzio et al., 2017; Górecki et al., 2018; Zinna et al., 2019). Concerning the MD contribution to the total transition dipole moment in a f–f transition, Richardson classified those into types DI, DII, and DIII where DI is expected to exhibit the largest dissymmetric factor (e.g., $^5D_0 \rightarrow {}^7F_1$ in Eu^{3+}) and DII and DIII lower values, for instance, $^4G_{5/2} \rightarrow {}^6H_{5/2}$ and $^5D_4 \rightarrow {}^7F_5$ in Sm^{3+} and Tb^{3+}, respectively, which are type DII transitions (Richardson, 1980). With this in mind, the trivalent lanthanide Ln^{3+} ions gathered in **Figure 1** represent a straightforward choice, within the periodic table, to induce strong g_{lum} in molecular complexes and materials. However, several key requirements must be fulfilled in order to obtain efficient (high quantum yields) luminescent chiral complexes with a strong dissymmetry factor for realistic applications.

TABLE 1 | Selection rules for electronic transitions of lanthanides ions (Eliseeva and Bünzli, 2010; Tanner, 2013).

Type of transition	Parity	$\lvert\Delta S\rvert$	$\lvert\Delta L\rvert$	$\lvert\Delta J\rvert$	Order of magnitude of the oscillator strength
Electric dipole (ED)	Opposite	0	$\leq 1^a$	$\leq 1^b$	∼0.01–1
Judd forced ED	Same	0	$= 0, 1, 3, 5^{a,c}$ $= 2, 4, 6^{a,d}$	$= 0, 1, 3, 5^{b,c}$ $= 2, 4, 6^{b,d}$	$\sim 10^{-4}$
Magnetic dipole (MD)	Same	0	0	$\leq 1^b$	$\sim 10^{-6}$
Electric quadrupole (EQ)	Same	0	$\leq 2^e$	$\leq 2^f$	$\sim 10^{-10}$

[a] $L = 0 \leftrightarrow L' = 0$ are forbidden.
[b] $J = 0 \leftrightarrow J' = 0$ are forbidden.
[c] If J and $J' \neq 0$.
[d] If J or $J' = 0$.
[e] $L = 0 \leftrightarrow L' = 0, 1$ are forbidden.
[f] $J = 0 \leftrightarrow J' = 0, 1$ are forbidden.

Strategy for Achieving Highly Luminescent CPL Emission Using Ln^{3+}

A classical strategy to overcome the low molar absorptivity of f–f transitions relies on the coordination of trivalent lanthanides, Ln^{3+}, to an organic chromophore, which can act as an efficient antenna, when excited, followed by an energy transfer onto the close lanthanide metal ion. This mechanism results in an efficient population of the lanthanide excited states that can relax to the ground state *via* radiative (luminescence) or non-radiative pathways. Therefore, to prepare highly luminescent chiral Ln^{III}-based complexes, the following points should be kept in mind. (i) The organic chromophore should be able to harvest a considerable amount of energy by absorbing UV-Vis light and to efficiently transfer it onto the lanthanide-excited states. (ii) The ligand should favor high coordination numbers for protecting Ln^{III} from interactions with solvent molecules and subsequent non-radiative de-excitation pathways. (iii) The kinetic inertness

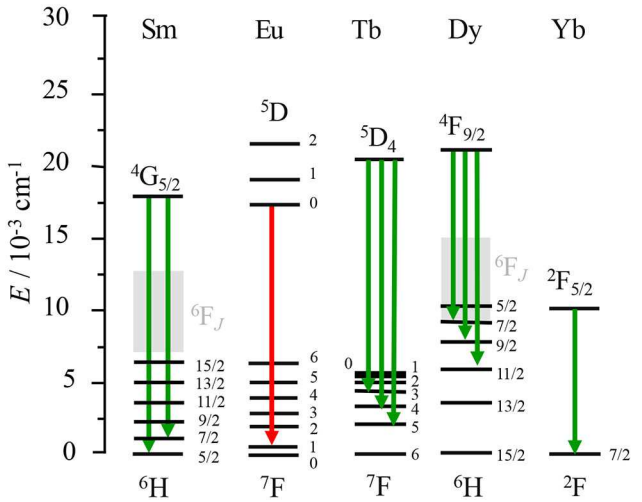

FIGURE 1 | Dieke diagram of the energy of the spectroscopic levels ($^{2S+1}L_J$) for some Ln^{3+}. Green arrows represent the magnetic dipole (MD)-allowed and electric dipole (ED)-allowed transitions whereas the red one represents the optimal case of an MD-allowed and ED-forbidden transition.

and thermodynamic stability of the resulting complex is of major importance since dissociation could lead to the formation of several luminescent species in solution and to a decrease in the luminescence intensity. (iv) The resulting complex should preferably not be fluxional or at least it should display a slow racemization rate constant compared to the time scale of the experiment (Metcalf et al., 1990). (v) Enantiopure species are desired in order to get unambiguous structure/property relationships and to induce maximum CPL performances. On the other hand, the chirality of lanthanide complexes may arise from (i) the helical twist of the ligands around the metal ions, (ii) the stereochemical orientation of the ligating arms of multidentate ligands, or (iii) the incorporation of stereocenters directly onto the ligand scaffold. As regards the first two options, the coordination of an achiral ligand (e.g., DPA = dipicolinic acid or tpy = terpyridine) to a lanthanide ion indeed produces the *Δ* or *M* (right-handed) and *Λ* or *P* (left-handed) isomers in racemic proportions. However, chiral resolution with the help of chromatographic techniques are quite challenging because of the kinetically fast interconversion (racemization) occurring between the two enantiomers (Kreidt et al., 2017). Therefore, the use of enantiopure chiral ligands (point iii, above) appeared to be the most promising strategy to prepare chiral lanthanide complexes, although the chiral induction of the Ln coordination sphere is not always quantitative and the associated stereoisomeric excess is only sporadically reported. In this context, Raymond and coworkers reported on a chiral octadentate ligand (**L1**) that strongly binds Ln^{3+} and protects it from interactions with solvent molecules (**Figure 2A**) (Petoud et al., 2007). The authors were able to prepare a family of luminescent complexes emitting in the visible range (Sm^{3+}, Eu^{3+}, Tb^{3+}, and Dy^{3+}) with modest to reasonable quantum yields (0.8–62%) and CPL activities. Remarkable dissymmetry factors could be measured for these complexes with $g_{lum}(Eu(\mathbf{L1})) = \pm 0.296(2)$ at 596 nm, $g_{lum}(Tb(\mathbf{L1})) = \pm 0.046(2)$ at 543 nm, $g_{lum}(Sm(\mathbf{L1})) = -0.027$ at 565 nm and −0.028 at 597 nm, and $g_{lum}(Dy(\mathbf{L1})) = 0.013$ at 669 nm. It is worth noting that this contribution reported on the first chiral Sm^{3+} complex showing CPL activity. From a more application-oriented point of view, Parker and coworkers provided numerous examples of versatile macrocycles (e.g., cyclen and triazacyclononane) bearing different coordinating side arms decorated with N-donors, amides, phosphinates, and carboxylate groups that are able to both complex and sensitize lanthanide ions for ultimate biomolecule sensing. Chirality elements can be introduced within the ring or within the side arms of these versatile scaffolds (**L2** and **L3** in **Figure 2A**).

These nitrogen-containing macrocycles served as starting materials for the synthesis of a huge number of Ln^{3+} complexes with remarkable thermodynamic stabilities and kinetic inertness. The most famous is probably 1,4,7,10-tetraazacyclododecane-1,4,7,10-tetraacetic acid (DOTA) (**Figure 2A**, **L2**) which usually gives nine-coordinated complexes when one additional water molecule is bound to the lanthanide (Parker et al., 2002). However, lanthanide complexes based on DOTA derivatives exist as four dynamically interconvertible stereoisomers which can be best described as two enantiomeric pairs (Aime et al., 1999). This has an unfavorable effect on the CPL performance. The introduction of chiral substituents into the cyclen ring and/or into the pendant arms of the DOTA derivative drives the formation of one stereoisomer over the others (Dickins et al., 1997, 1999; Ranganathan et al., 2002; Woods et al., 2003). This is of crucial importance for controlling the degree of local helicity and the associated dissymmetry factor (Carr et al., 2012; Dai et al., 2019). These complexes have been widely used as CPL probes for sensing small molecules and proteins thanks to the great sensitivity of the CPL signals of Tb^{3+}, Eu^{3+}, Dy^{3+}, Yb^{3+}, and Nd^{3+} to conformational and structural modifications (Beeby et al., 2000). Dissymmetry factors $|g_{lum}|$ around 0.5 correspond to the largest values reported for Eu^{3+} and Tb^{3+} chiral DOTA-based complexes. Triazonane-based europium complexes based on **L3** (**Figure 2A**) and **L3** derivatives are powerful tools for anion sensing (Neil et al., 2016). It is worth noticing that **L3** in its tautomeric form (tautomery between P–OH and P=O) is achiral, but it becomes a persistent stereochemical element when coordinated to a metal. In fact, Parker's group prepared a family of highly emissive Eu complexes, the chiroptical properties of which could be induced upon addition of chiral anions. Furthermore, the same authors exploited this property for the analysis of enantiomeric purity. Other complexes with interesting chiroptical properties have been reported, and most of them belong to the family of β-diketonate ligands. These bidentate anionic ligands are efficient to coordinate Ln^{3+} because of both the oxophilicity of Ln^{3+} and the electrostatic attraction between the cationic Ln^{3+} and the anionic ligands. Furthermore, β-diketonates are good sensitizers for inducing Ln^{3+} emission since they possess strong $\pi \rightarrow \pi^*$ transitions usually located in the UV region. The introduction of different substituents at the 1 or 3 position allows some energy tuning of the ligand triplet state of the antenna effect but also of the crystal field splitting affecting the $^{2S+1}L_J$

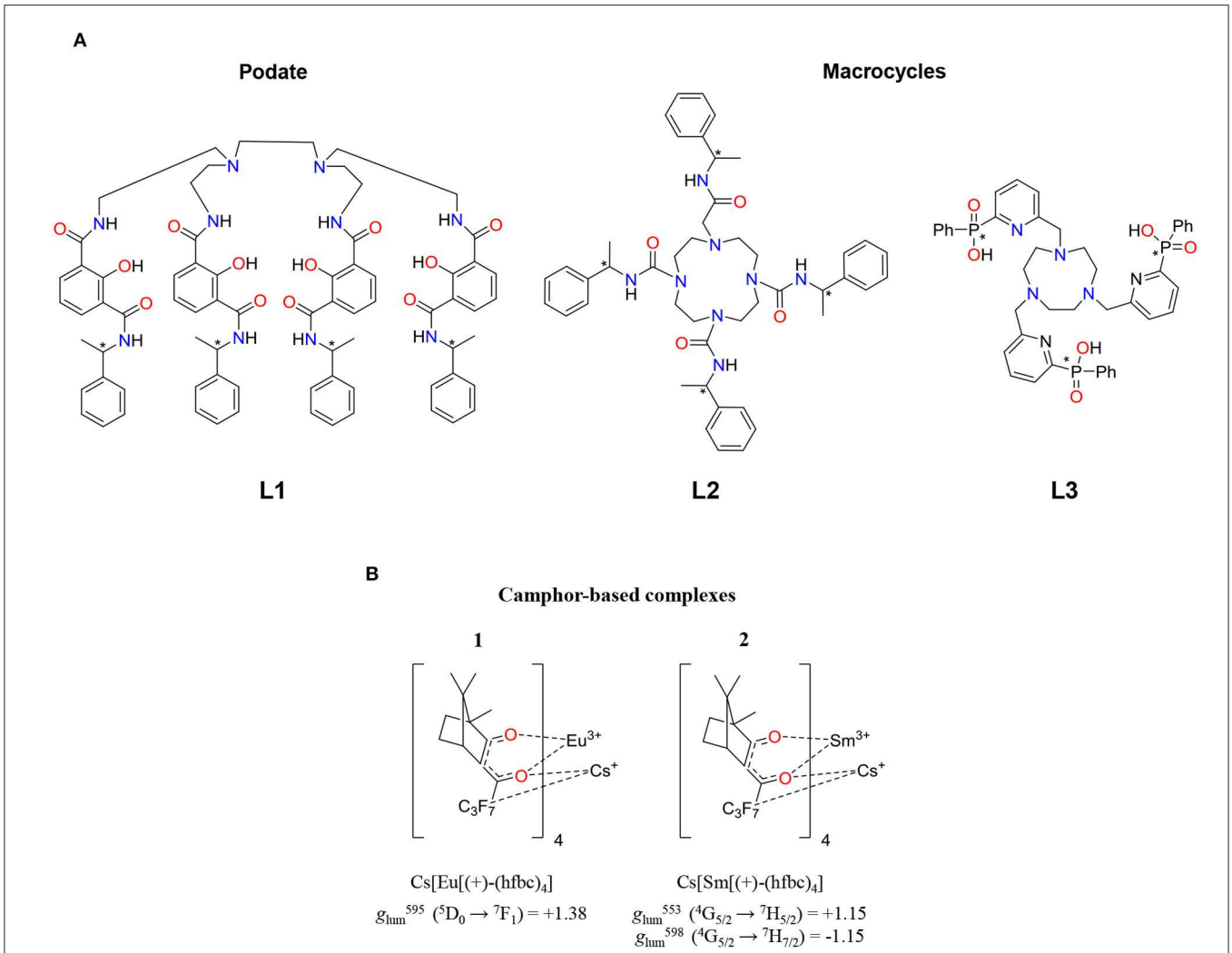

FIGURE 2 | (A) Structure of the podate ligand (L1) reported by Raymond and coworkers for the preparation of chiral Sm, Eu, Tb, and Dy complexes. Macrocycle-based cyclen (L2) and triazacyclononane (L3) used by Parker and coworkers for the preparation of chiral lanthanide-based CPL probes (Parker et al., 2002; Petoud et al., 2007; Neil et al., 2016). **(B)** Isostructural Eu^{3+} and Sm^{3+} complexes, Cs[Ln((+)-hfbc)$_4$] (Ln = Eu^{3+} or Sm^{3+}), and their corresponding record g_{lum} values associated with their MD-allowed transitions.

terms of the coordinated lanthanide complexes (Gálico et al., 2019). Taking advantage of the versatility of β-diketonate ligands, chiral derivatives can be easily prepared using cheap enantiopure ketones. Hence, the Eu^{3+} and Sm^{3+} complexes based on the hfbc ligand [hfbc = (+)-3-heptafluorobutylyrylcamphorato, **Figure 2B**] were straightforwardly prepared. They gave rise to extraordinary chiroptical properties affording the highest g_{lum} reported to date (+1.38 at 595 nm for the Eu^{3+} derivative). This value exceeds the previous record of −0.78 at 588 nm found for a similar camphor-based ligand, Cs[Eu((-)-facam)$_4$] where facam is 3-trifluoroacetyl-d-camphorato (Riehl and Richardson, 1986; Riehl and Muller, 2004). In its pivotal work, Muller and coworkers examined the CPL properties of M^I[Eu((+)-hfbc)$_4$] complexes (M^I = Cs and Na) in $CHCl_3$ and EtOH. They found that the magnitude of $|g_{lum}|$ is affected by the size of the alkali counter-ion and, to a less extend, by the nature of the solvent. In going from Cs^+ to Na^+, $|g_{lum}|$ drops to 0.15, a 9-fold reduction compared to 1.38 found for the Cs^+ derivative. This difference has been associated with a decrease in the degree of helical twist and hence of the chiral environment of the complex, upon reducing the size of the interacting alkali cation (Lunkley et al., 2011). Last but not least, a solvent dependence was also observed in going from $CHCl_3$ to EtOH, thus giving rise to lower dissymmetry factors of +1.32 and +0.06 at 595 nm for the Cs^+ and Na^+ derivatives. Subsequently, Di Bari and coworkers pointed out the crucial role played by the centered β-diketonane $\pi \rightarrow \pi^*$ transitions on the dynamic coupling mechanism (DC) operating in these complexes (Di Pietro and Di Bari, 2012). Alternatively, the combination of achiral β-diketonate antenna, including acetylacetonate (acac) or hexafluoracetylacetonate (hfac), with commercially available chiral tridentate ligands, such as 2,6-bis[(4R)-4-phenyl-2-oxazolinyl]pyridine (**L6**, Ph-Pybox)

or analogous **L5** (iPr-Pybox) and **L7** (Me-Ph-Pybox) represents an efficient approach for preparing enantiopure heteroleptic chiral trivalent lanthanides with high emission properties and interesting CPL properties (**Figure 3**, top) (Górecki et al., 2018). For instance, by changing the nature of the ancillary ligand in going from [Eu(**L5**)(hfbc)$_3$] to [Eu(**L7**)(hfbc)$_3$] (**Figure 3**, bottom), g_{lum} remains similar. However, the replacement of the chiral β-diketonate co-ligand (facam) with achiral acac in [Eu(**L6**)(acac)$_3$] resulted in a considerable drop in magnitude of the dissymmetry factor (**Figure 3**, bottom). This points out empirically the importance of having a large amount of chiral centers around the Ln^{3+} coordination environment for enhancing the dissymmetry factor. By replacing Eu^{3+} with Yb^{3+}, Di Bari and coworkers obtained [Yb(**L5**)(tta)$_3$] and [Yb(**L6**)(tta)$_3$] (tta = thenoyltrifluoroacetone), for which $|g_{lum}|$ values of 0.019 and 0.029 could be recorded for the $^2F_{7/2} \rightarrow {}^2F_{5/2}$ transition (Zinna et al., 2019), one of the rare examples of the NIR-CPL signal reported up to date.

Axial chiral ligands, such as (*R*/*S*)-2,2′-bis(diphenylphosphoryl)-1,1′-binaphthyl (BINAPO) have been also proven to be appropriate for inducing CPL (Harada et al., 2009; Liu et al., 2018; Cotter et al., 2019). Chiral terpyridine (tpy) ligands allowed Muller and coworkers to prepare helical complexes (Ln = Eu^{3+} and Tb^{3+}) which showed poor quantum yields (4% and 0.022%) and moderate g_{lum} of 0.028 and 0.020 for Eu^{3+} and Tb^{3+}, respectively (Muller et al., 2002). Along this line, the same authors used enantiopure dipicolinic acid-based ligands, which produce helical arrangements around the metal center mirroring those previously described for tpy-based complex ligands (Golesorkhi et al., 2018). At this occasion, they observed a considerable improvement of the chiroptical properties by measuring a g_{lum} of −0.18 for the Eu^{3+} derivative (Bonsall et al., 2007). Other important works using dipicolinic acid-based ligands have been reported, some of them leading to supramolecular structures (Leonard et al., 2007; Lincheneau et al., 2011; Kitchen et al., 2012; Bradberry et al., 2015; Zhang G. et al., 2015).

So far, we have focused our analysis on small chiral complexes, but more sophisticated structures, such as helicates, cages, or wheels showing interesting CPL properties have also been reported (**Figure 4**). For instance, Piguet and coworkers prepared the first enantiomerically pure inert nonadentate receptor [Cr(**L9**)$_3$]$^{3+}$ (Cantuel et al., 2004). Its complexation to Ln^{3+} generates the triple-stranded helicates [LnCr(**L9**)$_3$]$^{6+}$ (e.g., Ln = Eu, Tb), the CPL spectrum of which revealed a dual polarized emission for [EuCr(**L9**)$_3$]$^{6+}$ arising from the spin–flip $Cr^{III}(^2E \rightarrow {}^4A_2)$ transition with $|g_{lum}| = 0.01$ at 744 nm and from the $Eu^{III}(^5D_0 \rightarrow {}^7F_1)$ transition with $|g_{lum}| = 0.16$ at 594 nm. Due to the quantitative intramolecular Tb → Cr energy transfer, [TbCr(**L9**)$_3$]$^{6+}$ showed exclusively the polarized emission of Cr^{3+} with a g_{lum} value identical to that observed for the Eu derivative. Mamula et al. were able to prepare a trinuclear Eu_3(**L10**)$_2$ array through a diastereoselective assembly process harnessing the so-called chiral cooperativity approach and using an enantiopure bipyridine-carboxylate ligand (**L10,** $|g_{lum}| = 0.16$ for the $Eu(^5D_0 \rightarrow {}^7F_1)$ transition) (Mamula et al., 2005). Similarly, Gunnlaugsson and coworkers prepared the [Eu_2(**L8**)$_3$]$^{6+}$ triple-stranded helicate by self-assembly of enantiomerically pure **L8** and $Eu(CF_3SO_3)_3$ salts (Stomeo et al., 2009). CPL measurements showed a large g_{lum} of −0.23 at 593 nm corresponding to the magnetic allowed $^5D_0 \rightarrow {}^7F_1$ transition. Mazzanti and coworkers prepared a chiral heptanuclear Eu^{3+} wheel using the dissymmetric tetradentate ligand **L11** (Bozoklu et al., 2012). This system showed a reasonable quantum yield of 27% with a $|g_{lum}|$ of 0.1 for the $^5D_0 \rightarrow {}^7F_1$ transition. Other assemblies, such as tetrahedral and cubic cages, triangles, wheels, and clusters have been also reported, most of them based on Eu^{3+} with $|g_{lum}|$ ranging from 0.04 to 0.20 (Mamula et al., 2006; Tang et al., 2009; Yan et al., 2015; Li X.-Z. et al., 2017; Yeung et al., 2017; Bing et al., 2018; Zhou et al., 2019).

Although far to be comprehensive, the selected contributions commented above represent important and illustrative results in the field of lanthanide's CPL. The usual strategy to prepare chiral Ln^{3+}-based complexes deals with the introduction of stereogenic centers in the ligand skeleton that itself should (i) act as an efficient antenna for inducing the lanthanide emission and (ii) provide a DC mechanism for inducing considerable CPL. Thus, chiral Eu^{3+}, Tb^{3+}, and Sm^{3+} complexes have been largely exploited and they are now well-recognized for having strong CPL in the visible range whereas Yb^{3+} and Nd^{3+} centers have also been proven to show remarkable CPL emission in the NIR. This has led to the preparation of a plethora of optically active complexes with reasonable quantum yields. Despite the many examples reported to date, the relationship between the structure of the complex and the value of g_{lum}, which is of fundamental importance for molecular programming, remains challenging. This weakness mainly relies on the difficulties of performing theoretical CPL studies accessible to synthetic coordination chemists (Gendron et al., 2019). The potential applications of CPL arising from chiral Ln^{3+} systems is of considerable importance in biology and biochemistry because they have shown to be very sensitive to small changes in the molecular structure which can be detected as a change in the CPL emission. Therefore, they can be used as molecular probe for amino acid, anion, and biomolecule sensing. However, the high cost owed to the difficult purification of lanthanides and the theoretical complications associated with the operation of intermediate to strong spin–orbit coupling are non-negligible limitations for applications. Therefore, alternatives regarding the replacement of the optically active lanthanide center with transition metals might be of interest. Furthermore, the chemical lability of most of lanthanide complexes (apart from cryptates or anionic multidentate podates) is a severe drawback that usually prevents chiral resolution.

SECOND- AND THIRD-ROW TRANSITION METAL COMPLEXES FOR CPL

The 4d and 5d metal complexes benefit from their kinetic inertness, which allows their stereoisomeric separation, purification, and easy incorporation into devices. Those chemical advantages are supplemented by the strong and

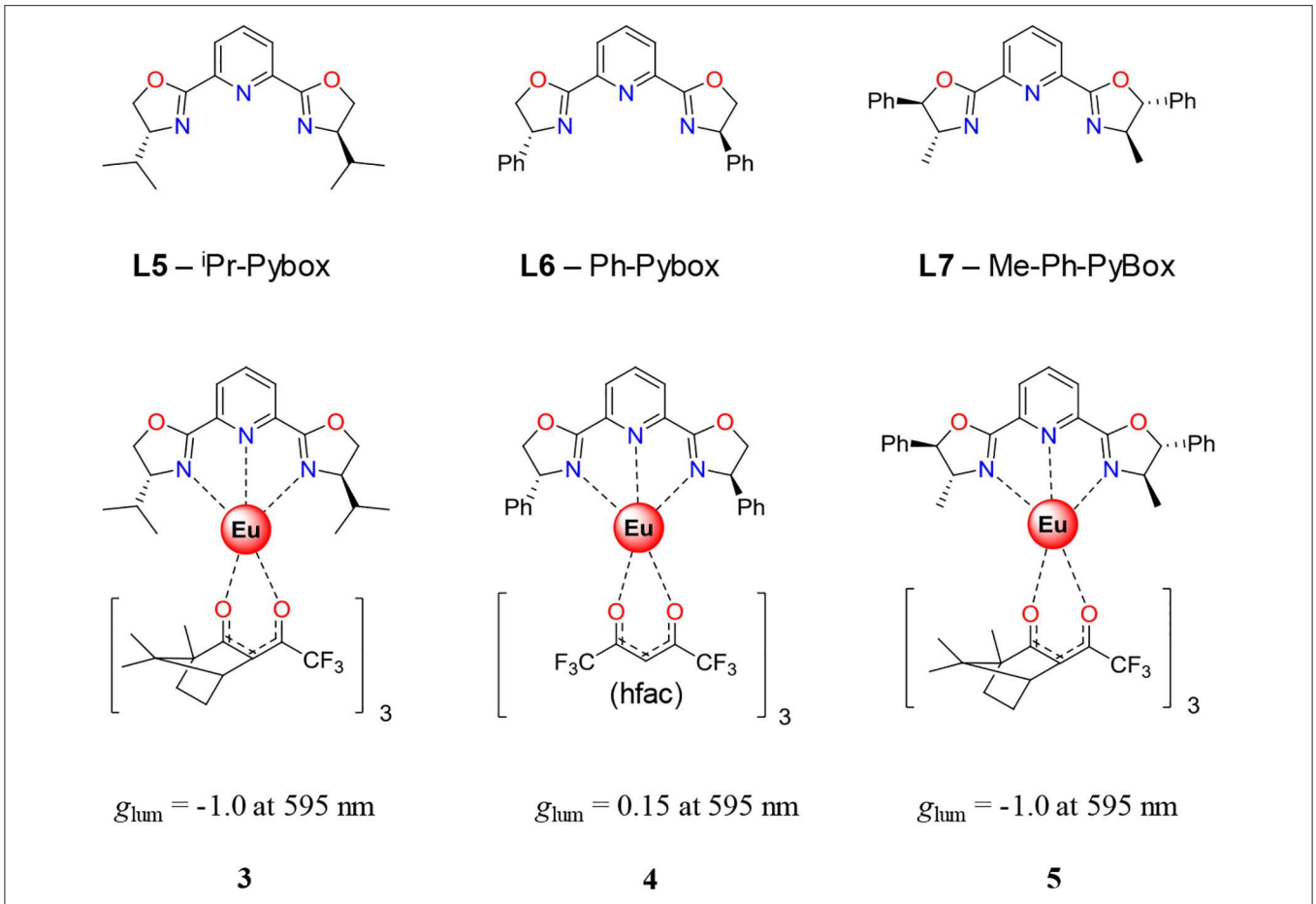

FIGURE 3 | (Top) Widely used enantiomerically pure ligand (L5, L6, and L7) used for the preparation of (bottom) chiral lanthanide complexes with the corresponding g_{lum} associated with the $Eu^{III}(^5D_0 \rightarrow {}^7F_1)$ transition.

tunable emission properties covering the visible part of the electromagnetic spectrum with sometimes impressive quantum yields, which are important advantages for modern applications (i.e., OLED or bio-probes) (Guerchais and Fillaut, 2011; Zhou et al., 2011). The efficient emission from the ^{3}LC or ^{3}MLCT transitions is due to the strong ligand field of complexes holding large metal ions and showing important covalence. In particular, the low spin d^6 (Ru^{II}, Os^{II}, Rh^{III}, Ir^{III}) or d^8 (Pt^{II}) configurations in octahedral and square planar geometries, respectively, promote the ^{3}MC quencher levels to high energy, which prevents ^{3}LC/^{3}MLCT→^{3}MC energy transfers (**Figure 5**). Increasing the emission quantum yield is thus indebted to the ligand field increase, a concept often harnessed to generate more efficient Ru^{II} emitters.

Among the d^6 metals, the strong-field and chiral emissive Ir^{III} cyclometallated complexes cover the visible spectral range and have been thus widely used as CPL emitters (Han et al., 2018). This important feature together with their appealing total luminescence properties have opened new perspectives for life science applications (Caporale and Massi, 2018), bio-imaging (Lo et al., 2011), electroluminescence (Kapturkiewicz, 2016), phototherapy (Zamora et al., 2018), and OLEDs (Zhou et al., 2011). The emission of the Ir^{III} cyclometallated complexes arised from a ^{3}LC/^{3}MLCT manifold displaying excited states lifetimes around 50 and 5 μs, respectively (Flamigni et al., 2007). Harnessing the Ir^{III} emission for CPL requires chiral complexes, and apart from a sole example of a chiral complex $[Ir(N^C^N')(C^N)X]$ ($X^- = Cl^-$ or CN^-) holding a tridentate, a bidentate, and a monodentate ligand, the enantiomers of which were separated by chiral HPLC ($g_{lum} = 4 \times 10^{-3}$) (Ashizawa et al., 2009), the chiral environments of Ir^{III} complexes were mainly produced with the help of pseudo-octahedral ter-bidentate environments leading to Δ/Λ stereoisomers in the $[Ir(X^X)_3]^{n+}$ complexes. Moreover, the use of unsymmetrical cyclometalated ligands in ter-bidentate $[Ir(X^Y)_3]^{n+}$ complexes induces the potential formation of *fac*/*mer* configurational isomers (**Figure 6A**); a synthetic issue that could be partially overcome thanks to the so-called *trans* effect since *mer* and *fac* isomers can be quantitatively formed, respectively at low (meridional conformation, kinetic product) and high temperatures (facial isomer, thermodynamic product) (Tamayo et al., 2003). The formation of heteroleptic

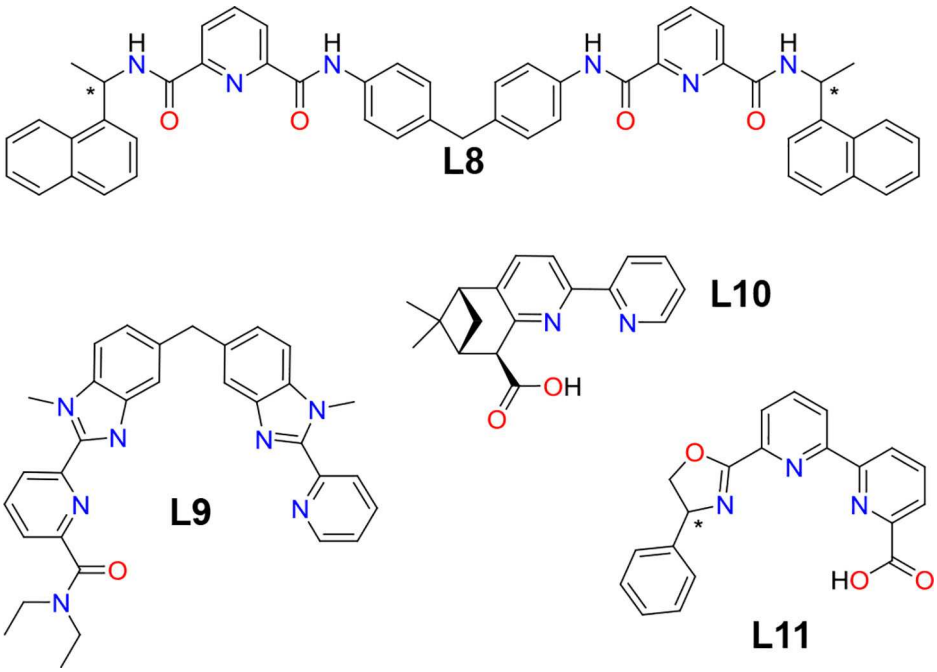

FIGURE 4 | Multidentate ligands L8, L9, L10, and L11 that have been used for the preparation of chiral supramolecular assemblies, such as helicates (L8 and L9), trinuclear assemblies (L10), and wheels (L11) mainly by complexation to Eu^{3+}.

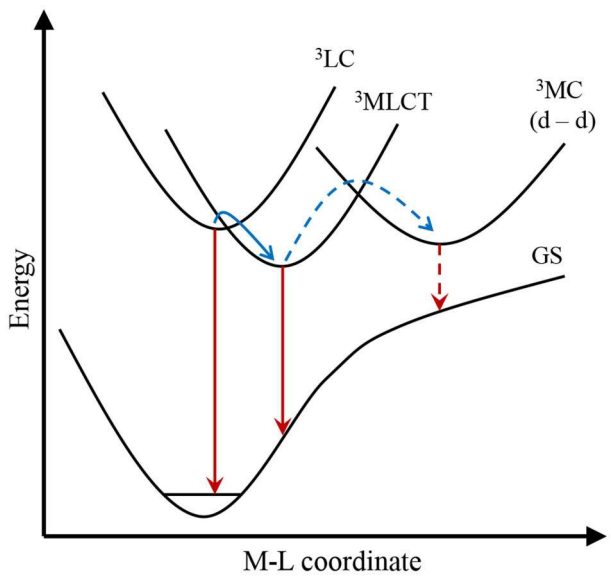

FIGURE 5 | Energy diagram established for a d^6 second- or third-row transition metal complex showing relaxation processes from triplet states via emission (red arrows) and energy transfer (blue arrows). The manifold ^{3}LC/^{3}MLCT emission and conversion are highlighted with plain arrows, whereas the potential quenching by the ^{3}MC state is shown with dashed arrows.

complexes $[Ir(C^\wedge N)_2(X^\wedge Y)]^{n+}$ further increases the number of available isomers (**Figure 6B**). Owing to the easy access to the intermediates $[Ir(C^\wedge N)_2Cl_2]^-$ or $[(Ir(C^\wedge N)_2Cl)_2]$ showing N–Ir–N *trans* configuration (**Figure 6C**), all heteroleptic Ir^{III} complexes of $[Ir(C^\wedge N)_2(X^\wedge Y)]^{n+}$ type reported to date for CPL investigations have been designed to possess a N–Ir–N *trans* configuration in order to avoid mixture of isomers.

In order to obtain enantiopure ter-bidentate Ir^{III} complexes for CPL, a first strategy relies on a unique source of chirality induced by the metal taken as the stereogenic center and using achiral bidentate ligands. Such method produces a pair of helical enantiomers as a racemate which should be further resolved by chiral HPLC. The latter separation technique was successfully achieved for simple mixtures of *fac*/*mer*-$[Ir(ppy)_3]$ (**6**) (ppy = 2-phenylpyridine) complexes to give *mer*-Λ-$[Ir(ppy)_3]$, *mer*-Δ-$[Ir(ppy)_3]$, *fac*-Λ-$[Ir(ppy)_3]$, and *fac*-Δ-$[Ir(ppy)_3]$ (Li et al., 2015), as well as for the more sophisticated complex **7** (**Figure 7A**) (Coughlin et al., 2008). Interestingly, the dissymmetry factor of *fac*-**6** is one order of magnitude superior to its *mer* counterpart, which might explain the popularity of *fac* isomers in CPL.

The previously introduced synthetic method for preparing $[Ir(C^\wedge N)_2(X^\wedge Y)]^{n+}$ afforded some heteroleptic complexes holding different achiral ligands (**Figure 7B**). Because of the use of unresolved $[Ir(C^\wedge N)_2Cl_2]^-$ or $[(Ir(C^\wedge N)_2Cl)_2]$ precursors, chiral resolution of the synthetized Δ/Λ-$[Ir(C^\wedge N)_2(X^\wedge Y)]^{n+}$ racemate **8** (Hellou et al., 2017), **9**, **10** (Li et al., 2015), and **11**, **12** (Coughlin et al., 2008) was performed by chiral supercritical fluid chromatography, before CPL measurement. Since the isolation of pure enantiomers requires sophisticated chiral resolution, the latter method is neither the most popular nor the first exploited to generate enantiopure Ir^{III} complex for CPL. An alternative strategy exploits the coordination of an

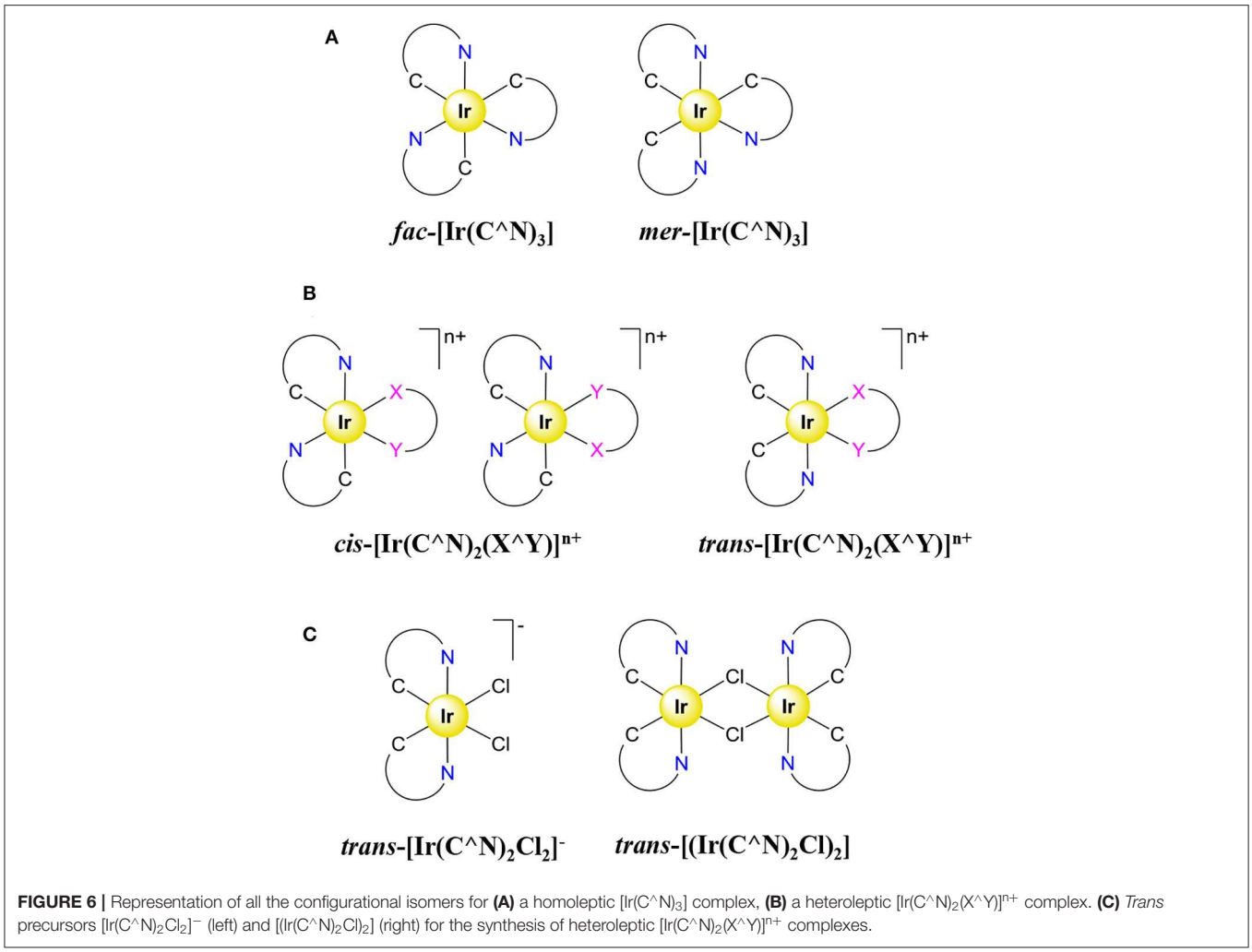

FIGURE 6 | Representation of all the configurational isomers for **(A)** a homoleptic $[Ir(C^N)_3]$ complex, **(B)** a heteroleptic $[Ir(C^N)_2(X^Y)]^{n+}$ complex. **(C)** *Trans* precursors $[Ir(C^N)_2Cl_2]^-$ (left) and $[(Ir(C^N)_2Cl)_2]$ (right) for the synthesis of heteroleptic $[Ir(C^N)_2(X^Y)]^{n+}$ complexes.

enantiopure chiral ligand to Ir^{III}, which provides a pair of diastereoisomers allowing (i) chiral induction, (ii) quantification of diastereomeric excess by NMR, and (iii) diastereoisomer separation by conventional chemical techniques, such as crystallization, precipitation, or chromatography. Actually, the first CPL measurement performed on an Ir^{III} complex used an homoleptic $[Ir(pppy)_3]$ (**12**) complex (pppy = (8R,10R)-2-(2′-phenyl)-4,5-pinenopyridine) synthetized according to the chiral induction methodology (**Figure 8A**) (Schaffner-Hamann et al., 2004). The reaction of $Ir(acac)_3$ with pppy at 190°C in glycerol afforded pure *fac*-$[Ir(pppy)_3]$ with a diastereomeric Λ/Δ ratio of 2/3. Further separation of the two diastereoisomers was achieved on a silica plate and afforded g_{lum} of -3.2×10^{-3} and $+2.8 \times 10^{-3}$ for *fac*-Δ-$[Ir(pppy)_3]$ and *fac*-Λ-$[Ir(pppy)_3]$, respectively.

Apart from **13**, the chemical attention usually focused on heteroleptic $[Ir(C^N)_2(X^Y)]^{n+}$ complexes probably because they are obtained by the simple reaction of the aforementioned Ir^{III} intermediates ($[Ir(C^N)_2Cl_2]^-$ or $[(Ir(C^N)_2Cl)_2]$) with enantiopure ligands, a versatile strategy which produces a library of complexes with various chiral ligands. In particular, the combination of achiral C^N ligands with a chiral X^Y one afforded the most important library of $[Ir(C^N)_2(X^Y)]^{n+}$ complexes for CPL, mainly based on central chirality (**14**–**17**) (Li et al., 2016; Mazzeo et al., 2016; Li L.-P. et al., 2017; Manguin et al., 2019), albeit axial chirality was occasionally exploited with ligands containing 1,1′-bi-2-naphthol derivatives (**18**–**19**) (**Figure 8B**) (Han et al., 2017b; Yan et al., 2019a). Although a few examples report on full chiral induction (**14**) (Li L.-P. et al., 2017), in most cases the separation of the formed diastereoisomer pair was achieved by selective diasteroisomer precipitation (**15**) (Mazzeo et al., 2016), by HPLC (**16**) (Li et al., 2016), or by silica column chromatography (**17**–**19**) (Manguin et al., 2019; Yan et al., 2019a). Alternatively, the ligand chirality can be introduced on the C^N ligand held by the precursor Ir^{III} complex prepared as an unresolved diasteroisomeric mixture. Hence, the coordination of acac (X^Y) to a precursor containing enantiopure 2-phenyl-5,6-pinenepyridine (C^N) resulted in a surprising full chiral induction with the exclusive formation of the Δ compound (**20**) (**Figure 8C**) (Yang et al., 2009). Finally, the introduction of both enantiopure C^N and X^Y ligands provided 8 stereoisomers from the overall 3 stereogenic centers (**21**) (**Figure 8D**) (Yan et al., 2018). The various mixtures of

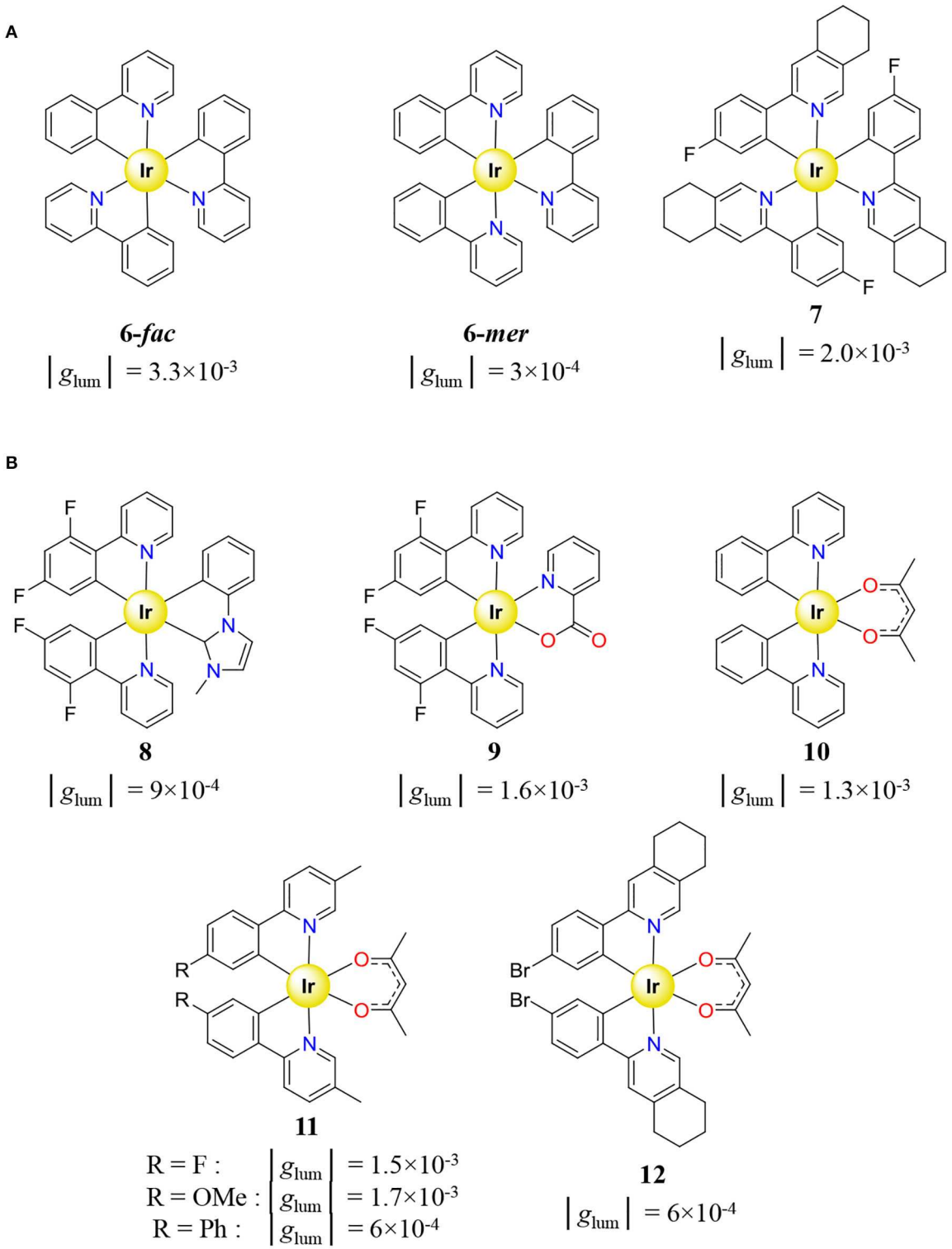

FIGURE 7 | (A) Homoleptic $[Ir(C^N)_3]$ (Coughlin et al., 2008; Li et al., 2015) and **(B)** heteroleptic $[Ir(C^N)_2(X^Y)]$ (Coughlin et al., 2008; Li et al., 2015; Hellou et al., 2017), cyclometallated Ir^{III} complexes holding achiral ligands displaying CPL, and associated dissymmetry factor g_{lum}.

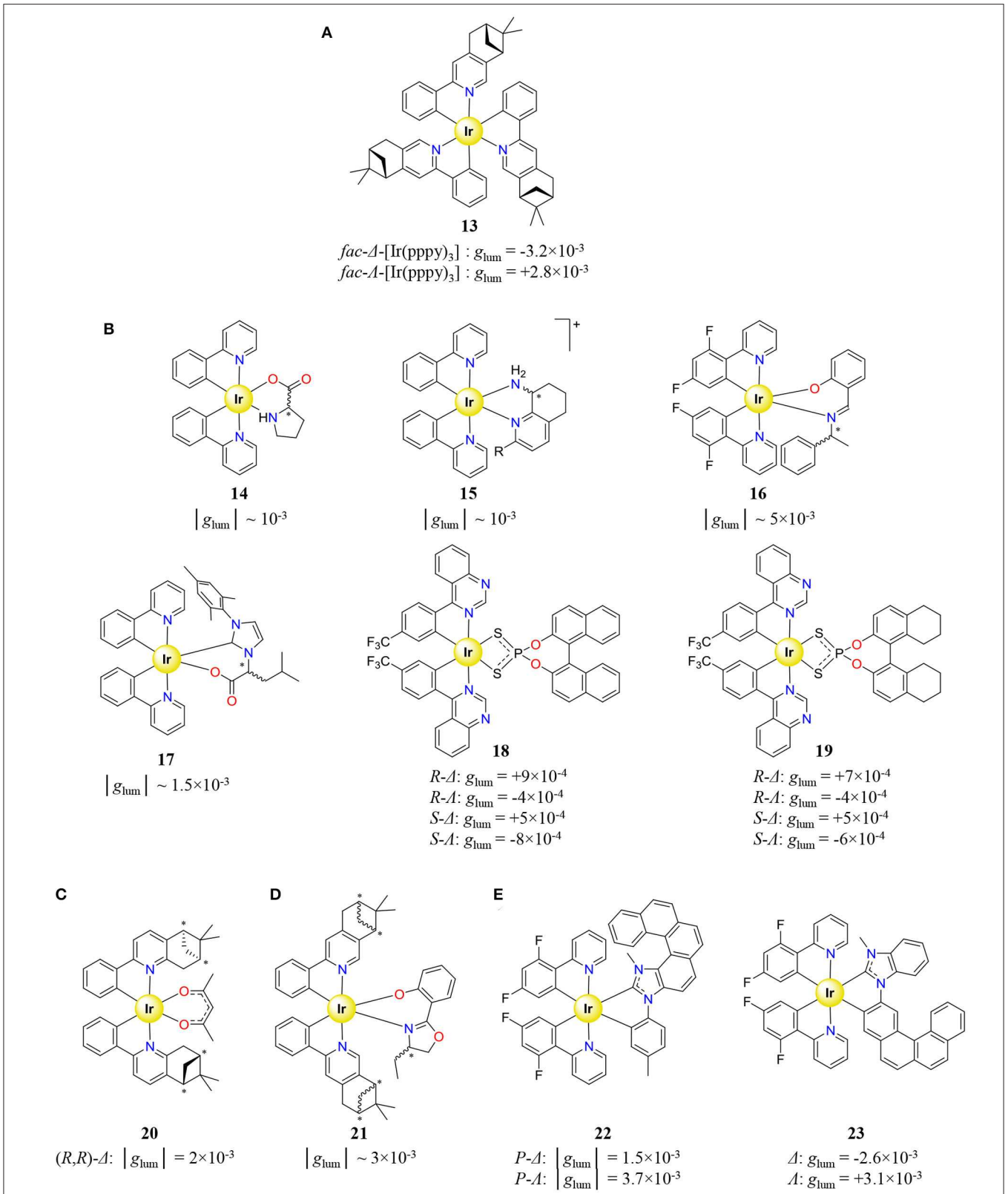

FIGURE 8 | Cyclometallated Ir^{III} complexes holding chiral ligands, displaying CPL, and associated dissymmetry factor g_{lum}. **(A)** Homoleptic *fac*-[Ir(pppy)$_3$] complex (Schaffner-Hamann et al., 2004). Heteroleptic complexes $[Ir(C^N)_2(X^Y)]^{n+}$ holding **(B)** achiral C^N and chiral X^Y ligands (Li et al., 2016; Mazzeo et al., 2016; Li L.-P. et al., 2017; Manguin et al., 2019; Yan et al., 2019a), **(C)** chiral C^N and achiral X^Y ligands (Yang et al., 2009), **(D)** chiral C^N and X^Y ligands (Yan et al., 2018), and **(E)** helicenic–NHC chiral ligand X^Y (Hellou et al., 2017; Macé et al., 2019).

diastereoisomers could be successfully separated by silica column chromatography. Even if chiral induction is an outstanding strategy for the easy preparation of stereoisomerically pure Ir^{III} complexes, this method requires kinetically inert enantiopure ligands. Nevertheless, the synthesis of a $[Ir(C^N)_2(X^Y)]^{n+}$-type complex with a helicenic–NHC as ligand X^Y (**22**–**23**) was conducted despite the observed racemization of the unbound helicene (**Figure 8E**) (Hellou et al., 2017; Macé et al., 2019). Since racemization is inhibited upon coordination, the chiral resolution of the four stereoisomers could be performed by chiral HPLC. In spite of all the remarkable synthetic efforts made for generating libraries of enantiopure Ir^{III} emissive complexes, the CPL measurements always show weak and comparable dissymmetry factors in the range of 10^{-4} -5 × 10^{-3}, an observation which is consistent with the nature of the electric-dipole allowed transitions characterizing mixed ^{3}LC/^{3}MLCT manifolds.

Recently, neutral Pt^{II} complexes received increasing attention as CPL emitters because they combine (i) chemical and kinetic advantages similar to Ir^{III} complexes, (ii) important emission quantum yield from ^{3}MLCT state or even ^{3}MMLCT state due to Pt–Pt bonds, and (iii) emission in the red-to-NIR region, which is an asset for biological applications. Pt^{II} (d^8) complexes usually display square planar geometry with a coordination number of 4 compatible with additional intermolecular axial interactions produced by molecule pilling which permit the tuning of the ^{3}MMLCT emission energy via Pt–Pt bond formation. Contrary to aforementioned pseudo-octahedral Ir^{III} ter-bidentate complexes, the square planar Pt^{II} ones possess an intrinsically achiral first coordination sphere, which affords an easy route for the preparation of enantiopure complexes. Indeed, the coordination of chiral enantiopure ligands generates the corresponding complex without the appearance of an additional stereogenic center upon coordination—a convenient synthetic pathway, which makes Pt^{II} complexes particularly appealing for CPL. The first CPL of a Pt^{II} complexes was thus reported by Crassous and coworkers in 2014. They correspond to the coordination of cyclometalated bidentate helicene ligands, with an acac anion completing the coordination sphere (**24**–**26**) (**Figure 9A**) (Shen et al., 2014). While **24** and **25** display weak dissymmetry factors, the related complex **26** shows g_{lum} one order of magnitude higher than that measured for the Ir^{III} analogs, this despite the simple ligand-centered chirality. This confirms the efficiency of the DC mechanism and the option of avoiding metal-centered chirality for producing large CPL signals. Owing to its outstanding $g_{lum} = 1.3 \times 10^{-2}$ for a d-block complex, **26** was recently incorporated into an electroluminescent device which provided an electroluminescent dissymmetry factor (g_{el}) one order of magnitude higher than its photoluminescent counterpart (g_{lum})—a result probably due to an additional helical arrangement in the condensed phase (Brandt et al., 2016). The impressive g_{el} is sensitive to weak structural modifications since the similar complex **27** showed much weaker values (Yan et al., 2019b). Motivated by the seminal work of Crassous and coworkers, numerous chiral Pt^{II} complexes for CPL studies were synthesized with the help of bidentate ligands possessing helical chirality (**27**–**28**, **Figure 9A**) (Biet et al., 2017), central chirality (**29**–**31**, **Figure 9B**) (Ionescu et al., 2017; Lu et al., 2017; Usuki et al., 2019), or axial chirality (**32**–**33**, **Figure 9C**) (Song J. et al., 2018; Song et al., 2019).

The fluorinated version of the bimetallic complex **33** shows a g_{lum} of 10^{-2} due to the helical shape induced by the BINOL ligand, which highlights that the pilling of complexes in an overall helical architecture is a promising strategy for g_{lum} enhancement (Song et al., 2019). The latter strategy was repeated with complex **34**, which is used as a dopant in achiral analog for the formation of helical co-assemblies with improved g_{lum} for the ^{3}MMLCT transition via Pt–Pt bonding interactions (**Figure 10A**) (Park et al., 2019).

In order to provide efficient stacking and intermolecular Pt–Pt bonding interactions, Pt^{II} complexes holding a tridentate and a monodentate ligand were developed (**35**, **36**, **38**, **Figure 10**) (Ikeda et al., 2015, 2018; Zhang X.-P. et al., 2015; Tanaka et al., 2016). Despite positioning the stereogenic centers on the ligand far from the emissive moiety, the resulting aggregates and helical supramolecular structures often display important dissymmetry factor around 10^{-2}. Moreover, the reversible entropic control of the aggregation process transforming CPL active assemblies (at low *T*) into discrete molecules with no CPL signal (at high *T*) provides a noteworthy CPL switch (**36**–**38**, **Figure 10B**) (Ikeda et al., 2015, 2018; Zhang X.-P. et al., 2015; Fu et al., 2016). The tuning of the CPL property can nonetheless be achieved in solution by controlling the intermetallic distance in a bimetallic architecture *via* the choice of the spacer length between complexes (**39**, **Figure 11A**) (Zhang et al., 2018).

A remarkable modulation of the CPL property in solution could be achieved with the cyclometallated Pt^{II}-helicene complex (**40**, **Figure 11A**), for which reversible protonation of the bidentate helical ligand provided a modification of g_{lum} albeit its absolute value remains weak (Saleh et al., 2015a). Aside from complexes owing their chirality to stereogenic centers located on the ligand, Clever and coworkers reported in 2017 a remarkable Pt^{II} cyclometallated complex built with an achiral ligand and showing metal-centered chirality despite the square planar geometry of the first coordination sphere (**41**, **Figure 11B**) (Schulte et al., 2017). In this complex, the chirality arises from an appropriate choice of the ligand coordination vectors, which permit the unusual orthogonal coordination of the two bidentate ligands.

Beyond the most popular Ir^{III} and Pt^{II} neutral complexes, the CPL of second- and third-row transition metal complexes is currently restricted, to the best of our knowledge, to three reports dealing with chiral and charged Ru^{II} (**42**) (Oyler et al., 2007), Re^{I} (**43**) (Saleh et al., 2015b), and Os^{II} (**44**) (Gunde et al., 1997) complexes (**Figure 12**).

The use of $[Ru^{II}(R\text{-bipy})_3]$ chromophores restores the difficulties associated with the prospective formation of Δ/Λ stereoisomers as well as *fac*/*mer* regioisomers. Nevertheless, those synthetic drawbacks were finally overcome by the use of enantiopure ter-bidentate podand, the coordination of which solely provides the *fac* isomer **42** (Oyler et al., 2007). Moreover, the three stereogenic centers located on the hexadentate ligand induce the complete diastereoselective formation of the Δ-(-)-**42** and Λ-(+)-**42** complexes which showed weak g_{lum} value of 7.7

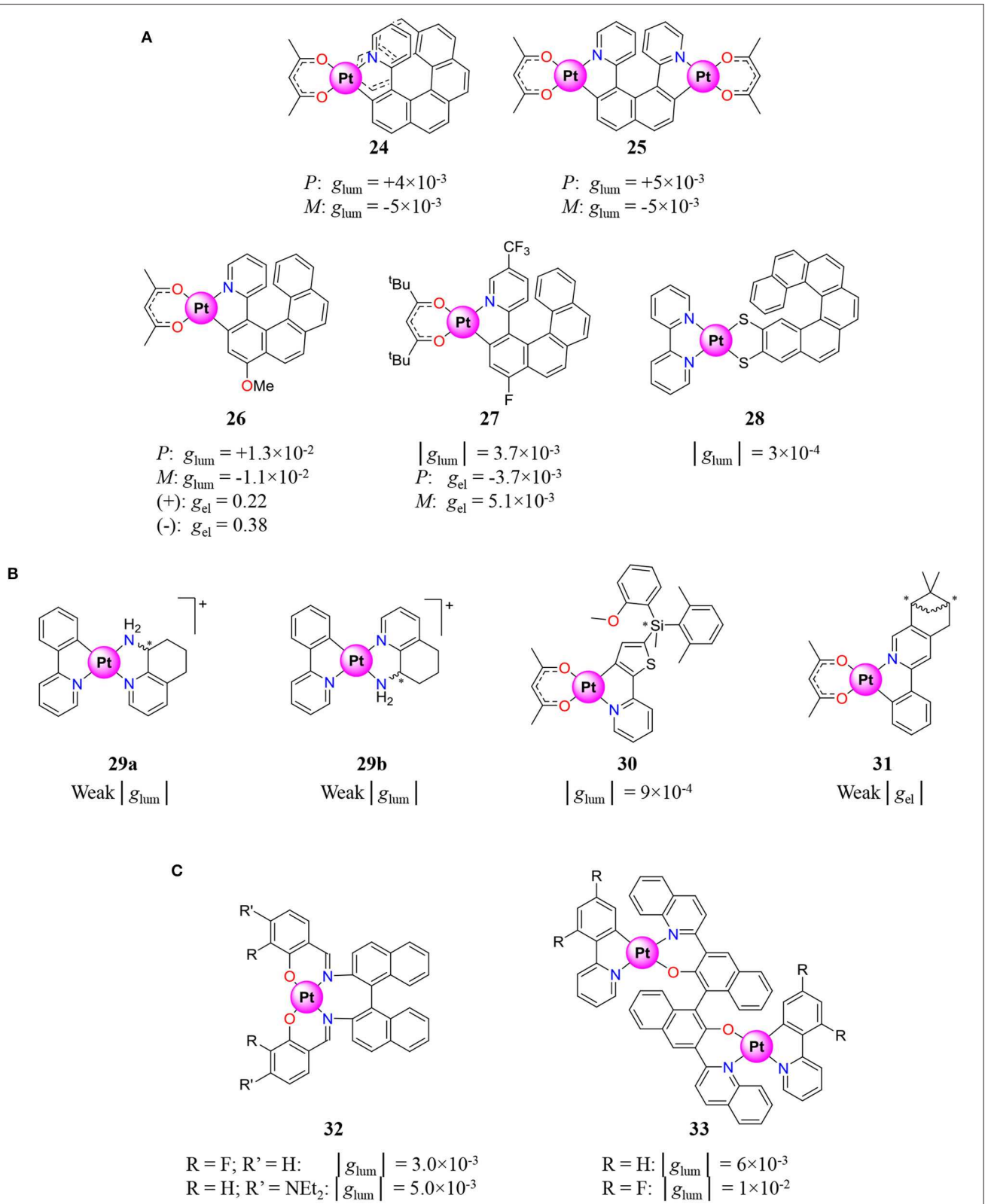

FIGURE 9 | Pt^{II} complexes coordinated by **(A)** helicene ligands (Shen et al., 2014; Brandt et al., 2016; Biet et al., 2017; Yan et al., 2019b), **(B)** bidentate ligands showing central chirality (Ionescu et al., 2017; Lu et al., 2017; Usuki et al., 2019), and **(C)** bidentate ligands showing axial chirality (Song J. et al., 2018; Song et al., 2019), and associated luminescence dissymmetry factor g_{lum} and electroluminescence dissymmetry factor g_{el}.

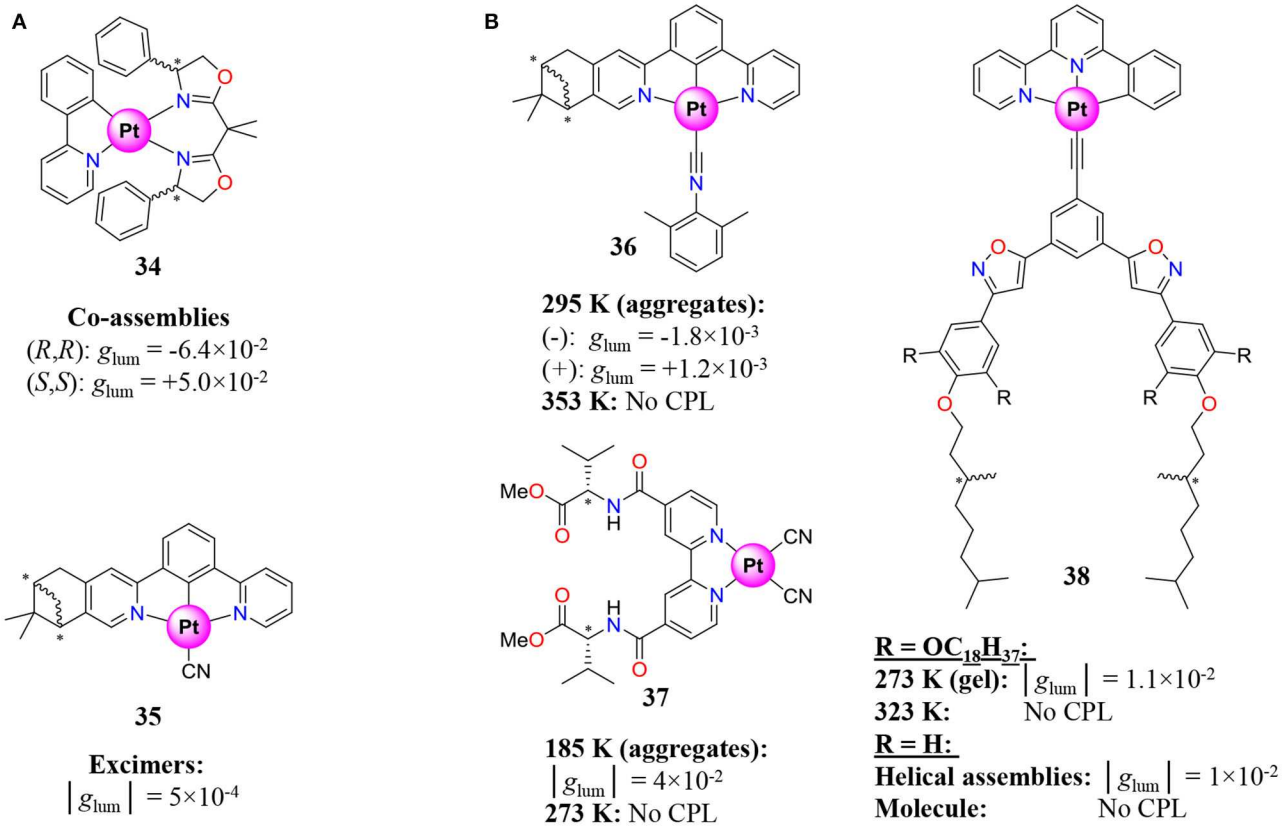

FIGURE 10 | Pt^{II} complexes **(A)** showing aggregation (Tanaka et al., 2016; Park et al., 2019), **(B)** showing reversible aggregation and switchable CPL and associated dissymmetry factor g_{lum} (Ikeda et al., 2015, 2018; Zhang X.-P. et al., 2015; Fu et al., 2016).

$\times 10^{-4}$. More recently, the complex **43** was obtained through the coordination of a helicenic ligand to a Re^{I} metal center with intrinsic achiral coordination sphere (Saleh et al., 2015b). Although this straightforward method provides enantiopure complexes, the associated dissymmetry factors remain weak, and only few further synthesis were performed for CPL application (Gauthier et al., 2020). Finally ligand-centered CPL were casually tuned or switched by a closed shell d-block metal like Ag^{I} or Au^{I}. While Au^{I} can be used to rigidify and organize organic chromophores to enhance its emission (Zhang J. et al., 2019), the interaction of Ag^{I} with organic moieties provides CPL switch and ratiometric CPL probe (Reiné et al., 2018a; Resa et al., 2018). Furthermore, CPL emission can be observed from nanoclusters of silver or gold in their metallic state (Kumar et al., 2017; Shi et al., 2017).

Excluding the outstanding electroluminescence of **26**, the CPL-active 4d and 5d metal complexes reported to date display a systematically weak dissymmetry factor ($<7 \times 10^{-2}$) in line with the limitations ascribed to ED-allowed and MD-forbidden charge transfer or ligand-centered transitions. Similarly to the lanthanide-based f–f transitions, the d–d transitions in the second and third-row metal complexes should display strong CPL, albeit there are non-emissive because of the low-lying MLCT. In order to observe emissive metal centered d–d transitions, the strong ligand field of 4d and 5d metal complexes should be reduced until the energy of MC states becomes lower than those of MLCT states, a criterion more easily fulfilled with 3d metal complexes.

EXTENSION TOWARD 3D METAL COMPLEXES. THE PROMISING CASE OF EARTH-ABUNDANT CHROMIUM CENTERS

The earth-abundant first-row d-block metals seem appealing in the field of CPL because of their low cost and the theoretically promising dissymmetry factors arising from the d–d transitions. Assuming very weak spin–orbit coupling and pure metal character of d orbitals, the d–d transitions with $\Delta L = 0$ are indeed ED-forbidden and MD-allowed. However, pure metal-centered emission in 3d coordination complexes, as found in 4f-block analogs, is rare because of the considerable covalencies of the M–L bonds that promote mixing with ligand-based wave functions, efficient coupling with vibration modes, and some significant quenching of the luminescence. Regarding this last point, a favorable situation for an emissive 3d metal excited level requires (i) a minimum perturbation by the ligand field in order

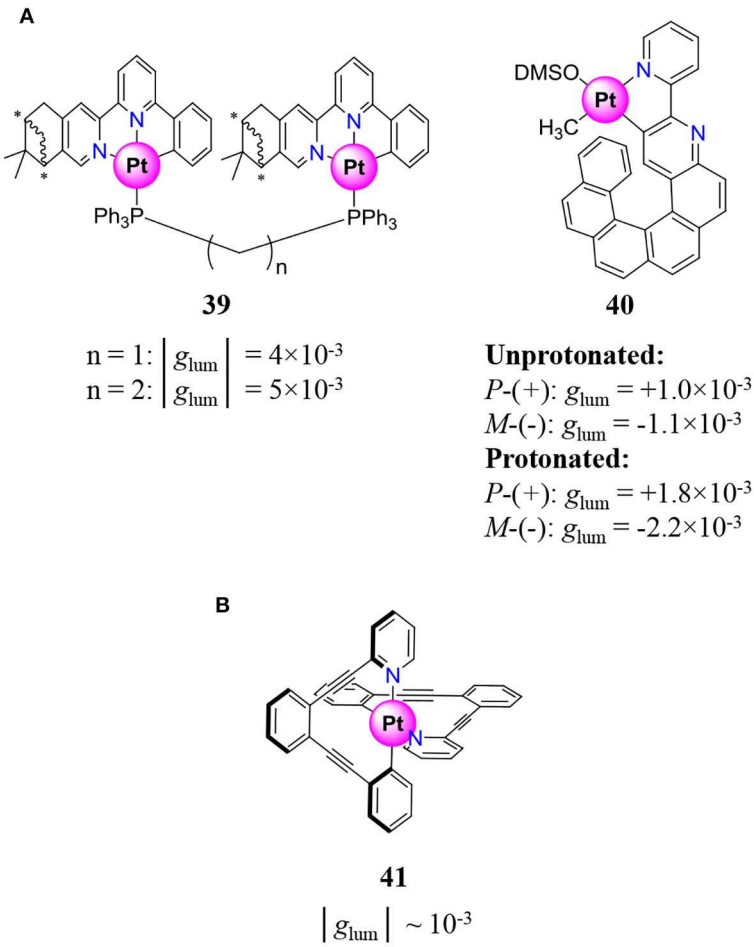

FIGURE 11 | (A) Pt^{II} complexes showing CPL signals tunable by spacer length (left) or switchable by protonation/deprotonation (right) (Saleh et al., 2015a; Zhang et al., 2018). **(B)** Pt^{II} cyclometallated complexes holding achiral ligands and showing metal centered chirality (Schulte et al., 2017), and associated dissymmetry factor g_{lum}.

to retain the almost pure d–d character of the transition and (ii) an important energy gap with upper excited levels in order to prevent deleterious back inter system crossing (BISC). Because of those sophisticated conditions, the use of first-row metals is mainly restricted to closed shell ions with d^{10} configuration, such as Zn^{II} complexes showing ligand-based emission (Isla et al., 2016; Kögel et al., 2016; Aoki et al., 2017; Reiné et al., 2018b; Maeda et al., 2019), or in Cu^{I} complexes displaying MLCT emission (Zhang M.-M. et al., 2019; Deng et al., 2020). In the first case, the Zn^{II} ions are responsible, upon their coordination to an organic ligand, for conformational changes affecting the optical and chiroptical properties, particularly in the CPL emission. However, g_{lum} remains low ranging from 10^{-2} to 10^{-4} as it arises from the organic moiety of the complex. One can note that chiral porphyrin-based ligand platforms have been widely used for such purposes. Interestingly, Cu^{I} has been recently exploited for the preparation of enantiopure organometallic complexes based on chiral carbene ligands. These complexes have the advantage of being prepared directly from enantiopure ligands and so there is no need for chiral resolution. However, the highest g_{lum} value recorded up to now reaches only 10^{-3}, but this strategy opens a new way to prepare enantiopure complexes based on earth-abundant metals acting as CPL emitters.

Significant g_{lum} enhancement thus requires moving from charge transfer to ED-forbidden/MD-allowed metal-centered transitions operating in 3d open-shell metal ions, but only few studies were reported on first-row transition metals, mainly on Cr^{III} and once on Mn^{II} showing CPL in the solid state (Zhao et al., 2019). Although the use of labile Mn^{II} is compatible with chiral induction produced by enantiopure ligands, the ideal metal complexes should be inert enough to tolerate separation techniques, such as chromatogaphy, a criterion only fulfilled with Co^{III}, Fe^{III}, or Cr^{III}. While the two former ions are known to be non-emissive, Cr^{III} complexes are known to show NIR emission in the 600–800 nm region, arising from the two low-lying $Cr^{III}(^2E)$ and $Cr^{III}(^2T_1)$ spin–flip excited states (**Figure 13**) (Jamieson et al., 1981; Kirk, 1981, 1999; Forster, 1990, 2002; Buldt and Wenger, 2017; Otto et al., 2018). In fact, Cr^{III} complexes

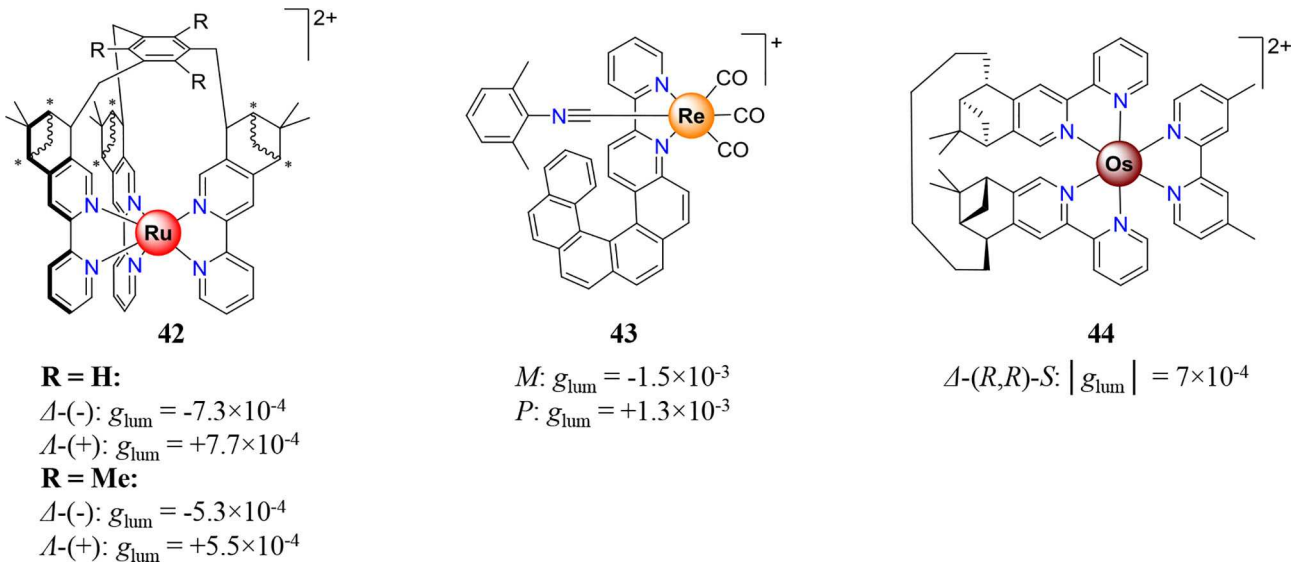

FIGURE 12 | Ru^{II} **(left)** (Oyler et al., 2007), Re^{I} **(center)** (Saleh et al., 2015b), and Os^{II} **(right)** (Gunde et al., 1997) complexes showing CPL, and associated dissymmetry factor g_{lum}.

have long been known to exhibit interesting photophysical and photochemical properties as illustrated by the archetypal terbidentate $[Cr(phen)_3]^{3+}$ (Serpone et al., 1979; Ryu and Endicott, 1988; Isaacs et al., 2006; Donnay et al., 2007; Vandiver et al., 2010; Vasudevan et al., 2010; Doistau et al., 2018, 2020), bis-terdentate $[Cr(tpy)_2]^{3+}$ (Serpone et al., 1979; Scarborough et al., 2012; Constable et al., 2014; Schönle et al., 2015a,b; Barbour et al., 2017), and analogs (Zare et al., 2017b; Jiménez et al., 2018). In all cases, the ligand-field strength induced by the phen and tpy ligands is strong enough to induce near-infrared phosphorescence arising from the lowest-lying $Cr(^2T_1)$ and $Cr(^2E)$ excited states, but the associated very low quantum yields (<0.2%) are strong limitations for their use as CPL probes. Thus, much effort was focused on the optimization of the Cr^{III} complexes in order to improve their photophysical properties. The introduction of six-membered chelated rings in the terdetante ligands (ddpd = *N*, *N*′-dimethyl-*N*, *N*′-dipyridin-2-ylpyridine-2,6-diamine or dqp = 2,6-di(quinolin-8-yl) ligands) has proven to be an efficient approach to increase both the quantum yield and the lifetimes of the $Cr(^2T_1)$ and $Cr(^2E)$ excited states in $[Cr(ddpd)_2]^{3+}$ and $[Cr(dqp)_2]^{3+}$ (Otto et al., 2015; Wang et al., 2017; Jiménez et al., 2018, 2019; Treiling et al., 2019).

In the frame of CPL, Cr^{III} complexes holding strong nitrogen donors as ligands are valuable candidates because the energy gap with the upper ligand field state ($^4T_2$) is large enough to prevent BISC and subsequent quenching (Fucaloro et al., 1983; Doistau et al., 2018; Otto et al., 2018). In addition, the Tanabe–Sugano diagram pertinent to a d^3 electronic configuration indicates that the $Cr^{III}(^2T_1,^2E)$ energy levels are almost insensitive to the ligand field strength, which preserve the ED-forbidden/MD-allowed character of the $Cr^{III}(^2T_1,^2E \rightarrow {}^4A_2)$ transitions (Lever, 1984; Zare et al., 2017b; Jiménez et al., 2018). Hence, the $Cr^{III}N_6$ complex NIR emission seems to fulfill the established criteria

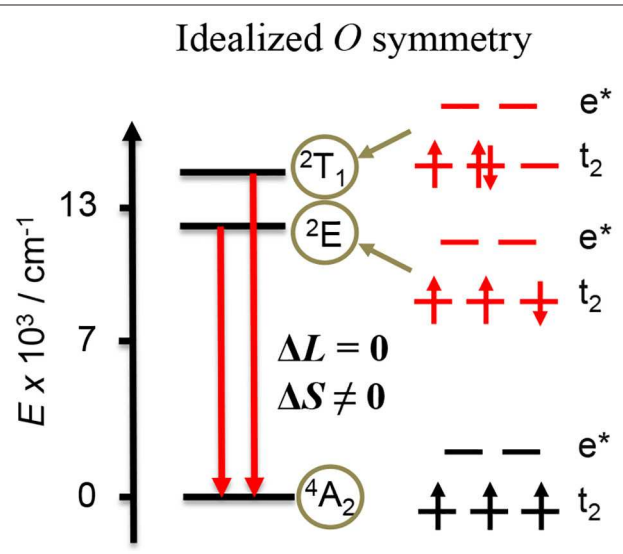

FIGURE 13 | Low-energy part of the energy level diagram for a $Cr^{III}N_6$ chromophore in octahedral symmetry. The two red arrows represent the emissive spin–flip transitions from the two low-lying excited states ($^2T_1$ and ^2E). The electronic arrangement is highlighted in the right part of the diagram.

for exhibiting strong CPL with high g_{lum}. It is however worth stressing here that, although the spin–flip $Cr^{III}(^2T_1,^2E \rightarrow {}^4A_2)$ emissive transitions are both strictly Laporte and spin-forbidden, the former rule is released in non-centrosymmetric systems and considerable intensity can be also gained through the vibronic coupling with unsymmetrical modes. Hence, the distortion from a perfect centrosymmetric octahedral should have a deleterious

effect on the ED/MD ratio because of increasing covalence in the t_{2g} orbitals—a consequence also triggered by strong π interactions and by strong nephelauxetic effect. Finally, the $Cr^{III}N_6$ complexes may allow discriminating the contribution of both ligand-field splitting and Racah parameters to the magnitude of g_{lum}–a feature which remains unexplored. During the early seventies, there was an ephemeral interest for chiral Cr^{3+} complexes that gave rise to the first reports on the circularly polarized emission arising from first raw transition metal complexes. In their seminal work, Emeis and Oosterhoff reported in 1967 that the simple chiral complexes $[Cr(en)_3]^{3+}$ (en = ethylenediamine) showed, despite a weak quantum yield, a remarkable $|g_{lum}| = 0.028$ for the spin–flip $Cr^{III}(^2E \rightarrow {}^4A_2)$ transition (Emeis and Oosterhoff, 1967), a result boosted to 0.046 in an ethylene glycol/water solution by Richardson and coworkers 10 years later (Hilmes et al., 1977). This $|g_{lum}|$ value is quite high compared with p-block systems and with 4d- and 5d-block-based complexes, which confirms the potential of Cr^{III} ions for inducing large g_{lum}. Despite those promising results, only scarce studies focused on Cr^{III} complexes reported CPL measurements in condensed phases (Manson and Shah, 1977; Yamaga et al., 1990; Nobuhiro et al., 2001; Anzai et al., 2003, 2006; Seyler et al., 2018), or in solution except for some triple helical complexes $[Cr(en)_3]^{3+}$ (Madaras and Brittain, 1980; Morita et al., 1984; Herren et al., 1996), $[Cr(ox)_3]^{3+}$ (ox = oxalate) (Herren et al., 1996), $[Cr(pn)_3]^{3+}$ (pn = 1,2-propanediamine) (Morita et al., 1984; Herren et al., 1996), and $[Cr(ala)_3]$ (ala = alaninato) (Tsubomura et al., 1988; Taro et al., 1991).

In 2001, Piguet and coworkers took advantage of the Cr^{III} complex inertness to prepare and resolve the enantiomerically pure triple-stranded helicates $[LnCr(\mathbf{L9})_3]^{6+}$ (e.g., Ln = Eu, Tb) (**Figure 14A**) which revealed Cr^{III}-centered polarized emission arising from the spin–flip $Cr^{III}(^2E \rightarrow {}^4A_2)$ transition with a $|g_{lum}|$ of 0.01 at 744 nm (Cantuel et al., 2004). More recently, the chiral resolution of the cationic kinetically inert $[Cr(dqp)_2]^{3+}$ complex (dqp = 2,6-di(quinolin-8-yl)) displaying extraordinary dual CPL emission was achieved. The wrapped arrangement of the dqp ligand around the Cr^{III} provides a helical configuration which generates a chiral bis-terdentate monometallic Cr^{III} helix as a racemic mixture. The two enantiomers *PP*-$[Cr(dqp)_2]^{3+}$ and *MM*-$[Cr(dqp)_2]^{3+}$ (**Figure 14C**) were separated by chromatography and isolated by cation exchange. The CPL spectra recorded in CH_3CN solutions showed two polarized emission bands at 724 nm and 747 nm corresponding to the spin–flip $Cr^{III}(^2T_1 \rightarrow {}^4A_2)$ and $Cr^{III}(^2E \rightarrow {}^4A_2)$ transitions with g_{lum} values of ±0.1 and ±0.2, respectively (Jiménez et al., 2019). These values are the highest reported up to date for any transition metal complex, and they are comparable to those found in chiral lanthanide-based f–f complexes. Subsequently, Heinze and coworkers were able to partially resolve the chiral complex $[Cr(ddpd)_2]^{3+}$ by HPLC (**Figure 14B**). CPL measurements displayed g_{lum} values as high as 0.098 for the $Cr^{III}(^2E \rightarrow {}^4A_2)$ transition (Dee et al., 2019).

Interestingly, the $[EuCr(\mathbf{L9})_3]^{6+}$ and $[Cr(en)_3]^{3+}$ complexes, which show intrinsic chirality of the CrN_6 coordination sphere due to D_3 local symmetry, display g_{lum} significantly lower than the $[Cr(dqp)_2]^{3+}$ and $[Cr(ddpd)_2]^{3+}$ complexes where their chirality arises from the helical disposition of the coordination ligands and not from the metal environment. The latter feature highlights the efficiency of the DC mechanism compared to SC. Nevertheless, the distortion from perfect octahedral can be also incriminated since it reduces the pure metal character of the t_{2g} orbitals in the D_3 symmetric coordination sphere holding five-membered chelate rings, while the $[Cr(dqp)_2]^{3+}$ and $[Cr(ddpd)_2]^{3+}$ complexes show a nearly undistorted octahedral first-coordination sphere (Perkovic et al., 1991). Finally, the importance for strong CPL due to a helical wrapping of the ligands around the metal should not be underestimated.

In summary, binding semirigid achiral bis six-membered chelate rings (dqp or ddpd) to form helical Cr^{III} complexes and further chiral resolution to generate enantiopure samples makes these systems promising candidates for working as

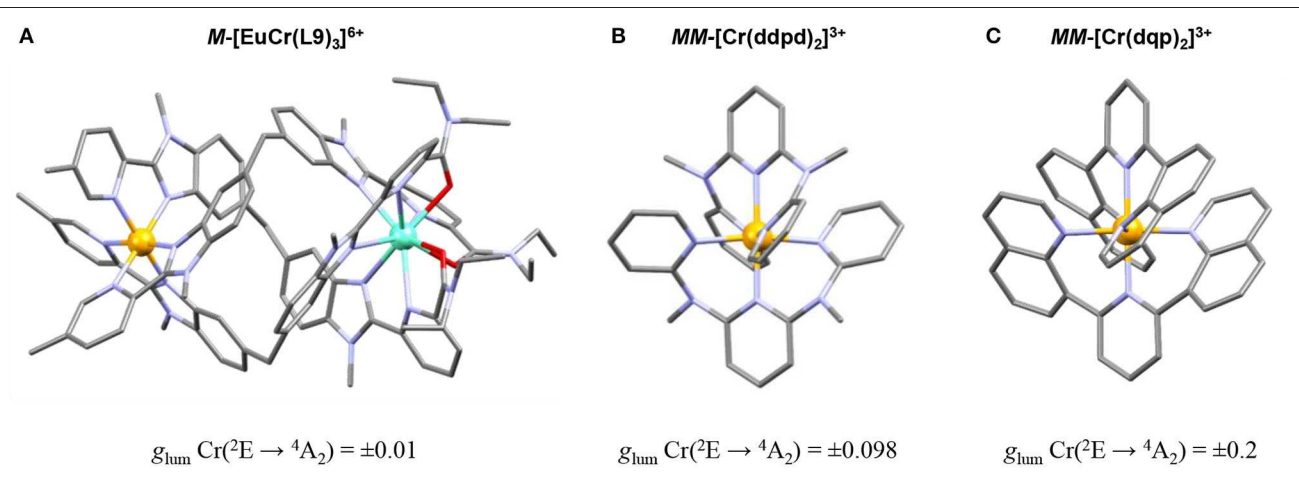

FIGURE 14 | (A–C) Crystal structures of chiral Cr^{III} based polypyridyl complexes and their respective g_{lum} values for the spin–flip $Cr^{III}(^2E \rightarrow {}^4A_2)$ transition. Color code: Cr (orange), Eu (sky blue), C (gray), N (purple), O (red), H, and counter-ions are omitted for clarity.

NIR CPL emitters. In these conditions, this earth-abundant metal could become a good competitor to rare earths for chiroptical applications.

CONCLUSION

Since the beginning of the twenty-first century, increasing efforts have been devoted to the synthesis of molecules or materials displaying strong CPL with large g_{lum}. These materials were found appealing for the design of devices, such as CP-OLEDs, the brightness of which can be enhanced compared with their linearly polarized counterparts, or for bio-imaging because of the lower scattering of the circularly polarized light. In terms of processability and adaptability to specific applications, the kinetically inert organic chromophores, as well as 4d and 5d coordination complexes, were systematically exploited despite the rather weak dissymmetry factors ($g_{lum} < 7 \times 10^{-2}$) associated with electric dipole allowed $\pi \rightarrow \pi^*$ and charge transfer transitions. Chiral single-wall carbon nano-ring and Pt^{II}-helicene complexes have been shown to exhibit the largest g_{lum} and g_{el} within that family of CPL materials. Improving g_{lum} requires ED-forbidden/MD-allowed transition; thus, pure metal-centered transitions ($\Delta L = 0$) are probably the best choice. In this context, the f–f transitions benefit from low covalence due to the inner character of the f orbitals, which are responsible for weak crystal field splittings (100–1,000 cm^{-1}) and almost pure intrashell character for the f–f transitions. Because of the strong spin–orbit coupling, all f–f transitions are not equally promising for displaying large g_{lum} and the target MD-allowed transitions obey specific selection rules applied on ΔJ values. A large number of chiral lanthanide complexes showing important dissymmetric factors in the range 0.01–2 have been reported with a record value of 1.38 at 595 nm for a europium complex. Nevertheless, the costly lanthanides metals and the kinetic lability of most of Ln^{III}-based complexes are severe drawbacks for the preparation of inert enantiopure complexes and their subsequent applications in material science. In order to combine large g_{lum}, kinetic inertness, and low cost, some 3d metal complexes represent a valuable alternative since the d–d transitions should display similar advantages as those described for f–f, except that they suffer from more important covalence and vibronic coupling. In particular, some Cr^{III} inert complexes have been shown to be compatible with enantiomeric resolution and strong CPL emission due to the spin–flip $Cr^{III}(^2T_1, ^2E \rightarrow {}^4A_2)$ transitions. The pure d–d character of the latter transitions is respected as long as the Cr^{III} coordination sphere is close to a perfect octahedron (no distortion)— a geometry observed for the $[Cr(dqp)_2]^{3+}$ complex which possesses the record g_{lum} value of 0.2 within the family of transition metal complexes. Although a deep theoretical understanding of the g_{lum}/structure relationship remains somehow elusive, this review dealing with CPL emitters allows the identification of empirical strategies for inducing large g_{lum}. Firstly, the SC mechanism induced by the intrinsic chirality of the chromophore does not provide the strongest CPL signals. On the contrary, introducing chirality on an aside moiety provides efficient DC mechanism, which has been proven to be an efficient tool for inducing important g_{lum}–an effect often enhanced when the number of stereogenic moieties increases. Secondly, the favorable MD transition can be enhanced upon implementing (i) helicity *via* aggregate formation or helical ligand coordination/wrapping or (ii) circular skeleton permitting current loop. Finally, in chiral coordination complexes, it is important to reduce the covalence and the mixing of the metal/ligand wave functions in order to retain the Laporte rule ($\Delta L = 0$) which controls the intensity of ED and MD transitions. This latter feature is fulfilled for (i) f–f transitions in weak crystal field complexes and for (ii) d–d transitions operating on in close-to perfect centrosymmetrical complexes.

AUTHOR CONTRIBUTIONS

BD and J-RJ equally contributed to both bibliography and writing of the manuscript. CP got the financial support for the project, supervised the research group, and corrected the manuscript. All authors contributed to the article and approved the submitted version.

FUNDING

This work was financially supported by the University of Geneva and by the Swiss National Science Foundation (grant numbers 200020_178758 and 206021_183324).

ACKNOWLEDGMENTS

CP thanks Professor Oliver Wenger (University of Basel) for fruitful discussions.

REFERENCES

Aime, S., Barge, A., Bruce, J. I., Botta, M., Howard, J. A. K., Moloney, J. M., et al. (1999). NMR, relaxometric, and structural studies of the hydration and exchange dynamics of cationic lanthanide complexes of macrocyclic tetraamide ligands. *J. Am. Chem. Soc.* 121, 5762–5771. doi: 10.1021/ja990225d

Anzai, N., Kurihara, H., Sone, M., Furukawa, H., Watanabe, T., Horie, K., et al. (2006). Light-induced formation of curved needle texture by circularly polarized light irradiation on a discotic liquid crystal containing a racemic chromium complex. *Liq. Cryst.* 33, 671–679. doi: 10.1080/02678290600647998

Anzai, N., Machida, S., and Horie, K. (2003). Light-induced control of textures and cholesteric pitch in liquid crystals containing chromium complexes, by means of circular and linear polarized light. *Liq. Cryst.* 30, 359–366. doi: 10.1080/0267829031000083740

Aoki, R., Toyoda, R., Kögel, J. F., Sakamoto, R., Kumar, J., Kitagawa, Y., et al. (2017). Bis(dipyrrinato)zinc(II) complex chiroptical wires: exfoliation into single strands and intensification of circularly polarized luminescence. *J. Am. Chem. Soc.* 139, 16024–16027. doi: 10.1021/jacs.7b07077

Ashizawa, M., Yang, L., Kobayashi, K., Sato, H., Yamagishi, A., Okuda, F., et al. (2009). Syntheses and photophysical properties of optical-active blue-phosphorescent iridium complexes bearing asymmetric tridentate ligands. *Dalton Trans.* 2009, 1700–1702. doi: 10.1039/B820821M

Aspinall, H. C. (2002). Chiral lanthanide complexes: coordination chemistry and applications. *Chem. Rev.* 102, 1807–1850. doi: 10.1021/cr010288q

Barbour, J. C., Kim, A. J. I., deVries, E., Shaner, S. E., and Lovaasen, B. M. (2017). Chromium(III) bis-arylterpyridyl complexes with enhanced visible absorption via incorporation of intraligand charge-transfer transitions. *Inorg. Chem.* 56, 8212–8222. doi: 10.1021/acs.inorgchem.7b00953

Barron, L. D. (2008). Chirality and life. *Space Sci. Rev.* 135, 187–201. doi: 10.1007/s11214-007-9254-7

Beeby, A., Dickins, R. S., FitzGerald, S., Govenlock, L. J., Maupin, C. L., Parker, D., et al. (2000). Porphyrin sensitization of circularly polarised near-IR lanthanide luminescence: enhanced emission with nucleic acid binding. *Chem. Commun.* 2000, 1183–1184. doi: 10.1039/B002452J

Benincori, T., Appoloni, G., Mussini, P. R., Arnaboldi, S., Cirilli, R., Quartapelle Procopio, E., et al. (2018). Searching for models exhibiting high circularly polarized luminescence: electroactive inherently chiral oligothiophenes. *Chem. Eur. J.* 24, 11082–11093. doi: 10.1002/chem.201801158

Berova, N., Bari, L. D., and Pescitelli, G. (2007). Application of electronic circular dichroism in configurational and conformational analysis of organic compounds. *Chem. Soc. Rev.* 36, 914–931. doi: 10.1039/B515476F

Beychok, S. (1968). Rotatory dispersion and circular dichroism. *Annu. Rev. Biochem.* 37, 437–462. doi: 10.1146/annurev.bi.37.070168.002253

Biet, T., Cauchy, T., Sun, Q., Ding, J., Hauser, A., Oulevey, P., et al. (2017). Triplet state CPL active helicene–dithiolene platinum bipyridine complexes. *Chem. Commun.* 53, 9210–9213. doi: 10.1039/C7CC05198K

Bing, T. Y., Kawai, T., and Yuasa, J. (2018). Ligand-to-ligand interactions that direct formation of D2-symmetrical alternating circular helicate. *J. Am. Chem. Soc.* 140, 3683–3689. doi: 10.1021/jacs.7b12663

Bonsall, S. D., Houcheime, M., Straus, D. A., and Muller, G. (2007). Optical isomers of *N*, *N*′-bis(1-phenylethyl)-2,6-pyridinedicarboxamide coordinated to europium(iii) ions as reliable circularly polarized luminescence calibration standards. *Chem. Commun.* 2007, 3676–3678. doi: 10.1039/B704346E

Bozoklu, G., Gateau, C., Imbert, D., Pécaut, J., Robeyns, K., Filinchuk, Y., et al. (2012). Metal-controlled diastereoselective self-assembly and circularly polarized luminescence of a chiral heptanuclear europium wheel. *J. Am. Chem. Soc.* 134, 8372–8375. doi: 10.1021/ja3020814

Bradberry, S. J., Savyasachi, A. J., Peacock, R. D., and Gunnlaugsson, T. (2015). Quantifying the formation of chiral luminescent lanthanide assemblies in an aqueous medium through chiroptical spectroscopy and generation of luminescent hydrogels. *Faraday Discuss.* 185, 413–431. doi: 10.1039/C5FD00105F

Brandt, J. R., Salerno, F., and Fuchter, M. J. (2017). The added value of small-molecule chirality in technological applications. *Nat. Rev. Chem.* 1:45. doi: 10.1038/s41570-017-0045

Brandt, J. R., Wang, X., Yang, Y., Campbell, A. J., and Fuchter, M. J. (2016). Circularly polarized phosphorescent electroluminescence with a high dissymmetry factor from PHOLEDs based on a platinahelicene. *J. Am. Chem. Soc.* 138, 9743–9746. doi: 10.1021/jacs.6b02463

Browne, W. R., and Feringa, B. L. (eds.). (2011). "Chiroptical molecular switches," in *Molecular Switches* (Wiley-VCH Verlag GmbH & Co. KGaA), 121–179. doi: 10.1002/9783527634408.ch5

Buldt, L. A., and Wenger, O. S. (2017). Chromium complexes for luminescence, solar cells, photoredox catalysis, upconversion, and phototriggered NO release. *Chem. Sci.* 8, 7359–7367. doi: 10.1039/C7SC03372A

Cantuel, M., Bernardinelli, G., Muller, G., Riehl, J. P., and Piguet, C. (2004). The first enantiomerically pure helical noncovalent tripod for assembling nine-coordinate lanthanide(III) podates. *Inorg. Chem.* 43, 1840–1849. doi: 10.1021/ic035292u

Caporale, C., and Massi, M. (2018). Cyclometalated iridium(III) complexes for life science. *Coord. Chem. Rev.* 363, 71–91. doi: 10.1016/j.ccr.2018.02.006

Carr, R., Evans, N. H., and Parker, D. (2012). Lanthanide complexes as chiral probes exploiting circularly polarized luminescence. *Chem. Soc. Rev.* 41, 7673–7686. doi: 10.1039/C2CS35242G

Casanovas, B., Zinna, F., Di Bari, L., El Fallah, M. S., Font-Bardía, M., and Vicente, R. (2017). Circularly polarized luminescence on dinuclear Tb(iii) and Eu(iii) complexes with (S-) and (R-) 2-phenylpropionate. *Dalton Trans.* 46, 6349–6357. doi: 10.1039/C6DT04686J

Chambron, J.-C., Dietrich-Buchecker, C., and Sauvage, J.-P. (1993). "From classical chirality to topologically chiral catenands and knots," in *Supramolecular Chemistry I - Directed Synthesis and Molecular Recognition*, eds J. Canceill, J.-C. Chambron, A. Collet, Ch. Dietrich-Buchecker, H. D. Durst, J.-P. Dutasta, F. H. Kohnke, B. Lozach, J.-P. Mathias, S. Misumi, J.-P. Sauvage, J. F. Stoddart, D. A. Tomalia, and S. C. Zimmerman (Berlin; Heidelberg: Springer), 131–162. doi: 10.1007/BFb0111283

Chen, N., and Yan, B. (2018). Recent theoretical and experimental progress in circularly polarized luminescence of small organic molecules. *Molecules* 23:3376. doi: 10.3390/molecules23123376

Constable, E. C., Housecroft, C. E., Neuburger, M., Schonle, J., and Zampese, J. A. (2014). The surprising lability of bis(2,2′:6′,2″-terpyridine)chromium(iii) complexes. *Dalton Trans.* 43, 7227–7235. doi: 10.1039/C4DT00200H

Cotter, D., Dodder, S., Klimkowski, V. J., and Hopkins, T. A. (2019). Circularly polarized luminescence of Sm (III) and Eu (III) complexes with chiral ligand (R/S)-BINAPO. *Chirality* 31, 301–311. doi: 10.1002/chir.23056

Coughlin, F. J., Westrol, M. S., Oyler, K. D., Byrne, N., Kraml, C., Zysman-Colman, E., et al. (2008). Synthesis, separation, and circularly polarized luminescence studies of enantiomers of iridium(III) luminophores. *Inorg. Chem.* 47, 2039–2048. doi: 10.1021/ic701747j

Crassous, J. (2009). Chiral transfer in coordination complexes: towards molecular materials. *Chem. Soc. Rev.* 38, 830–845. doi: 10.1039/B806203J

Crassous, J. (2012). Transfer of chirality from ligands to metal centers: recent examples. *Chem. Commun.* 48, 9687–9695. doi: 10.1039/C2CC31542D

Dai, L., Lo, W.-S., Coates, I. D., Pal, R., and Law, G.-L. (2016). New class of bright and highly stable chiral cyclen europium complexes for circularly polarized luminescence applications. *Inorg. Chem.* 55, 9065–9070. doi: 10.1021/acs.inorgchem.6b01546

Dai, L., Zhang, J., Chen, Y., Mackenzie, L. E., Pal, R., and Law, G.-L. (2019). Synthesis of water-soluble chiral DOTA lanthanide complexes with predominantly twisted square antiprism isomers and circularly polarized luminescence. *Inorg. Chem.* 58, 12506–12510. doi: 10.1021/acs.inorgchem.9b01799

Dee, C., Zinna, F., Kitzmann, W. R., Pescitelli, G., Heinze, K., Di Bari, L., et al. (2019). Strong circularly polarized luminescence of an octahedral chromium(iii) complex. *Chem. Commun.* 55, 13078–13081. doi: 10.1039/C9CC06909G

Deng, M., Mukthar, N. F. M., Schley, N. D., and Ung, G. (2020). Yellow circularly polarized luminescence from C1-symmetrical copper(I) complexes. *Angew. Chem. Int. Ed.* 59, 1228–1231. doi: 10.1002/anie.201913672

Dhbaibi, K., Favereau, L., and Crassous, J. (2019). Enantioenriched helicenes and helicenoids containing main-group elements (B, Si, N, P). *Chem. Rev.* 119, 8846–8953. doi: 10.1021/acs.chemrev.9b00033

Di Pietro, S., and Di Bari, L. (2012). The structure of MLn(hfbc)4 and a key to high circularly polarized luminescence. *Inorg. Chem.* 51, 12007–12014. doi: 10.1021/ic3018979

Dickins, R. S., Howard, J. A. K., Lehmann, C. W., Moloney, J., Parker, D., and Peacock, R. D. (1997). Structural rigidity and luminescence of chiral lanthanide tetraamide complexes based on 1,4,7,10-tetraazacyclododecane. *Angew. Chem. Int. Ed.* 36, 521–523. doi: 10.1002/anie.199705211

Dickins, R. S., Howard, J. A. K., Maupin, C. L., Moloney, J. M., Parker, D., Riehl, J. P., et al. (1999). Synthesis, time-resolved luminescence, NMR spectroscopy, circular dichroism and circularly polarised luminescence studies of enantiopure macrocyclic lanthanide tetraamide complexes. *Chem. Eur. J.* 5, 1095–1105. doi: 10.1002/(sici)1521-3765(19990301)5:3<1095::aid-chem1095>3.0.co;2-c

Doistau, B., Collet, G., Bolomey, E. A., Sadat-Noorbakhsh, V., Besnard, C., and Piguet, C. (2018). Heteroleptic ter–bidentate Cr(III) complexes as tunable optical sensitizers. *Inorg. Chem.* 57, 14362–14373. doi: 10.1021/acs.inorgchem.8b02530

Doistau, B., Jiménez, J.-R., Guerra, S., Besnard, C., and Piguet, C. (2020). Key strategy for the rational incorporation of long-lived NIR emissive Cr(III) chromophores into polymetallic architectures. *Inorg. Chem.* 59, 1424–1435. doi: 10.1021/acs.inorgchem.9b03163

Donnay, E. G., Schaeper, J. P., Brooksbank, R. D., Fox, J. L., Potts, R. G., Davidson, R. M., et al. (2007). Synthesis and characterization of tris(heteroleptic) diimine complexes of chromium(III). *Inorg. Chim. Acta* 360, 3272–3280. doi: 10.1016/j.ica.2007.03.055

Eliseeva, S. V., and Bünzli, J.-C. G. (2010). Lanthanide luminescence for functional materials and bio-sciences. *Chem. Soc. Rev.* 39, 189–227. doi: 10.1039/B905604C

Emeis, C. A., and Oosterhoff, L. J. (1967). Emission of circularly-polarised radiation by optically-active compounds. *Chem. Phys. Lett.* 1, 129–132. doi: 10.1016/0009-2614(67)85007-3

Feringa, B. L. (2007). The art of building small: from molecular switches to molecular motors. *J. Org. Chem.* 72, 6635–6652. doi: 10.1021/jo070394d

Feringa, B. L., van Delden, R. A., Koumura, N., and Geertsema, E. M. (2000). Chiroptical molecular switches. *Chem. Rev.* 100, 1789–1816. doi: 10.1021/cr9900228

Flamigni, L., Barbieri, A., Sabatini, C., Ventura, B., and Barigelletti, F. (2007). "Photochemistry and photophysics of coordination compounds: iridium," in *Photochemistry and Photophysics of Coordination Compounds II*, eds V. Balzani and S. Campagna (Berlin; Heidelberg: Springer Berlin Heidelberg), 143–203. doi: 10.1007/128_2007_131

Forster, L. S. (1990). The photophysics of chromium(III) complexes. *Chem. Rev.* 90, 331–353. doi: 10.1021/cr00100a001

Forster, L. S. (2002). Thermal relaxation in excited electronic states of d3 and d6 metal complexes. *Coord. Chem. Rev.* 227, 59–92. doi: 10.1016/S0010-8545(01)00458-1

Fu, H. L.-K., Po, C., He, H., Leung, S. Y.-L., Wong, K. S., and Yam, V. W.-W. (2016). Tuning of supramolecular architectures of l-valine-containing dicyanoplatinum(II) 2,2′-bipyridine complexes by metal–metal, π-π stacking, and hydrogen-bonding interactions. *Chem. Eur. J.* 22, 11826–11836. doi: 10.1002/chem.201601983

Fucaloro, A. F., Forster, L. S., Rund, J. V., and Lin, S. H. (1983). 2E relaxation in mixed-ligand Cr(NH3)6-nXn complexes. *J. Phys. Chem.* 87, 1796–1799. doi: 10.1021/j100233a028

Gálico, D. A., Marin, R., Brunet, G., Errulat, D., Hemmer, E., Sigoli, F. A., et al. (2019). Triplet-state position and crystal-field tuning in opto-magnetic lanthanide complexes: two sides of the same coin. *Chem. Eur. J.* 25, 14625–14637. doi: 10.1002/chem.201902837

Gao, X., Qin, X., Yang, X., Li, Y., and Duan, P. (2019). (R)-Binaphthyl derivatives as chiral dopants: substituent position controlled circularly polarized luminescence in liquid crystals. *Chem. Commun.* 55, 5914–5917. doi: 10.1039/C9CC02253H

Gauthier, E. S., Abella, L., Hellou, N., Darquié, B., Caytan, E., Roisnel, T., et al. (2020). Long-lived circularly polarized phosphorescence in helicene-NHC rhenium(i) complexes: the influence of helicene, halogen, and stereochemistry on emission properties. *Angew. Chem. Int. Ed.* 59, 8394–8400. doi: 10.1002/ange.2020023878394

Gendron, F., Moore Ii, B., Cador, O., Pointillart, F., Autschbach, J., and Le Guennic, B. (2019). *Ab initio* study of circular dichroism and circularly polarized luminescence of spin-allowed and spin-forbidden transitions: from organic ketones to lanthanide complexes. *J. Chem. Theory Comput.* 15, 4140–4155. doi: 10.1021/acs.jctc.9b00286

Geng, Y., Trajkovska, A., Culligan, S. W., Ou, J. J., Chen, H. M. P., Katsis, D., et al. (2003). Origin of strong chiroptical activities in films of nonafluorenes with a varying extent of pendant chirality. *J. Am. Chem. Soc.* 125, 14032–14038. doi: 10.1021/ja037733e

Gilot, J., Abbel, R., Lakhwani, G., Meijer, E. W., Schenning, A. P. H. J., and Meskers, S. C. J. (2010). Polymer photovoltaic cells sensitive to the circular polarization of light. *Adv. Mater.* 22, E131–E134. doi: 10.1002/adma.200903995

Golesorkhi, B., Guénée, L., Nozary, H., Fürstenberg, A., Suffren, Y., Eliseeva, S. V., et al. (2018). Thermodynamic programming of erbium(III) coordination complexes for dual visible/near-infrared luminescence. *Chem. Eur. J.* 24, 13158–13169. doi: 10.1002/chem.201802277

Górecki, M., Carpita, L., Arrico, L., Zinna, F., and Di Bari, L. (2018). Chiroptical methods in a wide wavelength range for obtaining Ln3+ complexes with circularly polarized luminescence of practical interest. *Dalton Trans.* 47, 7166–7177. doi: 10.1039/C8DT00865E

Goto, H. (2018). Liquid crystal auto-induction and amplification function for circularly polarized luminescence (CPL) with high gem-value, and dynamically controllable CPL devices. *Mol. Cryst. Liq. Cryst.* 669, 27–35. doi: 10.1080/15421406.2019.1569355

Gregolinski, J., Starynowicz, P., Hua, K. T., Lunkley, J. L., Muller, G., and Lisowski, J. (2008). Helical lanthanide(III) complexes with chiral nonaaza macrocycle. *J. Am. Chem. Soc.* 130, 17761–17773. doi: 10.1021/ja805033j

Guerchais, V., and Fillaut, J.-L. (2011). Sensory luminescent iridium(III) and platinum(II) complexes for cation recognition. *Coord. Chem. Rev.* 255, 2448–2457. doi: 10.1016/j.ccr.2011.04.006

Gunde, K. E., Credi, A., Jandrasics, E., von Zelewsky, A., and Richardson, F. S. (1997). Chiroptical absorption and luminescence spectra of a dissymmetric osmium(II)–polypyridyl complex containing an optically active bis(bipyridine)-type ligand of well-defined structural chirality. *Inorg. Chem.* 36, 426–434. doi: 10.1021/ic9609012

Han, J., Duan, P., Li, X., and Liu, M. (2017a). Amplification of circularly polarized luminescence through triplet–triplet annihilation-based photon upconversion. *J. Am. Chem. Soc.* 139, 9783–9786. doi: 10.1021/jacs.7b04611

Han, J., Guo, S., Lu, H., Liu, S., Zhao, Q., and Huang, W. (2018). Recent progress on circularly polarized luminescent materials for organic optoelectronic devices. *Adv. Opt. Mater.* 6:1800538. doi: 10.1002/adom.201800538

Han, J., Guo, S., Wang, J., Wei, L., Zhuang, Y., Liu, S., et al. (2017b). Circularly polarized phosphorescent electroluminescence from chiral cationic iridium(III) isocyanide complexes. *Adv. Opt. Mater.* 5:1700359. doi: 10.1002/adom.201700359

Harada, T., Nakano, Y., Fujiki, M., Naito, M., Kawai, T., and Hasegawa, Y. (2009). Circularly polarized luminescence of Eu(III) complexes with point- and axis-chiral ligands dependent on coordination structures. *Inorg. Chem.* 48, 11242–11250. doi: 10.1021/ic901663w

Hasenknopf, B., Micoine, K., Lacôte, E., Thorimbert, S., Malacria, M., and Thouvenot, R. (2008). Chirality in polyoxometalate chemistry. *Eur. J. Inorg. Chem.* 2008, 5001–5013. doi: 10.1002/ejic.200800759

Hellou, N., Srebro-Hooper, M., Favereau, L., Zinna, F., Caytan, E., Toupet, L., et al. (2017). Enantiopure cycloiridiated complexes bearing a pentahelicenic N-heterocyclic carbene and displaying long-lived circularly polarized phosphorescence. *Angew. Chem. Int. Ed.* 56, 8236–8239. doi: 10.1002/anie.201704263

Hembury, G. A., Borovkov, V. V., and Inoue, Y. (2008). Chirality-sensing supramolecular systems. *Chem. Rev.* 108, 1–73. doi: 10.1021/cr050005k

Herren, M., Horikoshi, H., and Morita, M. (1996). Photoluminescence of enantio-selectively formed chromium(III) double salts. *Mol. Cryst. Liq. Cryst. Sci. Technol. A* 286, 251–256. doi: 10.1080/10587259608042294

Hilmes, G. L., Brittain, H. G., and Richardson, F. S. (1977). Optical activity of the 4A2.tautm. 2E transition in chromium(en)33+. *Inorg. Chem.* 16, 528–533. doi: 10.1021/ic50169a005

Huck, N. P. M., Jager, W. F., de Lange, B., and Feringa, B. L. (1996). Dynamic control and amplification of molecular chirality by circular polarized light. *Science* 273, 1686–1688. doi: 10.1126/science.273.5282.1686

Ikeda, T., Hirano, K., and Haino, T. (2018). A circularly polarized luminescent organogel based on a Pt(ii) complex possessing phenylisoxazoles. *Mater. Chem. Front.* 2, 468–474. doi: 10.1039/C7QM00564D

Ikeda, T., Takayama, M., Kumar, J., Kawai, T., and Haino, T. (2015). Novel helical assembly of a Pt(ii) phenylbipyridine complex directed by metal–metal interaction and aggregation-induced circularly polarized emission. *Dalton Trans.* 44, 13156–13162. doi: 10.1039/C5DT01284H

Ionescu, A., Godbert, N., Ricciardi, L., La Deda, M., Aiello, I., Ghedini, M., et al. (2017). Luminescent water-soluble cycloplatinated complexes: structural, photophysical, electrochemical and chiroptical properties. *Inorg. Chim. Acta* 461, 267–274. doi: 10.1016/j.ica.2017.02.026

Isaacs, M., Sykes, A. G., and Ronco, S. (2006). Synthesis, characterization and photophysical properties of mixed ligand tris(polypyridyl)chromium(III) complexes, $[Cr(phen)2L]^{3+}$. *Inorg. Chim. Acta* 359, 3847–3854. doi: 10.1016/j.ica.2006.04.036

Isla, H., and Crassous, J. (2016). Helicene-based chiroptical switches. *C. R. Chim.* 19, 39–49. doi: 10.1016/j.crci.2015.06.014

Isla, H., Srebro-Hooper, M., Jean, M., Vanthuyne, N., Roisnel, T., Lunkley, J. L., et al. (2016). Conformational changes and chiroptical switching of enantiopure bis-helicenic terpyridine upon Zn^{2+} binding. *Chem. Commun.* 52, 5932–5935. doi: 10.1039/C6CC01748G

Ito, H., Sakai, H., Okayasu, Y., Yuasa, J., Mori, T., and Hasobe, T. (2018). Significant enhancement of absorption and luminescence dissymmetry factors in the far-red region: a zinc(II) homoleptic helicate formed by a

pair of achiral dipyrromethene ligands. *Chem. Eur. J.* 24, 16889–16894. doi: 10.1002/chem.201804171

Jamieson, E. M. G., Modicom, F., and Goldup, S. M. (2018). Chirality in rotaxanes and catenanes. *Chem. Soc. Rev.* 47, 5266–5311. doi: 10.1039/C8CS00097B

Jamieson, M. A., Serpone, N., and Hoffman, M. Z. (1981). Advances in the photochemistry and photophysics of chromium(iii) polypyridyl complexes in fluid media. *Coord. Chem. Rev.* 39, 121–179. doi: 10.1016/S0010-8545(00)80513-5

Jiménez, J.-R., Doistau, B., Besnard, C., and Piguet, C. (2018). Versatile heteroleptic bis-terdentate Cr(iii) chromophores displaying room temperature millisecond excited state lifetimes. *Chem. Commun.* 54, 13228–13231. doi: 10.1039/C8CC07671E

Jiménez, J.-R., Doistau, B., Cruz, C. M., Besnard, C., Cuerva, J. M., Campaña, A. G., et al. (2019). Chiral molecular ruby $[Cr(dqp)_2]^{3+}$ with long-lived circularly polarized luminescence. *J. Am. Chem. Soc.* 141, 13244–13252. doi: 10.1021/jacs.9b06524

Kapturkiewicz, A. (2016). Cyclometalated iridium(III) chelates—a new exceptional class of the electrochemiluminescent luminophores. *Anal. Bioanal. Chem.* 408, 7013–7033. doi: 10.1007/s00216-016-9615-8

Kim, B.-C., Choi, H.-J., Lee, J.-J., Araoka, F., and Choi, S.-W. (2019). Circularly polarized luminescence induced by chiral super nanospaces. *Adv. Funct. Mater.* 29:1903246. doi: 10.1002/adfm.201903246

Kirk, A. D. (1981). Chromium(iii) photochemistry and photophysics. *Coord. Chem. Rev.* 39, 225–263. doi: 10.1016/S0010-8545(00)80515-9

Kirk, A. D. (1999). Photochemistry and photophysics of chromium(III) complexes. *Chem. Rev.* 99, 1607–1640. doi: 10.1021/cr960111

Kitchen, J. A., Barry, D. E., Mercs, L., Albrecht, M., Peacock, R. D., and Gunnlaugsson, T. (2012). Circularly polarized lanthanide luminescence from langmuir–blodgett films formed from optically active and amphiphilic euiii-based self-assembly complexes. *Angew. Chem. Int. Ed.* 51, 704–708. doi: 10.1002/anie.201106863

Knof, U., and von Zelewsky, A. (1999). Predetermined chirality at metal centers. *Angew. Chem. Int. Ed.* 38, 302–322. doi: 10.1002/(sici)1521-3773(19990201)38:3<302::aid-anie302>3.0.co;2-g

Kögel, J. F., Kusaka, S., Sakamoto, R., Iwashima, T., Tsuchiya, M., Toyoda, R., et al. (2016). Heteroleptic [bis(oxazoline)](dipyrrinato)zinc(II) complexes: bright and circularly polarized luminescence from an originally achiral dipyrrinato ligand. *Angew. Chem. Int. Ed.* 55, 1377–1381. doi: 10.1002/anie.201509411

Kono, Y., Hara, N., Shizuma, M., Fujiki, M., and Imai, Y. (2017). Complexes of Eu(iii)(hfa)3 with a planar chiral P(iii) ligand (phanephos): solvent-sensitive sign inversion of circularly polarised luminescence. *Dalton Trans.* 46, 5170–5174. doi: 10.1039/C7DT00741H

Kotova, O., Kitchen, J. A., Lincheneau, C., Peacock, R. D., and Gunnlaugsson, T. (2013). Probing the effects of ligand isomerism in chiral luminescent lanthanide supramolecular self-assemblies: a europium "trinity sliotar" study. *Chem. Eur. J.* 19, 16181–16186. doi: 10.1002/chem.201303660

Kreidt, E., Arrico, L., Zinna, F., Di Bari, L., and Seitz, M. (2018). Circularly polarised luminescence in enantiopure samarium and europium cryptates. *Chem. Eur. J.* 24, 13556–13564. doi: 10.1002/chem.201802196

Kreidt, E., Dee, C., and Seitz, M. (2017). Chiral resolution of lanthanoid cryptates with extreme configurational stability. *Inorg. Chem.* 56, 8752–8754. doi: 10.1021/acs.inorgchem.7b01407

Kudernac, T., Ruangsupapichat, N., Parschau, M., Maciá, B., Katsonis, N., Harutyunyan, S. R., et al. (2011). Electrically driven directional motion of a four-wheeled molecule on a metal surface. *Nature* 479, 208–211. doi: 10.1038/nature10587

Kumar, J., Kawai, T., and Nakashima, T. (2017). Circularly polarized luminescence in chiral silver nanoclusters. *Chem. Commun.* 53, 1269–1272. doi: 10.1039/C6CC09476G

Kumar, J., Nakashima, T., and Kawai, T. (2015). Circularly polarized luminescence in chiral molecules and supramolecular assemblies. *J. Phys. Chem. Lett.* 6, 3445–3452. doi: 10.1021/acs.jpclett.5b01452

Leigh, D. A., and Pérez, E. M. (2006). "Dynamic chirality: molecular shuttles and motors," in *Supramolecular Chirality*, eds M. Crego-Calama and D. N. Reinhoudt (Berlin; Heidelberg: Springer Berlin Heidelberg), 185–208. doi: 10.1007/128_039

Leonard, J. P., Jensen, P., McCabe, T., O'Brien, J. E., Peacock, R. D., Kruger, P. E., et al. (2007). Self-assembly of chiral luminescent lanthanide coordination bundles. *J. Am. Chem. Soc.* 129, 10986–10987. doi: 10.1021/ja073049e

Leonzio, M., Melchior, A., Faura, G., Tolazzi, M., Zinna, F., Di Bari, L., et al. (2017). Strongly circularly polarized emission from water-soluble Eu(III)- and Tb(III)-based complexes: a structural and spectroscopic study. *Inorg. Chem.* 56, 4413–4421. doi: 10.1021/acs.inorgchem.7b00430

Lever, A. B. P. (1984). *Inorganic Electronic Spectroscopy*. Weinheim: Elsevier.

Li, L.-P., Yao, S.-Y., Ou, Y.-L., Wei, L.-Q., and Ye, B.-H. (2017). Diastereoselective synthesis and photophysical properties of bis-cyclometalated Ir(III) stereoisomers with dual stereocenters. *Organometallics* 36, 3257–3265. doi: 10.1021/acs.organomet.7b00406

Li, T.-Y., Jing, Y.-M., Liu, X., Zhao, Y., Shi, L., Tang, Z., et al. (2015). Circularly polarised phosphorescent photoluminescence and electroluminescence of iridium complexes. *Sci. Rep.* 5:14912. doi: 10.1038/srep14912

Li, T.-Y., Zheng, Y.-X., and Zhou, Y.-H. (2016). Iridium(iii) phosphorescent complexes with dual stereogenic centers: single crystal, electronic circular dichroism evidence and circularly polarized luminescence properties. *Dalton Trans.* 45, 19234–19237. doi: 10.1039/C6DT04030F

Li, X., Hu, W., Wang, Y., Quan, Y., and Cheng, Y. (2019). Strong CPL of achiral AIE-active dyes induced by supramolecular self-assembly in chiral nematic liquid crystals (AIE-N*-LCs). *Chem. Commun.* 55, 5179–5182. doi: 10.1039/C9CC01678C

Li, X.-Z., Zhou, L.-P., Yan, L.-L., Yuan, D.-Q., Lin, C.-S., and Sun, Q.-F. (2017). Evolution of luminescent supramolecular lanthanide $M_{2n}L_{3n}$ complexes from helicates and tetrahedra to cubes. *J. Am. Chem. Soc.* 139, 8237–8244. doi: 10.1021/jacs.7b02764

Lincheneau, C., Destribats, C., Barry, D. E., Kitchen, J. A., Peacock, R. D., and Gunnlaugsson, T. (2011). Lanthanide directed self-assembly synthesis and photophysical evaluation of chiral Eu(iii) luminescent "half-helicates." *Dalton Trans.* 40, 12056–12059. doi: 10.1039/C1DT11225B

Liu, D., Zhou, Y., Zhang, Y., Li, H., Chen, P., Sun, W., et al. (2018). Chiral BINAPO-controlled diastereoselective self-assembly and circularly polarized luminescence in triple-stranded europium(III) podates. *Inorg. Chem.* 57, 8332–8337. doi: 10.1021/acs.inorgchem.8b00986

Liu, M., Zhang, L., and Wang, T. (2015). Supramolecular chirality in self-assembled systems. *Chem. Rev.* 115, 7304–7397. doi: 10.1021/cr500671p

Lo, K. K.-W., Li, S. P.-Y., and Zhang, K. Y. (2011). Development of luminescent iridium(iii) polypyridine complexes as chemical and biological probes. *New J. Chem.* 35, 265–287. doi: 10.1039/C0NJ00478B

Longhi, G., Castiglioni, E., Koshoubu, J., Mazzeo, G., and Abbate, S. (2016). Circularly polarized luminescence: a review of experimental and theoretical aspects. *Chirality* 28, 696–707. doi: 10.1002/chir.22647

Lu, G.-Z., Su, N., Li, Y., and Zheng, Y.-X. (2017). Efficient electroluminescence of platinum complexes containing pinene sterically hindered spacer. *J. Organomet. Chem.* 842, 39–46. doi: 10.1016/j.jorganchem.2017.05.011

Lunkley, J. L., Shirotani, D., Yamanari, K., Kaizaki, S., and Muller, G. (2008). Extraordinary circularly polarized luminescence activity exhibited by cesium tetrakis(3-heptafluoro-butylryl-(+)-camphorato) Eu(III) complexes in EtOH and $CHCl_3$ solutions. *J. Am. Chem. Soc.* 130, 13814–13815. doi: 10.1021/ja805681w

Lunkley, J. L., Shirotani, D., Yamanari, K., Kaizaki, S., and Muller, G. (2011). Chiroptical spectra of a series of tetrakis((+)-3-heptafluorobutylyrylcamphorato)lanthanide(III) with an encapsulated alkali metal ion: circularly polarized luminescence and absolute chiral structures for the Eu(III) and Sm(III) complexes. *Inorg. Chem.* 50, 12724–12732. doi: 10.1021/ic201851r

Macé, A., Hellou, N., Hammoud, J., Martin, C., Gauthier, E. S., Favereau, L., et al. (2019). An enantiopure cyclometallated iridium complex displaying long-lived phosphorescence both in solution and in the solid state. *Helv. Chim. Acta* 102:e1900044. doi: 10.1002/hlca.201900044

Madaras, J. S., and Brittain, H. G. (1980). Induced optical activity in the terbium(III) complex of pyridine-2, 6-dicarboxylic acid through association with resolved tris(ethylenediamine)chromium(III). *Inorg. Chem.* 19, 3841–3842. doi: 10.1021/ic50214a051

Maeda, C., Ogawa, K., Sadanaga, K., Takaishi, K., and Ema, T. (2019). Chiroptical and catalytic properties of doubly binaphthyl-strapped chiral porphyrins. *Chem. Commun.* 55, 1064–1067. doi: 10.1039/C8CC09114E

Malta, O. L., and Carlos, L. D. (2003). Intensities of 4f-4f transitions in glass materials. *Quim. Nova* 26, 889–895. doi: 10.1590/S0100-40422003000600018

Mamula, O., Lama, M., Stoeckli-Evans, H., and Shova, S. (2006). Switchable chiral architectures containing PrIII ions: an example of solvent-induced adaptive behavior. *Angew. Chem. Int. Ed.* 45, 4940–4944. doi: 10.1002/anie.200601939

Mamula, O., Lama, M., Telfer, S. G., Nakamura, A., Kuroda, R., Stoeckli-Evans, H., et al. (2005). A trinuclear euIII array within a diastereoselectively self-assembled helix formed by chiral bipyridine-carboxylate ligands. *Angew. Chem. Int. Ed.* 44, 2527–2531. doi: 10.1002/anie.200500094

Manguin, R., Pichon, D., Tarrieu, R., Vives, T., Roisnel, T., Dorcet, V., et al. (2019). A kinetic resolution strategy for the synthesis of chiral octahedral NHC–iridium(iii) catalysts. *Chem. Commun.* 55, 6058–6061. doi: 10.1039/C9CC02434D

Manson, N. B., and Shah, G. A. (1977). Coupling of T_{1u} and T_{2u} vibrations to the 2Eg to 4A2g transition in MgO:V^{2+} and MgO:Cr^{3+}. *J. Phys. C Solid State Phys.* 10, 1991–2003. doi: 10.1088/0022-3719/10/11/034

Mason, S. F. (1971). Optical rotatory power of co-ordination compounds. Part XV. Regional rules and electronic mechanisms for the optical activity of d→ d transitions. *J. Chem. Soc. A Inorg. Phys. Theor.* 1971, 667–676. doi: 10.1039/J19710000667

Mason, S. F., and Seal, R. H. (1975). Complementation of the crystal field for dihedral optical activity. *Chem. Commun.* 1975, 331–333. doi: 10.1039/C39750000331

Mason, S. F., and Seal, R. H. (1976). The optical activity of cobalt(III) chelate diamine complexes. *Mol. Phys.* 31, 755–775. doi: 10.1080/00268977600100581

Mateos-Timoneda, M. A., Crego-Calama, M., and Reinhoudt, D. N. (2004). Supramolecular chirality of self-assembled systems in solution. *Chem. Soc. Rev.* 33, 363–372. doi: 10.1039/B305550G

Maupin, C. L., Dickins, R. S., Govenlock, L. G., Mathieu, C. E., Parker, D., Williams, J. A. G., et al. (2000). The measurement of circular polarization in the near-IR luminescence from chiral complexes of Yb(III) and Nd(III). *J. Phys. Chem. A* 104, 6709–6717. doi: 10.1021/jp000648y

Maupin, C. L., Parker, D., Williams, J. A. G., and Riehl, J. P. (1998). Circularly polarized luminescence from chiral octadentate complexes of Yb(III) in the near-infrared. *J. Am. Chem. Soc.* 120, 10563–10564. doi: 10.1021/ja982147k

Mazzeo, G., Fusè, M., Longhi, G., Rimoldi, I., Cesarotti, E., Crispini, A., et al. (2016). Vibrational circular dichroism and chiroptical properties of chiral Ir(iii) luminescent complexes. *Dalton Trans.* 45, 992–999. doi: 10.1039/C5DT03642A

Metcalf, D. H., and Richardson, F. S. (1994). The determination of chiroptical dissymmetry factors and electric-vs. magnetic-dipole transition amplitude ratios from circularly polarized excitation and emission measurements on racemic Eu(dpa)$^{33-}$ in aqueous solution. *J. Alloys Compd.* 207–208, 59–61. doi: 10.1016/0925-8388(94)90176-7

Metcalf, D. H., Snyder, S. W., Demas, J. N., and Richardson, F. S. (1990). Excited-state racemization kinetics and chiroptical activity of a labile metal complex in aqueous solution. Time-resolved circularly polarized luminescence study of tris(dipicolinato)europate (3-) in water and deuterium oxide. *J. Am. Chem. Soc.* 112, 469–479. doi: 10.1021/ja00158a001

Mori, K. (2011). Bioactive natural products and chirality. *Chirality* 23, 449–462. doi: 10.1002/chir.20930

Morita, M., Eguchi, K., Shishikura, M., Nishikawa, H., and Inoue, M. (1984). Circularly polarized luminescense of (-)D-[Cr(R-pn)$_3$]$^{3+}$ and related chiral chromium (III) complexes using a microcomputer-based digital spectrophotometer system. *J. Lumin.* 31–32, 558–560. doi: 10.1016/0022-2313(84)90059-0

Morita, M., Herren, M., Ansai, T., and Rau, D. (2000). Excited-state chiral discrimination of Tb(III) complexes of (S,S′)- and (R,R′)-ethylenediamine-*N*, *N*′-disuccinic acid in circularly polarized luminescence and luminescence decay profiles. *J. Lumin.* 87–89, 976–979. doi: 10.1016/S0022-2313(99)00498-6

Muller, G., Bünzli, J.-C. G., Riehl, J. P., Suhr, D., Zelewsky, A. v., and Mürner, H. (2002). First diastereoselective formation of lanthanide triple helical complexes with a terdentate chiral C2 symmetric ligand. *Chem. Commun.* 2002, 1522–1523. doi: 10.1039/B203691F

Neil, E. R., Fox, M. A., Pal, R., and Parker, D. (2016). Induced europium CPL for the selective signalling of phosphorylated amino-acids and O-phosphorylated hexapeptides. *Dalton Trans.* 45, 8355–8366. doi: 10.1039/C6DT01212D

Nobuhiro, A., Shinjiro, M., and Kazuyuki, H. (2001). Chirooptical control of liquid crystalline textures containing chromium complex by irradiation of circular polarized light. *Chem. Lett.* 30, 888–889. doi: 10.1246/cl.2001.888

Otto, S., Dorn, M., Förster, C., Bauer, M., Seitz, M., and Heinze, K. (2018). Understanding and exploiting long-lived near-infrared emission of a molecular ruby. *Coord. Chem. Rev.* 359, 102–111. doi: 10.1016/j.ccr.2018.01.004

Otto, S., Grabolle, M., Förster, C., Kreitner, C., Resch-Genger, U., and Heinze, K. (2015). [Cr(ddpd)$_2$]$^{3+}$: a molecular, water-soluble, highly NIR-emissive ruby analogue. *Angew. Chem. Int. Ed.* 54, 11572–11576. doi: 10.1002/anie.201504894

Oyler, K. D., Coughlin, F. J., and Bernhard, S. (2007). Controlling the helicity of 2,2′-bipyridyl ruthenium(II) and zinc(II) hemicage complexes. *J. Am. Chem. Soc.* 129, 210–217. doi: 10.1021/ja067016v

Park, G., Kim, H., Yang, H., Park, K. R., Song, I., Oh, J. H., et al. (2019). Amplified circularly polarized phosphorescence from co-assemblies of platinum(ii) complexes. *Chem. Sci.* 10, 1294–1301. doi: 10.1039/C8SC04509G

Parker, D., Dickins, R. S., Puschmann, H., Crossland, C., and Howard, J. A. K. (2002). Being excited by lanthanide coordination complexes: aqua species, chirality, excited-state chemistry, and exchange dynamics. *Chem. Rev.* 102, 1977–2010. doi: 10.1021/cr010452

Perkovic, M. W., Heeg, M. J., and Endicott, J. F. (1991). Stereochemical perturbations of the relaxation behavior of (2E)chromium(III). Ground-state x-ray crystal structure, photophysics, and molecular mechanics simulations of the quasi-cage complex [4,4′,4″-ethylidynetris(3-azabutan-1-amine)]chromium tribromide. *Inorg. Chem.* 30, 3140–3147. doi: 10.1021/ic00016a009

Pescitelli, G., Di Bari, L., and Berova, N. (2011). Conformational aspects in the studies of organic compounds by electronic circular dichroism. *Chem. Soc. Rev.* 40, 4603–4625. doi: 10.1039/C1CS15036G

Pescitelli, G., Di Bari, L., and Berova, N. (2014). Application of electronic circular dichroism in the study of supramolecular systems. *Chem. Soc. Rev.* 43, 5211–5233. doi: 10.1039/C4CS00104D

Petoud, S., Muller, G., Moore, E. G., Xu, J., Sokolnicki, J., Riehl, J. P., et al. (2007). Brilliant Sm, Eu, Tb, and Dy chiral lanthanide complexes with strong circularly polarized luminescence. *J. Am. Chem. Soc.* 129, 77–83. doi: 10.1021/ja064902x

Ranganathan, R. S., Pillai, R. K., Raju, N., Fan, H., Nguyen, H., Tweedle, M. F., et al. (2002). Polymethylated DOTA ligands. 1. Synthesis of rigidified ligands and studies on the effects of alkyl substitution on acid–base properties and conformational mobility. *Inorg. Chem.* 41, 6846–6855. doi: 10.1021/ic025657v

Reiné, P., Justicia, J., Morcillo, S. P., Abbate, S., Vaz, B., Ribagorda, M., et al. (2018a). Pyrene-containing ortho-oligo(phenylene)ethynylene foldamer as a ratiometric probe based on circularly polarized luminescence. *J. Org. Chem.* 83, 4455–4463. doi: 10.1021/acs.joc.8b00162

Reiné, P., Ortuño, A. M., Resa, S., Álvarez de Cienfuegos, L., Blanco, V., Ruedas-Rama, M. J., et al. (2018b). OFF/ON switching of circularly polarized luminescence by oxophilic interaction of homochiral sulfoxide-containing o-OPEs with metal cations. *Chem. Commun.* 54, 13985–13988. doi: 10.1039/C8CC08395A

Resa, S., Miguel, D., Guisán-Ceinos, S., Mazzeo, G., Choquesillo-Lazarte, D., Abbate, S., et al. (2018). Sulfoxide-induced homochiral folding of ortho-phenylene ethynylenes (o-OPEs) by silver(I) templating: structure and chiroptical properties. *Chem. Eur. J.* 24, 2653–2662. doi: 10.1002/chem.201704897

Réthoré, C., Avarvari, N., Canadell, E., Auban-Senzier, P., and Fourmigué, M. (2005). Chiral molecular metals: syntheses, structures, and properties of the AsF6-salts of racemic (±)-, (R)-, and (S)-tetrathiafulvalene–oxazoline derivatives. *J. Am. Chem. Soc.* 127, 5748–5749. doi: 10.1021/ja0503884

Richardson, F. S. (1971). Optical activity of transition metal compounds. I. Sector rules for metal complexes of the pseudotetragonal class. *J. Chem. Phys.* 54, 2453–2468. doi: 10.1063/1.1675200

Richardson, F. S. (1979). Theory of optical activity in the ligand-field transitions of chiral transition metal complexes. *Chem. Rev.* 79, 17–36. doi: 10.1021/cr60317a003

Richardson, F. S. (1980). Selection rules for lanthanide optical activity. *Inorg. Chem.* 19, 2806–2812. doi: 10.1021/ic50211a063

Rickhaus, M., Mayor, M., and Juríček, M. (2017). Chirality in curved polyaromatic systems. *Chem. Soc. Rev.* 46, 1643–1660. doi: 10.1039/C6CS00623J

Riehl, J. P., and Muller, G. (2004). "Circularly polarized luminescence spectroscopy from lanthanide systems," in Handbook on the Physics and Chemistry of Rare

Earths, Vol. 34, eds K. A. Gschneidner, J.-C. Bunzli, and V. Pecharsky (North Holland: Elsevier), 289–357. doi: 10.1016/S0168-1273(04)34003-1

Riehl, J. P., and Richardson, F. S. (1986). Circularly polarized luminescence spectroscopy. *Chem. Rev.* 86, 1–16. doi: 10.1021/cr00071a001

Rikken, G. L. J. A., and Raupach, E. (1997). Observation of magneto-chiral dichroism. *Nature* 390, 493–494. doi: 10.1038/37323

Roose, J., Tang, B. Z., and Wong, K. S. (2016). Circularly-polarized luminescence (CPL) from chiral AIE molecules and macrostructures. *Small* 12, 6495–6512. doi: 10.1002/smll.201601455

Ryu, C. K., and Endicott, J. F. (1988). Synthesis, spectroscopy, and photophysical behavior of mixed-ligand mono- and bis(polypyridyl)chromium(III) complexes. Examples of efficient, thermally activated excited-state relaxation without back intersystem crossing. *Inorg. Chem.* 27, 2203–2214. doi: 10.1021/ic00286a002

Saleh, N., Moore II, B., Srebro, M., Vanthuyne, N., Toupet, L., Williams, J. A. G., et al. (2015a). Acid/base-triggered switching of circularly polarized luminescence and electronic circular dichroism in organic and organometallic helicenes. *Chem. Eur. J.* 21, 1673–1681. doi: 10.1002/chem.201405176

Saleh, N., Srebro, M., Reynaldo, T., Vanthuyne, N., Toupet, L., Chang, V. Y., et al. (2015b). Enantio-enriched CPL-active helicene–bipyridine–rhenium complexes. *Chem. Commun.* 51, 3754–3757. doi: 10.1039/C5CC00453E

Sánchez-Carnerero, E. M., Agarrabeitia, A. R., Moreno, F., Maroto, B. L., Muller, G., Ortiz, M. J., et al. (2015). Circularly polarized luminescence from simple organic molecules. *Chem. Eur. J.* 21, 13488–13500. doi: 10.1002/chem.201501178

Sang, Y., Han, J., Zhao, T., Duan, P., and Liu, M. (2019). Circularly polarized luminescence in nanoassemblies: generation, amplification, and application. *Adv. Mater.* 2019:1900110. doi: 10.1002/adma.201900110

Sato, S., Yoshii, A., Takahashi, S., Furumi, S., Takeuchi, M., and Isobe, H. (2017). Chiral intertwined spirals and magnetic transition dipole moments dictated by cylinder helicity. *Proc. Natl. Acad. Sci. U.S.A.* 114, 13097–13101. doi: 10.1073/pnas.1717524114

Sawada, Y., Furumi, S., Takai, A., Takeuchi, M., Noguchi, K., and Tanaka, K. (2012). Rhodium-catalyzed enantioselective synthesis, crystal structures, and photophysical properties of helically chiral 1,1′-bitriphenylenes. *J. Am. Chem. Soc.* 134, 4080–4083. doi: 10.1021/ja300278e

Scarborough, C. C., Lancaster, K. M., DeBeer, S., Weyhermüller, T., Sproules, S., and Wieghardt, K. (2012). Experimental fingerprints for redox-active terpyridine in $[Cr(tpy)_2](PF6)_n$ ($n = 3–0$), and the Remarkable Electronic Structure of $[Cr(tpy)_2]^{1-}$. *Inorg. Chem.* 51, 3718–3732. doi: 10.1021/ic2027219

Schaffner-Hamann, C., von Zelewsky, A., Barbieri, A., Barigelletti, F., Muller, G., Riehl, J. P., et al. (2004). Diastereoselective formation of chiral tris-cyclometalated iridium (III) complexes: characterization and photophysical properties. *J. Am. Chem. Soc.* 126, 9339–9348. doi: 10.1021/ja048655d

Schellman, J. A. (1975). Circular dichroism and optical rotation. *Chem. Rev.* 75, 323–331. doi: 10.1021/cr60295a004

Schönle, J., Constable, E. C., Housecroft, C. E., and Neuburger, M. (2015a). Tuning peripheral π-stacking motifs in $\{Cr(tpy)_2\}^3$ + domains (tpy = 2,2′:6′,2″-terpyridine). *Inorg. Chem. Commun.* 53, 80–83. doi: 10.1016/j.inoche.2015.01.014

Schönle, J., Constable, E. C., Housecroft, C. E., Prescimone, A., and Zampese, J. A. (2015b). Homoleptic and heteroleptic complexes of chromium(III) containing 4′-diphenylamino-2,2′:6′,2″-terpyridine ligands. *Polyhedron* 89, 182–188. doi: 10.1016/j.poly.2015.01.015

Schulte, T. R., Holstein, J. J., Krause, L., Michel, R., Stalke, D., Sakuda, E., et al. (2017). Chiral-at-metal phosphorescent square-planar Pt(II)-complexes from an achiral organometallic ligand. *J. Am. Chem. Soc.* 139, 6863–6866. doi: 10.1021/jacs.7b03963

Seeber, G., Tiedemann, B. E. F., and Raymond, K. N. (2006). "Supramolecular chirality in coordination chemistry," in *Supramolecular Chirality*, eds M. Crego-Calama and D. N. Reinhoudt (Berlin; Heidelberg: Springer Berlin Heidelberg), 147–183. doi: 10.1007/128_033

Serpone, N., Jamieson, M. A., Henry, M. S., Hoffman, M. Z., Bolletta, F., and Maestri, M. (1979). Excited-state behavior of polypyridyl complexes of chromium(III). *J. Am. Chem. Soc.* 101, 2907–2916. doi: 10.1021/ja00505a019

Seyler, K. L., Zhong, D., Klein, D. R., Gao, S., Zhang, X., Huang, B., et al. (2018). Ligand-field helical luminescence in a 2D ferromagnetic insulator. *Nat. Phys.* 14, 277–281. doi: 10.1038/s41567-017-0006-7

Shen, C., Anger, E., Srebro, M., Vanthuyne, N., Deol, K. K., Jefferson, T. D., et al. (2014). Straightforward access to mono- and bis-cycloplatinated helicenes displaying circularly polarized phosphorescence by using crystallization resolution methods. *Chem. Sci.* 5, 1915–1927. doi: 10.1039/C3SC53442A

Sheng, Y., Ma, J., Liu, S., Wang, Y., Zhu, C., and Cheng, Y. (2016). Strong and reversible circularly polarized luminescence emission of a chiral 1,8-naphthalimide fluorophore induced by excimer emission and orderly aggregation. *Chem. Eur. J.* 22, 9519–9522. doi: 10.1002/chem.201600891

Shi, L., Zhu, L., Guo, J., Zhang, L., Shi, Y., Zhang, Y., et al. (2017). Self-assembly of chiral gold clusters into crystalline nanocubes of exceptional optical activity. *Angew. Chem. Int. Ed.* 56, 15397–15401. doi: 10.1002/anie.201709827

Song, F., Xu, Z., Zhang, Q., Zhao, Z., Zhang, H., Zhao, W., et al. (2018). Highly efficient circularly polarized electroluminescence from aggregation-induced emission luminogens with amplified chirality and delayed fluorescence. *Adv. Funct. Mater.* 28:1800051. doi: 10.1002/adfm.201800051

Song, J., Wang, M., Xu, X., Qu, L., Zhou, X., and Xiang, H. (2019). 1D-helical platinum(ii) complexes bearing metal-induced chirality, aggregation-induced red phosphorescence, and circularly polarized luminescence. *Dalton Trans.* 48, 4420–4428. doi: 10.1039/C8DT03615B

Song, J., Wang, M., Zhou, X., and Xiang, H. (2018). Unusual circularly polarized and aggregation-induced near-infrared phosphorescence of helical platinum(II) complexes with tetradentate salen ligands. *Chem. Eur. J.* 24, 7128–7132. doi: 10.1002/chem.201801414

Sprafke, J. K., Kondratuk, D. V., Wykes, M., Thompson, A. L., Hoffmann, M., Drevinskas, R., et al. (2011). Belt-shaped π-systems: relating geometry to electronic structure in a six-porphyrin nanoring. *J. Am. Chem. Soc.* 133, 17262–17273. doi: 10.1021/ja2045919

Stomeo, F., Lincheneau, C., Leonard, J. P., O'Brien, J. E., Peacock, R. D., McCoy, C. P., et al. (2009). Metal-directed synthesis of enantiomerially pure dimetallic lanthanide luminescent triple-stranded helicates. *J. Am. Chem. Soc.* 131, 9636–9637. doi: 10.1021/ja9032204

Strickland, R. W., and Richardson, F. S. (1976). Optical activity of d-d transitions in copper(II) complexes of amino acids, dipeptides, and tripeptides. Dynamical coupling model. *J. Phys. Chem.* 80, 164–173. doi: 10.1021/j100543a017

Tamayo, A. B., Alleyne, B. D., Djurovich, P. I., Lamansky, S., Tsyba, I., Ho, N. N., et al. (2003). Synthesis and characterization of facial and meridional tris-cyclometalated iridium(III) complexes. *J. Am. Chem. Soc.* 125, 7377–7387. doi: 10.1021/ja034537z

Tanaka, H., Ikenosako, M., Kato, Y., Fujiki, M., Inoue, Y., and Mori, T. (2018b). Symmetry-based rational design for boosting chiroptical responses. *Commun. Chem.* 1:38. doi: 10.1038/s42004-018-0035-x

Tanaka, H., Inoue, Y., and Mori, T. (2018a). Circularly polarized luminescence and circular dichroisms in small organic molecules: correlation between excitation and emission dissymmetry factors. *ChemPhotoChem* 2, 386–402. doi: 10.1002/cptc.201800015

Tanaka, H., Kato, Y., Fujiki, M., Inoue, Y., and Mori, T. (2018c). Combined experimental and theoretical study on circular dichroism and circularly polarized luminescence of configurationally robust D3-symmetric triple pentahelicene. *J. Phys. Chem. A* 122, 7378–7384. doi: 10.1021/acs.jpca.8b05247

Tanaka, S., Sato, K., Ichida, K., Abe, T., Tsubomura, T., Suzuki, T., et al. (2016). Circularly polarized luminescence of chiral Pt(pppb)Cl (pppbH=1-pyridyl-3-(4, 5-pinenopyridyl)benzene) aggregate in the excited state. *Chem. Asian J.* 11, 265–273. doi: 10.1002/asia.201500985

Tang, X.-L., Wang, W.-H., Dou, W., Jiang, J., Liu, W.-S., Qin, W.-W., et al. (2009). Olive-shaped chiral supramolecules: simultaneous self-assembly of heptameric lanthanum clusters and carbon dioxide fixation. *Angew. Chem. Int. Ed.* 48, 3499–3502. doi: 10.1002/anie.200900838

Tanner, P. A. (2013). Some misconceptions concerning the electronic spectra of tri-positive europium and cerium. *Chem. Soc. Rev.* 42, 5090–5101. doi: 10.1039/C3CS60033E

Taro, T., Iwao, O., and Makoto, M. (1991). Luminescence and circularly polarized luminescence of mononuclear and binuclear chromium(III) L-alaninato complexes. *Bull. Chem. Soc. Jpn.* 64, 2341–2348. doi: 10.1246/bcsj.64.2341

Tóth, É., Vauthey, S., Pubanz, D., and Merbach, A. E. (1996). Water exchange and rotational dynamics of the dimeric gadolinium(III) complex $[BO\{Gd(DO3A)(H_2O)\}^2]$: a variable-temperature and -pressure 17O NMR study 1. *Inorg. Chem.* 35, 3375–3379. doi: 10.1021/ic951492x

Train, C., Gruselle, M., and Verdaguer, M. (2011). The fruitful introduction of chirality and control of absolute configurations in molecular magnets. *Chem. Soc. Rev.* 40, 3297–3312. doi: 10.1039/C1CS15012J

Treiling, S., Wang, C., Förster, C., Reichenauer, F., Kalmbach, J., Boden, P., et al. (2019). Luminescence and light-driven energy and electron transfer from an exceptionally long-lived excited state of a non-innocent chromium(III) complex. *Angew. Chem. Int. Ed.* 58, 18075–18085. doi: 10.1002/anie.201909325

Tsubomura, T., Morita, M., and Ohkouchi, I. (1988). Luminescence of chronium(III) l-alaninato and other related complexes. *J. Lumin.* 40–41, 268–269. doi: 10.1016/0022-2313(88)90188-3

Uchida, T.-A., Nozaki, K., and Iwamura, M. (2016). Chiral sensing of various amino acids using induced circularly polarized luminescence from europium(III) complexes of phenanthroline dicarboxylic acid derivatives. *Chem. Asian J.* 11, 2415–2422. doi: 10.1002/asia.201600798

Usuki, T., Uchida, H., Omoto, K., Yamanoi, Y., Yamada, A., Iwamura, M., et al. (2019). Enhancement of the photofunction of phosphorescent Pt(II) cyclometalated complexes driven by substituents: solid-state luminescence and circularly polarized luminescence. *J. Org. Chem.* 84, 10749–10756. doi: 10.1021/acs.joc.9b01285

van Leeuwen, T., Lubbe, A. S., Štacko, P., Wezenberg, S. J., and Feringa, B. L. (2017). Dynamic control of function by light-driven molecular motors. *Nat. Rev. Chem.* 1:0096. doi: 10.1038/s41570-017-0096

Vandiver, M. S., Bridges, E. P., Koon, R. L., Kinnaird, A. N., Glaeser, J. W., Campbell, J. F., et al. (2010). Effect of ancillary ligands on the DNA interaction of $[Cr(diimine)_3]^{3+}$ complexes containing the intercalating dipyridophenazine ligand. *Inorg. Chem.* 49, 839–848. doi: 10.1021/ic9013619

Vasudevan, S., Smith, J. A., Wojdyla, M., McCabe, T., Fletcher, N. C., Quinn, S. J., et al. (2010). Substituted dipyridophenazine complexes of Cr(iii): synthesis, enantiomeric resolution and binding interactions with calf thymus DNA. *Dalton Trans.* 39, 3990–3998. doi: 10.1039/C000150C

Wada, S., Kitagawa, Y., Nakanishi, T., Gon, M., Tanaka, K., Fushimi, K., et al. (2018). Electronic chirality inversion of lanthanide complex induced by achiral molecules. *Sci. Rep.* 8:16395. doi: 10.1038/s41598-018-34790-0

Walton, J. W., Bari, L. D., Parker, D., Pescitelli, G., Puschmann, H., and Yufit, D. S. (2011). Structure, resolution and chiroptical analysis of stable lanthanide complexes of a pyridylphenylphosphinate triazacyclononane ligand. *Chem. Commun.* 47, 12289–12291. doi: 10.1039/C1CC14904K

Wang, C., Otto, S., Dorn, M., Kreidt, E., Lebon, J., Sršan, L., et al. (2017). Deuterated molecular ruby with record luminescence quantum yield. *Angew. Chem. Int. Ed.* 57, 1112–1116. doi: 10.1002/anie.201711350

Watanabe, K., and Akagi, K. (2014). Helically assembled π-conjugated polymers with circularly polarized luminescence. *Sci. Technol. Adv. Mater.* 15:044203. doi: 10.1088/1468-6996/15/4/044203

Woods, M., Kovacs, Z., Zhang, S., and Sherry, A. D. (2003). Towards the rational design of magnetic resonance imaging contrast agents: isolation of the two coordination isomers of lanthanide DOTA-type complexes. *Angew. Chem. Int. Ed.* 42, 5889–5892. doi: 10.1002/anie.200352234

Woody, R. W. (1995). Circular dichroism. *Methods Enzymol.* 246, 34–71. doi: 10.1016/0076-6879(95)46006-3

Wu, T., You, X.-Z., and Bour, P. (2015). Applications of chiroptical spectroscopy to coordination compounds. *Coord. Chem. Rev.* 284, 1–18. doi: 10.1016/j.ccr.2014.09.012

Yamaga, M., Marshall, A., O'Donnell, K. P., and Henderson, B. (1990). Polarized photoluminescence from Cr^{3+} ions in laser host crystals III. $ZnWO_4$. *J. Lumin.* 47, 65–70. doi: 10.1016/0022-2313(90)90060-O

Yan, L.-L., Tan, C.-H., Zhang, G.-L., Zhou, L.-P., Bünzli, J.-C., and Sun, Q.-F. (2015). Stereocontrolled self-assembly and self-sorting of luminescent europium tetrahedral cages. *J. Am. Chem. Soc.* 137, 8550–8555. doi: 10.1021/jacs.5b03972

Yan, Z.-P., Liao, K., Han, H.-B., Su, J., Zheng, Y.-X., and Zuo, J.-L. (2019a). Chiral iridium(iii) complexes with four-membered Ir–S–P–S chelating rings for high-performance circularly polarized OLEDs. *Chem. Commun.* 55, 8215–8218. doi: 10.1039/C9CC03915E

Yan, Z.-P., Luo, X.-F., Liao, K., Lin, Z.-X., Wu, Z.-G., Zhou, Y.-H., et al. (2018). The Taiji and Eight Trigrams chemistry philosophy of chiral iridium(iii) complexes with triplex stereogenic centers. *Dalton Trans.* 47, 4045–4048. doi: 10.1039/C8DT00264A

Yan, Z.-P., Luo, X.-F., Liu, W.-Q., Wu, Z.-G., Liang, X., Liao, K., et al. (2019b). Configurationally stable platinahelicene enantiomers for efficient circularly polarized phosphorescent organic light-emitting diodes. *Chem. Eur. J.* 25, 5672–5676. doi: 10.1002/chem.201900955

Yang, D., Han, J., Liu, M., and Duan, P. (2019). Photon upconverted circularly polarized luminescence via triplet–triplet annihilation. *Adv. Mater.* 31:1805683. doi: 10.1002/adma.201805683

Yang, L., Zelewsky, A. v., Nguyen, H. P., Muller, G., Labat, G., and Stoeckli-Evans, H. (2009). Stereoselective synthesis of cyclometalated iridium(III) complexes: characterization and photophysical properties. *Inorg. Chim. Acta* 362, 3853–3856. doi: 10.1016/j.ica.2008.10.011

Yang, X., Han, J., Wang, Y., and Duan, P. (2019). Photon-upconverting chiral liquid crystal: significantly amplified upconverted circularly polarized luminescence. *Chem. Sci.* 10, 172–178. doi: 10.1039/C8SC03806F

Yang, Y., da Costa, R. C., Fuchter, M. J., and Campbell, A. J. (2013). Circularly polarized light detection by a chiral organic semiconductor transistor. *Nat. Photon.* 7:634. doi: 10.1038/nphoton.2013.176

Yeung, C.-T., Yim, K.-H., Wong, H.-Y., Pal, R., Lo, W.-S., Yan, S.-C., et al. (2017). Chiral transcription in self-assembled tetrahedral Eu4L6 chiral cages displaying sizable circularly polarized luminescence. *Nat. Commun.* 8:1128. doi: 10.1038/s41467-017-01025-1

Zamora, A., Vigueras, G., Rodríguez, V., Santana, M. D., and Ruiz, J. (2018). Cyclometalated iridium(III) luminescent complexes in therapy and phototherapy. *Coord. Chem. Rev.* 360, 34–76. doi: 10.1016/j.ccr.2018.01.010

Zare, D., Doistau, B., Nozary, H., Besnard, C., Guenee, L., Suffren, Y., et al. (2017b). CrIII as an alternative to ruII in metallo-supramolecular chemistry. *Dalton Trans.* 46, 8992–9009. doi: 10.1039/C7DT01747B

Zare, D., Suffren, Y., Nozary, H., Hauser, A., and Piguet, C. (2017a). Controlling lanthanide exchange in triple-stranded helicates: a way to optimize molecular light-upconversion. *Angew. Chem. Int. Ed.* 56, 14612–14617. doi: 10.1002/anie.201709156

Zercher, B., and Hopkins, T. A. (2016). Induction of circularly polarized luminescence from europium by amino acid based ionic liquids. *Inorg. Chem.* 55, 10899–10906. doi: 10.1021/acs.inorgchem.6b01343

Zhang, G., Gil-Ramírez, G., Markevicius, A., Browne, C., Vitorica-Yrezabal, I. J., and Leigh, D. A. (2015). Lanthanide template synthesis of trefoil knots of single handedness. *J. Am. Chem. Soc.* 137, 10437–10442. doi: 10.1021/jacs.5b07069

Zhang, J., Liu, Q., Wu, W., Peng, J., Zhang, H., Song, F., et al. (2019). Real-time monitoring of hierarchical self-assembly and induction of circularly polarized luminescence from achiral luminogens. *ACS Nano* 13, 3618–3628. doi: 10.1021/acsnano.9b00218

Zhang, M.-M., Dong, X.-Y., Wang, Z.-Y., Li, H.-Y., Li, S.-J., Zhao, X., et al. (2019). AIE triggers the circularly polarized luminescence of atomically precise enantiomeric copper(I) alkynyl clusters. *Angew. Chem. Int. Ed.* n/a. doi: 10.1002/anie.201908909

Zhang, X.-P., Chang, V. Y., Liu, J., Yang, X.-L., Huang, W., Li, Y., et al. (2015). Potential switchable circularly polarized luminescence from chiral cyclometalated platinum(II) complexes. *Inorg. Chem.* 54, 143–152. doi: 10.1021/ic5019136

Zhang, X.-P., Wang, L.-L., Qi, X.-W., Zhang, D.-S., Yang, Q.-Y., Shi, Z.-F., et al. (2018). Pt…Pt interaction triggered tuning of circularly polarized luminescence activity in chiral dinuclear platinum(ii) complexes. *Dalton Trans.* 47, 10179–10186. doi: 10.1039/C8DT02277A

Zhao, J., Zhang, T., Dong, X.-Y., Sun, M.-E., Zhang, C., Li, X., et al. (2019). Circularly polarized luminescence from achiral single crystals of hybrid manganese halides. *J. Am. Chem. Soc.* 141, 15755–15760. doi: 10.1021/jacs.9b08780

Zhou, G., Wong, W.-Y., and Yang, X. (2011). New design tactics in OLEDs using functionalized 2-phenylpyridine-type cyclometalates of iridium(III) and platinum(II). *Chem. Asian J.* 6, 1706–1727. doi: 10.1002/asia.201000928

Zhou, Y., Li, H., Zhu, T., Gao, T., and Yan, P. (2019). A highly luminescent chiral tetrahedral $Eu_4L_4(L')_4$ cage: chirality induction, chirality memory, and circularly polarized luminescence. *J. Am. Chem. Soc.* 141, 19634–19643. doi: 10.1021/jacs.9b07178

Zinna, F., Arrico, L., and Di Bari, L. (2019). Near-infrared circularly polarized luminescence from chiral Yb(iii)-diketonates. *Chem. Commun.* 55, 6607–6609. doi: 10.1039/C9CC03032H

Zinna, F., and Di Bari, L. (2015). Lanthanide circularly polarized luminescence: bases and applications. *Chirality* 27, 1–13. doi: 10.1002/chir.22382

Zinna, F., Pasini, M., Galeotti, F., Botta, C., Di Bari, L., and Giovanella, U. (2017). Design of lanthanide-based OLEDs with remarkable circularly polarized electroluminescence. *Adv. Funct. Mater.* 27:1603719. doi: 10.1002/adfm.201603719

Conflict of Interest: The authors declare that the research was conducted in the absence of any commercial or financial relationships that could be construed as a potential conflict of interest.

frontiers in Chemistry

ORIGINAL RESEARCH
published: 15 September 2020
doi: 10.3389/fchem.2020.00801

Theoretical Investigation of the Circularly Polarized Luminescence of a Chiral Boron Dipyrromethene (BODIPY) Dye

*Qin Yang, Marco Fusè and Julien Bloino**

Scuola Normale Superiore, Pisa, Italy

Over the last decade, molecules capable of emitting circularly polarized light have attracted growing attention for potential technological and biological applications. The efficiency of such devices depend on multiple parameters, in particular the magnitude and wavelength of the peak of emitted light, and also on the dissymmetry factor for chiral applications. In light of these considerations, molecular systems with tunable optical properties, preferably in the visible spectral region, are particularly appealing. This is the case of boron dipyrromethene (BODIPY) dyes, which exhibit large molecular absorption coefficients, have high fluorescence yields, are very stable, both thermally and photochemically, and can be easily functionalized. The latter property has been extensively exploited in the literature to produce chromophores with a wide range of optical properties. Nevertheless, only a few chiral BODIPYs have been synthetized and investigated so far. Using a recently reported axially chiral BODIPY derivative where an axially chiral BINOL unit has been attached to the chromophore unit, we present a comprehensive computational protocol to predict and interpret the one-photon absorption and emission spectra, together with their chiroptical counterparts. From the physico-chemical properties of this molecule, it will be possible to understand the origin of the circularly polarized luminescence better, thus helping to fine-tune the properties of interest. The sensitivity of such processes require accurate results, which can be achieved through a proper account of the vibrational structure in optical spectra. Methodologies to compute vibrationally-resolved electronic spectra can now be applied on relatively large chromophores, such as BODIPYs, but require more extensive computational protocols. For this reason, particular attention is paid in the description of the different steps of the protocol, and the potential pitfalls. Finally, we show how, by means of appropriate tools and approaches, data from intermediate steps of the simulation of the final spectra can be used to obtain further insights into the properties of the molecular system under investigation and the origin of the visible bands.

Keywords: circularly polarized luminescence, vibronic spectroscopy, chirality, BODIPY, mode mixing, Franck-Condon, electronic transition current density

OPEN ACCESS

Edited by:
Tao Wu,
Academy of Sciences of the Czech Republic (ASCR), Czechia

Reviewed by:
Monika Srebro-Hooper, Jagiellonian University, Poland
Jakub Kaminsky, Academy of Sciences of the Czech Republic, Czechia

****Correspondence:***
Julien Bloino
julien.bloino@sns.it

Specialty section:
This article was submitted to Physical Chemistry and Chemical Physics, a section of the journal Frontiers in Chemistry

Received: *30 April 2020*
Accepted: *30 July 2020*
Published: *15 September 2020*

Citation:
Yang Q, Fusè M and Bloino J (2020) Theoretical Investigation of the Circularly Polarized Luminescence of a Chiral Boron Dipyrromethene (BODIPY) Dye. Front. Chem. 8:801. doi: 10.3389/fchem.2020.00801

1. INTRODUCTION

Circularly polarized luminescence (CPL) processes have gained interest over the years for their potential use in technological applications, such as data storage or optical displays, as well as for the design of novel biological probes (Riehl and Richardson, 1986; Furumi, 2010; Carr et al., 2012; Kumar et al., 2015; Sánchez-Carnerero et al., 2015; Zinna and Di Bari, 2015; Longhi et al., 2016; Jimènez et al., 2017; Li et al., 2018). A significant hurdle in passing from the proof of concept to potential industrial applications is the emitted signal. Besides the problem of performance, suitable candidates must meet a number of criteria in terms of stability, production cost, and toxicity. A relatively straightforward strategy is to start with a promising core structure, whose physico-chemical properties can be tuned through chemical substitutions or additions.

Among such tunable systems, Boron dipyrrin (4-bora-3a,4a-diaza-*s*-indacene, BODIPY) derivatives represent an important family of organic molecules that have shown excellent performance in photonic applications, such as 3D optical displays, storage, spintronics, or biological probes (Durán-Sampedro et al., 2013; Lifschitz et al., 2013; Wang et al., 2013; Liu et al., 2014; Zhao et al., 2015; Kaur and Singh, 2019; Turksoy et al., 2019), thanks to their absorption and emission properties in the visible spectra region, which can be easily manipulated (Loudet and Burgess, 2007; Ulrich et al., 2008; Wang et al., 2013; Liu et al., 2014; Zhao et al., 2015). They are also very stable and highly soluble in an extensive range of common organic solvents, and have the advantage of being economically more affordable and less hazardous than other light-emitting complexes based on rare earth or radioactive atoms (Kamkaew et al., 2013; Shivran et al., 2016; Zhang et al., 2020). These features make them appealing for the development of OLED devices or biological probes, for instance. While for the latter, the importance of chirality is well-established, interesting possibilities brought by the use of chiroptical signals in displays have also been proposed. However, most BODIPYs are achiral, so they do not exhibit any circular dichroism (CD) or CPL signals. For this reason, research groups have been exploring the possibility of synthetizing chiral BODIPYs, by adding chiral substituents or by tweaking the structure to be intrinsically chiral (Sánchez-Carnerero et al., 2014; Zinna et al., 2016; Alnoman et al., 2016; Lu et al., 2016; Jimènez et al., 2017; Abbate et al., 2017; Pop et al., 2019). The broad structural possibilities can pose a significant challenge in identifying the most suitable candidates. The inherent complexity of such a task can be reduced with the assistance of computational chemistry, which can help understanding the physico-chemical properties at the origin of the observed phenomena, and rationalize the chemical design. Thanks to hardware and software improvements, quantum chemical calculations can now be routinely done on molecular systems of increasing size and complexity, encompassing a large number of BODIPYs. Nevertheless, computational cost and accuracy still need to be carefully balanced, and the definition of a suitable computational protocol can be a complex task in view of the many methods available. The difficulty is further aggravated by the sensitivity of chiroptical spectroscopies, so that common models, which may be sufficient for non-chiral properties, may fall short, being unable to describe properly the properties involved and the radiative processes. This begins from the choice of the electronic structure calculation method, but also includes the representation of the potential energy surfaces and their vibrational structures. The latter is often disregarded but plays an essential role in determining the shape and intensity of absorption and emission spectra (Le Guennic et al., 2012; Pedone et al., 2012; Avila Ferrer et al., 2013; Barone et al., 2014; Hodecker et al., 2016; Liu et al., 2016; Padula et al., 2016; Hu et al., 2017; Fortino et al., 2019). With these considerations in mind, an extensive study of the methods available to describe excited-states properties of molecular systems of this size can be highly valuable. Through a description and illustration of their capabilities, it will be possible to design a comprehensive, but also evolutive, protocol for the study of chiroptical spectra of medium-to-large molecular systems beyond the standard, purely electronic methods.

As a test subject, we have chosen a derivative of BODIPY, called O-BODIPY by the original authors, where an axially chiral 1,1′-binaphthyl unit is orthogonally attached to the O-BODIPY chromophore, which was recently synthetized and studied experimentally (Sánchez-Carnerero et al., 2014; Gartzia-Rivero et al., 2017; Jiménez et al., 2019). Electronic circular dichroism (ECD) and CPL were used to characterize the chiroptical properties of such a design, shown in **Figure 1**. Both provide complementary information to the standard UV-visible absorption and fluorescence spectroscopies to get a comprehensive picture of the excited states of those molecules. Despite the low dissymmetry ratio ($g_{lum}(\lambda) = 2(I_L(\lambda) - I_R(\lambda))/(I_L(\lambda) + I_R(\lambda))$, with I_L and I_R the left- and right-circularly polarized emitted lights, respectively), an interesting property of this system is to show a sign inversion between ECD and CPL for the lowest-energy band. This phenomenon was speculated to be connected to the presence of an intramolecular charge transfer before the emission. With the aim of characterizing the nature of this process and understand the chiroptical properties of this chiral O-BODIPY, we present an extensive computational protocol, starting from the definition of the electronic structure calculation method based on their overall performance up to the simulation of the vibrationally-resolved electronic spectra. We will introduce available methodologies rooted in the time-independent formalism to simulate the latter, with a discussion on their strengths and possible pitfalls. The whole procedure is sustained by suitable graphical representations, with intermediate data generated during the simulations providing valuable information to check the reliability of the results and get further insights into the properties of the system (Licari et al., 2015; Fusè et al., 2019).

The manuscript is organized as follows. In the first part, the main concepts used for the analysis of the results will be recalled and summarized. The discussion will be done as an incremental process, starting from the identification of conformers and their relative abundances, followed by the simulation of spectra with a growing level of sophistication. At each point, the reliability and potential caveats will be studied. Finally, following the protocol identified to be performing the best, an in-depth vibrational

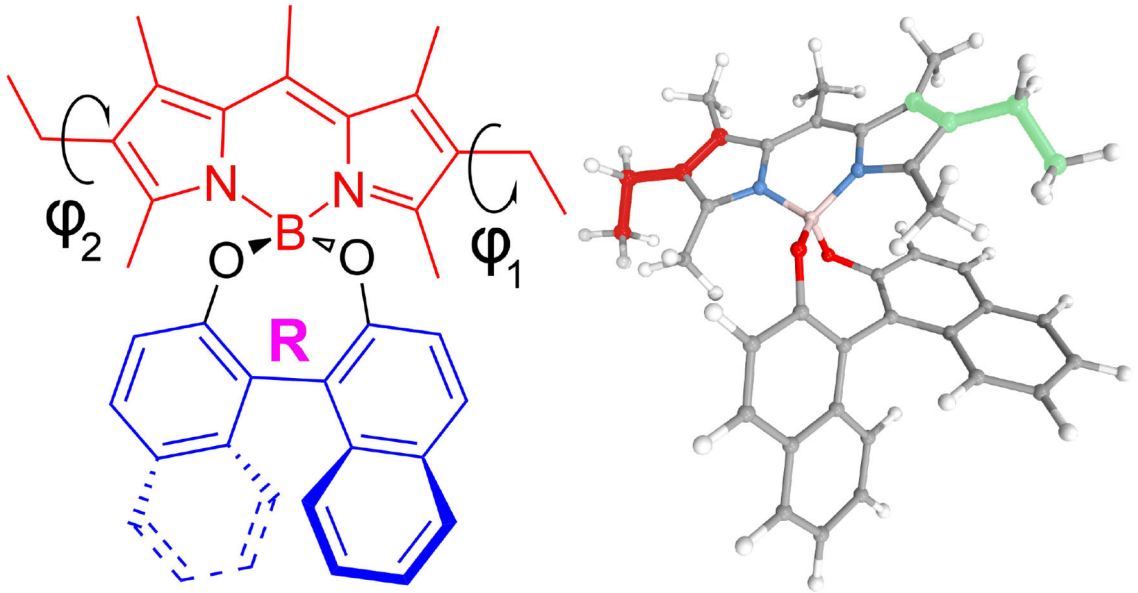

FIGURE 1 | 2D and 3D representations of (*R*)-O-BODIPY. ϕ_1 (red in the 3D representation) and ϕ_2 (green) represent the torsion angles for the scan.

analysis will be carried out, with an analysis of the most relevant data produced by the vibronic simulation, which can shed light on structural optimization to enhance the properties of those systems.

2. METHODS

2.1. General Overview

Expressed in general terms, the simulation of spectra will require two steps, the proper definition of the sample, to match experimental conditions and setup, and the choice of a suitable level of theory for the modeling of the response of the sample itself. Regarding the former, solvent can play an important role and, in case of direct interactions with the solute or if the solvent molecules have a significant impact on the overall spectra, must be treated explicitly, with the inclusion of solvent molecules. In the present case, polarizable continuum models, which reproduce the overall electrostatic properties of the solvent, are sufficient and were used. With a pure sample, the main issue in the modeling is the possible presence of conformers, which requires an investigation of the so-called conformational space, that is, the ensemble of all structures reachable by structural deformations with no bond breaking. Topological search or dynamics-based samplings are commonly used but can be time-consuming. For semi-rigid systems, like this is the case here, the actual degrees of freedoms are limited and a more directed search, based on chemical intuition is often more efficient.

It should be noted that the identification of stable conformers require a sufficient level of theory, which can be far lower than what needs to be employed for the simulation of spectra. With medium-large molecules like the ones of interest here, a trade-off between accuracy and computational cost is unavoidable. Density functional theory (DFT) remains the method of choice for such applications, with the well-known problem of identifying the best-suited functional. The standard approach is thus through a benchmark, which can be reduced to a small subset, based on existing knowledge accumulated in the literature. In the present case, because the target is not pure electronic spectra, but more sophisticated approaches, the problem of error compensation during this step must be kept in mind. Hence, instead of a best-performing functional for a given spectrum, it is more important to choose a well-balanced method, from which the potential energy surface and the transition moments of the properties of interest will be defined. The next subsections present the overall computational details for standard calculations, with emphasis on the methodological aspects related to the less common vibronic calculations.

2.2. Computational Details

All computations were done with a locally modified version of the GAUSSIAN suite of quantum chemical programs, able to handle internal coordinates in vibronic calculations (Frisch et al., 2019). Methods rooted in DFT—for the electronic ground state—and its time-dependent extension (TD-DFT)—for the excited states—have been employed as they represent the most suitable choice in terms of efficiency and accuracy for systems of this size. For all calculations, the 6-31+G(d) basis set was employed, except where specified otherwise, and an ultrafine grid (99 radial shells and 590 angular points per shell) was used to integrate the exchange-correlation kernel. To match experimental condition, solvent effects due to the presence of chloroform were included by means of the polarizable continuum model in its integral equation formalism (IEF-PCM) (Cancès

et al., 1997). The solute cavity was built as a combination of interlocking spheres centered on each atom with a diameter equal to their van der Waals radii scaled by a factor of 1.1. Equilibrium structures were reached using tight convergence criteria (maximum forces and displacements smaller than 1.5×10^{-5} Hartree/Bohr and 6×10^{-5} Å, respectively) for the geometry optimization of the ground electronic states, and loose criteria (1.67×10^{-3} Hartree/Bohr and 1.6×10^{-3} Å) for excited states, the latter being chosen to provide a balance between computational cost and accuracy. The quality of the "loose" convergence was checked for the first singlet excited state of one of the conformers of (*R*)-O-BODIPY (PC, see the next section for details) in terms of geometrical changes and frequencies. Maximum and mean deviations of 2.7×10^{-2} and 4×10^{-3} Å for the geometry, and 1.7 and 0.1 cm^{-1} for the vibrations were found. Analytic frequencies are available for both ground and excited states and were used to check that the true minima had been obtained.

The electronic transition current densities (ETCDs) were computed with a locally modified version of the CUBEGEN utility of GAUSSIAN and saved as a discretized volumetric dataset in plain-text cube files. 3D ETCD figures representing the vector field were obtained as described in Fusè et al. (2019). Space partitioning within the QTAIM (Quantum theory of atoms in molecules) theory was done with the MULTIWFN package (Lu and Chen, 2012) and volumetric datasets were processed with Python scripts.

For all spectra, Gaussian distribution functions were used to simulate the natural broadening observed in experimental spectra. In most cases, the value of the half-width at half-maximum was chosen to match the reference band-shape.

2.3. Vibronic Calculations

For vibrationally resolved electronic spectra, also referred to vibronic spectra in the following, the protocol extensively described in Bloino et al. (2016) was followed. We will just summarize here the most relevant aspects. Two complementary formalisms were adopted here. The sum-over-state approach (or time-independent, TI) was used to check the convergence of the spectrum and obtain information on the origin of the bands where relevant. The former represents the ratio between the calculated intensity obtained by summing the contributions from the individual transitions between each populated initial state and the manifold of final vibrational states, and the total intensity calculated by applying analytic sum rules. A low value, caused by the contribution of an exceedingly large number of low-intensity transitions, is often indicative of a strong mixing or displacement of the vibrational modes in conjunction with the electronic transition. This is due to significant structural changes, which may hint at a potential breakdown of the underlying Franck-Condon principle. Indeed, the theory used here assumes that the system is sufficiently rigid and the electronic transition induces relatively small geometrical deformations. The path-integral (or time-dependent, TD) formalism provides converged band-shapes, in presence of temperature effects as well. Once the reliability of the model has been validated with TI, which is generally done in absence of temperature effects to limit the pre-screening issues described below, TD can be applied to obtain fully converged band-shapes, in presence of temperature effects, and the details on the contribution of the most intense transitions superimposed to the result. For the sum-over-states approach, the class-based pre-screening method described in Santoro et al. (2007a,b, 2008), Barone et al. (2009), and Bloino et al. (2010) has been applied to select *a priori* the most intense transitions within a virtually infinite set. We refer interested readers to those articles for theoretical details on the algorithm. We will just mention here that the pre-screening relies on an internal database built from the transition intensities of overtones (vibrational progressions) and 2-modes combinations (mode couplings) to set the highest number of quanta each mode can reach when involved in 3-modes combinations (class 3) and above, up to a limit of 7 simultaneously excited modes (class 7). For class 1 (C_1, overtones) and class 2 (C_2, binary combinations), a maximum number of quanta reachable by each mode is set, respectively $C_1^{\max} = 100$ and $C_2^{\max} = 80$. For each class above, the maximum number of quanta for each mode was set so that no more that 4×10^8 transitions are treated. For the path integral formalism, the autocorrelation function was computed over a total time of 10^{-10} s divided in 2^{18} steps (Baiardi et al., 2013). To match the experimental conditions in Sánchez-Carnerero et al. (2014), a temperature of 298 K was set.

The harmonic description used to represent the potential energy surfaces (PESs) can have a significant impact on the reliability of the overlap integrals between the initial and final vibronic states. If the minima of the PESs are nearly superimposed (small shift), the standard calculation of the force constants (Hessian matrices) at the corresponding equilibrium geometry is a good approximation of their curvatures in the region of maximum overlap. As the shift increases, this can become unsatisfactory and a better alternative is to compute the force constants in the final state about the equilibrium geometry of the initial one. The former approach will be called adiabatic Hessian (AH), and the latter vertical Hessian (VH). It should be mentioned that the vibrational energies, hence the band positions, are generally more accurate with AH, while VH can reproduce better the band intensities. However, the latter is also more sensitive to the anharmonicity of the final-state PES, with the risk of imaginary frequencies being present. Because two frequency calculations are required, which can be expensive, especially for the excited states where analytic frequency calculations may not be available, approximated alternatives have been proposed in the literature, respectively adiabatic shift (AS) for AH and vertical gradient (VG, also called linear coupling model) for VH (Blazej and Peticolas, 1980; Macak et al., 2000; Bloino et al., 2010). In those models, the final-state PES is assumed equal to the initial one. It is noteworthy that these models were primarily defined for absorption spectra, where the lower initial state is almost systematically the electronic ground state and thus less expensive to compute. This is not the case for emission spectra (OPE and CPL here), and two strategies can be adopted, depending if the state of reference, for which the frequencies are actually calculated, is the lower one, labeled with the subscript "abs" since it assumes a behavior close to absorption processes, or the excited, actual initial state, labeled with the "emi" subscript. The advantages in terms

of overall computational cost of the latter is generally not considerable but will provide here a more complete picture of the validity of such approximations. Regarding the modeling of the solvent effects, for VG and VH, like for pure electronic transitions, the linear-response (LR-PCM/TD-DFT) approach for the non-equilibrium regime was employed, while the state-specific (SS-PCM/TD-DFT) was chosen for AH and AS in excited-states calculations.

Finally, both the Franck-Condon approximation (FC) and its Herzberg-Teller (HT) extension will be used for the representation of the electronic transition moments of the properties of interest, the electric and magnetic dipoles. As a matter of fact, those quantities cannot be expressed analytically with respect to the nuclear motions. The simplest way is to assume them constant, which corresponds to the FC approximation. This has two significant limitations. First, it is not able to reproduce sign alternations in the vibronic structure of chiral spectra, the spectra obtained this way being scaled versions of their non-chiral counterparts. Second, it can be a crude approximation for semi-rigid systems who undergo some deformation upon the electronic transition. A linear dependence with respect to the normal coordinates will also be included in what will be labeled the FCHT approximation. In this definition, the transition moment of a property **P** will be assumed to have the form,

$$\mathbf{P}(\mathbf{Q}) = \mathbf{P}(\mathbf{Q}^{\mathrm{eq}}) + \sum_{i=1}^{N} \frac{\partial \mathbf{P}}{\partial Q_i} Q_i$$

where **Q** is a vector of mass-weighted normal coordinates, and $\mathbf{Q}^{\mathrm{eq}}$ refers to the equilibrium geometry of the state of reference. The first term in the right-hand side corresponds to the FC approximation mentioned before.

In the following, the model used for the simulation of vibronic spectra will be defined starting from the framework (TI, TD), followed by the representation of the PESs (AH, VH, AS, VG), terminated by the form of the transition moments (FC, FCHT), e.g., "TI AH|FC." Where obvious, some of the terms will be omitted for the sake of readability.

2.4. Internal Coordinates

A final remark concerns the choice of coordinates for the simulation of vibronic spectra. The Cartesian-based normal coordinates are often preferred for their simplicity and versatility, but can overestimate the mode mixing and the contributions of the combination bands, resulting in excessively broad bands. Internal coordinates can reduce this phenomenon, providing a better localization of the vibrational modes (Reimers, 2001; Beenken and Lischka, 2005; Borrelli and Peluso, 2008; Cerezo et al., 2013; Baiardi et al., 2016). Unfortunately, their definition is not unique and building a preliminary set containing all relevant coordinates on such a large system is not straightforward. Here, the generalized internal coordinates (GICs) implemented in GAUSSIAN have been used. An initial set was automatically generated by the program and used as a starting point. To maximize the convergence of the spectra, *ad hoc* coordinates were defined to describe better the structural shift. Because the latter is extrapolated in the case of vertical models, different coordinates were added for adiabatic and vertical models. From them, a set of non-redundant, weighted internal coordinates (WICs, Lindh et al., 1999) was built upon it. This scheme emphasizes the localization of coordinates of different types, by weighing each one by the bond order of the atoms involved in it (Swart and Bickelhaupt, 2006). Details on the construction of the set used in our program can be found in Baiardi et al. (2016).

2.5. Reduced Dimensionality

For systems of this size exhibiting some flexibility, low-energy large-amplitude vibrational motions are often present and may cause a breakdown of the vibronic models despite contributing marginally to the overall spectrum. It has been shown that these modes can be ignored to provide results in very good agreement with experiment (Biczysko et al., 2011; Egidi et al., 2014, 2018; Aranda et al., 2018; Fortino et al., 2019). However, for the latter to be meaningful, it is necessary to rigorously isolate the modes to be removed from the rest of the system in a consistent way. This is done here by checking their overlap on the normal-modes basis of the other electronic state, using to this end the Duschinsky matrix, which relates the normal modes of the initial ($\mathbf{Q}_I$) and final ($\mathbf{Q}_F$) states in an affine transformation,

$$\mathbf{Q}_I = \mathbf{J}\mathbf{Q}_F + \mathbf{K}$$

with **J** the Duschinsky matrix and **K** the shift vector.

The so-called reduced-dimensionality procedure is as follows. For each mode of the initial (or final) electronic state, the elements of **J** (or $\mathbf{J}^{-1}$) along the corresponding row are squared and sorted by decreasing values. Then, all significant elements of this list are selected and the modes relative to the corresponding columns of **J** (or $\mathbf{J}^{-1}$) are selected to be removed too. This procedure carries on iteratively for both electronic states, alternating initial and final ones, until the lists of modes to remove stabilize with no new elements chosen. The corresponding M elements are removed, and the vibronic calculations are done over the $(N - M)$ modes remaining in each state. For a system of this size, a perfect localization of the modes is extremely difficult and a residual mode mixing is generally observed over large regions. As a result, selecting all elements in a given row with non-negligible values would result in an excessive reduction of the system. In practice, a threshold is defined, here set to 0.7, so that only the first m elements of the list of squared row elements ordered by decreasing values are selected, so that their sum is greater or equal to the chosen threshold. It should be also noted that **J** in internal coordinates is rarely orthogonal, so that the total sum of the squared elements will vary for each row and column. For this reason, the elements of **J** and its inverse are first normalized by setting the highest element in absolute value to 1. Further details can be found in Bloino et al. (2016). As a final remark, the number of normal modes to be removed should be kept as low as possible so the model retains most of the properties of the full system.

3. RESULTS AND DISCUSSIONS

In what follows, the results for the BODIPY dye will be presented, following the workflow described in the previous section, which can be summarized as: (i) exploration of the conformational space in order to define the low-lying conformational ensemble; (ii) choice of the best level of theory to reproduce the spectroscopic property of interest; (iii) inclusion of vibrational effects to the pure electronic transitions.

As it will be shown, the analysis of data generated in the last two steps allows for further insight on the underlying processes.

3.1. Conformational Analysis

The molecule, displayed in **Figure 1**, has two flexible ethyl groups, so an initial identification of the possible conformers was carried out through a relaxed scan. The values of the dihedral angles ϕ_1 and ϕ_2 (see **Figure 1** for details) were sequentially varied from 0 to 330° by steps of 30°. The calculations were carried out in the electronic ground state at the MN15/6-31G level, this functional having shown good results on some BODIPYs systems (Fortino et al., 2019), and the overall cost being still manageable for a system of this size. As visible in **Figure 2**, four conformers can be identified, labeled PC1 and PC2 (for a pseudo- "cis" configuration), and PT1 and PT2 (for "trans"). Each pair of conformers is equivalent, so only one representative of each type was chosen, shown in **Figure 3**, simply labeled "PC" and "PT" in the following.

The overall spectra are the sum of the "PC" and "PT" spectra weighed by their relative abundances at 298 K. The free energy differences at the MN15/6-31+(d) level of theory were used to compute the Boltzmann populations at room temperature. In order to avoid non-reliable contributions due to the presence of large amplitude motions (see subsection 3.4), the vibrational correction to the free energy was neglected.

3.2. Electronic Structure Calculation Methods and Optical Spectra

Although benchmarks on related molecules are present in literature (see for instance Fortino et al., 2019), they predominantly focus on non-chiral spectroscopies. Therefore, in order to identify the functional most suited to simulate all spectroscopies of interest, preliminary benchmarks based on both the OPA and ECD spectra were performed. A subset of functionals known to provide reliable results on similar system was chosen, namely CAM-B3LYP (Yanai et al., 2004), LC-ωPBE (Vydrov and Scuseria, 2006), M06-2X (Valero et al., 2008), MN15 (Haoyu et al., 2016), PBE0 (Adamo and Barone, 1999), and ωB97X-D (Chai and Head-Gordon, 2008). For CAM-B3LYP and PBE0, the D3 formulation of the empirical dispersion correction proposed by Grimme et al. (2010), in conjunction with the Becke-Johnson (BJ) damping (Grimme et al., 2011) were used. It should be noted that, for consistency and to avoid errors in the input files, the same parameters were used for each electronic structure calculation method, so the empirical dispersion was included in all computations involving CAM-B3LYP and PBE0. The resulting spectra are compared to experiment in **Figure 4**.

Considering one-photon absorption (OPA) first, all functionals give pretty similar results for the first band, shifted by about 60–70 nm with respect to experiment. The position of the second main band observed at about 350 nm is also an important indication of the relative energy gap between electronic transitions. PBE0 correctly reproduces the absolute position of the second band but not its relative energy with respect to the first one. LC-ωPBE gives the best overall result

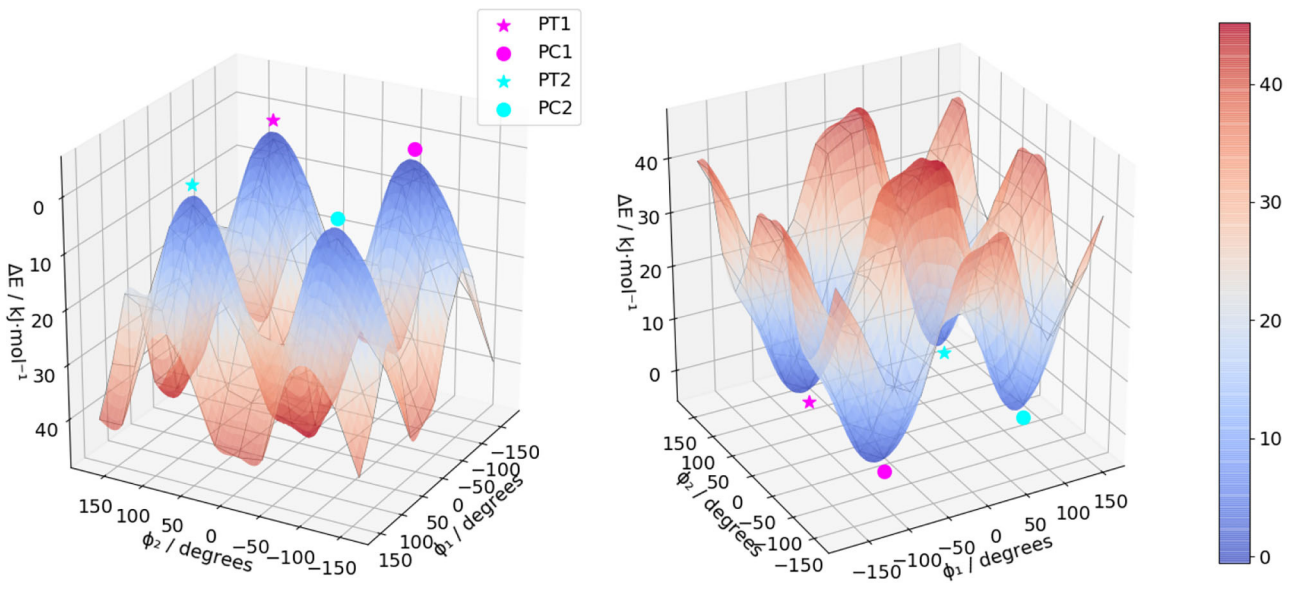

FIGURE 2 | Electronic energy of (*R*)-O-BODIPY at the MN15/6-31G with different values of the torsional angles ϕ_1 and ϕ_2.

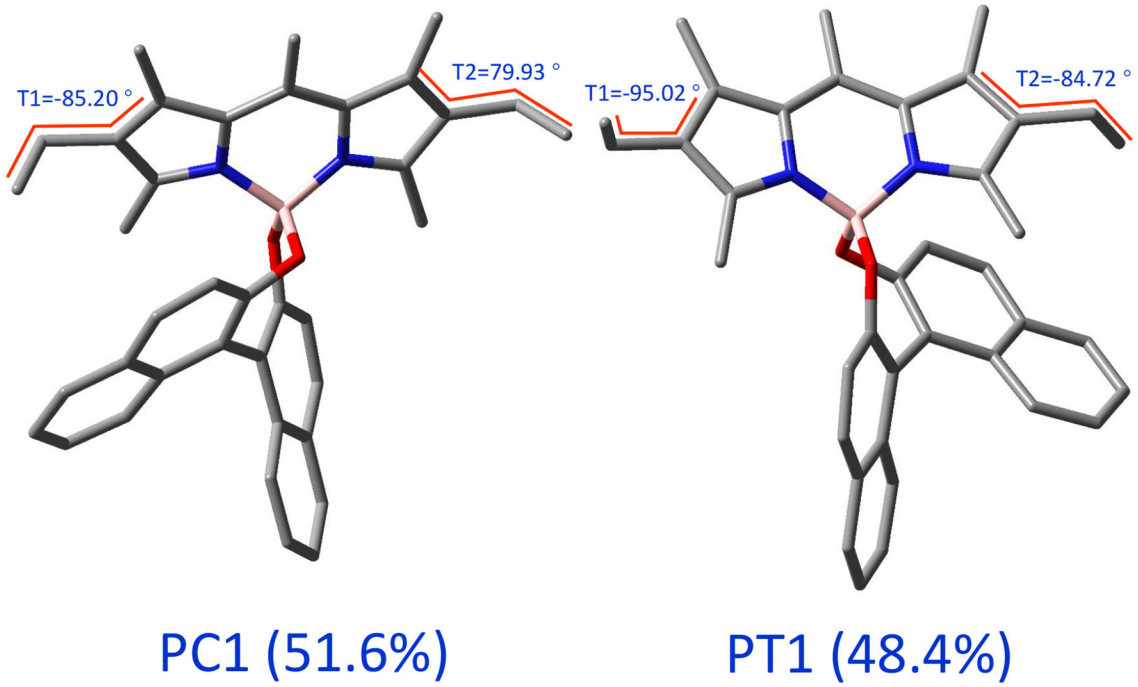

FIGURE 3 | 3D representations of the two types of conformers of (*R*)-O-BODIPY. The values of the angles are for the optimized geometries in the electronic ground state at the MN15/6-31+G(d).

in this case, with a gap very close to the experimental one, and a spectrum shifted by about 65 nm. Regarding the shape of the bands, all functionals show a relatively similar trend in comparison with experiment, with a relatively good agreement in terms of intensity for the first band, and a significant overestimation of the second one. A low-intensity, large shoulder in the lower-energy side of the second band can be observed in the experimental spectrum, which seems to be qualitatively reproduced by PBE0. However, in terms of relative intensity with the second band, it appears underestimated, while MN15 and ωB97X-D show comparatively more intense, but narrower shoulders. Nevertheless, the limited resolution does not allow us to draw further conclusions. To conclude, LC-ωPBE provides the best relative band positions, while MN15 provides overall satisfactory band patterns, displaying the best agreement with experiment. A benchmark purely on OPA does not guarantee success in the simulation of chiroptical spectroscopies, and the performance of the functionals in describing the electronic transition moment of the magnetic dipole and its relative orientation with the electric dipole's needs to be careful evaluated too. In **Figure 4B**, the benchmark results for electronic circular dichroism (ECD) are reported. The ECD spectrum, like OPA, shows two main bands, of opposite sign but close height. Besides the problem of band positions, already addressed for OPA, we can note that the sign pattern is globally correctly reproduced by all functionals regarding the main features. Relatively similar heights are obtained for the first band, slightly underestimated in all cases, except for PBE0, which appears broader and weaker, while all others have only one transition in this region. The pattern for the second band is far more diverse than for OPA. All functionals significantly overestimate its intensity, and most of them also show a weaker, lower-energy band of positive (for CAM-B3LYP, ω97X-D) or negative (LC-ωPBE, M06-2X, MN15) sign, which cannot be confirmed on the experimental spectrum. The latter, however, shows a broad, nearly flat positive band at about 410 nm, which can be identified only for MN15. While clearly visible by comparison with the ECD spectrum of its enantiomer, the features of this band are too small for further analysis. Overall, the similar performance of the chosen functionals for the first transition is mostly confirmed in **Table 1**, except for PBE0, which exhibit two close transitions in the energy region of the first band (at about 460 and 440 nm), which complement each other for OPA but lead to a broad feature for ECD. To summarize, all functionals are capable of reproducing qualitatively the first band for both OPA and ECD spectroscopies. However OPA intensities result slightly overestimated whereas the ECD ones are underestimated. This leads to smaller values of g_{abs} for all the functionals compared to the experimental one, from about one fourth for PBE0 to nearly half of the value for MN15 (see **Table 1** for details).

As MN15 shows a more consistent behavior with respect to experimental OPA and ECD spectra, and following the strategy described previously (Bloino et al., 2016), all calculations will be done from now on at the MN15/6-31+G(d). The electronic energies, and thus the band positions, will be corrected by using those obtained at the LC-ωPBE/6-31+G(d) when multiple electronic states are involved (see **Figures S1, S2**).

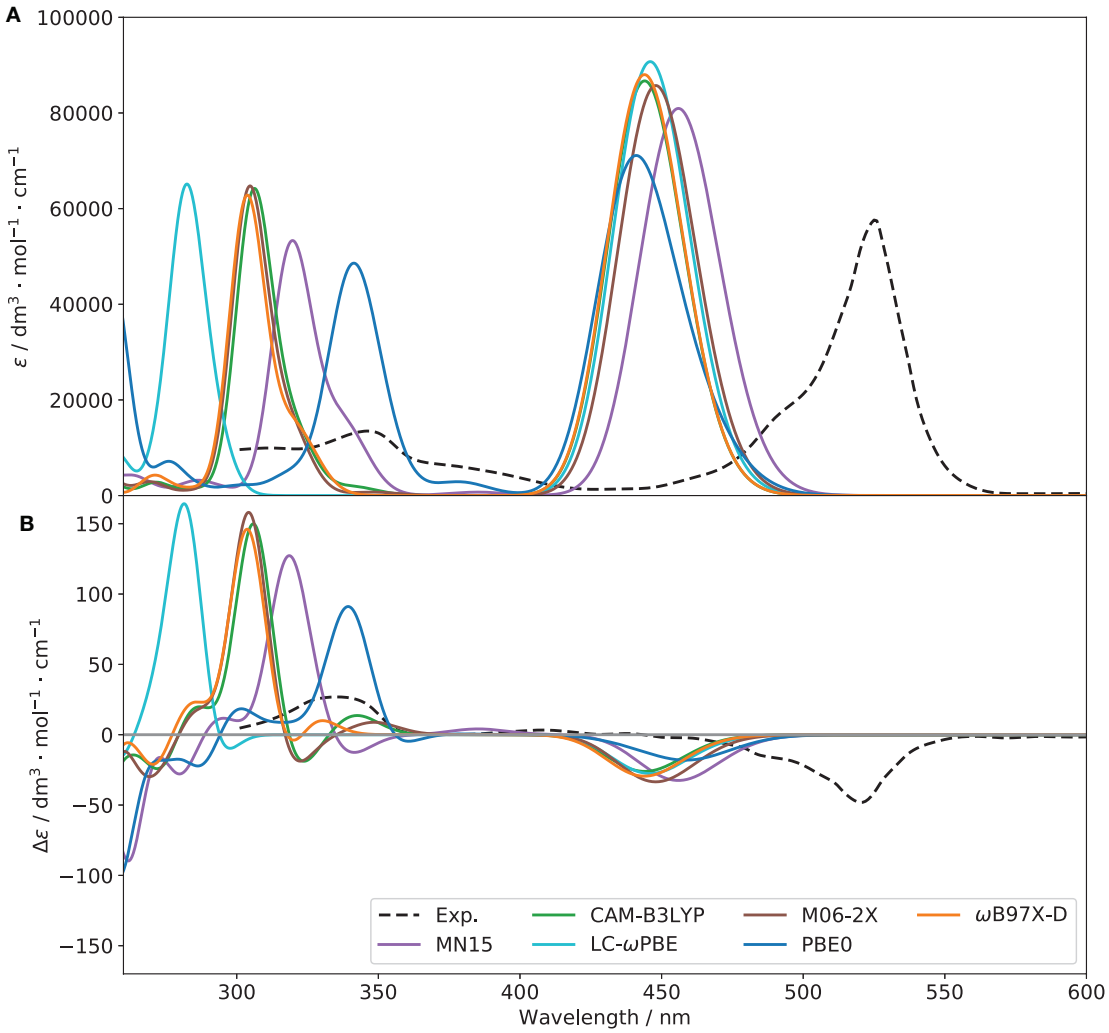

FIGURE 4 | OPA **(A)** and ECD **(B)** spectra of (*R*)-O-BODIPY with different functionals [basis set: 6-31+G(d)]. The broadening was simulated by means of Gaussian functions with half-widths at half-maximum of 800 cm^{-1}.

TABLE 1 | Energy (*E* in nm), dipole strength (*D*, in 10^{-36} esu^2 cm^2), oscillator strength (*f*), and rotatory strength (*R*, in 10^{-40} erg esu cm/Gauss) for the $S_1 \leftarrow S_0$ transition.

Functionals	*E*	*D*	*f*	*R*	ϵ_{max}	$\Delta\epsilon_{max}$	g_{abs}	Color
MN15	456.37	58.7279	0.6001	−57.7876	80,944	−33	-4.0×10^{-4}	
CAM-B3LYP-D3BJ	444.43	56.6468	0.6181	−45.3828	86,703	−26	-3.0×10^{-4}	
LC-ωPBE	446.41	59.5265	0.6467	−48.0030	90,733	−28	-3.0×10^{-4}	
M06-2X	448.39	61.1846	0.6359	−58.8453	85,734	−34	-3.9×10^{-4}	
PBE0-D3BJ	460.81	10.0846	0.1054	−29.9259	71,107	−18	-2.5×10^{-4}	
ωB97X-D	444.37	57.6935	0.6285	−51.1510	88,015	−29	-3.3×10^{-4}	
Exp.	525	—	—	—	57,618	−48	-8.4×10^{-4}	

ϵ_{max} and $\Delta\epsilon_{max}$ corresponds to the maximum of absorption (in OPA and ECD) for the first band (with a broadening obtained by applying Gaussian distribution functions with half-widths at half-maximum of 500 cm^{-1}), and the dissymmetry ratio is computed as $g_{abs} = \Delta\epsilon_{max}/\epsilon_{max}$. The perceived color is computed over the full visible spectral range.

Moving to the emission spectra, as recalled in the introduction, the CPL and ECD experimental spectra show different signs. This is interesting because, within the Frank-Condon regime, usually the first absorption and emission transitions involve the same states, and therefore should have the same sign. In Gartzia-Rivero et al. (2017), the authors suggested that an intramolecular charge transfer (ICT) between close electronic states was likely at the origin of the change of sign observed in the experimental CPL spectrum (see **Figure 5**) compared to the ECD spectrum reported in **Figure 4**. For this

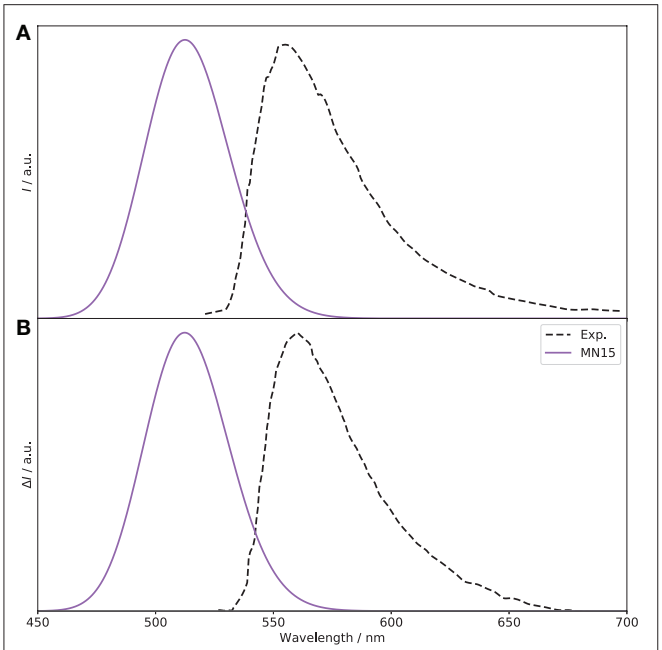

FIGURE 5 | $S_1 \rightarrow S_0$ OPE **(A)** and CPL **(B)** spectra of (*R*)-O-BODIPY at the MN15/6-31+G(d) level, compared to experiment. The broadening was simulated by means of Gaussian functions with half-widths at half-maximum of 800 cm^{-1}. The spectra are normalized in intensity for comparison.

reason, the first two electronic states (S_1 and S_2) have been considered here, and separate geometry optimizations were carried out. As expected, the sign of the CPL spectrum from the original S_1 state is negative. Looking at the rotatory strengths (*R*, in the following given as 10^{-40} esu^2cm^2), they are respectively −34.4 for PC and −3.8 for PT, compared to −77.1 and −37.2, respectively, for the $S_1 \leftarrow S_0$ transition. Interestingly, a crossing is observed between the first and second excited singlet electronic states, with an inversion of the energy order. The previously second excited state becomes the lowest and most likely source of emission. More details on the non-radiative process requires *ad hoc* tools going beyond the scope of the present study and will be deferred to a separate work. Compared to the transition at the previous S_1 minimum, PT is the largest contributor, with a rotatory strength of +30.9 (−1.9 for PC). The resulting fluorescence and CPL spectra are shown in **Figure 5**. A shift of about 50 nm is observed with respect to experiment, a value relatively close to absorption ($\simeq$ 60 nm), and the sign of the CPL band is correctly reproduced, with a g_{lum} of 0.9×10^{-4}, compared to 7.1×10^{-4} reported experimentally. To get further insight, it is interesting to consider the molecular orbitals and electronic structure.

3.3. Molecular Orbitals and Transition Current Density

In the following, only PT will be discussed, as both conformers show very similar trends (the results for PC can be found in **Figures S3, S4**). In BODIPY systems, the lowest-energy transition is expected to be a dipole-allowed $\pi \rightarrow \pi^*$ transition (Bergström et al., 2002). Thus, the first absorption band is mostly described as a HOMO to LUMO transition, which contributes for more than 97% in both isomers (see **Table S2**). Indeed, as displayed in **Figure 6**, HOMO and LUMO are well-localized on the BODIPY moiety of the molecule. The figure also displays the frontier orbitals of the molecule at both the ground-state geometry and at the geometry of the lowest excited state after crossing. Though extremely similar, the HOMO and HOMO-1 are less localized at the excited state geometry. Although the lower transition still has prevalently a HOMO to LUMO nature (95%), it also has a minor contribution from the HOMO-1 to LUMO pair (4%). The electron density difference ($\Delta\rho$) shown in the left panels of **Figure 7** confirms the origin of the orientation of the electric dipole transition moment, but is little informative about the change in sign observed between ECD and CPL.

To investigate further the phenomenon, we look at the electronic transition current density (ETCD) (Nafie, 1994, 1997). ETCD is a vector field, which represents the paths connecting two different probability densities and its integral is associated with the velocity form of the electric dipole transition moments. What makes appealing this density function, as firstly described by Nafie and co-workers (Freedman et al., 1997, 1998, 2002; Nafie, 1997) and recently re-proposed for the vibrational case (Fusè et al., 2019), is the visualization of the vector fields. It shows linear and curved patterns in the charge flow occurring upon excitation, which can be related to the electric and magnetic dipole transition moments, respectively. In the central panels of **Figure 7** (**Figure S4** for PC), ETCDs at the two geometry are represented using "streamtubes" representation, obtained by interpolating the vector field (Telea, 2007). The radius and the color of the represented tubes are proportional to the magnitude of the field (from low intense in light blue to high in tones of yellow). As expected in $\pi \rightarrow \pi^*$ transitions (Nafie, 1994), the ETCD crosses the conjugated systems with an intense linear pattern responsible of the electric dipole transition moment, coherently with the $\Delta\rho$ plots. Considering its C_{2v} point group symmetry, BODIPY is not providing a chiral response itself. Once a chiral group is attached, a chiral response can rise from the dipolar coupling of the electric dipole transition moments lying on the achiral chromophore (BODIPY) and the magnetic dipole transition moment originating from the chiral portion (BINOL) (Lu et al., 2016). Nevertheless, in dipole-allowed transitions, the electric dipole transition moments is expected to be orders of magnitude more intense than the magnetic ones, making difficult to spot the contributions on BINOL. Thus, we tried to partition the ETCD on the two molecular fragments, namely the BODIPY and the BINOL units. To accomplish this, we relied on the quantum theory of atoms in molecules (Bader, 1991) to partition the total space, according to the topology of the initial state electron density, into atomic basins. Then, these basins were combined according to fragments, giving the fragments' subspace. In the right panels of **Figure 7**, "Hedgehog" representations of the ETCD in which the BINOL contribution (depicted in blue shades) was magnified by 15 times, are reported. As can be seen, asides from the linear flow on the BODIPY fragment (in red shades), regions

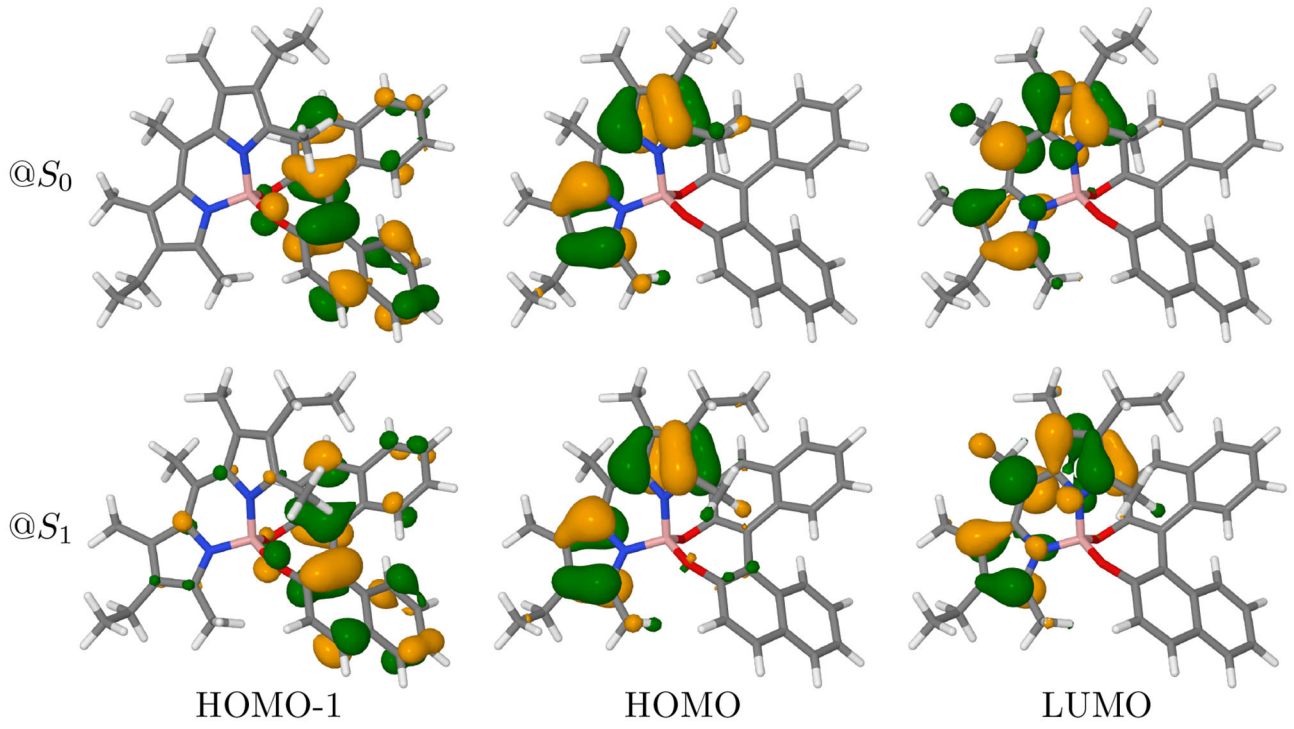

FIGURE 6 | Frontiers molecular orbitals of PT conformer at S_0 and S_1 geometries (isodensity surfaces at ± 0.04 $(e/bohr^3)^{1/2}$).

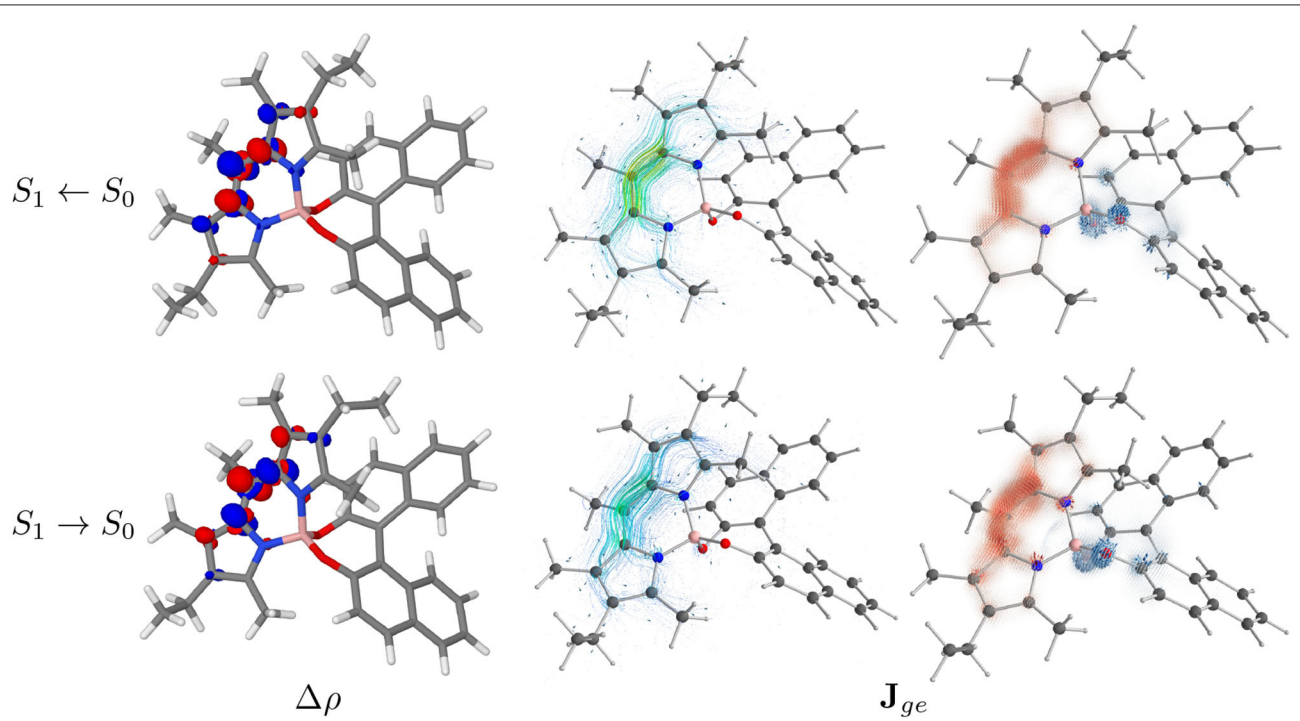

FIGURE 7 | In the left panels the difference between the electronic density of the final and the initial states ($\Delta\rho$) of PT conformer is represented as isosurfaces (isodensity surfaces at ± 0.004 $(e/bohr^3)$; red isosurfaces: depletion, blue isosurfaces: accumulation). In the central panels the ETCD ($\mathbf{J}_{ge}$) vector fields are represented by means of streamline objects. In the right panels, the ETCDs have been partitioned between BODIPY and BINOL contributions, with the BINOL field being magnified 15 times. The resulting fields are represented by the means of Hedgehog representation.

of circulation of charge are present on the BINOL fragment, in particular on the oxygen atoms. **Tables S3, S5** report the fragments contribution to the transition dipoles and, in turn, to the dipole strength (DS) and to the rotatory strength (RS). Focusing on the $S_1 \leftarrow S_0$ transition, the major contribution determining the sign of the first ECD band is the interaction term between the electric dipole transition moment on the BODIPY and the magnetic one on the BINOL. By comparing the upper and the lower panels in **Figure 7**, clues on the origin of the sign inversion between ECD and CPL can be obtained. In fact, the bending of the BODIPY frame upon excitation (see **Figure S20** and *vide infra* for a comparison between the two structures) leads to a slight reduction of the linear flow and to more curved flows in portions of the BODIPY itself. As a result, the interaction term between the electric dipole transition moment on the BODIPY and the magnetic one on BINOL is reduced whereas the BODIPY intra-fragment term and the coupling between the magnetic dipole transition moment on the BODIPY and the electric one of the BINOL gains more relevance. These rearrangements in the flows in the $S_1 \rightarrow S_0$ transition substantially revert the sign of CPL in the PT case and almost cause the cancellation of the CPL signal in the PC one (changes in the ETCD vector fields between transition from the first two excited states at their respective minima are shown in **Figure S5**).

3.4. Vibrationally-Resolved Electronic Spectra

The electronic structure provides already interesting information in understanding the experimental results. However, they neglect the vibrational structure contained in the experimental spectra, which can play a significant role in chiroptical spectroscopies (Lin et al., 2008a,b, 2009; Bloino et al., 2010; Pritchard and Autschbach, 2010; Santoro and Barone, 2010; Egidi et al., 2013, 2018).

To get a more accurate and complete picture, a proper account of the former is necessary. As shown in the previous section, a relatively broad range of models can be built, and it is useful to correctly assess their strengths and limits in light of the present system. Because it offers a balanced representation of the two PESs involved in the electronic transition, AH is first used as reference on the OPA and ECD spectra to check the basic setup in the definition of the vibronic system, namely the underlying coordinates system and the applicability of reduced-dimensionality schemes.

3.4.1. Coordinate Systems

Let us initiate with the coordinates. As noted before, Cartesian coordinates provide an unequivocal basis, easier to manipulate. However, it can perform poorly in presence of a system undergoing structural changes associated to the electronic transition by overestimating the mode mixing induced by it. Conversely, curvilinear linear coordinates can do a better job in describing the transformation, localizing the coordinates involved and recovering some of the intrinsic anharmonicity of the vibrational motions, reducing this way the coupling between the modes and resulting in narrower bands. However, this can be achieved only with a suitable set of coordinates, able to represent in a minimal basis the structural changes. For AH, the initial, automatically generated set of GICs, combined with the use of weights to build the non-redundant group of internal coordinates was sufficient (Lindh et al., 1999; Baiardi et al., 2016). The $S_1 \leftarrow S_0$ OPA and ECD spectra are shown in **Figure 8**. The time-dependent framework was chosen to avoid convergence issues, which could distort the analysis. Only the FC approximation is considered at first, so that the electronic transition moments of the electric and magnetic dipoles act as simple scaling factors, and the band-shape is dictated purely by the vibronic structure. To visualize better the impact of vibronic transitions, two different widths of broadening were applied, with half-widths at half-maximum of 500 cm^{-1} to match more closely experiment, and 250 cm^{-1} for finer details. As expected, all models are able to recover the asymmetry of the experimental first band. The shift with experiment is also improved with an overall shift of about 30 nm. However, the OPA band with Cartesian-based normal modes ("Cart") is excessively wide. Furthermore, it exhibits a second, relatively flat band at about 420 nm not observed in the experimental spectrum. Reducing the broadening from 500 to 250 cm^{-1} barely improves the band shape. At variance, internal coordinates ("WICs") provide a narrower, more intense band, with a smaller shift from the experimental band by about 10 nm (482 compared to 490 nm). The second band is not present here, which confirms that this is an artifact caused by the coordinates set. A flat band, even with a lower empirical broadening, is generally due to the contributions of a multitude of low-intensity transitions, which hint at an excessive mixing of the modes. This can be confirmed by analyzing the Duschinsky matrix **J**. As a visual aid for the analysis, **J** and the shift vector are graphically represented in **Figures S6, S7**, respectively. A few introductory comments on the chosen representations are in order. Displaying the raw numbers would produce excessively large, truncated tables, which would be difficult to analyze. Thus, it is convenient to represent each element as a square block filled with a shade of gray corresponding to the squared value of this element (J_{ik}^2), from white for a null value to black for 1. Because **J** is not orthogonal for internal coordinates, each row was individually normalized. The shift vector is represented in absolute value, since the most important information here is the magnitude of the shift. The pattern exhibited by **J** is relatively similar between the two sets of coordinates, with a block-diagonal structure mostly close to the diagonal, which indicates that the mode mixing is not excessive and mostly involve modes close in energy, in particular in the mid-infrared region. The magnitude of the coupling is, however, harder to assess with the normalization scheme applied, and its impact on the intensity of the combination bands can be only inferred this way. To evaluate better the effects of the magnitude of the couplings, a basic sum-over-states calculation was done with the same parameters to generate the so-called Sharp and Rosenstock **C** matrix (Sharp and Rosenstock, 1963), given as,

$$\mathbf{C} = 2\boldsymbol{\Gamma}_F^{1/2}(\mathbf{J}^T\boldsymbol{\Gamma}_I\mathbf{J} + \boldsymbol{\Gamma}_F)^{-1}\boldsymbol{\Gamma}_F^{1/2} - \mathbf{I}$$

with $\boldsymbol{\Gamma}$ the diagonal matrix of reduced frequencies.

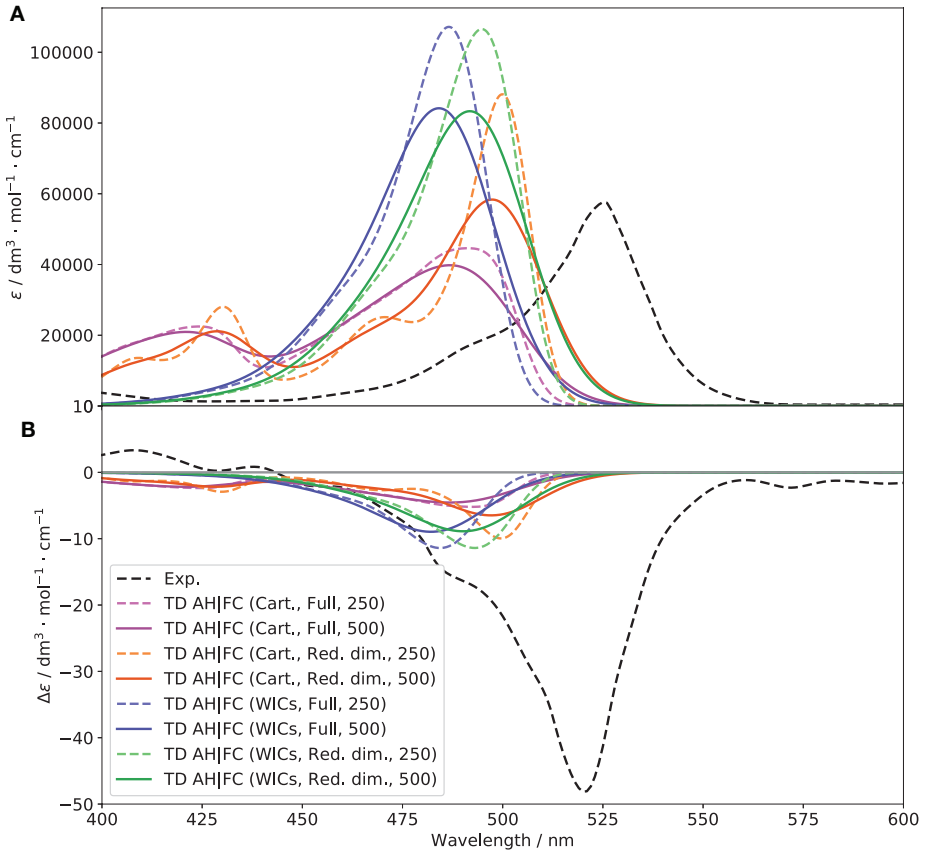

FIGURE 8 | Vibronic $S_1 \leftarrow S_0$ OPA **(A)** and ECD **(B)** spectra of (*R*)-O-BODIPY at the AH|FC level within the time-dependent framework at T = 298 K, compared to experiment. The broadening was simulated by means of Gaussian functions with half-widths at half-maximum of 250 (dashed lines) and 500 cm^{-1} (solid lines).

The interest of **C** is that it is directly related to the intensity of the combination bands in the recursive formulation proposed by Ruhoff (1994) through its off-diagonal elements, and is even the only contribution in absence of temperature effects (it remains a predominant term at room temperature). The **C** matrix (shown in **Figure S8**) shows more difference between the coordinates sets, and in particular a large coupling of modes at higher energy (195–220) with the rest of the system, which explains the large contributions of combinations bands in Cartesian coordinates. It is noteworthy that the diagonal terms of those modes are also larger, which result in a higher contribution of the corresponding overtones in the energy region of the second band observed for this case. The shift vector (**Figure S7**) shows a significant shift of the first mode and in general the lower-energy ones. The combination of low energy and large shift make their contribution to the main band features marginal but will often cause an excessive broadening of the bands. For this reason, modes below 50 cm^{-1} and with shift above 100 $\sqrt{m_e}a_0$ were initially set to be removed. Following the block construction algorithm described in the computational details, five modes were removed for PC, and eight for PT. The resulting spectra are displayed as "Red. dim." in **Figure 9**. We observe for both coordinates sets a narrowing of the band. However, the overall shape is still incorrect for Cartesian-based coordinates, with the second band being even more visible. This is to be expected, as low-energy modes, which contributed to some of the overall broadening are removed, while the higher-energy ones, whose vibrational progressions played a role in the second band are still present. For ECD, the results are more difficult to interpret. The intensity appears very low compared to the pure electronic one which matched quite well the first band but strongly overestimated the second, hinting at a likely compensation of errors in this case. Nevertheless, "WICs" with the reduced-dimensionality scheme seems to perform slightly better in terms of intensity. For this reason, and in the following, internal coordinates in conjunction with a reduced model system where strongly displaced, low-frequency modes are removed, will be used. As a final check, the convergence of the sum-over-states approach in the same conditions was evaluated to confirm that there was no fundamental issue with the general Franck-Condon principle used for the vibronic calculations (spectra are shown in **Figure S10**). Convergences of 84.7 and 92.7% were obtained for PC and PT, respectively, relatively high values in comparison of the system size and flexibility, which confirm the good performance of the overall model. It should be noted that, besides the problem of convergence highlighted earlier, the explicit sum

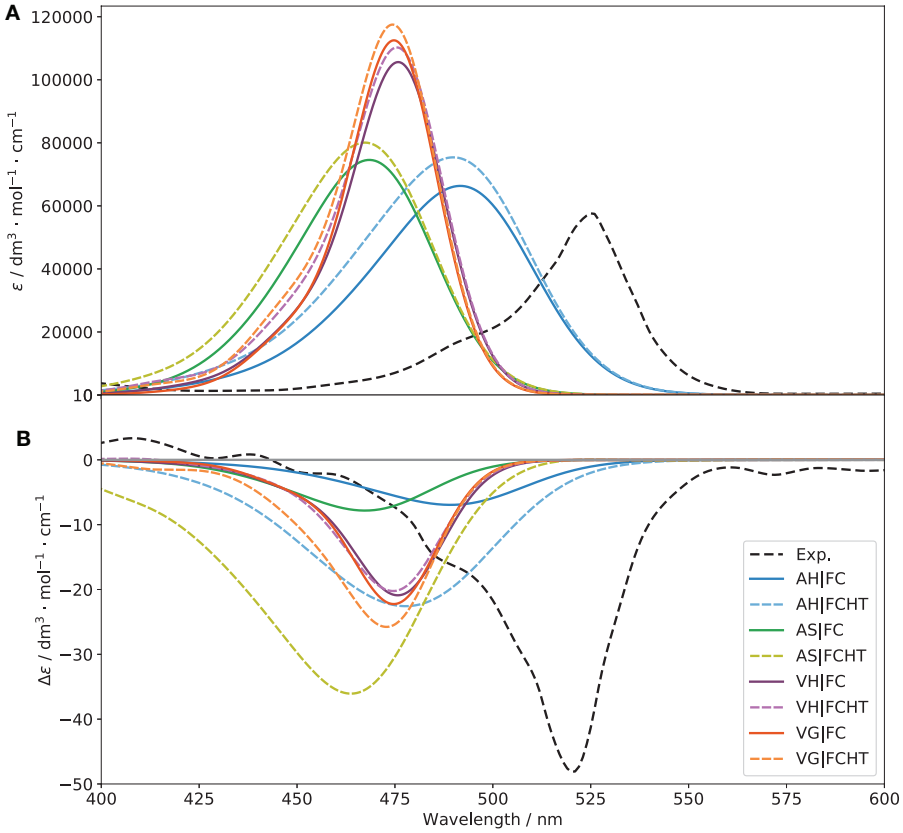

FIGURE 9 | Vibronic $S_1 \leftarrow S_0$ OPA **(A)** and ECD **(B)** spectra of (*R*)-O-BODIPY computed with different vibronic models at T = 298 K, with and without Herzberg-Teller effects, compared to experiment. The broadening was simulated by means of Gaussian functions with half-widths at half-maximum of 500 cm^{-1}.

of single vibronic transitions is computationally slow due to the manifold of initial vibrational states to take into account. For these reasons, calculations will be done within the TD framework to match experimental conditions at room temperature.

3.4.2. Vibronic Models

Figure 9 shows the $S_1 \leftarrow S_0$ OPA and ECD spectra with different representations of the PES involved in the transition, with and without Herzberg-Teller effects. Normalized spectra, which emphasize the changes in the shape of the bands are shown in **Figure S9**.

Let us first consider the non-approximated models, AH and VH. For VH, the S_1 harmonic force constants are computed at the S_0 equilibrium geometry, and the shift vector, which is normally related to the structural differences between the minima of the two PESs is extrapolated assuming a parabolic curvature. As a result, the Duschinsky matrix (represented in **Figure S11**) and the shift vector (**Figure S12**) are expected to be different. As a matter of fact, **J** is slightly more diagonal, hinting at a lower mode mixing. The shift vector, however, shows one of the potential pitfalls of vertical modes, with an excessively large shift of the low-energy modes, beyond 1,000 atomic units ($\sqrt{m_e}a_0$). This is related to the definition of **K** itself, which has a magnitude roughly proportional to the squared inverse of the energy of the vibrations. For this reason, the low-frequencies can exhibit unphysical shifts. Following a common practice adopted for vertical models, modes with wavenumbers below 150 cm^{-1} were selected to be removed in the reduced-dimensionality scheme, which corresponds to about 16 modes out of 234 for both conformers. This model system has been used to generate the VH (and VG) spectra shown in **Figure 9**. As was inferred from the shape of **J**, VH provides a narrower band-shape compared to AH, an observation confirmed by the shape of the C matrix (**Figure S13**). Moreover, the high-energy wing shows a small shoulder, in agreement with experiment where it is, however, more pronounced. For ECD, the intensity is still significantly underestimated but the agreement slightly improves for VH especially in terms of band width, too large with AH. Inclusion of HT contributions improves marginally the intensity of the OPA band for VH, and has no noticeable effect on ECD. For AH, the intensity improves but the width also increases, as visible on the normalized spectra. Overall, AH tends to overestimate the mode mixing, leading to an excessive band broadening. VH appears to perform better, with a good overall band-shape, still strongly underestimated for ECD, which may be due to limitations in the ability of the underlying electronic structure calculation methods in fully describing the electronic transition magnetic dipole moment or its relative orientation with the electric dipole. The

good performance can be explained by the underestimation of the structural shift from the extrapolation, which leads to a better overlap with the initial state and compensate the limitations of the harmonic approximation. At variance, the BODIPY moiety at the true S_1 minimum is visibly displaced compared to S_0, in particular the alkyl groups attached to it (see **Figure S14** for a comparison of the reference structures used by each models). As mentioned in the computational details, the main advantage of approximated models, AS and VG, is to reduce, potentially in a significant way, the computational cost by assuming that the two PESs are equal. In practice, since the normal modes are the same in both states, there is no mode mixing (**J** is the identity matrix). Based on these observations, the results obtained here are not necessarily intuitive. Indeed, because of the lack of mode mixing, narrower, more intense bands would be expected. For VG, on OPA, the bands with FC or FCHT are very close to their VH counterparts. This can be related to the limited mode-mixing observed for VH, so VG is a good approximation for this case, and with the limited definition of the band. The same trend is observed for ECD, with a slight improvement of the band intensity with FCHT. For AS, the results are close to AH, with a slightly larger band for both OPA and ECD. Hence, the mode mixing seem to help mitigating some of the larger shifts (the shift vector is the same for AS and AH), so that AS is here poorly suited to describe such transitions.

The good performance of VG|FC makes it applicable to simulate the OPA and ECD spectra of (*R*)-O-BODIPY over a larger energy range, involving multiple electronic states. To do so, energy gradients of the first 15 excited electronic states were computed at the S_0 equilibrium geometries and the relative $S_n \leftarrow S_0$ OPA and ECD spectra simulated. Then, the resulting spectra were combined to obtain **Figure 10**. For OPA, a significant improvement of the second band experimentally at about 350 nm can be noted, but the overestimation of the first band has slightly worsened. The band positions are also shifted toward a better agreement. For ECD, the higher-energy band has improved in terms of position, shape and intensity. The low-intensity band at about 410 nm in the experimental spectrum is nearly invisible in VG|FC, similarly to what was seen for the pure electronic spectrum. In this case, inclusion of HT contributions could be beneficial, but the calculation of the derivatives of the transition dipole moments over this large number of states would significantly increase the overall computational cost. The first band, due to the $S_1 \leftarrow S_0$ transition, is still strongly underestimated, with a g_{abs} of about -2×10^{-4}.

Let us now consider the emission spectra. In absence of explicit units for the experimental spectra (Sánchez-Carnerero et al., 2014), the same scale as for the electronic OPE and CPL spectra was used to facilitate our discussion. The simulated spectra obtained with the adiabatic and vertical models are shown in **Figure 11** (the normalized spectra are shown in **Figure S15**). For OPE, the intensity of the VH|FC band is slightly higher than the pure electronic one, a trend relatively similar to what was observed for OPA. The asymmetry of the experimental shape is well-reproduced. HT effects are small, which is to be expected since the transition probability is relatively high (oscillator strength of 0.6). For AH, an excessive broadening is observed here in addition to a significant lowering of the intensity, halved. These observations mirror what was found for OPA. Looking at the Duschinsky matrix and shift vector (**Figures S16, S17**), we can observe more differences between AH and VH than for OPA. Indeed, the mode mixing is significantly higher, in particularly for low- and high-energy modes, and the shift vector has more elements with high amplitudes. As a matter of fact, to obtain the AH|FC spectrum shown in **Figure 11**, modes below 100 cm^{-1} were systematically removed, resulting in the first 30 modes excluded after consistency check (the criteria and number of modes excluded remain unchanged for VH). Even with this smaller system, the coupling remains large, as can be observed in the **C** matrix (**Figure S18**), which exhibits a very large number of non-negligible off-diagonal elements of magnitude similar to the diagonal terms. Looking at the geometrical changes between the S_1 (noted ${}^{S_2}S_1$ since originally S_2 at the S_0 equilibrium) and S_0 minima (**Figure S19**), we can note important shifts of the BODIPY moiety, with an overall tilt, combined with rotations of the peripheral alkyl group. As the electronic transition is mainly centered on this fragment of the molecule, the overall shift explains primarily the poorer performance of AH. When comparing the equilibrium geometries of the ground and first two excited electronic states (**Figure S20**), we can observe that the changes related to the absorption process are relatively contained, while the starting geometry for the emission process is further shifted, which explains the worse performance of the adiabatic model. Conversely, the calculated shift from VH is relatively small, leading to an extrapolated equilibrium geometry very close to the minimum of the initial state, S_1 (${}^{S_2}S_1$ in the figure). Like VH, HT contributions for AH are marginal. Shifting to CPL, VH|FC reproduces well the fitted experimental spectrum, with an intensity higher than the pure electronic one. The sign is also correctly predicted. The HT effects are here apparent, leading to an increase of the intensity by about 40%, bringing the VH|FCHT intensity close to the electronic one, but with a stronger luminescence dissymmetry ratio g_{lum} of 1.5×10^{-4} (1.0×10^{-4} for VH|FC) and a good qualitative agreement with the experimental band-shape. Since electronic transition dipole moments act as scaling factors within the FC approximation, the excessive broadening of AH|FC observed for OPE is visible on CPL too. The intensity remains low compared to VH|FC too. Adding HT contributions results in a sign alternation with a first negative band at about 540 nm followed by a wide positive band above 600 nm (see **Figure S21** for details). This phenomenon is due to the fact that at this level, the two conformers have broad band-shapes of opposite signs but similar magnitudes, resulting in a destructive combination. The sign alternation reflects the dominance of one conformer's contribution over the one, with PT negative and PC positive.

Let us conclude our analysis on the use of approximated models. As explained in the computational details, their definition is less straightforward than in absorption. Indeed, from a theoretical point of view, it is assumed that the PES remains unaltered by the transition, simply shifted, so that the PES of the final state is the same as the initial one. From a computational perspective, excited-state frequency calculations are generally more expensive, in particular in absence of

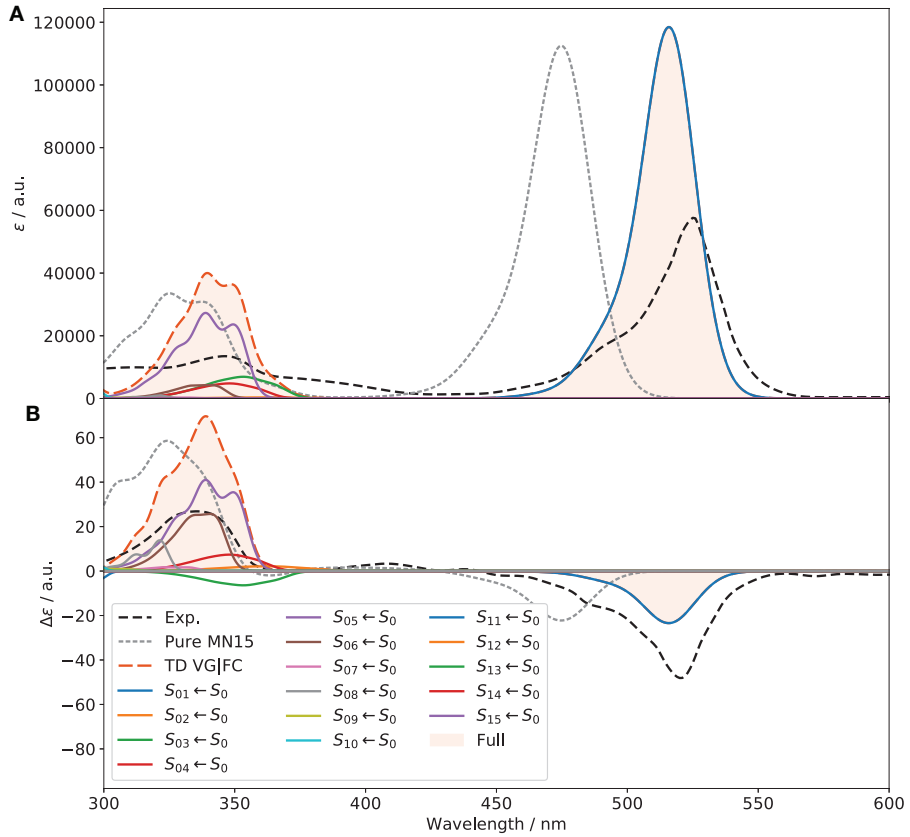

FIGURE 10 | Full vibronic OPA **(A)** and ECD **(B)** spectra of (*R*)-O-BODIPY at the VG|FC level within the time-dependent framework at T = 298 K, compared to experiment. The electronic transitions from S_0 to the first 15 electronic states are included. The broadening was simulated by means of Gaussian functions with half-width at half-maximum of 500 cm^{-1}. Only the first 12 excitations are visible within the displayed spectral range.

analytical frequencies. For emission spectra, theoretical and practical considerations have opposite implications. The two are shown in the **Supplementary Material** (**Figures S21, S22** for the normalized spectrum), "abs" using the ground state as reference, "emi" the initial, exited state. Both approximated vertical models give very close results for OPE and HT contributions are negligible. On the other hand, adiabatic models perform poorly, with AS_{abs} giving a nearly flat spectrum, with a peak at about 200 nm. This behavior can be directly related to the significant structural shift between the minima of the two states, mitigated by the mode mixing in AH. Switching to a description based on the normal coordinates of the excited state (AS_{emi}) improves the results, but with still an excessive mixing. As for OPA, HT contributions are very small. On CPL, the trend remains relatively similar for all methods at the FC level. However, inclusion of HT effects give very disparate results. While VG_{abs} produces a significantly narrower and more intense band compared to VH with a slightly negative, flat band between 550 and 650 nm, VG_{emi} exhibits an almost symmetric pattern, starting with a relatively narrow negative band, followed by a low-intensity positive band. Both diverge significantly from VH and the experimental data. AS_{abs} remains unusable at all levels, and AS_{emi} gives the same, broad and weaker band with and without HT contributions. These results show that approximated modes need to be carefully handled and can give poor results if the structural deformations are non-negligible.

3.5. Influence of the Vibronic Structure

Based on its performance, VH is used here for the analysis of the band contributions. TI VH|FC and VH|FCHT calculations were done in the same conditions as TD, with different broadenings to see the evolution of the band pattern. In the following, the transitions of interest are reported with their intensity given in terms of rotatory strength (R, in 10^{-44} esu^2cm^2).

Starting from the ECD spectra (shown in **Figure S23**), the 0–0 transition, between the vibrational ground states, is the main transition at both FC and FCHT levels for both PC (*cis*-conformer) and PT (*trans*-conformer). The intensity of the main transition of PC is three times that of PT at 477 nm in the spectra (−114.545 vs. −40.009). Hence, increasing the abundance of the *cis* conformer through structural modifications or environmental perturbations will lead to a higher ECD signal. The position of the band maximum is modulated by the contributions of lower-intensity transitions. For the PC conformer, fundamentals of modes 22, 62, and 137, at 473, 465, and 451 nm, respectively, are visible at both FC and FCHT levels.

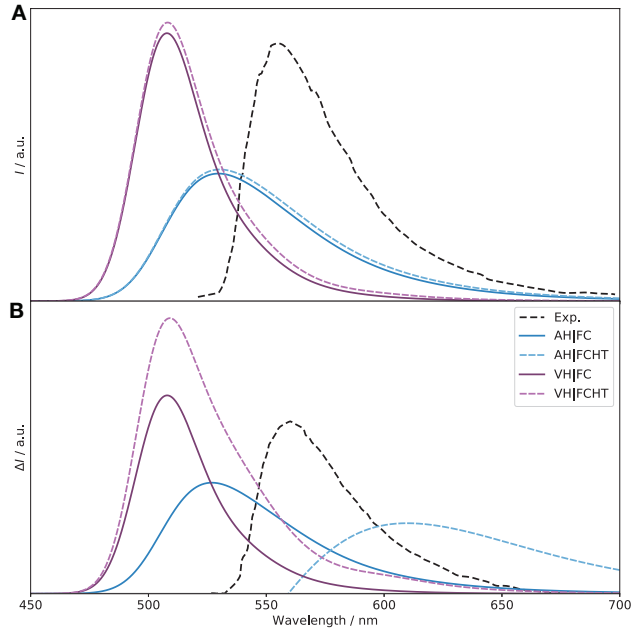

FIGURE 11 | Vibronic $S_1 \rightarrow S_0$ OPE **(A)** and CPL **(B)** spectra of (*R*)-O-BODIPY computed with the AH and VH models at T = 298 K, with and without Herzberg-Teller effects, compared to experiment. The broadening was simulated by means of Gaussian functions with half-width at half-maximum of 500 cm^{-1}.

These three modes correspond to vibrations centered on the BINOL moiety, especially for mode 137, fully localized on the BINOL part. Mode 22 is also accompanied by a motion of the ethyl groups, while mode 62 also involves a ring distortion on the achiral perylene moiety. For PT, the 0–0 transition is clearly dominant at both FC and FCHT level. The other transitions have a small impact at the FC level, while contributions from the fundamentals of modes 20, 22, and 50, at 474, 473, and 468 nm, respectively, can be noted with FCHT. Similarly to PC, these three modes are strongly connected to the BINOL moiety, especially vibrational mode 50, characterized by a bending of two naphthol groups. For modes 20 and 22, motions of the methyl or ethyl groups can also be observed. From the vibronic analysis above, it can be concluded that the vibrational motions of the BINOL moiety give rise to the most significant vibronic transitions. This is also in line with the analysis from ETCD and the structural differences reported in **Figure S14**. Besides the relative weights of PC and PT, the contribution of modes related to BINOL motions is also another important entry point for tuning the ECD properties of this system, even if the relatively sparse vibronic contribution makes a tailored modification of the current structure difficult to anticipate.

The vibronic structure in the CPL spectra, shown in **Figure 12**, is richer than for ECD. At variance with the ECD spectrum, the PT conformer is the largest contributor and gives the sign of the CPL band, both at FC and FCHT levels, whereas PC, of opposite sign, has a canceling effect. Therefore, reducing the population of the *cis*-conformer for this system would lead to a notable enhancement of the CPL signal. At the FC level, the transition at about 504 nm, between the vibrational ground states, dominates for both PC and PT, but with opposite signs. The rotatory strength of the 0–0 transition of PC is negative and about thirty times lower in magnitude than PT (−2.084 vs. 56.974). Then, the most notable contribution is the fundamental of mode 25 of PT at 509 nm, with an intensity doubled compared to the 0–0 transition of PC. This mode is characterized by the bending of the two naphthol groups in the BINOL moiety, accompanied by a slight motion of the ethyl groups. This vibration matches the displacement of the naphthyl group observed between the S_1 and S_0 true minima reported in **Figure S19**, which is in line with the vibrational progression observed. Aside from this one, modes 53 and 138, at 516 and 551 nm, respectively, also contribute noticeably to the CPL spectrum of PT. Mode 53 is characterized by a deformation of the rings on the BINOL moiety, while mode 138 corresponds to a deformation of the six-member ring in the BODIPY unit around the boron atom. For PC, no other noticeable contributions can be identified at the FC level. At the FCHT level, an enhancement effect observed on the overall band-shape for both conformers, which can be related to a few significant changes in the vibronic transitions. The intensity of the fundamental transitions for mode 25 in PT is doubled, while modes 53 and 138 are increased by one fourth. Additional contributions become more visible, related to the fundamentals of modes 19, 20, 24, 27, 42, 61, 75, 78, and 163. Except for mode 163, relatively similar to mode 138, the other vibrations are directly related to the BINOL moiety. For PC, HT contributions give rise to new vibronic contributions. The most significant one is the fundamental transition of mode 22, which has twice the intensity of the 0–0 one (−16.622 vs. −9.010). The energy of mode 22 is very close to mode 25 of PT, at 509 nm, and corresponds to a very similar vibration, characterized by the bending of the naphthol groups in the BINOL moiety. By its major contribution, this transition causes a slight shift in the emission maximum with respect to PT. The transitions to the fundamentals of modes 23 and 25 should be also mentioned, with intensities comparable to the 0–0 transitions. Both are characterized by the bending of the two naphthol groups in the BINOL moiety but with opposite sign (23 is negative, 25 positive). The vibrational analysis of the CPL spectra shows the significant contribution of the BINOL unit to the CPL sign, shape and intensity for both PC and PT. Therefore substitutions aimed to move the center of mass toward the BINOL fragment can sensibly modify the band shape and in turn the position of the band. The strategy can be combined with *ad hoc* modifications of the push-pull property of the molecule. This is also in line with ETCD Results, that an higher electron current density within the BINOL can lead to an enhancement of the CPL signal.

4. CONCLUSIONS

We present here an extensive protocol for the study of chiroptical spectra of medium-to-large molecular systems beyond the standard, purely electronic, methods. The inclusion

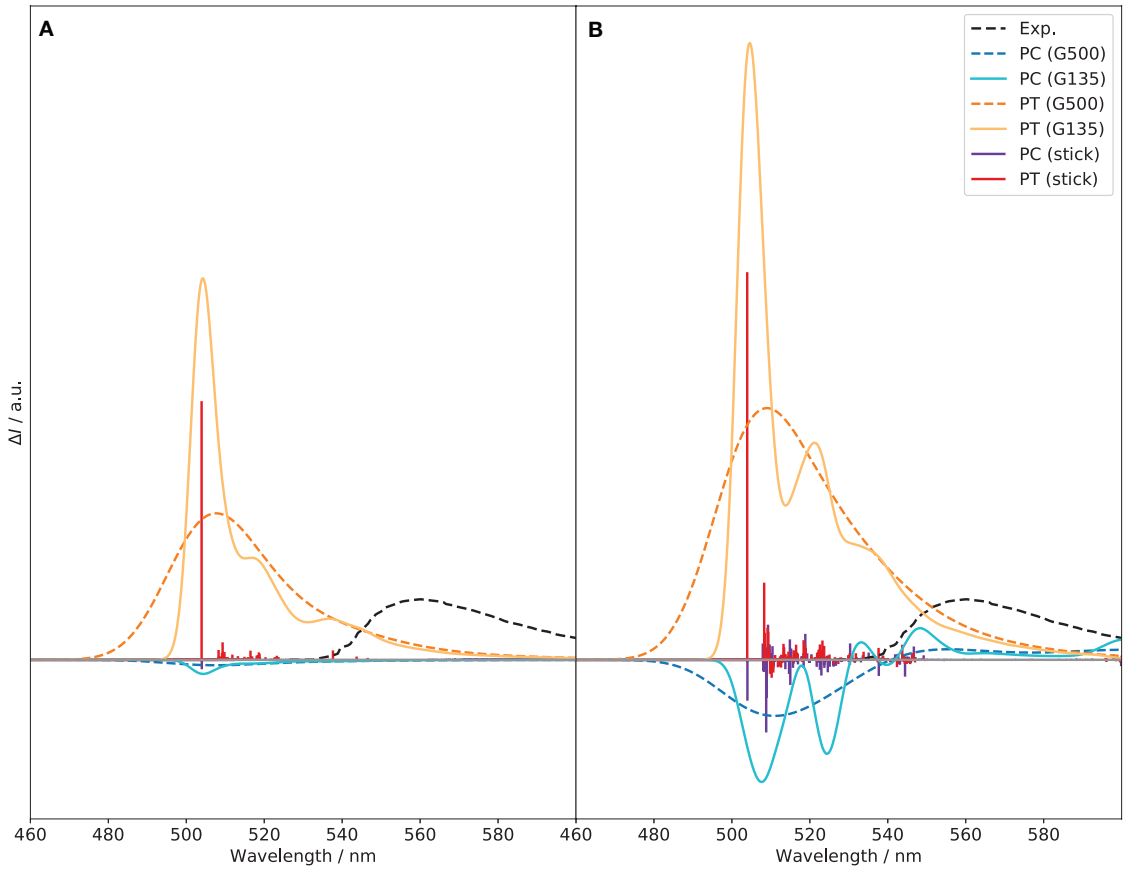

FIGURE 12 | Vibronic $S_1 \rightarrow S_0$ CPL spectra of the PC and PT conformers of (*R*)-O-BODIPY computed at the TI VH|FC **(A)** and VH|FCHT **(B)** levels with different broadenings. Gaussian distribution functions are used with half-widths at half-maximum of 135 ("G135") and 500 cm^{-1} ("G500"). The stick spectra were arbitrarily scaled to fit in the figure.

of vibrational contributions improves on overall the agreement with experiment, giving further insights on the origin of the spectral band-shape observed experimentally. Coupled with tailored graphical representations, like electronic transition current density, which shows the local contributions to the electric and magnetic transition dipole moments, it allows identifying the regions contributing more to the main features and the intensity of the bands. By identifying the excited states actually involved and the weight of each conformer in the CPL spectrum, it is possible to provide precise band assignments. This information can in turn be used to rationalize the design choice and propose paths to improvements in the performance of chiral BODIPYs, both in terms of intensity of emission and luminescence dissymmetry ratio. The results confirm the key role played by the conformational analysis in spectroscopic studies, especially in the present case. Two major conformations were found with opposite chiroptical properties in emission. The performance of the investigated functionals for the first band is close, with some marked differences at higher energies and for the chiral spectra. Overall, MN15 showed more consistent results for both OPA and ECD spectra, confirming to be a reliable choice for describing BODIPY systems (Fortino et al., 2019). Concerning vibronic effects, several aspects can be tuned to better describe the system: (i) Internal coordinates can better represent structural changes induced by the electronic transition, thus whenever a suitable set of coordinates are available they should be preferred over Cartesian ones. In the present system, weighted coordinates (WICs) prove to be particularly effective; (ii) The analysis of the Duschinsky transformation, namely the **J** matrix and **K** vector, aided the choice of the most suitable vibronic model and, combined with the **C** matrix (from time-independent calculations), the definition of the reduced model. Here, vertical models performed better, in particular the VH model resulted to be the best suited for both absorption and emission spectra, which is expected for low-resolution spectra were a correct description of the peaks intensity is more critical. In absorption spectra, the good performance of VG allowed to extend the vibronic simulation on a wider energy range. Finally, TI spectra computed with the best model can be used to highlight the most relevant vibrational contributions.

Besides the clear value in supporting experimental studies, such a comprehensive protocol is also relevant as a diagnostics tools for approximated methods, including those based on pure electronic structure calculations. Indeed, a proper account of the

vibrational structure can help check the quality of the potential energy surface, and will modulate the position of the band-shape and its intensity, revealing potential risks of error compensation. Furthermore, Herzberg-Teller terms can highlight important intensity-borrowing effects, potentially causing significant shift in intensity and band patterns.

Thanks to ongoing efforts in different groups, vibronic spectra can be routinely computed for a growing number of systems of increasing size and complexity. Nevertheless, structural deformations associated to the electronic transition still represent a complex challenge to reach a full black-box procedure. The choice of coordinates can play a critical role in the quality of the band-shape, and the treatment of large amplitude motions, which often give very low contributions, remains a difficult task. Automated procedures can now significantly reduce the work required to set up a proper computational protocol, but still require some careful checks of the produced data. By exploiting some of the representations shown here, paths of improvements can be devised in making such controls autonomous, with little input requested from the users.

DATA AVAILABILITY STATEMENT

The raw data used to generate the figures and supporting the conclusions of this article are available upon request.

AUTHOR CONTRIBUTIONS

All authors listed have made a substantial, direct and intellectual contribution to the work, and approved it for publication.

FUNDING

This work has been supported by the Italian MIUR (PRIN 2017, project Physico-chemical Heuristic Approaches: Nanoscale Theory Of Molecular Spectroscopy, PHANTOMS, prot. 2017A4XRCA).

ACKNOWLEDGMENTS

The high performance computer facilities of the SMART Laboratory (http://smart.sns.it) are acknowledged for providing computer resources. JB thanks Dr. Alberto Baiardi for fruitful discussions in the preparation of this manuscript.

SUPPLEMENTARY MATERIAL

The Supplementary Material for this article can be found online at: https://www.frontiersin.org/articles/10.3389/fchem.2020.00801/full#supplementary-material

REFERENCES

Abbate, S., Bruhn, T., Pescitelli, G., and Longhi, G. (2017). Vibrational optical activity of BODIPY dimers: the role of magnetic–electric coupling in vibrational excitons. *J. Phys. Chem. A* 121, 394–400. doi: 10.1021/acs.jpca.6b11327

Adamo, C., and Barone, V. (1999). Toward reliable density functional methods without adjustable parameters: the PBE0 model. *J. Chem. Phys.* 110, 6158–6170. doi: 10.1063/1.478522

Alnoman, R. B., Rihn, S., O'Connor, D. C., Black, F. A., Costello, B., Waddell, P. G., et al. (2016). Circularly polarized luminescence from helically chiral N,N,O,O-boron-chelated dipyrromethenes. *Chem. Eur. J.* 22, 93–96. doi: 10.1002/chem.201504484

Aranda, D., Cerezo, J., Pescitelli, G., Ferrer, F. J. A., Soto, J., and Santoro, F. (2018). A computational study of the vibrationally-resolved electronic circular dichroism spectra of single-chain transoid and cisoid oligothiophenes in chiral conformations. *Phys. Chem. Chem. Phys.* 20, 21864–21880. doi: 10.1039/C8CP03482F

Avila Ferrer, F. J., Cerezo, J., Stendardo, E., Improta, R., and Santoro, F. (2013). Insights for an accurate comparison of computational data to experimental absorption and emission spectra: beyond the vertical transition approximation. *J. Chem. Theory Comput.* 9, 2072–2082. doi: 10.1021/ct301107m

Bader, R. F. W. (1991). A quantum theory of molecular structure and its applications. *Chem. Rev.* 91, 893–928. doi: 10.1021/cr00005a013

Baiardi, A., Bloino, J., and Barone, V. (2013). General time dependent approach to vibronic spectroscopy including Franck–Condon, Herzberg–Teller, and duschinsky effects. *J. Chem. Theory Comput.* 9, 4097–4115. doi: 10.1021/ct400450k

Baiardi, A., Bloino, J., and Barone, V. (2016). General formulation of vibronic spectroscopy in internal coordinates. *J. Chem. Phys.* 144:084114. doi: 10.1063/1.4942165

Barone, V., Biczysko, M., Borkowska-Panek, M., and Bloino, J. (2014). A multifrequency virtual spectrometer for complex bio-organic systems: vibronic and environmental effects on the uv/vis spectrum of chlorophyll a. *ChemPhysChem* 15, 3355–3364. doi: 10.1002/cphc.201402300

Barone, V., Bloino, J., Biczysko, M., and Santoro, F. (2009). Fully integrated approach to compute vibrationally resolved optical spectra: from small molecules to macrosystems. *J. Chem. Theory Comput.* 5, 540–554. doi: 10.1021/ct8004744

Beenken, W. J. D., and Lischka, H. (2005). Spectral broadening and diffusion by torsional motion in biphenyl. *J. Chem. Phys.* 123:144311. doi: 10.1063/1.2049269

Bergström, F., Mikhalyov, I., Hägglöf, P., Wortmann, R., Ny, T., and Johansson, L. B.-Å. (2002). Dimers of dipyrrometheneboron difluoride (BODIPY) with light spectroscopic applications in chemistry and biology. *J. Am. Chem. Soc.* 124, 196–204. doi: 10.1021/ja010983f

Biczysko, M., Bloino, J., Santoro, F., and Barone, V. (2011). "Chapter: time independent approaches to simulate electronic spectra lineshapes: from small molecules to macrosystems," in *Computational Strategies for Spectroscopy, From Small Molecules to Nano Systems*, ed V. Barone (Chichester: John Wiley and Sons Ltd), 361–443.

Blazej, D. C., and Peticolas, W. L. (1980). Ultraviolet resonance Raman excitation profiles of pyrimidine nucleotides. *J. Chem. Phys.* 72, 3134–3142. doi: 10.1063/1.439547

Bloino, J., Baiardi, A., and Biczysko, M. (2016). Aiming at an accurate prediction of vibrational and electronic spectra for medium-to-large molecules: an overview. *Int. J. Quantum Chem.* 116, 1543–1574. doi: 10.1002/qua.25188

Bloino, J., Biczysko, M., Santoro, F., and Barone, V. (2010). General approach to compute vibrationally resolved one-photon electronic spectra. *J. Chem. Theory Comput.* 6, 1256–1274. doi: 10.1021/ct9006772

Borrelli, R., and Peluso, A. (2008). The electron photodetachment spectrum of c-$C_4F_8^-$: a test case for the computation of Franck-Condon factors of highly flexible molecules. *J. Chem. Phys.* 128:044303. doi: 10.1063/1.2819061

Cancès, E., Mennucci, B., and Tomasi, J. (1997). A new integral equation formalism for the polarizable continuum model: theoretical background and applications to isotropic and anisotropic dielectrics. *J. Chem. Phys.* 107, 3032–3041. doi: 10.1063/1.474659

Carr, R., Evans, N. H., and Parker, D. (2012). Lanthanide complexes as chiral probes exploiting circularly polarized luminescence. *Chem. Soc. Rev.* 41, 7673–7686. doi: 10.1039/C2CS35242G

Cerezo, J., Zúñiga, J., Requena, A., Ávila Ferrer, F. J., and Santoro, F. (2013). Harmonic models in cartesian and internal coordinates to simulate the absorption spectra of carotenoids at finite temperatures. *J. Chem. Theory Comput.* 9, 4947–4958. doi: 10.1021/ct4005849

Chai, J.-D., and Head-Gordon, M. (2008). Long-range corrected hybrid density functionals with damped atom-atom dispersion corrections. *Phys. Chem. Chem. Phys.* 10, 6615–6620. doi: 10.1039/b810189b

Durán-Sampedro, G., Agarrabeitia, A. R., Cerdán, L., Pérez-Ojeda, M. E., Costela, A., García-Moreno, I., et al. (2013). Carboxylates versus fluorines: boosting the emission properties of commercial BODIPYs in liquid and solid media. *Adv. Funct. Mater.* 23, 4195–4205. doi: 10.1002/adfm.201300198

Egidi, F., Bloino, J., Cappelli, C., and Barone, V. (2013). Development of a virtual spectrometer for chiroptical spectroscopies: the case of nicotine. *Chirality* 25, 701–708. doi: 10.1002/chir.22200

Egidi, F., Bloino, J., Cappelli, C., and Barone, V. (2014). A robust and effective time-independent route to the calculation of resonance raman spectra of large molecules in condensed phases with the inclusion of Duschinsky, Herzberg–Teller, anharmonic, and environmental effects. *J. Chem. Theory Comput.* 10, 346–363. doi: 10.1021/ct400932e

Egidi, F., Fusè, M., Baiardi, A., Bloino, J., Li, X., and Barone, V. (2018). Computational simulation of vibrationally resolved spectra for spin-forbidden transitions. *Chirality* 30, 850–865. doi: 10.1002/chir.22864

Fortino, M., Bloino, J., Collini, E., Bolzonello, L., Trapani, M., Faglioni, F., et al. (2019). On the simulation of vibrationally resolved electronic spectra of medium-size molecules: the case of styryl substituted BODIPYs. *Phys. Chem. Chem. Phys.* 21, 3512–3526. doi: 10.1039/C8CP02845A

Freedman, T. B., Lee, E., and Zhao, T. (2002). "Vibrational transition current density: visualizing the origin of vibrational circular dichroism and infrared intensities," in *Chirality: Physical Chemistry, Chapter 5*, ed J. M. Hicks (Washington, DC: American Chemical Society), 65–78.

Freedman, T. B., Shih, M.-L., Lee, E., and Nafie, L. A. (1997). Electron transition current density in molecules. 3. *Ab initio* calculations for vibrational transitions in ethylene and formaldehyde. *J. Am. Chem. Soc.* 119, 10620–10626. doi: 10.1021/ja9701568

Freedman, T. B., Shih, M.-L., Lee, E., and Nafie, L. A. (1998). Electron transition current density in molecules. 2. *Ab initio* calculations for electronic transitions in ethylene and formaldehyde. *J. Phys. Chem. A* 102, 3352–3357. doi: 10.1021/jp972345i

Frisch, M. J., Trucks, G. W., Schlegel, H. B., Scuseria, G. E., Robb, M. A., Cheeseman, J. R., et al. (2019). *Gaussian Development Version, Revision J.05*. Wallingford, CT: Gaussian, Inc.

Furumi, S. (2010). Recent progress in chiral photonic band-gap liquid crystals for laser applications. *Chem. Rec.* 10, 394–408. doi: 10.1002/tcr.201000013

Fusè, M., Egidi, F., and Bloino, J. (2019). Vibrational circular dichroism under the quantum magnifying glass: from the electronic flow to the spectroscopic observable. *Phys. Chem. Chem. Phys.* 21, 4224–4239. doi: 10.1039/C8CP06514D

Gartzia-Rivero, L., Sánchez-Carnerero, E. M., Jiménez, J., Bañuelos, J., Moreno, F., Maroto, B. L., et al. (2017). Modulation of ict probability in bi (polyarene)-based O-BODIPYs: towards the development of low-cost bright arene-BODIPY dyads. *Dalton Trans.* 46, 11830–11839. doi: 10.1039/C7DT01984J

Grimme, S., Antony, J., Ehrlich, S., and Krieg, H. (2010). A consistent and accurate ab initio parametrization of density functional dispersion correction (DFT-D) for the 94 elements H-PU. *J. Chem. Phys.* 132:154104. doi: 10.1063/1.3382344

Grimme, S., Ehrlich, S., and Goerigk, L. (2011). Effect of the damping function in dispersion corrected density functional theory. *J. Comput. Chem.* 32, 1456–1465. doi: 10.1002/jcc.21759

Haoyu, S. Y., He, X., Li, S. L., and Truhlar, D. G. (2016). MN15: a Kohn–Sham global-hybrid exchange–correlation density functional with broad accuracy for multi-reference and single-reference systems and non-covalent interactions. *Chem. Sci.* 7, 5032–5051. doi: 10.1039/C6SC00705H

Hodecker, M., Biczysko, M., Dreuw, A., and Barone, V. (2016). Simulation of vacuum UV absorption and electronic circular dichroism spectra of methyl oxirane: the role of vibrational effects. *J. Chem. Theory Comput.* 12, 2820–2833. doi: 10.1021/acs.jctc.6b00121

Hu, Y., Wang, C.-W., Zhu, C., Gu, F., and Lin, S.-H. (2017). Franck–Condon simulation for unraveling vibronic origin in solvent enhanced absorption and fluorescence spectra of rubrene. *RSC Adv.* 7, 12407–12418. doi: 10.1039/C7RA00417F

Jimènez, J., Cerdàn, L., Moreno, F., Maroto, B. L., García-Moreno, I., Lunkley, J. L., et al. (2017). Chiral organic dyes endowed with circularly polarized laser emission. *J. Phys. Chem. C* 121, 5287–5292. doi: 10.1021/acs.jpcc.7b00654

Jiménez, J., Moreno, F., Maroto, B. L., Cabreros, T. A., Huy, A. S., Muller, G., et al. (2019). Modulating ICT emission: a new strategy to manipulate the CPL sign in chiral emitters. *Chem. Commun.* 55, 1631–1634. doi: 10.1039/C8CC09401B

Kamkaew, A., Lim, S. H., Lee, H. B., Kiew, L. V., Chung, L. Y., and Burgess, K. (2013). BODIPY dyes in photodynamic therapy. *Chem. Soc. Rev.* 42, 77–88. doi: 10.1039/C2CS35216H

Kaur, P., and Singh, K. (2019). Recent advances in the application of BODIPY in bioimaging and chemosensing. *J. Mater. Chem. C* 7, 11361–11405. doi: 10.1039/C9TC03719E

Kumar, J., Nakashima, T., and Kawai, T. (2015). Circularly polarized luminescence in chiral molecules and supramolecular assemblies. *J. Phys. Chem. Lett.* 6, 3445–3452. doi: 10.1021/acs.jpclett.5b01452

Le Guennic, B., Maury, O., and Jacquemin, D. (2012). Aza-boron-dipyrromethene dyes: TD-DFT benchmarks, spectral analysis and design of original near-IR structures. *Phys. Chem. Chem. Phys.* 14, 157–164. doi: 10.1039/C1CP22396H

Li, M., Li, S.-H., Zhang, D., Cai, M., Duan, L., Fung, M.-K., et al. (2018). Stable enantiomers displaying thermally activated delayed fluorescence: efficient OLEDs with circularly polarized electroluminescence. *Angew. Chem. Int. Ed.* 57, 2889–2893. doi: 10.1002/anie.201800198

Licari, D., Baiardi, A., Biczysko, M., Egidi, F., Latouche, C., and Barone, V. (2015). Implementation of a graphical user interface for the virtual multifrequency spectrometer: the VMS-draw tool. *J. Comput. Chem.* 36, 321–334. doi: 10.1002/jcc.23785

Lifschitz, A. M., Shade, C. M., Spokoyny, A. M., Mendez-Arroyo, J., Stern, C. L., Sarjeant, A. A., et al. (2013). Boron-dipyrromethene-functionalized hemilabile ligands as "turn-on" fluorescent probes for coordination changes in weak-link approach complexes. *Inorg. Chem.* 52, 5484–5492. doi: 10.1021/ic400383t

Lin, N., Luo, Y., Santoro, F., Zhao, X., and Rizzo, A. (2008a). Vibronically-induced change in the chiral response of molecules revealed by electronic circular dichroism. *Chem. Phys. Lett.* 464, 144–149. doi: 10.1016/j.cplett.2008.09.013

Lin, N., Santoro, F., Rizzo, A., Luo, Y., Zhao, X., and Barone, V. (2009). Theory for vibrationally resolved two-photon circular dichroism spectra. application to (*R*)-(+)-3-methylcyclopentanone. *J. Phys. Chem. A* 113, 4198–4207. doi: 10.1021/jp8105925

Lin, N., Santoro, F., Zhao, X., Rizzo, A., and Barone, V. (2008b). Vibronically resolved electronic circular dichroism spectra of (*R*)-(+)-3-methylcyclopentanone: a theoretical study. *J. Phys. Chem. A* 112, 12401–12411. doi: 10.1021/jp8064695

Lindh, R., Bernhardsson, A., and Schütz, M. (1999). Force-constant weighted redundant coordinates in molecular geometry optimizations. *Chem. Phys. Lett.* 303, 567–575. doi: 10.1016/S0009-2614(99)00247-X

Liu, S., Shi, Z., Xu, W., Yang, H., Xi, N., Liu, X., et al. (2014). A class of wavelength-tunable near-infrared AZA-BODIPY dyes and their application for sensing mercury ion. *Dyes Pigm.* 103, 145–153. doi: 10.1016/j.dyepig.2013.12.00410.1016/j.dyepig.2013.12.004

Liu, Y., Cerezo, J., Mazzeo, G., Lin, N., Zhao, X., Longhi, G., et al. (2016). Vibronic coupling explains the different shape of electronic circular dichroism and of circularly polarized luminescence spectra of hexahelicenes. *J. Chem. Theory Comput.* 12, 2799–2819. doi: 10.1021/acs.jctc.6b00109

Longhi, G., Castiglioni, E., Koshoubu, J., Mazzeo, G., and Abbate, S. (2016). Circularly polarized luminescence: a review of experimental and theoretical aspects. *Chirality* 28, 696–707. doi: 10.1002/chir.22647

Loudet, A., and Burgess, K. (2007). Bodipy dyes and their derivatives: syntheses and spectroscopic properties. *Chem. Rev.* 107, 4891–4932. doi: 10.1021/cr078381n

Lu, H., Mack, J., Nyokong, T., Kobayashi, N., and Shen, Z. (2016). Optically active BODIPYs. *Coord. Chem. Rev.* 318, 1–15. doi: 10.1016/j.ccr.2016.03.015

Lu, T., and Chen, F. (2012). Multiwfn: a multifunctional wavefunction analyzer. *J. Comput. Chem.* 33, 580–592. doi: 10.1002/jcc.22885

Macak, P., Luo, Y., and Ågren, H. (2000). Simulations of vibronic profiles in two-photon absorption. *Chem. Phys. Lett.* 330, 447–457. doi: 10.1016/S0009-2614(00)01096-4

Nafie, L. A. (1994). "Molecular electronic transition current density, Chapter 4," in *Molecular and Biomolecular Electronics*, ed R. R. Birge (Washington, DC: American Chemical Society), 63–80.

Nafie, L. A. (1997). Electron transition current density in molecules. 1. non-Born-Oppenheimer theory of vibronic and vibrational transitions. *J. Phys. Chem. A* 101, 7826–7833. doi: 10.1021/jp9706137

Padula, D., Santoro, F., and Pescitelli, G. (2016). A simple dimeric model accounts for the vibronic ECD spectra of chiral polythiophenes in their aggregated states. *RSC Adv.* 6, 37938–37943. doi: 10.1039/C6RA05500A

Pedone, A., Bloino, J., and Barone, V. (2012). Role of host–guest interactions in tuning the optical properties of coumarin derivatives incorporated in MCM-41: A TD-DFT investigation. *J. Phys. Chem. C* 116, 17807–17818. doi: 10.1021/jp305294u

Pop, F., Zigon, N., and Avarvari, N. (2019). Main-group-based electro- and photoactive chiral materials. *Chem. Rev.* 119, 8435–8478. doi: 10.1021/acs.chemrev.8b00770

Pritchard, B., and Autschbach, J. (2010). Calculation of the vibrationally resolved, circularly polarized luminescence of d-camphorquinone and (*S*, *S*)-trans-β-hydrindanone. *ChemPhysChem* 11, 2409–2415. doi: 10.1002/cphc.20100005410.1002/cphc.201000054

Reimers, J. R. (2001). A practical method for the use of curvilinear coordinates in calculations of normal-mode-projected displacements and duschinsky rotation matrices for large molecules. *J. Chem. Phys.* 115, 9103–9109. doi: 10.1063/1.1412875

Riehl, J. P., and Richardson, F. S. (1986). Circularly polarized luminescence spectroscopy. *Chem. Rev.* 86, 1–16. doi: 10.1021/cr00071a001

Ruhoff, P. T. (1994). Recursion relations for multi-dimensional Franck-Condon overlap integrals. *Chem. Phys.* 186, 355–374. doi: 10.1016/0301-0104(94)00173-1

Sánchez-Carnerero, E. M., Agarrabeitia, A. R., Moreno, F., Maroto, B. L., Muller, G., Ortiz, M. J., et al. (2015). Circularly polarized luminescence from simple organic molecules. *Chem. Eur. J.* 21, 13488–13500. doi: 10.1002/chem.201501178

Sánchez-Carnerero, E. M., Moreno, F., Maroto, B. L., Agarrabeitia, A. R., Ortiz, M. J., Vo, B. G., et al. (2014). Circularly polarized luminescence by visible-light absorption in a chiral O-BODIPY dye: Unprecedented design of CPL organic molecules from achiral chromophores. *J. Am. Chem. Soc.* 136, 3346–3349. doi: 10.1021/ja412294s

Santoro, F., and Barone, V. (2010). Computational approach to the study of the lineshape of absorption and electronic circular dichroism spectra. *Int. J. Quantum Chem.* 110, 476–486. doi: 10.1002/qua.22197

Santoro, F., Improta, R., Lami, A., Bloino, J., and Barone, V. (2007a). Effective method to compute Franck-Condon integrals for optical spectra of large molecules in solution. *J. Chem. Phys.* 126:084509. doi: 10.1063/1.2437197

Santoro, F., Lami, A., Improta, R., and Barone, V. (2007b). Effective method to compute vibrationally resolved optical spectra of large molecules at finite temperature in gas phase and in solution. *J. Chem. Phys.* 126:184102. doi: 10.1063/1.2721539

Santoro, F., Lami, A., Improta, R., Bloino, J., and Barone, V. (2008). Effective method for the computation of optical spectra of large molecules at finite temperature including the Duschinsky and Herzberg-Teller effect: the q_X band of porphyrin as a case study. *J. Chem. Phys.* 128:224311. doi: 10.1063/1.2929846

Sharp, T. E., and Rosenstock, H. M. (1963). Franck–Condon factors for polyatomic molecules. *J. Chem. Phys.* 41, 3453–3463. doi: 10.1063/1.1725748

Shivran, N., Tyagi, M., Mula, S., Gupta, P., Saha, B., Patro, B. S., et al. (2016). Syntheses and photodynamic activity of some glucose-conjugated BODIPY dyes. *Eur. J. Med. Chem.* 122, 352–365. doi: 10.1016/j.ejmech.2016.06.050

Swart, M., and Bickelhaupt, F. M. (2006). Optimization of strong and weak coordinates. *Int. J. Quantum Chem.* 106, 2536–2544. doi: 10.1002/qua.21049

Telea, A. C. (2007). *Data Visualization: Principles and Practice*. Boca Raton, FL: AK Peters; CRC Press.

Turksoy, A., Yildiz, D., and Akkaya, E. U. (2019). Photosensitization and controlled photosensitization with BODIPY dyes. *Coord. Chem. Rev.* 379, 47–64. doi: 10.1016/j.ccr.2017.09.029

Ulrich, G., Ziessel, R., and Harriman, A. (2008). The chemistry of fluorescent BODIPY dyes: versatility unsurpassed. *Angew. Chem. Int. Ed.* 47, 1184–1201. doi: 10.1002/anie.200702070

Valero, R., Costa, R., Moreira, I. D. P. R., Truhlar, D. G., and Illas, F. (2008). Performance of the M06 family of exchange-correlation functionals for predicting magnetic coupling in organic and inorganic molecules. *J. Chem. Phys.* 128:114103. doi: 10.1063/1.2838987

Vydrov, O. A., and Scuseria, G. E. (2006). Assessment of a long-range corrected hybrid functional. *J. Chem. Phys.* 125:234109. doi: 10.1063/1.2409292

Wang, T., Douglass Jr., E. F., Fitzgerald, K. J., and Spiegel, D. A. (2013). A "turn-on" fluorescent sensor for methylglyoxal. *J. Am. Chem. Soc.* 135, 12429–12433. doi: 10.1021/ja406077j

Yanai, T., Tew, D. P., and Handy, N. C. (2004). A new hybrid exchange–correlation functional using the coulomb-attenuating method (CAM-B3LYP). *Chem. Phys. Lett.* 393, 51–57. doi: 10.1016/j.cplett.2004.06.011

Zhang, X., Liu, Y., Xu, C., Teng, L., Liu, H., Ren, T.-B., et al. (2020). pH stimuli-disaggregated BODIPY: an activated photodynamic/photothermal sensitizer applicable to tumor ablation. *Chem. Commun. (Camb).* 56, 1956–1959. doi: 10.1039/C9CC09790B

Zhao, J., Xu, K., Yang, W., Wang, Z., and Zhong, F. (2015). The triplet excited state of BODIPY: formation, modulation and application. *Chem. Soc. Rev.* 44, 8904–8939. doi: 10.1039/C5CS00364D

Zinna, F., Bruhn, T., Guido, C. A., Ahrens, J., Bröring, M., Di Bari, L., et al. (2016). Circularly polarized luminescence from axially chiral BODIPY DYEmers: an experimental and computational study. *Chem. Eur. J.* 22, 16089–16098. doi: 10.1002/chem.201602684

Zinna, F., and Di Bari, L. (2015). Lanthanide circularly polarized luminescence: bases and applications. *Chirality* 27, 1–13. doi: 10.1002/chir.22382

Conflict of Interest: The authors declare that the research was conducted in the absence of any commercial or financial relationships that could be construed as a potential conflict of interest.

frontiers in Chemistry

MINI REVIEW
published: 29 October 2020
doi: 10.3389/fchem.2020.00700

[2.2]Paracyclophane-Based Chiral Platforms for Circularly Polarized Luminescence Fluorophores and Their Chiroptical Properties: Past and Future

*Ken-ichi Sugiura**

Department of Chemistry, Tokyo Metropolitan University, Hachioji, Japan

Quality of CPL fluorophore is defined by the vectors of electric dipole transition moment and imaginary magnetic dipole transition moment. The aim of this review is to introduce readers to a chiral moiety applicable to CPL studies focusing on chiral cyclophanes because the rigid cyclophanes are able to hold the vector directions of electric dipole transition moment and imaginary magnetic dipole transition moment.

Keywords: carbazole, chirality, circularly polarized luminescence, cyclophane, multi-layer, pyrene

OPEN ACCESS

Edited by:
Ga-Lai Law,
Hong Kong Polytechnic University,
Hong Kong

Reviewed by:
Son Tung Ngo,
Ton Duc Thang University, Vietnam
Lipeng Xin,
Xi'an Jiaotong University, China

***Correspondence:**
Ken-ichi Sugiura
sugiura@porphyrin.jp

Specialty section:
This article was submitted to Physical Chemistry and Chemical Physics, a section of the journal Frontiers in Chemistry

Received: *08 April 2020*
Accepted: *07 July 2020*
Published: *29 October 2020*

Citation:
Sugiura K-i (2020) [2.2]Paracyclophane-Based Chiral Platforms for Circularly Polarized Luminescence Fluorophores and Their Chiroptical Properties: Past and Future. Front. Chem. 8:700. doi: 10.3389/fchem.2020.00700

INTRODUCTION

Circularly polarized luminescence (CPL) is both an old and a new research field. As far as the author knows, the first CPL observation could be the spectrum for a chiral crystal of uranyl acetate ($Na[UO_2(CH_3COO)_3]$) recorded at liq. He temperature in 1948 (Samoilov, 1948; Ferrari et al., 1959; Golovnya, 1963; Murata et al., 1979). Soon, researchers noticed the versatile applications of CPL and CPL science started attracting much attention. From the 1970's onwards, excellent reviews of the physics of CPL and the materials that show CPL have been published, reflecting the vast interest of scientists and engineers in CPL phenomena (Richardson and Riehl, 1977; Steinberg, 1978; Riehl and Richardson, 1986; Gussakovsky, 2008; Bradberry et al., 2014; Watanabe and Akagi, 2014; Sanchez-Carnerero et al., 2015; Zinna and Di Bari, 2015; Longhi et al., 2016; Han et al., 2018; Tanaka et al., 2018; Akagi, 2019). Basic theoretical background was already established in 1970' (Richardson and Riehl, 1977), however, the lack of a commercially available CPL apparatus hindered the progress of this research field and only a limited number of researchers who could make the apparatus were able to conduct research of CPL. The author likens CPL research in the 1980's to the *dark ages*.

In the 1980's, commercially available apparatus, i.e., *haute couture* apparatus, appeared in the market. Because of this, researchers, particularly synthetic chemists, gradually became accustomed to measuring CPL spectra. Today, many publications on CPL and related phenomena are available. CPL evolved into one of the fundamental physical properties to be reported when a researcher synthesizes a new chiral molecule, similarly to NMR, mass, IR, absorption, and conventional emission spectra.

One of the most important research topics in CPL science is how to improve the *g*-value of the fluorophore because the *g*-value is one of the most important indexes and/or the degree of CPL expressing the quality of a CPL fluorophore. Then, how does a researcher obtain high *g*-values? The

g-value is defined by the ratio of the difference in intensity divided by the average total luminescence intensity, as follows:

$$g = \frac{\triangle l}{\frac{1}{2}l} = \frac{l_L - l_R}{\frac{1}{2}(l_L - l_R)} = 4\frac{m}{\mu}\cos\theta_{\mu,m}$$

where μ and m are the vectors of electric dipole transition moment and imaginary magnetic dipole transition moment, respectively, and $\theta_{\mu,m}$ is the angle between them (Zinna and Di Bari, 2015). The g-value is a function of μ and m. We can qualitatively estimate μ of the molecule; in other words, we can design a fluorophore having a large μ (Berova et al., 2007). However, the estimation of m is non-objective and it is too difficult to translate m into a molecular structure. Therefore, the development of good CPL fluorophores is literally a continuous process of *trial* and *error* and largely depends on a researcher's intuition.

The CPL fluorophores used in the early stage of this science were simple. For example, chiral ketone **1** is a milestone molecule studied in CPL science in the 1960's through the 1970's. Unfortunately, the low quantum yield of this chromophore prevented its application (Emeis and Oosterhoff, 1967). Along with the progress of asymmetric synthesis using chiral catalysts prepared from 1,1′-bi-2-naphthol (BINOL) **2** and related compounds, this molecule was also applied in CPL science. In contrast to the excellent results of asymmetric synthesis using **2**, the low quantum yield ($\Phi = 0.04$) of **2** might have prevented the progress of CPL science (Hassan et al., 2015). In addition, the functionalization of **2** for CPL studies was usually carried out on the hydroxyl group(s) and the resultant ether linkage had a flexible conformation that led to ambiguous μ and m directions.

The aim of this review is to introduce readers to a chiral moiety applicable to CPL studies. Details of the physics of CPL and the proposed applications have been omitted because we already have many excellent reviews including those in this special issue. The author focuses on chiral cyclophanes for reasons discussed in the following section. Because the chemistry of chiral cyclophanes has a long and rich history, reports of these molecules are abundant (Hassan et al., 2020a). The author believes that a good CPL fluorophore having a high g-value could be obtained using the cyclophane skeleton. Actually, Tani and his coworkers reported one of the highest g-value for their carbazole-based cyclophanes, $|1.3 \times 10^{-2}|$ (*vide infra*) (Tani et al., 2001, 2020). Furthermore, as most of the reported chiral cyclophanes lack chiroptical properties, the author also believes that a good CPL fluorophore already exists among them. In this review, the author also introduces reported chiral cyclophanes such as pyrenophanes, which show great potential in CPL science. This information is expected to benefit readers.

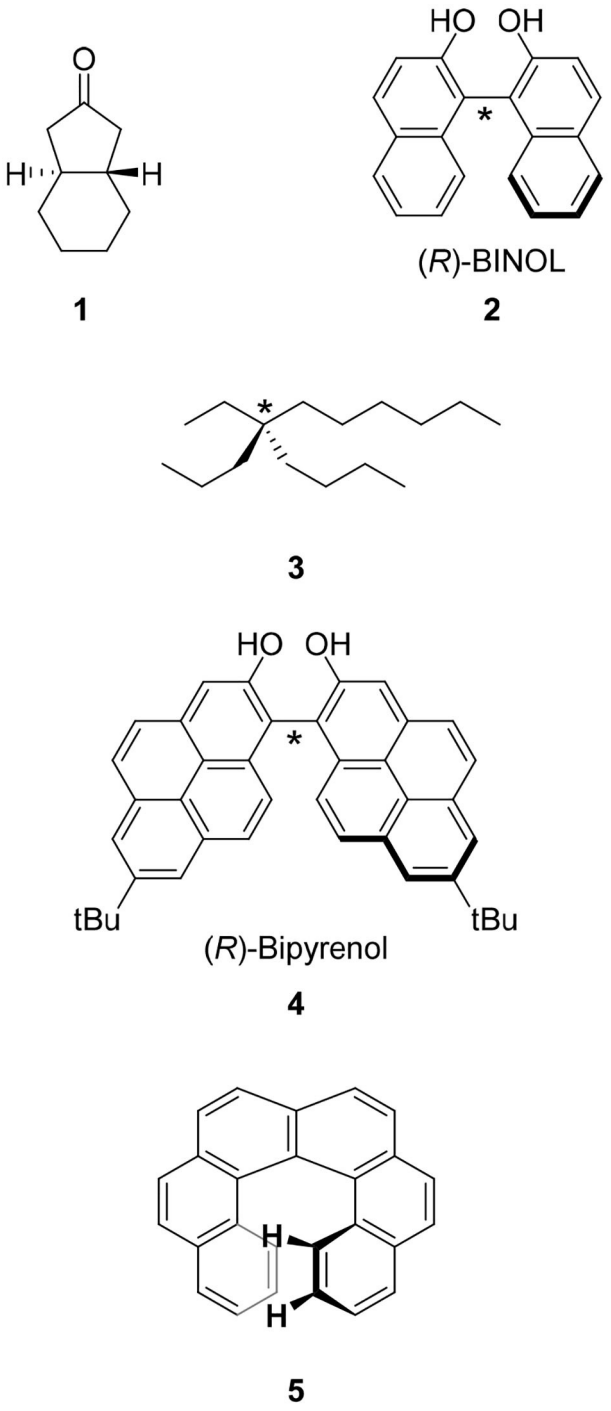

FIGURE 1 | Molecular structures of CPL fluorophores studied in the early stage of this science. Molecular structures of one of the isomers of **1**–**5** are shown. The chiral center and chiral axes of 2-4 are indicated with asterisks.

DEFINITION OF CHIRAL MOLECULE, CLASSIFICATION OF CHIRALITY, AND CRYPTOCHIRALITY IN CPL SCIENCE

A CPL fluorophore should be chiral. Because chirality is one of the most important concepts in chemistry, several definitions of a chiral molecule are known. The simplest definition is that a chiral molecule is a molecule having (a) carbon atom(s) to which four different groups are attached. For example, 5-ethyl-5-propyl-undecane **3**, in which one carbon has ethyl, propyl,

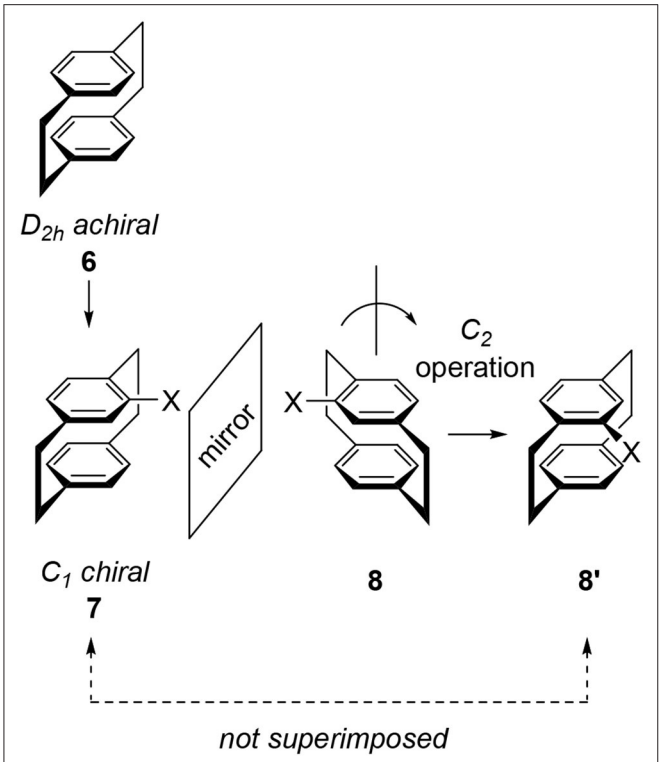

FIGURE 2 | Molecular structures of [2.2]paracyclophane **6** and its monosubstituted derivative **7**. **8** or **8′** are the mirror image of **7** and **8**/**8′** is different from **7**. Therefore, **7** and **8** are enantiomers.

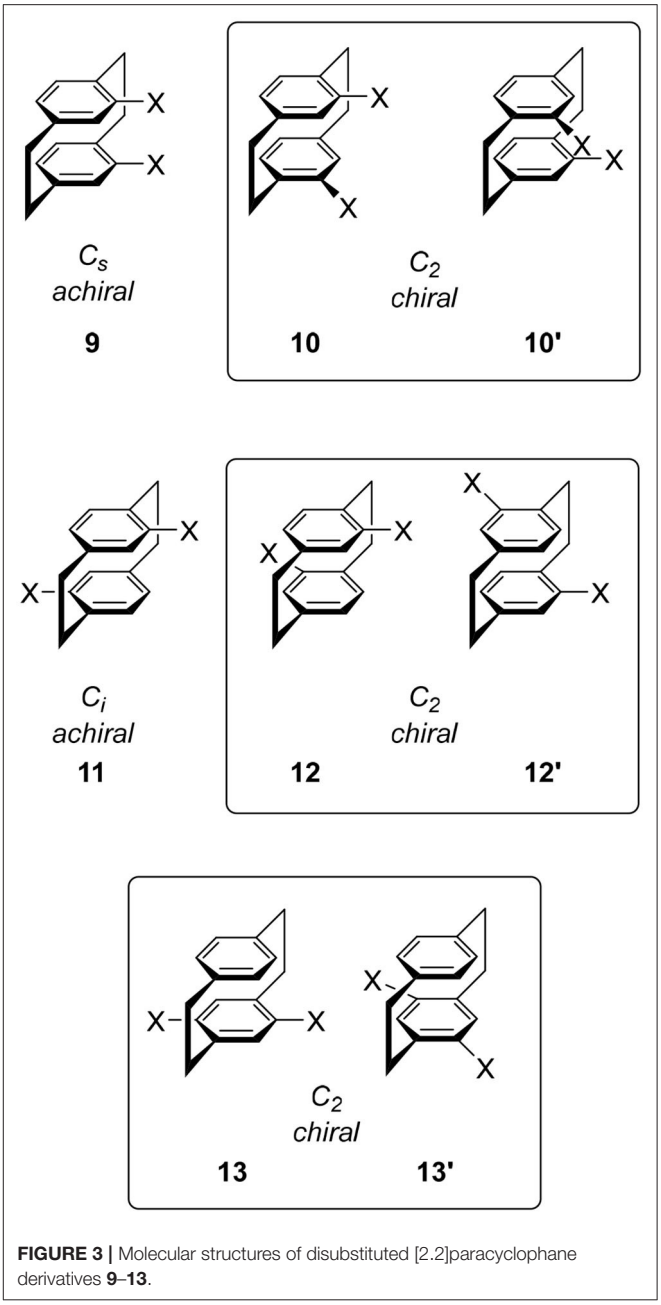

FIGURE 3 | Molecular structures of disubstituted [2.2]paracyclophane derivatives **9**–**13**.

butyl, and hexyl groups attached, is a chiral molecule (*vide infra*) (Rabjohn and Latina, 1954). The type of this chirality is called central chirality and the corresponding molecules belong to the C_1 point group. In CPL science, molecules classified under this chirality type are few (*vide infra*).

Most of the chiral molecules studied in CPL science are not central chirality molecules. As described in the previous section, BINOL **2** is one of the most frequently used chiral groups in contemporary CPL science. This molecule has no carbon atom having four different groups. The chirality of BINOL is generated by the C-C bond between the two naphthalene moieties and this bond is called chiral axis (the chiral axis of **2** is denoted by "*" in **Figure 1**). This type of chirality is called axial chirality. In CPL science, a molecule must be able to emit light and therefore, arenes are the main category of molecules. The connection of two fluorescent arenes at the hindered position to restrict free rotation induces axial chirality. Based on this consideration, the author reported bipyrenol **4** having an improved quantum yield (Hassan et al., 2015).

Apart from central and axial chiralities is planar chirality. This type of chirality is found in chiral cyclophane, the main topic of this review. The detailed behavior of planar chirality is introduced in the following section using cyclophanes as example. We also have helical chirality represented by helicene, i.e., π-expanded arenes. However, such helicenes as [6]helicene **5** show extremely low quantum yields (Birks et al., 1976). The CPL science based on helical chirality and helicenes is an issue for the future.

Next, the author would like to refresh readers' minds regarding *cryptochirality*. An important example is the optical rotation of chiral molecule **3**. Optical rotation measurement was carried out for optically pure 3 but the spectra were silent (Wynberg et al., 1965; Wynberg and Hulshof, 1974) because the electrons of the four structurally similar substituents induced negligible perturbation of the electric fields. Later, the term *cryptochirality* was coined to describe this phenomenon. This phenomenon is applicable to CPL science, namely, even if we design a chiral fluorophore, the molecule would not always emit

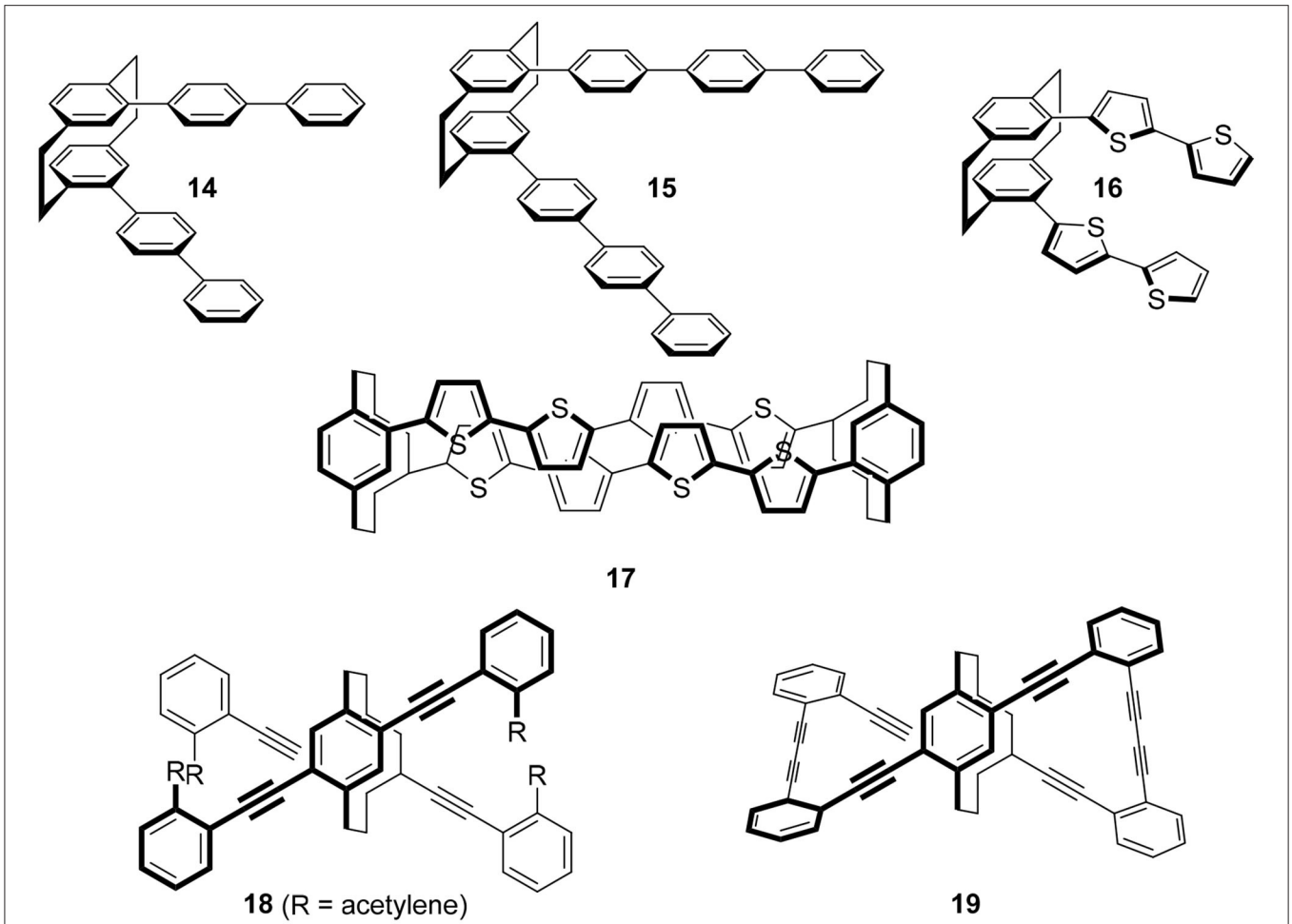

FIGURE 4 | Molecular structures of CPL fluorophores **14–19** based on [2.2]paracyclophane skeleton. The substituents were omitted for clarity.

CPL. Revealing the reason would be tantamount to revealing the molecular design of a CPL fluorophore. Therefore, the author sincerely hopes that researchers report negligible CPL behaviors of chiral fluorophores. These "undesirable" information could open doors to the synthetic strategy of a CPL fluorophore.

CHIRALITIES OF SUBSTITUTED [2.2]PARACYCLOPHANES

"Cyclophane" is the general term for arenes having cyclic moieties and various types of molecules are known (Vögtle, 1993; Gleiter and Hopf, 2004). In this review, the author only deals with stacked arene dimers connected by ethylene bridges and their related compounds. A representative example is achiral [2.2]paracyclophane **6**, a symmetrical molecule classified into the D_2h point group (**Figure 2**). The introduction of substituent *X* onto the benzene ring of **6** produces monosubstituted cyclophane **7**, a chiral molecule. Here we examine this chirality by reflecting **7** on a mirror to give image **8**. To compare the generated molecular shape of **8** with the molecular shape of original **7**, a rotation operation is carried out to produce another image **8′**. Obtained **8′** is different from **7** and therefore, **7** and **8** are enantiomers. Monosubstituted **7** is chiral and its point group is C_1.

The disubstitution of **6** also induces chirality. Recently, an excellent review of the substitution manner of [2.2]paracyclophane was published and a systematic consideration of the chirality of the disubstituted molecule was introduced (Hassan et al., 2020b). To avoid duplication, important derivatives in CPL science are introduced here. When we introduce one substituent each onto the two benzenes, we obtain four types of isomers **9**, **10**, **11**, and **12**. The point groups of **9** and **11** are C_s and C_i, respectively, and these molecules are not chiral. In contrast, the point groups of **10** and **12** are C_2, i.e., these molecules are chiral. The structures of the corresponding enantiomers **10′** and **12′** are shown in **Figure 3**. The introduction of two substituents on one benzene ring also forms a chiral cyclophane, e.g., **13**, which belongs to the C_2 point group generating enantiomer **13′**. This substitution manner is the key to multilayered chiral cyclophanes (*vide infra*).

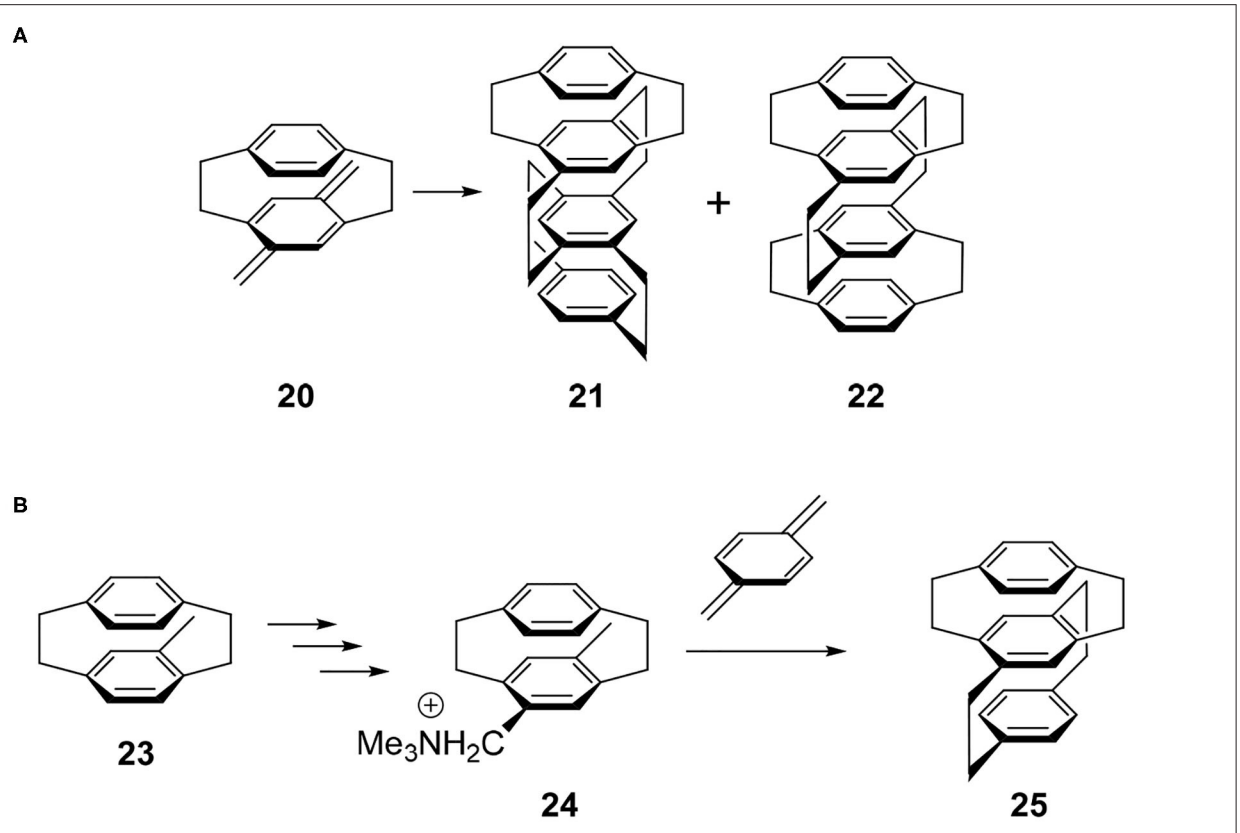

FIGURE 5 | (A) Synthesis of multilayered [2.2]paracyclophane derivatives **21** and **22**. **(B)** Stereoselective synthesis of four-layered cyclophane.

[2.2]PARACYCLOPHANE-BASED CPL FLUOROPHORE

As discussed above, monosubstituted **7** and disubstituted **10**, **12**, and **13** are chiral [2.2]paracyclophanes. When we introduce fluorescent group *X* onto these cyclophanes using, e.g., Pd-catalyzed coupling reactions, candidates for CPL are generated. In this review, three important examples are introduced, as follows.

The molecule to be introduced first is the simplest yet most informative example (**Figure 4**). Hasegawa and coworkers focused on *para*-phenylene fluorophores and introduced these fluorophores onto chiral **10** (X = Br) by the Suzuki coupling reaction to produce **14** and **15**, respectively (Ishioka et al., 2019). The two terphenyls in **14** and the two quaterphenyls in **15** are arranged in a chiral manner, and the termini of these fluorophores interact strongly through the [2.2]paracyclophane skeletons. Their quantum yields are dependent on the introduced para-phenylenes, i.e., Φ = 0.20 and 0.64 for **14** and **15**, respectively. Reflecting these chiral alignments, the expected CPL spectra were observed and $g = |4.2 \times 10^{-3}|$ (at 381 nm) and $g = |1.5 \times 10^{-3}|$ (at 385 nm) for **14** and **15**, respectively.

Although the publication years of the papers are back and forth, this strategy has produced various CPL fluorophores by replacing the *X* of **10**. For example, the replacement of *para*-phenylenes of **14** and **15** with oligothiophenes (OTs) gave **16** because OTs are one of the most important molecules in photochemistry. Then, the terminus of this molecule was capped with the [2.2]paracyclophane derivative to afford **17** (Hasegawa et al., 2017). Although they did not measure CPL of these molecules, the clear CD spectra of these molecules have enhanced expectations of their potential applications.

Other than thiophene, various π-systems were introduced as *X* of **10** and characteristic chiral molecules were synthesized. Morisaki's group introduced acetylenes using the Sonogashira coupling, **18** (Morisaki et al., 2014). Acetylenes offer the advantage of further functionalization under mild reaction conditions. Subsequently, they carried out the Glaser-type diacetylene formation reaction, which produced *Escher's trompe l'œil* style cyclic molecule **19**. Although the quantum yield was moderate, Φ = 0.45, its *g*-value was extremely high as a small organic molecule, $|1.1 \times 10^{-2}|$. Presumably, the rigidity of cyclophane and the strong interaction of the chromophore via the cyclophane unit would contribute to these chiroptical properties.

MULTILAYERED CYCLOPHANE

In the following two sections, the author introduces old molecules synthesized in the 1970's through the 1980's. Of

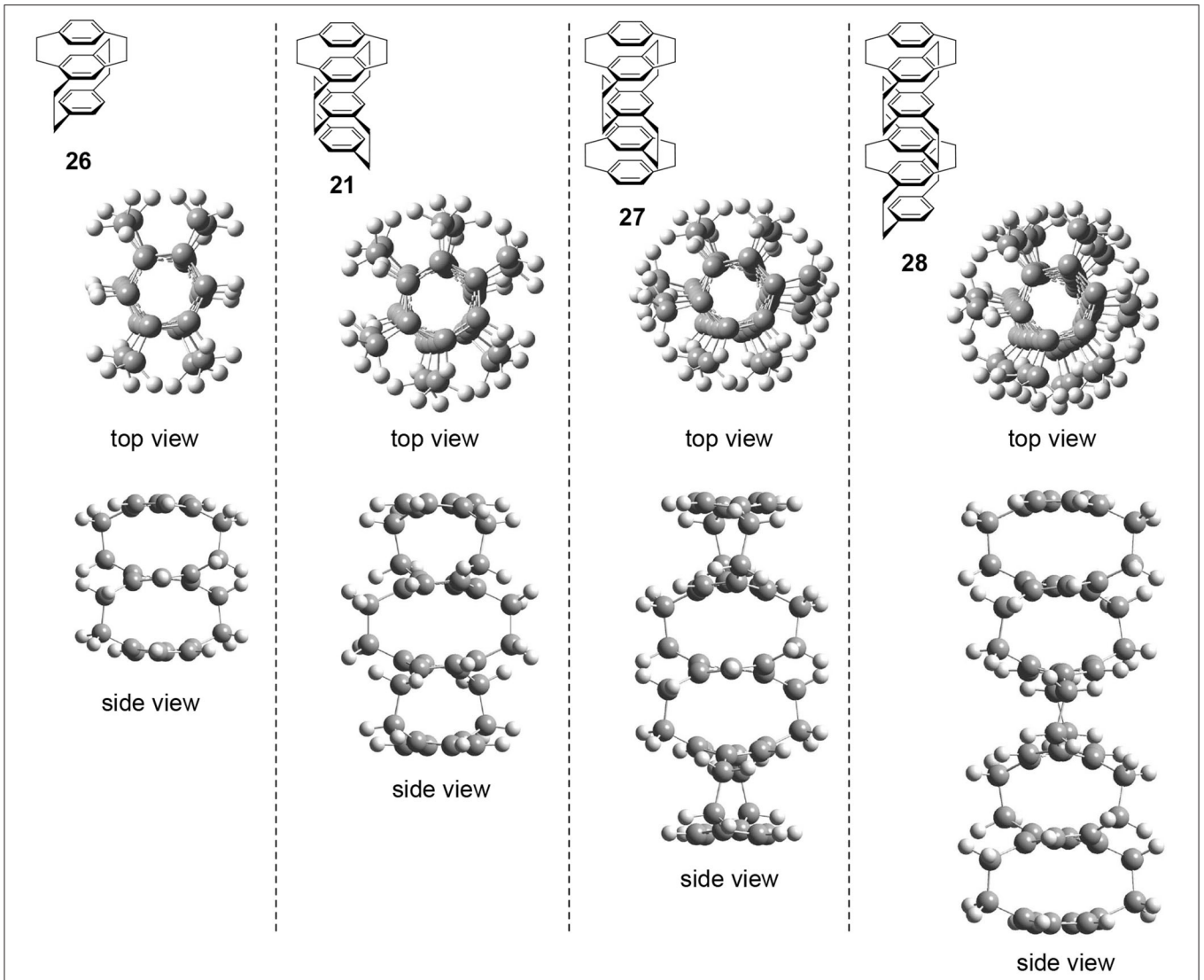

FIGURE 6 | Top and side views of theoretically optimized structures of multilayered [2.2]paracyclophane derivatives **26**, **21**, **27**, and **28** [B3LYP/6-31G(d)].

course, no synthetic chemists measured the CPL spectra of those molecules at that time. However, the author believes that the molecule(s) shown here could become leading compound(s) in future CPL science, inspiring breakthroughs.

The synthetic study of multilayered cyclophanes is one of the most exciting research topics in the history of cyclophanes (Misumi, 1983). The motivation of this chemistry was to reveal the through-space π-π interaction and ring current effects between the arenes. As far as the author knows, the first multilayered [2.2]cyclophane was a four-layered cyclophane (Longone and Chow, 1964, 1970). This molecule was prepared by the dimerization reaction of thermally generated *para*-xylylene intermediate **20** and this reaction afforded a mixture of **21** and **22** (**Figure 5A**). Later, Otsubo and Misumi performed fractional crystallization to give readily and sparingly soluble fractions. Comparing the spectra with those of authentic samples synthesized from structurally well-confirmed precursors, the readily soluble solid was determined to be **21** belonging to the D_2 point group, a chiral molecule focused in this review. Product **21** should be a thermodynamically controlled product to avoid steric repulsion of the bridges, whereas **22** could be a kinetically controlled product.

Because above-mentioned chiral molecule **21** was racemic, Yamamoto and Nakazaki achieved a stereoselective synthesis using a known optically pure cyclophane precursor (Nakazaki et al., 1977). For example, optically pure **23** was converted into **24** and the subsequent coupling reaction with *para*-xylylene afforded optically pure three-layered compound **25** (**Figure 5B**). Along with this compound, they reported the CD spectra of a series of optically pure cyclophanes ranging from two- to six-layered compounds.

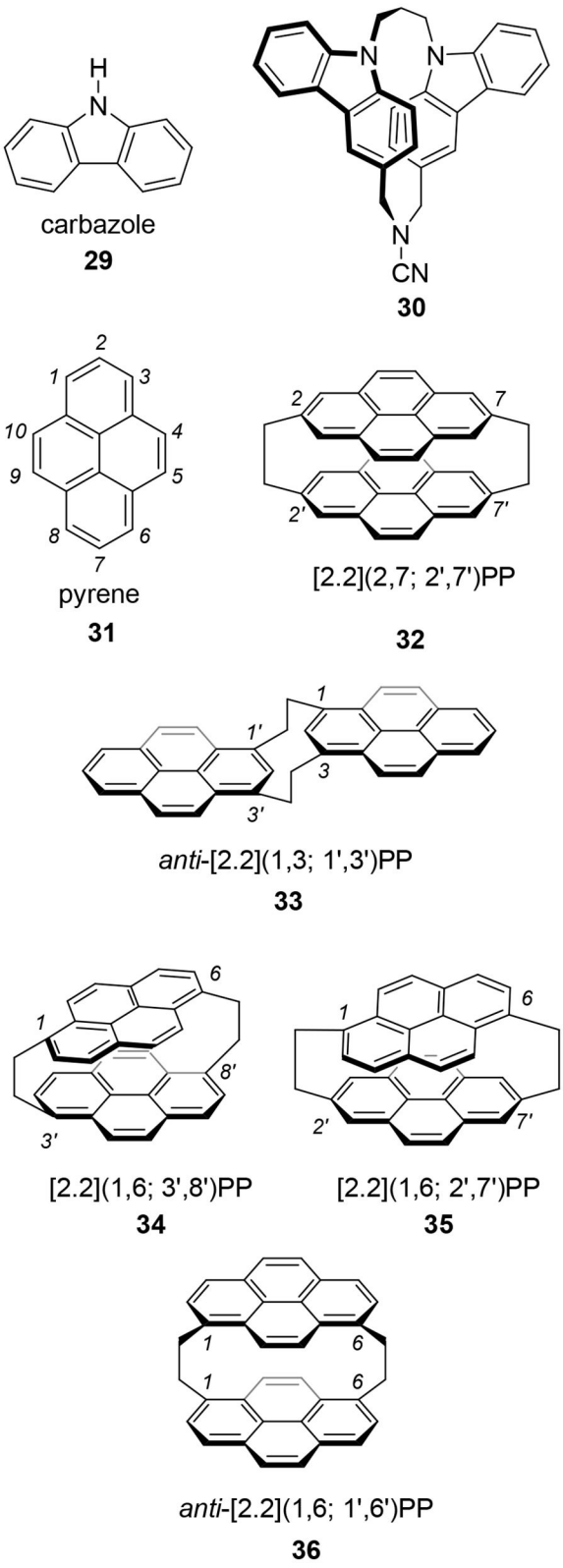

FIGURE 7 | Cyclophane derivatives using carbazole **29** and pyrene **31**.

The author performed preliminary theoretical studies of these multilayered chiral cyclophanes, i.e., three-layered **26**, four-layered **21**, five-layered **27**, and six-layered **28**. The optimized structures are shown in **Figure 6**. First of all, the author points out that all of these molecules belong to the D_2 point group regardless of the odd or even number of benzenes. The obtained structures reproduce the experimental result, i.e., the twisted boat conformation of the interior benzenes. The top views of the molecules suggest that the stacked benzenes take a screw alignment similar to the helical assembly of a chiral discotic liquid crystal that shows CPL (Wu et al., 2017). Therefore, CPL studies of multilayered cyclophanes could be important to reveal the molecular design strategy of the chromophore.

CYCLOPHANES USING ARENES OTHER THAN BENZENE: CARBAZOLOPHANE AND PYRENOPHANE

The chiral cyclophanes introduced in the previous sections show moderate *g*-values. However, their quantum yields are not so high for practical applications. If we replace the benzene moieties of **6** with fluorescent arenes, what will happen? As described, the author replaced the naphthalene of **2** with pyrene, a standard molecule in photochemistry, and good CPL fluorophore **4** was obtained (Hassan et al., 2015). A similar strategy could be applicable to other molecular systems (**Figure 7**).

Tani's group focused on carbazole **29** as the best candidate because carbazole is one of the widely applied molecules in photoelectronic technologies (Tani et al., 2001, 2020). They prepared chiral carbazolophane **30** and its enantiomer. Although its quantum yield was low, $\Phi = 0.047$, its *g*-value was extremely high as a small organic molecule, $|1.3 \times 10^{-2}|$. That they used propylene ([3.3]) as the linkage suggests that a shorter [2.2] linkage is not always needed for a good CPL fluorophore showing a high *g*-value.

Pyrene **31** is one of the most popular fluorophores in chemistry (Winnik, 1993; Casas-Solvas et al., 2014). Therefore, CPL research of a pyrene-based cyclophane, pyrenophane (PP), should be interesting. Using two ethylene bridges, i.e., [2.2] linkage, various [2.2](n,m; n′,m′)pyrenophanes are possible, where n, m, n′, and m′ are the position numbers of each pyrene. In the 1970's, several isomers were reported. At that time, the motivation for PP research was the model of a pyrene excimer. In 1975, Misumi reported the first PPs, i.e., [2.2](2,7; 2′,7′) **32** (Umemoto et al., 1975b; Staab and Kirrstetter, 1979) and *anti*-[2.2](1,3; 1′,3′) 33 (Umemoto et al., 1975a). Later, Misumi synthesized other isomers: [2.2](1,6; 3′,8′) 34, [2.2](1,6; 2′,7′) **35**, and [2.2](1,3; 1′,3′) **36** (Kawashima et al., 1978). Among these five isomers, **34** and **35** are chiral and their point groups are D_2 and C_2, respectively. It is unfortunate that few photophysical properties of these molecules are known because the synthesis of these molecules is time-consuming and difficult. However, the author hopes a revised synthetic scheme would be developed using contemporary

reactions to provide **34** and **35** for chiroptical studies in the future.

CONCLUSION

In this short review, the author introduced cyclophane-based CPL fluorophores along with chiral cyclophanes having potential as a CPL fluorophore. Contemporary research of CPL has just started. Along with the basic photophysical chemistry achievements introduced in the literatures shown in introduction section, fundamental research topics, e.g., the relationship between the chirality and light (Ayuso et al., 2019), are also ongoing.

Experiments for known chiral fluorophores is just as important as the synthesis of a new fluorophore for CPL study. Cyclophane derivatives are favorable for CPL science because these rigid molecules are able to hold the vector directions of electric dipole transition moment μ and imaginary magnetic dipole transition moment m. Using known synthetic methods of cyclophanes, researchers could arrange the orientations of fluorophores as desired. Currently, the relationship between bridge length and CPL and/or chiroptical properties is unknown. However, it should be an important parameter for molecular design. Past synthetic methods of cyclophanes could also solve these problems.

AUTHOR CONTRIBUTIONS

The author confirms being the sole contributor of this work and has approved it for publication.

FUNDING

This work was supported in part by the Cooperative Research Program of Network Joint Research Center for Materials and Devices: Dynamic Alliance for Open Innovation Bridging Human, Environment and Materials Grant Number 20201317, and the Priority Research Program sponsored by the Asian Human Resources Fund of Tokyo Metropolitan Government (TMG).

REFERENCES

Akagi, K. (2019). Interdisciplinary chemistry based on integration of liquid crystals and conjugated polymers: development and progress. *Bull. Chem. Soc. Jpn.* 92, 1509–1655. doi: 10.1246/bcsj.20190092

Ayuso, D., Neufeld, O., Ordonez, A. F., Decleva, P., Lerner, G., Cohen, O., et al. (2019). Synthetic chiral light for efficient control of chiral light–matter interaction. *Nat. Photonics* 13, 866–871. doi: 10.1038/s41566-019-0531-2

Berova, N., Di Bari, L., and Pescitelli, G. (2007). Application of electronic circular dichroism in configurational and conformational analysis of organic compounds. *Chem. Soc. Rev.* 36, 914–931. doi: 10.1039/b515476f

Birks, J. B., Birch, D. J. S., Cordemans, E., and Vander Donckt, E. (1976). Fluorescence of the higher helicenes. *Chem. Phys. Lett.* 43, 33–36. doi: 10.1016/0009-2614(76)80750-6

Bradberry, S. J., Savyasachi, A. J., Martinez-Calvo, M., and Gunnlaugsson, T. (2014). Development of responsive visibly and NIR luminescent and supramolecular coordination self-assemblies using lanthanide ion directed synthesis. *Coord. Chem. Rev.* 273–274, 226–241. doi: 10.1016/j.ccr.2014.03.023

Casas-Solvas, J. M., Howgego, J. D., and Davis, A. P. (2014). Synthesis of substituted pyrenes by indirect methods. *Org. Biomol. Chem.* 12, 212–232. doi: 10.1039/C3OB41993B

Emeis, C. A., and Oosterhoff, L. J. (1967). Emission of circularly-polarized radiation by optically-active compounds. *Chem. Phys. Lett.* 1, 129–132. doi: 10.1016/0009-2614(67)85007-3

Ferrari, A., Cavalca, L., and Tani, M. E. (1959). Uranyl compounds. tetragonal uranylacetates of univalent metals. *Gazz. Chim. Ital.* 89, 1534–1538.

Gleiter, R., and Hopf, H. (Eds.). (2004). *Modern Cyclophane Chemistry*. Weinheim: Wiley-VCH. doi: 10.1002/3527603964

Golovnya, V. A. (1963). Complex nature of the uranyl acetates. *L. K. Shubochkin. Zh. Neorgan. Khim.* 8, 1116–1121.

Gussakovsky, E. (2008). "Circularly Polarized Luminescence (CPL) of proteins and protein complexes," in *Reviews in Fluorescence 2008*, ed C. D. Geddes (Basel: Springer Nature Switzerland AG), 425–459. doi: 10.1007/978-1-4419-1260-2_18

Han, J., Guo, S., Lu, H., Liu, S., Zhao, Q., and Huang, W. (2018). Recent progress on circularly polarized luminescent materials for organic optoelectronic devices. *Adv. Opt. Mater.* 6:1800538. doi: 10.1002/adom.201800538

Hasegawa, M., Kobayakawa, K., Matsuzawa, H., Nishinaga, T., Hirose, T., Sako, K., et al. (2017). Macrocyclic oligothiophene with stereogenic [2.2]paracyclophane scaffolds: chiroptical properties from π-transannular interactions. *Chem. Eur. J.* 23, 3267–3271. doi: 10.1002/chem.201605842

Hassan, K., Yamashita, K.-I., Hirabayashi, K., Shimizu, T., Nakabayashi, K., Imai, Y., et al. (2015). π-Expanded axially chiral biaryls and their emissions: molecular design, syntheses, optical resolution, absolute configuration, and circularly polarized luminescence of 1,1′-Bipyrene-2,2′-diols. *Chem. Lett.* 44, 1607–1609. doi: 10.1246/cl.150704

Hassan, Z., Spuling, E., Knoll, D. M., and Braese, S. (2020a). Regioselective functionalization of [2.2]paracyclophanes: recent synthetic progress and perspectives. *Angew. Chem. Int. Ed.* 59, 2156–2170. doi: 10.1002/anie.201904863

Hassan, Z., Spuling, E., Knoll, D. M., and Brase, S. (2020b). Regioselective functionalization of [2.2]paracyclophanes: recent synthetic progress and perspectives. *Angew. Chem.* 59, 2156–2170.

Ishioka, S., Hasegawa, M., Hara, N., Sasaki, H., Nojima, Y., Imai, Y., et al. (2019). Chiroptical properties of oligophenylenes anchoring with stereogenic [2.2]paracyclophane. *Chem. Lett.* 48, 640–643. doi: 10.1246/cl.190149

Kawashima, T., Otsubo, T., Sakata, Y., and Misumi, S. (1978). Layered compounds. LVIII. Syntheses of three [2.2]pyrenophanes as an excimer model. *Tetrahedron Lett.* 51, 5115–5118. doi: 10.1016/S0040-4039(01)85826-3

Longhi, G., Castiglioni, E., Koshoubu, J., Mazzeo, G., and Abbate, S. (2016). Circularly polarized luminescence: a review of experimental and theoretical aspects. *Chirality* 28, 696–707. doi: 10.1002/chir.22647

Longone, D. T., and Chow, H. S. (1964). Paracyclophanes. IV. A multilayered [2.2]paracyclophane. *J. Am. Chem. Soc.* 86, 3898–3899. doi: 10.1021/ja01072a080

Longone, D. T., and Chow, H. S. (1970). Multilayered [2.2]paracyclophane. Synthesis and properties. *J. Am. Chem. Soc.* 92, 994–998. doi: 10.1021/ja00707a042

Misumi, S. (1983). "Multilayered cyclophanes," in *Cyclophanes, Vol. 2*, ed P. M. Keehn and S. M. Rosenfeld (New York, NY: Academic Press), 573–628. doi: 10.1016/B978-0-12-403002-2.50011-X

Morisaki, Y., Gon, M., Sasamori, T., Tokitoh, N., and Chujo, Y. (2014). Planar chiral tetrasubstituted [2.2]paracyclophane: optical resolution and functionalization. *J. Am. Chem. Soc.* 136, 3350–3353. doi: 10.1021/ja412197j

Murata, K., Yamazaki, Y., and Morita, M. (1979). Circular dichroism in uranyl ions in crystals detected by fluorescence. *J. Lumin.* 18–19, 407–410. doi: 10.1016/0022-2313(79)90150-9

Nakazaki, M., Yamamoto, K., Tanaka, S., and Kametani, H. (1977). Syntheses of the optically active multilayered [2.2]paracyclophanes with known absolute configurations. *J. Org. Chem.* 42, 287–291. doi: 10.1021/jo00422a026

Rabjohn, N., and Latina, M. J. (1954). Unsymmetrical tetraalkylmethanes. I. Coupling of alkylmagnesium bromides with tertiary bromides.

J. Am. Chem. Soc. 76, 1389–1390. doi: 10.1021/ja01634a074

Richardson, F. S., and Riehl, J. P. (1977). Circularly polarized luminescence spectroscopy. *Chem. Rev.* 77, 773–792. doi: 10.1021/cr60310a001

Riehl, J. P., and Richardson, F. S. (1986). Circularly polarized luminescence spectroscopy. *Chem. Rev.* 86, 1–16. doi: 10.1021/cr00071a001

Samoilov, B. N. (1948). Absorption and luminescence spectra of uranyl salts at the temperature of liquid helium. *Zh. Eksp. Teor. Fiz.* 18, 1030–1040.

Sanchez-Carnerero, E. M., Agarrabeitia, A. R., Moreno, F., Maroto, B. L., Muller, G., Ortiz, M. J., et al. (2015). Circularly polarized luminescence from simple organic molecules. *Chem. Eur. J.* 21, 13488–13500. doi: 10.1002/chem.201501178

Staab, H. A., and Kirrstetter, R. G. H. (1979). [2.2](2,7)Pyrenophane as an excimer model: synthesis and spectroscopic properties. *Liebigs Ann. Chem.* 1979, 886–898. doi: 10.1002/jlac.197919790618

Steinberg, I. Z. (1978). Circular polarization of luminescence: biochemical and biophysical applications. *Annu. Rev. Biophys. Bioeng.* 7, 113–137. doi: 10.1146/annurev.bb.07.060178.000553

Tanaka, H., Inoue, Y., and Mori, T. (2018). Circularly polarized luminescence and circular dichroisms in small organic molecules: correlation between excitation and emission dissymmetry factors. *ChemPhotoChem* 2, 386–402. doi: 10.1002/cptc.201800015

Tani, K., Imafuku, R., Miyanaga, K., Masaki, M. E., Kato, H., Hori, K., et al. (2020). Combined experimental and theoretical studies on planar chirality of partially overlapped C2-symmetric [3.3](3,9)dicarbazolophanes. *J. Phys. Chem. A* 124, 2057–2063. doi: 10.1021/acs.jpca.0c00286

Tani, K., Tohda, Y., Takemura, H., Ohkita, H., Ito, S., and Yamamoto, M. (2001). Synthesis and photophysical properties of [3.3](3,9)carbazolophanes. *Chem. Commun.*, 1914–1915. doi: 10.1039/b104101k

Umemoto, T., Kawashima, T., Sakata, Y., and Misumi, S. (1975a). Layered compounds. XXVIII. [2.2](1,3)pyrenophane and another triple-layered metacyclopyrenophane. *Chem. Lett.* 8, 837–840. doi: 10.1246/cl.1975.837

Umemoto, T., Satani, S., Sakata, Y., and Misumi, S. (1975b). Layered compounds. XXIX. [2.2](2,7)pyrenophane and its 1,13-diene. *Chem. Lett.* 8, 3159–3162. doi: 10.1016/S0040-4039(00)91483-7

Vögtle, F. (1993). *Cyclophane Chemistry: Synthesis, Structures and Reactions*. Chichester: John, Wiley and Sons.

Watanabe, K., and Akagi, K. (2014). Helically assembled π-conjugated polymers with circularly polarized luminescence. *Sci. Technol. Adv. Mater.* 15:44203. doi: 10.1088/1468-6996/15/4/044203

Winnik, F. M. (1993). Photophysics of preassociated pyrenes in aqueous polymer solutions. *Chem. Rev.* 93, 587–614. doi: 10.1021/cr00018a001

Wu, H., Zhou, Y., Yin, L., Hang, C., Li, X., Agren, H., et al. (2017). Helical self-assembly-induced singlet-triplet emissive switching in a mechanically sensitive system. *J. Am. Chem. Soc.* 139, 785–791. doi: 10.1021/jacs.6b10550

Wynberg, H., Hekkert, G. L., Houbiers, J. P. M., and Bosch, H. W. (1965). The optical activity of butylethylhexylpropylmethane. *J. Am. Chem. Soc.* 87, 2635–2639. doi: 10.1021/ja01090a020

Wynberg, H., and Hulshof, L. A. (1974). Optical activity of hydrocarbons. *Tetrahedron* 30, 1775–1782. doi: 10.1016/S0040-4020(01)97312-0

Zinna, F., and Di Bari, L. (2015). Lanthanide circularly polarized luminescence: bases and applications. *Chirality* 27, 1–13. doi: 10.1002/chir.22382

Conflict of Interest: The author declares that the research was conducted in the absence of any commercial or financial relationships that could be construed as a potential conflict of interest.

frontiers in Chemistry

MINI REVIEW
published: 15 January 2021
doi: 10.3389/fchem.2020.557650

Template Assisted Generation of Chiral Luminescence in Organic Fluorophores

*Sonia Maniappan, Ashok Badrinarayan Jadhav and Jatish Kumar**

Department of Chemistry, Indian Institute of Science Education and Research (IISER) Tirupati, Tirupati, India

Development of efficient ways of fabricating chiral light emitting materials is an active area of research due to the vast potential offered by these materials in the field of optoelectronic devices, data storage, and asymmetric synthesis. Among the various methods employed, template assisted generation of chiral luminescence is gaining enormous attention due to its simplicity, applicability over a wide range of fluorescent molecules/dyes, and the display of high anisotropic values.

Keywords: circularly polarized luminescence, chiral templates, nematic liquid crystals, chiral gelators, molecular aggregates, biomolecules

OPEN ACCESS

Edited by:
Giovanna Longhi,
University of Brescia, Italy

Reviewed by:
Paola Rizzo,
University of Salerno, Italy
Delia Miguel,
University of Granada, Spain

****Correspondence:***
Jatish Kumar
jatish@iisertirupati.ac.in

Specialty section:
This article was submitted to Physical Chemistry and Chemical Physics, a section of the journal Frontiers in Chemistry

Received: *30 April 2020*
Accepted: *18 September 2020*
Published: *15 January 2021*

Citation:
Maniappan S, Jadhav AB and Kumar J (2021) Template Assisted Generation of Chiral Luminescence in Organic Fluorophores. Front. Chem. 8:557650. doi: 10.3389/fchem.2020.557650

INTRODUCTION

The term polarization of light is enclosed with advanced optical phenomenon which provides vital information on the notable optical features like surface shape, material content etc. Circular polarization is considered to be of significance among the other forms of polarized light as it has gained immense popularity due its inevitable applications in 3D displays, optical sensors, bio-imaging, electroluminescent devices and asymmetric synthesis (Schadt, 1997; Maeda et al., 2011). Single photon exists in two circular polarization states due to their quantum properties (uncharged, massless bosons with quantized spin of ± 1 ħ) (Andrews, 2011; Sánchez-Carnerero et al., 2015). When the path followed by the electric and magnetic field vectors is in clockwise helix as the wave propagates to the observer, then it is termed as right circular polarized state whereas when the path followed is in anti-clockwise direction it is said to be left circular polarization state. Circularly polarized luminescence (CPL) spectroscopy is based on the differential emission of the left and right circularly polarized light by intrinsically chiral non-racemic luminescent systems, or from the luminophores that are present in chiral environment. Circular dichroism spectroscopy is often employed to study the ground state properties of chiral material whereas CPL measurement gives information on the excited state chiral properties. Hence, CPL can be employed for the observation of certain transitions which cannot be readily visualized in absorption (Nakanishi et al., 2013; Sang et al., 2019).

Materials in an asymmetric environment and exhibiting luminescence properties show CPL activity. The magnitude of CPL is generally quantified using a term known as luminescence dissymmetry factor (g_{lum}), which is described as the ratio of difference in the intensities of the left (I_L) and right (I_R) circularly polarized light to the average total luminescence intensity (Zinna and Di Bari, 2015).

$$g_{lum} = 2\left(\frac{I_L - I_R}{I_L + I_R}\right)$$

To date, a variety of CPL active molecules and materials have been developed. Chiral lanthanide complexes, transition metal complexes, π-conjugated polymers and small organic molecules, are

some examples of systems exhibiting chiral emissive property. Lanthanide complexes, owing to their magnetic dipole allowed transitions, exhibit high g_{lum} values; however, narrow and fixed emission bands, and weak luminescence quantum yields are the limiting factors (Zinna and Di Bari, 2015). In contrast, organic chromophores, due to their high luminescence and tunable emission, have attracted vast attention. However, CPL anisotropy is in general weak and in the order of 10^{-3} or less (Sánchez-Carnerero et al., 2015). Various strategies have been adopted for the generation as well as enhancement of CPL activity in these molecular systems. These include techniques like chiral blending, supramolecular assemblies, and template-assisted CPL generation (Maeda et al., 2011; Kumar et al., 2015b). There are comprehensive reviews on the enhancement of CPL activity through supramolecular approaches (Kumar et al., 2015a). Even though, the anisotropy factor could be increased by around an order of magnitude, the values remained low for any technological applications. In contrast, helical templates or chiral host matrices can lead to chiral induction in achiral chromophores through the symmetry breaking imposed by the asymmetric nature of the scaffold (**Figure 1**). Owing to its large chiral induction effects, these techniques have displayed great potential for the fabrication of CPL active materials with enhanced luminescence dissymmetry (Mei et al., 2015). This review mainly focuses on the generation of CPL active organic luminescent molecules utilizing the template assisted methods and provides an overview about the various templates employed till date.

LIQUID CRYSTALS

Chiral liquid crystals are the most widely used templates for the induction of optical activity in molecules and materials. Liquid crystals are classic soft materials having intermediate phase between solid crystal and isotropic liquid (Kim et al., 2019). They possess long-range orientational order exhibiting interesting thermal, mechanical and optoelectrical properties. Chiral nematic liquid crystals (*NLCs) can be obtained (i) directly from cholesteric liquid crystals or (ii) from nematic liquid crystals doped with chiral additives. Owing to their helical order and periodic structure, *NLCs exhibit fascinating optical properties (Li et al., 2018). One of the most interesting features that make these materials attractive is the selective reflection of circularly polarized light passing through them. When the wavelength of incident light is in resonance with the wavelength of selective reflection, circularly polarized light of same handedness as the liquid crystalline matrix is selectively reflected and light with opposite handedness is transmitted. This is in particular important for the generation of high anisotropic factors from *NLCs-based nanosystems (San Jose et al., 2014). The wavelength of the reflected light (λ_0) depends on the helical pitch (P), refractive index of the cholesteric material (n) as well as the angle (θ) between the incident light and the cholesteric layers (Fernandes et al., 2019). It can be defined as:

$$\lambda_0 = nP\sin\theta$$

Furthermore, induced chirality can be generated by the helical arrangement of achiral molecules on chiral templates. Thus, liquid crystalline materials doped with achiral molecules exhibit intense chiroptical signals and have great potential for applications in stereoscopic displays and color-image projection.

The idea of generating CPL with high anisotropic factor by using liquid crystalline template was introduced by Pollmann et al. (1976) by embedding fluorescent dye in a *NLC host. Later, experimental and theoretical studies were carried out by Shi et al. (1998) for emission outside the selective reflection band (or the resonance region) of the liquid crystalline material. *NLC films doped with a fluorescent dye displayed CPL with chiral anisotropy factor around 0.8 (Shi et al., 1998). In contrast, for emission inside the resonance region, almost pure circular polarization ($g_{lum} = \sim 2$) was observed for *NLC films embedded with light-emitting dopants (Chen et al., 1999). Later, a large variety of liquid crystalline matrices and achiral fluorophores were employed for the generation of intense CPL signals. Akagi's group has extensively reported on the research topic. One of their works demonstrated the preparation of a CPL-switchable cell containing a CPL-emitting film and chiral disubstituted liquid-crystalline polyacetylene (di-LCPA) merged with a thermoresponsive N*-LC cell. CPL switching and amplification could be achieved by the changes in the phase of thermotropic *NLC cell and the selective transmission of CPL in *NLC (San Jose et al., 2014). Another area in which these materials have been used widely is the polymerization reactions, wherein *NLC function as chiral solvents. Helical network polymers exhibiting CPL activity was synthesized through photo-crosslinking polymerization of functionalized methacrylates in chiral *NLC as asymmetric solvent for polymerization (Park et al., 2015).

The major limitation with systems having high concentration of fluorophores in *NCs is the quenching associated with aggregation. To overcome this, Zhao et al. (2016) used organic luminogens possessing aggregation-induced emission (AIE)

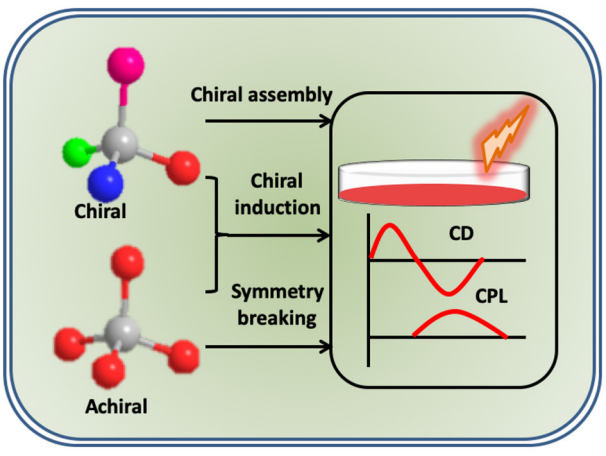

FIGURE 1 | Scheme illustrating the different approaches adopted for the enhancement of optical activity in chiral and achiral molecular systems.

property. AIE-LC synthesized by doping tetraphenylethylene-propylphenylethyne (TPE-PPE) in chiral *NLCs showed intense CPL properties (Zhao et al., 2016). Li et al. (2018) in contrary, developed nanocomposites by embedding a chiral AIE luminogen, *R*/*S* BINOL-CN into achiral NLC (N-LC, E7). Considerably high CPL response with a g_{lum} value of +0.41 was obtained due to the dipolar interactions between polar cyano groups and π-π interactions between binaphthyl moiety of *R*/*S*-BINOL-CN and biphenyl/terphenyl groups of the E7 host (Li et al., 2018). Due to their unique properties, *NLCs were also used as scaffolds for the generation of photon upconverted CPL. Triplet–triplet annihilation-based photon upconversion as well as upconverted CPL was observed by dispersing a chiral emitter and a triplet donor into the *NLC (Yang X. et al., 2019).

Among various *NLC materials, cellulose nanocrystals (CNC) have attracted special attention due to their abundance, stability and robustness. Different approaches such as application of stress, addition of metal salt, change in pH and solvent polarity have been employed to tune the CPL emission of achiral luminogens embedded in CNC templates. In most cases, variations in the pitch of the helix induced by external stimuli were the major cause for the changes in optical properties (**Figure 2A**). The inversion in the sign of CPL and the tuning of CPL wavelength could be achieved (Zheng et al., 2018; He et al., 2019). Moreover, suitably designed fluorescence resonance energy transfer (FRET) and charge transfer systems have also been used to tailor the CPL emission using *NLC templates (Li et al., 2020; Lin et al., 2020). Thus, it is observed that doping achiral fluorescent dyes with *NLC is emerging as an effortless and efficient way of generating CPL active materials.

BIOMOLECULES

While substantial progress has been made in the development of CPL active materials with different chiral templates, the development of probes using nucleic acids or related biostructures has remained unexplored to large extend. Biomolecules such as DNA and RNA owing to their well-defined molecular backbone has the advantage of having functional groups placed at a defined space and distance. This enables ordered arrangement of guest molecules at specified locations on the scaffold resulting in a distinct helical organization of the luminophores. The helical assembly gives rise to reproducible chiral luminescence due to the robustness of the template. Nakamura et al. (2016) demonstrated that the pyrene fluorophores when assembled helically like a zipper along the RNA duplex resulted in strong excimer fluorescence as well as CPL. The chiral emission exhibited a dissymmetric factor around 3.5×10^{-2} in a dilute aqueous solution (Nakamura et al., 2016). They further extended their investigations to DNA duplexes possessing varying number of pyrenes modified non-nucleosidic linkers wherein CPL emission was observed from the pyrene excimers (Nakamura et al., 2018). In an interesting investigation, Jiang Q. et al. (2019) demonstrated the development of a new class of CPL-active biomaterials using achiral carbazole-based biscyanine fluorophores assembled on chiral DNA scaffold (**Figure 2B**). Electrostatic attraction drives the binding of achiral cyanine molecules to the minor groove of DNA leading to chirality transfer from the DNA molecules to the cyanine dyes. This resulted in a remarkably high CPL emission from the dye molecules which could be regulated by varying the structure of the template (Jiang Q. et al., 2019). Further, Chen et al. (2019) demonstrated CPL activity in achiral ThT dyes through the interaction with human telomeric G-quadruplex. Statistical analysis of different DNA sequences and structures revealed that right- and left-handed CPL are induced on the parallel and antiparallel G4 structure, respectively (Chen et al., 2019). Hence, the exploration of biocompatible templates for CPL emission is emerging as an attractive area of research due to the vast potential of these materials as biosensing and bioimaging platforms.

MOLECULAR AGGREGATES

Molecular self-assembly has been demonstrated as an efficient approach for the enhancement of chiral luminescence, particularly, in chiral organic systems. However, there are few reports in which supramolecular assemblies have been employed as chiral templates to induce optical activity in achiral molecules. In a recent report, Liang et al. (2020) utilized the helical microtubes formed by the self-assembly of β-cyclodextrin-sodium dodecyl sulfate supramolecular complex to induce CPL in achiral dyes loaded in the microtubes (**Figure 2C**). The systems exhibited chirality at different levels starting from β-CD to β-CD/SDS complex, their self-assembled microtubes and finally induced chirality in achiral dyes blended in the microtubes. The achiral dyes exhibited strong induced CPL with a g_{lum} value of 0.1 (Liang et al., 2020). Zhang et al. (2019) synthesized two AIE-active chiral Au(I) complexes which undergo spontaneous hierarchical self-assembly transforming from vesicles to helical fibers. Utilizing the enantiomers as chiral transcription templates, induction of CPL signals from achiral luminogens were successfully achieved with g_{lum} values around 10^{-3} (Zhang et al., 2019). Goto et al. (2017) could successfully induce CPL in commercially available achiral dyes using chiral nanofibrillar templates synthesized from L-glutamic acid substituted amphiphilic molecules. The nanosystem exhibited enhanced CPL activity with a g_{lum} value as high as 0.1 in dilute solution (Goto et al., 2017). The advantages with such self-assembled molecular templates is that they provide wide range of possibility in the choice of molecular building blocks thereby enabling the development of CPL active materials with tailored optical properties.

CHIRAL GELATORS

Supramolecular organogels comprising of hydrogels and low-molecular-weight organogels (LMWGs) are an important class of soft materials that have shown a lot of advancement over the last decades. These are another class of molecular self-assembling systems that form nanostructures like strands, tapes, fibers, ribbons, platelets, and other aggregates with high

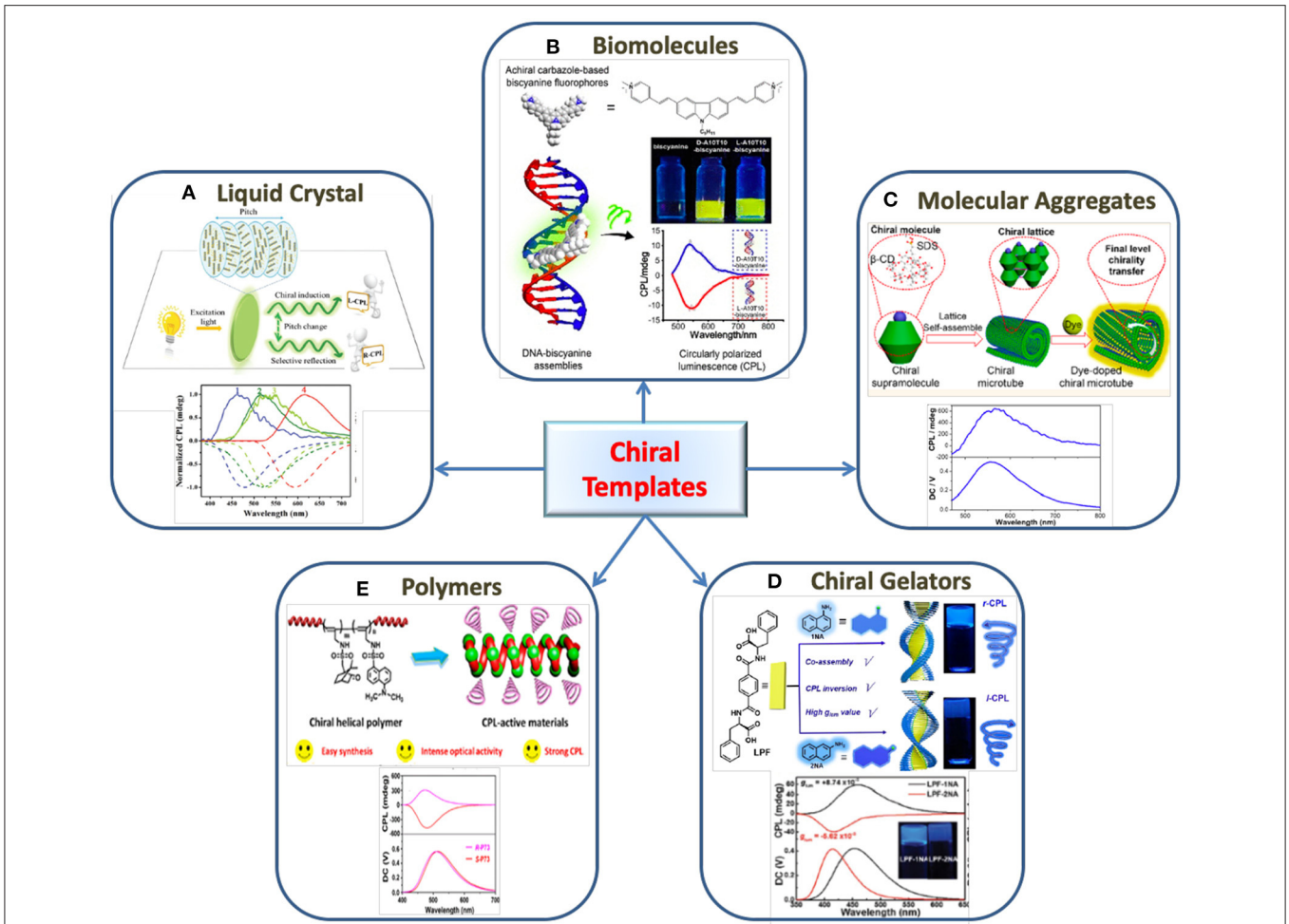

FIGURE 2 | The use of various chiral templates for the generation of CPL in organic fluorophores. **(A)** Liquid crystals: Schematic illustration represents the generation of R-CPL and L-CPL from CNC- fluorescent dyes composite film with respect to helical pitch change and their corresponding CPL spectra. Reproduced with permission from He et al. (2019). Copyright (2019) The Royal Society of Chemistry. **(B)** Biomolecules: Fabrication of CPL material composed of achiral biscyanine and DNA duplex as chiral template. Reproduced with permission from Jiang Q. et al. (2019). Copyright (2019) American Chemical Society. **(C)** Molecular aggregates: Induced CPL generated by blending achiral dyes into helical microtube obtained from self-assembly of β-cyclodextrin (β- CD) and sodium dodecyl sulfate (SDS). Reproduced with permission from Liang et al. (2020). Copyright (2020) American Chemical Society. **(D)** Chiral gelators: scheme illustrates the chirality transfer from a C2-symmteric hydrogelator (LPF) to achiral naphthylamine isomers and the CPL inversion. Reproduced with permission from Yang L. et al. (2019). Copyright (2019) The Royal Society of Chemistry. **(E)** Polymers: CPL obtained from a chiral fluorescent helical mono-substituted polyacetylenes prepared by the copolymerization between a chiral monomer and achiral fluorescent monomer. Reproduced with permission from Zhao et al. (2018). Copyright (2018) American Chemical Society.

aspect ratio upon gelation (Terech and Weiss, 1997). They form 3D network structures depending on their interaction with the solvent molecules, and disable the movement of organic solvents by capillary forces and surface tension. CPL materials can be fabricated by introducing a chiral source and achiral fluorophore which co-assembles through non-covalent interactions like hydrogen bonding, π-π stacking, and electrostatic interactions (Shen et al., 2015; Han et al., 2017). The intensity and handedness of CPL can be controlled by the controlling the interactions and position of achiral fluorophores on the template (Liu et al., 2018; Xing and Zhao, 2018). Herein, we describe the recent advancements in CPL systems created by the interaction of achiral dopants with chiral gelator.

Han et al. (2017) developed a CPL system by utilizing a C3 symmetrical L-glutamic acid-based host gelator 1,3,5-benzenetricarbonyl L-glutamate diethylester and AIE active dyes. The host gelator formed hexagonal nanotubes providing chiral space for encapsulating the AIE luminogen. The CPL signal showed a g_{lum} value in the order of 10^{-3} (Han et al., 2017). Another notable work, Li et al. (2019) demonstrated the development of CPL material containing chiral amphiphilic D-glutamic acid gelator (DGG) and achiral pyridine-functionalized tetraphenylethylenes (PTPE). An interesting feature of this work is the stoichiometry-controlled inversion of supramolecular chirality and CPL handedness. Left- and right-handed CPL were observed when the molar ratio of PTPE/DGG was 1:100 and 1:16, respectively (Li et al., 2019). Hydrogels have also been explored

as a template to synthesize CPL materials. The CPL handedness of phenylalanine-based hydrogels was tailored by achiral isomers of naphthylamine through intermolecular hydrogen bonds and π-π stacking (**Figure 2D**). The CPL inversion is assisted by non-covalent interactions between the chiral and achiral molecules thereby inducing reorientations in the assembled molecules. The co-assembled hydrogels showed a $|g_{lum}|$ value in the order of 10^{-3} (Yang L. et al., 2019). Wang et al. (2019) chose chiral phenylalanine based hydrogelator in which achiral coumarin derivatives were co-assembled. The fabricated system exhibited high CPL performance with a g_{lum} value around -1.9×10^{-2}. Even though the g_{lum} values are not very high, chiral gelators are emerging as promising templates for the development of a variety of CPL based composite systems.

POLYMERS

The use of a chiral helical polymer templates for the generation of CPL is another area of attraction (Fukao and Fujiki, 2009; Nishikawa et al., 2017; Kulkarni et al., 2018). Zhao et al. (2018) reported a CPL material *via* co-polymerization of helical monosubstituted polyacetylene (PA) polymers and achiral fluorescent monomer in presence of a rhodium-based catalyst (**Figure 2E**). The achiral fluorescent monomers were attached to the polymer backbone through covalent bonds and CPL was generated only when helical structure of one handedness was formed (Zhao et al., 2018). They have further achieved a tunable CPL emission with high g_{lum} value of 0.1 using chiral helical substituted polyacetylenes (HSPAs) and fluorophores. The generation of CPL was attributed to the circularly polarized scattering and fluorescence-selective absorption effects of chiral HSPAs (Zhao et al., 2019). The CPL response from a syndiotactic polystyrene (s-PS) polymer films generated by the sorption of chiral molecules on crystallization was reported by Rizzo and coworkers. The polymeric film thus obtained, exhibited a CPL signal around 320 nm with a g_{lum} value of 0.03. CPL emission from an achiral fluorophore, fluorescein was also obtained on passing it through s-PS film (Rizzo et al., 2011, 2017).

OTHER TEMPLATES

In addition to the templates described above, there are various other scaffolds employed for the fabrication of CPL active materials. Chiral silica is one such template that has been effectively utilized. Tsunega et al. (2019) have developed a CPL active material with inorganic silica as chiral host material with acidic fluorophores embedded in it. The surface modification of chiral silica provided the binding pocket for encapsulation of fluorophores. Recently, chiral nematic mesoporous silica films (CNMS) was used for generation of right-handed CPL from luminophores capped in it. Restricting the transmission of light with the same chirality, selective reflection band of CNMS enables R-CPL emission with g_{lum} value up to 0.38 (Jiang H. et al., 2019). In addition to these templates, chiral solvents have also been employed for generation for CPL in fluorescent materials and nanoparticles, however, we have restricted our discussions to template assisted chiral luminescence in organic fluorophores.

CONCLUSIONS AND FUTURE PERSPECTIVE

The major drawback associated with CPL studies on simple organic systems is the tedious protocols associated with the synthesis, purification and characterization of chiral molecules with high enantiopurity. Moreover, the systems exhibit low g_{lum} values. Molecular self-assembly has been demonstrated as an efficient technique to enhance the CPL of organic molecules. However, reproducibility and stability of the supramolecular systems is a major concern. The g_{lum} could be enhanced by an order of magnitude in most cases, which is still low for any technological applications. Under these circumstances, template assisted chiral induction has enormous potential and is gaining vast attention due to its attractive features. Template-driven CPL generation offers several advantages over the conventional CPL observed in molecular systems; (i) since the scaffold-based approach uses simple achiral fluorescent molecules, a wide range of molecules/dyes can be used, imposing minimal restrictions on the choice of molecular system, (ii) easy tuning of the emission wavelength is facilitated by the proper selection of molecules/dye, (iii) as highly ordered structures are used as templates, the chiral properties can be tailored through the control of template morphologies, (iv) the technique is cost effective as it can be applied on cheap host and guest materials, and (v) simple procedure involving mixing of the chiral host and achiral guest in most cases. While large number of templates have been employed, liquid crystalline materials have shown promise due to their unique selective reflection property. Since any chiral medium can function as a template for CPL generation, research is actively pursued to explore large number of novel templates capable of generating enhanced CPL. The incorporation of simple organic molecules into diverse chiral templates stipulates versatile strategy for the rational design and scalable manufacturing of organic-based CPL materials that can open new avenues for technological advances in field of photonic devices.

AUTHOR CONTRIBUTIONS

SM and JK conceived, designed the project, edited, and revised the review. SM, ABJ, and JK contributed to the writing and literature research. All the authors approved the final draft.

FUNDING

JK acknowledges financial support from DST-SERB, Government of India (Project No. CRG/2019/002715) and IISER Tirupati. SM acknowledges DST-INSPIRE and ABJ acknowledges IISER Tirupati for fellowship.

REFERENCES

Andrews, D. L. (2011). Introduction to quantum optics: from the semi-classical approach to quantized light, by gilbert grynberg, alain aspect and claude fabre. *Contemp. Phys.* 52, 627–628. doi: 10.1080/00107514.2011.604134

Chen, J., Chen, Y., Zhao, L., Feng, L., Xing, F., Zhao, C., et al. (2019). G-quadruplex DNA regulates invertible circularly polarized luminescence. *J. Mater. Chem. C* 7, 13947–13952. doi: 10.1039/C9TC04508B

Chen, S. H., Katsis, D., Schmid, A. W., Mastrangelo, J. C., Tsutsui, T., and Blanton, T. N. (1999). Circularly polarized light generated by photoexcitation of luminophores in glassy liquid-crystal films. *Nature* 397, 506–508. doi: 10.1038/17343

Fernandes, S. N., Lopes, L. F., and Godinho, M. H. (2019). Recent advances in the manipulation of circularly polarised light with cellulose nanocrystal films. *Curr. Opin. Solid State Mater. Sci.* 23, 63–73. doi: 10.1016/j.cossms.2018.11.004

Fukao, S., and Fujiki, M. (2009). Circularly polarized luminescence and circular dichroism from Si-Si-bonded network polymers. *Macromolecules* 42, 8062–8067. doi: 10.1021/ma901427v

Goto, T., Okazaki, Y., Ueki, M., Kuwahara, Y., Takafuji, M., Oda, R., et al. (2017). Induction of strong and tunable circularly polarized luminescence of nonchiral, nonmetal, low-molecular-weight fluorophores using chiral nanotemplates. *Angew. Chem. Int. Ed.* 56, 2989–2993. doi: 10.1002/anie.201612331

Han, J., You, J., Li, X., Duan, P., and Liu, M. (2017). Full-color tunable circularly polarized luminescent nanoassemblies of achiral AIEgens in confined chiral nanotubes. *Adv. Mater.* 29:1606503. doi: 10.1002/adma.201606503

He, J., Bian, K., Li, N., and Piao, G. (2019). Generation of full-color and switchable circularly polarized luminescence from nonchiral dyes assembled in cholesteric cellulose films. *J. Mater. Chem. C* 7, 9278–9283. doi: 10.1039/C9TC01956A

Jiang, H., Qu, D., Zou, C., Zheng, H., and Xu, Y. (2019). Chiral nematic mesoporous silica films enabling multi-colour and on-off switchable circularly polarized luminescence. *New J. Chem.* 43, 6111–6115. doi: 10.1039/C9NJ00724E

Jiang, Q., Xu, X., Yin, P. A., Ma, K., Zhen, Y., Duan, P., et al. (2019). Circularly polarized luminescence of achiral cyanine molecules assembled on DNA templates. *J. Am. Chem. Soc.* 141, 9490–9494. doi: 10.1021/jacs.9b03305

Kim, Y. K., Noh, J., Nayani, K., and Abbott, N. L. (2019). Soft matter from liquid crystals. *Soft Matter.* 15, 6913–6929. doi: 10.1039/C9SM01424A

Kulkarni, C., Meskers, S. C. J., Palmans, A. R. A., and Meijer, E. W. (2018). Amplifying chiroptical properties of conjugated polymer thin-film using an achiral additive. *Macromolecules* 51, 5883–5890. doi: 10.1021/acs.macromol.8b01077

Kumar, J., Nakashima, T., and Kawai, T. (2015a). Circularly polarized luminescence in chiral molecules and supramolecular assemblies. *J. Phys. Chem. Lett.* 6, 3445–3452. doi: 10.1021/acs.jpclett.5b01452

Kumar, J., Tsumatori, H., Yuasa, J., Kawai, T., and Nakashima, T. (2015b). Self-discriminating termination of chiral supramolecular polymerization: tuning the length of nanofibers. *Angew. Chem. Int. Ed.* 54, 5943–5947. doi: 10.1002/anie.201500292

Li, P., Lü, B., Han, D., Duan, P., Liu, M., and Yin, M. (2019). Stoichiometry-controlled inversion of circularly polarized luminescence in co-assembly of chiral gelators with an achiral tetraphenylethylene derivative. *Chem. Commun.* 55, 2194–2197. doi: 10.1039/C8CC08924H

Li, X., Li, Q., Wang, Y., Quan, Y., Chen, D., and Cheng, Y. (2018). Strong aggregation-induced CPL response promoted by chiral emissive nematic liquid crystals (N*-LCs). *Chem. A Eur. J.* 24, 12607–12612. doi: 10.1002/chem.201801186

Li, Y., Liu, K., Li, X., Quan, Y., and Cheng, Y. (2020). The amplified circularly polarized luminescence regulated from D-A type AIE-active chiral emitters via liquid crystals system. *Chem. Commun.* 56, 1117–1120. doi: 10.1039/C9CC09067C

Liang, J., Guo, P., Qin, X., Gao, X., Ma, K., Zhu, X., et al. (2020). Hierarchically chiral lattice self-assembly induced circularly polarized luminescence. *ACS Nano* 14, 3190–3198. doi: 10.1021/acsnano.9b08408

Lin, S., Sun, H., Qiao, J., Ding, X., and Guo, J. (2020). Phototuning energy transfer in self-organized luminescent helical superstructures for photonic applications. *Adv. Opt. Mater.* 8:2000107. doi: 10.1002/adom.202000107

Liu, G., Sheng, J., Wu, H., Yang, C., Yang, G., Li, Y., et al. (2018). Controlling supramolecular chirality of two-component hydrogels by J- and H-aggregation of building blocks. *J. Am. Chem. Soc.* 140, 6467–6473. doi: 10.1021/jacs.8b03309

Maeda, H., Bando, Y., Shimomura, K., Yamada, I., Naito, M., Nobusawa, K., et al. (2011). Chemical-stimuli-controllable circularly polarized luminescence from anion-responsive π-conjugated molecules. *J. Am. Chem. Soc.* 133, 9266–9269. doi: 10.1021/ja203206g

Mei, J., Leung, N. L. C., Kwok, R. T. K., Lam, J. W. Y., and Tang, B. Z. (2015). Aggregation-induced emission: together we shine, united we soar! *Chem. Rev.* 115, 11718–11940. doi: 10.1021/acs.chemrev.5b00263

Nakamura, M., Ota, F., Takada, T., Akagi, K., and Yamana, K. (2018). Circularly polarized luminescence of helically assembled pyrene π-stacks on RNA and DNA duplexes. *Chirality* 30, 602–608. doi: 10.1002/chir.22838

Nakamura, M., Suzuki, J., Ota, F., Takada, T., Akagi, K., and Yamana, K. (2016). Helically assembled pyrene arrays on an RNA duplex that exhibit circularly polarized luminescence with excimer formation. *Chem. A Eur. J.* 22, 9121–9124. doi: 10.1002/chem.201602043

Nakanishi, K., Berova, N., Polavarapu, P. L., and Woody, R. W. (2013). *Comprehensive Chiroptical Spectroscopy: Instrumentation, Methodologies, and Theoretical Simulations*. Weinheim: Wiley-VCH Verlag GmbH Co. KGaA.

Nishikawa, T., Nagata, Y., and Suginome, M. (2017). Poly(quinoxaline-2,3-diyl) as a multifunctional chiral scaffold for circularly polarized luminescent materials: color tuning, energy transfer, and switching of the CPL handedness. *ACS Macro Lett.* 6, 431–435. doi: 10.1021/acsmacrolett.7b00131

Park, J., Yu, T., Inagaki, T., and Akagi, K. (2015). Helical network polymers exhibiting circularly polarized luminescence with thermal stability. Synthesis via photo-cross-link polymerizations of methacrylate derivatives in a chiral nematic liquid crystal. *Macromolecules* 48, 1930–1940. doi: 10.1021/acs.macromol.5b00063

Pollmann, P., Mainisch, K. J., and Stegkmeyer, H. (1976). Circularpolarisation der fluoreszenz achiraler moleküle in cholesterischen flüssigkristallphasen. *Zeitschrift Phys. Chem.* 103, 295–309. doi: 10.1524/zpch.1976.103.5_6.295

Rizzo, P., Abbate, S., Longhi, G., and Guerra, G. (2017). Circularly polarized luminescence of syndiotactic polystyrene. *Opt. Mater.* 73, 595–601. doi: 10.1016/j.optmat.2017.09.010

Rizzo, P., Montefusco, T., and Guerra, G. (2011). Chiral optical films based on achiral chromophore guests. *J. Am. Chem. Soc.* 133, 9872–9877. doi: 10.1021/ja2021087

San Jose, B. A., Yan, J., and Akagi, K. (2014). Dynamic switching of the circularly polarized luminescence of disubstituted polyacetylene by selective transmission through a thermotropic chiral nematic liquid crystal. *Angew. Chem. Int. Ed.* 53, 10641–10644. doi: 10.1002/anie.201404250

Sánchez-Carnerero, E. M., Agarrabeitia, A. R., Moreno, F., Maroto, B. L., Muller, G., Ortiz, M. J., et al. (2015). Circularly polarized luminescence from simple organic molecules. *Chem. A Eur. J.* 21, 13488–13500. doi: 10.1002/chem.201501178

Sang, Y., Han, J., Zhao, T., Duan, P., and Liu, M. (2019). Circularly polarized luminescence in nanoassemblies: generation, amplification, and application. *Adv. Mater.* 32:1900110. doi: 10.1002/adma.201900110

Schadt, M. (1997). Liquid crystal materials and liquid crystal displays. *Annu. Rev. Mater. Sci.* 27, 305–379. doi: 10.1146/annurev.matsci.27.1.305

Shen, Z., Wang, T., Shi, L., Tang, Z., and Liu, M. (2015). Strong circularly polarized luminescence from the supramolecular gels of an achiral gelator: tunable intensity and handedness. *Chem. Sci.* 6, 4267–4272. doi: 10.1039/C5SC01056J

Shi, H., Conger, B. M., Katsis, D., and Chen, S. H. (1998). Circularly polarized fluorescence from chiral nematic liquid crystalline films: theory and experiment. *Liq. Cryst.* 24, 163–172. doi: 10.1080/026782998207334

Terech, P., and Weiss, R. G. (1997). Low molecular mass gelators of organic liquids and the properties of their gels. *Chem. Rev.* 97, 3133–3160. doi: 10.1021/cr9700282

Tsunega, S., Jin, R. H., Nakashima, T., and Kawai, T. (2019). Transfer of chiral information from silica hosts to achiral luminescent guests: a simple approach to accessing circularly polarized luminescent systems. *Chempluschem* 85, 619–626. doi: 10.1002/cplu.201900615

Wang, F., Ji, W., Yang, P., and Feng, C. L. (2019). Inversion of circularly polarized luminescence of nanofibrous hydrogels through co-assembly with achiral coumarin derivatives. *ACS Nano* 13, 7281–7290. doi: 10.1021/acsnano.9b03255

Xing, P., and Zhao, Y. (2018). Controlling supramolecular chirality in multicomponent self-assembled systems. *Acc. Chem. Res.* 51, 2324–2334. doi: 10.1021/acs.accounts.8b00312

Yang, L., Wang, F., Auphedeous, D. I. Y., and Feng, C. (2019). Achiral isomers controlled circularly polarized luminescence in supramolecular hydrogels. *Nanoscale* 11, 14210–14215. doi: 10.1039/C9NR05033G

Yang, X., Han, J., Wang, Y., and Duan, P. (2019). Photon-upconverting chiral liquid crystal: significantly amplified upconverted circularly polarized luminescence. *Chem. Sci.* 10, 172–178. doi: 10.1039/C8SC03806F

Zhang, J., Liu, Q., Wu, W., Peng, J., Zhang, H., Song, F., et al. (2019). Real-time monitoring of hierarchical self-assembly and induction of circularly polarized luminescence from achiral luminogens. *ACS Nano* 13, 3618–3628. doi: 10.1021/acsnano.9b00218

Zhao, B., Pan, K., and Deng, J. (2018). Intense circularly polarized luminescence contributed by helical chirality of monosubstituted polyacetylenes. *Macromolecules* 51, 7104–7111. doi: 10.1021/acs.macromol.8b01545

Zhao, B., Pan, K., and Deng, J. (2019). Combining chiral helical polymer with achiral luminophores for generating full-color, on-off, and switchable circularly polarized luminescence. *Macromolecules* 52, 376–384. doi: 10.1021/acs.macromol.8b02305

Zhao, D., He, H., Gu, X., Guo, L., Wong, K. S., Lam, J. W. Y., et al. (2016). Circularly polarized luminescence and a reflective photoluminescent chiral nematic liquid crystal display based on an aggregation-induced emission luminogen. *Adv. Opt. Mater.* 4, 534–539. doi: 10.1002/adom.201500646

Zheng, H., Li, W., Li, W., Wang, X., Tang, Z., Zhang, S. X. A., et al. (2018). Uncovering the circular polarization potential of chiral photonic cellulose films for photonic applications. *Adv. Mater.* 30:1705948. doi: 10.1002/adma.201705948

Zinna, F., and Di Bari, L. (2015). Lanthanide circularly polarized luminescence: bases and applications. *Chirality* 27, 1–13. doi: 10.1002/chir.22382

Conflict of Interest: The authors declare that the research was conducted in the absence of any commercial or financial relationships that could be construed as a potential conflict of interest.

frontiers in Chemistry

EDITORIAL
published: 23 February 2021
doi: 10.3389/fchem.2021.635655

Chiral Organic Chromophoric Systems in the Enhancement of Circularly Polarized Luminescence

Tao Wu[1], You-Xuan Zheng[2], Giovanna Longhi[3] and Ga-Lai Law[4]*

[1]Institute of Organic Chemistry and Biochemistry, Academy of Sciences of the Czech Republic (ASCR), Prague, Czechia, [2]Nanjing University, Nanjing, China, [3]University of Brescia, Brescia, Italy, [4]Hong Kong Polytechnic University, Kowloon, Hong Kong

Keywords: circularly polarized luminescence, organic chromophore, molecular chirality, excited state, chiral enhancement

Editorial on the Research Topic

Chiral Organic Chromophoric Systems in the Enhancement of Circularly Polarized luminescence

Circularly polarized luminescence (CPL) discloses rich information about molecular chirality in the excited state. The number of reports on CPL studies has increased significantly since 2010: with the progress of instrumental techniques and calculation methods, CPL is widely used in the development of smart materials for advanced photonic technologies, 3D display and bio-responsive studies.

Recently, several significant overviews have been presented on CPL instrumental development and theoretical interpretation (Longhi et al., 2016), CPL of lanthanide complexes (Zinna and Di Bari, 2015), small organic molecules (Sanchez-Carnerero et al., 2015; Mori, 2020) and supramolecular assemblies (Kumar et al., 2015). A key factor to evaluate the enhancement of CPL is the dissymmetry factor g_{lum}. A general theoretical aspect to achieve high value of the g_{lum} is the manipulation of optical transitions with strong magnetic and weak electric dipole transition moment contribution.

This Special Issue includes 12 contributions (1 Perspective, 2 Reviews, 3 mini-reviews, and 6 research papers) that touch experimental and theoretical aspects of CPL enhancement studies, including small organic molecules, polymers, aggregates, and metal complexes.

In a perspective paper, Kondo et al. summarize the KBr pellet method for CPL measurement, providing a protocol for solid-state CPL measurement and temperature-dependent samples.

Doistau et al. discuss the strategies to obtain strong CPL activity, and compare optical properties of CPL materials based on chiral d-block and f-block metal complexes, demonstrating an empirical protocol for CPL applications with cheap transitional metals.

Gao et al. review the most recent advances in switchable CPL aspects toward external stimuli, giving an overview of CPL switches for various technical applications.

Nagata and Mori present a specific mini-review on simultaneous improvement of luminescence quantum yields and dissymmetry factors, paving a way for obtaining excellent organic CPL materials.

A special focus on cyclophane-based chromophore in CPL materials is reported in the mini-review by Sugiura. Upon synthetic chemical tools, one may manipulate the orientations of fluorophores and obtain strong CPL materials as desired.

In the mini-review by Kumar et al., they discuss several chiral templates such as liquid crystals, biomolecules, molecular self-assemblies and chiral gelators utilized for generating enhanced CPL in organic luminophores.

OPEN ACCESS

Edited and reviewed by:
Doo Soo Chung,
Seoul National University, South Korea

****Correspondence:***
Tao Wu
wu@uochb.cas.cz

Specialty section:
This article was submitted to Physical Chemistry and Chemical Physics, a section of the journal Frontiers in Chemistry

Received: *30 November 2020*
Accepted: *11 January 2021*
Published: *23 February 2021*

Citation:
Wu T, Zheng Y-X, Longhi G and Law G-L (2021) Chiral Organic Chromophoric Systems in the Enhancement of Circularly Polarized Luminescence. Front. Chem. 9:635655. doi: 10.3389/fchem.2021.635655

Theoretical evaluations on electric dipole forbidden and magnetic dipole allowed transitions represent a particularly appealing approach for understanding the origin of CPL, thus aiding the interpretation of CPL enhancement mechanism.

Del Galdo et al. introduce an economic computational way for the simulation of solvatochromic shifts of medium-size flexible chromophores in condensed phases. Yang et al. present an extensive protocol for the interpretation of CPL spectra of medium-to-large molecular systems. Incorporation of vibrational participations provides comprehensive insights on the origin of the measured spectral band-shape.

From an industrial point of view, CPL enhancement plays a key role in the development of chiral materials applied in optoelectronic devices, e.g. circularly polarized organic light-emitting diodes (CP-OLEDs), chiral photovoltaics and transistors.

Dhbaibi et al. report on the synthesis of chiral diketopyrrolopyrrole-helicene polymers showing red CPL, which gives a fascinating example demonstrating the potential of π-conjugated helical polymers for chiral optoelectronic applications.

In another research paper, Reine et al. present an enantiopure bis-perylenediimide cyclohexane derivative with CPL response. The optical properties can be easily tuned by self-assembly or by functionalization of the electron-deficient organic chromophore.

The diversity of coordination environment with chiral ligands makes Pt(II) complexes quite appealing for CPL studies. Yang et al. present a case on manipulation of CPL enhancement in phosphorescent chiral Pt(II) complexes by inclusion of bulky ligands.

Finally, Yan et al. present the design and synthesis of a pair of chiral platinahelicene enantiomers with CPL activity. The evaporated CP-OLEDs based on platinahelicene display deep-red emission as well as distinct CP electroluminescence (CPEL) signals, providing an excellent example to improve the CPL properties of organic chromophore to cope with the future application in CP-OLEDs.

The editorial team would like to thank all authors for their excellent contributions to this exciting topic. The Editors suggest that such a rich palette of articles, manifests the essential features of the chiral chromophores in the enhancement of CPL, and will serve to guide and promote future development in the field.

AUTHOR CONTRIBUTIONS

TW, YXZ, GL, and GLL wrote the manuscript

REFERENCES

Kumar, J., Nakashima, T., and Kawai, T. (2015). Circularly polarized luminescence in chiral molecules and supramolecular assemblies. *J. Phys. Chem. Lett.* 6, 3445–3452. doi:10.1021/acs.jpclett.5b01452

Longhi, G., Castiglioni, E., Koshoubu, J., Mazzeo, G., and Abbate, S. (2016). Circularly polarized luminescence: a review of experimental and theoretical aspects. *Chirality* 28, 696–707. doi:10.1002/chir.22647

Mori, T. (2020). "Frontiers of circularly polarized luminescence Chemistry of isolated small organic molecules," in *Circularly polarized luminescence of isolated small organic molecules*. Editor T. Mori (Singapore: Springer Singapore), 1–10.

Sanchez-Carnerero, E. M., Agarrabeitia, A. R., Moreno, F., Maroto, B. L., Muller, G., Ortiz, M. J., et al. (2015). Circularly polarized luminescence from simple organic molecules. *Chemistry* 21, 13488–13500. doi:10.1002/chem.201501178

Zinna, F., and Di Bari, L. (2015). Lanthanide circularly polarized luminescence: bases and applications. *Chirality* 27, 1–13. doi:10.1002/chir.22382

Conflict of Interest: The authors declare that the research was conducted in the absence of any commercial or financial relationships that could be construed as a potential conflict of interest.

Advantages of publishing in Frontiers

OPEN ACCESS
Articles are free to read for greatest visibility and readership

FAST PUBLICATION
Around 90 days from submission to decision

HIGH QUALITY PEER-REVIEW
Rigorous, collaborative, and constructive peer-review

TRANSPARENT PEER-REVIEW
Editors and reviewers acknowledged by name on published articles

Frontiers
Avenue du Tribunal-Fédéral 34
1005 Lausanne | Switzerland

Visit us: www.frontiersin.org
Contact us: frontiersin.org/about/contact

REPRODUCIBILITY OF RESEARCH
Support open data and methods to enhance research reproducibility

DIGITAL PUBLISHING
Articles designed for optimal readership across devices

FOLLOW US
@frontiersin

IMPACT METRICS
Advanced article metrics track visibility across digital media

EXTENSIVE PROMOTION
Marketing and promotion of impactful research

LOOP RESEARCH NETWORK
Our network increases your article's readership